Transactions of the ASME

PUBLISHING STAFF
Mng. Dir., Publ., J. J. FREY
Director, Technical Publishing, JOS. SANSONE
Managing Editor, CORNELIA MONAHAN
Production Editor, JACK RUMMEL
Editorial Production Asst. BETH DARCHI
Associate Editors
Air Pollution Control R. E. HALL
Diesel and Gas Engine Power W. R. TABER, Jr.
Gas Turbine G. K. SEROVY
Power N. T. NEFF
Advanced Energy Systems J. SNELL
Fuels J. PAPAMARCOS
Nuclear Engineering B. D. ZIELS

BOARD ON COMMUNICATIONS
Chairman and Vice-President M. J. RABINS

Members-at-Large
W. BEGELL
J. CALLAHAN
M. HELMICH
D. KOENIG
M. KUTZ
F. LANDIS
J. W. LOCKE
J. E. ORTLOFF
C. PHILLIPS
K. REID

President, SERGE GRATCH
Deputy Executive Director PAUL F. ALLMENDINGER
Treasurer, ROBERT A. BENNETT

Journal of Engineering for Power (ISSN 0022-0825) is edited and published quarterly at the offices of The American Society of Mechanical Engineers, United Engineering Center, 345 E. 47th St., New York, N.Y. 10017. ASME-TWX No. 710-581-5267, New York. Second Class postage paid at New York, N.Y., and at additional mailing offices.

CHANGES OF ADDRESS must be received at Society headquarters seven weeks before they are to be effective. Please send old label and new address.

PRICES: To members, $36.00, annually; to nonmembers, $72.00. Single copies, $24.00 each. Add $5.00 for postage to countries outside the United States and Canada.

INDEXED by the Engineering Index, Inc.

Journal of Engineering for Power

Published Quarterly by The American Society of Mechanical Engineers

VOLUME 104 • NUMBER 4 • OCTOBER 1982

TECHNICAL PAPERS

(Contents continued on p. 728)

(Contents Continued)

ANNOUNCEMENTS

B. M. Burnside
Department of Mechanical Engineering,
Heriot-Watt University,
Riccarton, Edinburgh EH14 4AS,
United Kingdom

A Simplified Immiscible Liquid Dual Pressure Cycle for Gas Turbine Waste Heat Recovery

Introduction

The open cycle gas turbine/steam turbine combined cycle continues to be one of the world's most efficient fossil fuel to electricity converters. Developments continue to increase gas turbine top temperature and it has been suggested [1, 2] that the introduction of reheat might increase the performance still further. While it is obviously sensible to concentrate development effort at the most rewarding high temperature end of the heat supply range, the possibility of improving the amount and effectiveness of energy recovery from the gas turbine exhaust must not be neglected.

The presently used dual pressure steam cycle is a very effective simple means of bottoming the gas turbine. However, it has been shown [3] that a hybrid dual pressure steam/nonane cycle is capable of significantly greater specific work output per kg of exhaust. There are two reasons for this improvement. The higher molecular weight organic fluid, present in the heat exchangers at the stack end of the heat recovery generator, matches the cooling gas better than steam. Thus more heat can be recovered from the gas. Further, the mixture of steam and nonane vapour expanding in the L.P. turbine exhausts a fraction above its dew point. There is no liquid in the flow, and higher turbine efficiency should be possible if stage loading and compressibility effects are kept at the same level as in the steam turbine of the conventional cycle. Penalties are a larger condenser and more L.P. economiser surface. The hybrid cycle is shown in Fig. 1 and has been described elsewhere [3].

Using steam only at the high temperature end and the very stable nonane, the hybrid cycle is not subject to the usual fluid stability limitations of organic cycles. Steam and water buffer seals can be used to prevent the organic leakage at rotating shafts which is otherwise a major problem in a large plant incorporating organic turbines and pumps. Despite these advantages and its thermodynamic suitability there are a number of control problems inherent in implementation of the cycle:

(*a*) control of low steam fraction in the L.P. boiler
(*b*) design of rising temperature non-eutectic boiler
(*c*) separation of immiscible water and nonane at 158°C

Points (*a*) and (*b*) are related problems. They may be dealt with successfully no doubt by making use of the sensitivity of dew point temperature to steam mass fraction. Separation of the liquids at the cycle conditions proposed dictates some form of mechanical separation to eliminate the large containing vessel which otherwise is required. These factors lead to a more sophisticated and hence more expensive plant.

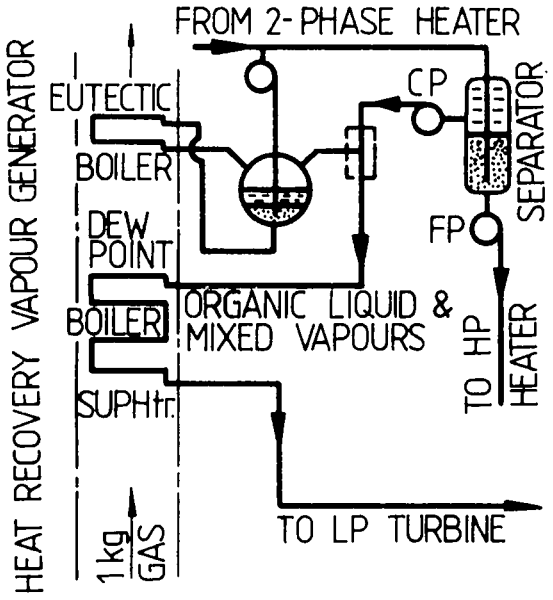

Fig. 1 Hybrid dual pressure cycle B

Earlier work [3] suggested that simpler hybrid steam/organic cycles can be developed with performance aproaching that of the cycle shown in Fig. 1 (cycle B). This paper is concerned with the formulation and analysis of three of these cycles and some of the modifications required to the conventional steam dual pressure cycle if they were to be used in combined cycle plant.

A Simplified Hybrid Cycle

The first of these cycles (cycle C) is shown in Fig. 2. Unlike cycle B, water and nonane, following separation immediately after condensation, are separately preheated, evaporated, and superheated. As before, only steam flows through the high temperature end of the vapour generator and H.P. turbine. The L.P. circuit fluid is entirely nonane which mixes with the exhaust from the H.P. turbine before expanding in the L.P. turbine down to the condenser pressure. H.P. and L.P.

Contributed by the Gas Turbine Division of THE AMERICAN SOCIETY OF MECHANICAL ENGINEERS and presented at the 27th International Gas Turbine Conference and Exhibit, London, England, April 18 22, 1982. Manuscript received at ASME Headquarters November 4, 1981. Paper No. 82-GT-1.

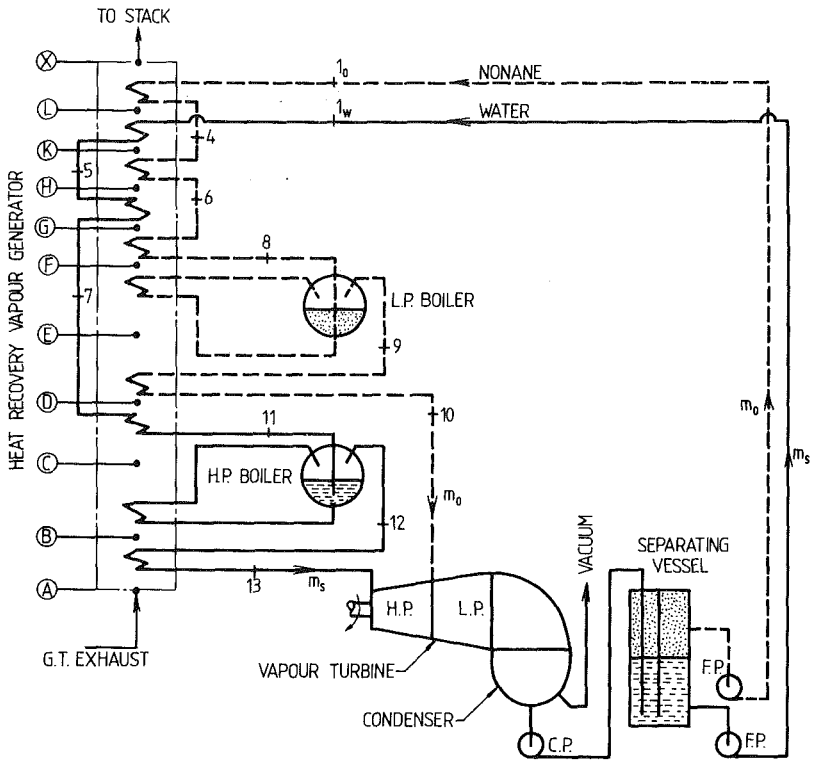

Fig. 2 Plant diagram cycle C

preheaters are positioned alternately in the gas stream. In all there are three stages, each of water and nonane preheat. Proportions of steam and nonane entering the L.P. turbine are such that an entirely dry expansion, exhausting just before the dew point, results.

Figure 3 shows the matching diagram for cycle C. There is a pinch-point at outlet from each stage of preheat. Single component evaporation only occurs and separation takes place only at the condensate temperature where the solubility of nonane in water is at its lowest (1 part in 10^5 by mass). A further simplification is the requirement for two feed pumps only.

Cycle Analysis. The following simplifying assumptions were made in the cycle analysis:

(*a*) flow conditions other than in heat exchangers are adiabatic

(*b*) circulating pump (but not feed pump) power, and pressure losses ignored

(*c*) steam/nonane vapour mixtures assumed to be ideal mixtures of real gases

(*d*) liquids approach evaporators saturated

(*e*) Pump efficiencies and turbine efficiencies before wetness corrections are applied are the same for steam and steam/nonane cycles.

The last assumption implies that the steam/nonane turbine is of conventional design with the same level of stage loading and compressibility effects as the steam turbine. Since the expansion in the mixed vapour turbine is entirely dry, wetness corrections amounting to 1 percent reduction in stage efficiency per 1 percent average wetness in the stage need be applied to the steam turbine only. All of the assumptions are identical with those made before [3] in analysing the conventional steam/steam dual pressure cycle and cycle B, Fig. 1. The results obtained here are therefore directly comparable with these cycles.

The following are the key equations for determination of the cycle state points. Steam and organic mass flows are given by

$$m_s = (h_A - h_0)/h_{13} - h_{11}) \tag{1}$$

and

$$m_0 = ((h_A - h_X) - m_s(h_{13} - h_{1w}))/(h_9 - h_{1_0}) \tag{2}$$

Nomenclature

a = specific available energy, kJ/kg
c_p = specific heat at constant pressure, kJ/kgK
ϵ_m = mean heat exchanger effectiveness
h = specific enthalpy, kJ/kg
H.P. = high pressure
L.M.T.D. = log. mean temperature difference, K
L.P. = low pressure
m_0 = organic: air flow ratio
m_s = steam: air flow ratio
P_H = high pressure, bar
P_L = intermediate pressure, bar
s = specific entropy, kJ/kgK
t = temperature, Celsius
T = temperature, K
W = specific work output kJ/kg gas.
x = mass fraction steam
Δt = pinch point tempt. difference, K
ϵ = 2nd Law effectiveness
ϵ_R = efficiency ratio
η = isentropic efficiency
Σ = summation

Subscripts

1-13 = cycle state points
A-X = gas status
cond = condenser
d = datum state
L.P.in = L.P. turbine inlet
0 = organic, dead state
turb = turbine
w = water

Table 1 Fixed conditions

Gas inlet temp. t_A °C	513.0
enthalpy h_A	506.0
datum temp. t_d °C	30.0
Superheat temp. t_{13} °C	475.0
Condenser temp. t °C	30.0
All pinch point Δts K	30.0
Efficiencies, pump η_s	0.70
turbines H.P. η_s	0.82
L.P. η_s	0.86

Table 2 Cycle details

Cycle	A	B	C	D	E
w	129.9	137.0	132.5	133.3	134.1
p_H	50.0	80.0	100.0	100.0	100.0
p_L	3.5	7.5	5.0	5.0	5.0
m_0	–	0.145	0.172	0.178	0.184
t_X	110.0	90.0	104.0	100.0	96.0
x_{LPturb}	–	0.436	0.355	0.348	0.341
t_{cond}	30.0	30.0	30.0	30.0	30.0
t_2	–	–	–	–	89.0
t_3	–	–	–	91.0	126.0
t_4	–	–	105.0	134.0	156.0
t_5	–	–	147.0	163.0	176.0
t_6	–	–	181.0	189.0	196.0
t_7	–	–	203.0	206.0	209.0
t_8	139.0	158.0	223.0	223.0	223.0
t_{10}	208.0	231.0	223.0	223.0	223.0
t_{LPin}	191.0	216.0	193.0	193.0	194.0

respectively. The vapour generator L.P. outlet enthalpy is

$$h_{10} = h_{1_0} + (h_A - h_X)/m_0 - (h_{13} - h_{1w})(m_S/m_0) \quad (3)$$

and the enthalpy and temperature at inlet to the final water preheater

$$h_7 = h_{11} - (c_p/m_S)(t_{11} - t_8 + \Delta 1 - \Delta 2) - (m_0/m_S)h_8 \quad (4)$$

and

$$t_7 = t_w(h_7) \quad (5)$$

The enthalpy h_6 is dependent on h_5

$$h_6 = h_6(\Delta 1 + \Delta 4 - \Delta 2 - \Delta 5 + t_{11} - t_8 - (m_s/c_p)(h_{11} - h_5) - (\mathrm{m_0}/c_p)(\mathrm{h_{10}} - \mathrm{h_8}) + \mathrm{t_7}) \quad (6)$$

and the temperature

$$t_6 = t_0(h_6) \quad (7)$$

Also

$$h_F - c_p(t_7 + \Delta 4 - t_d) = m_0(h_8 - h_6) \quad (8)$$

The organic flow, m_0, given by (2) is the maximum possible and corresponds to no organic superheat. Under equilibrium conditions, after mixing with the steam exhaust from the H.P. turbine, the condition of the steam nonane mixture at L.P. turbine entry will be well superheated even although the organic stream is saturated nonane vapor. Any carryover of liquid nonane should therefore evaporate. If necessary, the organic stream can be superheated with only a very small reduction in performance.

Given cycle pressures, H.P. superheat, and pinch point temperature differences, a stack temperature t_x is selected. m_0 and m_s are calculated using equations (1) and (2) and h_7 from (4) and (5). Equation (6) can then be written in the form

$$h_6 = h_6(h_5)$$

allowing the calculation of h_5 from equation (8). All the gas and fluid enthalpies and temperatures upstream of the second organic heater are then calculable. Selecting the required value for $\Delta 6$, $\Delta 7$ is determined. If the value of $\Delta 7$ is not satisfactory, all calculations are repeated at different values of stack temperature until it is. In all the cycles described in this paper, the L.P. turbine exhaust condition was just above the dew point. Thus no desuperheater is required before condensation.

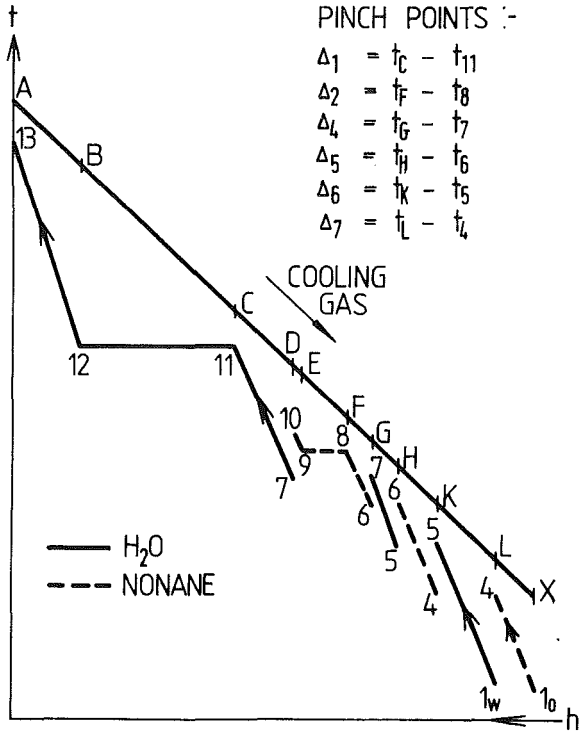

Fig. 3 Matching diagram cycle c

Calculated Performance. Calculations were carried out over a range of cycle conditions. The results presented here are based on the fixed values in Table 1 which were used [3] in comparing the conventional steam/steam cycle and cycle B. A range of pressures p_H and p_L were tried. In general, the highest value gave the maximum cycle specific work, but to avoid wet conditions in the H.P. turbine p_H was set at 100 bar. There is also an upper limit for p_L for which a solution of equations (4) and (5) is possible with p_H = 100 bar. p_L was set at 5 bar.

The principal cycle conditions determined are shown in Table 2. A maximum specific work output of 132.5 kJ/kg gas was obtained for the cycle, which is just 2 percent improvement on the conventional dual pressure steam cycle. The stack temperature is 104°C.

Raising Specific Work Output

Specific work output of cycle C is lower than that of cycle B. As explained above, there is a limit to organic flow rate through the heaters consistent with a predetermined minimum pinch point temperature difference $\Delta 7$ in the first organic heater, Fig. 3. By adding another water heater at the stack end, a higher organic flow is possible for the same pinch point temperature difference at lower stack temperature. This cycle D is shown in Fig. 4, and its matching diagram in Fig. 5.

Calculations were carried out as described above for cycle conditions and gas temperatures upstream of the second water heater. Conditions in the first three heaters were determined by trial and error. A guess was made of the proportion of the heat transfer occurring in each heater at a selected stack temperature t_X and the pinch point temperature differences $\Delta 7$ and $\Delta 8$ calculated. These proportions were altered until $\Delta 7 = \Delta 8$. If necessary, stack temperature T_X was altered and the whole calculation repeated until the predetermined values of $\Delta 7$ and $\Delta 8$ were obtained.

Principal cycle conditions are shown in Table 2. The main effect is an increase in organic mass flow, a reduced stack temperature of 100°C, and an increased specific work of 133.3 kJ/kg gas, a 2.6 percent improvement on the con-

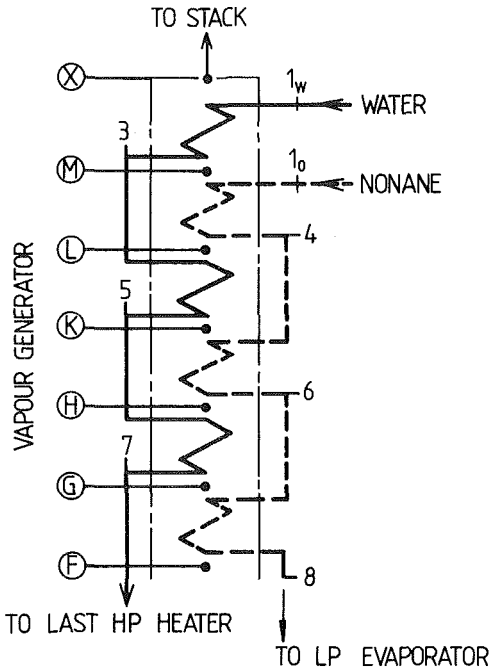

Fig. 4 Low temperature section cycle D

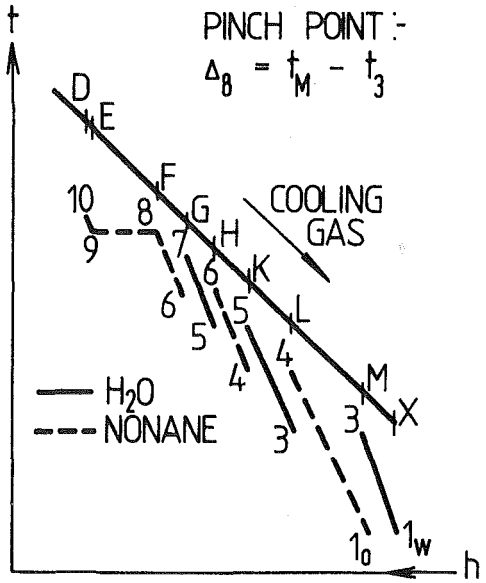

Fig. 5 Matching diagram cycle D

ventional all steam cycle A. Specific work output is still lower than in cycle B.

The effect of adding a further organic heater at the stack end was investigated. This cycle E is shown in Fig. 6 and the matching diagram in Fig. 7. Calculations were carried out in the same way as for cycle D. The same pressure levels p_H = 100 bar, p_L = 5.0 bar proved to optimize cycle work. Table 2 shows the cycle details. A further rise in specific work to 134.1 kJ/kg gas resulted, again due to better matching. The stack temperature is down to 96°C. Cycle E shows an improvement in work output of 3.2 percent on cycle A but is still inferior in this respect to cycle B.

Discussion

Although none of the three new cycles proposed attains the output of cycle B, a trend of increasing output with increased intermingling of water and organic heaters is evident. The

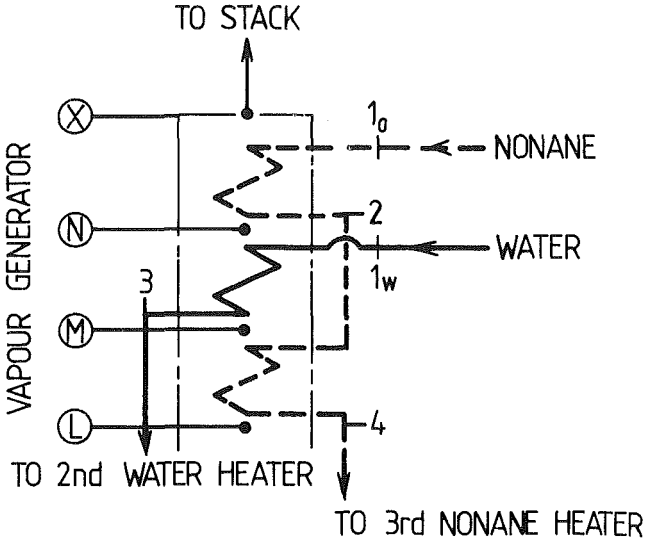

Fig. 6 Low temperature end cycle E

more heaters there are, the greater the permissible organic flow and the more heat is extracted from the gas. Thus 4.2 kJ more heat is extracted per kg of gas in cycle E compared to cycle D. The specific work output has increased by 0.8 kJ so that the conversion efficiency is apprently 19 percent compared with the Carnot value of 18 percent. In fact, an average reduction in heat exchange per heater of 12 percent caused by the addition of the extra heater in cycle E results in lower fluid temperature rises in the heaters. This leads to lower average temperature differences between gas and fluid streams for given pinch point temperature differences and hence less irreversibility in the first six or seven heaters.

Available Energy Losses in Low Temperature Water Heaters. The above argument can be made more precise by 2nd Law analysis of the heat exchange in the heat recovery vapour generator. The maximum efficiency of conversion of heat in the gas to work is given by

$$\eta_{max} = 1 - (T_{cond}/(T_A - T_{cond}))1n(T_A/T_{cond})$$

With the conditions of Table 1 η_{max} = 40.2 percent or a maximum specific work output of 203 kJ/kg gas. Table 4 shows the proportion of this available energy which is actually converted to work in the five cycles referred to here. The total loss in available energy therefore amounts to 50–60 percent of the cycle output under the conditions of Table 1. Most of this loss occurs in the vapour generator due to irreversibilities in the heat exchangers and loss to the stack. The results of an analysis of these losses is presented in Table 4. The figures are based on a dead state temperature T_0 of 15°C. Stack loss is expressed as a percentage of the available energy in the gas entering the vapour generator.

The effectiveness, ϵ, is defined (4) as

$$\epsilon = \frac{\text{available energy gain of heated fluid}}{\text{available energy loss of heating gas}}$$

where the specific available energy, a, is defined by

$$a = h - T_0 s - (h_0 - T_0 s_0)$$

Pressure losses were neglected in the calculations and the effectiveness referred to in Table 4 is the average value for all the heat exchangers in the vapour generator defined as

$$e_M = -\Sigma(\Delta\text{A.E. of the fluid})/\Sigma(\Delta\text{A.E. of gas})$$

the summations extending over all the heat exchangers.

Referring to Table 4, it is evident that the progressive improvement in cycle output of cycles C, D, and E is due not only to a decrease in stack loss but also to a decrease in the

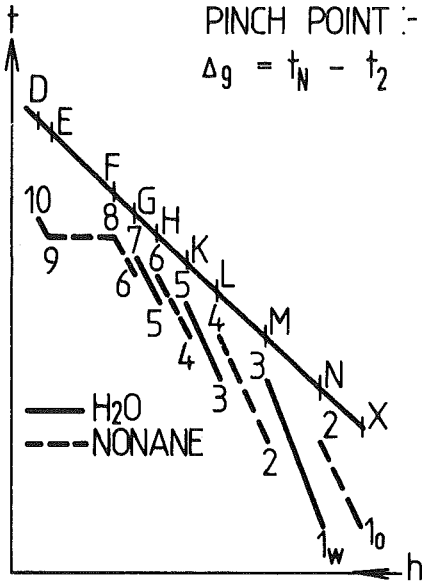

Fig. 7 Matching diagram cycle E

average irreversibility of the heat exchange in the vapor generator. Between cycles A and the others, part of the reduction in performance is due to wetness losses in the steam turbine.

The best of the new cycles, E, produces 2.9 kJ/kg gas less output than the more elaborate cycle B, although a maximum of only 1.1 kJ/kg gas of energy is made available by the reduced stack temperature and the effectiveness of the overall heat exchange is lower. Because the mass fraction of water entering the condenser in cycles C, D, and E is below the eutectic value, part of the condensation occurs at temperatures above the eutectic temperature, 30°C, which is the minimum cycle temperature. Thus there is an extra loss in available energy in these cycles which does not occur in cycle B, where the vapour entering the condenser has the eutectic composition.

Possibility of Further Improvement in Performance. Calculations indicate that cycle work can be increased by further addition of heaters at the stack end and increase of cycle pressure levels. The rise in pressure results in a higher optimum steam fraction in the L.P. turbine flow which reduces the condenser irreversibilities as described above. However, for the same stack temperature, more heaters are required when the cycle pressures are higher. Further performance improvements are possible, perhaps up to the cycle B level, by increasing cycle pressures and the number of heaters.

Another possibility is the use of an octane/nonane mixture to alter the eutectic composition itself. Examination [5] of the alkane series for suitable working fluids reveals that the octane/steam and nonane/steam systems have eutectic steam mass fractions of about 21 and 43 percent, respectively. These mass fractions usually straddle the optimum mixture for most applications, leading to reduction of cycle efficiency and undesirable condensation of organic rich mixtures if the best compromise-nonane/steam mixtures is adopted. Cycle B is unique among the dual pressure cycles studied so far in having the optimum match between heated fluid and cooling gas at the eutectic composition.

Design Problems. To the extent that mixture boiling and separation at elevated temperatures have been eliminated in substituting the new cycles for cycle B, the control and design problems of the plant have been considerably simplified. The fluids are mixed only in the L.P. turbine and condenser. However a new problem, multiple pinch points, is created. It may be thought that the problem is no worse than in the vapour generator of an organic cycle using a fluid at supercritical pressure. In the latter application the working fluid and cooling gas are within a pinch point temperature difference over a large temperature range. In the present case this situation corresponds to cycle E with a infinite number of alternate nonane and water heaters. However, in the supercritical cycle the fluid flowrate can be altered if the design heat-transfer areas are initially incorrect or if, subsequently, due to fouling or corrosion, heat-transfer rates decrease. In cycle E, there are two separate heater flows so design matching is more critical. A possible solution is the provision, at critical positions, of heating tubes which may or may not be bypassed.

Much more of the heat-transfer load is L.P. preheating in cycle E, than in the conventional cycle A. Table 5 shows the distribution of heat-transfer modes for cycle A, B, and E. Total preheat amounts to about half the total cycle heat supply compared with 38 percent in the high performance cycle B and 28 percent in the conventional steam dual pressure cycle A. Thus, there is a substantial shift from boiling to liquid preheating in cycle E. This is an inevitable consequence of extracting more heat from the gas and increasing the effectiveness of the heat exchangers in transferring available energy from gas to cycle working fluid. Basically, adding sensible heat to a liquid matches gas cooling much better than boiling. Table 6 shows the heat transfer weighted log mean temperature difference of the preheating sections of the cycles. The L.M.T.D. of cycle E is about 13 percent lower than that of the conventional cycle and 5 percent lower than cycle B.

Condenser and L.P. Turbine. Condensing the steam/nonane mixture of cycle E requires about 75 percent greater condensing surface than in the all steam cycle A. The reasons for this have been described before [3]. The cycle E L.P. turbine has about half the enthalpy drop of the cycle A steam turbine. The sonic velocity in the nonane/steam turbine is 70 percent and the required enthalpy drop 53 percent of that in the steam turbine of cycle A. Thus about the same number of stages is required at 70 percent of the steam turbine blade speeds.

Table 3 Cycle efficiency ratios

Cycle	A	B	C	D	E
ϵ_R percent	63.7	67.4	65.2	65.6	66.0

Table 4 Analysis of vapour generator losses

Cycle	A	B	C	D	E
Stack loss percent	6.2	4.0	5.5	5.0	4.6
Mean heat exchanger effectiveness, e_M percent	83.9	83.5	84.8	85.1	85.4

Table 5 Distribution of heat transfer, percent

Cycle	A	B	E
L.P. preheat	14.6	23.0	37.7
L.P. boiling	16.2	16.7	9.9
L.P. supht.	1.1	0.7	0.0
H.P. preheat	13.8	14.8	11.2
H.P. boiling	40.1	32.1	28.6
H.P. supht.	14.2	12.7	12.6

Table 6 Heat transfer mean L.M.T.D., K

Cycle	A	B	E
L.M.T.D.	54.3	49.5	47.2

Conclusion

The hybrid steam/steam-nonane dual pressure cycle (cycle B) has previously been shown capable of extracting

significantly more of the available energy in gas turbine exhausts than the conventional steam cycle (cycle A). Some awkward control and liquid separation problems are features of this cycle. This paper proposes a simpler steam/nonane cycle in which the steam and nonane flows are kept separate in the heat recovery vapour generator so that liquid separation at condensate temperatures only is necessary. The specific work output of this cycle is shown to be capable of development to cycle B levels.

In the new cycle much more of the heat uptake from the gas occurs in the liquid heaters and there are multiple pinch points. Compared to the conventional cycle, a much larger condensing surface is required, but the L.P. turbine requires about the same number of stages if it is of conventional design. Like cycle B, the turbine expansion is entirely dry and all shafts can have steam or water buffer seals, eliminating the possibility of fluid leakage usually associated with organic working fluids in power cycles.

References

1 Rice, I. G., "The Combined Reheat Gas Turbine/Steam Turbine Cycle," ASME JOURNAL OF ENGINEERING FOR POWER, Vol. 102, Jan. 1980, pp. 35–49.

2 Mori, K., Kitajima, J., and Kimura, T., "Preliminary Study on Reheat Combustor for Advanced Gas Turbine," ASME Paper No. 81-GT-29, Gas Turbine Conference, Houston, Mar. 1981.

3 Burnside, B. M., "Dual Pressure Steam/Immiscible Liquid Cycles for Gas Turbine Exhaust Heat Recovery," ASME Paper No. 81-GT-55, Gas Turbine Conference, Houston, Mar. 1981.

4 Reistad, G. M., "Available Energy Conversion and Utilization in the United States," ASME Paper No. 74-WA/Pwr-1, Winter Annual Meeting, New York, 1974.

5 Burnside, B. M., "Immiscible Liquid Cycle in Large Scale Medium Temperature Waste Heat Recovery," *Third Conference on Waste Heat Management and Utilization*, Miami Beach, May 1981.

R. P. Dring
Manager, Gas Turbine Technology.

H. D. Joslyn
Research Engineer.

L. W. Hardin
Research Engineer.

J. H. Wagner
Associate Research Engineer.

United Technologies Research Center,
East Hartford, Conn. 06108

Turbine Rotor-Stator Interaction

The aerodynamic interaction between the rotor and stator airfoils of a large scale axial turbine stage have been studied experimentally. The data included measurements of the time averaged and instantaneous surface pressures and surface thin film gage output on both the rotor and stator at midspan. The data also included measurement of the stator suction and pressure surface time averaged heat transfer at midspan. The data was acquired with rotor-stator axial gaps of 15 and 65 percent of axial chord. The upstream potential flow influence of the rotor on the stator was seen as well as the downstream potential flow and wake influences of the stator on the rotor. It was also seen that at the 15 percent axial gap, the stator heat-transfer coefficient was typically 25 percent higher than that at the 65 percent gap.

Introduction

Turbine airfoil design is presently at the point where accurate design analyses are available for the compressible potential (inviscid) flow through cascades and for the boundary layer flows on airfoil surfaces. The designer can, through subtle changes in the airfoil contour, carefully optimize both the inviscid and viscous character of the flow. This optimization includes not only the aerodynamic performance but also the cooling design. The vast majority of these analyses, however, are based on the assumption that the rotor and stator rows are spaced far enough apart such that the flow in each is steady, i.e., that there is no unsteadiness of any sort due to rotor-stator aerodynamic interaction. It is clear, however, that when rows are closely spaced there can be a strong interaction which will impact the aerodynamic, thermal, and structural performance of the airfoils. Furthermore, the rows of current turbines (and compressors) are already very closely spaced. Axial gaps between adjacent rows of approximately 1/4 to 1/2 of the airfoil chord are common practice. Thus, the problem of rotor-stator interaction is having an impact on existing turbine designs. Future designs with higher loading and lower aspect ratios, i.e., fewer and bigger airfoils, and the ever present desire to minimize engine length, will aggravate this condition even further. The reason for this probelm is due to the fact that currently there are few practical analytical tools or detailed experimental results that can provide guidance to the designer as to the magnitude or impact of this unsteadiness.

The phenomenology of rotor-stator aerodynamic interaction may be divided into two separate areas. These are first, potential flow (inviscid) interaction and, second, wake (viscous) interaction. The gradients due to the potential flow over an airfoil extend both upstream and downstream of the airfoil and typically these gradients decay with a length scale equal to the pitch (or chord) of the cascade. The potential flow over a row of airfoils can cause unsteadiness in both the upstream and downstream rows if the axial gap between them is less than approximately the airfoil chord. The wake, on the other hand, is convected downstream. The far field rate of decay of the wake, however, is much more gradual than that of the potential flow. It may still be felt several chords downstream. Thus, wake interaction will be present even when adjacent rows are spaced far apart. Under most circumstances, both mechanisms are occurring simultaneously.

One of the earliest studies of the interaction problem was conducted by Kemp and Sears ([1] and [2]). After applying a number of "classical" simplifying assumptions, that is, a linearized potential flow solution for thin airfoils with small turning, they came to the conclusion that for realistically close axial spacing of two rows of airfoils the unsteady lift amplitude could be as much as 18 percent of the steady value. Furthermore, the unsteadiness of the flow over the upstream row was much larger than that of the downstream row. They also found that "the unsteady forces arising from passage (of an airfoil) through viscous wakes are of about the same size" as those due to the potential flow interaction. Giesing ([3] and [4]) carried out an "exact" solution of unsteady potential flow, and in particular, for the case of the interaction of two moving lifting bodies. Although there were no quantitative results of direct value to the present problem, the qualitative results were impressive as to the complexity of the problem and of the flows that were produced.

In a series of combined analytical and experimental studies, Parker et al. (references [5–8]) provided a number of significant insights into the nature of rotor-stator interaction. They carried out a solution for the quasi-steady potential flow interaction of two rows of airfoils accounting for their relative motion. They concluded that the principle mechanism of potential flow interaction was the prevention of the accelerations normal to the surface of the closely coupled

Contributed by the Gas Turbine Division of THE AMERICAN SOCIETY OF MECHANICAL ENGINEERS and presented at the 27th International Gas Turbine Conference and Exhibit, London, England, April 18–22, 1982. Manuscript received at ASME Headquarters November 9, 1981. Paper No. 82-GT-3.

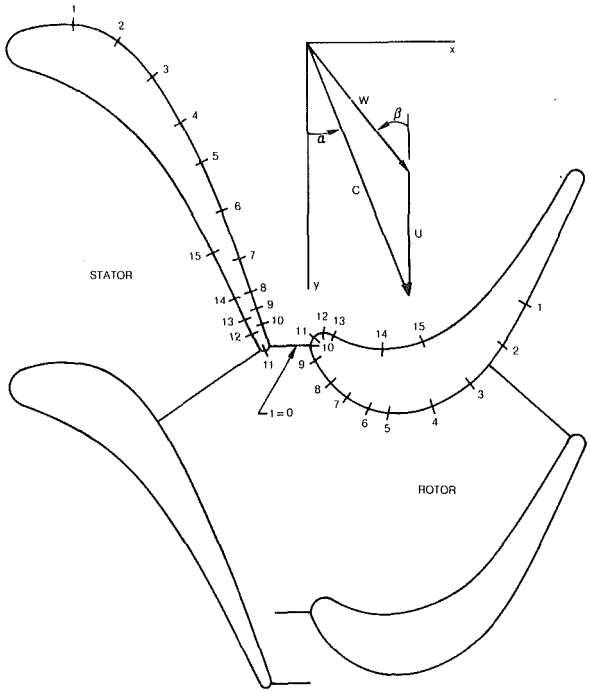

Fig. 1 Turbine stage at 15 percent gap (Kulite sites)

airfoils which would have occurred at those locations if the rows were not closely spaced. In addition, the unsteady pressure differences they computed on the surface of one of the airfoils of two interacting rows was roughly three times the computed pressure fluctuation amplitude at the same point without interaction, i.e., with only the moving row present. From these results, Parker raised the question of cyclic separation resulting from periodic locally strong negative pressure gradients. This would have strong implications for both the aerodynamic and thermal (heat tranfer) performance of an airfoil. Although these solutions did not account for unsteady shed vorticity, they did show better agreement with measured data trends with the assumption of constant airfoil circulation than for the assumption of a fixed Kutta point.

This question of an appropriate Kutta condition for unsteady flow at intermediate values of the frequency parameter (k) was the subject of papers by Gostelow [9] and by Satyanarayana and Davis [10]. For steady flow and in fact even in unsteady flow at low values of the frequency parameter ($k < 0.6$) the classical Kutta condition, i.e., no trailing edge loading, appeared to be reasonably accurate. However, "for problems involving rotor-stator interaction, usually at frequency parameters higher by an order of magnitude or more, the probability of instantaneous trailing edge loading is strong" [9]. Such trailing edge loading was subsequently demonstrated experimentally [10]. The importance of this question and its centrality to any analytical attack on the rotor-stator interaction problem was evident from the discussion following the presentation of the papers at the AGARD conference on usteady phenomena in turbomachinery [11].

Adachi and Murakami [12] studied the passage of a wake from a moving circular cylinder as it was convected through a row of compressor stator airfoils. The instantaneous stator pressure distribution was also measured and its fluctuations were related to the instantaneous wake disturbance in the blade channel. Gallus et al. [13] examined rotor-stator interaction in a compressor stage having an axial gap of 60 percent of the rotor axial chord. Unsteady pressures were measured at midspan at seven locations on the rotor and at ten locations on the stator. The unsteady lift coefficient calculated from this data for the stator was sensitive to flow coefficient but typically had an amplitude of ± 0.04. The rotor data indicated only very weak potential flow interaction with the stator at this large axial spacing. Scholz [14] reported data taken by Ohashi and by Speidel which indicated how the total pressure loss of a row of airfoils could vary as a function of the location and motion of an upstream blade row. He described how a suitably defined Strouhal number could characterize this rotor-stator wake interaction effect. The physics here were much the same as those described by Evans [15] when he showed that the boundary layer profile on a downstream airfoil could oscillate between characteristically laminar and turbulent conditions periodically with the passing of the wake of a moving upstream blade row.

Although investigators have been examining the problem for many years, the main result is that more questions and concerns have been raised. There is still precious little in the way of analytical tools or experimental results to guide the designer. The only exception to this is that there is a great deal of overall performance data for turbines and compressors from a wide variety of sources (references [16–22]). The conclusion from reviewing all of these results is: (*a*) that there is an optimum axial gap between rotors and stators, (*b*) that the value of this optimum spacing is hard to generalize, and

Nomenclature

B = airfoil chord
B_x = airfoil axial chord
C = absolute flow speed
C_p = specific heat
C_p = pressure coefficient, $(P_{T1} - P)/Q_2$
$\bar{C}_p$ = steady state pressure coefficient: $(P_{T1} - \bar{P})/Q_2$
$\tilde{C}_p$ = amplitude pressure coefficient: $(P_{max} - P_{min})/Q_2$
C_p' = fluctuation pressure coefficient: $(P(t) - \bar{P})/Q_2$
$C_{p,U}$ = pressure coefficient: $(P_{T0} - P)/1/2\rho U_m^2$
h = stream tube height
H = heat-transfer coefficient
k = reduced frequency, $N\Omega B/2C$)
N = number of airfoils in a row
P = static pressure
P_T = total pressure
Q = dynamic pressure
r = radius
S = surface arc length
St = Stanton number: $(H\rho C_p/C_1)$
t = normalized time: $(T - T_0)$/airfoil passing period
T = time
T_0 = reference time
U = wheel speed
W = relative flow speed
x = axial distance
y = tangential distance
Y = total pressure loss, $(\Delta P_T/Q)$
α = absolute flow angle
β = relative flow angle
δ_w = stator wake half width at mid-depth
δ^* = displacement thickness
ρ = density
τ = airfoil pitch
Ω = rotor angular rotation (radians per second)
θ = tangential angle
Θ = momentum thickness

Subscripts

0 = stator inlet
1 = stator exit and rotor inlet (general inlet)
2 = rotor exit (general exit)
x = axial
r = radial
θ = tangential
m = midspan
R = rotor
S = stator
p = pressure surface
s = suction surface

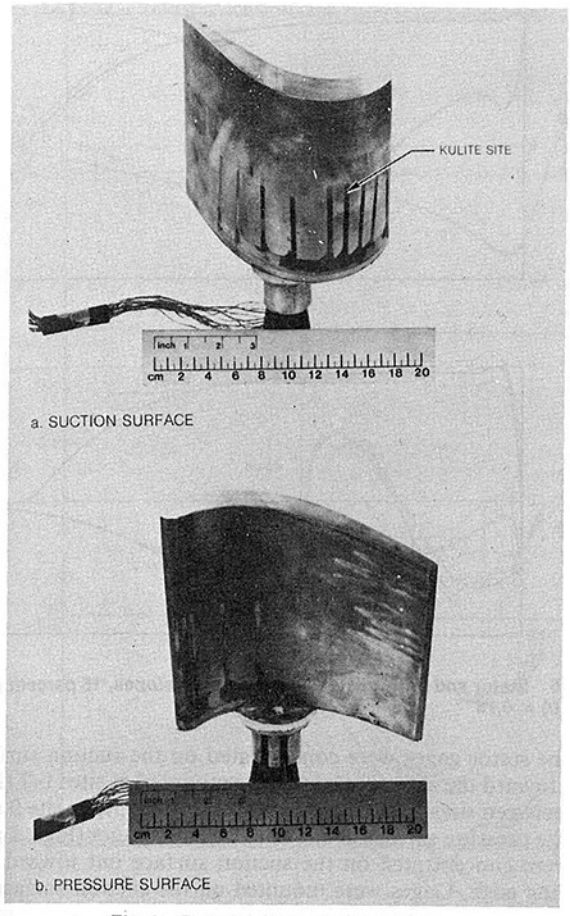

Fig. 2 Rotor Kulite instrumentation

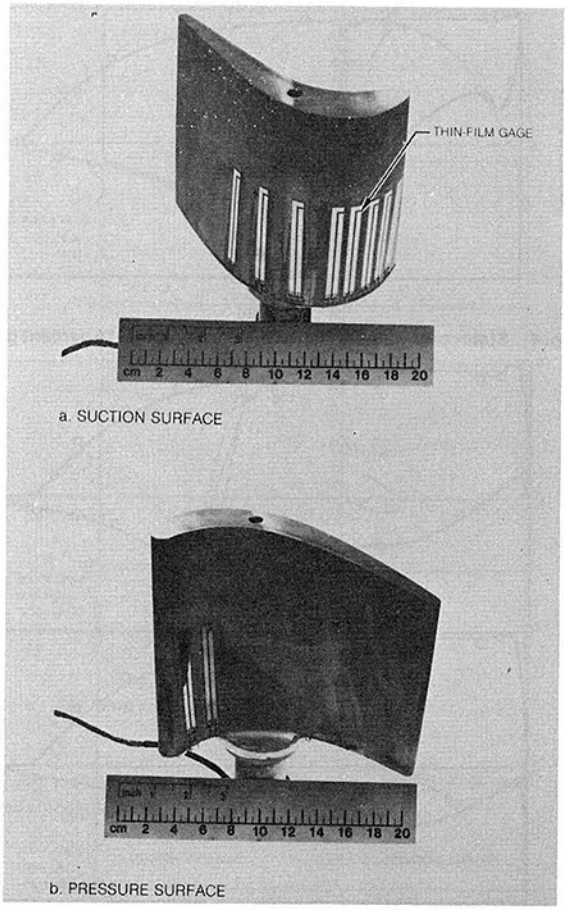

Fig. 3 Rotor thin film gage instrumentation

(*c*) that for changes in axial spacing over the ranges commonly found in current engines the change in overall turbine or compressor efficiently can be as much as 2 percent.

Experimental Facility

The United Technologies Research Center (UTRC) Large Scale Rotating Rig No. I (LSRR-I) is 5 ft (1.52 m) in dia and it can accept a wide variety of turbine and compressor models ranging in hub/tip ratio from 0.5 to 0.8. The turbine model (0.8 hub/tip ratio) has three rows of airfoils; first vane, first blade and second vane. For the present program only the first vane (stator) and the first blade (rotor) were installed (Fig. 1). Both airfoils had aspect ratios (span/axial chord) of approximately unity. The airfoil chords are approximately 5 times engine scale. The large scale of the rig is a distinct advantage because it permits the use of extensive instrumentation on both the stationary and rotating airfoils. The large scale also has the advantage of giving Reynolds numbers which are typical of high pressure turbines at nominal model running conditions of 410 rpm and a test section average axial flow velocity of 75 ft/s (23 m/s). The various absolute and relative flow angles and the airfoils that produce them (Fig. 1) are also typical of current high pressure turbine stages. Airfoil geometry and nominal operating conditions are summarized in Table I. Unless otherwise stated, all conditions and dimensions quoted are at midspan (r_m = 27 in.). The major departure from actual engine aerodynamic parameters is that the flow is virtually incompressible. The airfoil exit Mach numbers are approximately 0.2. Thus, the facility is limited to the study of phenomena which are insensitive to compressibility effects.

For all values of (C_x/U) at which data was obtained the axial flow velocity was held constant at a nominal value of 75 ft/s. Variation of (C_x/U) was achieved by varying the rotor speed. The motivation for this approach was to hold the airfoil Reynolds numbers (based on exit velocity) constant at all test conditions.

A complete description of the computerized steady-state data acquisition and control system and the steady-state transducer calibration procedure were presented by Dring and Joslyn [23]. The specialized instrumentation used in the present program are described in context below and in detail in reference [24].

Steady-State and High Response Aerodynamic Instrumentation

The program consisted of acquiring and analyzing high response pressure and thin film gage data at midspan on the rotor and stator airfoils at three flow conditions corresponding to the rotor design incidence ($C_x/U = 0.78$, $\beta_1 = 40$ deg) and at ± 5 deg of rotor incidence ($C_x/U = 0.96$, $\beta_1 = 35$ deg and $C_x/U = 0.68$, $\beta_1 = 45$ deg). Data were required at two rotor-stator axial spacings. The closest spacing was 15 percent of the nominal (average) axial chord, as in Fig. 1, and the largest spacing was 65 percent of the nominal axial chord.

Both the rotor and the stator had 22 pressure taps around their perimeters at midspan which were used to establish the steady state, or time averaged, pressure distributions. These rotor and stator pressure taps were each connected to 48 channel Scanivalves (Scanivalve, model 48J9-1290) mounted in the rotating and stationary frames of reference, respectively. Transducer calibration procedures for these Scanivalves were discussed in reference [23].

Both the rotor and the stator had 15 miniature high response pressure transducers (Kulite, model XCS-093 ± 2D) distributed around each airfoil at midspan (Figs. 1 and 2). The transducers were inserted into chambers which were connected to the airfoil surface by a 0.020 in. dia hole. The

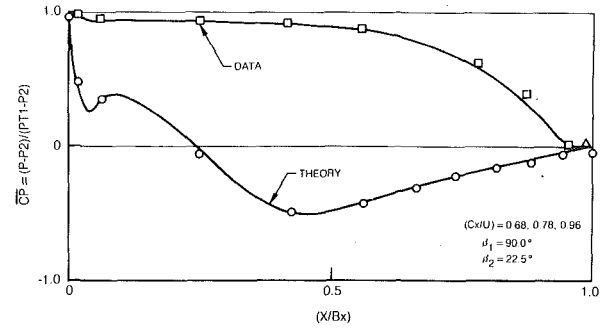

Fig. 4 Stator pressure distribution—time average, 15 percent gap

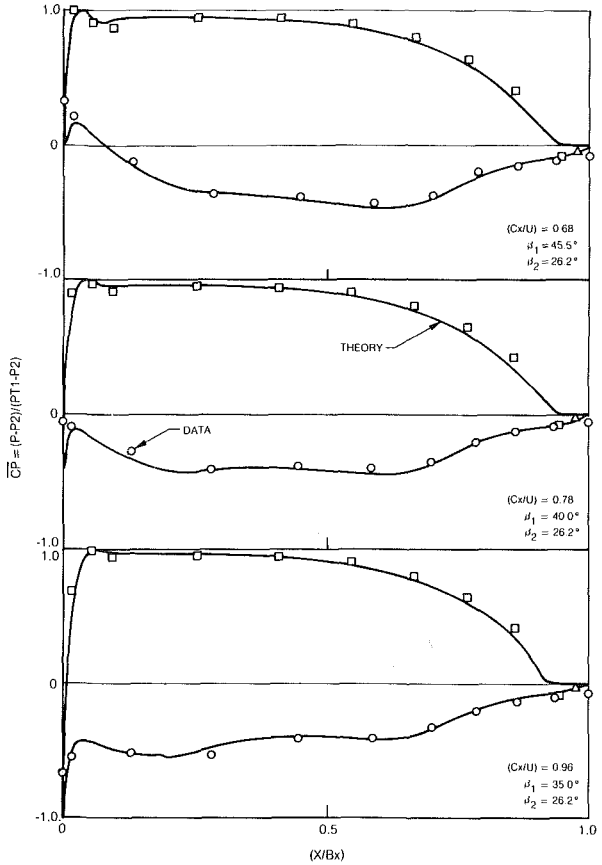

Fig. 5 Rotor pressure distribution—time average, 15 percent gap

geometry of the installation was such that a frequency response of approximately 10 kHz was realized. This response was 50 times blade passing frequency and hence it was judged to be adequate for the present application. The stator transducers were concentrated on the suction surface, toward the trailing edge, in the uncovered portion of the airfoil surface, i.e. downstream of the throat. The rotor transducers were concentrated on the suction surface, toward the leading edge. The transducers were located in these regions since the interaction was expected to be strongest here due to close proximity to the stator and the rotor.

Both the rotor and the stator had 10 thin film gages distributed around each airfoil at midspan (Fig. 3). These gages were custom manufactured for this application by DISA. The custom gage configuration was similar to the DISA model 55R47 but it allowed all lead connections to be confined to a region near the tip of the stator and to a region near the root of the rotor where they would create no significant disturbances in the airfoil boundary layers. The gages themselves were bonded into depressions which had been chemically etched into the airfoil surfaces to a depth of 0.003 in. The result was a smooth airfoil surface which would not artificially trip the boundary layer.

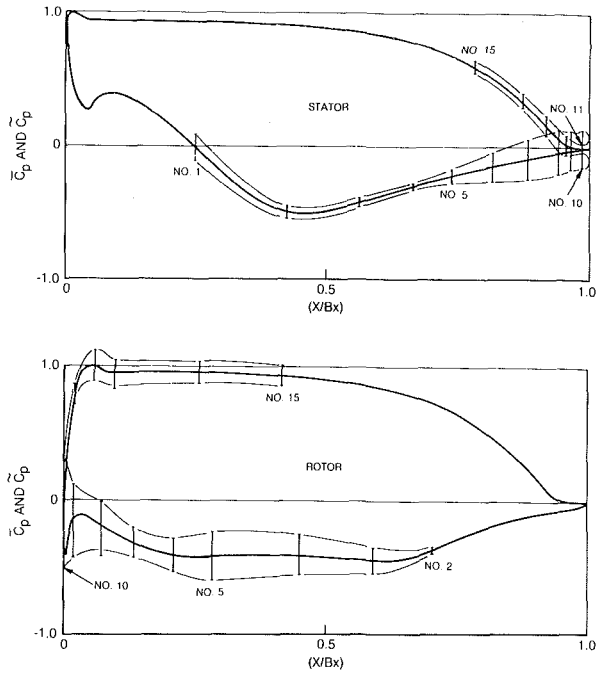

Fig. 6 Stator and rotor unsteady pressure envelopes, 15 percent gap, $(C_x/U) = 0.78$

The stator gages were concentrated on the suction surface and toward the aft end. Gages were mounted at sites 1–7 (Fig. 1), between sites 7 and 8 (referred to as site 7.5), at site 9 and on the pressure surface at site 13. The rotor gages (Figs. 1 and 3) were concentrated on the suction surface but toward the leading edge. Gages were mounted on the suction surface at sites 2–9, and on the pressure surface between sites 13 and 14 (referred to as site 13.5) and between sites 14 and 15 (referred to as site 14.5). The gages were operated in a constant temperature mode at a nominal resistance ratio of 1.5.

The high response pressure transducer output and the thin film gage output were acquired and recorded in digital form for subsequent off-time processing by the Aeromechanics Transient Logging and Analysis System (ATLAS) which accepted up to 26 channels of data. Each channel may be amplified and filtered as required. The heart of the system was a 26-channel transient recorder which digitized and stored each channel simultaneously at sampling rates up to 200 kHz as selected by the operator. The system was run in the external trigger mode so that data could be synchronized with the rotor position. An optical sensor (Optron, OPB-253-A) which detected the passing of a polished rotor blade tip provided the trigger pulse. The system was programmed to self-calibrate and then to acquire and write onto tape 100 rotor revolutions of data. Each scan consisted of 1024 samples for each channel acquired at 40,000 samples per second. Typical rotor speeds yielded data over approximately 5 blade pitches (roughly 200 samples per blade passing period). Since the speed of the rig was very stable, the 100 scans taken at each flow configuration could be averaged to remove random variations in the blade surface pressures (referred to as phase-locked or ensemble averaging). The thin film gage data were not averaged but rather was reduced on an instantaneous (rev. by rev.) basis to preserve any random fluctuations which might signify turbulence or separation.

Rotor-Stator Aerodynamic Interaction

Steady-State Pressure Distributions. The results of the steady-state stator and rotor midspan pressure distribution measurements are summarized in Figs. 4 and 5, respectively. The steady pressure coefficient ($\bar{C}_p$) for the stator (Fig. 4) was based on the measured stator inlet total pressure and a

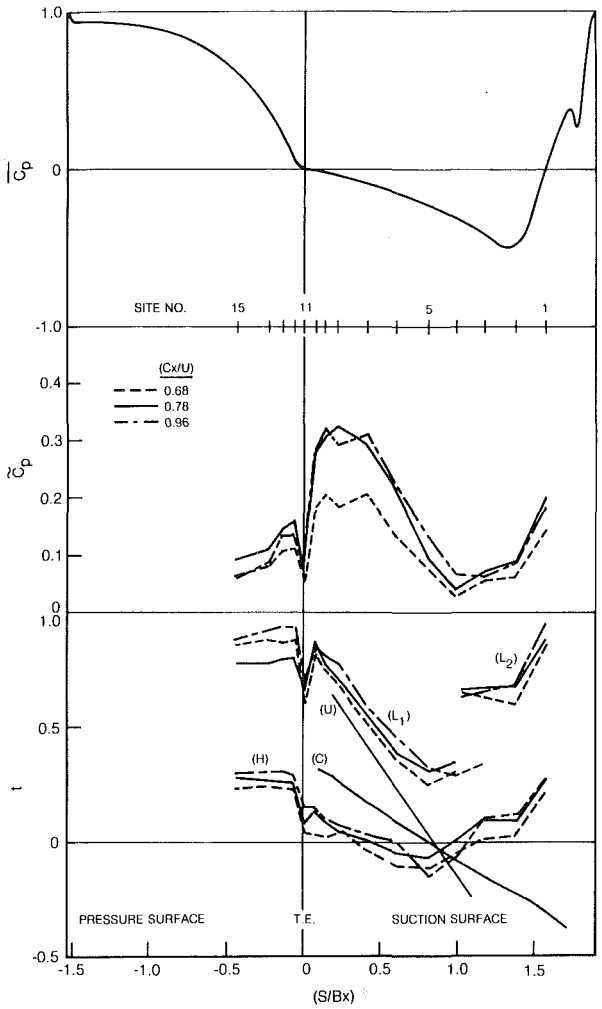

Fig. 7 Stator unsteady pressure, 15 percent gap

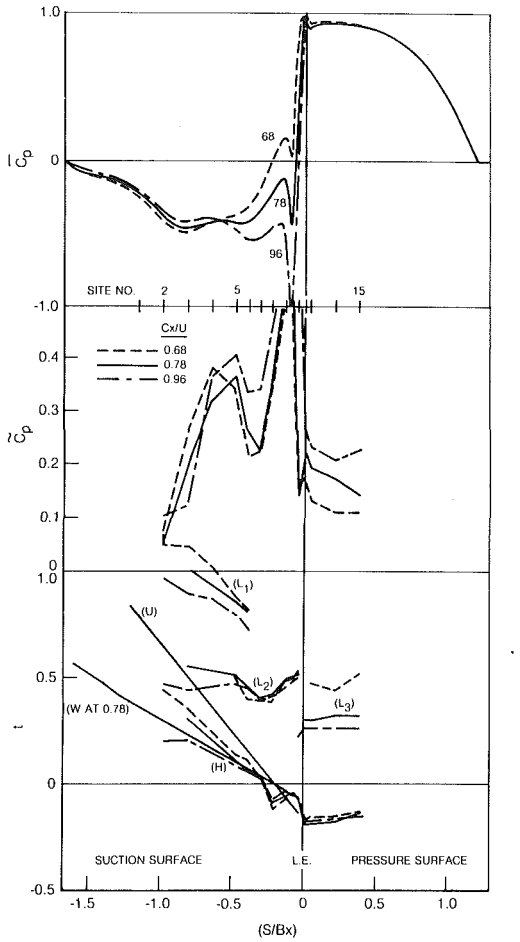

Fig. 8 Rotor unsteady pressure, 15 percent gap

midspan exit static pressure based on a free vortex interpolation between the measured flowpath static pressures at the hub and tip. The measured data (symbols) were compared with a theoretical distribution (curve) based on the method of Caspar et al. [25] which accounts for total pressure loss and stream tube contraction. The excellent agreement between the measured and computed results was obtained by varying the exit flow angle in the calculation until a best match occurred. For the 15 percent axial gap this occurred at an exit flow angle of 22.5 deg for all three values of (C_x/U) at which data was obtained (0.68, 0.78, and 0.96). At the 65 percent axial gap and data was also invariant with (C_x/U) and differed from the 15 percent gap data by no more than 0.03 in $\bar{C}_p$. This very small difference occurred in the throat. Practically speaking, then, the stator steady-state pressure distribution was invariant with rotor speed and rotor-stator axial gap and the data agree well with potential flow for an exit angle of 22.5 deg. From the pressure distribution it could be seen that the suction surface recompression occurred smoothly from the throat to the trailing edge, showing no evidence of boundary layer separation. Previous surface flow visualization studies had indicated the same result of attached and nearly two-dimensional boundary layers on both the suction and pressure surfaces of the stator at midspan.

The steady-state pressure coefficient for the rotor (Fig. 5) was based on an incident relative total pressure whose level was inferred from the surface static pressure measured on the rotor pressure surface at 24 percent chord. This method was described in greater detail in references [23] and [26]. As with the stator, the rotor exit midspan static pressure was based on a free vortex interpolation between measured values at the hub and tip. Measured and computed [25] pressure distributions are shown for all three values of (C_x/U) examined. Here again, the excellent agreement between the measured and computed results was obtained by varying the inlet and exit flow angles in the calculation until a best match occurred. At the 15 percent axial gap (Fig. 5) this occurred at an exit angle of 26.2 deg for all three values of (C_x/U). At the 65 percent axial gap the pressure coefficient in the throat region $(X/B_x = 0.7)$ was slightly higher $(\Delta\bar{C}_p = 0.06)$, and a match was obtained for an exit flow angle of 25.5 deg for all three values of (C_x/U). The present data taken at this larger spacing was practically identical with data taken earlier at this spacing [23] and [26] where the same exit angle provided a best match.

The best match with the data at the three values of (C_x/U), 0.68, 0.78, and 0.96 occurred at rotor relative inlet angles of 45, 40, and 35 deg, respectively. These inlet flow angles gave excellent agreement at both axial spacings and they correspond to an absolute stator exit angle of 22 deg (compared to the 22.5 deg flow angle inferred from the stator pressure distributions). This agreement was believed to be excellent and within the level of experimental and analytical matching uncertainty.

In summary, the steady-state flow over the rotor showed a weak dependence on axial gap and the expected dependence on relative inlet air angle. The suction and pressure surface flows were well behaved, showing no indication of boundary layer separation over the entire inlet flow angle range from 35–45 deg. The absence of midspan boundary layer separation on either surface had been demonstrated by previous flow visualization [23]. Note, however, that there was strong radial flow on the pressure surface [23] and [26] due to inviscid

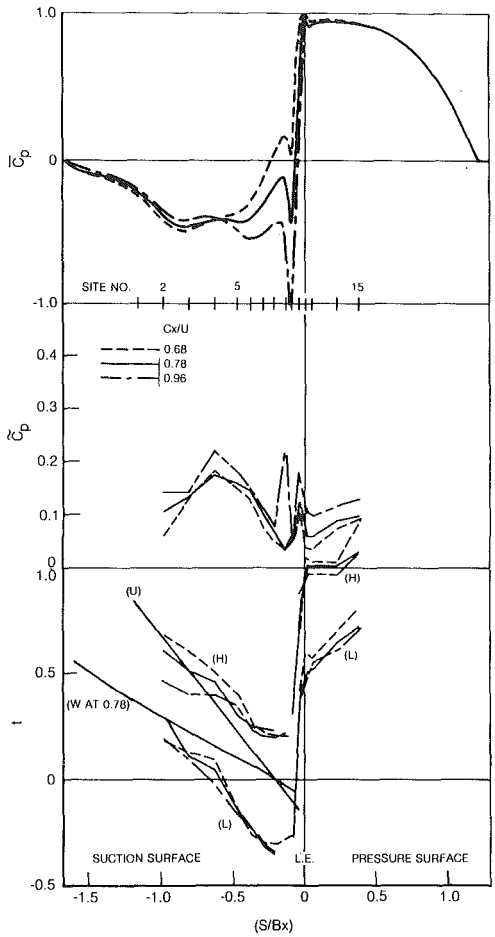

Fig. 9 Rotor unsteady pressure, 65 percent gap

effects. For reasons that were suggested in reference 23, these radial flows had little impact on the pressure distribution. There were also strong radial flows on the rotor suction surface due to secondary flow in the endwall regions. It was shown in reference [23] that these radial flows do penetrate to the midspan region downstream of the throat but that they had only a relatively weak impact on the pressure distribution.

Unsteady Pressure Envelopes. The envelopes defined by the maximum and minimum unsteady pressures on the stator and rotor at the 15 percent gap and at the design conditions (C_x/U) = 0.78 (β_1 = 40 deg), are shown superimposed on the theoretical steady-state pressure distributions in Fig. 6. The maximum and minimum of the periodic (ensemble averaged) pressure fluctuations are plotted symmetrically above and below the computed result at each site. In order to relate this data to physical locations on the airfoils (Fig. 1), site numbers are indicated. For the stator it may be seen that the amplitude decreased on the suction surface going from site 1 aft to site 4 (which was located just downstream of the throat, on the uncovered portion of the suction surface, Fig. 1). From site 4 aft toward the trailing edge (site 10) the amplitude increased to ± 15 percent of Q_2. There was an abrupt drop in amplitude at the trailing edge at site 11 on the mean camber line. The amplitude increased going around to the pressure surface (site 12), and then decreased gradually going forward on the pressure surface (to site 15). This periodically fluctuating pressure on the stator was due to the potential flow interaction with the rotor passing by downstream. Of particular interest were the relatively large amplitude (± 15 percent of Q_2) and the fact that the pressure fluctuations penetrate very far forward on the stator. When considering the unsteady potential flow fluctuations on the stator due to the rotor it should be kept in mind that the rotor was moving relativley slowly, i.e., at typically half the stator exit absolute flow speed (see Fig. 1).

The rotor unsteady pressure envelope at the 15 percent gap and at an inlet angle of 40 deg is shown in Fig. 6. There was a failure in the transducer at site 1 and no data was obtained there. The amplitude decreased toward the trailing edge. On the suction surface, however, there was a weak minimum at site 7 (reminiscent of the minimum at site 4 on the stator) and on the pressure surface the decay with distance aft was very gradual. The amplitude at site 5 on the suction surface was ± 18 percent of Q_2. Near the leading edge (at site 10) the amplitude of the fluctuation is ± 36 percent of Q_2 or ± 80 percent of Q_1. On the pressure surface the amplitude is typically ± 9 percent of Q_2. These large amplitude periodic pressure fluctuations on the rotor pressure and suction surfaces were due to the combined influences of (*a*) the potential (inviscid) flow and (*b*) the viscous wake of the stator passing by upstream (see Appendix I). In the light of the presence of the stator wake it was not surprising that the fluctuation amplitude on the rotor was in general larger than that on the stator. When considering the fluctuations on the rotor due to the stator is should be kept in mind that the stator was moving (relative to the rotor) at typically 80 percent of the rotor inlet relative flow speed (see Fig. 1).

Unsteady Pressure Wave Amplitude and Phase. The unsteady pressure distributions on the rotor and on the stator all had as their reference initial time (t = 0) the instant when the stator trailing edge circle center was in line with the rotor leading edge circle center. This condition is illustrated by the top two airfoils in Fig. 1. All events were referenced to this moment for both high response pressure and thin film gage instrumented rotors and stators. The unsteady stator and rotor pressures were examined in terms of fluctuation amplitude and phase (relative to t = 0). This data is presented in Fig. 7 for the stator at the 15 percent gap and in Figs. 8 and 9 for the rotor at the 15 precent and 65 percent gaps, respectively.

The fluctuating pressure data for the stator for the 15 percent gap is shown in Fig. 7. Included on the figure is (*a*) the theoretical steady-state pressure distribution ($\bar{C}_p$), (*b*) the fluctating pressure amplitude distribution ($\tilde{C}_p$) and (*c*) the phase relationships of the various pressure maxima and minima (relative to t = 0), all three plotted against arc length from the trailing edge mean camber line (S) normalized by stator axial chord (B_x).

The variation in unsteady pressure amplitude around the stator can be seen clearly here (Fig. 7). The increase in amplitude on the uncovered portion of the suction surface toward the trailing edge and the minima occurring at site 4 and at the trailing edge (site 11) are particularly evident. The phase is indicated for the high (H) points of the pressure wave (maxima) and for the low (L1 and L2) points of the wave (minima). Included on the figure for comparison purposes is the phase of a disturbance traveling at the local convective velocity (C) and also the phase of a disturbance traveling at wheel speed (U). It can be seen that pressure waves were traveling upstream and downstream from about site 5. This was close to the location where the fluctuation amplitude was at a minimum (site 4). It appeared from the data that the pressure wave from the rotor blade first struck the uncovered portion of the stator suction surface around sites 4 and 5 and that waves traveled fore and aft from that point. The low pressure region of the forward traveling wave (L2) was distinctly separate from the low pressure region of the rearward traveling wave (L1). Such a distinction could not be made for the high pressure region (H).

In the uncovered portion of the channel (sites 4–10) the pressure maxima (H) were traveling aft faster than the local

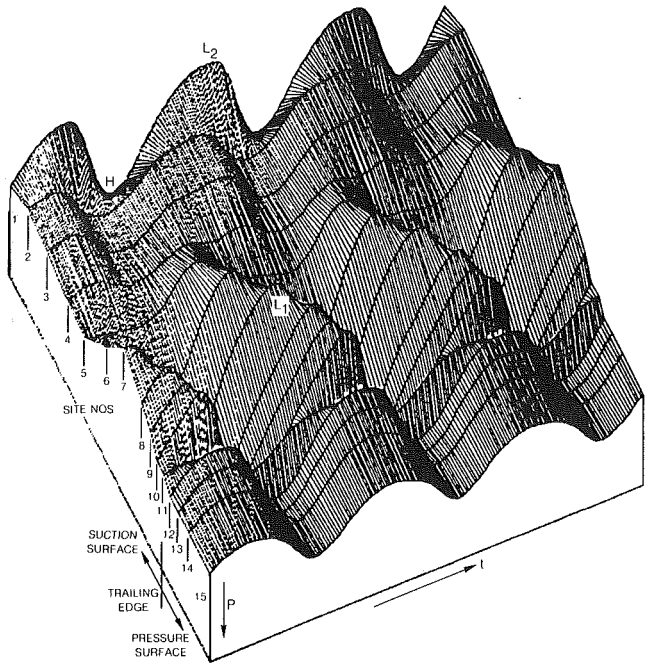

Fig. 10 Stator pressure time history, 15 percent gap, $(C_x/U) = 0.78$

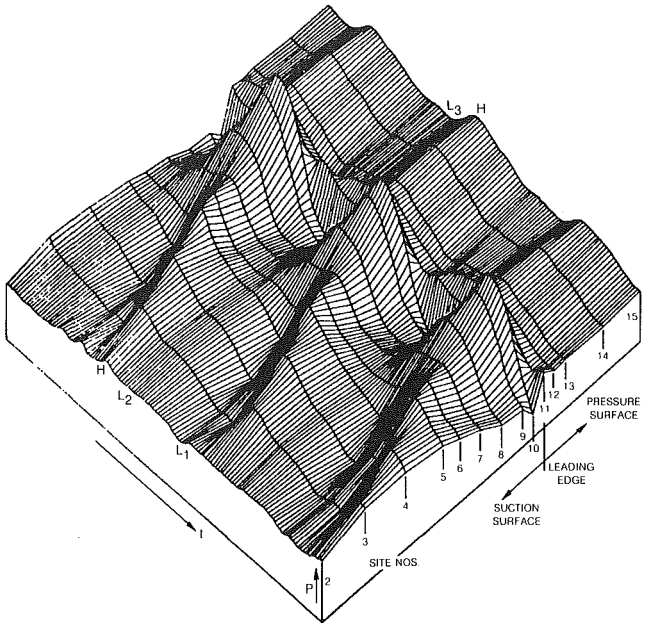

Fig. 11 Rotor pressure time history, 15 percent gap, $(C_x/U) = 0.78$

flow velocity, and the minima (L1) were traveling aft more slowly than the local flow velocity, but not as slow as wheel speed. These differences were evident in the different slopes of the phase plots in these regions. This indicated a steepening of the pressure rise portion of the wave as it proceeded aft. This distorted wave form was indeed seen in the data near the trailing edge. There was a sudden variation in amplitude and phase around the trailing edge. This indicated that for unsteady flow of this type, i.e., with reduced frequency on the order of unity, that the steady Kutta condition of no loading at trailing edge no longer applied. This matter will be explored more fully below in the discussion of Fig. 12.

Another interesting feature of the unsteady pressures on the stator was seen by comparing the nearly constant phase on the suction surface between sites 2 and 4 (located just upstream of the throat) with that on the pressure surface at sites 12–15. If these sites had been on the same channel instead of on the same airfoil, i.e., if sites 12–15 had been on the pressure surface of the adjacent airfoil facing sites 2 and 4 on the suction surface, then they would all have been very nearly in phase. Moving Sites 12 through 15 to the adjacent airfoil would have advanced their phase by $[1 - (22/28)] = 0.21$ of a blade passing period (or an interstator phase angle of 77 deg). This would be very close to the phase of sites 2 and 4. The conclusion was that when viewed as a channel, the fluctuations of the flow on both sides of the channel were nearly in phase.

The fluctuating pressure data for the rotor for the 15 percent gap is shown in Fig. 8. The format is the same as that for the stator (Fig. 7), except that for the rotor arc length (S) was measured from the leading edge stagnation point location at a $(C_x/U) = 0.78$ ($\beta_1 = 40$ deg). Aspects of the fluctuating pressure distribution ($\tilde{C}_p$) evident in the data include very high amplitudes at the leading edge (truncated at $\tilde{C}_p = 0.5$ in the figure), an amplitude decreasing with distance on the pressure surface, a local minimum amplitude on the suction surface between sites 6 and 7, a local maximum between sites 4 and 5 and a rapid decay in amplitude back to site 2. Recall that the transducer at site 1 was inoperative. The peak in amplitude at the leading edge occurred at site 10, which was at the minimum x location (Fig. 1). For inlet flow angles (C_x/U) of 35 deg (0.96), 40 deg (0.78) and 45 deg (0.68), the fluctuation amplitude ($\tilde{C}_p$) at site 10 was 0.98, 0.72, and 0.61, respectively.

The phase behavior of the rotor was considerably more complicated than that of the stator. The high pressure part of the wave (H) and one of the low pressure parts (L_1) were moving aft on the suction surface at approximately the local convective velocity (W). These high and low pressure regions will be shown to be associated with the flow between stator wakes. The low pressure region (L_2) will be shown to be associated with the flow in the stator wake and it could be seen to impact the entire suction surface almost at once (at $t \approx 0.5$), i.e., with a very high phase velocity. This matter will be discussed below in conjunction with Fig. 17, however, the possibility that the stator wake impacted a long region of the rotor suction surface all at once at $t \approx 0.5$ was not unreasonable. The uncovered portion of rotor suction surface (sites 5–9) reached the stator wake at about $t \approx 0.5$. This can be seen in Fig. 1 by extending the stator trailing edge mean camber line into the rotor channel. Using this extended mean camber line as an estimate of the stator wake position it can be seen that when the rotor had moved down 1/2 of the stator pitch ($t = 0.5$) the uncovered portion of the rotor suction surface was in line with stator wake. An event on the rotor occurring at $t = 0.5$ (such as L_2) would occur on the stator at $t = 0.5 \times (N_R/N_S) = 0.64$. Thus, the nearly constant phase low pressure region on the rotor suction surface (L_2) occurred at nearly the same instant as the constant phase low pressure region on the stator suction surface (L_2), i.e., at $t \approx 0.64$ (Fig. 7). Note that at this instant the stator trailing edge stagnation point streamline and the rotor leading edge stagnation point streamline were nearly coincident.

The fluctuation on the rotor pressure surface was in nearly constant phase. As with the stator, if the pressure surface sites had been in the same channel as the suction surface sites (as opposed to on the same airfoil), i.e., if sites 13–15 had been on the pressure surface of the adjacent airfoil facing sites 2–10 on the suction surface, then the low pressure regions L_2 and L_3 would have been approximately in phase. Moving sites 13–15 to the adjacent airfoil would have retarded their phase by $[(28/22) - 1] = 0.27$ of a stator passing period (or an interrotor phase angle of 98 deg). This would have put them close to the phase of sites 2–10. Thus, when viewed as a channel, the events at L_2 and L_3 were occurring nearly

simultaneously, particularly for the two higher values of (C_x/U).

The fluctuating pressure data for the rotor at the 65 percent gap is shown in Fig 9. The fluctuation amplitude at this larger spacing is reduced by typically a factor of 2 relative to that at the 15 percent gap. The high amplitude at the leading edge had moved from site 10 (the minimum x location, Fig. 1) at the 15 percent gap to site 11 (the mean camber line location) at the 65 percent gap. The magnitude of this peak had been reduced by typically a factor of 6. There was a second amplitude maximum at site 9 for a (C_x/U) of 0.96. This maximum may be related to the very steep gradient in the steady-state pressure distribution $(\bar{C}_p)$ at this location due to the positive incidence leading edge overspeed. It seemed reasonable to expect relatively high amplitude fluctuations to occur at regions of steep gradients in the steady-state pressure. This same reasoning provided some explanation for the curious increase in fluctuation amplitude observed on the stator at site 1 toward the leading edge. The gradient of the steady-state pressure was relatively steep there also. The phase plot indicated that the high pressure part of the wave (H) on the suction surface was moving aft at about the local convective velocity but that the low pressure part (L) was moving aft much more slowly, at about wheel speed. This was similar to what occurred on the stator. A large phase shift around the leading edge was also evident in the data.

Instantaneous Pressure Distributions. In an effort to provide some indication of the complex nature of the instantaneous pressure distributions (C_p'), pressure-time histories for the stator and the rotor are presented in Figs. 10 and 11. The data for both airfoils included the suction and pressure surface sites, and they were located along the coordinate axis at distances proportional to their arc length distance from the leading or trailing edge. Data was shown for several blade passing periods but for the sake of clarity the data at every instantaneous time was not included. Only enough instantaneous data was included to give a clear indication of the pressure-time history.

Since the most interesting features of the stator data were the low pressure region, it has been plotted with pressure decreasing in the upward direction (Fig. 10), i.e., low pressure regions appear as ridges and high pressure regions appear as valleys. The increase in unsteadiness amplitude from site 5 aft toward the trailing edge at site 11 can be seen along with the fact that the low pressure region L1 was a wave moving slowly aft on the airfoil, i.e., it was moving aft at a finite speed as seen by the way in which the wave crossed the lines of constant time. In contrast, the wave moving forward from site 5 toward site 1 (L2) was nearly at a constant phase, i.e, the low pressure occurred at nearly the same instant for sites 4 through 2. These phase relationships have also been discussed above in connection with Fig. 7. An unusual feature evident in Fig. 10 was that the minimum amplitude at site 4 (see also Fig. 7) occurred due to the wave moving toward the trailing edge being out of phase with the wave on the forward portion of the suction surface. Said another way, the low pressure region at sites 1–3 (L2) had its origin in the high pressure region at site 5 and the low pressure region moving aft from site 5 (L1) had its origin in the high pressure region at site 4. The abrupt changes in amplitude and phase at the trailing edge and the nearly constant phase behavior on the pressure surface can also be seen.

The rotor data is presented viewed from a different perspective and with pressure increasing in the upward direction in Fig. 11. The salient feature here was the high amplitude on the suction surface near the leading edge. The phase shift in the high pressure region (H) and in the low pressure region (L1) as they moved aft along the suction surface was evident here (and also in Fig. 8). The nearly constant phase of the suction surface low pressure region (L2) and the pressure surface high (H) and low (L3) regions could also be seen. This figure clearly illustrated the extremely high amplitude near the leading edge and its decay along the suction surface as well as the abrupt drop in amplitude going toward the pressure surface.

The instantaneous pressure distributions (C_p') on both airfoils had many extremes and many zero crossings. For this reason it would have been difficult to make an accurate estimate of the instantaneous force on the airfoils without a far more dense array of instrumentation around the entire perimeter of each airfoil. Both the stator and the rotor demonstrated the very complex nature of the pressure fluctuations that occur at reduced frequencies on the order of unity.

Unsteady Trailing Edge Loading. The fact that the fluctuating pressure produced unsteady loading at the stator trailing edge was illustrated in Fig. 12 where the pressure time history at the trailing edge mean camber line (site 11) was compared with those slightly upstream on the suction and pressure surfaces (sites 10 and 12, respectively). The existence of this unsteady loading at the stator trailing edge was mentioned above in conjunction with Fig. 7. From Fig. 7, it could also be seen that any phase shift in the pressure wave as it proceeded from sites 10 and 12 downstream to the trailing edge (a distance of 5.3 to 6.3 percent of axial chord) was small relative to the phase differences that existed between these sites. This was particularly true in comparing sites 11 and 12 since the phase gradient on the pressure surface was very small.

The fact that the pressure fluctuations at sites 10, 11, and 12 were (*a*) all considerably out of phase and (*b*) of significantly different amplitude, indicated the existence of unsteady trailing edge loading. The expectation (by Gostelow, [9] and by Satyanarayana and Davis, [10]) that unsteady trailing edge loading would become significant above a reduced frequency of 0.6 was born out by this data. The reduced frequency for

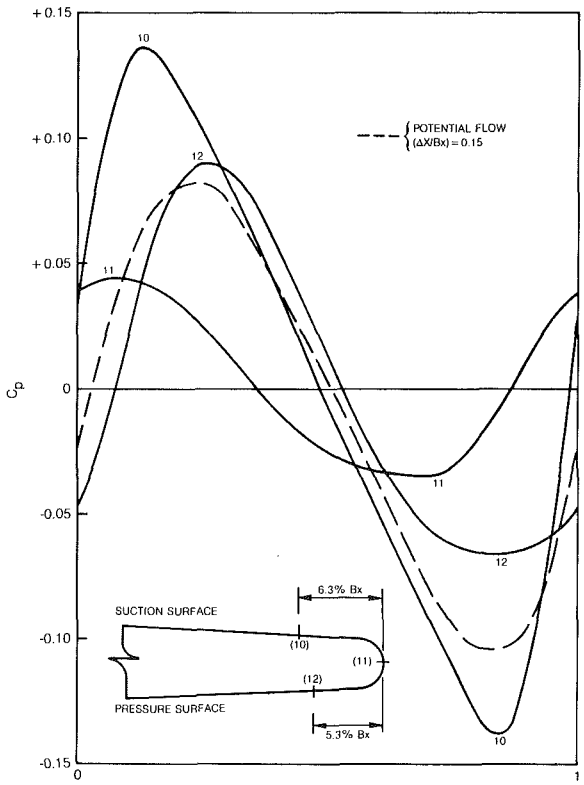

Fig. 12 Stator trailing edge unsteady pressure, 15 percent gap, $(C_x/U) = 0.78$

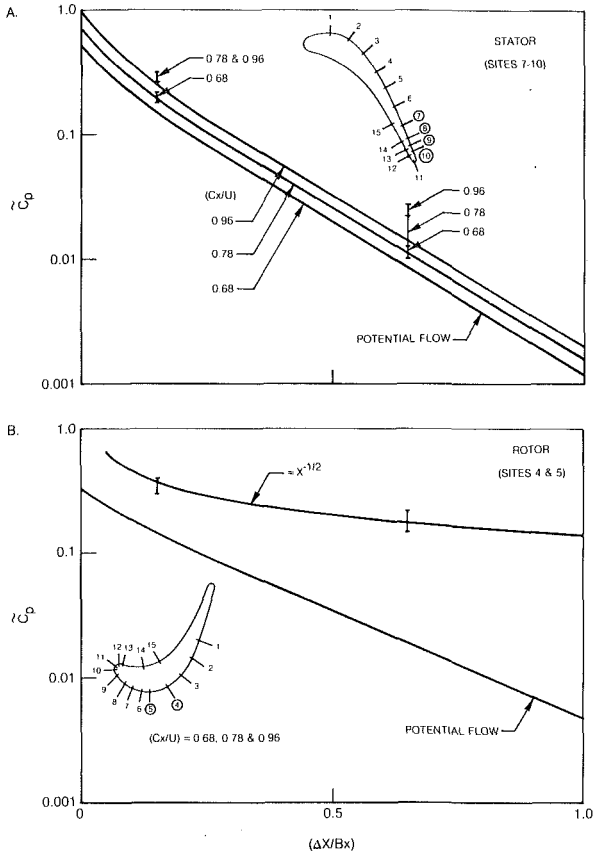

Fig. 13 Decay of unsteady pressure amplitude with axial gap

the stator was based on the true chord (B) and the absolute stator exit velocity (C) as follows:

$$k = \left(\frac{N_R \Omega B}{2C}\right) = \left(\frac{N_R}{2}\right)\left(\frac{B/R_m}{C_x/U}\right) \text{Sin } \alpha$$

For the range of values of (C_x/U) tested, 0.68, 0.78, and 0.96, the reduced frequencies were 2.7, 2.3, and 1.9. From these results, it appeared likely that any analytical model of the rotor-stator interaction process that did not account for unsteady trailing edge loading would be limited to low reduced frequencies.

The stator trailing edge pressure fluctuations (Fig. 12) were also examined with respect to their wave shape. In the discussion of Fig. 7 it had been pointed out that near the stator trailing edge the wave form was one of a rapid pressure rise ($\Delta t = 0.3 \sim 0.4$) and a relatively slow pressure drop ($\Delta t = 0.6 \sim 0.7$). This could be seen in the data from sites 10, 11, and 12. Also included in Fig. 12 was a prediction of the unsteady pressure wave based on the predicted [25] steady potential flow around the rotor. At an axial location upstream of the rotor leading edge corresponding to the 15 percent axial gap between the stator trailing edge and the rotor leading edge, the steady rotor pitchwise static pressure variation was used to determine C_p' at the stator trailing edge, i.e., the steady spatial variation in the rotor frame of reference was viewed as a temporal variation in the stator frame of reference (ignoring the presence of the stator). It was seen (Fig. 12) that this rather simple approach resulted in a surprisingly accurate prediction of the wave form, amplitude, and phase of the stator trailing edge pressure fluctuations. This relatively close agreement was contrary to the results of Parker [5], which indicated that the local amplitude with interaction was roughly 3 times that without interaction. Had this been the case, the computed amplitude in Fig. 12 would have been approximately half its actual value.

Decay of Unsteadiness with Axial Gap. The same potential flow analysis [25] that was used to predict the amplitude, phase, and wave form at the stator trailing edge (Fig. 12) was also used to predict the amplitude of the pressure fluctuations ($\tilde{C}_p$) on the rotor and the stator as the axial gap separating them was changed from 15 to 65 percent of axial chord. The theoretical potential flow results and the measured data are shown in Fig. 13. As in Fig. 12, the tangential variations in the computed static pressure downstream of the stator and upstream of the rotor were normalized with the exit dynamic pressure of the rotor and the stator, respectively. Note that the predicted $\tilde{C}_p$ for the stator was a function of (C_x/U) due to the changing rotor incidence, but that for the rotor it was independent of (C_x/U). The measured data were from the aft end of the stator suction surface, sites 7–10, and from the midchord region of the rotor surface, sites 4 and 5.

For the prediction on the stator, the agreement between the measured and predicted results was excellent as to level and the trends with (C_x/U) and with relative axial spacing. When the data was viewed in this manner it appeared possible that the indications from Parker's [5] results, that the presence of the upstream airfoil increased the fluctuation amplitude over what it would have been at that point without the airfoil present, may indeed be qualitatively correct. For the change in axial spacing from 15 to 65 percent gap there was a reduction by about a factor of 10 in unsteady pressure amplitude.

For the unsteady pressure amplitude on the rotor, however, the decrease with axial gap predicted by potential flow was much too strong and in general the predicted amplitude was much too low. This suggested that the influence of the stator wake was considerably stronger than that of the stator potential flow in determining the amplitudes on the rotor (at sites 4 and 5). The possibility that this unsteadiness on the rotor was primarily due to the stator wake was further strengthened when it was observed that the amplitude decay was nearly proportional to $X^{-1/2}$, i.e., the amplitude was decaying in the same manner as a wake. This observation was further supported by the fact that due to the velocity triangles of a turbine one would expect the stator wakes to migrate toward the rotor suction surface. In contrast to this behavior on the suction surface it was noticed that near the rotor leading edge stagnation point (sites 11 and 12), while the amplitudes were still much larger than predicted by potential flow, the decay in amplitude with increasing axial gap was much closer to the potential flow prediction. On the rotor both viscous and inviscid mechanisms of rotor-stator interaction are occurring, whereas on the stator it it purely a potential flow effect.

The computed results shown in Figs. 12 and 13 made possible a number of additional observations regarding the stator data presented in Fig. 7. Based on the decay with axial distance of the potential flow unsteadiness on the stator due to the rotor (Fig. 13), one would expect the unsteady pressure amplitude at the 15 percent gap condition to decrease by approximately a factor of 10 going from the trailing edge forward on the stator suction surface to site 4. From Fig. 7, it can be seen that this is very close to what was measured. From Fig. 12, it was shown that the unsteady pressure wave form on the stator (due to the rotor potential flow) closely matched the measured wave form near the trailing edge (at sites 10, 11, 12). It is reasonable, therefore, that the low pressure region (L_1) is moving downstream on the stator suction surface at a speed very close to wheel speed (U), i.e., it is moving with the rotor. However, the reason for the much higher phase velocity of the high pressure region (H) on the suction surface is not clear. As mentioned above, the different phase velocities of the high and low pressure regions cause a steepening of the pressure rise portion of the wave at it travels downstream. This change in wave form is also evident in the potential flow results. At an axial location 15 percent ahead of the rotor the

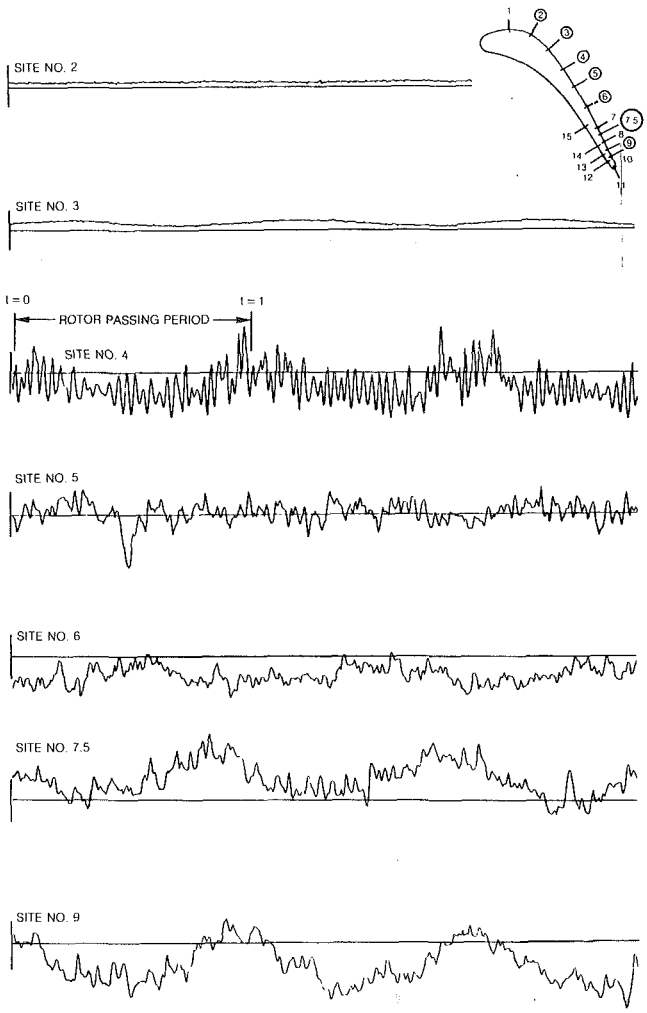

Fig. 14 Stator thin film data, 15 percent gap, $(C_x/U) = 0.78$

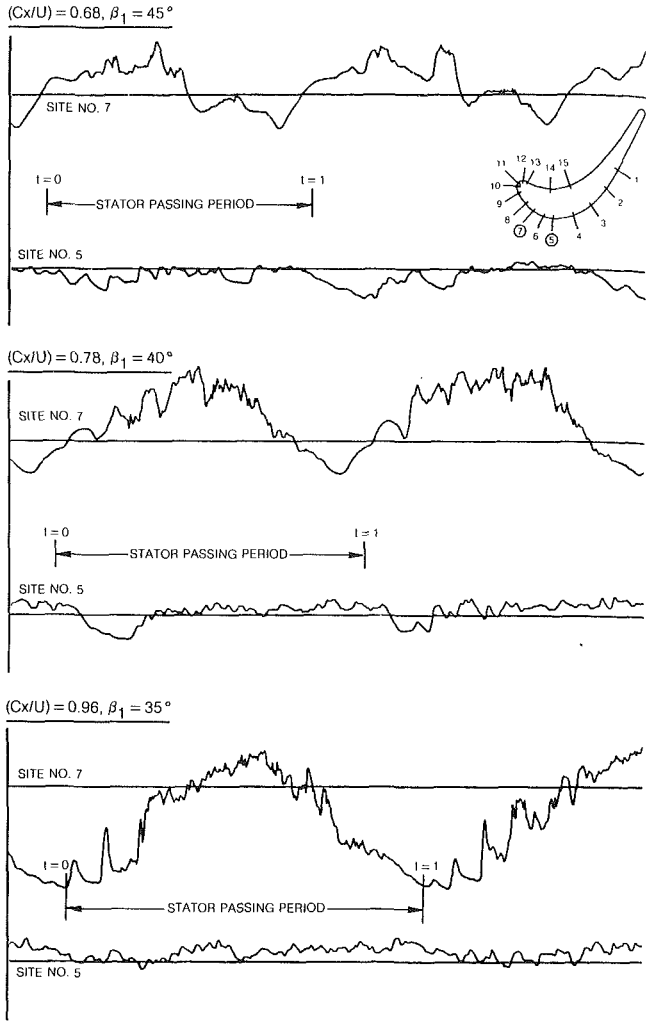

Fig. 15 Rotor thin film data, 15 percent gap

wave has nonsinusoidal rapid pressure rise (as seen in Fig. 12). However, as also seen in the data, at an axial location 50 percent ahead of the rotor the wave was nearly sinusoidal.

Thin Film Gage Results—Stator. Up to this point, discussion of the high response data has been focused purely on the ensemble averaged pressures. Turning our attention now to the thin film gage data it must be kept in mind that this data must be viewed on an instantaneous basis. All of the film data represented a portion of the data acquired over a single rotor revolution. It was not averaged over 100 revolutions as was the pressure data. This approach permitted one to distinguish, for example, the difference between laminar and turbulent portions of the flow. On all of the thin film data plots increased power input to the gage resulted in an increased output, i.e., positive (upward) deflection. The gages were all operated at the same sensitivity and hence the output amplitudes were directly comparable.

Typical thin film data for the stator at a (C_x/U) of 0.78 and a 15 percent gap is shown in Fig. 14 for most of the gages located on the suction surface (sites 2–9). Site 2 upstream of the throat indicated nearly steady laminar flow (as did site 1). This was somewhat surprising in light of the pressure fluctuations at this site (Fig. 7). At site 3, at the throat and just downstream of the minimum pressure, the flow was still laminar but there was a weak oscillation at rotor passing frequency. At site 4, in the recompression region, a very distinct high frequency oscillation was present superimposed on the oscillation at rotor passing frequency. This high frequency (approximately 6 kHz) was independent of rotor speed. It was seen on the spectrum analyses as a broad band from 5 to 7.5 kHz. It was also seen in the instantaneous Kulite data. Since boundary layer transition was expected to occur at or about site 4, these oscillations were examined in the light of Tollmien-Schlichting waves. Based on the results presented in reference [27] (Figs. 16.12 and 16.18), and those presented by Fink [28] and by Erens and Chasteau [29], it was estimated that Tollmien-Schlichting waves would have had a frequency of 4–7 kHz in the present stator situation. The conclusion reached was that these were indeed Tollmien-Schlichting waves. The stator suction surface boundary layer was turbulent from site 5 downstream to site 9 near the trailing edge. The superimposed periodic unsteadiness increased in magnitude significantly as the trailing edge was approached.

On the pressure surface the thin film gage at site 13 indicated a laminar boundary layer with a weak periodic oscillation at blade passing frequency. The data was very similar to that at site 3 on the suction surface. That the flow was laminar was not unexpected due to the strong acceleration up to this point (Fig. 4).

When the rotor-stator axial gap was increased from 15 to 65 percent the frequency of the Tollmien-Schlichting waves and the site at which they were observed on the suction surface were unchanged. The random fluctuations in the turbulent region were of the same magnitude (as at 15 percent) but the periodic fluctuations were virtually eliminated. This was consistent with the large reduction in the amplitude of the

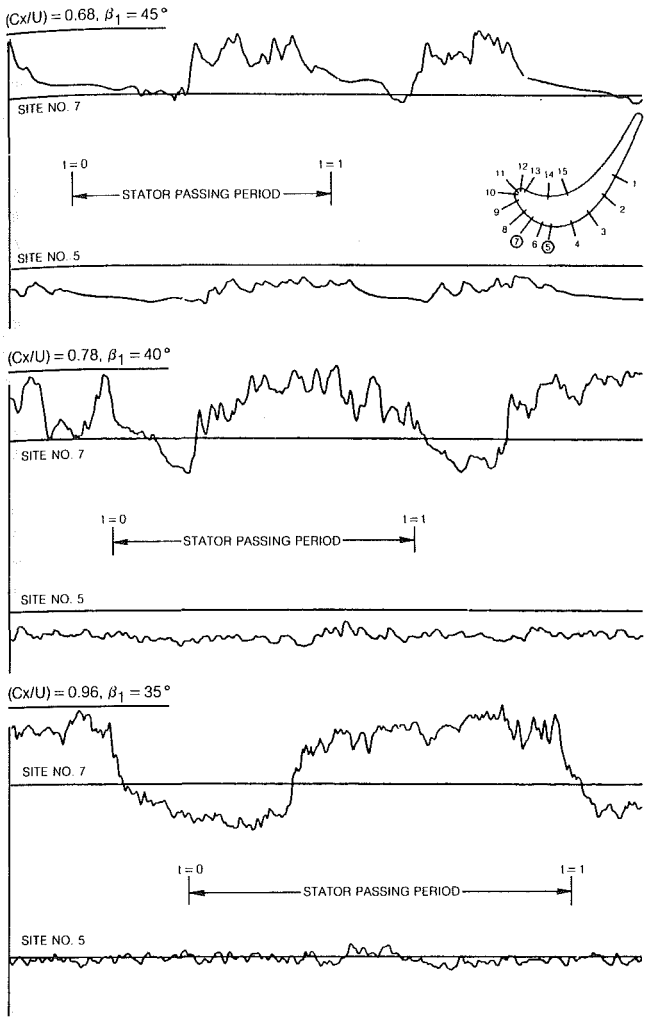

Fig. 16 Rotor thin film data, 65 percent gap

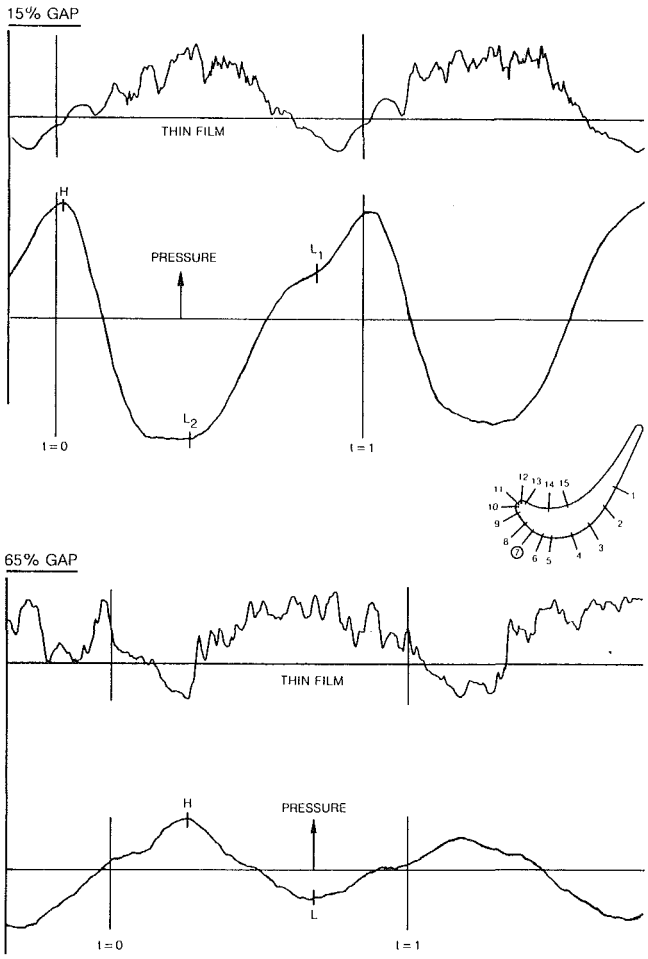

Fig. 17 Rotor pressure and thin film data at site 7, $(C_x/U) = 0.78$

periodic pressure fluctuations that occurred when the gap was increased to 65 percent.

Thin Film Gage Results—Rotor. Samples of the rotor thin film gage data for the three rotor inlet gas angles (35, 40, and 45 deg) were shown for the 15 percent gap in Fig. 15 and for the 65 percent gap in Fig. 16. Data was shown for sites 5 and 7 located on the suction surface toward the leading edge. For the rotor, periodic events occurred at the stator passing frequency which was indicated on the figures relative to $t = 0$. There was a strong unsteadiness at stator passing frequency at site 7 (near the leading edge) which was greatly reduced at the further downstream location on the rotor (site 5). Both locations for both spacings showed regions of large random fluctuation due to the turbulence in the stator wake superimposed on the periodic fluctuation. At site 7 there were portions of the stator passing period (between the stator wakes) where the randomness was very small. These occurred where the gage output was near a minimum. There were also indications of this type of behavior at site 5, especially at the 45 deg inlet angle ($C_x/U = 0.68$) for 65 percent axial spacing. In general, the portion of the stator passing period where the random fluctuations were small increased with increasing inlet gas angle, i.e., with reduced (C_x/U) or reduced turning. The reduced leading edge overspeed with reduced (C_x/U) at $\beta_1 = 45$ deg produced a laminar boundary layer on the rotor suction surface which was interrupted periodically by the impingement of the turbulent upstream stator wake. Evidence of these laminar regions at an inlet gas angle of 45 deg ($C_x/U = 0.68$) persisted all the way to the aft-most gage, particularly at the 65 percent gap. (The gage at site 9 had become inoperative early in the program.) The essentially laminar behavior at site 8 indicated that the leading edge overspeeds (Fig. 5) did not trip the boundary layer immediately. At the most positive incidence, however, the overspeed did appear to accelerate the transition process as seen by the increased random fluctuations in the low output regions between the stator wakes at both spacing. The periodic oscillation between laminar and turbulent boundary layer flow on the rotor suction surface was in agreement with similar observations made by Evans [15] and by Speidel (as reported by Scholz [14]).

The output of the high response pressure transducer and the thin film gage at site 7 on the rotor suction surface were compared at a (C_x/U) of 0.78 ($\beta_1 = 40$ deg) at both axial spacings in Fig. 17. At the 15 percent gap it was seen that the high pressure region (H, as in Fig. 8) corresponded to the laminar region between stator wakes and that the low pressure region (L_2) corresponded to the turbulent region within the stator wakes. As the rotor passed through the stator wake, the wake impacted a long region along the suction surface at about the same instant. This can be seen in Fig. 8 by the fact that the phase of L_2 is nearly constant from site 2 to site 10. This effect could be seen in the thin film output as well as in the pressures. The initial development of the second low pressure region (L_1) is also indicated (Figs. 8 and 17).

At the 65 percent gap, the high pressure region (H) at site 7 was again between the stator wakes and the low pressure region (L) was in the wakes. It was observed that at this downstream location the increased width of the turbulent region was in agreement with the increase in wake width

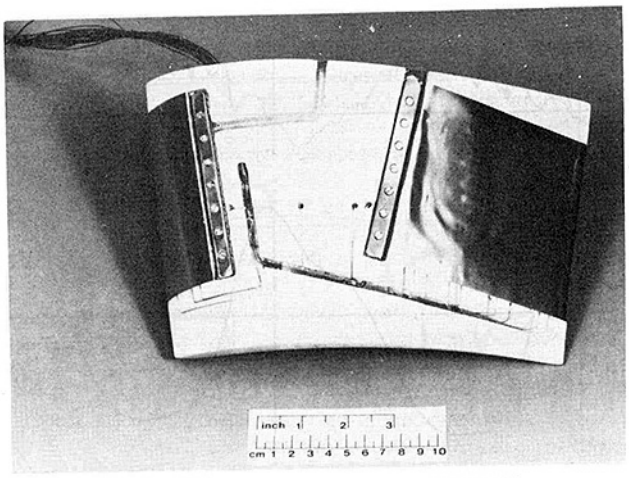

Fig. 18 Stator pressure surface transfer model

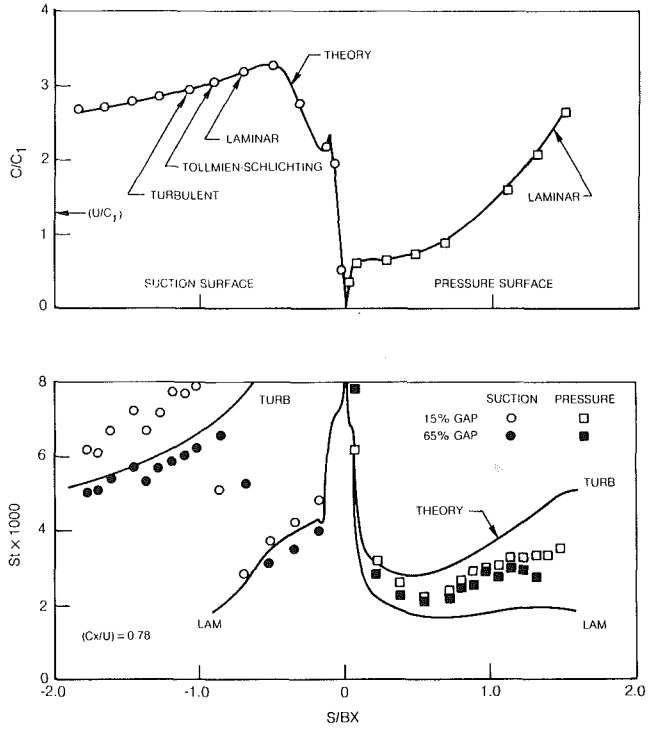

Fig. 19 Stator velocity and Stanton number distributions, $(C_x/U) = 0.78$

expected with downstream distance. The phase of the thin film output could only be distinguished in the data at the inlet flow angle of 45 deg. For this case, the phase was not constant as L_2 has been at the close spacing (Fig. 8), but rather the wake moved down the airfoil as indicated by the (H) and (L) in Fig. 9.

The rotor pressure surface thin film gage output (site 13.5) indicated weakly periodic turbulent flow at all combinations of spacing and incidence. The gage at site 14.5 was inoperative. Note from Fig. 9 that even though the motion of the wake on the pressure surface could not be clearly distinguished in the thin film gage data, its effect on surface pressure was distinct. In particular, unlike the constant wake phase on the pressure surface (L_3) at the close spacing, at the large spacing the wake effect was proceeding aft on the pressure surface in a manner similar to that on the suction surface, i.e., the phase was not constant.

Stator Heat Tranfer Model and Instrumentation

The stator heat transfer portion of the present program was conducted simultaneously with the aerodynamic measurements decribed previously. At both axial spacings (15 percent and 65 percent axial gap) stator heat-transfer data was acquired at the same three flow conditions at which aerodynamic data had been acquired, i.e., values of (C_x/U) of 0.68, 0.78, and 0.96.

The basic approach to the heat-transfer measurement was the same as that employed in references [30] and [31]. It consisted of fabricating a low thermal conductivity foam model of the stator and covering it with an instrumented heater strip. As with the aerodynamic measurements described above, the heat-transfer measurements were made at the midspan section of the stator.

Two stator heat-transfer models were fabricated, one for the suction surface and one for the pressure surface. The partially completed pressure surface model was shown in Fig. 18, viewed from the suction surface. An aluminum stator airfoil was used to make a mold. This mold was constructed using hydrocalic cement which had extremely low shrinkage and gave an accurate duplicate of the original metal airfoil. A metal structure consisting of hub and tip airfoil sections and two spanwise spars was constructed to provide structural integrity to the model. Urethane foam (Isofoam^R, Witco Chemical) was poured into the mold around the metal structure to form an accurate duplicate of the metal airfoil. This foam was chosen as a suitable airfoil material since its thermal conductivity was very low (0.02 ~ 0.03 Btu/hr ft °F), being close to that of still air. The effect was to minimize thermal conduction within the model. Buss bars (visible in Fig. 18) were installed to provide power to the heater foils. The foil was 0.001 in. thick stainless steel, which when electrical current was passed through it provided a nearly uniform surface heat flux. This foil was glued to one surface (pressure or suction) of the airfoil and typically 20 thermocouples (0.003 in. dia Chromel-Alumel) were welded to its back surface through predrilled holes in the foam. The foil was then wrapped around and glued to the remaining surface of the airfoil and connected to the buss bars. This was the condition of the airfoil in Fig. 18.

The back surface of the airfoil (i.e., with the buss bars and thermocouple leads) was restored to its original contour with joint compound and the entire airfoil was sprayed with flat black paint to obtain a known emissivity. The separate suction and pressure surface instrumented airfoils were mounted in the turbine model with several unheated airfoils separating them. The airfoils and endwalls in the channels facing the instrumented stator surfaces were also spray painted flat black to obtain a known emissivity. The thermocouples were connected to a programmable thermocouple scanning device. Power to heat the foil was provided by a single low ripple regulated d-c power supply. The d-c power passing through the foil was measured using two precision shunt resistors and a digital voltmeter.

Unsteady Effects on Stator Heat Transfer—Results

All of the stator heat tranfer testing was conducted at a constant stator Reynolds number (based on axial chord and exit velocity) of 5.9×10^5. All variations of (C_x/U) were obtained by changing the rotor speed. The tests were conducted with a nearly constant heater power input which gave temperature differences of typically 10 to 49 F°. At these levels, the radiant flux and the conduction loss (based on thermocouples on the back side of the airfoils) were typically 2 to 10 percent and 0 to 3 percent, respectively, of the total generated surface heat flux.

The measured suction and pressure surface heat-transfer data are presented in Fig. 19 along with the surface velocity distribution for a (C_x/U) of 0.78 as a function of distance from the stagnation point. The velocity distributions were included to provide perspective on the heat-transfer data. The

relative magnitude of the rotor speed ($U/C_1 = 0.78^{-1} = 1.28$) was included to demonstrate that it was moving relatively slowly behind the stator. The measured and computed [25] velocity distributions and the locations where the boundary layers were either laminar, turbulent or had Tollmien-Schlichting oscillations, were all included. Recall that all of these were very insensitive to (C_x/U) as well as to axial gap. The same could not be said for the heat-transfer results. They were presented in terms of a Stanton number based on inlet flow velocity. A significant drop was observed in the Stanton numbers as the rotor-stator axial gap was increased from 15 to 65 percent, particularly on the suction surface. The heat transfer data were compared with laminar and fully turbulent calculations based on the theory by Carter and Edwards [32]. The boundary layer calculations were in turn based on the surface velocity distribution computed by the method of Caspar et al. [25].

The suction surface heat-transfer results (Fig. 19) indicated that the boundary layer was laminar to an (S/BX) of about 0.75 and turbulent from about 1.0 to the trailing edge. This was in good agreement with the known locations of laminar, transitional, and turbulent flow based on the thin film data. The source of the small difference in transition location for the two gaps was uncertain since the thin film (and Kulite) data indicated no change. Generally speaking, at the 65 percent gap the measured and computed heat-transfer results were in good agreement. However, with the rotor stator gap reduced to 15 percent, the measured suction surface heat transfer coefficients increased by typically 25 percent. At this time the fundamental mechanism behind the increase is unclear. The pressure surface heat-transfer results indicated that the boundary layer was transitional over its entire length and that the change in axial gap had a much weaker impact on the heat transfer coefficient there.

The Stanton number distributions at the higher and lower values of (C_x/U) were very similar [24]. There was slight variations with (C_x/U) on the suction surface and little or no variations on the pressure surface. The present data were in qualitative agreement with that reported by Dunn and Hause [33] where stator heat-transfer data was reported both with and without a rotor present. Their data, however, indicated some sensitivity to the presence of the rotor on both the suction and pressure surface heat tranfer.

Conclusions

An extensive body of experimental data and analytical results for an axial turbine stage have been presented which provide detailed information on (*a*) the nature of the unsteadiness in the midspan flow over the rotor and the stator due to rotor-stator interaction, and (*b*) the impact of this unsteadiness on the stator midspan, time-averaged heat transfer. Specific conclusions in each of these areas were as follows:

Rotor-Stator Aerodynamic Interaction:

1 The stator midspan, time-averaged pressure distribution was in agreement with potential flow, and it was independent of rotor speed and only a very weak function of rotor-stator axial gap.

2 The rotor midspan, time-averaged pressure distribution was in excellent agreement with potential flow over a wide range of incidence, and it was only a weak function of rotor-stator axial gap.

3 The unsteady pressures on the stator at the 15 percent gap were as high as ±15 percent of the dynamic pressure with waves propagating both upstream and downstream on the suction surface.

4 The unsteady pressures on the rotor leading edge at the 15 percent gap were as high as ±80 percent of the incident relative dynamic pressure.

5 Unsteady stator trailing edge loading was observed to occur at the reduced frequencies present in this experiment (k = 1.9 to 2.7), and it is probably a required feature in any analytical model of rotor-stator interaction.

6 The variation of the fluctuating pressure on the stator with axial gap was well predicted by a steady rotor potential flow calculation.

7 The fluctuating pressure on the rotor was of a much larger amplitude than could be explained by the stator potential flow alone, and its decay with increased axial gap was similar to that of wake decay ($\approx x^{-1/2}$).

8 The stator boundary layer (as evidence by thin film gages) evolved from laminar, to transitional (with Tollmien-Schlichting waves), to turbulent, all with a periodic oscillation at rotor passing frequency.

9 The Tollmien-Schlichting waves were evident in the high response pressure transducer output.

10 The rotor suction surface boundary layer varied periodically between turbulent and laminar flow as it passed into and out of the stator wakes. This was particularly evident when the rotor was at negative incidence.

11 The instantaneous high or low pressures on the rotor suction surface occurred when the rotor was between or within the stator wakes, respectively.

12 No evidence was found to indicate that either the stator or the rotor was experiencing periodic separation and reattachment due to rotor-stator interaction.

Unsteady Effects on Stator Heat Tranfer:

1 At the 65 percent gap, the stator suction surface Stanton number was initially at a laminar level, went through transition, and was at a turbulent level to the trailing edge.

2 At the 65 percent gap, the laminar and turbulent suction surface Stanton number levels were in good agreement with a theoretical prediction.

3 At the 15 percent axial gap (on the suction surface), the same laminar, transitional, and turbulent flow was observed but the Stanton number was higher by typically 25 percent.

4 At both axial gaps, the transition location on the suction surface, as indicated by the Stanton number distributions, was very close to that indicated by the thin film gages and by the high response pressure transducers.

5 The pressure surface Stanton number distributions indicated transitional flow along the entire surface at both axial gaps and a much smaller increase due to reduced axial gap.

6 The stator Stanton number distribution was only a very weak function of rotor speed.

Acknowledgments

The work reported here was performed under Air Force contract under the direction of Dr. Kervyn Mach (APL/POTC), project engineer, Contract Number F33615-80-2008.

The authors are indepted to many people for the successful completion of the program and, in particular, to Dr. Kervyn Mach (AFAPL) for generating Figs. 10 and 11, to Mr. John Kostic for helping in the rig assembly, to Mr. Kenneth Dauphinais for writing the data reduction software and for doing the data reduction, to Mr.Charles Coffin for building the heat transfer models, and to the grace of God.

References

1 Kemp, N. H. and Sears, W. R., "Aereodynamic Interference Between Moving Blade Rows," *J. Aero. Sci.*, Vol. 20, No. 9, Sept. 1953, pp. 585–597.

2 Kemp, N. H. and Sears, W. R., "The Unsteady Forces Due to Viscous Wakes in Turbomachines," *J. Aero. Sci.*, Vol. 22, No. 7, July 1955, pp. 478–483.

3 Giesing, J. P., "Nonlinear Two-Dimensional Unsteady Potential Flow with Lift," *J. Aircraft*, Vol. 5, No. 2, Mar.-Apr. 1968, pp. 135–143.

4 Giesing, J. P., "Nonlinear Interaction of Two Lifting Bodies in Arbitrary Unsteady Motion," ASME *Journal of Basic Eng.*, Sept. 1968, pp. 387–394.

5 Parker, R., "Calculation of Flow Through Cascades of Blade Having Relative Motion and the Generation of Alternating Pressures and Forces Due to Interaction Effects," *Proceedings of the Institute of Mechanical Engineering*, Vol. 182, Pt. 1, No. 11, 1967-68, pp. 229-242.

6 Parker, R., "Pressure Fluctuations Due to Interaction Between Blade Rows in Axial Flow Compressors," *Proceedings of the Institute of Mechanical Engineering*, Vol. 183, Pt. 1, No. 7, 1968-89, pp. 154-164.

7 Parker, R., "Relation Between Blade Row Spacing and Potential Flow Interaction Effects in Turbomachines," *Proceedings of the Institute of Mechanical Engineering*, Vol. 184, Pt. 3G, No. 11, 1969-70, pp. 1-8.

8 Parker, R. and Watson, J. F., "Interaction Effects Between Blade Rows in Turbomachines," *Proceedings of the Institute of Mechanical Engineering*, Vol. 186, No. 21, 1972, pp. 331-340.

9 Gostelow, J. P., "Trailing Edge Flows Over Turbomachine Blades and the Kutta-Joukowsky Condition," ASME Paper No. 75-GT-94, Mar. 1975.

10 Satyanarayana, B. and Davis, S., "Experimental Studies of Unsteady Trailing-Edge Conditions," *AIAA Journal*, Vol. 16, No. 2, Feb. 1978, pp. 125-129.

11 *AGARD Conference Proceedings No. 177*, Unsteady Phenomena in Turbomachinery, 46th PEP Meeting, Sept. 22-26, 1975.

12 Adachi, T. and Murakami, Y., "Three-Dimensional Velocity Distribution between Stator Blades and Unsteady Force on a Blade due to Passing Wakes," JSME, Vol. 22, No. 170, Aug. 1979, pp. 1074-1082.

13 Gallus, H. E., Lambertz, J., and Wallmann, T., "Blade-Row Interaction in an Axial Flow Subsonic Compressor State, ASME JOURNAL OF ENGINEERING FOR POWER, Jan. 1980, Vol. 102, pp. 169-177.

14 Scholz, N., *Aerodynamics of Cascades*, Translated and revised by A. Kline, AGARD-AG-220, pp. 341-344.

15 Evans, R. L., "Boundary Layer Development on an Axial-Flow Compressor Stator Blade," ASME JOURNAL OF ENGINEERING FOR POWER, Vol. 100, Apr. 1978, pp. 287-293.

16 Smith, L. H., "Casing Boundary Layers in Multistage Compressor," *Flow Research in Blading*, edited by J. S. Dzung, Mar. 1969.

17 Mikolajczak, A. A., "The Practical Importance of Unsteady Flow," Paper No. 1 in reference [11].

18 Hetherington, R. and Moritz, R. R., "Influence of Unsteady Flow Phenomena on the Design and Operation of Aero Engines," Paper No. 2 in reference [11].

19 Kosyak, Yu. F., Sobolev, S. P., Yushkovich, Yu. E., Golamn, V. I., and Petrusenko, P. S., "Selecting the Axial Clearances Between the Stages of a Turbine," *Thermal Engineering*, Vol. 3, p. 22, from Tepolenergetika, Vol. 20, No. 3, 1973, pp. 17-18.

20 Messegee, J., "Influence of Axial and Radial Clearances on the Performance of a Turbine stage with Blunt Edge Non-Twisted Blades," A. E. thesis, U.S. Naval Postgraduate School, Sept. 1967.

21 Due, H. F., Easterling, A. E., and Rogo, C., "Cascade Research on Small, Axial High-Work, Cooled Turbine," ASME Paper No. 75-GT-62, Mar. 1975.

22 Okapuu, U., "Some Results From Tests on a High Work Axial Gas Generator Turbine," ASME Paper No. 74-GT-81, Mar. 1974.

23 Dring, R. P., and Joslyn, H. D., Measurements of Turbine Rotor Blade Flows," ASME JOURNAL OF ENGINEERING FOR POWER, Vol. 103, No. 2, Apr. 1981, pp. 400-405.

24 Dring, R. P., Joslyn, H. D., Hardin, L. W., and Wagner, J. H., "Research on Turbine Rotor-Stator Aerodynamic Interaction and Rotor Negative Incidence Stall," AFWAL-TR-81-2114, Components Branch (POTC) Turbine Engine Division (POT), Aero Propulsion Laboratory, Wright Aeronautical Laboratories, Wright-Patterson Air Force Base, Ohio.

25 Caspar, J. R., Hobbs, D. E., Davis, R. L., "Calculation of Two-Dimensional Potential Cascade Flow Using Finite Area Methods," *AIAA Journal*, Vol. 18, No. 1, Jan. 1980, pp. 103-109.

26 Dring, R. P., Blair, M. F., Joslyn, H. D., An Experimental Investigation of Film Cooling on a Turbine Rotor Blade, ASME JOURNAL OF ENGINEERING FOR POWER, Vol. 102, No. 1, Jan. 1980, pp. 81-87.

27 Schlichting, H., *Boundary Layer Theory*, 6th ed., 1968.

28 Fink, M. R., "Prediction of Airfoil Tone Frequencies," *J. Aircraft*, Vol. 12, No. 2, Feb. 1975, pp. 118-120.

29 Erens, P. J. and Chasteau, V. A. L., "Laminar Boundary-Layer Response to Freestream Disturbances," *AIAA Journal*, Vol. 12, No. 1, Jan. 1974, pp. 93-94.

30 Blair, M. F. and Werle, M. J., "The Influence of Free-Stream Turbulence on the Zero Pressure Gradient Fully Turbulent Boundary Layer," AFSOR Report, Sept. 1980.

31 Graziani, R. A., Blair, M. F., Taylor, J. R., and Mayle, R. E., "An Experimental Study of Endwall and Airfoil Surface Heat Transfer in a Large Scale Turbine Blade Cascade," ASME JOURNAL OF ENGINEERING FOR POWER, Apr. 1980, Vol. 102, pp. 257-267.

32 Edwards, D. E., Carter, J. E., and Werle, M. J., "Analysis of the Boundary Layer Equations Including a New Composite Coordinate Transformation," UTRC Report No. UTRC81-30, 1981.

33 Dunn, M. G. and Hause, A., "Measurements of Heat Flux and Pressure in a Turbine Stage," ASME Paper No. 81-GT-88, presented at the Gas Turbine Conference, Houston, Texas, Mar. 1981.

APPENDIX I

Stator Wake Characterization

The stator wake at midspan was documented to provide a basis for future analytical efforts in the area of the gust response of the rotor. The wake documentation was accomplished using a 5-hole probe at midspan at a flow coefficient (C_x/U) of 0.78. The circumferential traverse was conducted at a plane 17 percent of the stator axial chord axially aft of the stator trailing edge. The traverse was by necessity conducted with the 65 percent rotor-stator axial gap. The wake shape was analyzed using a linear variation for the "inviscid" velocity across the wake to establish the "ideal" velocity at the wake center (V_c). The stator wake was summarized by the following parameters:

$$Y_2 = 0.036$$

$$\delta_w/\tau = 0.045$$

$$\delta^*/\tau = 0.0172$$

$$\theta/\tau = 0.0149$$

$$H = 1.154$$

$$(V_c - V_m)/V_c = 0.182$$

$$K' = \frac{\dfrac{V_c - V_m}{V_c}}{1 - \dfrac{1}{H}} = 1.358$$

Table 1—Airfoil Geometry and Nominal Operating Conditions, $(C_x/U) = 0.78$

Airfoil	Stator vane	Rotor blade
Number	22.0	28.0
B_x (ins)	5.93	6.34
(τ/B_x)	1.30	0.96
Span (ins)	6.00	6.00
Stagger angle (deg)	49.5	32.7
(Span/B_x)	1.01	0.95
Inlet flow angle (deg)	90.0	40.0
Exit flow angle (deg)	22.5	25.5
Re(B_x, C_2 or W_2)	5.9×10^5	5.5×10^5

$C_x = 75$ ft/s ($\approx$ const)
$N = 410$ rpm (variable)

Influence of Free-Stream Turbulence on Boundary Layer Transition in Favorable Pressure Gradients

M. F. Blair
Senior Research Engineer,
Gas Turbine Technology Group,
United Technologies Research Center,
East Hartford, Conn. 06108
Mem. ASME

Results from an experimental study of large-scale, two-dimensional incompressible transitional boundary layer flows are presented. Tests were conducted on a heated flat wall with a zero pressure gradient and for two levels of "sink" streamwise acceleration; $k = \nu/U^2\ \partial U/\partial x = 0.2$ or 0.75×10^{-6}. Free-stream turbulence intensity levels ranged from approximately 0.7 to 5 percent with limited data obtained outside these values. Convective heat-transfer distributions, laminar, transitional, and fully turbulent boundary layer mean velocity and temperature profile data, and free-stream turbulence intensity distributions are presented. Boundary layer integral quantities and shape factors are also given. Transition onset Reynolds number data obtained for this program agreed well with the results of other experimental and theoretical studies for both zero pressure gradient and accelerating flows. Comparisons of the profile data and wall heat-transfer distribution data indicated that fully turbulent mean velocity profiles were achieved upstream of fully turbulent wall heat-transfer rates.

Introduction

Accurate prediction of the development of airfoil boundary layers is an important aspect of the design of gas turbine blading. The quality of these predictions can influence the airfoil aerodynamic efficiency and, through its impact on the cooling design, both the cycle efficiency and the hardware durability. One feature of the airfoil boundary layer development that has proved to be particularly difficult to compute is the region of transitional flow. Accurate prediction of both the onset and the length of the transitional flow can be very important; experimental evidence indicates that for certain gas turbine airfoils the boundary layer is transitional for over half the chord [1].

Two important factors which affect the onset and length of boundary layer transition on gas turbine airfoils are pressure gradient and mainstream turbulence level. These are but two of many phenomenon which influence transition in the actual engine environment where local separation bubbles, film cooling injection, boundary layer/shock interaction, surface curvature, wall/free-stream temperature ratios, surface roughness, and Mach number related effects may all be involved. In an effort to isolate mainstream turbulence and pressure gradient effects from this much more complex matrix of interacting phenomenon, numerous previous analytical and experimental studies have focused on the simplified case of accelerating, incompressible, two-dimensional flows along flat walls (e.g., references [2–6]; also see references [7] and [8] for extensive reviews of the available literature). These studies have shown that the net result of the combined influences of turbulence and pressure gradient is dependent upon the sign of the pressure gradient and the relative strengths of the two effects. For adverse pressure gradients both the turbulence and deceleration hasten the transition process. Because of this "compression" of the process the onset and length of transition can currently be predicted quite satisfactorily for decelerating flows [9]. For favorable pressure gradients, however, the flow acceleration acts to stabilize the boundary layer and tends to counteract the effect of the free-stream turbulence. This interplay of pressure gradient and turbulence can influence both the onset and the length of transition and the heat-transfer distribution of the transitional flow. Nearly all previous studies of flat wall transition with pressure gradient, however, have dealt with measurement or prediction of transition for adiabatic flows. As a result there presently exists very little information regarding the influence or relative importance of pressure gradient and turbulence on wall heat transfer through transition.

The present program was conducted to provide a set of fundamental wall heat-transfer, mean velocity, and temperature boundry layer profile data for zero pressure gradient and accelerating transitional flows with high free-stream turbulence. It is anticipated that these data will prove useful to workers in the field of boundary layer computation for the evaluation of analytical models of transitional flows.

The present data were obtained in incompressible, two-dimensional flat wall flows with large-scale boundary layers and only very slight wall heating (negligible density ratio effects). In order to focus on the interaction of the flow acceleration and turbulence level, the experimental test cases

Contributed by the Gas Turbine Division of THE AMERICAN SOCIETY OF MECHANICAL ENGINEERS and presented at the 27th International Gas Turbine Conference and Exhibit, London, England, April 18–22, 1982. Manuscript received at ASME Headquarters November 9, 1981. Paper No. 82-GT-4.

were selected such that the relative strengths of these two effects were about equal. To simplify the experiment as much as possible, testing was conducted for flows with zero or near constant accelerations ($k = \nu/U^2\ \partial U/\partial x = 0$, 0.2 and 0.75 $\times$ 10^{-6}) along the test wall. Turbulence levels ranging from 0.7 to 5 percent were generated through the use of rectangular bar grids. For the various test cases, measurements were obtained of the free-stream turbulence intensity, scale and spectrum, the streamwise test pressure distributions, the wall heat-transfer distributions, and for the accelerating cases, the mean velocity and temperature profiles.

The data for transition onset location obtained for this program agreed very well with the well-known theoretical predictions of van Driest and Blumer [6]. For the test cases with longer transition regions the mean velocity distributions appeared to assume fully turbulent characteristics earlier than did the boundary layer turbulence distributions. For these extended transition test cases the length of transitional flow as determined form the wall heat-transfer data was considerably longer (up to 70 percent) than was inferred from the associated velocity profile shape factor data.

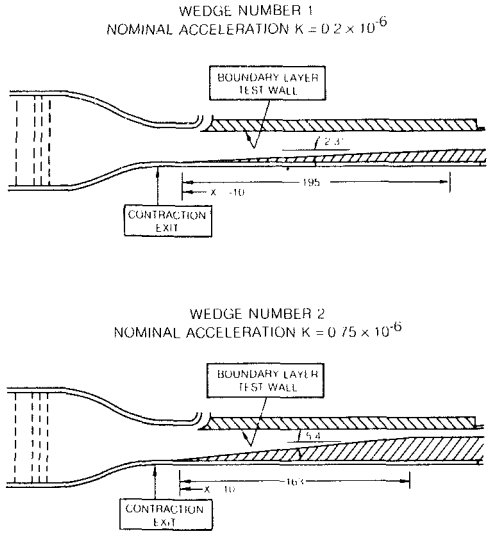

Fig. 1 Schematic of test configurations

Experimental Apparatus

Wind Tunnel and Heat-Transfer Test Surface. All experimental data for the present investigation were obtained in the United Technologies Research Center (UTRC) Boundary Layer Wind Tunnel. A complete description of this facility including measurements documenting the tunnel flow uniformity and two-dimensionality of the test boundary layers was given in reference [10]. The boundary layer test surface consisted of a flat, uniform heat flux electrically heated plate instrumented for both heat transfer and static pressure measurements. A description of the construction details of the heat-transfer plate and results from a series of zero pressure gradient evaluation tests can be found in reference [11]. Two wedge-shaped inserts, designed to produce constant acceleration levels along the test surface, served as the lower walls of the test section for the accelerating test cases. Diagrams of the test section configurations with the wedges installed are shown in Fig. 1.

To produce initially laminar, two-dimensional test boundary layers and to avoid premature transition, a 4 $\times$ 1 elliptical leading edge piece was installed onto the front of the test surface. The design of this leading edge was such that the test boundary layers grew from a short (4.3 cm) unheated starting length upstream of the heated test surface. Details of the leading edge and its adjustment are given in references [10] and [11].

Turbulence Generating Grids. As described in references [10] and [11], the wind tunnel had a relatively low residual test section turbulence level (1/4 percent). Higher turbulence levels required for this study were generated by inserting various square array biplane grids constructed from rectangular bars at the entrance to the main tunnel contraction. The advantage of this arrangement was that the generated turbulence was very homogeneous within the test section. The grids will be referred to as grid 1, 2, 3, and 4, corresponding to mesh widths, M, of 2.24, 6.51, 17.79, and 22.86 cm. The minimum turbulence configuration (no grid) will be referred to as grid 0. Details of the grid configurations and the characteristics of their turbulence in zero pressure gradient flow are given in references [10] and [11].

Boundary Layer Probes and Traverse Control. Boundary layer mean velocity profile data were measured using United Sensor Model BA-0.020 impact probes with flattened tips. Mean temperature data were measured with miniature thermocouple probes designed following reference [12]. The results of reference [12] indicate that a probe of this design was virtually free of wire conduction errors and was capable

Nomenclature

C_L = tunnel centerline
c_p = specific heat at constant pressure
h = heat-transfer coefficient
H = shape factor, δ^*/θ
K = acceleration parameter
Pr = molecular Prandtl number
Pr_t = turbulent Prandtl number
q = heat flux
Re_θ = Reynolds number based on boundary layer momentum thickness
Re_{δ^*} = Reynolds number based on boundary layer displacement thickness
St = Stanton number, $h/\rho_e U_e c_p$ (based on local velocity)
t = temperature
T = total turbulence intensity
T^+ = dimensionless temperature
u',v',w' = streamwise, normal, and transverse fluctuating velocities
U = velocity
U^+ = dimensionless velocity
U_τ = friction velocity
x = distance from test surface leading edge
y = distance from wall
Z = transverse distance from tunnel C_L
Y^+ = dimensionless distance from wall
Λ_θ = Pohlhausen acceleration parameter
δ = boundary layer thickness
δ^* = displacement thickness
θ = momentum thickness
ν = kinematic viscosity
ξ = unheated starting length
ρ = fluid density

Subscripts

e = freestream
w = wall
0 = value upstream of acceleration
0.995 = where $U = 0.995\ U_e$

Table 1 Test conditions

Flow condition	$KX10^6$	Grid	T nominal	U/U_0 m/s	q_{wall} watts/cm^2	t_e °C
1	0.0	0	1/4%	30.3	0.057	20.1
2	0.0	1	1%	30.3	0.087	20.4
3	0.0	2	2%	30.3	0.085	19.6
4	0.20	1	1%	15.9	0.051	22.4
5	0.20	2	2%	15.9	0.053	23.2
6	0.75	2	2%	9.9	0.048	26.3
7	0.75	3	4%	9.9	0.052	23.9

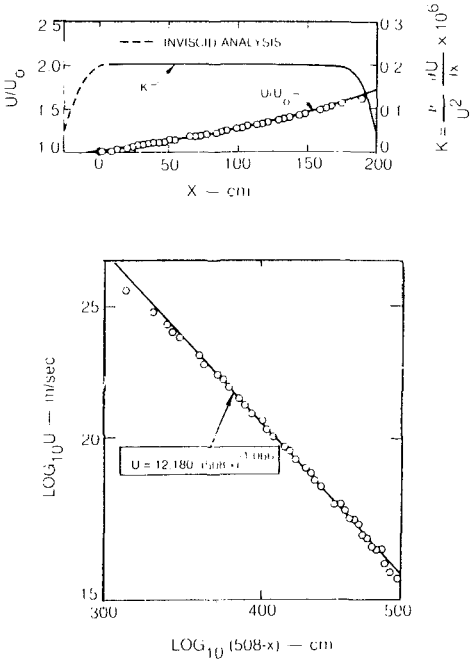

Fig. 2 Test wall velocity distribution—wedge # 1

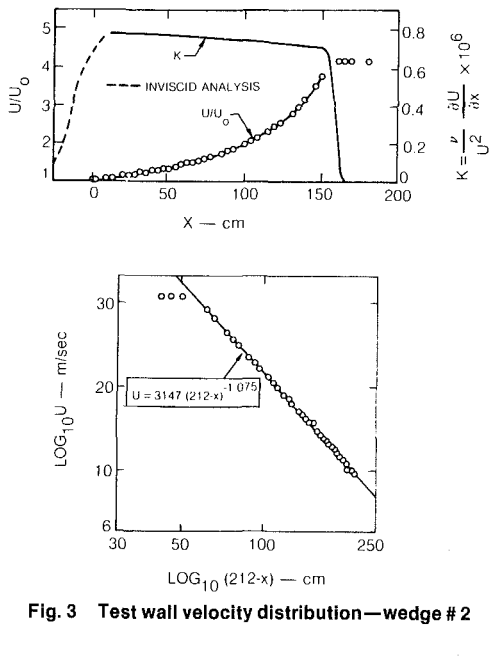

Fig. 3 Test wall velocity distribution—wedge # 2

of measuring boundary layer mean temperature profile data into the viscous sublayer region.

Movement of the boundary layer probes was achieved using a L. C. Smith ball/screw traverse drive capable of resolving probe location to within 0.01 mm. A telescope sighted through the plexiglass tunnel sidewall was used to accurately position probes relative to the test wall. Estimated absolute accuracy of measured probe distance from the test surface was 0.03 mm for any location in the test boundary layers.

Experimental Test Conditions

Test Section Velocity and Acceleration Distributions. The test section wedge inserts were designed to produce sink flow with near constant acceleration parameters, K. Sample velocity distributions measured with these wedge inserts installed are presented in Figs. 2 and 3. The test velocity distributions measured for the various grids agreed with the sample data of Figs. 2 and 3 within ±1 percent and are omitted for clarity. The following curve fits, shown in Figs. 2 and 3, provide accurate representations of the measured velocity data:

$$\text{wedge 1} \qquad U = 12{,}180(508\text{-}X)^{-1.066} \tag{1}$$

$$\text{wedge 2} \qquad U = 3{,}147(212\text{-}X)^{-1.075} \tag{2}$$

where U is in m/s and x is in cm. For both wedges the exponent of the velocity curve fit was near -1 (ideal sink flow), indicating that near constant acceleration distributions were achieved. Also shown in Figs. 2 and 3 are plots of the velocity ratios (U/U_0) and acceleration parameters (K). These curves were computed from equation (1) or (2) for their respective wedges.

For the constant velocity test cases the lower wall of the test section was adjusted to produce constant static pressure along the test wall.

The Test Matrix. Convective heat-transfer coefficients, wall static pressure distributions, and free-stream turbulence intensity, spectral, and longitudinal integral scale distributions were measured for the seven acceleration/turbulence grid combinations listed in Table I. For all test cases the test section static pressure was very near ambient.

In addition, for the accelerating test cases (flow conditions 4–7), the mean velocity and temperature boundary layer profiles were documented. These particular combinations were selected to parametrically cover a wide range of both acceleration and turbulence intensity.

Free-Stream Turbulence Intensity Distributions. Measurements of multicomponent turbulence intensity distributions for the various generating grids were obtained with TSI Model 1243 X hot film probes and a TSI series 1050 linearized, constant temperature, 2-channel anemometer system. The system employed a model 1052 polynomial linearizer, a model 1063 sum/difference unit and model 1076 RMS voltmeter. Descriptions of the anemometer and signal processing equipment used to obtain these data as well as descriptions of the techniques employed to reduce and interpret the measured quantities can be found in reference [11]. Surveys of the turbulence distributions were obtained over five planes along the test section. In each plane, measurements were obtained at three transverse locations ($Z = C_L$ and ± 15 cm) and at three uniformly spaced vertical locations.

A sample multicomponent (u', v', and w') turbulence intensity distribution for flow condition 5 (nominal turbulence of 2 percent) is presented in Fig. 4. All nine turbulence measurements obtained in the plane at each streamwise location fell within the plotting symbols. The data of Fig. 4, which were typical of the various test cases, demonstrate that the free-stream turbulence was nearly isotropic. For all test cases, the relationship between the magnitudes of the three components in the test section was $v' > w' > u'$ with the slight differences between the various components decreasing with increasing x.

Total turbulence distributions were calculated from the multicomponent turbulence data for the various flow conditions and are presented in the lower half of Fig. 4 for the four accelerating configurations. As indicated by the vertical bars of Fig. 4, the range of spatial nonuniformity of the turbulence for grid 3 ranged from ± 10 percent at $X = 0$ to near 0 by $X = 70$ cm. The results shown in Fig. 4 indicate that the total turbulence for grid 2 (flow conditions 5 and 6) was only slightly dependent on the acceleration level. The turbulence intensity distributions for the constant velocity cases were in close agreement with the distributions with acceleration and are omitted to avoid crowding on the figure. For flow condition 1 (grid 0) the free-stream turbulence level was approximately 1/4 percent. Details of these zero pressure gradient measurements are given in reference [10].

Turbulence Length Scale and Spectral Distributions. Measurements of the streamwise integral scale and power spectral density distributions for the various grids were obtained using single sensor TSI model 1220 hot film probes, a TSI 1050 constant temperature anemometer system, a Saicor Model SAI 42 correlator and a Spectral Dynamics Model SD 340 narrow-band spectrum analyzer. Autocorrelation measurements indicated that the growth of the streamwise integral scale was considerably faster for the accelerating cases than for the zero pressure gradient cases documented in reference 10 (for some grids growth rates were more than doubled). For all cases, the spectral distribution measurements were in good agreement with the von Karman one-dimensional spectrum. This result indicates that the turbulence had the characteristics of classical grid generated turbulence and that the spectral distributions were not altered by the flow acceleration. Details of both the length scale and spectral data are available in reference 11.

Two-Dimensionality of the Test Boundary Layers. For the accelerating cases (flow conditions 4–7) transitional boundary layer mean velocity and temperature profile data were obtained along with wall heat flux measurements. Profile data were obtained downstream of transition only for the zero pressure gradient test cases. These zero pressure gradient data are available in references [10] and [13]. For each of the measured profiles a thermal energy balance was computed. This balance consisted of a ratio between the total convective heat generated per-unit-tunnel-width upstream of any profile location to the measured thermal energy in the profile at that location.

$$\int_0^{\delta} \rho U c_P (T - T_e)\, dy \Big/ \int_0^{x} q\, dx$$

Convergence or divergence (non-two-dimensionality) of the test surface boundary layer flow would result in measured values of this ratio greater or less than one. An examination of these ratios revealed that the thermal energy balance was within approximately ± 10 percent of unity for all the measured profiles except those midway in the transition region. There deviations from unity on the order of ± 20 percent were calculated apparently as a result of the intermittent transition process causing imperfect time averaging of the pitot probe system. In general, the thermal balance

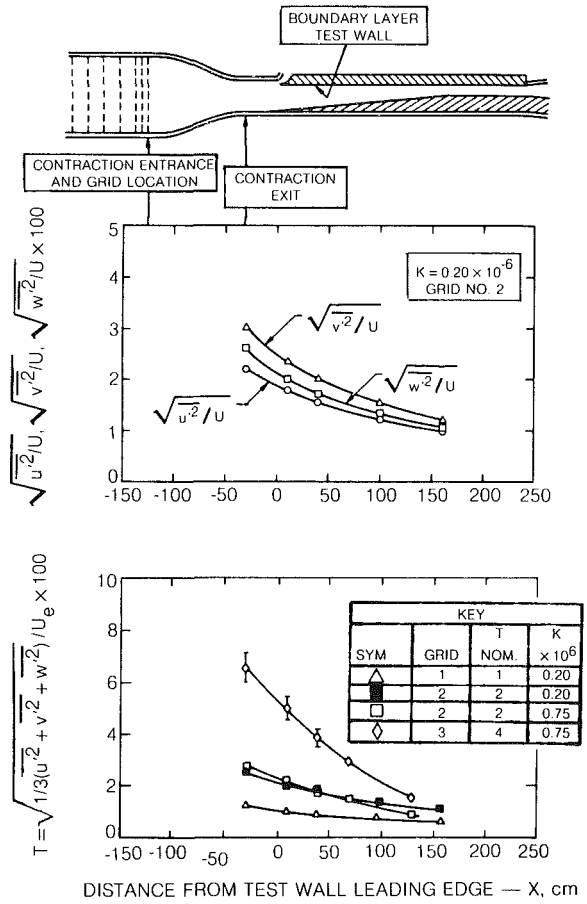

Fig. 4 Turbulence intensity distributions

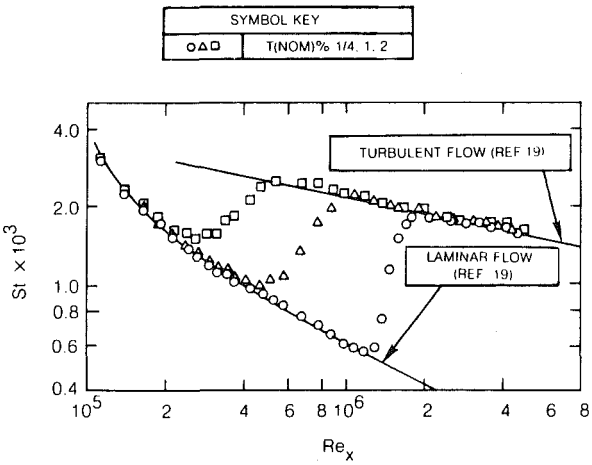

Fig. 5 Heat-transfer distributions for zero pressure gradient flow

comparisons indicate a high degree of accuracy, consistency and two-dimensionality for the measured profiles.

Results and Discussion

Transition Location. Two independent methods of determining the location of the onset and length of boundary layer transition were provided by the measurements of this study. For all test flow conditions the measured heat-transfer distributions were employed to locate both the onset (XT_0) and termination (XT_t) of transition. The location of the onset of transition was determined as the streamwise station where

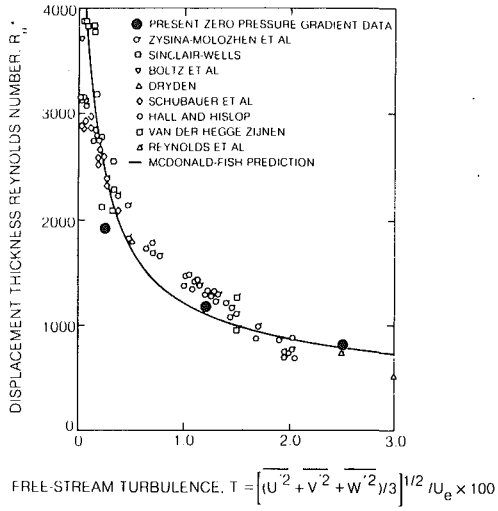

Fig. 6 Effect of free-stream turbulence upon the transition Reynolds number for zero pressure flow

the measured Stanton number first exceeded the laminar heat-transfer rate expected for the test velocity distribution (XT_0 – heat transfer). Transition was judged to be complete where the measured Stanton numbers merged with the expected fully turbulent heat transfer distribution (XT_t – heat transfer). For the accelerating test cases, the measured mean velocity and temperature profile data provided a second technique for locating the region of transition. The location of the onset of transition was inferred to coincide with the streamwise station at which the boundary layer shape factor dropped below the laminar value expected for the particular test acceleration level (XT_0 – profile). Transition was inferred to be complete where the measured shape factor first agreed with the expected turbulent shape factor (XT_T – profile).

Zero Pressure Gradient Flow. The heat-transfer distributions measured for flow conditions 1 through 3 are presented in Fig. 5. These data clearly show a forward movement of transition with increasing turbulence level. The absolute accuracy of these measurements is believed to be very good because the Stanton numbers measured both upstream and downstream of transition are in excellent agreement with the laminar or turbulent distributions of Kays [19]. The transition origin boundary layer Reynolds numbers determined from the heat-transfer distributions of Fig. 5 are presented in Fig. 6. For this figure the displacement thickness Reynolds number ($Re_{\delta}{}^*$) was calculated by assuming constant velocity laminar boundary layer development from the plate leading edge to the measured location of the onset of transition (XT_0 – heat transfer). Figure 6 includes measurements from eight other sources which all used techniques other than heat transfer to determine the onset of transition. Also given in Fig. 6 is the transition onset prediction of the McDonald-Fish [9] boundary layer computation scheme. The results from the present study for nominal $T = 1$ and 2 percent turbulence (exact values of turbulence at XT_0 were $T = 1.2$ and 2.5 percent, respectively) are in excellent agreement with the other data and the prediction of Fig. 6. For $T = 0.25$ percent (grid 0) the present transition onset measurement indicates slightly earlier transition than either the other data or the McDonald-Fish prediction. The cause of this early transition was that for this lowest test turbulence level transition was not two-dimensional but began near the tunnel side-walls (possible corner flow effects) and progressively encroached into the flat wall test flow. The data of Fig. 6 show that for the two higher turbulence levels the present test facility and instrumentation techniques produced transition results consistent with a large number of other experiments.

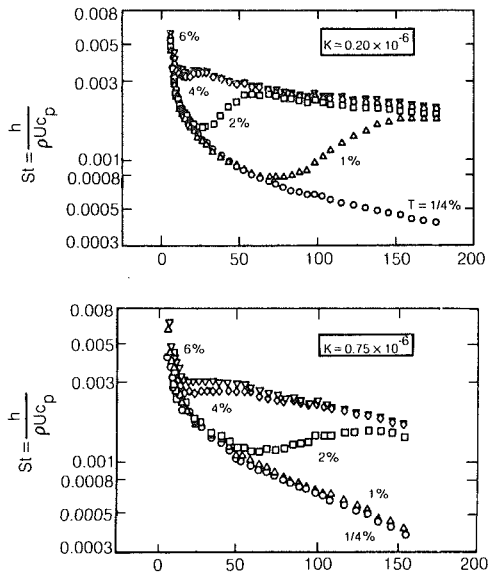

Fig. 7 Heat-transfer distributions for accelerating flows

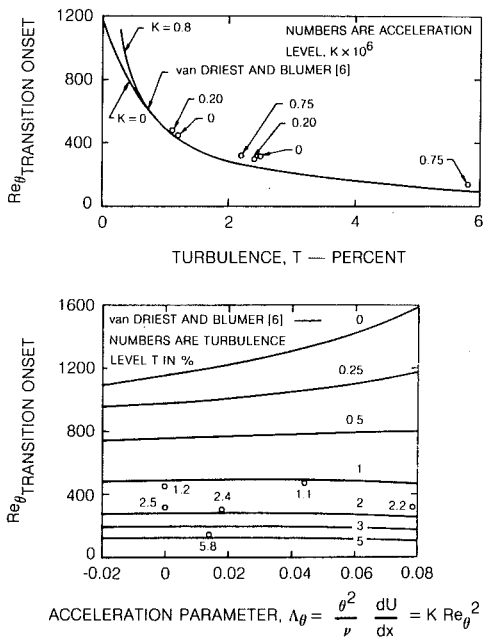

Fig. 8 Combined influence of streamwise pressure gradient and free-stream turbulence intensity on boundary layer transition

Accelerating Flow Test Cases. As previously discussed, the location of the onset and termination of transition for the accelerating test cases were determined both through the heat transfer and boundary layer profile measurements. The heat-transfer distributions measured for flow conditions 4–7 are presented in Fig. 7. To demonstrate the fact that the measurements obtained for these 4 accelerating flow conditions are part of a consistent trend, additional heat transfer distribution data obtained with no turbulence grid (grid 0) and with turbulence grids 1, 3 and 4 are included in Fig. 7. Freestream turbulence distribution data were not obtained for grids 0 or 4 (○ and ▽ symbols in Fig. 7) but measurements obtained in zero pressure gradient flow [10] indicate that these grids produced approximately 1/4 and 6 percent turbulence, respectively. The heat-transfer distributions presented in Fig. 7 demonstrate the interplay of the effects of acceleration and turbulence on the transition process. For grid 0 (T<1/4

percent), the boundary layers apparently remained laminar for the entire test length for both acceleration levels. In contrast, for very high turbulence the onset of transition moved far upstream. With grid 4 installed, transition began about 7 cm from the plate leading edge for both acceleration levels. There were, however, significant differences between the heat-transfer distributions measured for wedges 1 and 2. For the higher acceleration level (wedge 2), transition was suppressed for the entire test flow for both the grid 0 and grid 1 test cases. In addition, for grid 2 the length of the transition region was much greater for the more highly accelerated test case. The data of Fig. 7 also indicated that, as expected from the results of reference [13], for the fully turbulent regions of the various flows the free-stream turbulence level increased the heat transfer.

Mean velocity and temperature boundary layer profile data were obtained for flow conditions 4–7 for approximately twelve streamwise stations per test case. Integral thicknesses (δ^* and θ) and shape factors were calculated from these profile data and are available in reference [11]. In addition, the boundary layer data are available in tabular form upon request.

In Figs. 8(*a*) and 8(*b*), the present measurements for transition onset Reynolds number are compared to the theoretical predictions of van Driest and Blumer [6]. These predictions are presented in two formats: for Fig. 8(*a*), the transition onset Reynolds number for a fixed acceleration (K) versus turbulence level (T); for Fig. 8(*b*), the transition onset Reynolds number for a fixed turbulence level versus the Pohlhausen acceleration parameter. For Fig. 8, the measured boundary layer momentum thicknesses were employed to compute both the Reynolds number and Pohlhausen parameter while the locations of the onset of transition were determined from the heat-transfer distributions. The local turbulence intensity or acceleration level at the transition location is indicated beside each data point. Also included in Figs. 8(*a*) and 8(*b*) are the zero pressure gradient data of the present study. $Re_{\theta transition}$ for these zero pressure gradient data were calculated by assuming constant velocity laminar boundary layer growth to the location of the onset of transition as indicated by the heat-transfer data. Agreement between the present results and the predictions of van Driest and Blumer is excellent for both the constant velocity and accelerating cases. Both the predictions and the present data indicate a relative insensitivity of transition onset Reynolds number to this range of acceleration at even modest turbulence levels. Recent measurements of transition onset in adiabatic flows by Abu-Ghannam and Shaw [14] are also in excellent agreement with the van Driest-Blumer predictions. It should be noted that these present results are in marked disagreement with the suggested correlations of Hall and Gibbings [2] and Dunham [15], both of which predict rapid increases in $Re_{\theta transition}$ with increasing Λ_θ.

Sample mean velocity and temperature boundary layer profile measurements obtained for flow condition 5 ($K = 0.2\times10^{-6}/T \approx 2$ percent), are presented in Fig. 9. In Fig. 9, the developing mean velocity and temperature profiles are presented in the form of velocity and temperature ratio versus $y/\delta_{0.995}$ along with the growth of the velocity boundary layer thickness ($\delta_{0.995}$) along the test wall. Both the velocity and temperature profiles of Fig. 9 demonstrate the progressive change from laminar-like distributions to "full" turbulent profiles.

Momentum and displacement thicknesses and shape factors calculated from the measured boundary layer profile data of flow condition 5 are presented in Fig. 10. The profiles measured at various transverse but fixed streamwise locations on the test surface are in good agreement with the centerline values. The spanwise uniformity, along with the thermal energy balance check discussed earlier indicates that the test

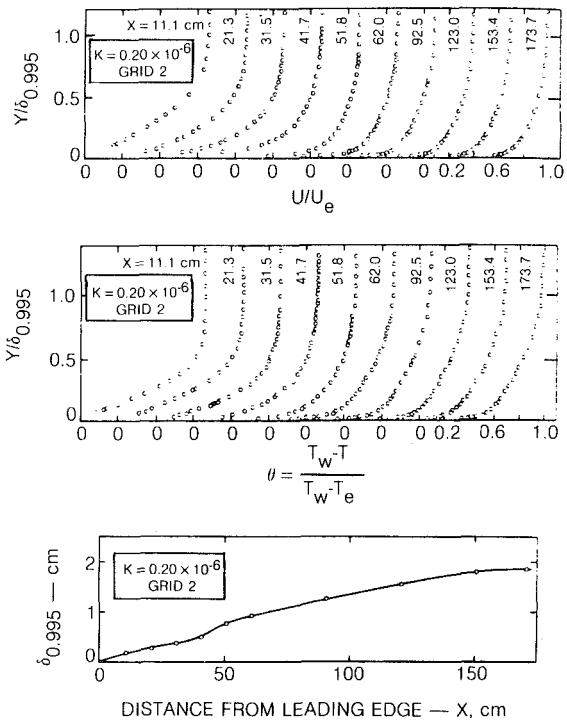

Fig. 9 Boundary layer profile development for T (NOM) = 2 percent

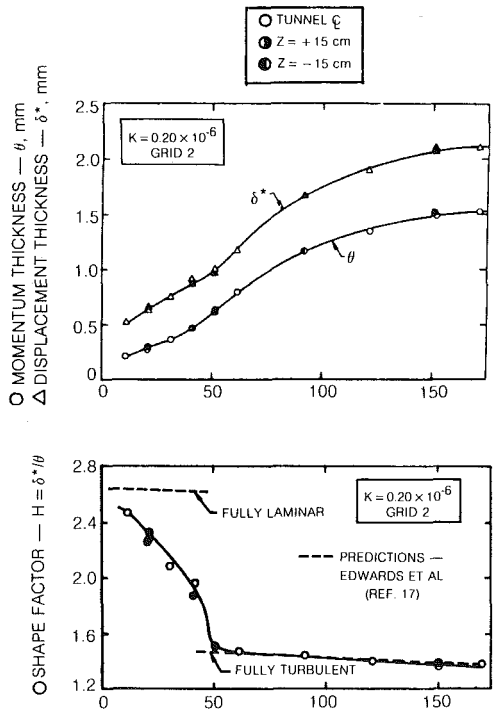

Fig. 10 Boundary layer integral thickness for T = 2 percent

boundary layer was highly two-dimensional. Shown in Fig. 10 are shape factor distributions for fully laminar and fully turbulent flow as predicted by the numerical boundary layer code of references [16] and [17] for the test velocity and wall heat flux distributions. The measured shape factors are in excellent agreement with the predicted fully turbulent values downstream of approximately X = 55 cm. Interpretation of

Table 2 Transition locations

Flow condition	XT_0 – cm (onset) Heat transfer	Profile	XT_T (termination) – cm Heat transfer	Profile	$XT_0 - XT_T$ (length) – cm Heat transfer	Profile
4	70	70	170	130	100	60
5	22	12	64	56	44	44
6	50	45	150	120	100	75
7	12	12	38	43	26	31

the most upstream profile data of Fig. 10 is difficult because of the experimental uncertainties associated with documenting these extremely thin boundary layers. The shape factor apparently was dropping rapidly by the first profile station (X = 11.1 cm). Within the accuracy allowed by the profile measurements, the shape factor data of Fig. 10 indicate that for flow condition 5, XT_0-profile ≈ 12 cm and XT_T-profile ≈ 56 cm.

Table 2 presents the measured locations of the origin and termination of transition for the various flow conditions as determined from both the heat transfer and profile data. Bearing in mind the uncertainties in the laminar profile measurements, comparisons of the locations of the onset of transition as indicated by the shape factor and heat transfer data show good agreement. For both test cases in which the turbulence intensity was high relative to the strength of the flow acceleration (flow conditions 5 and 7) the mean profile and wall heat-transfer distribution measurements were in very close agreement and indicated nearly identical transition termination (XT_T) locations. For both test cases in which the flow acceleration was relatively strong in relation to the turbulence intensity (flow conditions 4 and 6), however, there were significant differences in the transition length as indicated by the profile and heat-transfer measurements. For both flow conditions 4 and 6, the lengths of transitional flow as determined from the heat-transfer distributions were at least 1/3 longer than those indicated by the shape factor distributions. These limited results indicate that for cases with extended transitional flow the mean velocity profile reached a shape typical of a fully turbulent condition in a shorter length than was required for the boundary layer turbulence to assume its equilibrium structure. The wall heat transfer, which was dominated by the turbulent transport through the boundary layer, did not reach fully turbulent values until well downstream of the establishment of the fully turbulent mean velocity profile.

Figure 11 presents the velocity and temperature profile data of Figs. 9 and 10 in the universal turbulent coordinates of U^+ and T^+ versus Y^+. For the most upstream (laminar) profile (x = 11.1 cm), U_τ was determined from the slope of the mean velocity at the wall and the molecular viscosity. For the downstream (turbulent) profiles (x = 62.0, 94.5 and 173.7 cm), U_τ was determined from fits of the profile data to the zero pressure gradient law of the wall (for this relatively weak pressure gradient the "constants" in the law should be very close to their zero pressure gradient values). For the intermediate profiles, where no convenient technique for determining wall shear was available, U_τ was calculated using the two-dimensional von Karman momentum integral equation and the measured integrals of the mean velocity profiles. As can be seen from an examination of Fig. 11, there was an orderly change from laminar to fully turbulent velocity profiles with increasing distance along the wall. At x = 11.1 cm, the boundary layer was fully laminar with $U^+ = Y^+$ for $Y^+ \leq 20$. With the development of turbulent shear within the boundary layer, the profiles progressively assumed a more logarithmic-like shape with increasing x. For the most downstream profile (x = 173.7), the profile data fit the buffer region and logarithmic-wall laws for $Y^+ \leq 400$. The outer

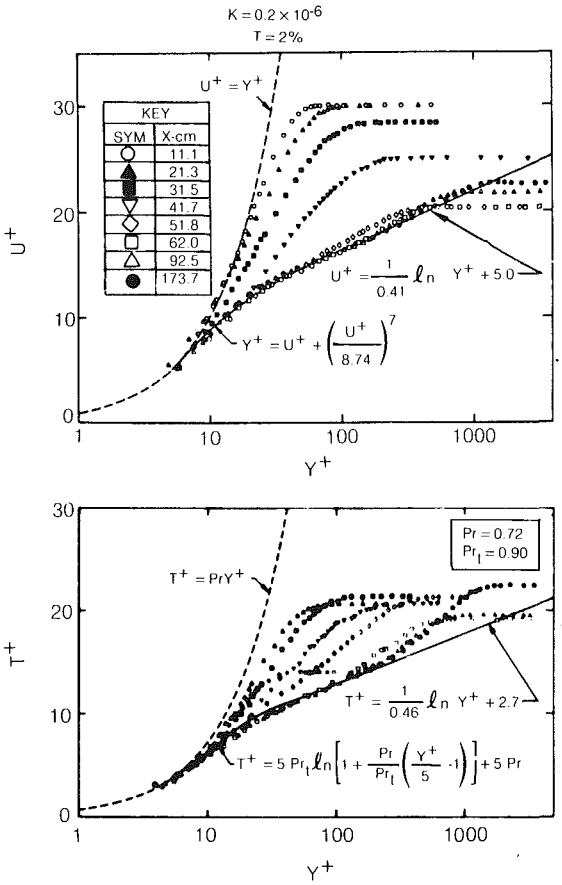

Fig. 11 Development of the mean velocity and temperature profiles along the test wall

region of this most downstream profile showed a weak wake appropriate for this low Reynolds number (Re_θ = 2470) and streamwise pressure gradient.

The mean temperature data are presented in the universal turbulent coordinates of T^+ versus Y^+ in the lower portion of Fig. 11. The dimensionless temperature (T^+) is a function of both the wall heat flux and skin friction. The friction velocities for these profiles were inferred from the respective velocity profiles. At the most upstream location (x = 11.1 cm), the mean temperature profile is seen to have been laminar-like and developing within the laminar velocity profile. At x = 11.1 cm, the laminar velocity profile extended to $Y^+ \approx 70$. The temperature profile at this same station extended to only $Y^+ \approx 40$. This difference between the velocity and temperature profile thicknesses at x = 11.1 cm resulted from the fact that there was a short but finite unheated length (ξ = 4.3 cm) on the leading edge of the heated test wall. At x = 11.1 cm the thermal and momentum boundary layers had not yet reached equilibrium. Similar measurements of a temperature profile developing within a velocity profile were presented by Blom [18]. For the profiles measured from x = 21.3–62.0 cm, the mean temperature profiles fell between the fully laminar and fully turbulent

limits. Note that the development of the transitional temperature profiles lagged that of the respective velocity profiles. This lag is clearly in evidence for $x = 51.8$ and 62.0 cm where the velocity profiles are in close agreement with the law of the wall while the temperature profiles exhibit no logarithmic region.

At the furthest downstream location ($x = 173.7$ cm) where the boundary layer was fully turbulent, the mean temperature profile agreed well with the buffer zone and logarithmic laws for $Y^+ \leq 200$. In contrast to the mean velocity profile at this station the outer region of the most downstream temperature profile showed a strong wake component. This difference between the velocity and temperature profiles was produced by the streamwise pressure distribution. The boundary layer velocity distribution was directly dependent on the mainstream acceleration through the equations of motion. The temperature distribution, however, was only indirectly linked to the pressure gradient through the effect of the acceleration on the turbulent transport of heat. For these reasons the most downstream temperature boundary layer was considerably thicker and less "full" than its velocity counterpart.

The velocity and temperature profile and wall heat-transfer data obtained in this study have been shown to be both self-consistent, accurate, and two-dimensional. It is anticipated that these results will provide a needed set of boundary layer transition experimental test cases to which analytical predictions of boundary layer transition can be compared.

Conclusions

1 Transition onset location data obtained in the present program agree very well with the theoretical predictions of van Driest and Blumer. Both indicate that the transition Reynolds number is relatively insensitive to acceleration at even moderate turbulence levels.

2 Comparisons of transition lengths inferred for the various test cases from the velocity profile shape factor and wall heat-transfer distribution data indicate that fully turbulent mean velocity profiles are achieved upstream of fully turbulent wall heat-transfer rates. The present data suggest that the mean velocity profile is established in a shorter length than is required for the development of the equilibrium turbulence distribution.

Acknowledgment

Research sponsored by the Air Force Office of Scientific Research (AFSC), under Contract F49620-78-C-0064. The United States Government is authorized to reproduce and distribute reprints for governmental purposes notwithstanding any copyright notation hereon. The contract monitors for this project were Col. Robert C. Smith (Ret.), Dr. D. George Samaras, and Dr. James D. Wilson.

References

1 Turner, A. B., "Local Heat Transfer Measurements on a Gas Turbine Blade," *Journal of Mechanical Engineering Science*, Vol. 13, No. 1, 1971.

2 Hall, D. J. and Gibbings, J. C., "Influence of Stream Turbulence and Pressure Gradient Upon Boundary Layer Transition," *Journal of Mechanical Engineering Science*, Vol. 14, No. 2, 1972.

3 Feindt, E. G., "Investigations on the Dependence of Laminar-Turbulent Transition in Surface Roughness and Pressure Gradient," *Fb. Schiffbautech. Ges.*, Vol. 50, 1957, p. 180.

4 Edwards, A. and Furber, B. N., "The Influence of Free Stream Turbulence on Heat Transfer by Convection from an Isolated Region of a Plane Surface in Parallel Air Flow," *Proceedings of the Institute of Mechanical Engineers*, Vol. 170, 1956.

5 Junkhan, G. H. and Serovy, G. K., "Effects of Free-Stream Turbulence and Pressure Gradient on Flat Plate Boundary-Layer Velocity Profiles and on Heat Transfer," ASME *Journal of Heat Transfer*, Vol. 169, 1967, pp. 169–176.

6 van Driest, E. R. and Blumer, C. B., "Boundary Layer Transition: Freestream Turbulence and Pressure Gradient Effects," *AIAA Journal*, Vol. 1, No. 6, June 1963.

7 Morkoven, M. W., "Instability, Transition to Turbulence and Predictability," AGARDograph 236, 1978.

8 Reshotko, E., "Boundary-Layer Stability and Transition," *Annual Review of Fluid Mechanics*, Vol. 8, 1976, pp. 311–350.

9 McDonald, H. and Fish, R. W., "Practical Calculations of Transitional Boundary Layers," *International Journal of Heat and Mass Transfer*, Vol. 16, No. 9, Sept. 1973, pp. 1729–1944.

10 Blair, M. F., Bailey, D. A., and Schlinker, R. H., "Development of a Large Scale Wind Tunnel for the Simulation of Turbomachinery Airfoil Boundary Layer," ASME JOURNAL OF ENGINEERING FOR POWER, Vol. 103, 1981, pp. 678–687.

11 Blair, M. F. and Werle, M. J., "Combined Influence of Free-Stream Turbulence and Favorable Pressure Gradients on Boundary Layer Transition and Heat Transfer," UTRC Report R81-914388-17, Mar. 1981.

12 Blackwell, B. F. and Moffat, R. J., "Design and Conduction of a Low Velocity Boundary-Layer Temperature Probe," AIAA Paper No. 74-709; ASME Paper No. 74-HT-29, July 1974.

13 Blair, M. F., "Influence of Free-Stream Turbulence on Turbulent Boundary Layer Heat Transfer and Mean Profile Development, Parts I & II," submitted to ASME *Journal of Heat Transfer*.

14 Abu-Ghannam, B. J. and Shaw, R., "Natural Transition of Boundary Layers—The Effects of Turbulence, Pressure Gradient and Flow History," *Journal of Mechanical Engineering Science*, Vol. 22, No. 5, 1980.

15 Dunham, J., "Predictions of Boundary Layer Transition in Turbomachinery Blades," AGARDograph No. 164, 1972.

16 Carter, J. E., Edwards, D. E., and Werle, M. J., "A New Coordinate Transformation for Turbulent Boundary Layer Flows—Numerical Grid Generation Techniques," NASA CP-2166, Oct. 6-7, 1980.

17 Edwards, D. E., Carter, J. E., and Werle, M. J., "Analysis of Boundary Layer Equation Including a New Adaptive Grid Technique," UTRC Report 81-30, May 1982.

18 Blom, J., "An Experimental Determination of the Turbulent Prandtl Number in a Developing Temperature Boundry Layer," Ph.D. thesis, Technological University, Eindhoven, The Netherlands, 1970.

19 Kays, W. M., *Convective Heat and Mass Transfer*, McGraw-Hill, New York, 1966, pp. 222 and 224.

R. H. Tindell
Group Head, Propulsion Fluid System.

C. A. Hoelzer
Group Head, Propulsion Systems.
Grumman Aerospace Corporation,
Bethpage, N.Y. 11714

D. Alexander
Propulsion and Power Division,
Naval Air Systems Command,
Washington, D.C. 20361

F-14 Inlet Development Experience

This paper reviews the F-14 inlet design and discusses the wind tunnel and flight test results of investigation that can contribute to move advanced inlet design.

Introduction

The F-14 inlet was designed to provide adequate amounts of sufficiently high-quality air to ensure good performance and stall-free operation of the TF30 engine. It was concurrently developed to efficiently accommodate advanced turbofan engines like the F401-PW-400 and the General Electric GE-F-101X. An advanced engine was to be selected shortly after the beginning of the F-14 development; however, the selection has yet to be made although both of the above advanced engines have been successfully demonstrated in F-14 flight tests.

Important inlet design decisions were made early in the development to meet the ambitious goal of a first flight within two years of contract award. This goal was achieved on December 24, 1970, after having conducted seven subscale inlet wind-tunnel tests, six small scale (1/12) and one large scale (1/7) isolated inlet tests, three large scale (1/7) inlet-forebody tests, and two full scale static inlet-engine tests. Subsequent flight testing corroborated most of the wind tunnel results, turned up new data not investigated in the wind tunnel, and generated some data that contradicted wind tunnel results.

This paper reviews the F-14 design and discusses the wind tunnel and flight test results of investigations that can contribute to more advanced inlet designs.

Inlet Description

The inlet has a two-dimensional, four-shock external compression system with essentially horizontally oriented ramps; the inlet is rolled 10 deg out of the horizontal plane (Fig. 1). It has a 3 deg initial fixed ramp and three computer-controlled variable compression ramps which are programmed to vary with Mach number only. Any airflow variation or angle-of-attack/yaw effects at any particular Mach number fall within the stable operating limits of the basic inlet ramp position. The inlet aspect ratio, H/W, is 1.35, and the duct is four engine diameters from cowl lip to engine compressor face; the centerline is essentially straight.

The compression ramp boundary layer is bled through a

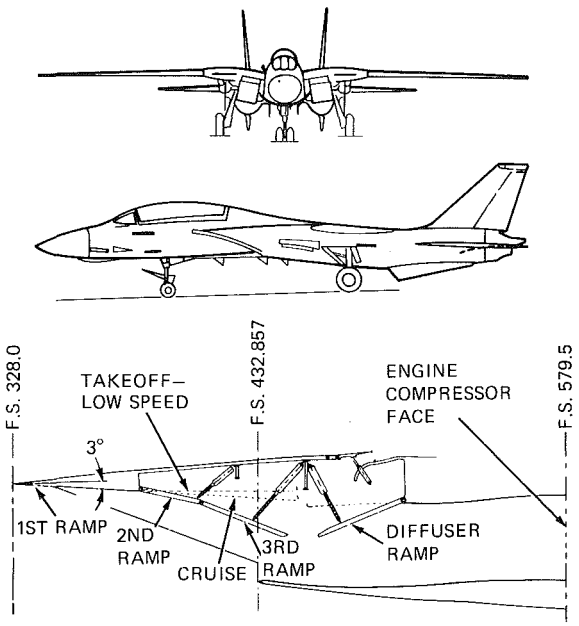

Fig. 1 F-14 inlet arrangement

throat bleed slot and dumped overboard through the bleed/bypass door. This door was variable during the flight test program but is fixed for production aircraft.

The inlet was designed to meet both the angle-of-attack/yaw and corrected airflow extremes shown on Figs. 2 and 3. These design limits were estimated based upon early wind-tunnel tests and engine test cell programs. In 1968, the angle-of-attack levels were as high as or higher than those obtainable by any then-current fighter aircraft. The supersonic high-alpha limits reflect control surface effectiveness at high altitudes and limited "g" loads, whichever is most constraining at any Mach number. The supersonic low-alpha limits reflect a design goal of $-1''g''$ above Mach 2.00 to preclude the requirement to vary inlet geometry with angle-of-attack. Extreme yaw angles during subsonic flight were anticipated to be quite large below $M = 0.60$.

In the Mach number range of $M = 0 - 0.90$, the duct has a diffusion area ratio of 1.09 and a maximum diffuser inlet

Contributed by the Gas Turbine Division of THE AMERICAN SOCIETY OF MECHANICAL ENGINEERS and presented at the 27th International Gas Turbine Conference and Exhibit, London, England, April 18–22, 1982. Manuscript received at ASME Headquarters November 9, 1981. Paper No. 82-GT-5.

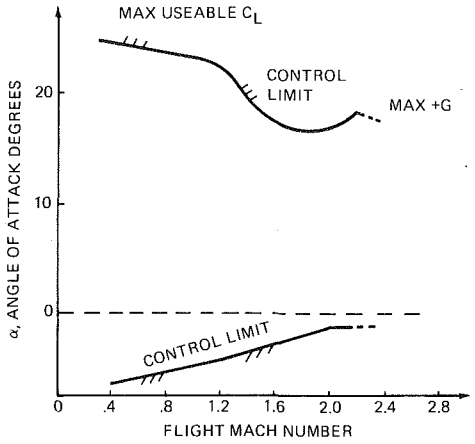

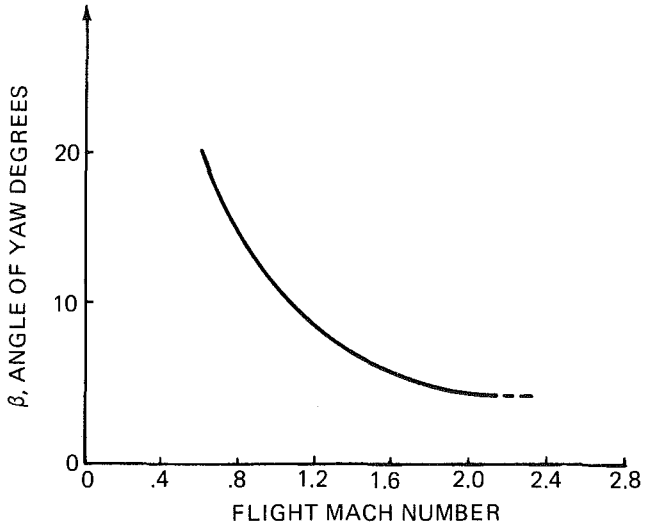

Fig. 2 F-14A inlet design limits

Mach number of M = 0.50 for the TF30 installation. The bleed/bypass door, located atop the wing glove, serves as an auxiliary inlet for static operation.

Each inlet is spaced a minimum of 8 in. from the fuselage wall and, due to the 10 deg inlet roll, this distance increases at lower waterlines. A 12 deg diverter separates the inlet and fuselage, terminating approximately 3 in. aft of the cowl lip station. The entrance to the Environmental Control System inlet also starts at this point.

There have been several basic inlet design changes during the wind tunnel studies and full-scale boiler plate static development tests (Fig. 4). The inlet capture area was increased by 10 percent to accommodate all of the potential advanced engine maximum airflows. The cowl lip internal

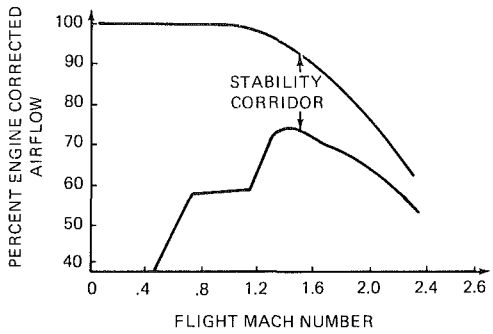

Fig. 3 F-14A inlet design limits

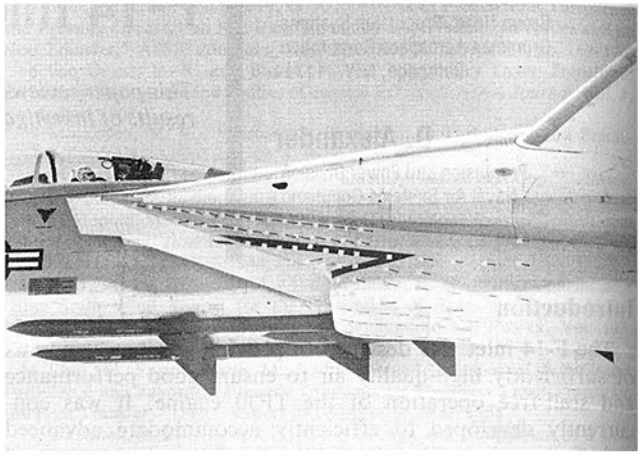

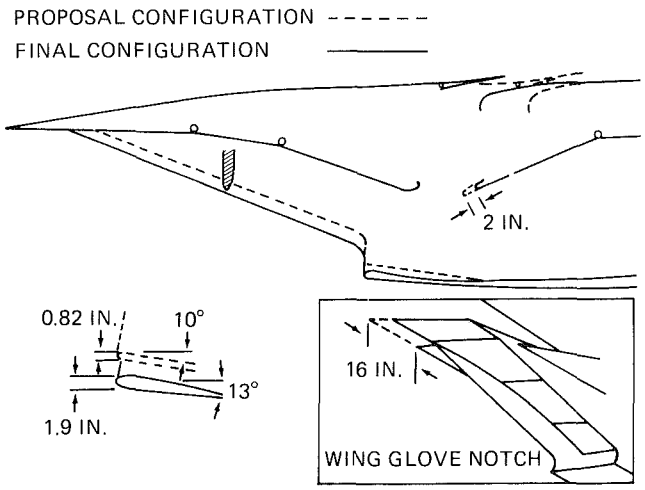

Fig. 4 Inlet design evolution

Nomenclature

A = area
$C.R$ = contraction ratio, A_{LE}/A_{MIN}
ΔH = scoop height
K_{D_2} = Pratt and Whitney distortion index
M = mach number
P_s = static pressure
P_t = total pressure
T_t = total temperature
W = weight flow
W_c = corrected weight flow $W\sqrt{\theta_t}/\delta_{t_2}$
X = distance
α = angle-of-attack
β = angle-of-yaw
δ = ramp turning angle
δ_t = $P_t/14.7$
θ = diffuser wall angle
θ_t = $T_t/518.7$

Subscripts

0 = free stream
2 = engine face
3 = third ramp
C = capture
E = exit
CAV = cavity
DR = diffuser ramp
LC = lower cowl
LE = leading edge
MIN = minimum
RMS = root mean square
TH = throat

Conversion Factors

m = 39.37 in. = 3.281 ft
m/s = 1.9439 KT
kg/sm^2 = 1.4194×10^{-3} (lb/s in.^{2})

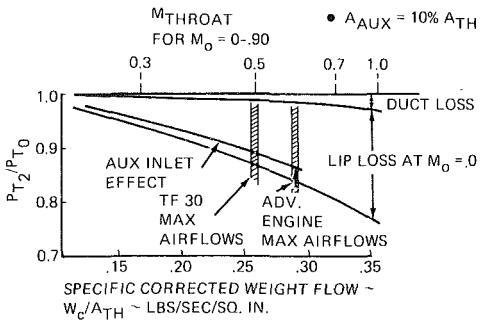

Fig. 5 Theoretical inlet performance

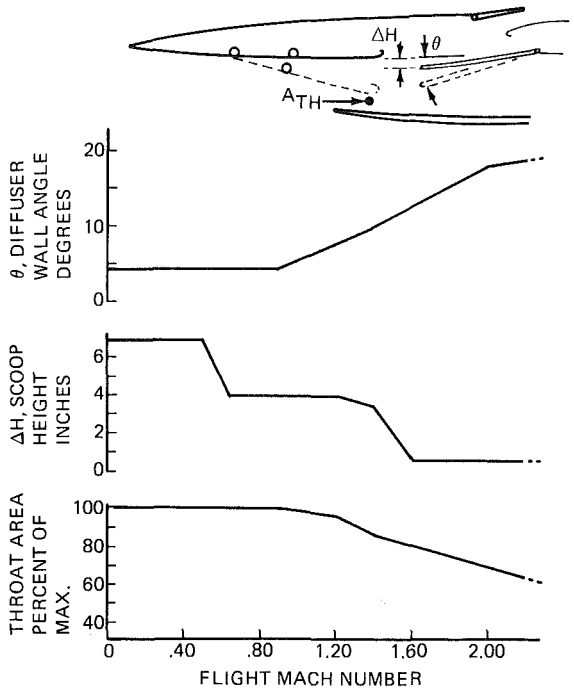

Fig. 6 Variable inlet geometry schedules

angle was increased to improve high-speed supersonic performance; the bleed exit was moved forward.

Static performance required two design changes; namely, thickening the cowl lip, and shortening the aft ramp to ease auxiliary intake flow from the bleed exit into the duct, a reversal of its normal operation flow direction.

Manèuver considerations dictated two additional basic inlet design changes. One was that the swept inlet side plates were substantially blunted to improve low-speed angle-of-attack lift/drag operation. The other was made because the intersection of the original diverter leading edge region and the fuselage was in an area where the inlet was unprotected by the inboard side plate. It was necessary to cut back the diverter 16 in. to alleviate the build-up of fuselage boundary layer air during a maneuver, which otherwise spilled into the inlet.

A theoretical calculation of the inlet's total pressure recovery characteristics for static operation and of the duct loss alone, which should approximate the inlet performance for $M = 0.5-1.0$, is illustrated on Fig. 5. Throat Mach numbers of $M = 0.70$ correspond to engine corrected airflows that are 22 percent greater than the TF30. Maximum airflows for advanced engines considered for the F-14 are approximately 10 percent greater than the TF30 levels.

Inlet Control System

The primary function of the Air Inlet Control System (AICS) is to position the three variable ramps in each inlet to

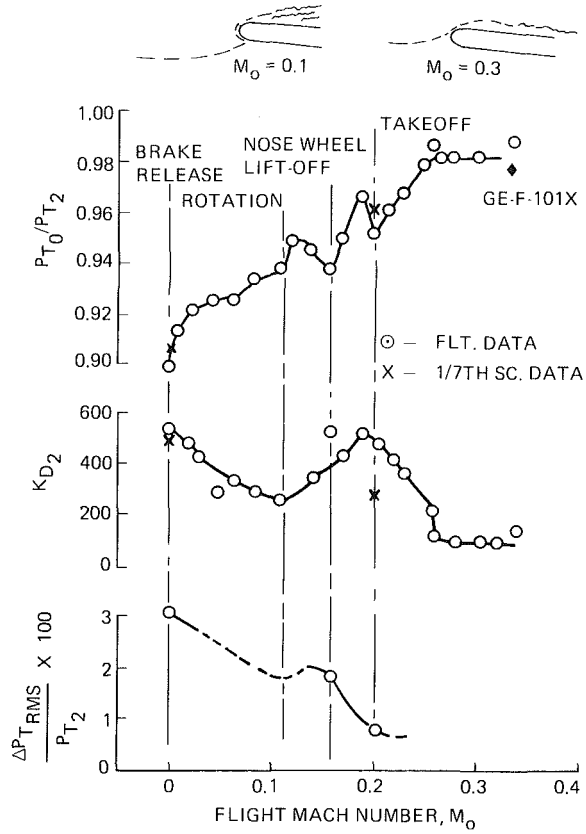

Fig. 7 Inlet performance during takeoff

some preset schedule of angles, which makes the ramp position a function of flight Mach number only. Each inlet is independently controlled by its own AICS; the required position derived from an averaged calibration using both the left-side and right-side, pilot-static probe data.

Left side-to-right side differences in local flow condition, especially at high angles-of-attack, cause small but inconsequential deviations in ramp positioning from side to side.

The variations of three important parameters that are determined by the variable ramp position schedule are shown on Fig. 6. At high supersonic speeds, the diffuser wall angle is on the order of 20 deg, the result of reserving the latter half of the duct length (two engine diameters) for a constant area section within which the rectangular-to-circular shape transition occurs.

The throat slot scoop height is very large subsonically, being tuned to the airflow matching requirements of the TF30. This is discussed in a subsequent section. Advanced engine installations would have smaller scoop heights subsonically to provide more duct area.

A near-constant value of throat area is provided throughout the subsonic regime, dropping off to approximately 60 percent of this value at high supersonic flight.

Engine adjustments, which brought engine airflow extremes within the stable inlet operating range at all Mach numbers and ambient conditions, precluded the need for a low airflow bleed door function as originally planned. The bleed exit door is now fixed.

The F-14 inlet control system is very simple and unsophisticated; it is aimed at providing adequate performance and stability while maximizing reliability and minimizing maintenance costs. Future mission requirements may dictate a more sophisticated control system; therefore, a study to investigate the benefits of integrating the inlet and engine controls is presently being conducted by Grumman and Pratt

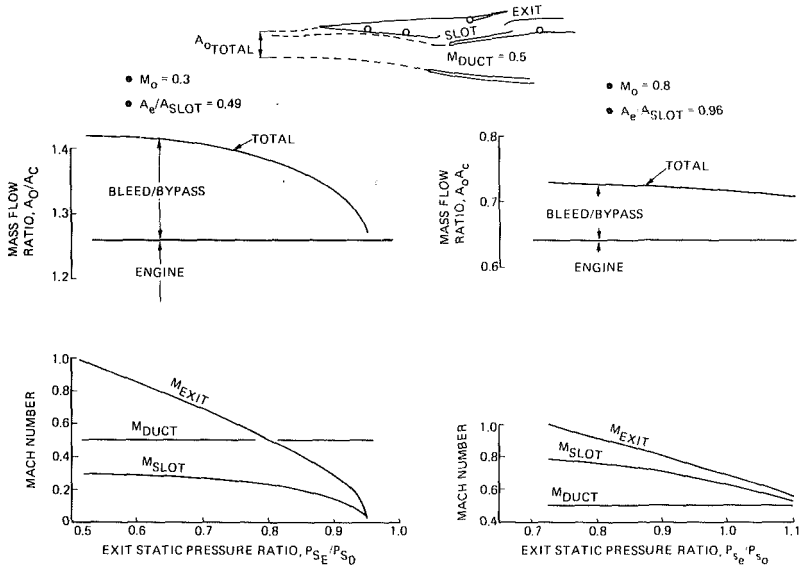

Fig. 8 Bleed/bypass system operation subsonic

and Whitney, under contract to the Naval Air Propulsion Center (NAPC) in Trenton, New Jersey. This study is evaluating more complex functional relationships between the inlet geometry and its governing parameters in order to provide a more efficient inlet-engine integration, using a full authority digital electronic control (FADEC) developed by Pratt and Whitney.

Bleed/Bypass System

The bleed/bypass system operates as an auxiliary inlet during ground operation, as long as there is an appropriate pressure ratio across it. When the exit static pressure becomes lower than the slot total pressure, then the system will pass duct flow out, rather than induct external air. This point is probably reached soon after the takeoff roll starts, although no measurements were ever made.

The engine face data of Fig. 7 show that there are no spurious effects of the bleed/bypass system operation on the inlet performance during takeoff. Both KD2 (the TF30 distortion index) and turbulence "cleanup" rapidly, turbulence improving to about the minimum expected level at $M_0 = 0.20$ and KD2 by about $M_0 = 0.30$. Typically, this cleanup is the result of reducing the internal lip separation due to moving the lip stagnation point forward along the external surface, thus reducing the inflow's acceleration around the lip and subsequent pressure gradient (see sketches on Fig. 7). Data points from the advanced engine flight tests are also shown.

A similar lip separation will occur at the leading edge of the diffuser ramp whenever the Mach number in the slot (above the ramp) is lower than the duct Mach number (below the ramp). Therefore, both the lower cowl lip and the diffuser ramp leading edge are potential sources of duct separation. The takeoff data of Fig. 7 show that all duct separation is eliminated in level flight by $M_0 \simeq 0.30$. There is good agreement between the wind tunnel model and flight test results.

A theoretical estimate of the bleed/bypass system operation is presented on Fig. 8, for $M_0 = 0.30$ and 0.80 at maximum engine corrected airflow. For the $M_0 = 0.30$ case, there is no flow when the exit static pressure ratio is slightly less than unity, depending upon the system total pressure recovery. This occurs, for the assumptions of this study, at $P_{se}/P_{so} = 0.960$. At lower ratios, which may result from operation at high angles-of-attack, the system Mach numbers increase. The bleed/bypass mass flow can be 10 percent of the total inlet flow.

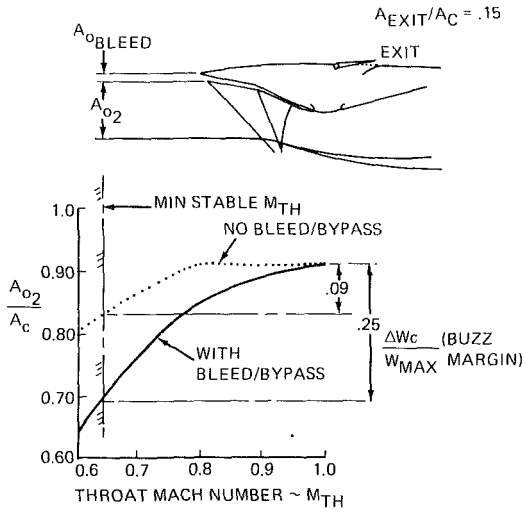

Fig. 9 Bleed/bypass system operation – supersonic

The system has been sized to ensure that the slot cannot get into a choked operating condition. The slot Mach number is generally quite low and, in conjunction with the duct Mach number of $M_{duct} = 0.50$, causes the stagnation point to be on the cavity side of the diffuser ramp leading edge.

At higher flight Mach numbers, the slot Mach number is greater than the duct Mach number, thereby requiring that the stagnation point be on the duct side of the diffuser ramp leading edge. This allows clean duct flow conditions, but suggests the possibility of separation on the cavity side of the ramp.

The results of theoretical calculations shown on Fig. 8, for $M_0 = 0.80$, are typical for the transonic Mach number range to about $M_0 = 1.30$. Notice that the bypass mass flow is still approximately 10 percent of the total value, but the mass-flow ratio values at this condition are about half of the low speed values at $M_0 = 0.30$. Another important difference is that the system can stand much more back pressure (exit static pressure ratio) without any significant loss in flow capability.

Supersonically, the bleed/bypass system provides the means for boundary layer removal as well as increased stable airflow range or buzz margin. Figure 9 presents the results of an analysis that shows almost a tripling of the buzz margin due to the bleed/bypass system. For the three-shock system used in the example, a throat Mach number of $M_b = .64$ is estimated to be the minimum stable case, using the methods

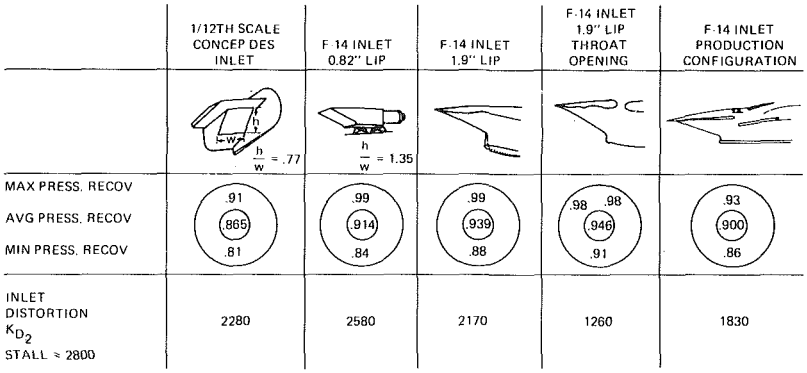

Fig. 10 F-14A static inlet test-development summary

of reference [1]. Only a 9 percent range of corrected airflow occurs for the no-bleed/bypass case, before the minimum stable throat Mach number is arrived at. The bleed/bypass configuration adds airflow to the throat area, thereby increasing the throat Mach number at the same engine mass flow ratio at which the no-bleed/bypass case was on the verge of buzz. An additional 16 percent in stable corrected airflow range is provided.

Static Test Results

The development of the inlet lip and throat configuration for static operation employed subscale model tests as well as full-scale inlet-engine evaluations. The full-scale tests were done with an iron-monster inlet rig and a TF30-P-12 engine. Figure 10 summarizes the main results at maximum engine airflow from a series of these tests.

The 1/12th scale model had the wrong aspect ratio but the proper lip shape to simulate the subsequently developed preliminary inlet lines. The results of this early test showed that lower lip separation probably affected the flow in the upper portion of the inlet which should incur only small losses. The distortion index, K_{D_2}, which includes an increment due to turbulence, is within 20 percent of the value at which engine stall would be expected for steady-state operation on a standard day. The total pressure recovery, although relatively low, does not cause any penalty to mission capability.

The first full-scale static test results reflected the proper aspect ratio, which tends to isolate the upper and lower surfaces. The results showed a slight improvement in lower lip pressure recovery, possibly due to the higher Reynolds number. The pressure in the upper flow was significantly increased to only a 1 percent loss, and the average overall pressure recovery was increased by more than 5 percent. The distortion index increased by 13 percent because of the average pressure increase and the fact that the minimum pressure remained approximately the same. The lower lip thickness was then increased to reduce the lip losses. A 5 percent increase in the lower flow total pressure was measured, which translated into a 3 percent increase in the overall total pressure recovery (see Fig. 10). A concurrent 15 percent reduction in distortion factor was achieved.

A crude simulation of the throat slot was then cut into the iron-monster inlet rig and performance was measured, with the thicker cowl lip. The auxiliary inlet effect of the slot causes an increase in the lower lip pressure and a small reduction in the upper flow pressure. The overall pressure recovery was improved by less than 1 percent, but the distortion was reduced by over 40 percent.

A more accurate simulation of the production aircraft configuration, including proper ramps and bleed/bypass cavity geometry, was subsequently tested. The internal geometry of this real-life configuration was much less conducive to efficient aerodynamics than the previous

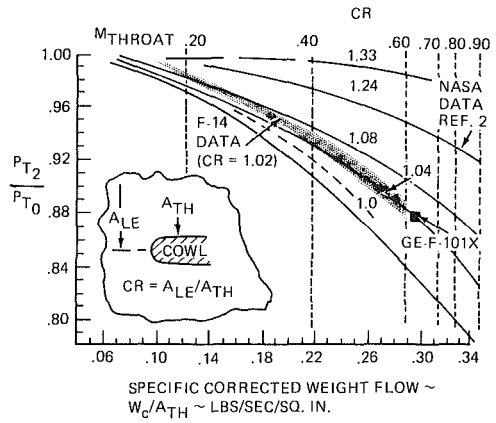

Fig. 11 Static inlet performance correlation

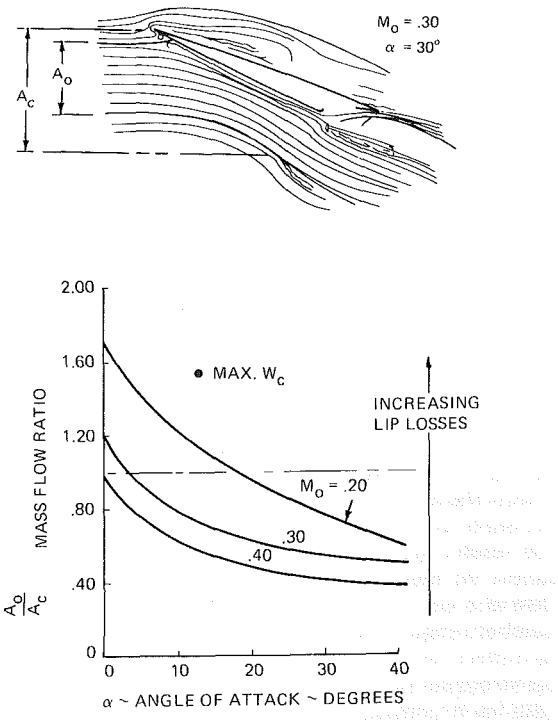

Fig. 12 Mass flow ratio characteristics

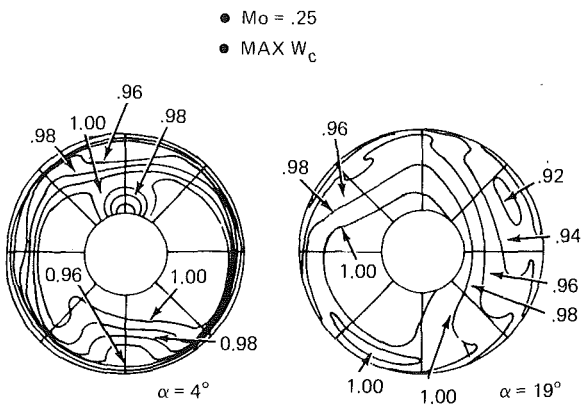

Fig. 13 Engine face pressures

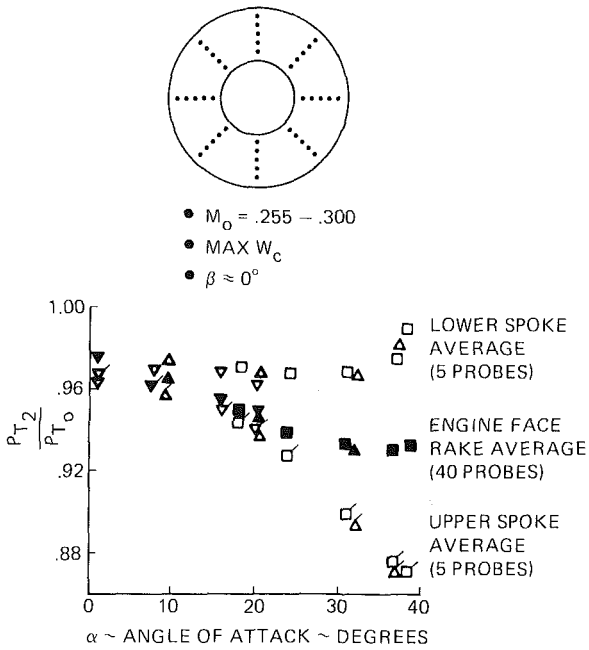

Fig. 14 Effects of attitude on flight test rake pressure distribution

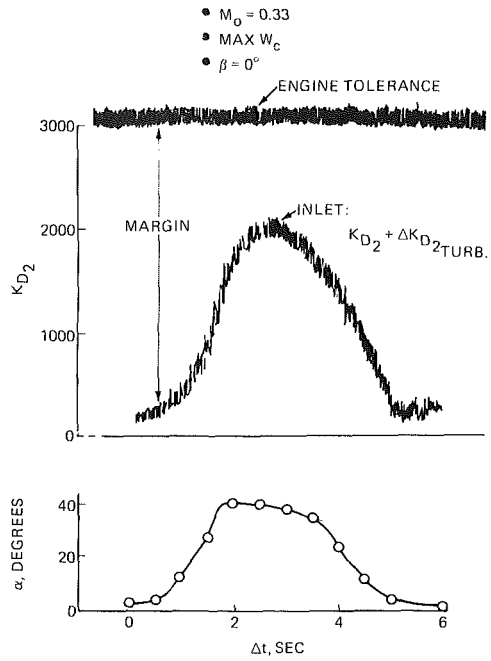

Fig. 15 Compatibility during low speed wind-up-turn

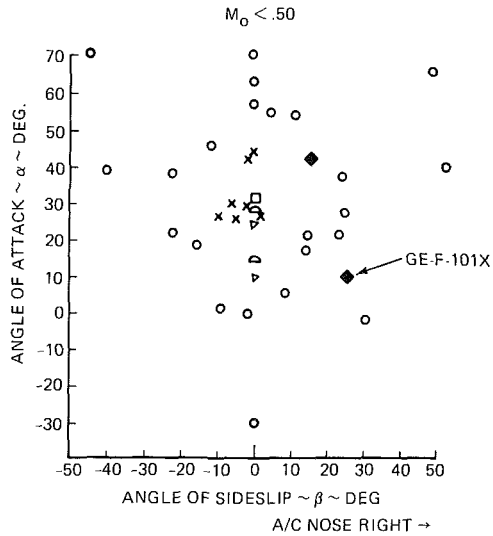

Fig. 16 Low speed maneuvering capability

simulation. To provide a minimum distortion index, K_{D_2}, for maximum airflow operation, the diffuser ramp was positioned to provide a reduced total pressure level in the upper flow at the engine face. This lowered the average overall pressure recovery level while not significantly affecting the minimum pressure level in the lower flow behind the lip. Thus, the upper flow quality was reduced to minimize distortion specifically for the TF30 installation. The total pressure recovery and distortion index are as shown on Fig. 10. An inlet-engine distortion margin, $(K_{D_{2_{STALL}}} - K_{D_{2_{INLET}}})/(K_{D_{2_{STALL}}}$, of approximately 34 percent is available.

The cowl lip provides an internal area contraction of 2 percent, and as discussed above, the lip thickness significantly affects the overall total pressure recovery. The F-14 inlet static pressure recovery characteristics are compared with NASA test results for configurations having a range of contraction ratios, on Fig. 11. The F-14 data correlate with the NASA data at a contraction ratio of 1.04 – 1.05 in the throat Mach number range above M_{TH} = .40. By adjusting the F-14 data to reflect the 10 percent auxiliary inlet area effect of the bleed/bypass system, a reasonable correlation with the NASA data at a contraction ratio of approximately CR = 1.02 occurs, as shown by the dashed line.

Subsonic Maneuvering

The inlet was designed to meet a maximum angle-of-attack of α = 25 deg; however, due to excellent lift characteristics of the aircraft, the useful angle-of-attack range runs in excess of α = 70 deg.

An estimate of the inlet streamline patterns during subsonic maneuvering (for M_0 = 0.30 and α = 30 deg) illustrates some of the mechanisms for potential losses (see sketch on Fig. 12). Most significant is the fact that the mass-flow ratio is much less than unity (m/m_0 = 0.55), thereby allowing the lower stagnation streamline to be located on the inner surface of the cowl lip. This tends to reduce internal flow separation at the lower lip. The curves on Fig. 12 show how mass flow ratio varies with flight Mach number and inlet attitude. When the inlet is operated at angles-of-attack less than α = 3.5 deg, for M_0 = 0.30, the mass flow ratio is greater than unity and the lower stagnating streamline would be located on the external lip surface, causing inlet flow to accelerate around the lip and to separate internally. Based upon this theoretical effect, we would expect the lower portion of the compressor face flow

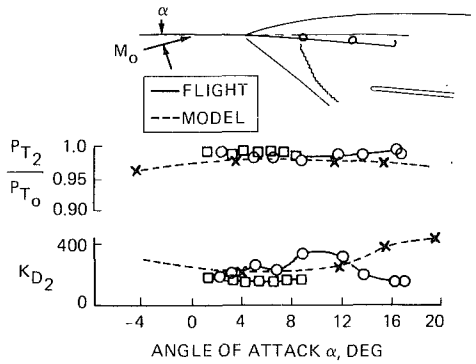

Fig. 17 Wind tunnel model & flight data at $M_0 = 1.25$

patterns, behind the lip, to have higher pressure recovery levels at high angles-of-attack than at lower ones. This is indeed the case shown on Fig. 13, which compares the engine face profiles for $\alpha = 4.0$ and 19.0 deg.

A closer look at the variations of the upper and lower portions of the compressor face, as angle-of-attack is varied, is shown on Fig. 14. The average of the lower spoke pressures (open symbols without ticks) remains high and even rises slightly to $\alpha = 40$ deg. The average of the upper spoke (ticked symbols) closely matches the engine face average (filled in symbols) up to $\alpha = 18$ deg, above which it is much lower. These results tend to support the theoretical effect discussed above.

Flight test results showing the distortion index developed during a wind-up-turn to $\alpha = 42$ deg are compared with the estimated engine tolerance on Fig. 15. A maximum pitch rate of 32 deg/s was measured. The minimum distortion margin for this maneuver is approximately 32 percent. This is similar to the distortion margin for static operation with maximum engine airflow discussed above.

The extreme attitudes achieved during the course of flight testing at Grumman are summarized on Fig. 16. These results were obtained with steady-state engine operation, that is, there were no severe throttle manipulations, and no engine stalls were experienced.

Supersonic Operation

A comparison of wind-tunnel model and flight test data for $M_0 = 1.25$ is shown on Fig. 17. Good agreement of pressure recovery data is illustrated, but the flight test distortion index data exhibits a strange rise and fall characteristic that lags what may be a similar variation in the wind tunnel data by about 10 deg. One reason for the differences between the wind tunnel and flight data might be the relative variability of M_0 with increasing angle-of-attack. The aircraft decelerates as angle-of-attack is increased due to increasing drag, while the wind tunnel test section Mach number is hardly changed at all. Reynolds number differences may also be partly responsible for these trends.

The comparison of wind tunnel and flight test data at $M_0 = 2.00$, Fig. 18, shows a significantly different result than for the transonic case. The angle-of-attack effects are more significant, especially at very low and high attitudes. The analytical characteristics tend to clarify some of the results.

The analysis is based on the use of a forward marching numerical computation which integrates the governing Euler equations in regions of continuous flow (see reference [3]).

The pressure recovery difference between the theoretical shock and the isolated inlet model levels are due to the internal duct losses (friction and diffusion effects). An analytical determination of the inviscid effects of the aircraft forebody (nose, canopy, etc.) on the local inlet angle-of-attack and total pressure recovery is shown by the hatched

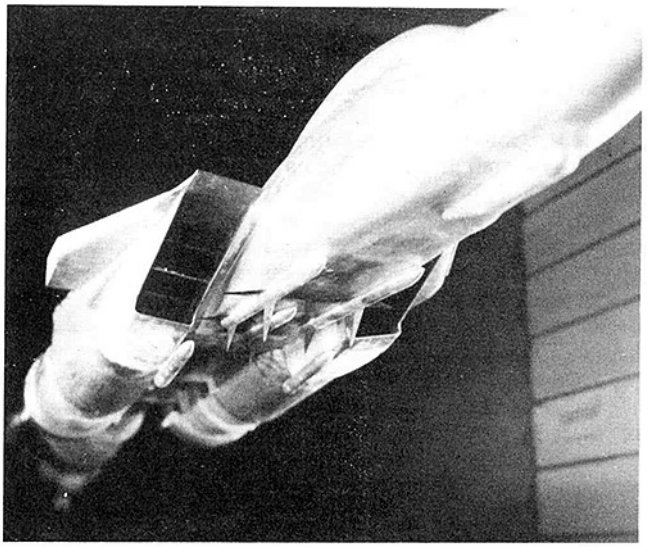

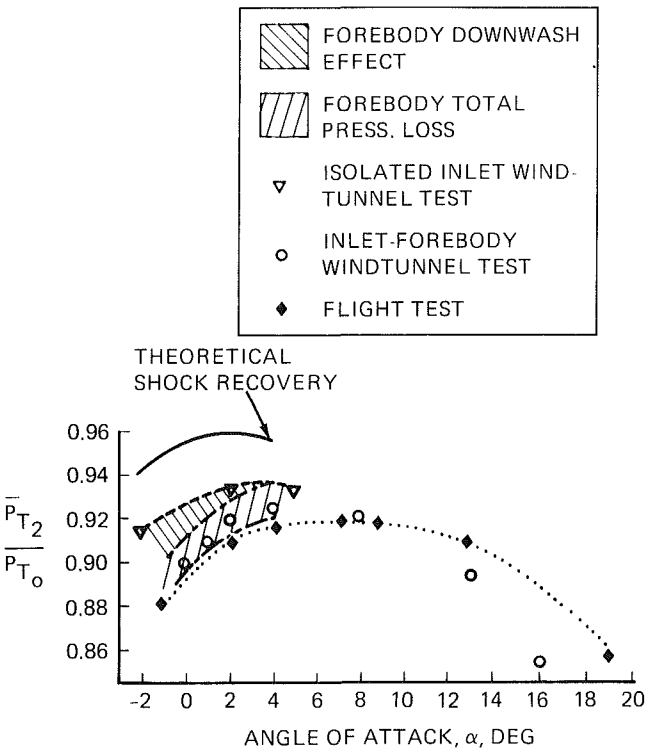

Fig. 18 Wind tunnel model & flight data at $M_0 = 2.00$

areas. The angle-of-attack effect (downwash) is reckoned relative to the isolated model data. There is no effect at an angle of 4 deg, but a significant downwash occurs at lower angles. The forebody total pressure recovery effect brings the predicted values to a level that is between the inlet-forebody model data and the flight data. It is within half of 1 percent of the flight data.

A comparison of the inlet-forebody model and flight data shows a nominal 1 percent lower level for the flight data at the low angles-of-attack, and the same value at about nine degrees. At higher angles-of-attack, the flight data shows much less sensitivity and higher levels of pressure recovery than the wind tunnel data. The counterclockwise rotation of the flight pressure recovery versus angle-of-attack characteristic, relative to the model characteristic, indicates that a downwash occurs on the flight inlet relative to the model inlet. This downwash beneficially affects high angle-of-attack performance, but is not significant at low angles.

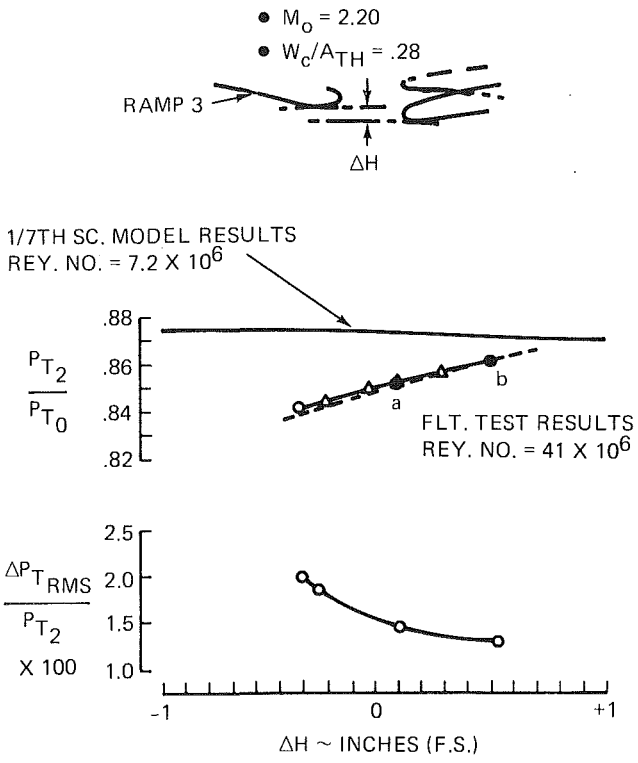

Fig. 19 Bleed slot scoop height effects

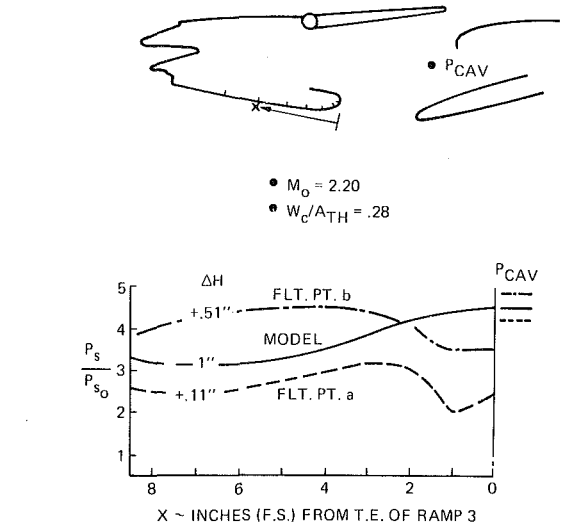

Fig. 20 Static pressures on ramp 3

Bleed/Bypass Geometry

Initial supersonic flight data showed a difference from wind tunnel results in the trend of engine face flow quality with the inlet scoop height. Figure 19 shows the slight but consistent improvement in total pressure recovery, as the aft (diffuser) ramp of the wind-tunnel model is raised in order to vary the scoop height from forward to aft facing configurations. The flight results show a much stronger and opposite trend in pressure recovery, which is supported by the accompanying trend in turbulence. These results prompted a modification to the ramp control system schedule as well as the inclusion of ramp static pressure instrumentation to aid in understanding this phenomenon.

Figure 20 shows a comparison of the flight and wind-tunnel model static pressure distributions along the last 8 in. of the

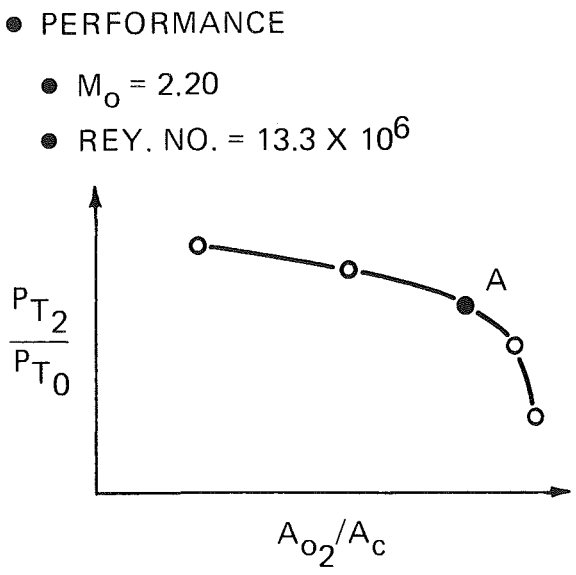

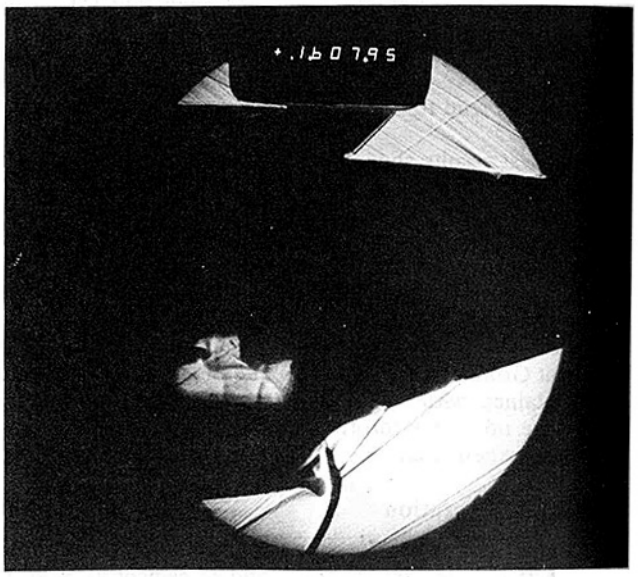

Fig. 21 1/7th Scale model internal aerodynamics

third ramp. This data is at the same flight Mach number, angle-of-attack, angle-of-yaw, and engine face Mach number. The Reynolds numbers are as shown on Fig. 19. The cavity pressure readings are shown to the right of the curves.

The backward facing scoop (ΔH = 1 in.) of the wind tunnel model shows a continually rising static pressure as the flow approaches the trailing edge of the ramp. The cavity pressure corresponds very closely to the highest ramp pressure level, that is, the value at the trailing edge. The two flight configurations, corresponding to points "a" and "b" of Fig. 19, both have forward facing scoops and show static pressure decreases as the flow approaches the end of the ramp, followed by an abrupt leveling out or slight rise within the last inch of the ramp. The larger scoop height configuration has considerably higher ramp and cavity pressures and corresponds to the better engine face flow quality.

This behavior is probably the result of separation occurring relatively farther upstream in the wind tunnel model flow (low Reynolds number), with the result that the remainder of the ramp surface acts as a separated boattail surface seeing relatively high pressures. In flight, the much higher Reynolds number conditions allow the flow to remain attached and

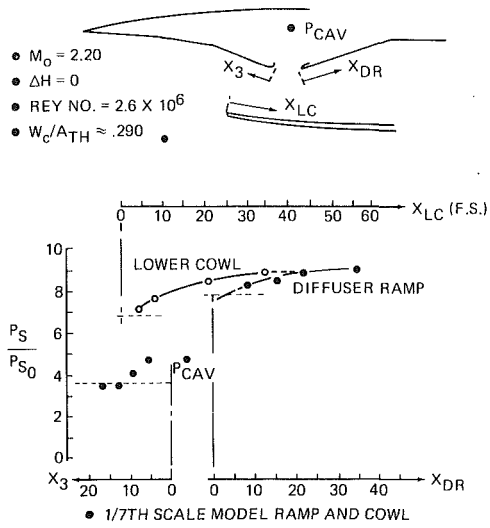

Fig. 22 Centerline static pressure distributions

expand around the ramp trailing edge to high terminal shock Mach numbers, thus incurring pressure recovery and turbulence penalties. The larger scoop heights cause less expansion of the flow to occur and, therefore, lower terminal shock Mach numbers.

Figure 21 shows a shadowgraph of the 1/7th scale model in the wind tunnel at $M_0 = 2.20$ with the bleed/bypass inlet slot visible through the walls of the model. There is some optical deformation but the essential elements of the flow are visible. The crossed shocks appearing under the diffuser ramp are in the external flow and should not be confused with inlet duct phenomena. The inlet bow shock is highly curved and impinges upstream of the trailing edge of the third ramp. There appears to be a Mach reflection at the point of boundary layer separation and a branching shock. Downstream of this there is a final normal shock that impinges on the aerodynamic boundary between the duct and cavity flows.

This boundary appears to flow into the diffuser ramp after having made a 90 deg turn, then flows forward and, subsequently, into the cavity. The upper strata of diffuser flow follows the large turning angle (as shown by the vortex sheet from the triple-point) which is the mechanism for adjusting the diffuser ramp upstream static pressures to the bow shock levels of the lower flow. These results are similar to those reported in reference [4], in which case the terminal shock was arranged to impinge upon the slot's aerodynamic boundary.

A comparison of the ramp and cowl static pressures with several theoretical estimates is shown in Fig. 22. These data are for a configuration which is similar to the one corresponding to the data in Fig. 21, although it is at a lower Reynolds number. The upstream pressures on the third ramp correspond closely to the two-dimensional theoretical estimate indicated by the dashed line. The static pressure rises over the last 14 in. of the ramp. Although there is no data available for the last five in., it is significant that the maximum pressure ratio achieved, 4.8, is very close to the cavity pressure reading. The theoretical static pressure downstream of the normal shock corresponds closely to the initial measurement on the lower cowl surface. Similarly, the pressures measured on the upper surface (diffuser ramp) agree fairly well with the theoretical calculation of the diffuser entrance pressure. It is obvious that most of the static pressure rise in the upper flow occurs within the section below the slot. This analysis agrees with the implications of the shadowgraph on Fig. 21.

At higher Reynolds numbers, because of the expansion around the trailing edge of the third ramp, the terminal shock structure will move downstream and may impinge on the aerodynamic boundary of the bleed slot flow. This is also true at higher mass flows, that is, less subcritical operation. In these cases, the strength of all shocks will be increased and shocks impinging on the bleed slot flow boundary may reflect as expansion waves, thus making the terminal shock even stronger. For very large expansions, terminal shocks that span the complete throat height and interact with the lower surface boundary layer have been observed.

The scoop height effect on total pressure recovery, described by the flight data of Fig. 19, can be correlated with the normal shock strength corresponding to expansions to higher Mach numbers just ahead of the leading edge of the diffuser ramp. These expansions may be calculated, albeit rather simplistically, using the minimum area under ramp 3 and the area at the diffuser entrance. This is shown by the dashed line on Fig. 19.

In the case of the F-14, it was relatively easy to solve the problem by rescheduling the ramps to provide adequate scoop heights at the appropriate Mach numbers. This might not always be possible. Therefore, it is recommended that the design and development of boundary layer removal systems be planned with sufficient consideration as to Reynolds number effects. As in this case, factors that tend to reduce flow separation can hurt system performance.

Conclusions

The F-14 inlet has demonstrated in-flight compatibility with two advanced engines, the F401-PW-400 and the GE-F-101X, as well as with the TF30.

The inlet control system concept is simple and unsophisticated to minimize maintenance and maximize reliability. We are presently studying the potential benefits of integrating inlet and engine controls in our NAVAIR-funded FADEC program.

To achieve low total pressure distortion for static operation, the total pressure recovery was intentionally lowered to minimize the difference between average and minimum pressures. This did not effect any other mission requirement.

Although the maximum design angle-of-attack was $\alpha = 25$ deg, the F-14 routinely flies through $\alpha = 40$–50 deg, and can maneuver to $\alpha \simeq 75$ deg, with very large concurrent yaw angles.

There is good agreement between subscale wind tunnel data and flight data. Supersonically, there is a beneficial downwash effect in flight at high angles-of-attack that provides higher performance than for the wind tunnel model.

Analytical estimates of aircraft forebody effects on the inlet flow field, using a three-dimensional, inviscid, supersonic flow field code, are fairly close to experimental results. This approach predicts shock losses as well as local flow direction.

The geometry of the inlet of the boundary layer removal system was adjusted during flight tests to accommodate the effects of Reynolds number differences between wind tunnel and flight. These effects are involved with the transonic flow in the terminal shock-diffuser entrance area. The aerodynamics in this flow regime are not well understood for the general case and should be investigated more completely.

References

1 Hall, G. R., "A Criterion for Prediction of Air-frame Integration Effects on Inlet Stability With Application to Advanced Fighter Aircraft," Technical Paper Presented at the AGARD Symposium on Airframe/Propulsion Interference, Rome, Italy, Sept. 1974.

2 Blackaby, J. R., and Watson, E. C., "An Experimental Investigation at Low Speeds of the Effects of Lip Shape on the Drag and Pressure Recovery of a Nose Inlet In a Body of Revolution," NACA TN 3170, Apr. 1954.

3 Marconi, F., et. al., "Development of a Computer Code for Calculating the Steady Super/Hypersonic Inviscid Flow Around Real Configurations," NASA CR-2675, 1975.

4 Laynaert, J., "Operation of an Internal Boundary Layer Trap of an Air Intake Under External Supersonic Compression," ONERA TP 288, 1966.

Three-Dimensional Flow Field in the Tip Region of a Compressor Rotor Passage—Part I: Mean Velocity Profiles and Annulus Wall Boundary Layer

B. Lakshminarayana
Director of Computational Fluid Dynamics Studies, and Professor of Aerospace Engineering
Fellow ASME

M. Pouagare

R. Davino
Graduate Assistant.

Department of Aerospace Engineering,
The Pennsylvania State University,
University Park, Pa. 16802

The flow field in the annulus wall and tip region of a compressor rotor was measured using a triaxial, hot-wire probe rotating with the rotor. The flow was surveyed across the entire passage at five axial locations (leading edge, 1/4 chord, 1/2 chord, 3/4 chord, and trailing edge locations) and at six radial locations inside the passage. The data derived include all three components of mean velocity. Blade-to-blade variations of the velocity components, pitch and yaw angles, as well as the passage-averaged mean properties of the annulus wall boundary layer, are derived from this data. The measurements indicate that the leakage flow starts beyond a quarter-chord and tends to roll up farther away from the suction surface than that observed in cascades. Substantial velocity deficiencies and radial inward velocities are observed in this region. The annulus wall boundary layer is well behaved up to half a chord, beyond which interactions with the leakage flow produce complex profiles.

Introduction

The complexity of the flow in the tip region of a turbomachinery rotor, shown in Fig. 1, is well-known. The presence and interaction of secondary flow, tip leakage flow, rotor blade, and annulus wall boundary layers result in large flow departure from design conditions. This region also accounts for a substantial (one-third to one-half) fraction of losses in turbomachinery. Further improvements in design, performance, and flow prediction in this region should come from a better understanding of the flow field. Due to the complexity of measurement in a rotor frame of reference, there has been no attempt to measure the passage flow in the tip region. The earlier measurement in this region was carried out by Lakshminarayana and Gorton [1] in an axial flow inducer passage, which substantially differs from that of a compressor rotor passage. Recent measurements by Dring et al. [2], Lakshminarayana and Ravindranath [3], and Davino and Lakshminarayana [4] at the *exit* of the rotor blade have revealed the complex interactions in this region resulting from the physical mechanisms occurring within the passage. The difficulty in interpreting these results in the absence of passage flow data is evident. It is the objective of this study to report and interpret such data.

Stationary cascades have been of great value in studying many of these mechanisms. The cascade, however, is unsuitable for the study of a variety of mechanisms which are present in turbomachinery. The effect of rotation, curvature, the relative motion between the rotor and the end wall, and other three-dimensional effects in the end wall region are most suitably studied in an actual turbomachine environment. The relative motion between the rotating rotor blade row and the stationary wall casing generates a region of complex flow interaction in the flow; this annulus wall region is greatly influenced by the effects of rotation, the tip leakage flow, the annulus wall boundary layer, the cascade secondary flow, and the blade boundary layer.

The primary objective of the current study reported in this paper has been to gather additional understanding of the complex inviscid and viscid effects in the annulus wall flow field, including the three components of mean velocity, turbulence intensity, and turbulence stress inside the rotor blade passage. This is accomplished by a complete survey of the rotor blade passage in the tip region utilizing a rotating three-sensor, hot-wire probe and by rotor blade static pressure measurements. It is hoped that the knowledge gained from this investigation will help serve in establishing a theoretical model for the eventual analysis of the three-dimensional flow in the annulus wall region.

Experimental Facility, Instrumentation, and Program

All the measurements reported in this paper were performed using the Axial Flow Compressor Facility in the Department of Aerospace Engineering of The Pennsylvania State University. All the data were acquired with a triaxial, hot-wire probe rotating with the rotor. The study included the measurement of mean velocities, turbulence intensities, and

Contributed by the Gas Turbine Division of THE AMERICAN SOCIETY OF MECHANICAL ENGINEERS and presented at the 27th International Gas Turbine Conference and Exhibit, London, England, April 18-22, 1982. Manuscript received at ASME Headquarters November 19, 1981. Paper No. 82-GT-11.

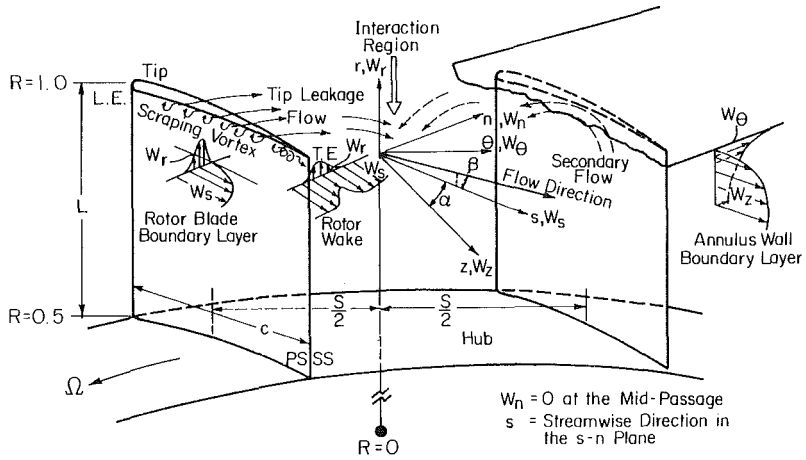

Fig. 1 Nature of flow in the tip region and notations used

Reynolds stresses. Only the mean velocity data are presented and interpreted in this paper. The turbulence data are described in a companion paper [5].

The Axial Flow Compressor Facility. A general description of the compressor stage is given by Smith [6], and a detailed discussion of the facility is given by Lakshminarayana [7]. Good peak efficiencies are exhibited by the rotor. The hub/annulus wall diameter ratio of the facility is 0.5, with the diameter of the annulus wall equal to 0.9377 m. The inlet guide vane row, which consists of 43 blades, is followed by the 21-bladed rotor. The rotor is driven by a 37 kw variable-speed motor through a belt and pulley system. The rotor is followed by a stator vane row of 25 blades. Downstream of the stator is located an axial flow fan with variable blade setting for the variation of pressure rise and mass flow. Operating conditions and rotor specifications are as follows: inlet velocity, 29 m/s; flow coefficient based on tip speed, 0.56; stage loading coefficient based on tip speed, 0.4864; speed of rotor, 1066 rpm; tip clearance, 0.25 to 0.3 cm. Blade element data at the tip are NASA 65 series; chord, 15.41 cm; spacing, 14.12 cm; maximum thickness, 5.10 percent of chord; stagger angle, 45.0 deg; and maximum camber height, 8 percent of chord. The blade element details of the rotor are given in Table 1 of reference [3].

Rotating Probe Traverse Mechanism and Data Acquisition System. The rotating probe traverse mechanism and the instrumentation system used in these rotor flow measurements are described in detail in reference [7]. A triaxial, hot-wire probe, similar to that used in references [3] and [4], was employed for all velocity measurements reported in this paper. The probe has been found to measure the three components of velocity and turbulence intensities accurately. The probe calibrations are corrected for the variations of temperature and aging of the wire. The signals from the rotating hot wire, rotating with the rotor, were taken through a ten-channel slip-ring unit to a stationary data-processing system described in reference [7]. The choice of the instrumentation was such that the raw data from the experiment could be used directly in the data-processing program developed by Gorton and Lakshminarayana [8]. The probe measurement programs incorporated the three-sensor, hot-wire calibration and operation techniques discussed in Chapter 3 of reference [9]. The yaw and pitch angle sensitivity of the passage-flow probe response was determined through the mat-plotting of the sensor response.

The measurements were taken at several radial and axial stations, and are tabulated in Table 1. The stationary hot-wire probe data at the *exit* of the rotor passage of these radii are presented in reference [4]. The rotating hot-wire probe data at the *exit* of the rotor passage at $R = 0.932$, 0.959, and 0.973 are presented and interpreted in reference [3]. All measurements reported in this paper were taken *inside* the rotor passage near the tip region. The measurements inside

Nomenclature

C_p = blade static pressure coefficient $[2(p - p_1)/\rho W_1^2]$
C_L = local lift coefficient based on inlet dynamic head of the relative flow
c = blade chord length
p = static pressure
PS = pressure side of the rotor blade passage
R = radius ratio (r/r_t), $R = 1$ at tip, $R = 0.5$ at hub
S = blade spacing
SS = suction side of the rotor blade passage
s,n,r = end wall flow coordinate system (streamwise, normal, and radial coordinate directions, Fig. 1)
U_t = blade tip speed
W = flow relative velocity
Y = tangential distance measured from camber line ($Y = 0$ on suction side, $Y = S$ on pressure side)
Z = streamwise distance from the rotor blade leading edge normalized by the rotor blade chord
z,θ,r = axial, tangential, and radial coordinate system (Fig. 1)
α = flow angle measured from the axial direction
β = flow meridional angle (measured from the cylindrical plane)
Θ^* = momentum thickness of the boundary layer (equation (2))
δ^* = displacement thickness of the boundary layer (equation (1))

Subscripts

1 = inlet value
s,n,r = values in the streamwise, normal, and radial coordinate directions, respectively (Fig. 1)
0/max = maximum values
t = blade tip location
z,θ,r = values in the axial, tangential, and radial coordinate directions, respectively (Fig. 1)

Superscript

— = passage-averaged values

Table 1 Maximum streamwise velocity (W_{s_0}/U_t) for the reported measurement stations*

Percent span from tip**	R \ Z	0.0	0.25	0.50	0.75	0.979
4.0	0.980	0.690	0.750	0.653	0.550	0.432
5.4	0.973	0.709	0.824	0.670	0.707	0.588
8.2	0.959	0.716	0.858	0.697	0.593	0.580
11.0	0.945	0.750	0.943	0.742	0.579	0.553
16.4	0.918	0.780	0.973	0.840	0.680	0.539
21.8	0.891	0.861	0.975	0.923	0.740	0.610

* Corresponding data at exit are tabulated in Table 2 of reference [4].

** The rotor blade static pressures were measured at $R = 0.918$, 0.962, 0.988, 0.996, and 0.998.

the tip clearance region for this rotor is presented in reference [10].

Experimental Results and Interpretation

The hot-wire measurements derived from the triaxial, hot-wire probe are plotted in the (s, n, r) coordinate system. The orientation of this coordinate system (s, n, r), as well as the flow angle, α, and the meridional angle, β, with respect to the compressor coordinate system (z, θ, r), are indicated in Fig. 1. The s, n, r coordinate system follows the projection of the flow at the mid-passage in the radial plane for the various axial measurement stations. s is the projection of the streamwise direction at mid-passage onto a cylindrical plane, n is the principal normal, and r is the radial direction. Therefore, at the mid-passage, $W_n = 0$. All velocities presented in this section are relative velocities and are normalized with respect to the corresponding maximum streamwise velocity in the blade passage. The normalization values [W_{s0}/U_t] are given in Table 1. The tangential distance is normalized by the blade spacing, with $Y/S = 0$ and $Y/S = 1$ representing the blade suction and pressure sides, respectively.

In addition, some quantitative measurements were obtained on the blade surface. These included the flow visualization on the blade surface as well as the blade static pressure measurements near the tip region.

The mean velocity and turbulence intensity profiles at inlet to the rotor (0.35-chord length upstream of the leading edge) are shown in Fig. 2. The annulus wall boundary layer thickness is approximately 12 to 14 percent of the span from the tip. The axial velocity profile is of the conventional type. The peak turbulence intensities (τ_θ is the tangential component, τ_z is the axial component, both normalized with respect to the local relative velocity) reach about 10 percent near the annulus wall, with free stream turbulent intensities averaging less than 2 percent.

Blade Surface Measurements. The rotor blade static pressures were measured at various radial locations, including one at the tip. These are plotted in Fig. 3. The suction peak decreases continuously as the tip of the blade is approached. The pressures on the pressure surface increase from $R = 0.918$ to approximately $R = 0.988$, beyond which there is a drastic decrease in pressures. The values of the local lift coefficient, based on the dynamic head of the inlet relative velocity, are also shown in Fig. 3. The local lift coefficient starts to decrease from $R = 0.962$ with a rapid decrease in the outer 2 percent of the blade.

The flow on the surface of the blade was visualized utilizing the ammonia streak filament method described in reference [11]. The limiting streamlines on both the pressure and the suction surfaces are shown in Fig. 4. The ammonia traces (shown schematically) on both pressure and suction surface reveal the presence of radial outward flow in the outer 4.5 percent of the blade tip. The outward flow on the pressure surface is caused by the blade boundary layer, where outward flow exists due to imbalance between the pressure forces and the centrifugal forces, and the leakage flow from pressure to suction surface at the tip. The flow on the suction surface is also outward, which is caused by the blade boundary layer and the entrainment of the jet due to the leakage flow issuing from the tip of the blade.

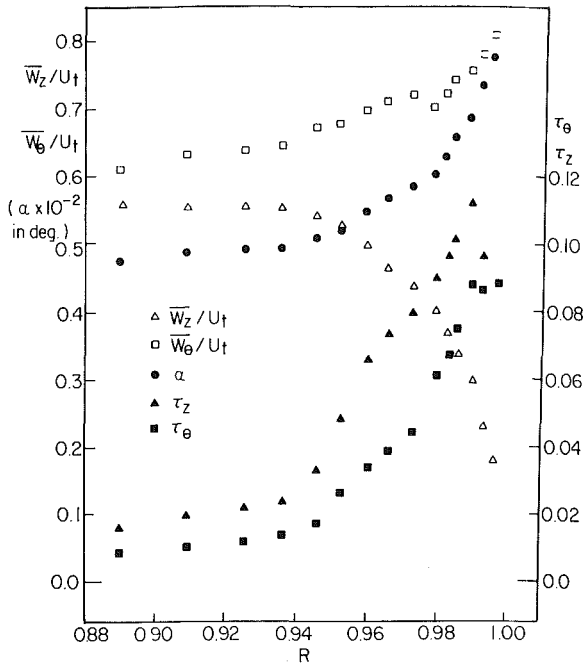

Fig. 2 Inlet velocity and turbulence profiles in the tip region upstream of the rotor ($Z = -0.35$)

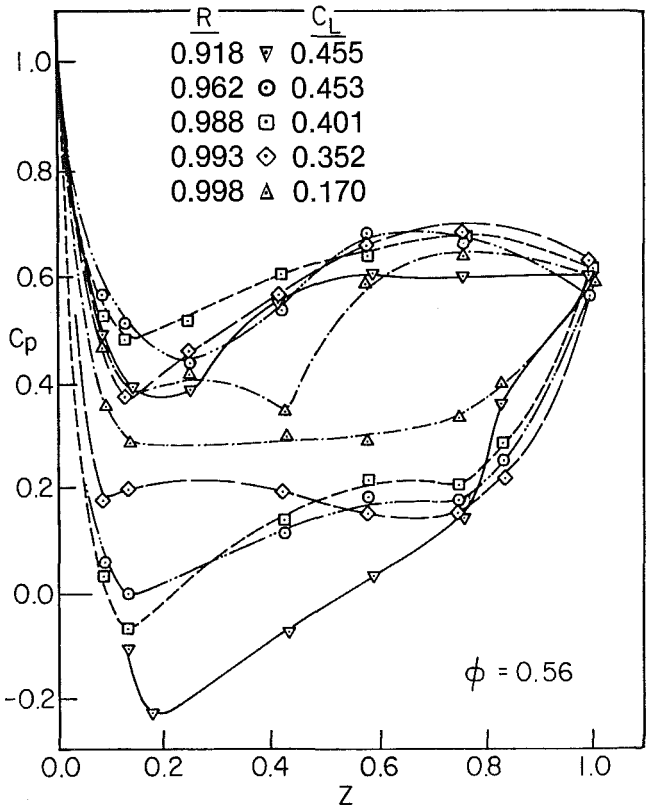

Fig. 3 Blade pressure distribution and blade lift coefficient in the blade tip region

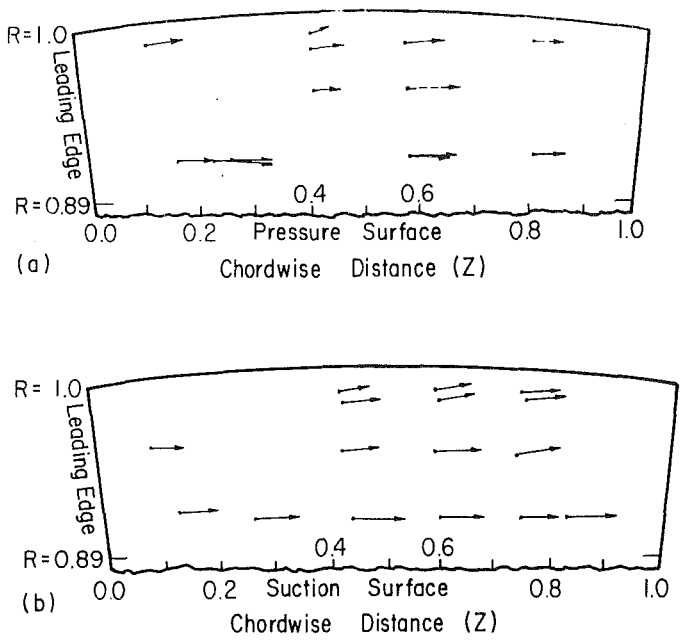

Fig. 4 The limiting streamline angles on the blade surface near the tip region

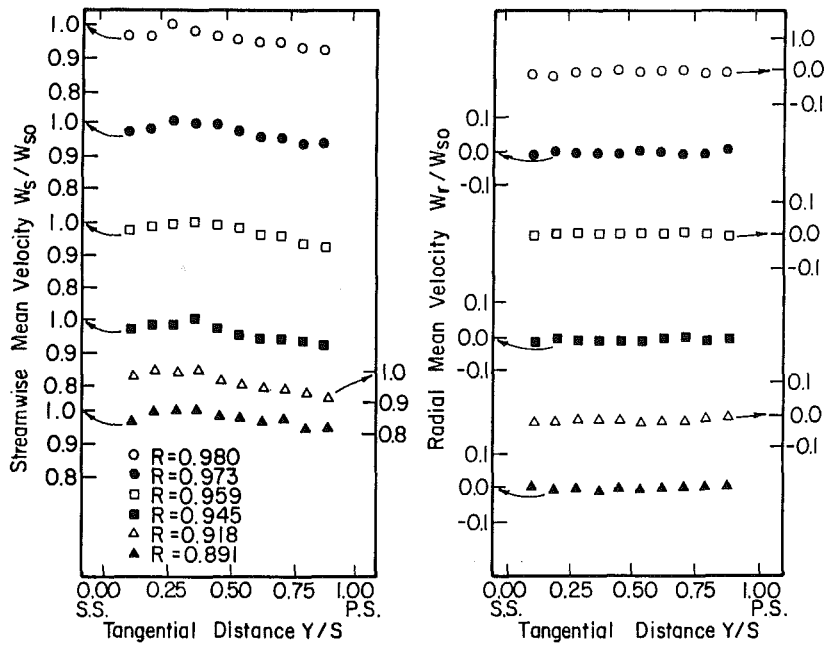

Fig. 5 Blade-to-blade distribution of the streamwise velocity and radial velocity at the leading edge ($Z = 0$)

Local and Passage-Averaged Relative Velocity Profiles and Flow Angles. The coordinate system used and notations employed were described earlier in this section.

Streamwise Mean Velocity. The variation of the streamwise velocity across the rotor blade row for various radial locations is shown plotted in Fig. 5 for the leading edge ($Z = 0$) location. Data for all other axial locations are shown in Fig. 6. The blade thickness is indicated on the abscissa of the figures. Due to the travel limitations of the probe traversing mechanism, the surveys do not extend completely to the blade surfaces. The data at $Z = 0$ shows that the variation across the passage is small, most of which is brought about by inviscid turning effects. The maximum value occurs closer to the suction surface at $Y/S = 0.3$. Referring to Table 1, it is clear that the maximum relative flow accelerates up to $Z = 0.25$, beyond which it decreases. The maximum value as well as passage-averaged values decrease continuously from $R = 0.891$ to $R = 0.98$, except at $Z = 0.75$ and 0.979.

At the axial location $Z = 0.25$ (Fig. 6), the flow has the typical inviscid trend. It shows almost a linear increase in streamwise velocity from pressure to suction side. Even though the tip leakage flow has not yet developed, its effect is clear at $R = 0.980$, where there is a substantial reduction in the tangential gradient of the relative velocity from those measured at $R = 0.973$. This is also evident from the blade static-pressure distribution shown in Fig. 3.

At the axial location $Z = 0.5$, a velocity deficiency near the mid-passage is noted at the last two radial locations. At the four lower radii ($R \leq 0.959$), the flow shows a predominantly

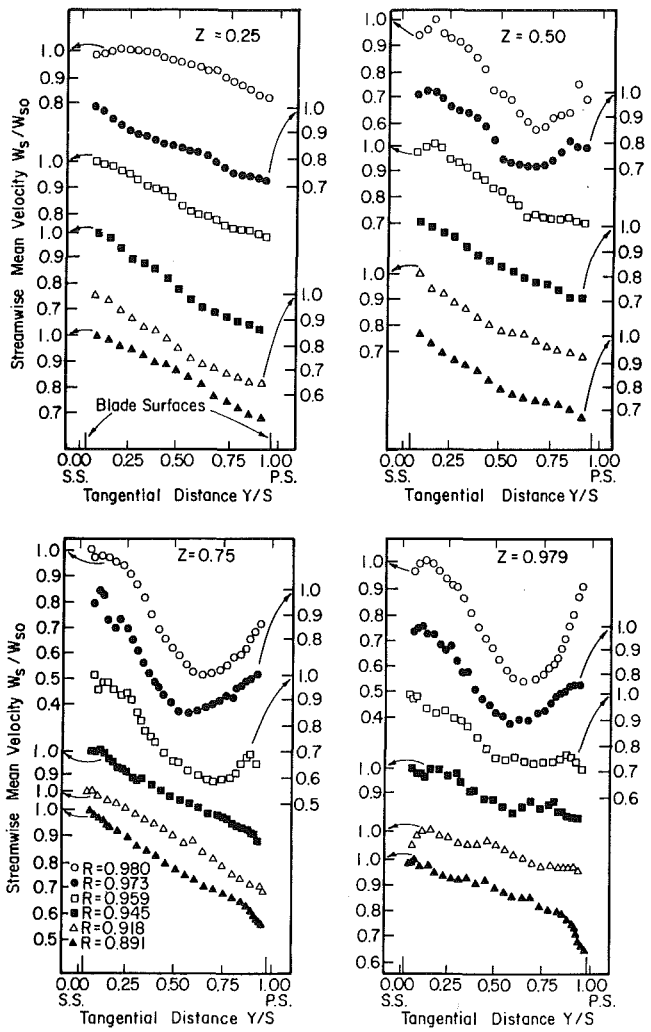

Fig. 6 Blade-to-blade distribution of the streamwise velocity (W_s) at Z = 0.25, 0.50, 0.75, 0.979

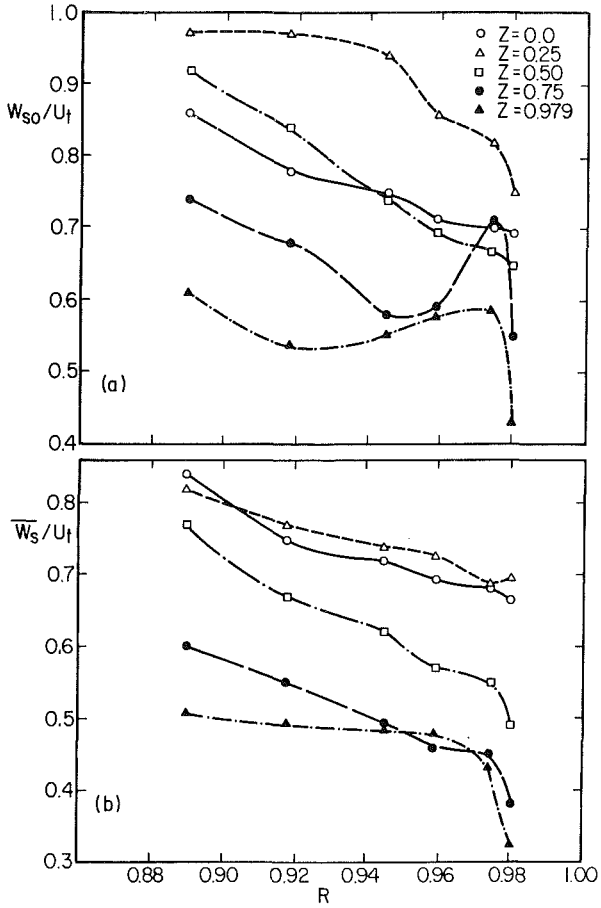

Fig. 7 Radial variation of the maximum and the passage-averaged streamwise velocity ($\overline{W_s}$)

inviscid trend. The deficiency of the streamwise velocity is maximum at $R = 0.98$, with a value of $\sim 0.2\ W_{s_0}$ at $Y/S = 0.65$. This deficiency is caused partly by the interaction of the blade boundary layer with the annulus wall boundary layer and mainly by the tip leakage flow which originates usually [12, 10] between $Z = 0.25$ and $Z = 0.5$. The leakage flow jet is augmented by the blade motion and, hence, travels farther away from the suction side. This feature will be evident from the secondary velocity vector contours presented later. The interaction of these flows forms a region of low-momentum fluid near the mid-passage of the blade tip. This unconventional "wake-type" of profile is attributed to inward radial flow which is a result of the interaction of the tip leakage flow, blade boundary layer, and annulus wall boundary layer. It is not clear from the data whether the radial inward flow (reported later) which causes this effect arises due to the blade boundary layer or the leakage flow. The radial outward flow in blade boundary layers, when encountered by the annulus wall, tends to move along the wall and then inward in the interaction region [13]. A similar trend exists for the leakage flow, which is in the form of a jet from the pressure to the suction surface in the gap region. Augmented by the wall motion, the jet due to the leakage flow moves farther away from the suction surface before rolling up as it moves radially inward from the tip [14]. Since the blade boundary layers are small in this case, it is speculated that the dominant phenomenon observed here is the leakage flow. The secondary-flow contribution to this deficiency should be small since the turning is very small at this axial location.

As the flow proceeds downstream ($Z = 0.75$, Fig. 6), the velocity deficiency near the mid-passage increases substantially, and this interaction region extends to lower radial locations. The maximum defect (interpolated from the inviscid trend that would exist) is $0.3\ W_{s_0}$ at $R = 0.980$, $Y/S = 0.65$, and the interaction region extends to $R = 0.959$. The inviscid flow at the lower radii shows a uniform increase in streamwise velocity from a value of $0.6\ W_{s_0}$ at the pressure side to W_{s_0} on the suction side. The blade passage data, however, cannot accurately describe the blade boundary layer due to the spatial limitation of the three-sensor probe and the probe traversing mechanism.

A trend similar to that observed at $R = 0.75$ can be seen in the streamwise velocity profiles at $Z = 0.979$. At this location, the predominantly inviscid flow is observed only at $R = 0.891$. The region of the velocity deficiency in the interaction region has extended to the lower radial location of $R = 0.945$. At this axial location, the velocity gradient from the suction to pressure surface of the blade passage in the inviscid region is not as large as that at $Z = 0.750$. A velocity gradient of only $0.10\ W_{s_0}$ to $0.20\ W_{s_0}$ is apparent. This reduction is due to the decreasing blade pressure difference as the trailing edge of the rotor blade is approached. With increasing radius, the region of the streamwise velocity deficiency becomes apparent. This velocity defect is again a maximum at $R = 0.980$ and $Y/S = 0.65$ with a value of $0.60\ W_{s_0}$ below an interpolated inviscid trend. The region of velocity deficiency increased with the axial distance from $Z = 0.25$ to 0.75, but essentially remained the same from $Z = 0.75$ to 0.979. The value of the maximum velocity defect increased by nearly 20 percent from $Z = 0.5$ to 0.75 but remained the same beyond $Z = 0.75$. The tangential location of this region has remained the same, however.

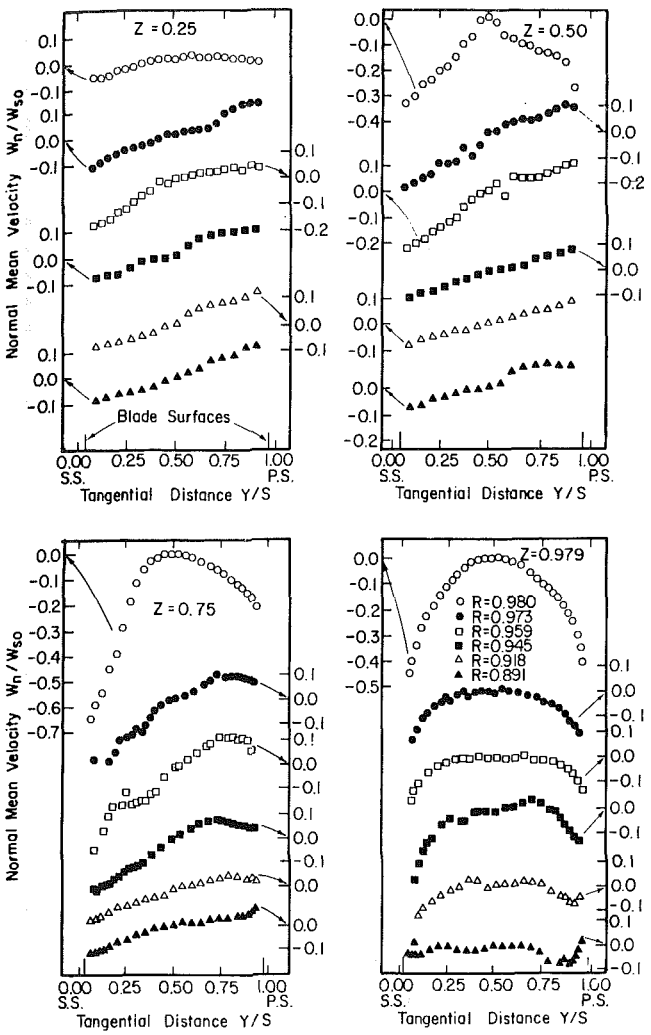

Fig. 8 Blade-to-blade distribution of the normal velocity (W_n) at Z = 0.25, 0.5, 0.75, 0.979

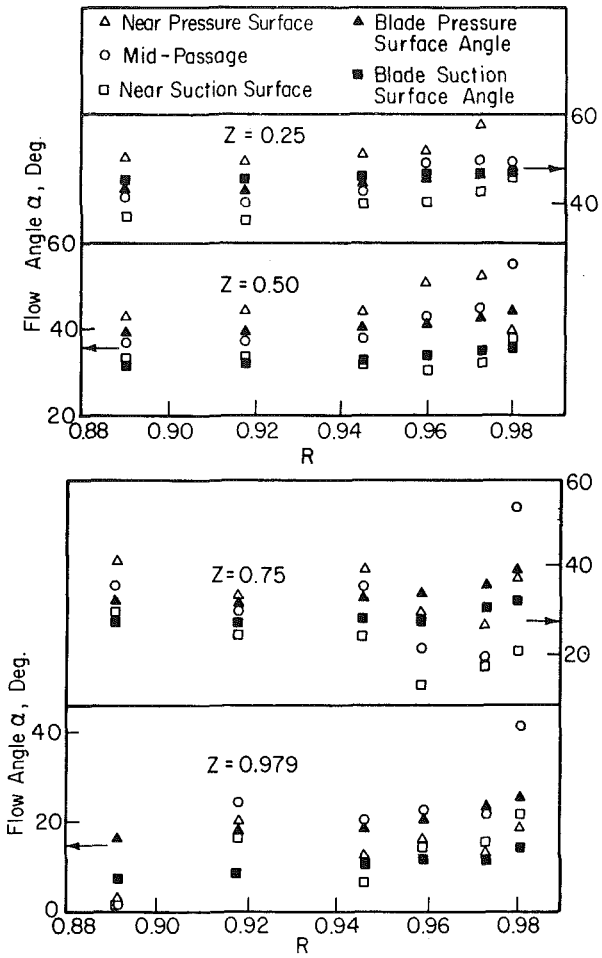

Fig. 9 Radial variation of the flow angle (α) near blade surfaces and the mid-passage at various axial locations

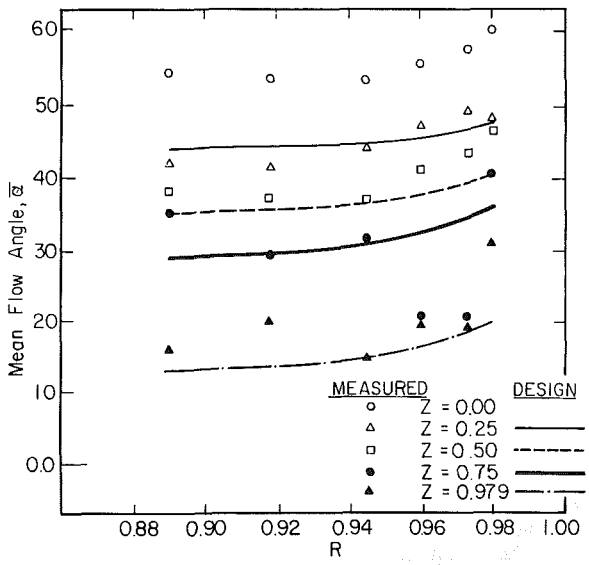

Fig. 10 Radial variation of passage-averaged flow angle ($\bar{\alpha}$)

The region of the streamwise velocity deficiency becomes especially pronounced at radial locations near the tip of the rotor blade. This is a region of maximum loss and considerable flow mixing which results in strong eddies and associated energy dissipation. A concentration of high turbulence intensities was measured in this region and is reported in reference [5].

The radial variation of the maximum values of the streamwise velocity (W_{s_0}/U_t) at various axial locations is shown in Fig. 7. It is evident that the relative flow accelerates from $Z = 0$ to $Z = 0.25$, beyond which considerable diffusion occurs. The flow is rather well behaved until $Z = 0.5$, beyond which a low velocity region is observed at $R = 0.959$ for $Z = 0.75$ and at $R = 0.918$ for $Z = 0.979$. The maximum velocity decreases continuously from $Z = 0.25$ to $Z = 0.979$, and it varies almost linearly in the radial direction from $Z = 0$ to $Z = 0.5$.

The passage-averaged values of the streamwise velocity ($\bar{W}_s/U_t$) at various axial and radial locations are plotted in Fig. 7. The development of the annulus wall boundary layer can be traced in this plot. The relative velocity decreases rapidly in the tip region. Large diffusion of the relative flow in this region can be attributed to mixing and turbulence effects. The change in the passage-averaged mean streamwise velocity is relatively small from $Z = 0$ to $Z = 0.25$.

Normal Velocity (W_n/U_t) and Flow Angle α. The normal velocity profiles across the passage at various radial and axial locations are shown in Fig. 8. By definition of the coordinate system (Fig. 1), the normal velocity is zero at the mid-passage location. The variation of the passage flow angle near the suction surface, at mid-passage, and near the pressure surface locations is shown in Fig. 9. The passage-averaged values of $\bar{\alpha}$ are compared with the design values in Fig. 10. These figures, combined with the normal velocity profiles (Fig. 8), allow proper intepretation of the passage flow relative to the blade geometry to be made.

At the axial location $Z = 0.0$, the flow is uniform across the passage with no normal component of velocity. Hence, this data is not shown. The average flow angles are shown in Fig. 10.

At the axial locations $Z = 0.25$ and $Z = 0.5$, the measurements indicate an increase in the normal velocity from the suction surface to the pressure surface of the blade at lower radii. This trend is due to inviscid turning of the flow. The flow angles plotted in Figs. 9 and 10 clearly show that the flow in the mid-passage region is underturned near the blade tip region. This results from the tip-leakage flow.

The normal velocity profiles shown at $Z = 0.5$ indicate that the inviscid effects persist up to $R = 0.973$. The distribution at $R = 0.980$ indicates substantial deviation from the mid-passage value at all passage locations. The flow is underturned at most of the radial locations. The normal velocity and the angles deviate considerably in the tip region of the pressure surface. This clearly indicates the presence of the leakage flow. Larger negative values of W_n on the suction side shown in Fig. 8 indicate overturning near the suction side in the tip region. This is confirmed by angles shown in Fig. 9, and is probably caused by the fact that the jet due to leakage flow rolls back and migrates towards the suction side. Arguments supporting this phenomenon are provided later. The shift from positive values to negative values on the pressure side (from $R = 0.973$ to 0.980) indicates the presence of underturning near the pressure surface. Hence, the flow near the tip at $Z = 0.5$ is significantly underturned. This effect can be attributed directly to the leakage flow.

At the axial location of $Z = 0.750$ and radial locations below $R = 0.959$, the data indicate (Fig. 8) an increase in normal velocity from the suction surface to the pressure surface of the blade. This trend is due to the turning of the flow by the blade row. Figure 10 shows that at these locations the flow nearly follows the blade camber line, thus following the inviscid streamlines. Figure 9 also shows that the flow is deflected away from the mean streamline near the suction surface and vice versa near the pressure surface of the blade. The turning of the passage-flow is an inviscid flow phenomenon which is also observed at $Z = 0.979$. Figures 8, 9, and 10 show that substantial deviations from the inviscid trend occur at radial locations near the blade tip. At $Z = 0.750$ and radial locations above $R = 0.945$, the flow is overturned. A maximum of 15 deg of overturning is seen to occur at $R = 0.959$ (Fig. 10). This flow overturning on the suction side of the blade passage is due to the interaction of the tip leakage flow and the main-stream flow. The tip leakage flow, upon leaving the tip clearance gap, begins to roll up and reverse its direction, which ultimately results in a vortex formation. Another possible reason for the overturning is the secondary flow. Since $R = 0.959$ is almost the edge of the annulus wall boundary layer (Fig. 2), the secondary flow is not the cause for such large overturning. It is suspected that the leakage flow and the scraping vortex play a major role in the overturning observed in these regions. At this location within the blade passage, the tip leakage flow rolls up toward the suction surface of the blade to produce substantial overturning of the flow.

The data (Fig. 8) at $Z = 0.979$ indicate that the normal velocity variation across the passage is negligibly small at lower radii at most passage locations. Appreciable variation of the normal velocity component near the blade surface is due to substantial blade boundary layer growth that occurs at this location (Figs. 6 and 8). The mean streamline as well as the streamlines near the suction surface are underturned as shown in Figs. 9 and 10. The pressure surface shows a small overturning in this region. It should be recognized that the change in the leakage flow velocities is small near this region due to small blade-pressure differences. This may account for the observed effect. The fact that the leakage flow peaks

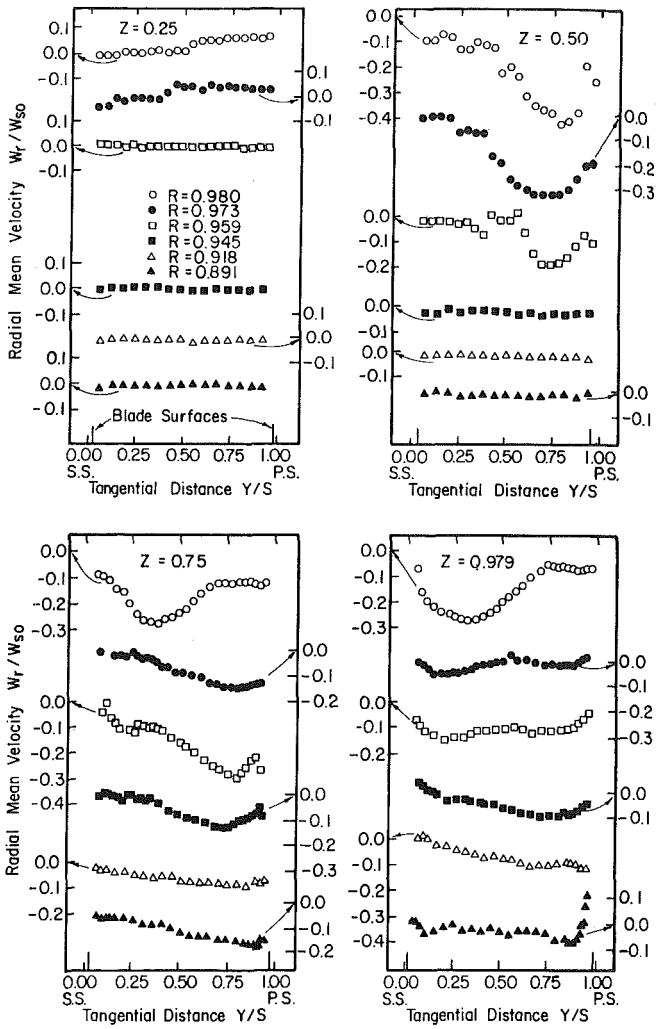

Fig. 11 Blade-to-blade distribution of the radial velocity (W_r) at Z = 0.25, 0.5, 0.75, and 0.979

beyond the mid-chord is evident from the comparison of the normal velocity plot near the tip at $Z = 0.5$, 0.75, and 0.979. The deviation in normal velocity is maximum at $Z = 0.75$ near both the surfaces (Figs. 8 and 9), as well as at the mid-passage (Figs. 9 and 10). The deviations are relatively small at the trailing edge (Figs. 8 and 10).

Radial Mean Velocity and Meridional Flow Angle (β). The radial component of velocity is negligibly small at the axial location $Z = 0$ as shown in Fig. 5. The radial velocity profiles at $Z = 0.25$, 0.5, 0.75, and 0.979 at all radii are plotted in Fig. 11.

At $Z = 0.25$, the radial component of velocity is zero, for $R \leq 0.959$. At $R = 0.973$ and $R = 0.98$, a small radial outward component of velocity exists between the mid-passage and the pressure side. A small negative radial component of velocity exists between the mid-passage and the suction side. This kind of radial velocity profile is typical of those arising from secondary flow. Even though the secondary flow is not strong due to the small turning, it is strong enough to produce this small radial velocity profile. Another possible explanation for the positive radial component of velocity between $Y/S \approx 0.5$ and $Y/S = 1$ is that the inception of the tip leakage flow starts at this location.

At $Z = 0.5$, strong radial inward velocities exist near the tip. The magnitude of these velocities decreases at lower radii, with negligibly small values at $R = 0.945$. At $R = 0.98$, the maximum value of the radial inward velocity is 0.41 W_{s_0} and

occurs at around $Y/S = 0.75$. Its values at $R = 0.973$ and 0.959 are 0.31 and 0.17, respectively. The region between the pressure side and the mid-passage has the most radial inward flow. Measurements at $Z = 0.75$ and $Z = 0.979$ show that this region moves towards the suction surface and also spreads inward into lower radii as the flow proceeds from $Z = 0.5$ to 0.75. This radial inward flow is probably caused by the cross-flow jet due to the tip leakage flow as explained earlier. The region where the radial velocity is inward is the location where the leakage flow tends to roll up. The flow near the blade surfaces is radially outward as shown in Fig. 4, but no measurements could be taken in the blade boundary region due to the limitations of the probe traverse, mechanical difficulties, and large probe errors that would result due to the wall vicinity.

The tangential variation of the radial velocity at $Z = 0.75$ (Fig. 11) indicates radial inward velocities for the radii near the tip with maximum values ($0.3\ W_{s_0}$) occurring at approximately 30 percent of the tangential distance from the suction surface of the blade.The radially inward flow at this location indicates the extent of interaction between the leakage flow and the annulus wall boundary layer. This type of profile also results from the interaction of the blade boundary layers and the annulus wall boundary layer as described in references [1] and [13]. The radial flows inside the suction and pressure-surface boundary layers tend to roll toward mid-passage, interact, and produce strong vortices and radially inward flows. Since the blade boundary layers are thin, as observed in Fig. 6, the most probable cause of this phenomenon is the leakage flow. The roll up of the jet has moved towards the mid-passage. The maximum radial inward velocity (W_r/W_{s_0}) of 0.28 at $Z = 0.750$ and $R = 0.980$ has diminished drastically at $R = 0.973$. This rapid decrease of the radial velocity is also seen at $Z = 0.979$. However, at $Z = 0.979$ the region of appreciable inward flow has increased to approximately 70 percent of the blade passage as compared to nearly 50 percent at $R = 0.750$. The region of maximum radial velocity has also moved toward the suction-surface of the rotor blade. At $Z = 0.979$ and $R = 0.890$, a radial outward flow is observed near the pressure surface, where the boundary layer is found to be thick (compare plots of Figs. 6 and 11 at this location).

The radial velocities near the blade tip are believed to be influenced by the tip leakage flow. This flow produces a vortex which rolls up and travels downstream along the suction surface of the blade. The complete structure of the tip leakage vortex is not evident from these data. Possible reasons for this are the limited radial traverse distance of the three-sensor probe and a possible unsteady character of the tip leakage flow. Furthermore, the leakage flow is still in the form of a jet and has not yet developed into a vortex.

Due to limitations of the probe traverse and mechanical difficulties, no measurement could be taken very close to the blade surface. Here the radial velocities should be outward as indicated in Fig. 4. These radially outward flows, however, are present in the profile of the rotor blade wake at this location [4]. Radial velocities in blade boundary layers are caused by an imbalance in the radial pressure gradient and the centrifugal forces. Physically, at either surface of the rotor blade, the radial velocities must be zero. The maximum outward radial velocities occur slightly away from the blade surface in the blade boundary layer. This feature is not present in the data presented due to reasons mentioned above.

The radial variation of the maximum inward or outward radial velocities occurring within the passage is shown plotted in Fig. 12 for various axial locations. The radial velocities are insignificant at $Z = 0.0$. The outward velocities have maximum value at $Z = 0.25$ near the tip and $Z = 0.979$ at $R = 0.89$. The inward velocity reaches a maximum value at $Z = 0.5$ near the tip of the blade. The magnitude of the maximum

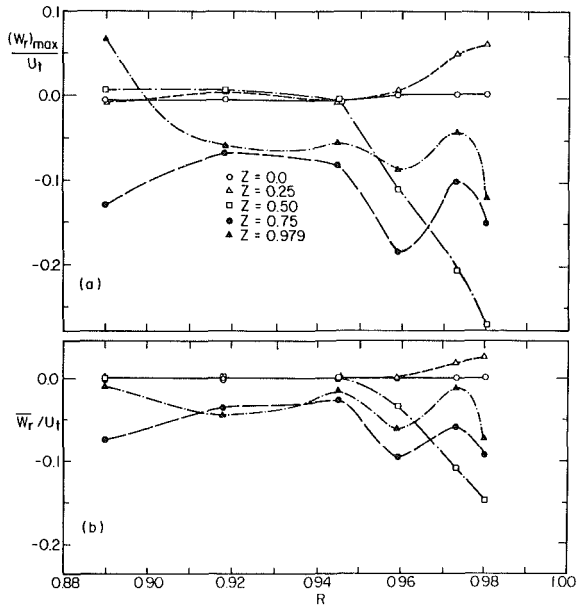

Fig. 12 Radial variation of the maximum and the passage-averaged radial velocities

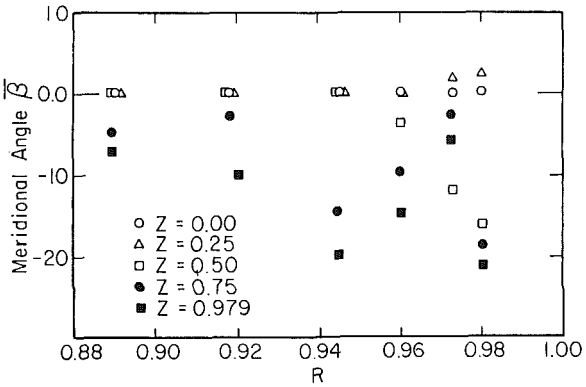

Fig. 13 Radial variation of the passage-averaged meridional angle ($\bar{\beta}$)

radial inward velocity decreases as the flow proceeds from $Z = 0.5$ to $Z = 0.979$.

The passage-averaged values of radial velocity are also shown plotted in Fig. 12. Here again, the passage-averaged radial velocities are negligibly small at $Z = 0$ and reach a maximum value near the tip at $Z = 0.5$. The region of large radial inward flow extends downward to lower radii, and the values of the average radial velocities decrease as the flow proceeds downstream.

A plot of the passage-averaged meriodional flow angle ($\bar{\beta}$) is shown in Fig. 13. The plot indicates that the meriodional angle ($\bar{\beta}$) increases continuously from the leading edge to the trailing edge of the blade and reaches a maximum value of -20 deg at $Z = 0.979$ and $R = 0.98$. Even though the radial velocities are highest at $Z = 0.5$ (Fig. 11), the streamwise velocities are also very high at this location. However, the radial velocities at $Z = 0.979$ are lower than those observed at $Z = 0.5$, and the streamwise velocity is also lower; hence, the meriodional flow angle is found to be highest at this axial location ($Z = 0.979$). The value of the average meriodional flow angle increases continuously from $Z = 0.25$ to $Z = 0.979$, and the increase is rapid from $Z = 0.25$ to 0.5. Furthermore, these angles are inward and their magnitude increases continuously from $R = 0.891$ to $R = 0.98$.

Velocity Vector Plots in s-n Plane and r-θ Plane. A plot of the velocity vectors in the s–n plane for $R = 0.98$ is shown in Fig. 14(a). The velocity in this plane is the resultant of W_s and W_n. As concluded earlier, the velocity vectors indicate that

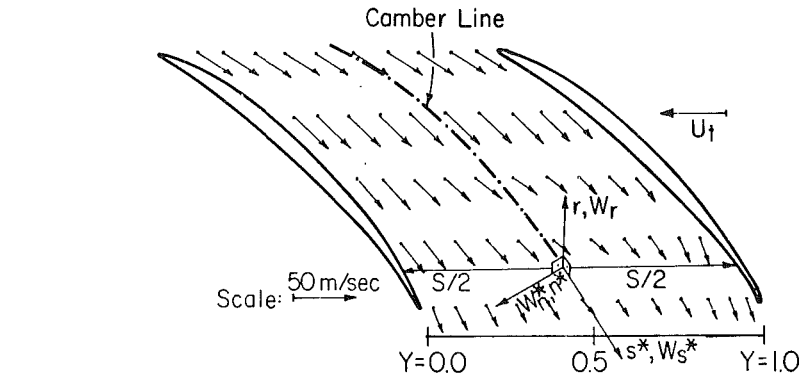

(a) Velocity Vectors in s-n Plane at R = 0.980.

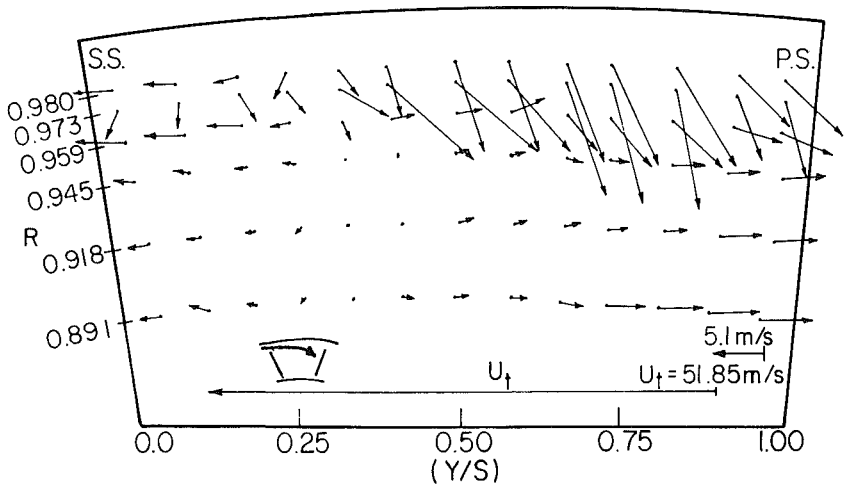

(b) Secondary Velocity ($\underline{W}_{sec}$) Vectors at Z = 0.500.

$$\underline{W}_{sec} = \underline{W}_{measured} - (\underline{W}_s^*)_{measured}$$

Fig. 14 Measured velocity vectors in the (*sn*) and (*rθ*) planes (see Fig. 14(*a*) and notation for the definition W_s^*)

the relative flow follows the blade passage very closely until $Z = 0.5$. Appreciable deviation in the flow is observed between the mid-passage and the pressure surface at this radial station. This departure is attributed to the leakage-flow jet originating from the pressure surface near the tip of the blade. The tangential motion of this jet is augmented by the blade motion. The jet shows a tendency to roll up to form a leakage vortex. This is evident from Fig. 14(*a*) as well as the secondary velocity vectors plotted in Fig. 14(*b*). The roll up and the resulting inward motion of the leakage flow are responsible for the appreciable velocity deficiency observed in Fig. 6. Figure 14(*a*) also indicates that the resultant velocity decreases continuously from $Z = 0.5$ to 0.979, with substantial reduction in velocity near the mid-passage at these axial locations.

The secondary velocity vectors (computed as the difference between the measured relative vector minus the measured component along the blade camber) represent the deviation of the flow from the mean streamline in both *r* and *n* directions in the *rθ* plane. From $R = 0.89$ to 0.945, the flow deviations are mainly in the normal direction; beyond $R > 0.945$, appreciable presence of radial velocity is observed. The motion of the jet due to the leakage flow, discussed earlier, is evident from this plot. The leakage flow tends to move downward in the tip region ($R > 0.945$) from mid-passage to suction surface. This phenomenon is illustrated in the insert of Fig. 14(*b*). It is evident that the leakage flow behavior is quite different from that observed in a cascade [12], where the leakage flow tends to roll up immediately near the suction surface. In a compressor rotor, the relative motion has a tendency to move the roll up farther away from the suction surface as evidenced from the secondary velocity vector contours shown in Fig. 14(*b*). This phenomenon has also been predicted by Wadia and Booth [15] by a theoretical analysis employing a simple model of the leakage flow.

Total Relative Velocity Contours. The distribution of the total relative velocity in the form of isocontour plots inside the blade passage at axial locations $Z = 0.750$ and $Z = 0.979$ is shown in Fig. 15. These isocontour plots clearly indicate the three-dimensional nature of the flow inside the blade passage. A distinct velocity deficiency is noted at approximately 65 percent of the distance from the suction surface at radial locations above $R = 0.945$. The low relative velocities near the tip result in a large stagnation (absolute) pressure rise in this region. This large pressure rise is not due to flow turning, but is caused by complex mixing and viscous interactions due to the leakage flow and the annulus wall boundary layer. This interaction region is an area of maximum loss, with considerable flow mixing which results in strong eddies and energy dissipation. The interference region is seen to grow with axial distance. At $Z = 0.750$, the total velocity is at a level of 0.3 to 0.4 W/U_t, and at $Z = 0.979$, the total velocity has decreased to a level of 0.2 to 0.3 W/U_t.

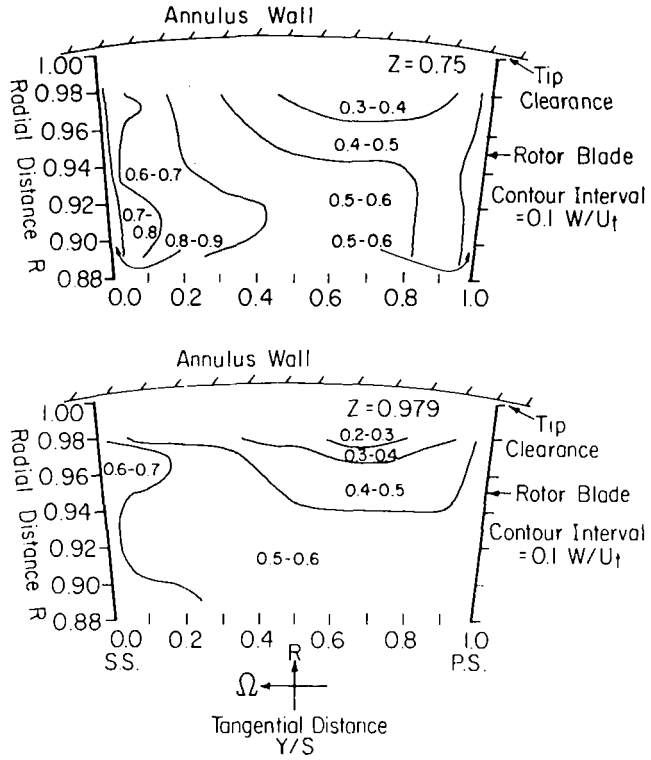

Fig. 15 Isocontours of total velocity at Z = 0.75 and 0.979

Mean Properties of the Annulus Wall Boundary Layer. The radial variation of the axial velocity and the relative tangential component of mean velocities averaged over the passage is plotted in Fig. 16.

The axial velocity profile is well-behaved near the leading edge and upstream ($Z = -0.35, 0$). The velocity gradients are not as steep. The profile shows a marked change for $Z \geq 0.25$. The influence of the leakage flow, which has the same effect as the blowing in a boundary layer, is felt at these stations. The flow velocities increase in magnitude from $R = 0.96$ to 0.98 as the flow travels downstream from $Z = 0$ to 0.25. The profiles are unconventional and complex for $Z \geq 0.25$. The axial velocities in the tip region decrease from $Z = 0.25$ to 0.5, and then increase again downstream of the blade.

The mean tangential velocities (relative) behave differently from the axial velocities. The absolute tangential velocity follows the conventional boundary layer profile and the relative tangential velocity is of the "wake" type with maximum velocities at the annulus wall and free stream with defects in between. This is evident from the plot shown in Fig. 16. The relative tangential velocities change rapidly from the tip of the blade ($R = 0.98$) to the annulus wall. On the basis of this plot, it can be concluded that the absolute tangential velocities are expected to be large at $R = 0.98$, decreasing towards the wall to reach zero values there. It is thus evident that large gradients in absolute tangential velocity exist in the tip region. The relative tangential velocities in the free stream decrease continuously from the leading edge to the trailing edge, which is as expected from the inviscid analysis or design.

The axial and tangential components of momentum thicknesses and the shape factor were derived from the data in Fig. 16 using the following equations:

$$\delta_z^* = \int_{R=0.891}^{R=1} \left(1 - \frac{\bar{W}_z}{\bar{W}_{z_0}}\right) dR,$$

$$\delta_\theta^* = \int_{R=0.891}^{R=1} \left(\frac{\bar{W}_\theta}{\bar{W}_{\theta_0}} - 1\right) dR \tag{1}$$

$$\Theta_z^* = \int_{R=0.891}^{R=1} \frac{\bar{W}_z}{\bar{W}_{z_0}} \left(1 - \frac{\bar{W}_z}{\bar{W}_{z_0}}\right) dR,$$

$$\Theta_\theta^* = \int_{R=0.891}^{R=1} \left(\frac{\bar{W}_\theta}{\bar{W}_{\theta_0}} - 1\right) \frac{\bar{W}_\theta}{\bar{W}_{\theta_0}} dR \tag{2}$$

and

$$H = \delta_z^* / \Theta_z^*$$

The expressions for the momentum and displacement thicknesses based on absolute tangential velocity are given by

$$(\delta_\theta^*)_{Abs} = \int_{R=0.891}^{R=1} \left(1 - \frac{\bar{V}_\theta}{\bar{V}_{\theta_0}}\right) dR,$$

$$(\Theta_\theta^*)_{Abs} = \int_{R=0.891}^{R=1} \frac{\bar{V}_\theta}{\bar{V}_{\theta_0}} \left(1 - \frac{\bar{V}_\theta}{\bar{V}_{\theta_0}}\right) dR \tag{3}$$

where V_θ is the absolute tangential velocity, and $\bar{W}_{z_0}$, $\bar{W}_{\theta_0}$, $\bar{V}_{\theta_0}$ are axial velocity, relative tangential velocity, and absolute tangential velocity, respectively, at $R = 0.891$, except at the $Z = 0.979$, where it refers to the values at $R = 0.918$. The momentum thicknesses at the exit of the blade row are given in reference [4].

The axial variation of the axial component of the displacement and momentum thicknesses and the shape factor is shown in Fig. 17. Both δ_z^* and Θ_z^* increase slowly from $Z = -0.35$ to 0.25, beyond which a rapid increase up to $Z = 0.5$ and a rapid decrease from $Z = 0.5$ to 0.75 are noticed. The rapid increase from $Z = 0.25$ to 0.5 is brought about by the adverse pressure gradients. The decrease in $Z = 0.5$ to 0.75 is caused by the leakage flow, which reenergizes the annulus wall boundary layer. This can be seen from the profiles plotted in Fig. 16. Further increase in the momentum and displacement thicknesses observed beyond $Z = 0.75$ is again brought about by the adverse pressure gradient in the blade passage.

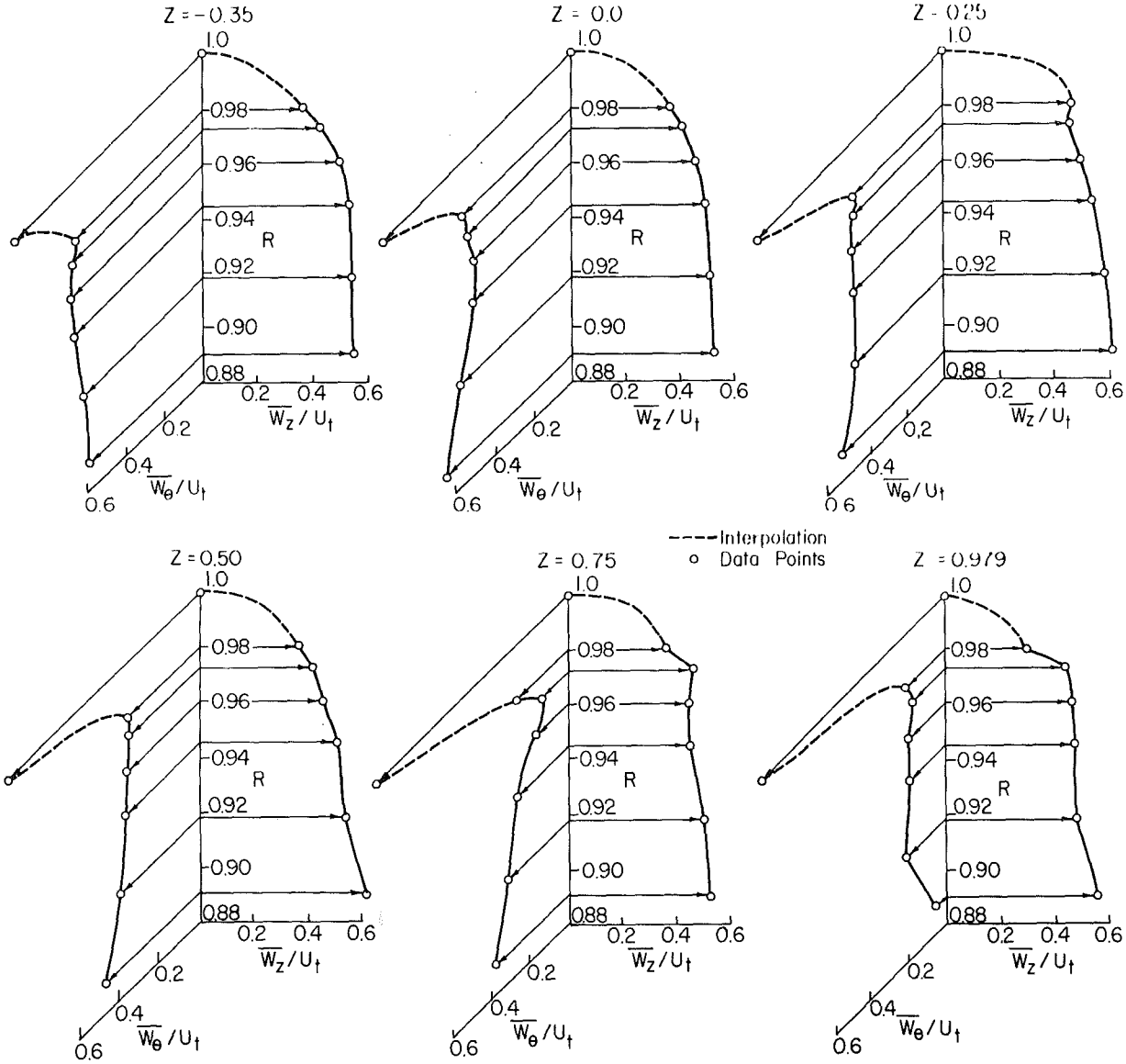

Fig. 16 Measured development of the three-dimensional annulus wall boundary layer

The tangential components of the displacement thickness and the momentum thickness, shown in Fig. 17, behave differently. The displacement thickness shows small values in the region (Z = 0.5 to 0.75) where the leakage flow is maximum, and the same region has the maximum momentum thickness. This trend is reversed for the displacement and momentum thicknesses based on the absolute tangential velocities as shown in Fig. 17. In the blade leading edge, a drastic decrease in momentum $[(\Theta^*_\theta)_{Abs}]$ and displacement thicknesses $[(\delta^*_\theta)_{Abs}]$ is brought about by an increase in the swirl velocity in the annulus wall region caused by the dragging of the fluid by the blade tip. An increase in these values between Z = 0.25 to Z = 0.5 is brought about by the leakage flow. Both the momentum and displacement thicknesses of the absolute flow decrease beyond Z = 0.5.

Conclusions

Some of the important conclusions derived from the measurements reported in this paper are as follows:

1 The tip leakage flow originates near quarter-chord, with peak values occurring near mid-chord. It is concluded that the leakage flow, which is in the form of a jet within the blade row, is augmented by the blade rotation and travels farther away from the suction surface than that observed in stationary blade rows and cascades. This leakage flow tends to roll up between the mid-passage and the pressure surface near the tip region. The vortex formation does not occur within the passage in this particular case.

2 The flow field near the annulus wall region is primarily inviscid in nature at radial locations below 10 percent of the blade span from the blade tip.

3 At locations within approximately 10 percent of the blade span near the blade tip, a region of intense viscous and leakage flow interaction and mixing occurs at 65 percent of the blade spacing from the suction side of the blade passage. The streamwise velocity deficiency reaches a maximum value of 0.6 W_{s_0}. The resulting "wake-type" profile is attributed to low-momentum fluid and inward radial flows generated by the interaction of the leakage flow and the annulus wall boundary layer. The magnitude of this velocity deficiency increases with the axial distance inside the blade passage.

4 Within the blade passage and at radial locations within 10 percent of the blade tip, the normal velocity indicates large

amounts of flow underturning and overturning which reveal the effect of the leakage flow. The flow overturning is due to the rolling up of the tip leakage flow by the mainstream flow. However, the normal velocity is reversed at higher radial locations near the blade tip. This underturning of the flow is due to the combined effect of the tip leakage flow and the annulus wall boundary layer.

5 The radial velocities are mostly inward in the tip region. Large radial inward velocities are observed near the outer 8 percent of the span, with maximum values occurring near the mid-passage in the tip region.

6 The annulus wall boundary profile undergoes substantial changes as it passes from the leading edge of the blade to the trailing edge. The boundary layer is energized by the leakage flow, resulting in a complex profile.

7 The axial components of displacement and momentum thicknesses of the annulus wall boundary layer also increase initially, reaching a maximum value near mid-chord. Subsequent decreases in the momentum and displacement thicknesses are attributed to the leakage flow.

Acknowledgment

This work was supported by the National Aeronautics and Space Administration through Grant No. NSG 3212, with P. M. Sockol as the project monitor. The data on the blade pressure distribution and the limiting streamline angle were provided by N. Sitaram and T. R. Govindan, respectively. The authors also wish to thank G. Kane and J. Fetterolf for their aid with the experimental set up and instrumentation.

References

1 Lakshminarayana, B. and Gorton, C. A., "Three-Dimensional Flow Field in Rocket Pump Inducers—Part 2," ASME *Journal of Fluids Engineering*, Vol. 99, Series I, No. 1, Mar. 1977, pp. 176–186.

2 Dring, R. P., Joslyn, H. D., and Hardin, L. W., "An Investigation of Axial Compressor Rotor Aerodynamics," ASME JOURNAL OF ENGINEERING FOR POWER, Vol. 104, No. 1, Jan 1982, p. 84.

3 Lakshminarayana, B. and Ravindranath, A., "Interaction of Compressor Rotor Blade Wake with Wall Boundary Layer/Vortex in the End Wall Region," ASME JOURNAL OF ENGINEERING FOR POWER, Vol. 104, No. 2, Apr. 1982, pp. 467–478.

4 Davino, R. and Lakshminarayana, B., "Characteristics of Mean Velocity in the Annulus Wall Region at the Exit of the Turbomachinery Rotor Passage," *AIAA Journal*, Vol. 20, No. 4, Mar. 1982, pp. 528–535.

5 Lakshminarayana, B., Davino, R., and Pouagare, M., "Three-Dimensional Flow Field in the Tip Region of a Compressor Rotor Passage—Part II: Turbulence Properties," ASME JOURNAL OF ENGINEERING FOR POWER (this issue).

6 Smith, L. H., "Three-Dimensional Flow in an Axial Flow Turbomachinery," WADC Technical Report 55-348, Vol. 2, John Hopkins University, 1956.

7 Lakshminarayana, B., "An Axial Flow Research Compressor Facility Designed for Flow Measurement in Rotor Passages," ASME *Journal Of Fluids Engineering*, Vol. 102, No. 4, Dec. 1980, pp. 402–411.

8 Gorton, C. A. and Lakshminarayana, B., "A Method of Measuring the Three-Dimensional Mean Flow and Turbulence Quantities Inside a Passage," ASME JOURNAL OF ENGINEERING FOR POWER, Vol. 98, No. 2, pp. 137–146.

9 Davino, R., "Three-Dimensional Mean Flow and Turbulence Characteristics in the Annulus-Wall Region of an Axial Flow Compressor Rotor Blade Passage," M.S. thesis, Department of Aerospace Engineering, The Pennsylvania State University, Nov. 1980.

10 Pandya, A. and Lakshminarayana, B., "Investigation of the Tip Clearance Flow Inside and at the Exit of a Compressor Rotor Passage, Part I: Mean Velocity Field," ASME Paper 82-GT-12 (to be published in ASME JOURNAL OF ENGINEERING FOR POWER).

11 Johnston, J. P., "A Wall Trace, Flow Visualization Technique for Rotating Surfaces in Air," *Journal of Basic Engineering*, 1964.

12 Lakshminarayana, B. and Horlock, M. H., "Leakage and Secondary Flows in Compressor Cascades," *British ARC R and M, 3483*, London, 1967, pp. 1–58.

13 Lakshminarayana, B., "Three-Dimensional Flow Field in Rocket Pump Inducers, Part I: Measured Flow Field Inside the Rotating Blade Passage and at the Exit," ASME *Journal of Fluids Engineering*, Vol. 95, No. 4, Dec. 1973, pp. 567–578.

14 Lakshminarayana, B., "Methods of Predicting the Tip Clearance Effects in Axial Flow Turbomachinery," *Journal of Basic Engineering*, Vol. 92, Sept. 1970, pp. 467–482.

15 Wadia, A. R. and Booth, T. C., "Rotor Tip Leakage, Part II: Design Optimization Through Viscous Analysis and Experiment," ASME JOURNAL OF ENGINEERING FOR POWER, Vol. 104, No. 1, Jan. 1982, p. 162.

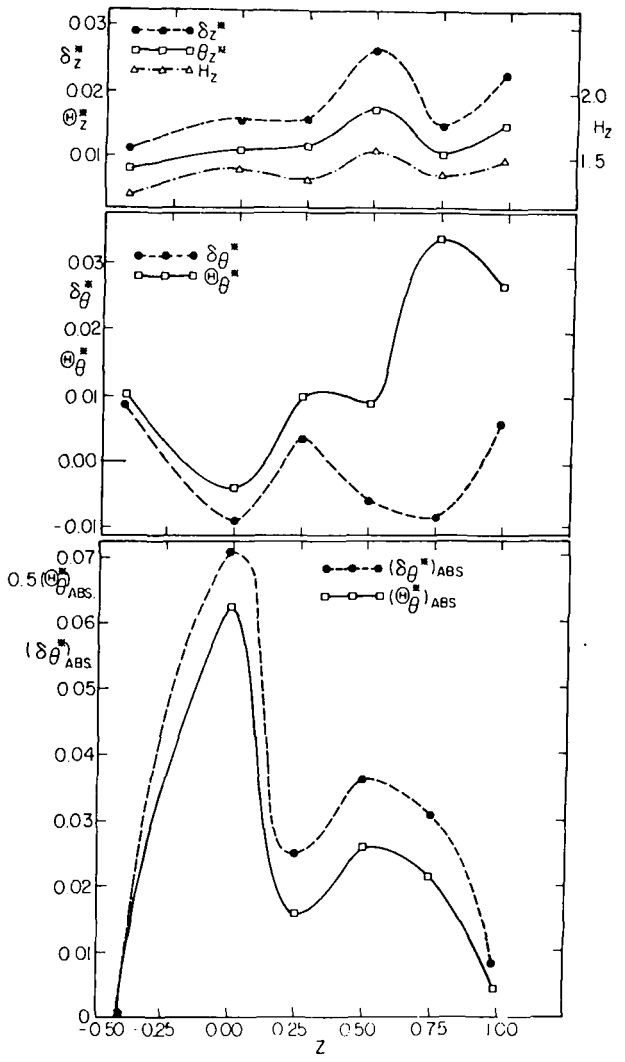

Fig. 17 Axial variation of the axial and tangential components of displacement and momentum thicknesses of the annulus wall boundary layer

Three-Dimensional Flow Field in the Tip Region of a Compressor Rotor Passage—Part II: Turbulence Properties

B. Lakshminarayana
Director of Computational Fluid Dynamics Studies, and Professor of Aerospace Engineering. Fellow ASME

R. Davino

M. Pouagare
Graduate Assistant.
Department of Aerospace Engineering, The Pennsylvania State University, University Park, Pa 16802

The turbulence properties in the annulus wall region of an axial flow compressor rotor was measured using a triaxial, hot-wire probe rotating with the rotor. The flow was surveyed across the entire passage at five axial locations (leading edge, 1/4 chord, 1/2 chord, 3/4 chord, and the trailing edge location) and at six radial locations in a low-speed compressor rotor. The data derived include all three components of turbulence intensity and three components of turbulence stress. A comprehensive interpretation of the data with emphasis on features related to rotation, leakage flow, annulus wall boundary layer, and blade boundary layer interactions is included. All the components of turbulent intensities and stresses are found to be high in the leakage-flow mixing region. The radial component of intensities and stresses is found to be much higher than the corresponding streamwise components. The turbulent spectra clearly reveal the decay process of the inlet-guide-vane wake within the rotor passage.

Introduction

The presence and interaction of the leakage flow, annulus wall boundary layer, secondary flow, scraping vortex, and the blade boundary layer in the end wall flow region of turbomachinery produce complex mixing and large turbulent fluctuations. This region accounts for a substantial fraction of losses (one-third to one-half) in turbomachinery. The existence of high turbulence in this region within the passage accounts for a substantial portion of this loss. Hence, a knowledge of the turbulence flow field in the tip region of turbomachinery is not only essential for understanding the sources of losses and three dimensionality introduced by this turbulence, but also in the development of a turbulence closure model for the prediction of the three-dimensional flow field in this region. The turbulence in this region is also responsible for mixing losses downstream, unsteady (random) flows, and noise generated by the subsequent stator blade row.

Further improvements in design, performance, and flow prediction in the end wall region should come from a better understanding of the flow field. Due to the complexity of measurement in a rotor frame of reference, there has been no attempt to measure the passage flow in the tip region. Stationary cascades have been of great value in studying some of these mechanisms. The cascade, however, is unsuitable for the study of a variety of mechanisms which are present in turbomachinery. The effects of rotation, curvature, the relative motion between the rotor and the end wall, and other three-dimensional effects in the end wall region are most suitably studied in an actual turbomachine environment.

The primary objective of the current study reported in this paper has been to gain an additional understanding of the complex turbulent flow field in the annulus wall region, including the three components of turbulence intensities and turbulence stresses inside the rotor blade passage. This is accomplished by a complete survey of the rotor blade passage in the tip region utilizing a rotating three-sensor, hot-wire probe and by rotor blade static pressure measurements [1]. It is hoped that the knowledge obtained from this investigation will help serve in establishing a theoretical model for the eventual analysis of the three-dimensional flow and losses in the annulus wall region.

This is a companion paper of reference [1]. The mean flow properties are discussed in [1], and the turbulence properties are presented in this paper. The turbulence properties at the exit, measured with a stationary three-sensor, hot-wire probe, are reported in reference [2].

Experimental Facility, Instrumentation, and Program

All the measurements reported in this paper were performed using the Axial Flow Compressor Facility in the Department of Aerospace Engineering of The Pennsylvania State University. All the data were acquired with a triaxial, hot-wire probe rotating with the rotor. The study included the measurement of mean velocities, turbulence intensities, and Reynolds stresses. Only the turbulence data is presented and interpreted in this paper. The mean flow data is described in a companion paper [1].

A general description of the compressor stage is given by

Contributed by the Gas Turbine Division of THE AMERICAN SOCIETY OF MECHANICAL ENGINEERS and presented at the 27th International Gas Turbine Conference and Exhibit, London, England, April 18-22, 1982, Manuscript received at ASME Headquarters December 15, 1981. Paper No. 82-GT-234.

Table 1 Maximum streamwise velocity (W_{s_0}/U_t) for the reported measurement stations

Percent span From tip	R \ Z	0.0	0.25	0.50	0.75	0.979
4	0.98	0.690	0.750	0.653	0.55	0.432
5	0.973	0.709	0.824	0.670	0.707	0.588
8	0.959	0.716	0.858	0.697	0.593	0.580
11	0.945	0.750	0.943	0.742	0.579	0.553
16	0.918	0.780	0.973	0.840	0.680	0.539
22	0.891	0.861	0.975	0.923	0.740	0.610

Smith [3], and a detailed discussion of the Axial Flow Compressor Facility is given by Lakshminarayana [4]. Good peak efficiencies are exhibited by the rotor. The hub/annulus wall diameter ratio of the facility is 0.5, with the diameter of the annulus wall equal to 0.932 m. The inlet guide vane row, which consists of 43 blades, is followed by the 21-bladed rotor. The rotor is driven by a 37 kw variable-speed motor through a belt-and-pulley system. The rotor is followed by a stator vane row of 25 blades. Downstream of the stator is located a Joy axial flow fan with variable blade setting for the variation of pressure rise and mass flow. Operating conditions and rotor specifications are as follows: inlet velocity, 29 m/s; flow coefficient based on tip speed, 0.56; stage loading coefficient based on tip speed, 0.486; speed of rotor, 1060 rpm; tip clearance, 0.25, to 0.30 cm. Blade element data at the tip are NASA 65 series; chord, 15.41 cm; spacing, 14.12 cm; maximum thickness, 5.10 percent of chord; stagger angle, 45.0 deg; and camber, 8 percent of chord. The blade element details of the rotor are given in Table 1 of reference [5].

The rotating-probe traverse mechanism and the instrumentation system used in these measurements are described in detail in [4]. A triaxial, hot-wire probe, similar to that used in [4] and [5], was employed for all turbulence measurements reported in this paper. The probe calibrations are corrected for the variations of temperature and aging of the wire. The signals from the rotating hot wire, rotating with the rotor, were taken through a ten-channel, slip-ring unit to a stationary data-processing system described in [4]. The choice of the instrumentation was made such that the raw data from the experiment could be used directly in the data-processing program developed by Gorton and Lakshminarayana [6]. The probe measurement programs incorporated the three-sensor, hot-wire calibration and operation techniques discussed in Chapter 3 of [7]. The yaw and pitch angle sensitivity of the passage-flow probe response was determined through calibration of the probe at various yaw and pitch angles and mat-plotting of the sensor response.

The measurements were taken at several radial and axial stations, and are tabulated in Table 1. The stationary hot-wire probe data on turbulence at the *exit* of the rotor passage at these radii are presented in [2]. All measurements reported in this paper were taken *inside* the rotor passage near the tip region.

Experimental Results and Interpretation

The hot-wire measurements derived from the triaxial, hot-wire probe are plotted in the (s, n, r) coordinate system. The orientation of this coordinate system (s, n, r), as well as the flow angle, α, and the meridional angle, β, with respect to the compressor coordinate system (z, θ, r), are indicated in Fig. 1. The s, n, r coordinate system follows the projection of the flow at the mid-passage in the radial plane for the various

Nomenclature

c = blade chord length
e = fluctuating voltage of the hot wire
PS = pressure side of the rotor blade passage
k = total energy of turbulence $(\overline{w_s^2} + \overline{w_n^2} + \overline{w_r^2})/2W^2_{so}$
R = radius ratio (r/r_{tip}), $R = 1$ at tip, $R = 0.5$ at hub
S = blade spacing
SS = suction side of the rotor blade passage
(s,n,r) = end-wall flow coordinate system (streamwise, normal, and radial coordinate directions, Fig. 1)
U_t = blade tip speed
W = relative flow velocity
w = fluctuating component of relative velocity
Y = tangential distance measured from camber line ($Y = 0$ on the suction side, $Y = S$ on the pressure side)
Z = streamwise distance from the rotor blade leading edge normalized by the rotor blade chord
(z,θ,r) = axial, tangential, and radial coordinate system (Fig. 1)
α = relative flow angle (Fig. 1)
τ_s,τ_n,τ_r = normalized turbulence intensities in the streamwise, normal, and radial directions, respectively $(\sqrt{\overline{w_s^2}}/W_s, \sqrt{\overline{w_n^2}}/W_s, \sqrt{\overline{w_r^2}}/W_s)$
$\tau_{sn},\tau_{rn},\tau_{rs}$ = Reynolds stress correlations given by $\overline{w_s w_n}/W_s^2, \overline{w_n w_r}/W^2_s, \overline{w_r w_s}/W^2_s$, respectively
τ_z,τ_θ = normalized turbulence intensities in the axial and tangential directions, respectively $\sqrt{\overline{w_z^2}}/W, \sqrt{\overline{w_\theta^2}}/W$
Ω = rotational speed of the rotor blade

Subscripts

1 = inlet value
0 = free stream value/maximum value
s,n,r = values in the streamwise, normal, and radial coordinate directions, respectively (Fig. 1)
t = blade tip location
z,θ,r = values in the axial, tangential, and radial coordinate directions, respectively (Fig. 1)
1,2,3 = hot wires 1, 2, and 3 in a three-sensor wire

Superscript

$-$ = time-averaged values

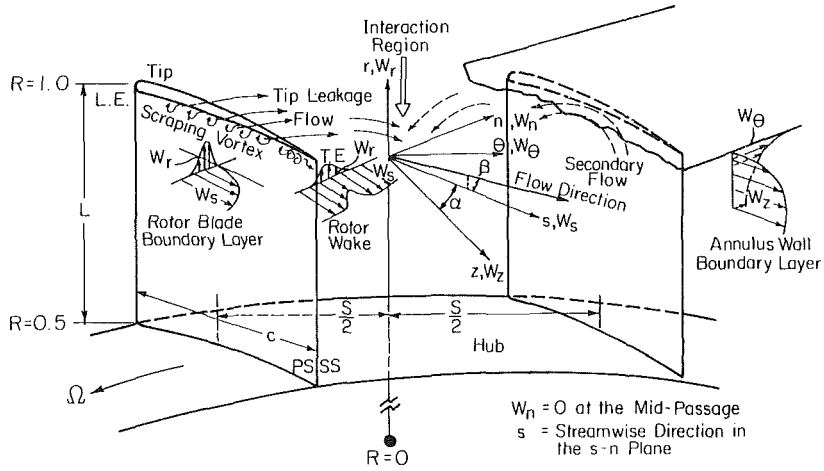

Fig. 1 Definition of streamwise (s,n,r) coordinate system

axial measurement stations. s is the projection of the streamwise direction at mid-passage onto a cylindrical plane, n is the principal normal, and r is the radial direction. Therefore, at the mid-passage $W_n = 0$. All intensities and shear stresses presented in this section are in a relative system and are normalized by the corresponding local streamwise velocity in the blade passage. The tangential distance is normalized by the blade spacing, with $Y/S = 0$ and $Y/S = 1$ representing the blade suction and pressure sides, respectively. The maximum values of the streamwise velocity $[(W_s)_0/U_t]$ are tabulated in Table 1.

The mean velocity and turbulence intensity profiles at inlet to the rotor (0.35 chord length upstream of the leading edge) are shown in Fig. 2. The annulus wall boundary layer thickness is approximately 12 to 14 percent of the span from the tip. The axial velocity profile is of the conventional type. The peak turbulence intensities (τ_θ is the tangential component, and τ_z is the axial component, both normalized with respect to the local relative velocity) reach about 10 percent near the annulus wall, with free stream turbulence intensities averaging less than 2 percent.

The blade-to-blade variation of the streamwise velocity (W_s) at various axial and radial stations is given in Fig. 3. Detailed interpretation of the data in this figure is given in [1]. The presence of velocity defect near the tip region ($R \geq 0.945$ at $Z \geq 0.5$) is caused by the presence of leakage flow and its interaction (roll up) with the main flow. All other data related to the mean velocity profile is presented and interpreted in [1].

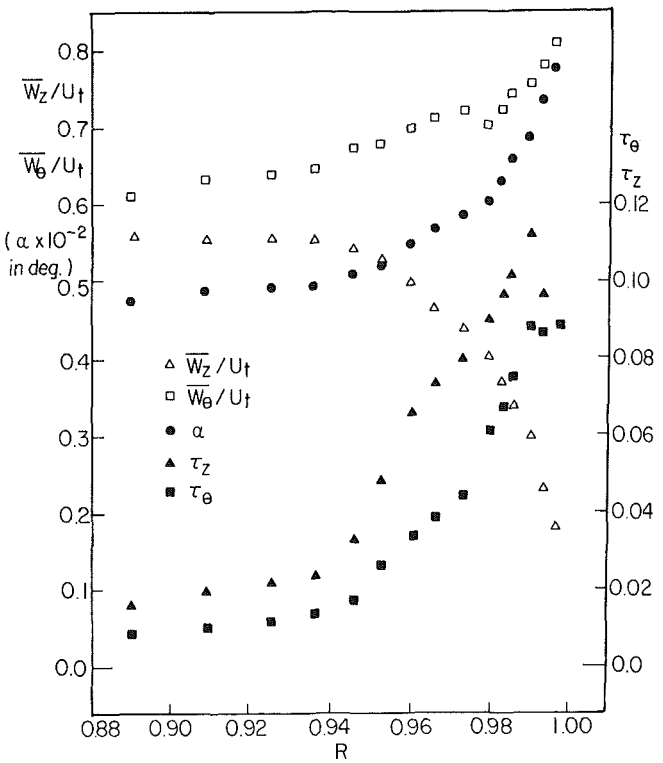

Fig. 2 Inlet velocity and turbulence profiles in the tip region upstream of the rotor ($Z = -0.35$)

Turbulence Intensity Profiles. The blade-to-blade variation of the turbulence intensity profiles at the blade leading edge is shown in Fig. 4. All three components of intensities are nearly uniform across the passage and show a slight increase in their values towards the pressure surface. The normal and the radial components of turbulence intensity vary from 5 to 7.5 percent from $R = 0.891$ to 0.980. The streamwise turbulence intensities vary from 2 to 5 percent from $R = 0.891$ to 0.980. All the shear stresses (only τ_{sn} is shown in Fig. 4) are zero at this location.

The blade-to-blade variation of the streamwise, normal, and radial components of turbulence intensity at all the other axial locations are shown in Figs. 5, 6, and 7, respectively. All intensities and stresses are normalized with respect to the local streamwise velocities.

Streamwise-Turbulence Intensity (τ_s). The blade-to-blade variation of the streamwise component of turbulence intensity at $Z = 0.25$, 0.5, 0.75, and 0.979 at various radial locations is shown in Fig. 5. Because of the mechanical limitations and the errors due to the wall vicinity, no measurements were taken very close to the blade surface.

At $Z = 0.25$, the streamwise-turbulence intensities are about the same as those observed at $Z = 0$ (Fig. 4), with a slight decrease in their magnitude at $R = 0.891$ near the suction side where the inviscid effects and flow acceleration are dominant features, and a slight increase at $R = 0.981$ and $R = 0.973$, where the annulus wall boundary layer is the dominant factor.

At $Z = 0.5$, the values of τ_s show a rapid increase from those measured at $Z = 0.25$, especially at higher radii. Since the flow is predominantly inviscid up to $R = 0.945$, the streamwise-turbulence intensities are nearly uniform here, with generally higher values than those measured at $Z = 0.25$. The streamwise-turbulence intensities are large in the tip region ($R = 0.959$ to 0.980), with peak intensities as high as 10 to 15 percent occurring near the mid-passage. Even the intensities in the "free stream" region have increased substantially, averaging about 7.5 percent at radii $R \geq 0.959$. The region of high turbulence intensity near the mid-passage is caused by the mixing of the leakage flow, as discussed in

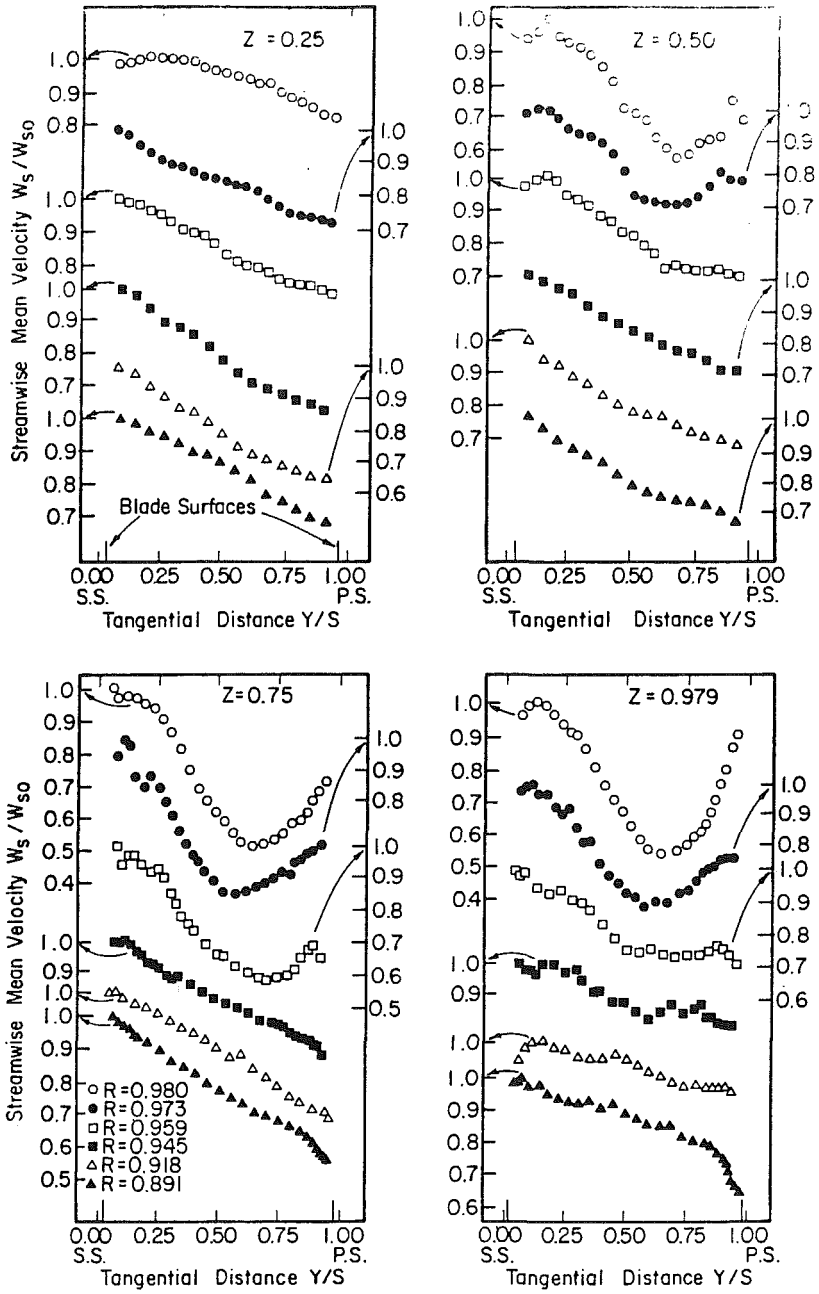

Fig. 3 Blade-to-blade distribution of the streamwise velocity (W_s) at Z = 0.25, 0.50, 0.75, 0.979

[1]. The leakage flow velocities are high at $Z = 0.5$, and this is augmented by the blade rotation. This has the effect of delaying the roll up or mixing of the leakage flow jet. Therefore, the "interference" or "mixing" region is almost near the mid-passage.

At the axial station $Z = 0.75$, the streamwise intensity profiles from $R = 0.891$ to $R = 0.959$ are similar to those measured at $Z = 0.5$. The values remain about the same, with large changes observed only at the higher radii, especially at $R = 0.980$. The blade-to-blade distribution of τ_s has become more uniform at $R = 0.980$, with its value ranging from 0.05 at the suction side to 0.10 at the pressure side. The "peaky" distribution observed at $R = 0.980$ seemed to have moved down to $R = 0.973$, indicating the movement of the leakage flow interaction region downward as the flow proceeds from $Z = 0.5$ to 0.75.

The location of the high turbulence levels corresponds to the interference region where considerable flow mixing occurs. As shown by the mean velocity profiles [1], this region is located at approximately 65 percent of the blade passage from the suction surface of the rotor blade. The region of increased turbulence intensity is seen to increase radially to the radial location of $R = 0.945$ at the axial location $Z = 0.979$. This indicates the spatial growth of the interference region as the end wall flow propagates downstream within the blade passage.

The streamwise-turbulence intensity is also seen to increase near the blade surfaces at $Z = 0.75$ and 0.979 near the pressure side. This increase is due to the production of turbulence by the mean velocity gradients in the blade boundary layers. A decrease should then occur very near the blade surface in the viscous layer. However, this was not observed since measurements could not be taken in this region due to the finite size of the probe.

A slight decrease in the peak turbulence intensities (τ_s) observed at $Z = 0.979$ may be due to the fact that the "mixing" region is spreading inward (compare plots at $Z = 0.75$ and 0.979), providing a decrease in intensities. The

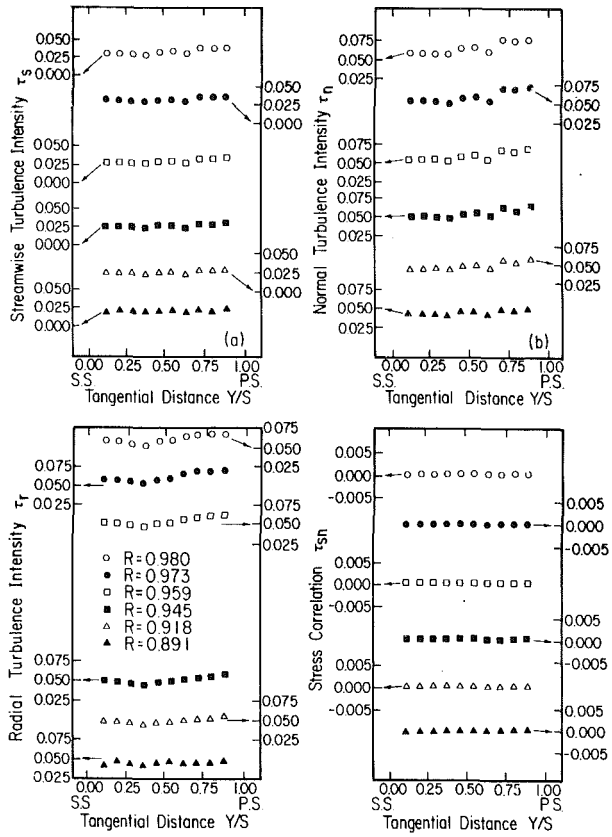

Fig. 4 Blade-to-blade distribution of the streamwise (τ_s), normal (τ_n) and radial (τ_r) turbulence intensities and stress correlation (τ_{sn}) at the leading edge ($Z = 0$)

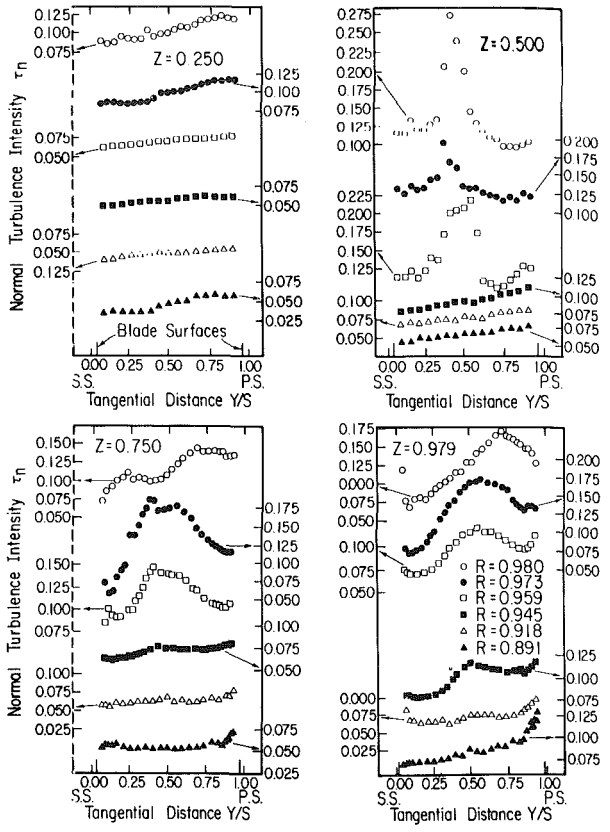

Fig. 6 Blade-to-blade distribution of the normal-turbulence intensity (τ_n) at $Z = 0.25, 0.5, 0.75, 0.979$

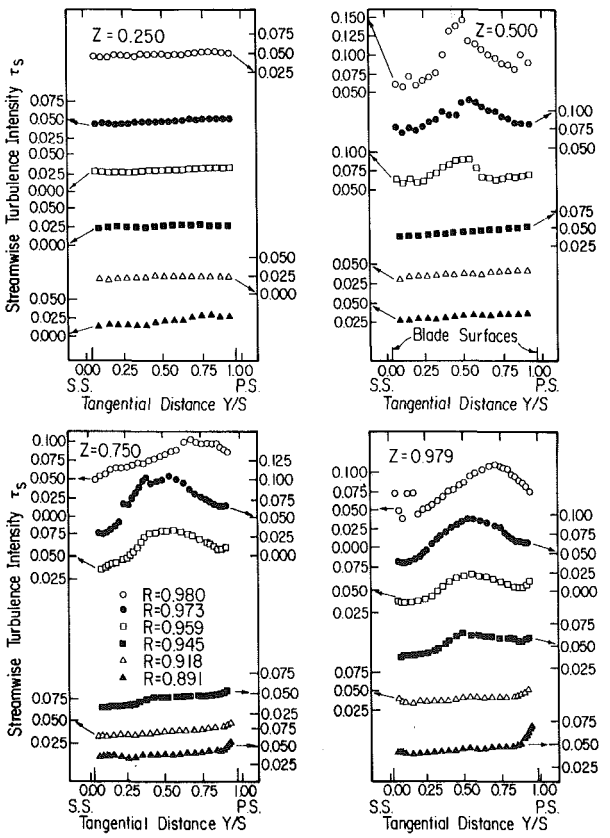

Fig. 5 Blade-to-blade distribution of the streamwise-turbulence intensity (τ_s) at $Z = 0.25, 0.5, 0.75, 0.979$

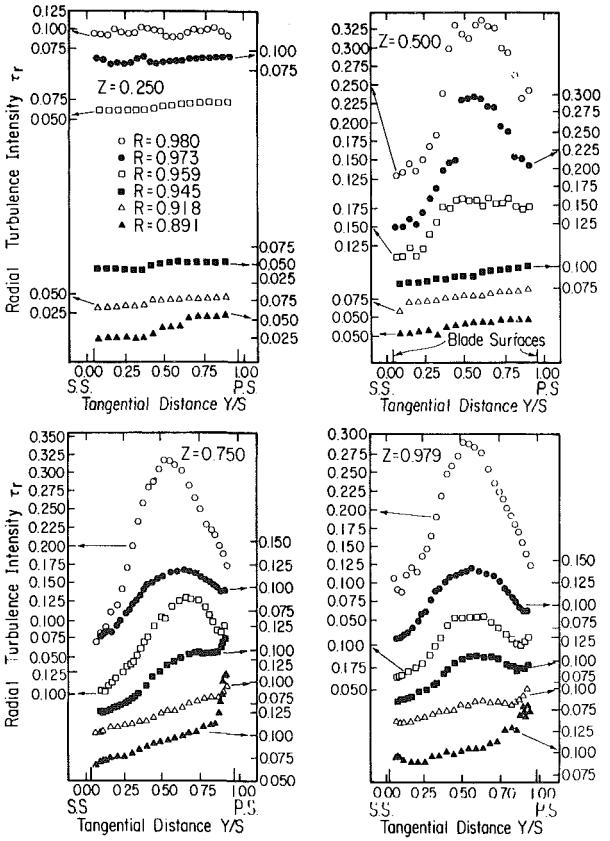

Fig. 7 Blade-to-blade distribution of the radial-turbulence intensity (τ_r) at $Z = 0.25, 0.5, 0.75, 0.979$

distribution of τ_s at $Z = 0.75$ and 0.979 is very similar, except at $R = 0.980$.

The streamwise-turbulence intensity profiles at the exit of the blade row at these radii are given in [2]. Considerable redistribution is observed, resulting in higher values of intensities in the free stream caused by the intense mixing downstream. At 4 percent chord downstream of the trailing edge, the free stream intensity increases to nearly 20 percent at $R = 0.980$.

Normal-Turbulence Intensity (τ_n). The blade-to-blade variation of the normal component of turbulence intensity at various axial and radial locations is shown plotted in Fig. 6. The distribution of τ_n is very similar to that of the streamwise-turbulence intensity, but the values are generally higher. Hence, the interpretation will be limited to only the new features.

At $Z = 0.25$, the normal-turbulence intensities are generally higher than those of the streamwise values, with peak intensity occurring near the pressure surface with values varying from 5 percent at $R = 0.891$ to 11 percent at $R = 0.980$.

At $Z = 0.5$, the normal-turbulence intensity profiles show the dramatic effect of the leakage flow, which is approximately in the blade normal direction. The mixing region has peak intensities near the mid-passage, decreasing continuously towards both blade surfaces. The τ_n profile shows a distribution characteristic of a free shear flow, with peak intensities increasing from 10 percent at $R = 0.945$ to 27.5 percent at the tip. This is almost twice as much as the streamwise intensity (τ_s) values. This indicates the highly anisotropic nature of turbulence in this region. The leakage flow is likely to be dominant in the direction normal to the blade at this axial location. This may also be interpreted as caused by the presence of a leakage vortex due to the roll up of the leakage flow jet. The shear stress distribution given later substantiates this conclusion.

Farther downstream ($Z = 0.75$), the "peaky" distribution of normal-turbulence intensities observed at $Z = 0.5$ seems to spread out across the passage as well as inward in the radial direction. The shear flow region is less than half the blade passage at $Z = 0.5$ for $R \geq 0.959$, but spreads out across the entire passage at $Z = 0.750$. The peak intensity has also decreased drastically. This indicates that the mixing region caused by the interaction of the leakage flow jet and the main flow at $Z = 0.5$ seems to spread out and decay as it moves downstream. This phenomenon can be compared to that of a confined jet mixing, with a secondary jet mixing with a primary jet. In this case, the two jets (leakage flow and the main flow) are nearly normal to each other.

As the flow approaches the trailing edge ($Z = 0.979$), the "mixing" region seems to become well developed with a rather smooth distribution in normal-turbulence intensities. The peak values move towards the pressure surface, an effect caused by the blade rotation. The normal-turbulence intensity increases again as the blade surface is approached. This is caused by the presence of the blade boundary layer.

The free stream value of normal-turbulence intensity increases after the flow leaves the passage [2]. The flow also tends to become isotropic at lower radial locations.

Radial-Turbulence Intensity (τ_r). The blade-to-blade distribution of the radial component of turbulence intensities is shown plotted in Fig. 7. The distributions are qualitatively similar to the normal and streamwise components, but the magnitudes are generally the highest compared to the streamwise and the normal components. The presence of the coriolis force in the radial direction influences the turbulent structure as analyzed in [8] and [9]. It is shown qualitatively [9] that this effect is to increase the radial intensity component

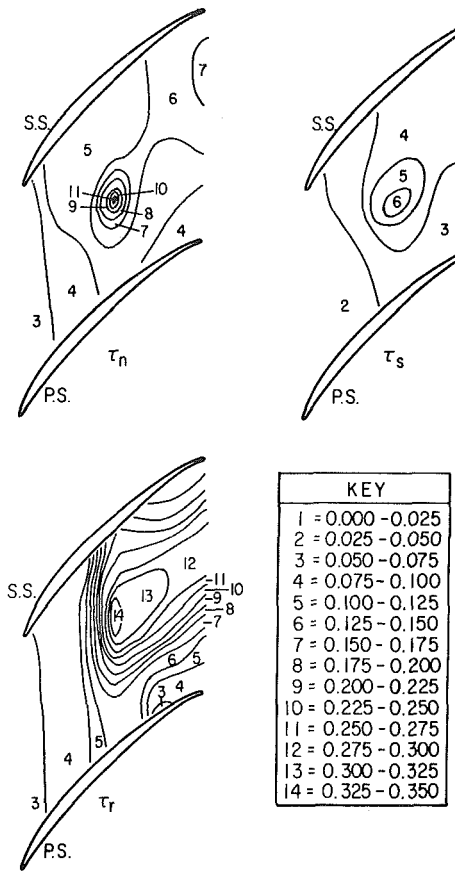

Fig. 8 Isocontours of streamwise (τ_s), normal (τ_n) and radial (τ_r) turbulence intensities in (sn or $Z\theta$) plane at $R = 0.98$

with a corresponding decrease in the streamwise component. This trend is clear from the data presented.

At $Z = 0.25$, the radial component of turbulence intensity is nearly uniform from blade to blade, with nearly the same magnitude as the normal-turbulence intensity, but a higher magnitude than the streamwise-turbulence intensity.

At $Z = 0.5$, the radial-turbulence intensities vary from 5 percent near the blade suction surface to nearly 10 percent near the pressure surface at lower radii ($R \leq 0.945$). At higher radii, the effect of the leakage flow and its mixing with the free stream is clearly evident. The peak intensity reaches as high a value as 32.5 percent at $Y/S = 0.6$ and $R = 0.980$. The radial velocity profiles shown in [1] indicate that the radial velocity is inward and maximum in these regions. The leakage flow jet seems to roll up and move inward at this location. This "mixing" effect and the coriolis force on the mixing layer results in the type of distribution shown in Fig. 7.

The distribution of the radial-turbulence intensity at $Z = 0.75$, shown in Fig. 7, seems to indicate that the mixing region has reached an equilibrium state, with very little change in turbulence intensity at $R = 0.980$, but substantial change at $R = 0.973$. The "mixing region" has spread to the entire passage at this axial location. This region spreads inward as indicated by the profiles at $Z = 0.979$. There is no substantial change in the turbulent structure between $Z = 0.75$ and 0.979. Peak intensities remain nearly the same beyond $Z = 0.75$. The data downstream of the blade row at these radial locations are given in reference [2].

In general, the magnitude of τ_r is generally much higher than those of τ_s and τ_n in the region of intense mixing as well as the free stream. Thus, the marked effect of rotation on the turbulence structures is clearly evident [8,9].

Isoturbulence Intensity Contours in the (sn or $Z\theta$) and ($r\theta$) Planes. The contours of equal intensities inside the blade

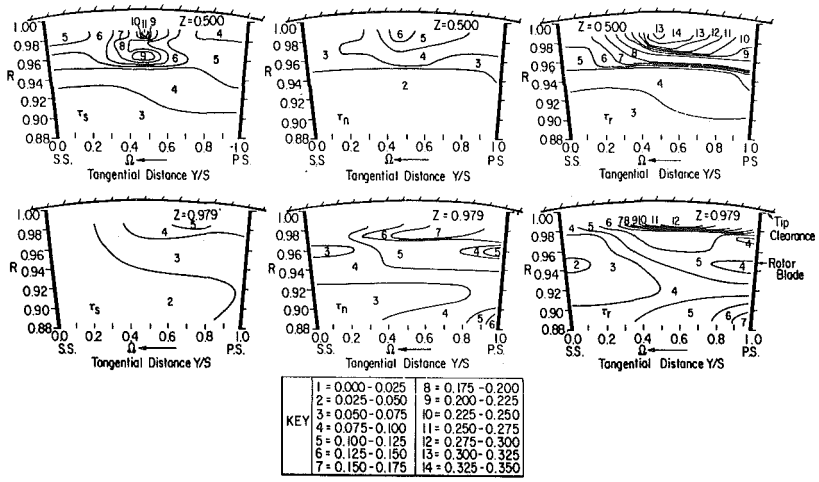

Fig. 9 Isocontours of streamwise (τ_s), normal (τ_n), and radial (τ_r) turbulence intensities in the $r\theta$ plane at Z = 0.500, 0.979

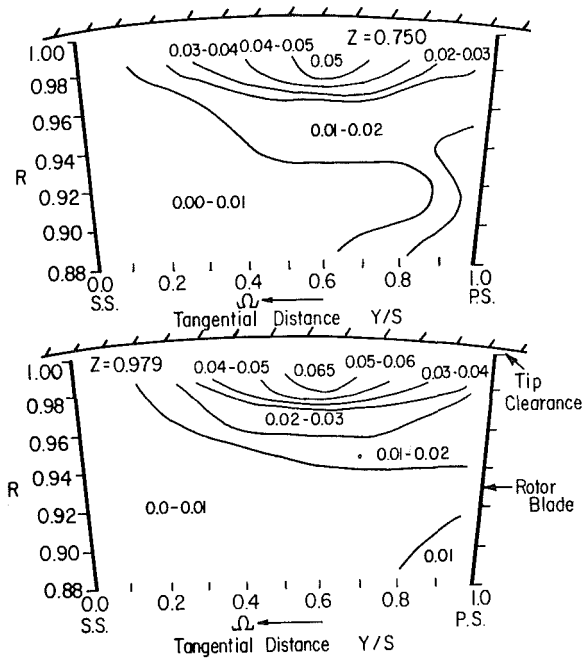

Fig. 10 Isocontours of total turbulent energy (k) at Z = 0.75, 0.979

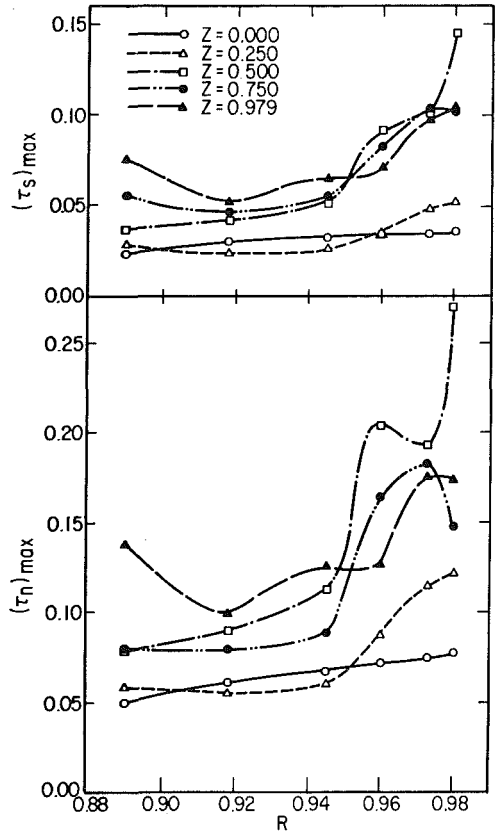

Fig. 11 Radial variation of the maximum streamwise (τ_s) and normal (τ_n) turbulence intensities

passage at R = 0.98 are shown in Fig. 8 for all the components of turbulence intensities. Peak intensities occur near the mid-chord and near the mid-passage regions. The intensities are relatively low up to mid-chord, increase rapidly beyond that region, then are nearly constant beyond Z = 0.75. The region of "mixing" of the leakage flow with the mainstream is dramatically illustrated by these contours. The leakage flow seems to travel away from the suction surface, augmented by the blade rotation, with the maximum mixing and the turbulence production occurring at the middle third of the passage. This may also be the region of the formation of the leakage vortex. These remarks are in conformity with the mean velocity profiles presented and interpreted in [1]. It is also clear that the radial-turbulence intensities are maximum, followed by the normal and the streamwise components. This is contrary to the distributions observed in stationary channels, where the streamwise component is likely to be the dominant, one followed by the normal and the radial components. The effect of the Coriolis force in altering the turbulence structure [8,9] is thus clearly evident from this plot.

The contours of equal turbulence intensity in the ($r\theta$) plane at Z = 0.5 and 0.979 are plotted in Fig. 9. The conclusion drawn earlier with regard to the relative magnitude of various components is evident in this plot also. The movement of the leakage flow jet and its eventual roll-up is also evident. At the axial station Z = 0.5, this mixing region extends from R = 1.0 (extrapolated) to R = 0.97, nearly 6 percent of the blade height. The location of the jet is still well-defined even at the trailing edge (Z = 0.979), even though the spreading of the jet inward is clearly evident in the iso-τ_r plot. The streamwise and normal-turbulence intensities are diffused, but the radial-turbulence intensities are still high in a fairly narrow region (R = 0.97 to 1.00) near the tip. This region has large radial inward velocities [1].

Total Turbulent Energy Inside the Blade Passage (k). Isocontour plots of the total turbulent energy, k, normalized by the $W_{s_0}^2$ are plotted in Fig. 10 for the axial locations Z = 0.750 and Z = 0.979. The three-dimensional

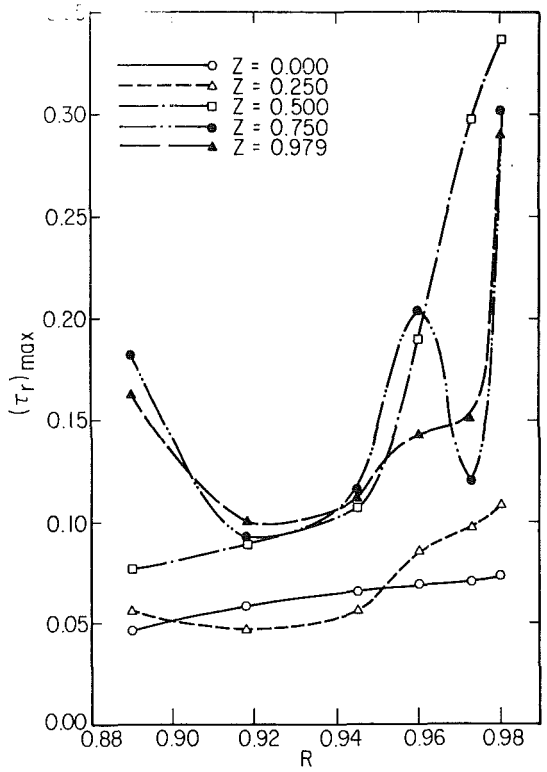

Fig. 12 Radial variation of the maximum radial-turbulence intensity (τ_r)

nature of the blade passage flow is clearly indicated. These contours show a core of high-turbulence energy centered at approximately 65 percent of the passage width from the suction surface. This core is seen to increase with axial distance. The core location and increase in size coincide with the location of the maximum total relative velocity deficiency reported in [1]. This core represents a region of high aerodynamic losses. The production of turbulent energy is maximum in this region. This clearly indicates the origin and magnitude of losses resulting from the leakage flow and its mixing. The turbulent kinetic energy increases from $Z = 0.75$ to 0.979, reaching a maximum value of 6.5 percent of the maximum kinetic energy in mean flow near the tip at $Z = 0.979$.

Radial and Axial Variation of Maximum Turbulence Intensity. The radial variation of the maximum streamwise and normal-turbulence intensities is shown in Fig. 11 and the corresponding plot for the radial component is given in Fig. 12. These maximum values occur near the middle of the passage, especially for $R \geq 0.945$, and hence are not due to the annulus wall boundary layer developing within the passage. It is evident from Fig. 11 that the maximum streamwise and normal-turbulence intensities increase rapidly towards the tip for $R \geq 0.945$. They increase gradually near the leading edge and rapidly near the mid-chord location, with maximum values occurring at the mid-chord location. The maximum radial intensity shows a similar trend, but the values are generally higher than the normal component and much higher than the streamwise component. Increased values of $(\tau_r)_{max}$ at the lowest radii are due to the turbulence in the blade boundary layer. The values of $(\tau_r)_{max}$ are much higher for $Z \geq 0.5$.

Turbulent Shear Stresses (τ_{sn}, τ_{rn}, τ_{sr}). The stress correlations τ_{sn}, τ_{rn}, and τ_{sr} are plotted in Figs. 13, 14, and 15, respectively. These are normalized by the local dynamic head based on the streamwise velocity (W_s^2). A detailed discussion of the errors involved in the hot-wire measurements is given in [7]. The maximum estimated error (including the spatial resolution, thermal inertia, etc.) for the stress correlation measurements inside the passage is 15 percent.

The streamwise components of Reynolds stresses, shown in Figs. 4 and 13, are negligibly small at $Z = 0$ and 0.25. The blade-to-blade distribution at $Z = 0.5$ and $R = 0.980$ indicates a type of distribution normally encountered in a free shear layer (jets, wakes, etc.) or a "vortex" in the region. Large positive and negative stresses in this region indicate the presence of the free shear layer caused by the "mixing" of the leakage flow and the mainstream. The streamwise stresses are zero at all radial locations $R < 0.973$ for this axial station. As the flow travels downstream, $Z = 0.75$, the streamwise shear stresses at $R = 0.980$ become vanishingly small and the stresses at $R = 0.973$ and 0.959 increase, indicating the diffusion of the mixing layer. Surprisingly, the streamwise Reynolds stresses vanish at all locations at $Z = 0.979$, except in the blade boundary layer regions at $R = 0.891$ and $R = 0.980$.

The radial component of Reynolds stresses, shown in Fig. 14, are negligibly small at all radii for $Z = 0.0$ (not shown) and 0.25. At the axial location $Z = 0.5$, the presence of large negative and positive values of the radial component of Reynolds shear stress is evident at $R = 0.980$ and to a lesser extent at $R = 0.973$. This distribution is similar to those observed for the streamwise component of Reynolds stress, but the maximum values of the radial component are two to three times as high as the corresponding streamwise component. Even the free stream values outside the leakage flow mixing region are high. The dominant effect of rotation is clearly evident. Even though the maximum radial velocities in this region are less than 50 percent of the streamwise velocities, the radial stresses are almost two to three times the streamwise component. The qualitative analysis developed by Lakshminarayana and Reynolds [9] predicts this trend. The radial components of stresses are zero away from the mixing region and at all radial locations $R \leq 0.959$. The radial components of stresses increase downstream, with peak values reaching about 0.023. The negative values of radial components of shear stresses observed at $Z = 0.5$ are absent at $Z = 0.75$ and 0.979. The reason for this behavior may be due to the diffusion of the leakage vortex downstream of the mid-chord position. The mixing region at $Z = 0.5$ is characterized by a reversal of the radial velocity gradient reported in [1]. Large values of radial stresses observed near the pressure surfaces for $R = 0.891$ at $Z = 0.75$ and 0.979 are due to the presence of the blade boundary layer. These values are generally much higher than the streamwise stresses at the same location.

The Reynolds stress correlations (τ_{rs}) plotted in Fig. 15 are much smaller than the corresponding radial and the streamwise stresses, even at the tip radii. This fact should be helpful in modeling the Reynolds stress equation in this region.

Turbulent Energy Spectra. Real-time spectrum analysis was carried out to evaluate the spectral content of the turbulence in the end wall region. These energy spectra were taken at various axial, radial, and tangential locations within the blade passage employing the rotating three-sensor, hot-wire probe. The results at $Z = 0.25$, 0.75, and 0.979 are shown in Figs. 16, 17, and 18, respectively. Each figure displays the spectra obtained by the three-sensor probe. Also at each axial and radial position the spectra obtained near the suction surface, at mid-passage, and near the pressure surface are given. It is seen from these figures that most of the energy in turbulence at the lower radial location, $R = 0.891$, is confined to the low-frequency range below 2 KHZ. However, at this radial location there is a sharp spike in the spectra. This spike corresponds to the blade-passing frequency of the inlet guide vane wakes. The vane-passing frequency (VPF) (speed

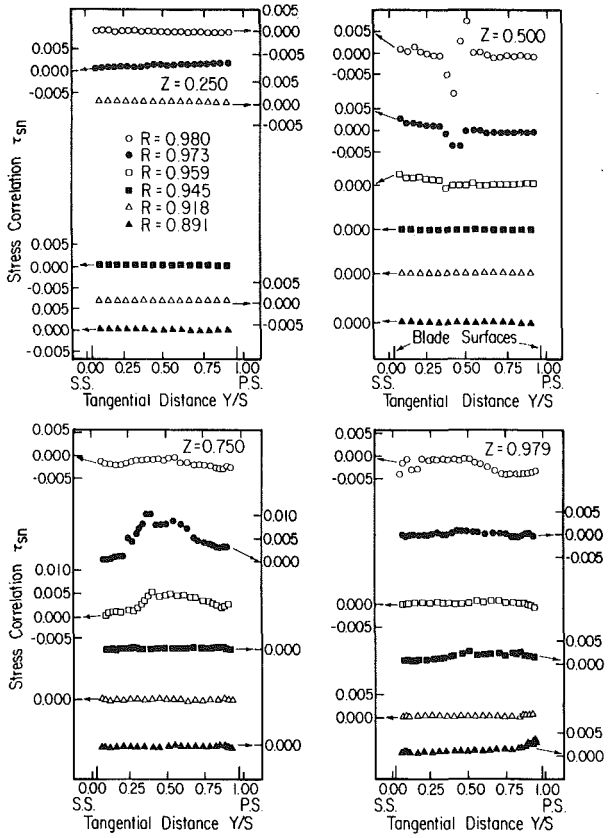

Fig. 13 Blade-to-blade distribution of the turbulent stress correlation (τ_{sn}) at Z = 0.25, 0.5, 0.75, 0.979

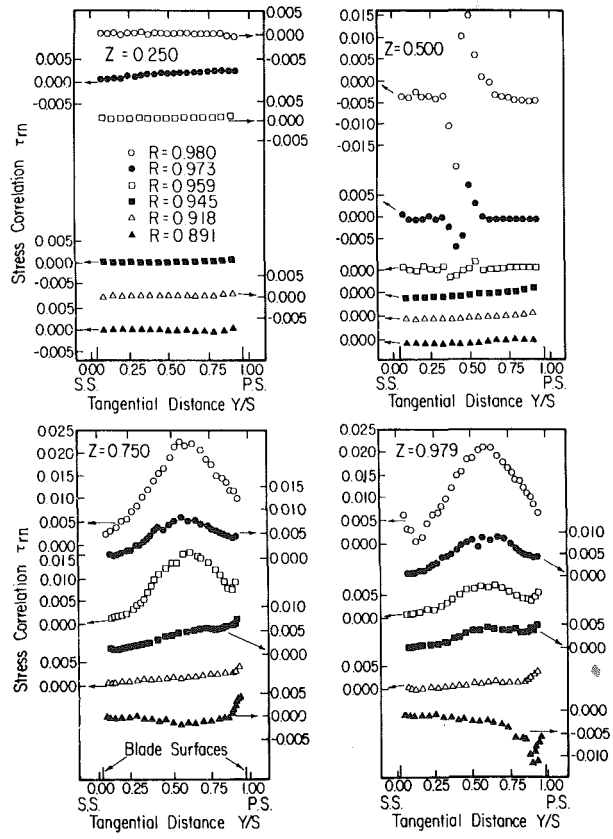

Fig. 14 Blade-to-blade distribution of the turbulent stress correlation (τ_{rn}) at Z = 0.25, 0.5, 0.75, 0.979

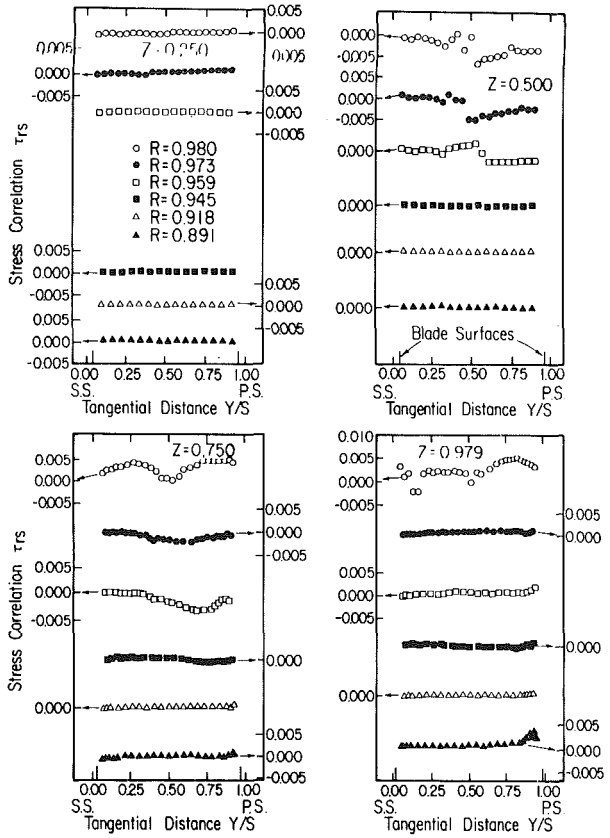

Fig. 15 Blade-to-blade distribution of the turbulent stress correlation (τ_{rs}) at Z = 0.25, 0.5, 0.75, 0.979

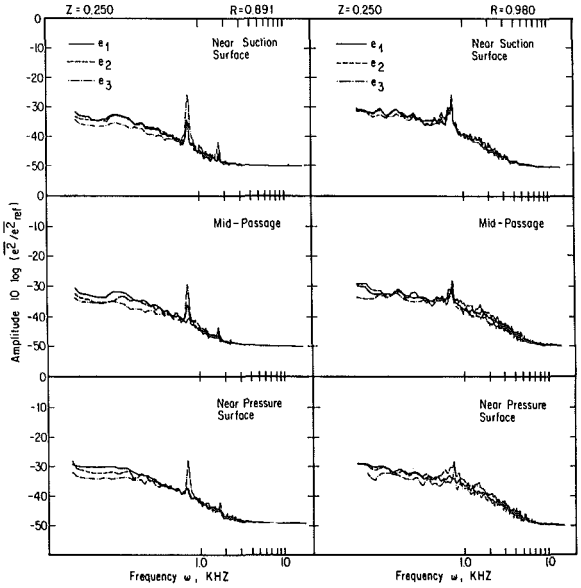

Fig. 16 Turbulence energy spectra in the relative frame of reference inside the blade passage at Z = 0.25 and at R = 0.891 and 0.980

(rpm) × number of IGV blades/60) is 0.759 KHZ. The area under the spikes represents the fraction of the total fluctuating energy contained in the periodic oscillations caused by the upstream inlet guide vane (IGV) wakes. The rotating hot-wire probe senses the inlet guide vane wakes as a source of turbulence. This spike decreases continuously from Z = 0.25 (Fig. 16) to Z = 0.979 (Fig. 18), and vanishes completely near the pressure surface at Z = 0.75 and 0.979. This indicates that the influence of the wake of IGV, located about three-chord lengths upstream of the rotor, persists up to Z = 0.75. The energy content of the turbulence fluctuations increases as the rotor blade tip is approached. This is seen markedly on the

pressure side of the blade passage and at the mid-passage location. The spike due to the inlet guide blade wake is overshadowed by the high turbulence in this region, and the IGV wake seems to diffuse much more rapidly here. The increase in the turbulence energy content is due to the development of the interference region discussed earlier. Associated with this region is a high degree of flow mixing and interaction of the leakage flow, main flow, and the annulus wall boundary layer.

The spectra at $R = 0.980$ at all axial locations exhibit typical energy distributions that exist in turbulent flows, with most of the energy contained within 10 KHZ. At the lowest radial station ($R = 0.891$), most of the turbulent energy is confined below 2 KHZ. However, with increasing radius the limiting frequency approaches 10 KHZ. The radial locations above $R = 0.945$ [7] show the higher values of turbulence occurring at tangential locations 65 percent of the distance from the suction surface of the rotor blade. This is the location of the loss core caused by the strong flow interactions of the tip leakage flow and the main flow.

Conclusions

1 Turbulence levels within the blade passage are high near the tip regions, especially near the mid-passage. A growing core of high turbulence is evident near 65 percent of the blade-passage distance from the suction side, which corresponds to the region of velocity deficiency reported earlier. Turbulence energy levels in the "mixing" region reach values of 6.5 percent of the kinetic energy in the mean flow.

2 The streamwise component of the turbulence intensity is found to be the lowest and the radial component to be the largest in the leakage flow mixing region. The maximum intensities measured are 32, 27.5, and 15 percent for the radial, normal, and streamwise components, respectively. These values occur at the tip near the mid-chord region, where the leakage flow and three-dimensional effects are found to be dominant. The effect of rotation is to attenuate the streamwise component and amplify the radial component of the turbulence intensity.

3 The turbulence intensities are found to be small at radial locations below 8 percent of the span from the tip.

4 The maximum radial component of the turbulent shear stress is found to be two to three times higher than the maximum streamwise stress. The maxima occur near the mid-passage at mid-chord, which is the location where the maximum leakage velocity is observed. The effect of rotation is to attenuate the streamwise stress and amplify the radial component. The distribution of stresses at the tip near the mid-chord is similar to that observed in a free shear layer or a vortex.

5 The turbulent energy spectra show that the energy is confined to 2 KHZ at lower radii, while the frequency content extends up to 10 KHZ near the tip.

6 The presence of the inlet guide vane (IGV) wake is evident from the spectra of turbulent kinetic energy measured. The IGV wakes decay rapidly near the blade pressure surface and persist even up to three-quarter-chord location along the blade passage.

Acknowledgment

This work was supported by the National Aeronautics and Space Administration through the Grant No. NSG 3212, with P. M. Sockol as the project monitor.

References

1 Lakshminarayana, B., Pouagare, M., and Davino, R., "Three Dimensional Flow Field in the Tip Region of a Compressor Rotor Passage—Part 1: Mean Velocity Profiles and Annulus Wall Boundary Layer," ASME JOURNAL OF ENGINEERING FOR POWER (this issue).

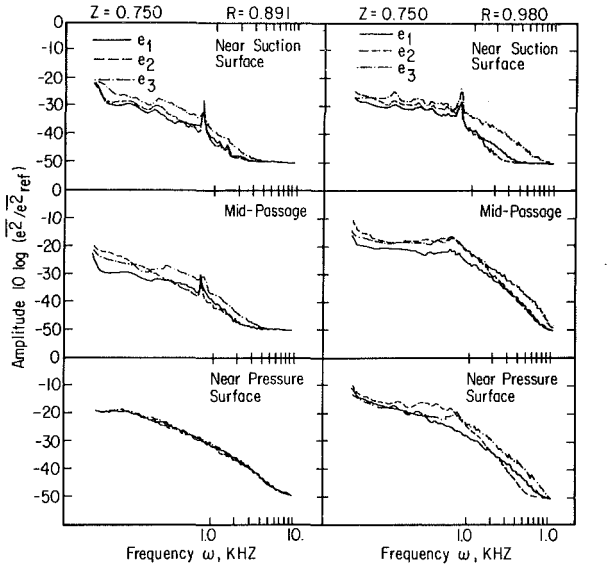

Fig. 17 Turbulence energy spectra in the relative frame of reference inside the blade passage at $Z = 0.75$ and at $R = 0.891$ and 0.980

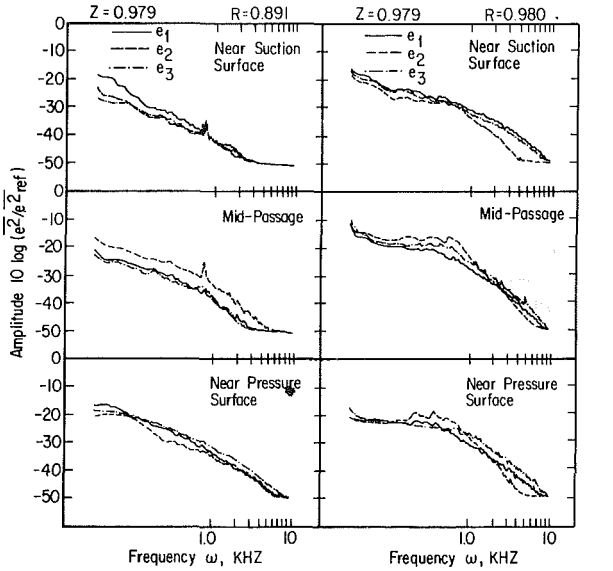

Fig. 18 Turbulence energy spectra in the relative frame of reference inside the blade passage at $Z = 0.979$ at $R = 0.891$ and 0.980

2 Davino, R. and Lakshminarayana, B., "Turbulence Characteristics in the Annulus Wall Boundary Layer and Wake Mixing Region of a Compressor Rotor Exit," ASME JOURNAL OF ENGINEERING FOR POWER, Vol. 104, July 1982, pp. 561–570.

3 Smith, L. H., "Three-Dimensional Flow in an Axial Flow Turbomachinery WADC Technical Report 55-348, Vol. 2, John Hopkins University, 1956.

4 Lakshminarayana, B., "An Axial Flow Research Compressor Facility Designed for Flow Measurement in Rotor Passages," ASME *Journal of Fluids Engineering*, Vol. 102, No. 4, Dec. 1980, pp. 402–411.

5 Lakshminarayana, B. and Ravindranath, A., "Interaction of Compressor Rotor Blade Wake with Wall Boundary Layer/Vortex in the End Wall Region," ASME JOURNAL OF ENGINEERING FOR POWER, Vol. 104, Apr. 1982, pp. 467–478.

6 Gorton, C. A. and Lakshminarayana, B., "A Method of Measuring the Three-Dimensional Mean Flow and Turbulence Quantities Inside a Passage," ASME JOURNAL OF ENGINEERING FOR POWER, Vol. 98, No. 2, 1976, pp. 137–146.

7 Davino, R., "Three-Dimensional Mean Flow and Turbulence Characteristics in the Annulus-Wall Region of an Axial Flow Compressor Rotor Blade Passage," M.S. thesis, Department of Aerospace Engineering, The Pennsylvania State University, Nov. 1980.

8 Raj, R. and Lumley, J. L., "A Theoretical Investigation on the Structure of Fan Wakes," ASME *Journal of Fluids Engineering*, Vol. 100, 1978, pp. 113–119.

9 Lakshminarayana, B. and Reynolds, B., "Turbulence Characteristics in the Near Wake of a Compressor Rotor Blade," *AIAA Journal*, Vol. 18, No. 11, Nov. 1980, pp. 1354–1362.

Hideaki Kosuge
Research Engineer.

Takane Ito
Senior Research Engineer.

Keiichi Nakanishi
Manager,
Project Control Section.

Engine Research Laboratory,
Central Engineering Laboratories,
Nissan Motor Co., Ltd.,
1 Natsushima-cho,
Yokosuka 237, Japan

A Consideration Concerning Stall and Surge Limitations Within Centrifugal Compressors

In order to understand the characteristics of an impeller independently, it is necessary that the impeller is tested without a diffuser. Using this method, the surge may be caused either by the inducer stall or impeller stall. Two types of impellers, with different inducer blade-to-blade shape, were employed to investigate the critical condition of stall and surge. Employing a one-dimensional-flow analysis within the impeller, various parameters for stall and surge were investigated. In this study, the relative velocity reduction between the inlet and throat of the inducer, and between the inlet and exit of the impeller were examined in comparison with the inducer throat Mach number.

Introduction

This experimental study was conducted to improve the understanding of surge and stall in centrifugal compressors. Compressor surge can be caused by many different factors, such as: (*a*) inducer stall, (*b*) impeller stall, (*c*) vaneless diffuser instability, (*d*) vaned diffuser stall, and (*e*) a combination of the above mentioned factors.

As matching the centrifugal compressor with a vaneless or vaned diffuser restricts the operating flow ranges, impellers were tested independently without a diffuser in this study.

The impeller is defined as the combined inducer and rotor of a radial compressor. Impeller surge, under a "diffuserless" condition, can be caused by the following two factors: inducer stall, and impeller stall.

Considering an impeller as a kind of diffuser, there could be a critical inlet/exit relative velocity ratio [2, 3, 4, 5, 7]. At the critical condition of inducer stall, it is suggested that the critical incidence angle at the inducer tip varies with the inducer tip relative Mach number. The ratio of relative velocities at the inducer tip and the inducer throat is constant over a range of low inlet relative Mach numbers [3, 7].

With regard to the surge limitation, it is suggested that the critical relative velocity ratio, impeller tip to inducer tip W_2/W_{1t}, is constant regardless of the impeller speed, provided that the relative inlet Mach number is not high. At higher Mach numbers, the compressor runs into surge as soon as the inducer is stalled [3, 7].

To investigate the effect of the inducer on surge, each stall and surge limitation was examined by employing two types of impellers with different inducer shape. In this paper, all parameters were calculated by a simple, one-dimensional flow analysis which assumes that the axial velocity is uniform at the inducer inlet.

Impeller Design

The test impellers were those designed and tested for application to a two-shaft regenerative gas turbine for heavy-duty vehicles [1]; and a nonregenerative gas turbine for emergency generator sets.

Two types of impellers, Type "A" and "B", were used in this study. The particular geometric details of the test impellers are shown in Table 1 and Fig. 1. The only geometric difference between impellers A and B is their inducer blade-to-blade shape.

Test Apparatus and Procedures

The impellers were driven by a d-c 440-kw dynamometer with 11 to 1 step-up gears. Airflow rate was measured utilizing a metering orifice in the suction line.

Surge was detected audibly at both high and low speeds using a microphone installed near the inlet bellmouth, and by an instantaneous temperature rise in the thermocouple installed near the inducer inlet. Inducer stall was detected by observing the pressure variation between inducer blades. This was measured by a miniature semiconductor transducer installed at the shroud.

The exit of the impeller was opened directly into a large collector to avoid stall in the vaneless diffuser. Use of the "diffuserless test rig" significantly facilitated our understanding of impeller characteristics and allowed us to better match the impeller and vaned diffusers [1].

Experimental Results and Considerations

Figure 2 shows the total-to-static pressure ratio versus the weight flow rate characteristics for the 6 speed lines examined. In this figure, the dotted lines indicate operation when the inducer is stalled. At the left end of each characteristic curve, the impeller runs into surge.

The different operating ranges, using each type of impeller, are shown in Fig. 3. Although it is suggested that the compressor runs into surge as soon as the inducer is stalled, in cases of the nominal inlet Mach number $M_t' \geqq 1.09$ [3] it can

Contributed by the Gas Turbine Division of THE AMERICAN SOCIETY OF MECHANICAL ENGINEERS and presented at the 27th International Gas Turbine Conference and Exhibit, London, England, April 18-22, 1982. Manuscript received at ASME Headquarters November 23, 1981. Paper No. 82-GT-15.

Table 1 Design specification of impellers

		Impeller Type A	Type B
Rotating speed	N	40000 rpm	
Type		Radial blade impeller, no prewhirl	
Impeller tip diameter	D_2	0.2116 m	
Inducer tip diameter	D_{1t}	0.142 m	
Inducer hub diameter	D_{1h}	0.040 m	
Impeller tip passage depth	b_2	0.0091 m	
Number of blades	inducer	15	
	impeller	30	
Inducer tip inlet blade angle		66 deg	62 deg
Total throat area/ annular area	F_{1th}/F_1	0.672	0.798

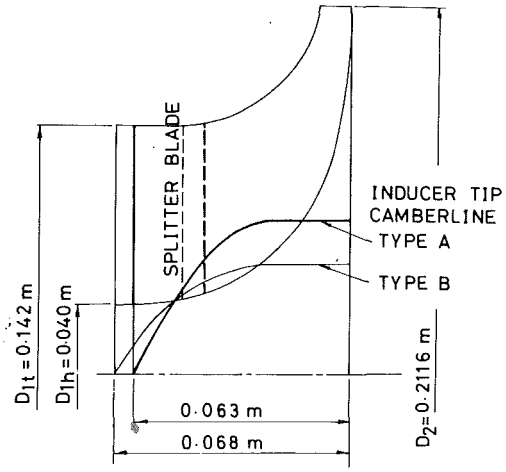

Fig. 1 Meridional geometry and blade camberline shape of test impellers

be observed (as shown in Fig. 3) that the critical Mach number, M_t' of surge-to-stall boundary differs with impeller geometries, and especially with inducer geometries.

Inducer Tip Relative Mach Number. The relationship between the inducer tip incidence at the critical condition of stall and surge and the inducer tip relative Mach number M_{rlt} is shown in Fig. 4. At the condition of inducer stall, almost all the data points are on a single curve for impellers A and B,

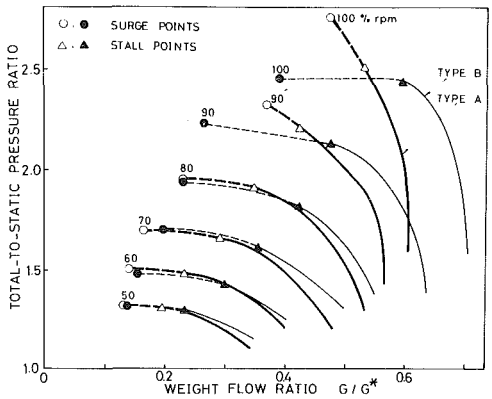

Fig. 2 Characteristics of impellers

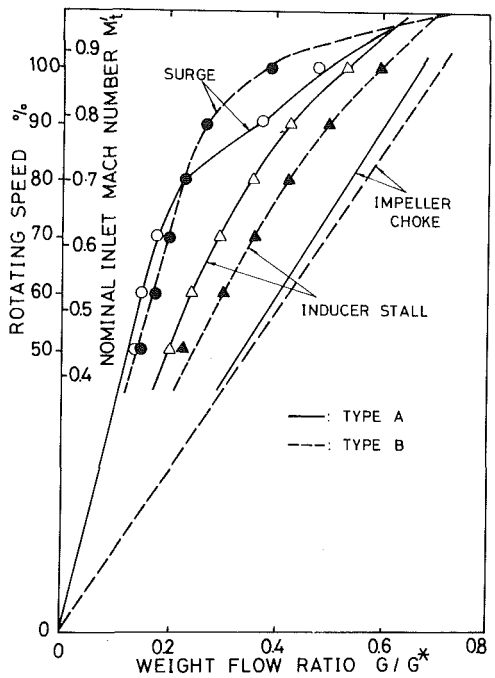

Fig. 3 Operating range of impellers

but the incidence angle at the impeller surge is different for each impeller type.

The real angle of incidence at the inducer-stall condition,

Nomenclature

a = acoustic velocity
b = passage depth
c = absolute velocity
C_p = specific heat at constant pressure
D = diameter
G = weight flow rate
G^* = weight flow rate choked at the intake duct
g = gravitational constant
i = incidence angle
J = Joules equivalent
F = area
M = Mach number
M_t' = inducer tip nominal Mach number = u_{1t}/a_0
N = rotating speed
P = total pressure
P_s = static pressure
q = nondimensional specific weight flow rate
R = gas constant
SF = slip factor
T = temperature
u = peripheral speed
W = relative velocity
W_2 = calculated relative velocity at impeller exit
W_2^* = measured relative velocity at impeller exit (see Appendix)
β = flow or blade angle
κ = ratio of specific heats
γ = density
η = efficiency

Subscripts

0 = suction plenum chamber
1 = impeller inlet
1th = inducer throat
2 = impeller exit
h = hub
t = tip
rms = root mean square
u = tangential component
m = meridional component

Superscript

* = choked condition or measured value

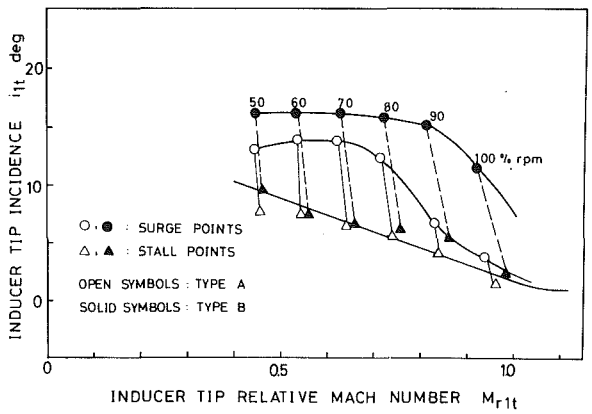

Fig. 4 Incidence versus inducer tip relative Mach number

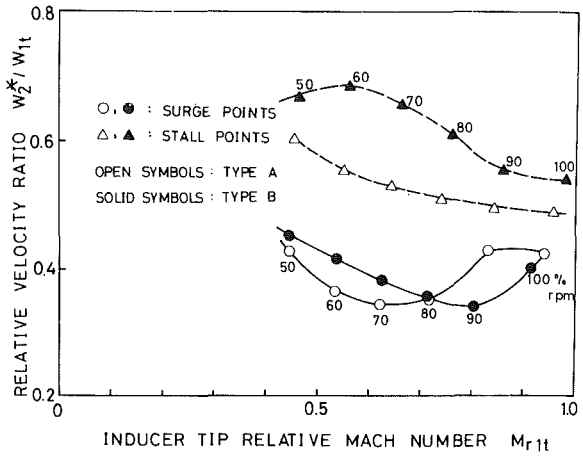

Fig. 5 Relative exit/inlet velocity ratio versus inducer tip relative Mach number

based on a quasi-three-dimensional flow analysis [8], is 4 deg less than that of the lines indicated in the figure, and furthermore the lines of impellers A and B are no longer depicted as one single curve.

The relationship between the inducer tip relative Mach number M_{r1t} and the relative exit/inlet velocity ratio W_2^*/W_{1t} is shown in Fig. 5. Although it is reported that the relative exit/inlet velocity ratio at the critical condition of surge is constant regardless of the impeller speed [3, 7], all data points of impellers A and B do not lie on the same flat line in this figure.

As shown in Figs. 4 and 5, it would seem that the inducer tip relative Mach number M_{r1t} is not an absolute parameter which influences the inducer tip incidence or the relative exit/inlet velocity ratio at the critical condition of stall and surge.

Inducer Throat Mach Number. The relative velocity pattern at the critical condition of impeller surge, calculated with the one-dimensional-flow analysis, is shown in Fig. 6 in the form of a meridional length along the shroud, versus a relative velocity ratio. It should be noted that in the diffuserless condition, inducer surge is distinctly different from impeller surge, that is, there is a difference in the relative velocity reduction between the inlet and the throat of the inducer, and the reduction between the inlet and the exit of the impeller.

It is suggested that the surge of impeller A along the 50–80 percent speed lines and of impeller B along the 50–90 percent speed lines may be caused by the blade loading along the shroud between the inlet and throat of inducer. Along these lines, it should be noticed that the flow downstream of the throat is accelerated and, stable notwithstanding, there is considerable relative velocity reduction between the impeller inlet and exit. Therefore, we have focused our attention on the inducer throat Mach number M_{1th}, which indicates the weight flow rate through the throat, because the inducer tip relative Mach number M_{r1t} mainly represents the rotating speed as shown in Figs. 4 and 5. This is only a parameter influencing the flow behavior at the inducer inlet.

Figure 7 shows the relative throat/inlet velocity ratio W_{1th}/W_{1t} versus the inducer throat Mach number. All the data points at the critical condition of inducer stall are on a single straight line ($\overline{b'a}$) with both impeller types. However, at the critical condition of surge, all data points are not on a single straight line, a inducer surge line ($\overline{c'd}$).

This disparity may be explained by a boundary value of the inducer throat Mach number. This is noted as the critical inducer throat Mach number $(M_{1th})_{cr}$ in Fig. 7. As the inducer tip relative Mach number M_{r1t} equals 1.0 with the increase of impeller speed, the impeller will run into surge as soon as the inducer is stalled by the shock wave. At this point, the inducer-surge line of $M_{r1t} > 1$ disappears. The boundary value at the location, d, on this inducer-surge line $\overline{c'd}$ becomes the critical inducer throat Mach number $(M_{1th})_{cr}$.

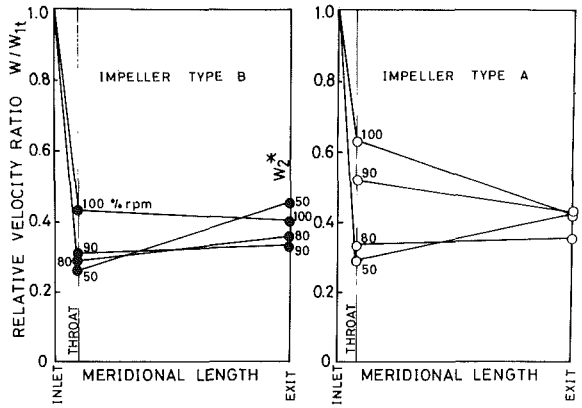

Fig. 6 Relative velocity pattern

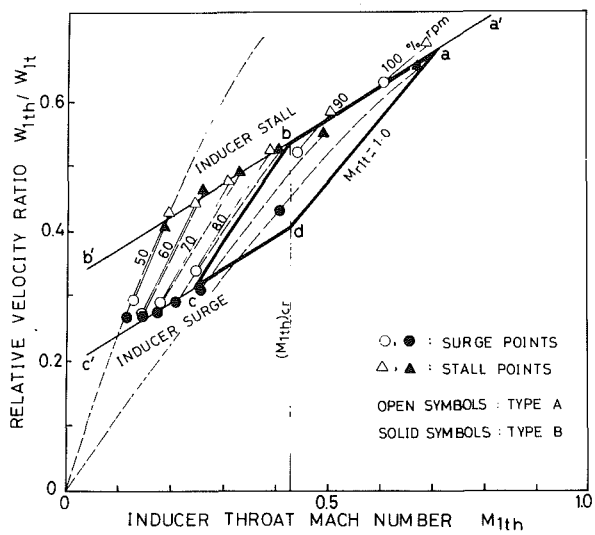

Fig. 7 Relative throat/inlet velocity ratio versus inducer throat Mach number

The lines of constant rotating speeds are represented in this figure by the dotted lines. It can be observed that the lines of constant rotating speeds change slightly with the inducer throat area. It should also be noticed that under the critical inducer throat Mach number, the inducer surge will occur and, above this number, the impeller surge will occur.

As a further explanation, in the case of inducer stall under the critical throat Mach number (line $\overline{b'b}$), the surge will occur at the critical velocity ratio of inlet to inducer throat, that is, the inducer surge (line $\overline{c'c}$).

As to the inducer stall above the critical inducer throat Mach number (line $\overline{ba'}$), the following three cases are suspected:

1 The relative velocity is reduced to the critical relative throat/inlet velocity line, cd, that is, the inducer-surge line.

2 Surge occurs at a constant value of the critical relative exit/inlet velocity ratio regardless of rotating speed; that is, the impeller surge. In this case, all the surge points are located above the critical inducer throat Mach number, (right side of the line $\overline{bd}$), as shown in the figure.

3 The impeller runs into surge as soon as the inducer is stalled above the critical inducer tip relative Mach number $M_{rlt} = 1$, (line $\overline{aa'}$).

The region, whether in case 1 or 2, is surrounded by the thick solid line ($\overline{abcd}$) in Fig. 7.

The relationship between the inducer inlet Mach number M_{1th} and the relative outlet/inlet velocity ratio W_2^*/W_{1t} (measured), W_2/W_{1t} (calculated) is shown in Figs. 8 and 9. The impeller tip relative velocity W_2^* is calculated using the measured static pressure at the impeller exit and the temperature rise, assuming that the slip factor is 0.90.

The relative velocity W_2 is calculated by assuming that the slip factor is 0.90 and the impeller efficiency is 0.88. By decreasing the weight flow rate, the operating lines of constant rotating speed converge to a single value (at the location b') as defined by the formula:

$$\left(\frac{W_2}{W_{1t}}\right)_{M_{1th}\to 0} = \frac{D_2}{D_{1t}}(1 - SF)$$

which is obtained on referring to equations (6) and (23) in the Appendix.

A border line $\overline{b'c'}$ may explain the separation of $\overline{ab}$ from $\overline{cd}$ in Figs. 8 and 9. It may also explain the tendencies given below.

The tendencies derived from the comparison of impellers A and B and from the trimming of impeller A are as follows:

1 Increasing the inducer throat area by cutting the inducer chord will increase the surge weight flow rate.

2 Decreasing the inducer annular area by cutting the inducer tip diameter will decrease the surge weight flow rate.

3 Decreasing the inducer throat area by redesigning the inducer blade curvature will decrease the stall weight flow rate.

4 Decreasing the impeller tip passage depth will decrease the surge weight flow rate.

With regard to the operating lines from inducer stall to surge of constant rotating speed in Figs. 8 and 9, as the inducer throat area increases, the operating lines incline and the relative velocity ratio at the critical condition of inducer stall assumes a higher value, that is, the stall-to-surge margin increases.

As shown in Fig. 7, as the inducer stall relative velocity ratio is limited by the fixed inducer throat Mach number at a given rotating speed, the impeller exit relative velocity W_2, with larger throat area, assumes a higher value (Tendency 3). Under the same condition, impeller tip passage depth will decrease (Tendency 4). By decreasing the inducer annular area by cutting the inducer tip diameter, it is discovered that the critical velocity ratio $(W_2/W_{1t})M_{1th}\to 0$ is proportional to $1/D_{1t}$ (Tendency 2).

At a low nominal inlet Mach number M_l', the surge weight flow rate is related to the inducer throat area (See Fig. 3). At a

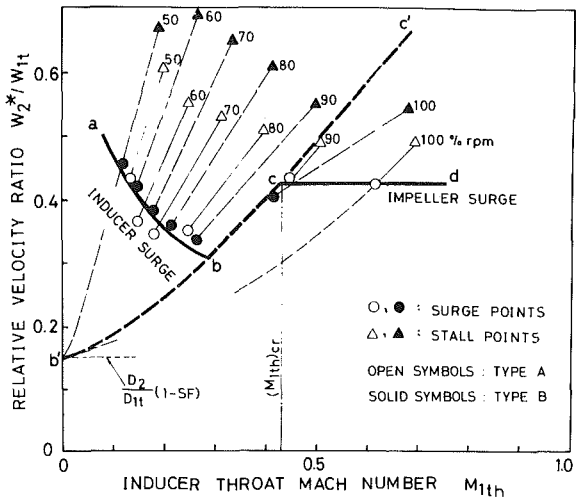

Fig. 8 Relative exit/inlet velocity ratio versus inducer throat Mach number

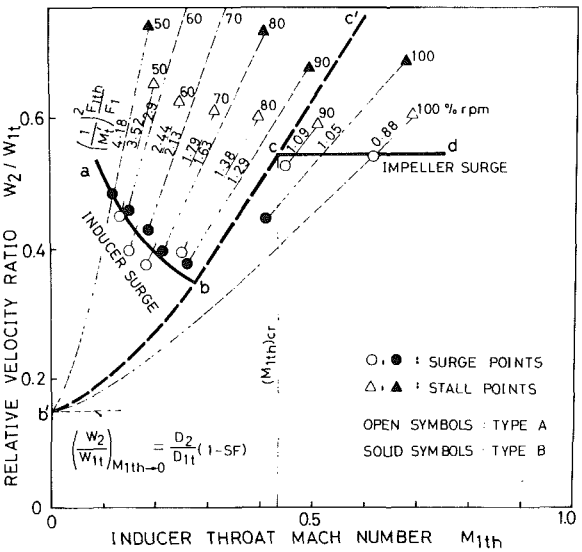

Fig. 9 Relative exit/inlet velocity ratio versus inducer throat Mach number

higher nominal inlet Mach number, the surge weight flow rate within the inducer throat area has a different tendency. After all, the side of border line ($\overline{b'c'}$) passed by the impeller operating line determines whether inducer surge or impeller surge will occur. This is the difference in the stall-to-surge margin as observed in Fig. 3.

While the data presented herein is limited in accuracy due to the poor sampling number of impellers, it is still possible to improve our level of understanding of impeller stall and surge. It should be emphasized that the stall and surge should be studied using the results displayed in Figs. 7-9. Furthermore, the operating lines of constant rotating speed may be distinguished empirically by the following parameter:

$$\left(\frac{1}{M_l'}\right)^2 \frac{F_{1th}}{F_1}$$

Conclusion

The results of the present investigation are summarized below.

1 The stall would occur at the critical relative velocity reduction between the inlet and the throat of the inducer, and

its velocity ratio was related to the inducer throat Mach number M_{1th}.

2 The surge would be caused by the critical relative velocity reduction either between the inlet and the throat of the inducer or between the inlet and the exit of the impeller.

3 The relative velocity ratio of the inlet to the throat of the inducer at the critical condition of surge was related to the inducer throat Mach number until the critical throat Mach number $(M_{1th})_{cr}$, where the inducer tip relative Mach number M_{r1t} approached 1.0.

At this condition, it was observed that the impeller would run into surge as soon as the inducer was stalled.

4 Surge above the critical inducer throat Mach number $(M_{1th})_{cr}$ was occurred at the critical velocity ratio of the inlet to the exit of the impeller, which has a fixed value.

Acknowledgement

The authors wish to express their thanks to Dr. Yasutoshi Senoo for his consistent guidance and encouragement in the design and development of the compressor. The would also like to thank Nissan Motor Co., Ltd. for permission to publish this paper. Finally, the authors wish to express their appreciation to Y. Nomura, Y. Ishii, and S. Takayanagi for their experimental work.

References

1 Nakanishi, K., et al., "Development of the Centrifugal Compressor for the Nissan Vehicular Gas Turbine," ASME Paper No. 77-GT-100.

2 Rodgers, C., "Impeller Stalling as Influenced by Diffusion Limitations," Trans. ASME *Journal of Fluids Engineering*, Vol. 99, 1977.

3 Senoo, Y., et al., "Experimental Study on Flow in a Supersonic Centrifugal Impeller," ASME JOURNAL OF ENGINEERING FOR POWER, Vol. 101, No. 1, 1979.

4 Dallenbach, F., "The Aerodynamic Design and Performance of Centrifugal and Mixed Flow Compressors," SAE Technical Progress Series, 1961.

5 Dean, R. C., "The Fluid Dynamic Design of Advanced Centrifugal Compressors," Creare Tenn., 1974, p. 185.

6 Yoshinaka, T., "Surge Responsibility and Range Characteristics of Centrifugal Compressors," *Proceedings of the 1977 Tokyo Joint Gas Turbine Congress*.

7 Mishina, H., et al., "An Investigation of the Influence of Relative Velocity Distributions on the Performance of Centrifugal Impellers," in Japanese, Trans. JSME, Vol. 46, No. 412, 1980.

8 Senoo, Y. and Nakase, Y., "An Analysis of Flow through a Mixed Flow Impeller," ASME *Journal of Fluids Engineering*, Vol. 94, No. 1, 1972.

APPENDIX

Properties at the Inducer Inlet

Inducer inlet area

$$F_1 = \frac{\pi}{4}(D_{1t}^2 - D_{1h}^2) - F_{1B} \tag{A1}$$

where F_{1B} area decreased by blades

Nondimensional specific weight flow rate

$$q_1 = \frac{G_1\sqrt{T_1}}{P_1 F_1} = M_1\left(1+\frac{\kappa-1}{2}M_1^2\right)^{-Z\frac{\kappa+1}{(\kappa-1)}}\sqrt{\frac{\kappa g}{R}} \tag{A2}$$

Inducer inlet Mach number M_1 is obtained by equation (2). Then,

$$\frac{T_{1s}}{T_1} = \frac{1}{1+\frac{\kappa-1}{2}M_1^2} \tag{A3}$$

$$a_1 = \sqrt{g\kappa R T_{1s}} \tag{A4}$$

$$c_1 = a_1 \cdot M_1 \tag{A5}$$

Inducer tip relative velocity

$$W_{1t} = \sqrt{c_1^2 + u_{1t}^2} \tag{A6}$$

Inducer tip relative Mach number

$$M_{r1t} = W_{1t}/a_1 \tag{A7}$$

Inducer inlet rms relative velocity

$$W_{1\text{rms}} = \sqrt{c_1^2 + u_{1\text{rms}}^2} \tag{A8}$$

Inducer tip flow angle

$$\beta_{1t} = \tan^{-1}\left(\frac{u_{1t}}{c_1}\right) \tag{A9}$$

Inducer tip incidence

$$i_{1t} = \beta_{1t} - \beta_{1tB} \tag{A10}$$

where β_{1tB} inducer tip blade angle

Properties at the Inducer Throat

Static temperature at the throat

$$T_{1ths} = T_1 - \frac{W_{1\text{rms}}^2}{2g\frac{\kappa}{\kappa-1}R} \tag{A11}$$

Static pressure at the throat

$$P_{1ths} = P_1\left(\frac{T_{1ths}}{T_1}\right)^{\frac{\kappa}{\kappa-1}} \tag{A12}$$

Relative total pressure at the throat

$$P_{1th} = P_{1ths}\left(1+\frac{\kappa-1}{2}M_{1th}^2\right)^{\frac{\kappa}{\kappa-1}} \tag{A13}$$

Relative total temperature at the throat

$$T_{1th} = T_{1ths}\left(1+\frac{\kappa-1}{2}M_{1th}^2\right) \tag{A14}$$

Nondimensional specific weight flow rate at the throat

$$q_{1th} = \frac{G_1\sqrt{T_{1th}}}{P_{1th}\cdot F_{1th}} = M_{1th}\left(1+\frac{\kappa-1}{2}M_{1th}^2\right)^{-\frac{\kappa+1}{2(\kappa-1)}}\sqrt{\frac{\kappa g}{R}} \tag{A15}$$

The inducer throat Mach number is obtained from equations (13–15).

Acoustic velocity at the throat

$$a_{1th} = \sqrt{g\kappa R T_{1ths}} \tag{A16}$$

Inducer throat relative velocity

$$W_{1th} = a_{1th}\cdot M_{1th} \tag{A17}$$

Properties at the Impeller Exit

Assuming the slip factor, the temperature rise through the impeller

$$\Delta T = SF\frac{u_2^2}{g\,JC_p} \tag{A18}$$

Assuming the first approximate value for the impeller exit flow angle, β_2, the impeller exit static temperature

$$T_{2s} = T_2 - \frac{C_2^2}{2g\frac{\kappa}{\kappa-1}R} \tag{A19}$$

The impeller exit total pressure is calculated from the assumed impeller efficiency. Impeller exit static pressure

$$P_{2s} = P_2 \left(\frac{T_{2s}}{T_2} \right)^{\frac{\kappa}{\kappa - 1}} \tag{A20}$$

Impeller exit meridional absolute velocity

$$C_{m2} = \frac{G_1}{\gamma_2 \cdot F_2} \tag{A21}$$

where F_2 impeller exit area, considering the blade thickness Therefore,

$$\beta_2' = \tan^{-1} \left(\frac{C_{u2}}{c_{m2}} \right) \tag{A22}$$

Repeat until β_2' is equal to β_2.

Impeller exit relative velocity

$$W_2 = \sqrt{(u_2 - c_{u2})^2 + c_{m2}^2} \tag{A23}$$

Another Method for Impeller Exit Relative Velocity

The impeller exit peripheral absolute velocity c_{u2}^* and exit absolute total temperature T_2 are obtained assuming the slip factor.

Then, employing the measured impeller exit static pressure P_{2s} and the first approximate impeller exit absolute velocity c_2, the meridional absolute velocity c_{m2}^* is calculated with equations (19–21).

Therefore,

$$c_2 = \sqrt{c_{m2}^{*2} + c_{u2}^{*2}} \tag{A24}$$

Repeat until c_2 is converged.

Impeller exit relative velocity

$$W_2^* = \sqrt{(u_2 - c_{u2}^*)^2 + c_{m2}^{*2}} \tag{A25}$$

Cao Ming-hua
Lecturer.

Jiang Hong-kun
Post Graduate Student.

Jet Propulsion Department,
Beijing Institute of Aeronautics
and Astronautics,
Beijing, People's Republic of China

Chin Ju-shan
Visiting Professor
of Mechanical Engineering,
Purdue University,
West Lafayette, Ind. 47907
Mem. ASME

Semiempirical Analysis of Liquid Fuel Distribution Downstream of a Plain Orifice Injector Under Cross-Stream Air Flow

An improved semiempirical analysis is presented for the liquid fuel distribution downstream of a plain orifice fuel injector under a cross-stream air flow of uniform high velocity and constant ambient temperature. The analysis is based on a simplified "flat-fan spray" model ($\epsilon-\psi$ model). A $\epsilon-\psi$ model is proposed which assumes that the fuel injected through the orifice forms a flat-fan liquid sheet with an average fan angle $2\psi_0$. Once the droplets have been formed, the trajectory of individual droplets determines the fuel distribution downstream. The validity of the analysis is confirmed by comparison of calculations based on the $\epsilon-\psi$ model and test data obtained from fuel distribution experiments under cross-stream air flow of ambient temperature. The agreement is shown to be very good. The semiempirical analysis presented offers a very useful approach in the preliminary design of the fan air flow path portion of turbofan afterburners.

Introduction

In a previous paper [1], the authors presented a flat-fan spray model for the semiempirical analysis of the liquid fuel distribution downstream of a plain orifice injector under cross-stream air flow. The present paper is a step further and a modification of that analysis. It has been improved from the previous paper [1] in the following aspects:

1 Removal of the assumption of a radial initial atomization delay distance by use of a correlation obtained from experimental data of [2]
2 Use a more accurate droplet drag coefficient equation
3 Use a correlation based on experimental data [2] for the average fan angle $2\psi_0$ as a function of ϵ
4 Consideration of the effect of fuel spray on the stream velocity in the region close to the injector
5 Initial fuel allocation with respect to the ψ angle is assumed to be distributed as a normal probability density distribution

The authors assume the fuel injected through the orifice is exposed to the aerodynamic force of the high-velocity cross air flow and immediately forms a flat-fan liquid sheet in *YOZ*-plane (see Fig. 1). The flat-fan liquid sheet so formed is perpendicular to the crossflow with a fan angle of $2\psi_0$. The initial fuel allocation with respect to the fan angle, ψ, is assumed to be distributed as a normal probability density distribution. The liquid flat-fan sheet is atomized under the aerodynamic force into droplets gradually within a certain distance. The fuel fraction remaining in the liquid sheet as unatomized is a function of a nondimensional breakup parameter, ϵ [2]. The function which was obtained based on experimental data is

$$\frac{A}{A_0} = [1+0.00392(7.68\epsilon-1)(\epsilon-1)^{2.34}]^{-1} \tag{1a}$$

$$\epsilon = \frac{\rho_g}{\rho_1}\left(1+\frac{V_g^{\,2}}{V_1^{\,2}}\right)\frac{\rho^2}{d_0^{\,2}} \tag{1b}$$

and is shown in Fig. 2. It is obvious that at $\epsilon = 15$ the liquid fuel has been fully atomized. In [2] it was suggested using the following expression to calculate the transverse spreading of the jet that

$$d_0 + 2\delta = d_0(1+2\epsilon) \tag{2}$$

As an approximation the present authors suggest that a straight line connected from $\rho_{\epsilon=1}$ to $\rho_{\epsilon=15}$ (see Fig. 1) can be used as the average edge of the flat-fan sheet, where $Z_{\epsilon=1} = d_0(1+\epsilon) = 2d_0$, $Z_{\epsilon=15} = d_0(1+\epsilon) = 16\,d_0$. All the droplets start to move at different initial positions in the *YOZ*-plane at different radial distance ρ_i away from *x*-axis and with different fan angle ψ_i with respect to the *XOY*-plane. The drop size distribution proposed in [3] is assumed. After the droplets have formed, the trajectories determine the liquid fuel distribution downstream and can be described by droplet motion equations. The drag coefficient expression

$$C_D = \frac{a}{\mathrm{Re}} + b\cdot\mathrm{Re}^c$$

Contributed by the Gas Turbine Division of THE AMERICAN SOCIETY OF MECHANICAL ENGINEERS and presented at the 27th International Gas Turbine Conference and Exhibit, London, England, April 18–22, 1982. Manuscript received at ASME Headquarters November 23, 1981. Paper No. 82-GT-16.

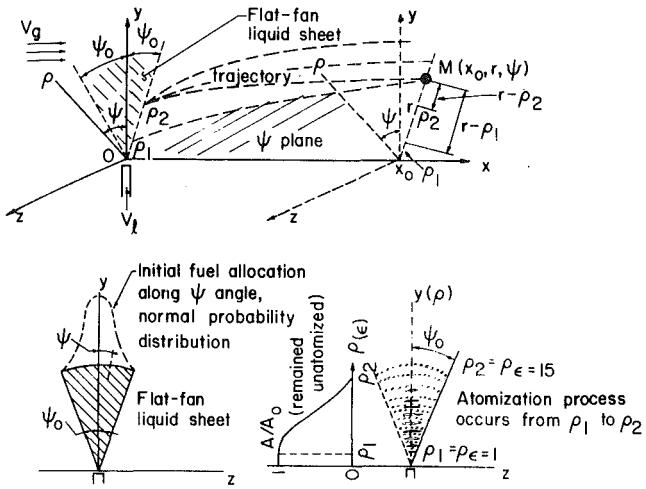

Fig. 1 Coordinate system and diagrammetic explanation of $\epsilon-\psi$ model

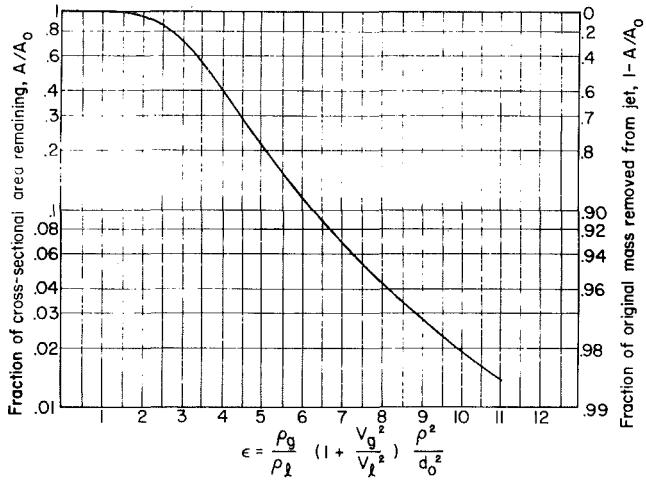

Fig. 2 Extent of breakup as function of breakup parameter

is used in this paper. Since the injection and atomization of the liquid sheet will certainly change the flow field, it may be desirable to have a correction term in the trajectory equation to take into account the influence of the spray exerted on the flow. Based on this model and using the empirical correlation mentioned, the authors were able to predict the fuel concentration at any point downstream of the fuel injector and compare the calculation results with the experimental data of fuel distribution tests. It is found the agreement is very good. This model is very useful for the preliminary design and for the development work of turbofan afterburners, such as overcoming the low frequency combustion instability problem. This analysis can also be used for the design of a premixed-prevaporized combustor of a aerogas turbine engine and dump combustor for a ram-jet engine.

This model can be used to predict the influence of air flow parameters (such as flow velocity, pressure, temperature, etc.), fuel properties (density, viscosity, surface tension), injector parameters (orifice diameter, injection velocity) and downstream distance on the liquid fuel distribution.

This analysis makes use of several simplifications. These are:

1 The fuel emanates from a geometrical point with a flow direction perpendicular to the cross-stream flow.

2 Fuel evaporation is neglected. Since this analysis is mainly for the fan air flow path of an afterburner, the temperature of the fan air flow is relatively low, and this simplification is allowable.

3 Turbulent droplet diffusion is neglected. The authors believe that at high velocity, cross-stream air flow, a high injection velocity, the turbulent droplet diffusion is not important.

In the following sections, an equation is first developed for the liquid fuel concentration (dQ/dF) at a point (x_0,r,ψ) in space. This equation is shown to depend on the following quantities:

(a) initial fuel allocation with respect to ψ, $dQ/d\psi$;
(b) initial droplet size distribution, dQ/dD;
(c) rate of change of droplet diameter with respect to radial distance from the orifice, $dD/d\rho$; and
(d) rate of fuel mass removed from the jet with respect to radial distance from the orifice, $d(1-A/A_0)/d\rho$.

Equations for items (a–d) are derived in sections 3, 4, 5, and

Nomenclature

A = cross-sectional area remaining in the jet
A_0 = initial cross-sectional area of the liquid jet
a, b, c = constants in drag coefficient equation
C_D = droplet drag coefficient
d = diameter
d_0 = orifice diameter
D = droplet diameter
D_{30} = volume-mean drop size
D_M = mean drop size
F = area
K = trajectory correction factor
m = mass of droplet
Q = volume fraction of drops having diameter smaller than D
$\frac{dQ}{dF}$ = liquid fuel concentration
r = radial distance
Re = Reynolds number for droplet motion $\rho_g W D/\mu_g$
Re′ = Reynolds number for atomization $\rho_l V_g \cdot d_0/\mu_g$
Re_0 = Reynolds number for droplet motion at initial condition $\rho_g W_0 D/\mu_g$
s = cross-section area of droplet
t = time
V = velocity
V_g, V_l = air flow velocity and fuel injection velocity
W = relative velocity between droplet and air flow
W_0 = initial relative velocity $= \sqrt{V_g{}^2 + V_l{}^2}$
We = Weber number $= \sigma/d_0\rho_g V_g{}^2$
X, Y, Z = coordinates
Y_M = the position of the maximum point of the fuel distribution curve ($z = 0$)
δ = the transverse spread of the jet
ϵ = nondimensional jet breakup parameter
μ_g, μ_l = viscosity of air and liquid viscosity
ρ_g, ρ_l = air density and liquid density
σ = surface tension
χ, ρ, ψ = cylindrical coordinates
ψ_0 = average flat-fan half-angle

6, respectively. Results obtained with the equations for several droplet drag coefficient formulations are compared with experimental data in section 8.

Fuel Concentration Equation

Downstream of the fuel injector, at any position, $M(x_0,r,\psi)$, within an element area of $\Delta\rho \cdot r \cdot \Delta\psi$, the fuel concentration will be

$$\frac{dQ}{dF} = \lim_{\Delta F \to 0} \frac{\Delta Q}{\Delta\rho \cdot r \cdot \Delta\psi} = \frac{1}{r} \cdot \frac{dQ}{d\psi} \cdot \frac{dQ}{d(D)} \cdot \frac{d(D)}{d\rho} \tag{3}$$

But the droplets are formed within a certain distance, that is, from

$$\rho_{\epsilon=1} = \sqrt{\frac{\rho_1}{\rho_g}\left(\frac{V_1^2}{V_1^2+V_g^2}\right)} \cdot d_0 \text{ to } \rho_{\epsilon=15} = \sqrt{15} \cdot \rho_{\epsilon=1}$$

The droplets formed at the YOZ-plane at radial distance, ρ, will have a mass fraction equal to

$$\left.\frac{d\left(1-\frac{A}{A_0}\right)}{d\rho}\right|_{\rho_{\epsilon=1}}$$

The droplets formed at $\rho_{\epsilon=1}$ will give a contribution to the fuel concentration at $M(x_0,r,\psi)$ as follows:

$$\left.\frac{dQ}{dF}\right|_{\substack{(x_0,r,\psi)\\ \text{from } \rho_{\epsilon=1}}} = \frac{1}{r} \cdot \frac{dQ}{d(D)} \cdot \frac{d(D)}{d\rho}\Big|_{r-\rho_{\epsilon=1}} \cdot \left.\frac{d\left(1-\frac{A}{A_0}\right)}{d\rho}\right|_{\rho_{\epsilon=1}}$$

By the same token, the droplets formed at $\rho_{\epsilon=15}$ will given contribution to the concentration at $M(x_0,r,\psi)$ as follows:

$$\left.\frac{dQ}{dF}\right|_{\substack{(x_0,r,\psi)\\ \text{from } \rho_{\epsilon=15}}} = \frac{1}{r} \cdot \frac{dQ}{d(D)} \cdot \frac{d(D)}{d\rho}\Big|_{r-\rho_{\epsilon=15}} \cdot \left.\frac{d\left(1-\frac{A}{A_0}\right)}{d\rho}\right|_{\rho_{\epsilon=15}}$$

So the fuel concentration at point $M(x_0,r,\psi)$ is the summation of all the contribution given by the droplets formed from $\rho_{\epsilon=1}$ to $\rho_{\epsilon=15}$

$$\left.\frac{dQ}{dF}\right|_{(x_0,r,\psi)} = \sum_{r-\rho_{\epsilon=15}}^{r-\rho_{\epsilon=1}} \frac{dQ}{d(D)} \cdot \frac{d(D)}{d\rho} \cdot \frac{d\left(1-\frac{A}{A_0}\right)}{d\rho} \cdot \Delta\rho \cdot \frac{1}{r} \cdot \frac{dQ}{d\psi}$$

The fuel concentration equation can be written as:

$$\left.\frac{dQ}{dF}\right|_{(x_0,r,\psi)} = \frac{1}{r} \cdot \frac{dQ}{d\psi} \cdot \int_{r-\rho_{\epsilon=15}}^{r-\rho_{\epsilon=1}} \frac{dQ}{d(D)} \cdot \frac{d(D)}{d\rho} \cdot \frac{d\left(1-\frac{A}{A_0}\right)}{d\rho} \tag{4}$$

where

$$\left.\frac{dQ}{dF}\right|_{(x_0,r,\psi)}$$

is the liquid fuel concentration at point $M(x_0,r,\psi)$ and is the percentage of the total fuel injected per square centimeter (percent/cm^2),

$$\frac{dQ}{d\psi}$$

is the initial fuel allocation along the ψ angle (percent/radius),

$$\frac{dQ}{d(D)}$$

is the fuel fraction in unit droplet size range (percent/μ),

$$\frac{d(D)}{d\rho}$$

is the droplet size changing in accordance with the change in unit radial distance which is determined by droplet trajectory (μ/cm),

$$\frac{d\left(1-\frac{A}{A_0}\right)}{d\rho}$$

is the initial atomization fraction in unit radial distance (percent/cm).

In order to calculate the fuel distribution, it is necessary to obtain the correct expression for

$$\frac{dQ}{d\psi}, \frac{dQ}{d(D)}, \frac{d(D)}{d\rho}, \text{ and } \frac{d\left(1-\frac{A}{A_0}\right)}{d\rho}$$

Initial FuelAllocation With Respect to ψ

It is assumed that the initial fuel allocation with respect to the ψ angle is a normal probability distribution. So it can be written as

$$\frac{dQ(\psi,\sigma)}{d\psi} = \frac{1}{\sqrt{2\pi}\cdot\sigma}\exp\left(\frac{-\psi^2}{2\sigma^2}\right) \tag{5}$$

When $\psi_0 = \pm 3\sigma$ the fuel fraction covered should be 99.7 percent of the total fuel amount, we take $\sigma = \psi_0/3$, $dQ/d\psi$ can be expressed as follows

$$\frac{dQ}{d\psi} = \frac{3}{\sqrt{2\pi}\psi_0}\exp\left(\frac{-4.5\psi^2}{\psi_0^2}\right) \text{at } -\psi_0 < \psi < \psi_0;\ 1/\text{radius} \tag{6}$$

Determination of ψ_0. In reference [2], based on experimental data, a simple expression was suggested for the transverse spreading of a jet injected into cross-stream flow

$$\delta = d_0 \cdot \epsilon$$

The present authors assume that if we draw a straight line between $\rho_{\epsilon=1}$ and $\rho_{\epsilon=15}$, this straight line can be seen as the lateral edge of the flat-fan liquid sheet and, based on this approximation, an equation can be obtained for ψ_0 as follows:

$$tg\psi_0 = \frac{\delta_{\epsilon=15}-\delta_{\epsilon=1}}{\rho_{\epsilon=15}-\rho_{\epsilon-1}} = \frac{14\,d_0}{(\sqrt{15}-1)d_0\sqrt{\rho_1/\rho_g[V_1^2/V_1^2+V_g^2}}$$

$$\psi_0 = \text{arc } tg\left[4.873\cdot\sqrt{\rho_g/\rho_1(1+V_g^2/V_1^2)}\right] \tag{7}$$

Initial Droplet Size Distribution

The droplet size distribution used in the present paper is the correlation proposed by Ingebo [3], which is

$$\frac{dQ}{dD} = 29.157\frac{D^5}{D_{30}^6}\exp\left(-3.9\frac{D}{D_{30}}\right) \tag{8}$$

where

$$D_{30} = 3.9\cdot d_0 \cdot \left(\frac{\text{We}}{\text{Re}'}\right)^{0.25} \tag{9}$$

Q = the volume fraction of droplets having diameter larger than D

We = Weber number $= \sigma/d_0\rho_g V_g^2$

Re′ = Reynolds number for atomization $= d_0\rho_l V_g/\mu_l$

Initial Atomization Fraction Along Radial Distance

As it is assumed, the flat-fan liquid sheet is in YOZ-plane and all the atomization process occurs in YOZ-plane.

From [2], the fraction of the original mass removed from the jet, that is, the fraction atomized is expressed as follows

$$1-\frac{A}{A_0}=1-[1+0.00392(7.68\epsilon-1)(\epsilon-1)^{2.34}]^{-1}$$

$$\frac{d\left(1-\frac{A}{A_0}\right)}{d\rho}=0.00784\cdot\left(\frac{A}{A_0}\right)^2\frac{\epsilon}{\rho}(25.6512\cdot\epsilon-10.02)\cdot(\epsilon-1)^{1.34} \tag{10}$$

Droplet Trajectory Equation and Expression for $dD/d\rho$

The droplet motion equation can be written as [4]

$$m\cdot\frac{dW}{dt}=-C_D\cdot\frac{\rho_g\cdot W^2}{2}\cdot s \tag{11}$$

Using the droplet drag coefficient equation

$$C_D=\frac{a}{\mathrm{Re}}+b\cdot\mathrm{Re}^c \tag{12}$$

We may rewrite equation (11) as follows

$$-\frac{d\left(\frac{W}{W_0}\right)}{dt}=\frac{3a\mu_g}{4D^2\rho_l}\cdot\left(\frac{W}{W_0}\right)+\frac{3b\rho_g{}^{(1+c)}W_0{}^{(1+c)}}{4\rho_l\mu_g{}^cD^{(1-c)}}\left(\frac{W}{W_0}\right)^{2+c}$$

where W_0 is the initial relative velocity $=\sqrt{V_g^2+V_l^2}$. If the following combinations are defined

$$A_1=\frac{3a\mu_g}{4D^2\rho_l}$$

$$A_2=\frac{3b\cdot\rho_g{}^{(1+c)}\cdot W_0{}^{(1+c)}}{4\rho_l\mu_g{}^cD^{(1-c)}}$$

and $f=2+c$, then equation (11) becomes

$$\frac{d\left(\frac{W}{W_0}\right)}{dt}+A_1\left(\frac{W}{W_0}\right)=-A_2\left(\frac{W}{W_0}\right)^f \tag{13}$$

The solution of equation (13) is

$$\frac{W}{W_0}=\left(1+\frac{A_2}{A_1}\right)^{\frac{1}{1-f}}\exp(-A_1t)\left[1-\frac{1}{\left(1+\frac{A_1}{A_2}\right)\exp[A_1(f-1)t]}\right]^{\frac{1}{1-f}} \tag{14}$$

By integrating equation (14), we have

$$\int_0^t\frac{W}{W_0}dt=\frac{\left[1+\frac{D^{1+c}}{A_4}\right]^{A_5}D^2}{A_4}\left\{\frac{1}{A_5}\left[\exp\left(\frac{A_4A_5}{D^2}\right)t-1\right]+\right.$$

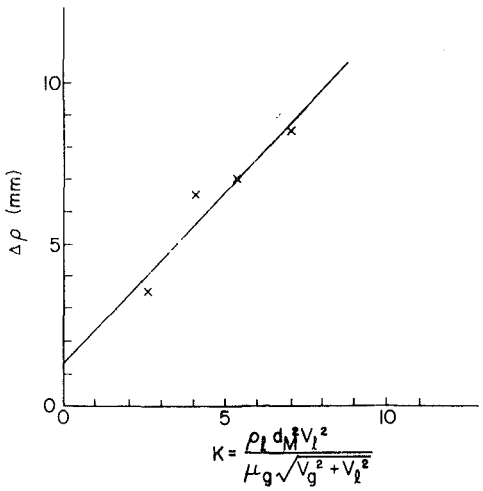

Fig. 3 Correction term for trajectory $\Delta\rho = f(K)$

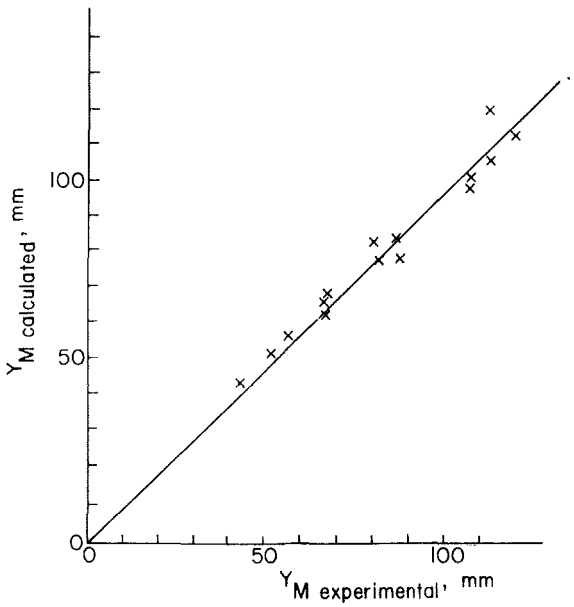

Fig. 4 Calculated and experimental Y_M

$$\sum_{i=1}^{100}\left\{\left(\frac{1}{A_3D^{-(1+c)}+1}\right)^i-\frac{A_5(A_5-1)\cdot\cdots\cdot(A_5-i+1)}{i!\,(A_5-i)}\cdot\left(\exp\left[\frac{(A_5-i)A_4}{D^2}t\right]-1\right)\right\} \tag{15}$$

where

$$A_3=\frac{a}{b}\left(\frac{\mu_g}{\rho_gW_0}\right)$$

$$A_4=\frac{3a(1+c)\mu_g}{4\rho_l}$$

$$A_5=\frac{1}{1-f}$$

When equation (14) is integrated to get equation (15), the last bracket in the right-hand side of equation (14) is expanded in a binomial series and then integrated term by term. Since it is an alternating series with very slow convergence, it is necessary to have one hundred terms to have the accuracy better than 2 percent.

Because the air velocity is uniform and purely in the X-

direction, the droplets initially formed at a fan angle, ψ, will always move in ψ-plane (see Fig. 1), which has an angle of ψ with the XOY-plane. Also, all the droplets start their trajectory from YOZ-plane. So at $t=0$, the starting point for droplet trajectory will be $X=0,\psi,\rho_i$. Thus, trajectory equations for droplets initially at ψ angle with the correction for the effect of spray on flow field (the same for droplets initially at any angle) are [4]:

$$\psi = \text{Const}$$

$$X = V_g t - V_0 \int_0^t \left(\frac{W}{W_0}\right) dt \tag{16}$$

$$\rho = V_1 \int_0^t \left(\frac{W}{W_0}\right) dt + \Delta\rho \tag{17}$$

where $\Delta\rho$ is the correction term.

The authors suggest that the following expression be used for the $\Delta\rho$ correction:

$$\Delta\rho = \Delta_1 + \Delta_2 \cdot K + \Delta_3 \cdot K^2 \tag{18}$$

and

$$K = \frac{\rho_1 \cdot d_M^2 V_1^2}{\mu_g \cdot \sqrt{V_g^2 + V_1^2}} \tag{19}$$

where d_M is the mean droplet size.

The correction coefficients Δ_1, Δ_2, Δ_3 are obtained by comparison of the calculation results with the experimental data at typical experimental conditions by means of curve fitting method, as shown in Fig. 3.

Rewrite equations (16) and (17) as

$$X = V_g \cdot t - V_g \cdot f_1(t,D) \tag{20}$$

$$\rho = V_1 \cdot f_1(t,D) + \Delta\rho \tag{21}$$

From equation (20) we have

$$V_g \cdot \frac{dt}{dD} - V_g\left(\frac{\partial f_1}{\partial t} \cdot \frac{dt}{dD} + \frac{\partial f_1}{\partial D}\right) = 0$$

$$\frac{dt}{dD} = \frac{\dfrac{\partial f_1}{\partial D}}{1 - \dfrac{\partial f_1}{\partial t}} \tag{22}$$

From equation (21) we have

$$\frac{d\rho}{dD} = \frac{\partial\rho}{\partial t}\frac{dt}{dD} + \frac{\partial\rho}{\partial D} = V_1 \frac{\partial f_1}{\partial t}\left(\frac{\dfrac{\partial f_1}{\partial D}}{1 - \dfrac{\partial f_1}{\partial t}}\right) + V_1 \frac{\partial f_1}{\partial D} \tag{23}$$

From equation (23) we obtain

$$\frac{dD}{d\rho} = \frac{1 - \dfrac{\partial f_1}{\partial t}}{V_1 \dfrac{\partial f_1}{\partial D}} \tag{24}$$

The terms $\partial f_1/\partial t$ and $\partial f_1/\partial D$ can be obtained by partial differentiating equation (15) as presented in Appendix B.

Droplet Drag Coefficient Equation

In the present paper, most calculations were done with the following droplet drag coefficient equation:

$$C_D = \frac{24}{\text{Re}}(1 + 0.15 \cdot \text{Re}^{0.687}) \tag{25}$$

But for comparison purposes some calculations were done with the following droplet drag coefficient equation:

$$C_D = \begin{cases} 27 \cdot \text{Re}^{-0.84} & 0 < \text{Re} < 80 \\ 0.271\ \text{Re}^{0.217} & 80 < \text{Re} < 10^4 \\ 2 & \text{Re} > 10^4 \end{cases} \tag{26}$$

Where Re is Reynolds number for droplet motion, $\text{Re} = \rho_g W D/\mu_g$. At $\text{Re}<350$ we use equation (25) and at $\text{Re}>350$ we use $C_D = 0.271 \cdot \text{Re}^{0.217}$. By using equation (4) together with equations (6–10), and (24) the fuel concentration can be calculated.

Calculation Results and Comparison With Experimental Data

The experimental data used to check the model were all obtained in the Jet Propulsion Lab, BIAA. Part of the data are listed in Appendix A. Using the $\epsilon-\psi$ model, the authors have calculated the position of the maximum point of fuel distribution curve $Y_M = Y_{dQ}/dF_{\max}$, and compared with experimental data as shown in Fig. 4. Y_M is measured and calculated at $Z=0$ or in XOY-plane. The agreement is very good.

The authors used the nondimensional parameter

$$\frac{\rho_g}{\rho_1}\left[1 + \left(\frac{V_g}{V_1}\right)^2\right]$$

to correlate Y_M; the correlation is very satisfactory. The curve fitting for the experimental data is

$$Y_M = 0.2566 - 49.219\left[\frac{\rho_g}{\rho_1}\left(1 + \frac{V_g^2}{V_1^2}\right)\right] + 2885\left[\frac{\rho_g}{\rho_1}\left(1 + \frac{V_g^2}{V_1^2}\right)\right]^2 \tag{27}$$

where Y_M is in meter.

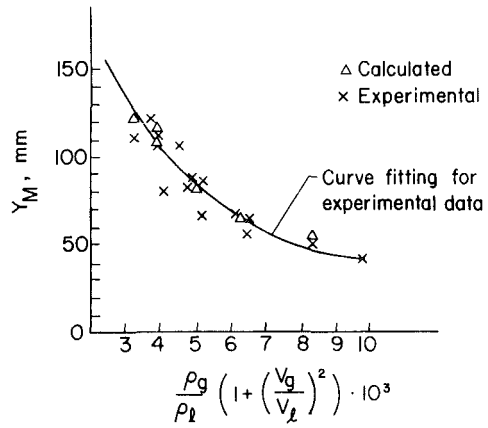

Fig. 5 Y_M correlation

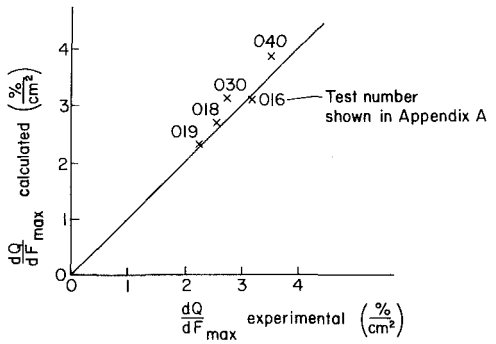

Fig. 6 Experimental and calculated dQ/dF

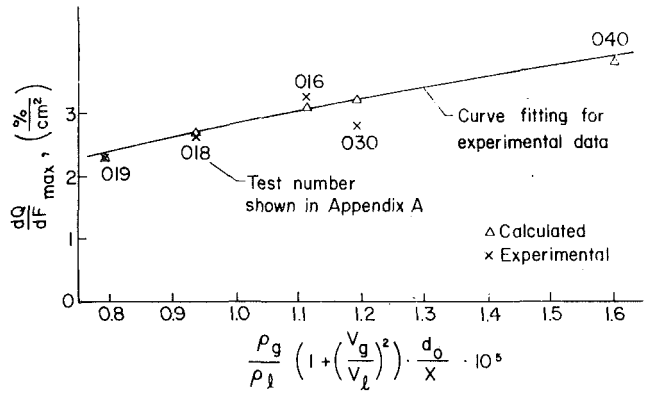

Fig. 7 dQ/dF_{max} correlation

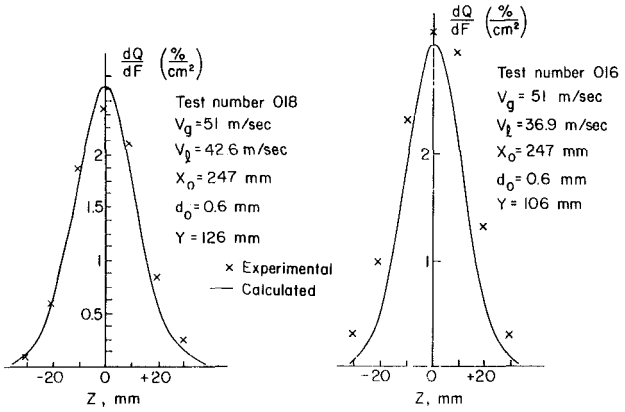

Fig. 8 Fuel concentration curve, Z-direction, comparison between experiment and calculation

The correlation of Y_M by the nondimensional parameter

$$\frac{\rho_g}{\rho_1}\left(1+\frac{V_g^2}{V_1^2}\right)$$

is shown in Fig. 5. In Fig. 5, the calculated values are also shown. It is obvious that the calculated Y_M agrees very well with the correlation curve.

The calculation results of the maximum value of fuel distributon curve dQ/dF_{max} are compared with the experimental data in Fig. 6. dQ/dF_{max} is measured and calculated at $Z=0$ or in XOY-plane. It can be seen the agreement is good.

The correlation of dQ/dF_{max} by the nondimensional parameter

$$\frac{\rho_g}{\rho_1}\left[1+\left(\frac{V_g}{V_1}\right)^2\right]\cdot\frac{d_0}{X}$$

is shown in Fig. 7. The correlation is very good. The curve fitting for the experimental data is

$$\frac{dQ}{dF_{max}} = -0.3072+749.95\left[\frac{\rho_g}{\rho_1}\cdot\left(1+\frac{V_g^2}{V_1^2}\right)\cdot\frac{d_0}{X}\right]^{1/2}$$
$$+71333\left[\frac{\rho_g}{\rho_1}\left(1+\frac{V_g^2}{V_1^2}\right)\frac{d_0}{X}\right] \qquad (28)$$

where dQ/dF_{max} is in percent/cm^2.

From Fig. 7, it can be seen that the $\epsilon-\psi$ model provides very good prediction on dQ/dF_{max} as the calculated values agree very well with the correlation curve.

The calculations of fuel concentration curve along the Z-direction are shown in Fig. 8 compared with experimental data. It shows that the $\epsilon-\psi$ model can be used to predict the fuel concentration curve along the Z-direction very well. The

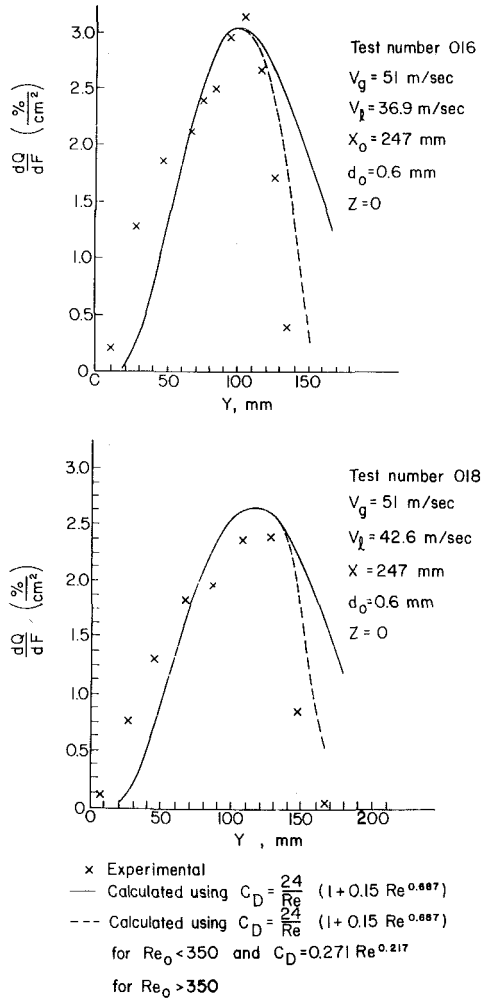

Fig. 9 Fuel concentration curve, Y-direction comparison between experimental and calculated values

authors used the model to calculate the fuel concentration curve along Y-direction. The results are shown in Fig. 9. In these figures the experimental data are shown along with calculated curves for different droplet drag coefficient equations. It is obvious that the agreement between prediction and experiment will be better if we use an appropriate droplet drag coefficient equation for each Reynolds number range considered. Equation

$$C_D=\frac{24}{\mathrm{Re}}(1+0.15\,\mathrm{Re}^{0.687})$$

is not suitable for Re>350. At high Reynolds numbers the drag will be increased with Re because of the deformation of the droplet. If the correct droplet drag coefficient equation is used, the $\epsilon-\psi$ model can predict the fuel concentration curve along Y-direction very well.

Discussion

Drag Coefficient Equation. From the calculation and the comparison with experimental data the authors suggest that the following equation for droplet drag coefficient should be used:

$$C_D=\frac{24}{\mathrm{Re}}\left(1+\frac{1}{6}\mathrm{Re}^{2/3}\right) \qquad \mathrm{Re}<350$$
$$C_D=0.271\cdot\mathrm{Re}^{0.217} \qquad \mathrm{Re}>350 \qquad (29)$$

The first one of equation (29) was suggested because it is easy to integrate the droplet trajectory equation, and that will help to reduce the total calculation work without sacrifice of accuracy. The integration of droplet trajectory equation and dD/d_p expression with

$$C_D = \frac{24}{\mathrm{Re}}\left(1 + \frac{1}{6}\mathrm{Re}^{2/3}\right)$$

are presented in Appendix C. The reason for suggesting using $C_D = 0.271 \cdot \mathrm{Re}^{0.217}$ for $\mathrm{Re} > 350$ is that in order to get good agreement with fuel distributon test data, the droplet drag coefficient should be increased with increasing Reynolds number at high Re range.

The Correction Term for Trajectory $\Delta\rho$. According to the authors' experience, if the correct droplet drag coefficient equation is used, there is no need to have the correction term for trajectory $\Delta\rho$. As a matter of fact, the correction terms $\Delta\rho$ in most of the calculation presented in this paper are of the order of 2–3mm, which, of course, are not significant.

Initial Fuel Allocation. The assumption that the initial fuel allocation with respect to the ψ angle is a normal probability distribution is proved to be correct as the calculation results of the fuel concentration curve in the Z-direction are in good agreement with the experimental data.

ψ_0. The approach the present paper suggests for calculating the spreading of the flat-fan sheet

$$\psi_0 = \mathrm{arc}tq\left\{4.873 \cdot \sqrt{\frac{\rho_g}{\rho_1}\left[1 + \left(\frac{V_g}{V_1}\right)^2\right]}\right\}$$

is basically correct. The ψ_0 angle calculated for some test conditions are listed below and they are in agreement with the experimental observation.

Test Number	019	018	016	030	040
ψ_0	15.57°	16.84°	18.20°	16.95°	16.96°

Conclusion

The $\epsilon - \psi$ model presented in this paper can be used to predict the liquid fuel distribution at any point downstream of a plain orifice injector under high-velocity, low-temperature uniform cross-stream air flow under a wide range of conditions with good accuracy.

References

1 Chin, J. S., Cao, M. H., Jiang, H. K., "Semiempirical Analysis of Liquid Fuel Distribution Downstream of a Plain Orifice Injector Under Cross-stream Air Flow," AIAA Paper 81-1467, 1981.

2 Clark, B. J., "Breakup of a Liquid Jet in a Transverse Flow of Gas," NASA TN D-2424, 1964.

3 Ingebo, R. D., Foster, H. H., "Drop-Size Distribution for Cross-current Breakup of Liquid Jets in Airstreams," NACA TN 4087, 1957.

4 "The Injection and Combustion of Liquid Fuels," WADC-TR-56-344, 1956.

APPENDIX A

Fuel Distribution Test Data

Test number	V_g m/s	V_1 m/s	X_0 mm	d_0 mm	$Y_M = y_{\frac{dQ}{dF_{\max}}}$ mm	
					Calculated	Experimental
042	61.2	42.3	147	0.6	80	86
021	63.3	42.6	247	0.6	86	86
019	51.5	49.6	247	0.6	122	111
026	73.4	42.4	247	0.6	70	66
016	51.0	36.9	247	0.6	100	106
018	51.1	42.6	247	0.6	115	119
030	51.2	42.2	197	0.6	108	111
040	50.8	42.4	147	0.6	102	106
047-7	73.4	36.0	97	0.6	53	51
047-8	73.4	42.3	97	0.6	58	56
042-9	73.4	49.4	97	0.6	68	66
047-1	51.1	36.0	97	0.6	80	81
047-4	61.2	36.0	97	0.6	64	66
047-6	61.2	49.4	97	0.6	85	79

All the tests were done under ambient pressures and temperature with Chinese kerosene fuel, the physical properties are all known and the same for all the tests.

APPENDIX B

Equations for $\frac{\partial f_1}{\partial t}$ and $\frac{\partial f_1}{\partial D}$:

$$\frac{\partial f_1}{\partial t} = \frac{\left[1 + \frac{D^{1+c}}{A_3}\right]^{A_5} D^2}{A_4}\left\{\frac{A_4}{D^2}\exp\left(\frac{A_5 A_4}{D^2}t\right) + \sum_{i=1}^{100}\left[\left(\frac{-1}{A_3 D^{-(1+c)}+1}\right)^i \cdot \frac{A_5(A_5-1)\cdot\cdots\cdot(A_5-i+1)}{i!} \cdot \frac{A_4}{D^2} \cdot \exp\left(\frac{(A_5-i)A_4}{D^2}t\right)\right]\right\} \quad \text{(B1)}$$

$$\frac{\partial f_1}{\partial D} = \frac{D}{A_3 A_4}\left[1+\frac{D^{1+c}}{A_3}\right]^{A_5-1}\left\{2A_3+[2+(1+c)A_5]\cdot D^{1+c}\right\}\cdot\left\{\frac{1}{A_5}\left[\exp\left(\frac{A_4 A_5}{D^2}t\right)-1\right]\right.$$

$$\left.+\sum_{i=1}^{100}\left[\left(\frac{-1}{A_3 D^{-(1+c)}+1}\right)^i \frac{A_5(A_5-1)\cdot\cdots\cdot(A_5-i\text{-}1)}{i!\,(A_5-i)}\right.\right.$$

$$\left.\left.\cdot\left(\exp\left[\frac{(A_5-i)A_4}{D^2}t\right]-1\right)\right]\right\}+\frac{\left[1+\frac{D^{1+c}}{A_3}\right]^{A_5}\cdot D^2}{A_4}\left(\frac{-2A_4 t}{D^2}\right)\cdot\exp\left(\frac{A_5 A_4}{D^3}t\right)$$

$$+\frac{\left(1+\frac{D^{1+c}}{A_3}\right)^{A_5} D^2}{A_4}\cdot\sum_{i=1}^{100}\left\{\left(\frac{1}{A_3 D^{-(1+c)}+1}\right)^i \frac{A_5(A_5-1)\cdot\cdots\cdot(A_5-i+1)}{i!}\right.$$

$$\left.\cdot\left[\exp\left(\frac{(A_5-i)A_4}{D^2}t\right)\cdot\left(\frac{A_3(1+c)D^{-(2+c)}}{(A_5-i)(A_3 D^{-1-c}+1)}-2A_4 t D^{-3}\right)-\frac{A_3(1+c)D^{-(2+c)}}{(A_5-i)[A_3 D^{-(1+c)}+1]}\right]\right\} \tag{B2}$$

Substituting equations (B1) and (B2) into equation (24) we obtain $\frac{dD}{d\rho}$.

APPENDIX C

Trajectory equation and $\frac{dD}{d\rho}$ expression with $C_D = \frac{24}{\mathrm{Re}}\left(1+\frac{1}{6}\cdot\mathrm{Re}^{2/3}\right)$

$$\frac{W}{W_0} = \left[\frac{1}{\left(1+\frac{1}{6}\cdot\mathrm{Re}_0^{2/3}\right)\exp\left(\frac{12\mu_g}{\rho_1 D^2}t\right)-\frac{1}{6}\mathrm{Re}_0^{2/3}}\right]^{3/2} \tag{C1}$$

$$\int_0^t \frac{W}{W_0}dt = \frac{2}{B_1 B_2}\left\{1-\left[(B_1+1)\exp(B_2 t)-B_1\right]^{-1/2}+\frac{1}{\sqrt{B_1}}\left[\mathrm{arctg}\sqrt{\left(1+\frac{1}{B_1}\right)\exp(B_2 t)-1}-\mathrm{arctg}\sqrt{\frac{1}{B_1}}\right]\right\} \tag{C2}$$

where

$$B_1 = \frac{1}{6}\cdot\mathrm{Re}_0^{2/3}$$

$$B_2 = \frac{12\mu_g}{\rho_1 D^2}$$

$$\frac{dD}{d\rho} = \frac{1-\frac{6\sqrt{6}}{B_3^3 B_4}\left(2+\frac{1}{B_4^2}\right)}{\frac{\sqrt{6}}{3}\frac{\rho_1}{\rho_g}\frac{V_1}{W_0}\left\{\frac{4}{\sqrt{6}}B_3-3\mathrm{arctg}\frac{\sqrt{6}}{B_3}+3\mathrm{arctg}B_4+\frac{\sqrt{6}B_3}{B_3^2+6}-\frac{4+3B_2 t+\frac{6D}{B_3^2+6}}{B_4}+\frac{\left(1-3B_2 t-\frac{18B_2}{B_3^2}\right)e^{B_2 t}-1}{B_4^3}\right\}} \tag{C3}$$

where

$$B_3 = \mathrm{Re}_0^{1/3} = (6\cdot B_1)^{1/2}$$

$$B_4 = \left[\left(1+\frac{6}{B_3^2}\right)e^{B_2 t}-1\right]^{1/2}$$

Fumikata Kano
Senior Researcher.

Noriyuki Tazawa
Researcher.

Yoshiteru Fukao
Researcher.

Mechanical Engineering Research Laboratory,
Kobe Steel, Ltd.,
Kobe, Japan

Aerodynamic Performance of Large Centrifugal Compressors

The aerodynamic performance of impellers and diffusers of the large centrifugal compressor were studied. A performance design procedure based on the quasi-three-dimensional flow analysis which is combined with the boundary layer theory was developed. The conditions of the boundary layer at the impeller exit and at the diffuser vane throat were calculated, and the three-dimensional measurements were carried out. This result shows that the low momentum flow is accumulated at the corner of the shroud and the blade suction side of the impeller. These results were applied to the development of a large four-stage isothermal compressor which handles the air for an air separation apparatus. This was tested in the field and showed an isothermal efficiency of 76 percent.

Introduction

The centrifugal compressor is an important piece of equipment in plants and recent trends indicate the need for a higher flow rates in them.

The efficiency of the compressor is also important for conserving energy. The flow within the impeller is three dimensional and is distorted due to boundary layer migration. The relation between impeller performance and inviscid flow velocity distribution has been reported by some researchers [1, 2]. The loss in the impeller is mainly caused by the total pressure decrease due to the friction and adverse pressure gradient. This depends on the velocity distribution and the shape of the impeller blade. It is important to investigate the boundary layer distribution as well as the inviscid flow in order to design good impellers and diffusers. The boundary layer analysis of backward curved impellers, in which the three-dimensional flow is considered approximately, was performed and the actual impeller exit flow was measured.

The vaned diffuser increases the efficiency of the centrifugal compressor. The channel type diffuser is more effective in converting dynamic pressure into static pressure than other types of diffusers, since it provides large static pressure recovery and the shape is simple. The performance of the two-dimensional channel diffuser with uniform inlet flow has been studied by many researchers. They have published many performance maps as functions of the area ratio, the aspect ratio, the length of channel, the Mach number, and the inlet blockage. However, it is not possible to apply this data to the diffuser in the centrifugal compressor, because the diffuser in the centrifugal compressor has a semivaneless region at the inlet, and the inlet flow is distorted three dimensionally. The vaned diffusers reported here have the shape of the NASA 65 series profile for the semivaneless region and a nearly straight two-dimensional channel downstream of the throat. A large static pressure recovery is obtained in the semivaneless region. This produces a boundary layer, and the throat boundary layer blockage affects the performance of the channel downstream of the throat. The diffusers were studied to determine their optimum incidence angle, performance, and stall. The analysis was made by dividing them into two regions: the semivaneless region and the channel region.

A worldwide large isothermal centrifugal compressor was designed. The specifications are as follows:

flow rate	70 m^3/s
total pressure ratio	6.9
number of stage	4 (in one shaft)
drive output	20,000 kW

In addition, a similar compressor which handles 55 m^3/s of air was also designed. These compressors have been serving as air compressors in air separation apparatus.

Experimental Facility and Measurements

Prior to designing the actual machine, experiments on scaled-down components were performed. The sectional view of the test rig of a centrifugal compressor is shown in Fig. 1. The centrifugal compressor is driven by an electric motor through a speed increasing gear. The air flows through a straightener at the inlet of the compressor. The inlet conditions were almost same as the ambient conditions. The external surface of the compressor casing is covered with a 60-mm thick insulation material to eliminate the heat leakage effect on the total temperature. Three impellers, which have backward leaning blades, and fourteen diffusers of various shapes were tested. The tests were performed with a vaneless diffuser to measure the three-dimensional velocity distribution in the vaneless diffuser and to measure the impeller characteristics. Vaned diffuser tests were then performed.

The measurements are as follows:

- Static pressure and total pressure distribution at impeller exit. Static pressure is measured on the diffuser wall at a

Contributed by the Gas Turbine Division of THE AMERICAN SOCIETY OF MECHANICAL ENGINEERS and presented at the 27th International Gas Turbine Conference and Exhibit, London, England, April 18-22, 1982. Manuscript received at ASME Headquarters November 23, 1981. Paper No. 82-GT-17.

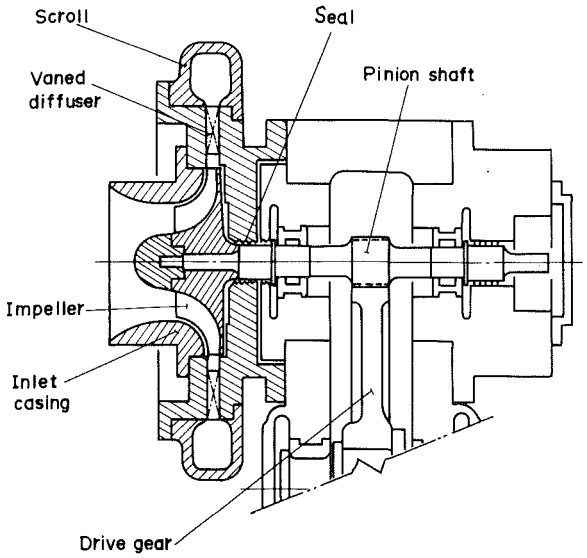

Fig. 1 Sectional view of the test rig of centrifugal compressor

radius of $r/r_2 = 1.05$. The total pressure distribution is measured by a three-hole cobra probe at positions of $r/r_2 = 1.05$, 1.10, and 1.20.

- Static pressure distribution at shroud side wall of vaned diffuser
- Total pressure distribution at diffuser throat, using a 1.0-mm dia, one hole yaw meter
- Time dependent pressure variation in vaned diffuser at the start of surge
- Time dependent total pressure variation at the impeller exit
- Total pressure, static pressure, and total temperature at the suction and discharge of compressor
- Discharge flow rate by orifice meter

The specifications of tested impellers and diffusers are shown in Table 1 and Table 2, respectively. The geometry of a typical vaned diffuser is shown in Fig. 2. The impellers are three-dimensional with backward leaning blades, but without a shroud. The divergence angle 2β of vaned diffuser is approximately 19 deg for the a-series and 14 deg. for the b-series. The incidence angle, $\bar{i}$, is the angle between the vane camber line and the flow angle, $\bar{\alpha}$, at the vane leading edge. All the diffusers have fifteen vanes each. The Reynolds number, $PS \times b_2/\nu$, is 3.0×10^5 for impeller A, 4.2×10^5 for impeller B, and 3.1×10^5 for impeller C. Impeller A was used with the diffusers of a-series and impeller B was used with the diffusers of b-series. Impeller C was used with diffuser b5.

Table 1 Parameters of tested impellers

Parameters	Impeller		
	A	B	C
Exit blade angle deg from tangential line	60	50	60
No. of blades	18	18	18
Specific speed, m^3/min,m,rpm	340	330	310
W_1/W_2	1.71	1.54	1.68
$Ws,max/W_2$	1.97	1.64	1.74
W_1/Wm,min	1.77	1.73	1.86
ΔW max/Wm	0.93	0.78	0.95
$(W_1/W_2)/(lo/D_2)$	4.50	4.21	3.94
Peripheral speed, m/s	330	387	400
Inducer tip diameter, mm	155	225	147
Inducer hub diameter, mm	75	90	61
Exit diameter, mm	250	380	250
Blade tip clearance, mm	0.4	0.7	0.4

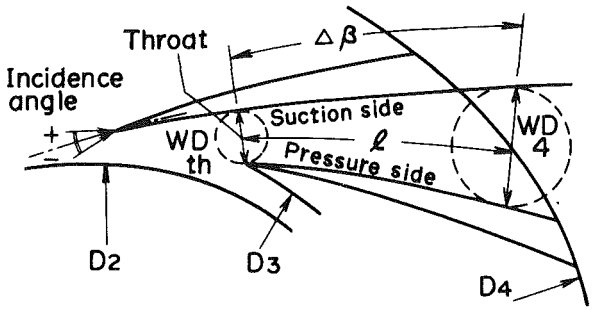

Fig. 2 Vaned diffuser geometry and nomenclature

Nomenclature

B = blockage due to boundary layer
b = meridional width
$\bar{C}$ = area averaged absolute velocity, $\int \rho C dA / \int \rho dA$
$\bar{\bar{C}}$ = mass averaged absolute velocity, $\int \rho C^2 dA / \int \rho C dA$
C_f = local skin friction factor
C_p = static pressure recovery coefficient
D = diameter
DF = velocity distortion factor, $\bar{C}/\bar{C}$
lo = length of blade shroud line
n = index for power-law profile
PS = peripheral speed
Q = flow rate
U = velocity at boundary layer edge
u = streamwise velocity component in boundary layer
v = crosswise velocity component in boundary layer
WD = diffuser width
W_1 = relative velocity at inducer shroud
W_2 = relative velocity at impeller exit
W_m = mean relative velocity on suction and pressure surface of blade along shroud line
W_s = relative velocity along shroud line on suction surface of blade
ΔW = relative velocity difference between pressure side and suction side of blade
x,y,z = streamline co-ordinate system, Fig. 3
$\bar{\alpha}$ = area averaged mean flow angle, $\tan^{-1} \bar{C}_m/\bar{C}_t$
$\bar{\bar{\alpha}}$ = mass averaged mean flow angle, $\tan^{-1} \bar{\bar{C}}_m/\bar{\bar{C}}_t$
$\Delta\alpha$ = $\bar{\bar{\alpha}} - \bar{\alpha}$
2β = divergence angle, $2 \tan^{-1} WD_4 - WD_{th}/2l$, where l is mean channel length
δ = boundary layer thickness, at $u = 0.99U$
δ_1 = boundary layer displacement thickness
θ = boundary layer momentum thickness
ν = kinematic viscosity
ρ = density
τ_{ox}, τ_{oz} = x and z components of wall shear stress

Subscripts

ch = channel region
d = design condition
i = semivaneless region
m = radial component
max = maximum
min = minimum
t = tangential component
th = vaned diffuser throat
2 = impeller exit
3 = vaned diffuser entrance
4 = vaned diffuser exit

Table 2 Specifications of tested vaned diffusers

Spec.	Diffuser No.	a1	a2	a3	a4	a5	a6	b1	b2	b3	b4	b5	b6	b7	b8
Incidence angle, $\bar{i}$, in design condition, (deg)		−3.5	−2.5	−1.5	−0.5	+0.5	+3.2	−2.0	−0.5	+2.0	+4.0	−0.5	+2.0	−0.5	+2.0
2β deg.		18.2	18.6	18.5	18.2	18.2	18.8	13.0	13.2	13.6	13.8	13.1	13.4	15.8	15.9
$\Delta\beta$ deg.		2.0	2.0	2.0	2.0	2.0	6.0	9.0	9.0	9.0	9.0	9.0	9.0	9.0	9.0
Aspect ratio															
b_{th}/WD_{th}		0.586	0.563	0.542	0.522	0.487	0.522	0.712	0.662	0.610	0.580	0.662	0.610	0.662	0.610
l/WD_{th}		3.49	3.29	3.13	3.00	2.69	3.18	5.23	4.90	4.53	4.37	4.72	4.40	4.85	4.49
WD_4/WD_{th}		2.12	2.08	2.02	1.96	1.86	2.05	2.20	2.14	2.08	2.06	2.08	2.04	2.35	2.26
D_3/D_2		1.17	1.16	1.16	1.15	1.14	1.14	1.10	1.10	1.09	1.08	1.10	1.09	1.10	1.09
D_4/D_2		1.66	1.67	1.67	1.69	1.66	1.68	1.72	1.73	1.76	1.77	1.70	1.73	1.71	1.73

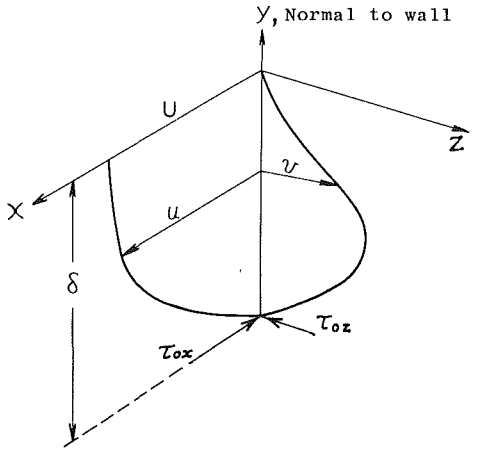

Fig. 3 Three-dimensional boundary layer velocity profile

Flow in Impeller

The secondary flow arising within the boundary layer which is induced by the pressure gradient causes the accumulation of low momentum fluid at the suction side of the blade. These phenomena have also been found by others [3, 4]. From these results, it seems that a core flow may exist. The core flow was analysed by using a quasi-three-dimensional method which assumed that the core flow was an inviscid and compressible flow. The boundary layer analysis was combined with the core flow analysis interactively. In the boundary layer flow, the centrifugal force caused by rotation and flow path curvature, the Coriolis force, and the pressure gradient do not balance. This unbalance causes the cross flow. A typical three-dimensional boundary layer velocity profile is illustrated in Fig. 3. The streamwise velocity profile and shear stress in a three-dimensional turbulent boundary layer were assumed to be represented by two-dimensional relations [5, 6]. The streamwise momentum integral equation is shown as

$$\frac{\partial\theta}{\partial x}+\left(2+\frac{\delta_1}{\theta}\right)\frac{\theta}{U}\frac{\partial U}{\partial x}+\frac{1}{U^2}\frac{\partial}{\partial z}\int_0^\delta (U-u)v\,dy=\frac{C_f}{2} \quad (1)$$

It is assumed that the streamwise velocity distribution is represented by a power-law profile.

$$\frac{u}{U}=\left(\frac{y}{\delta}\right)^{1/n} \quad (2)$$

In this analysis, the effects of curvature and rotation on the streamwise boundary layer growth are not considered, except the momentum transport resulting from cross flow. The local skin friction factor was determined by the next equation of Ludwieg & Tillmann.

$$C_f=0.246\times 10^{-0.678H}\times \mathrm{R}_{e\theta}{}^{-0.268} \quad (3)$$

The crossflow velocity profile is represented by the Prandtl-Mager model.

$$\frac{v}{U}=\frac{u}{U}\left(1-\frac{y}{\delta}\right)^2\epsilon \quad (4)$$

The factor, ϵ, is defined as the shear stress ratio on the wall.

$$\epsilon=\frac{\tau_{oz}}{\tau_{ox}} \quad (5)$$

This factor is variable and depends on the magnitude of the crossflow.

The momentum equation of the crossflow is defined for each stream line as

$$\frac{\partial}{\partial x}\int_0^\delta \rho uv\,dy+\frac{\partial}{\partial Z}\int_0^\delta \rho v^2\,dy=\frac{\partial}{\partial Z}\int_0^\delta p\,dy-\tau_{oz} \quad (6)$$

where p is the force per unit area which acts in the direction of

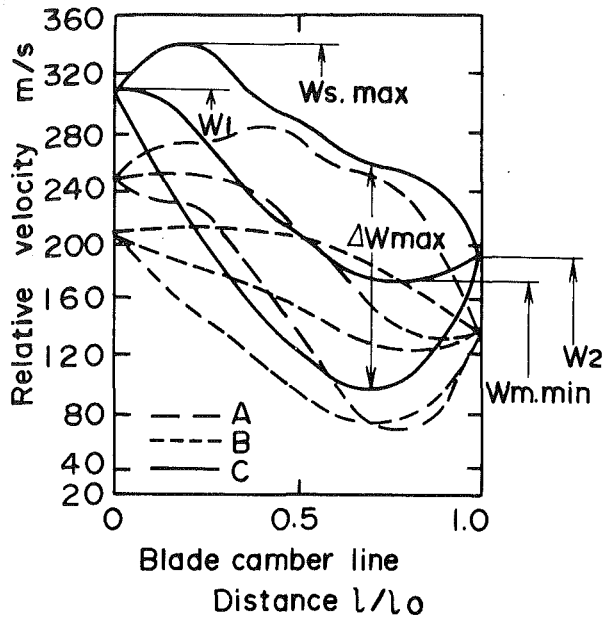

Fig. 4 Relative velocity distribution along shroud line of impeller

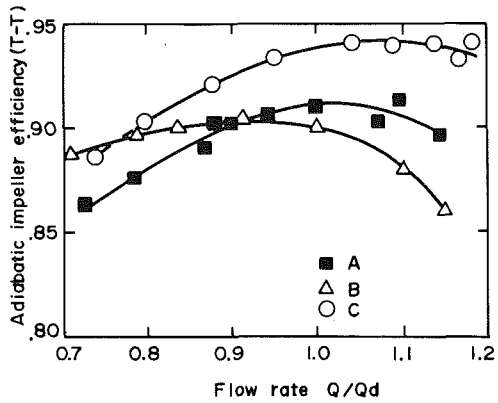

Fig. 5 Impeller efficiency

Z-axis. In this analysis, p is determined only from the pressure gradient normal to the stream line calculated by the core flow analysis, the centrifugal force due to flow line curvature, the Coriolis force in the streamwise boundary layer, and the centrifugal force by rotation.

The equations described above were applied to the internal flow in the impeller by assuming that the shape of flow path was simplified as the rotating flow channel which is curved two-dimensionally.

The boundary layer migrates through the corner regions. The boundary layer behavior in this region may be different from other areas. In the present analysis, this region was simply considered as the developed surface.

The boundary layer at the suction side of the impeller blade tends to separate in the radial portion of the impeller. This is mainly due to thickening by the migration of the boundary layer from pressure side of the blade, the hub and the shroud.

After the boundary layer separates, the wake is assumed to grow in the same manner as before the separation in the present analysis. On the surface of the blade presusre side and the hub, the low momentum fluid is taken away by the pressure gradient normal to the core flow, and the boundary layer on the surface does not grow so rapidly.

In the case of the open impeller, the fluid on the shroud surface flows in the combined direction of rotation and relative velocity of the core flow in the impeller. The boundary layer calculation should be performed in accordance with this combined direction. In addition, the blade tip acts to cut the boundary layer, and some fluid enters into the next flow path through the tip clearance. However, in the present analysis, the shroud side boundary layer was calculated by the same method used for the covered impeller to avoid the very complicated flow at the blade tip.

The internal loss of impeller can be approximated by the momentum thickness of the boundary layer.
The loss $\Delta\eta$ is represented by the following relation.

$$\Delta\eta = \frac{B_\theta \cdot \bar{w} \cdot w_{2c}}{g \cdot (1 - \mathbf{B}_{\delta 1}) \cdot H_0} \tag{7}$$

where B_θ is the blockage by the momentum thickness at impeller exit,

$$\frac{1}{A_2 \cdot w^2_{\max}} \int_{A_2} w(w_{\max} - w)\, dA$$

where A is flow path area, w is relative velocity, and $B_{\delta 1}$ is the blockage by the displacement thickness at impeller exit,

$$\frac{1}{A_2 \cdot w_{\max}} \int_{A_2} (w_{\max} - w)\, dA$$

Here:

$\bar{w}$ = mean relative velocity of the core flow along stream line from the root mean square radius at inlet to the exit
H_0 = theoretical head
w_{2c} = relative velocity of the core flow at impeller exit
g = acceleration due to gravity

Impeller Performance

The inviscid flow velocity distributions are shown in Fig. 4. The diffusion ratio along the suction surface of impeller A is higher than the other impellers. The loading of the blade $\Delta W_{\max}/W_m$, which is related to the blade-to-blade pressure difference, is smallest in impeller B. The mean velocity gradient along the shroud line, $(W_1/W_2)/(lo/D_2)$,is related to the boundary layer growth. This fact is maximum in impeller A and minimum in impeller C. The smaller mean relative velocity causes a lower friction loss due to the shear force on the bounding surface. On the other hand, the loss associated with the effect of adverse velocity gradients on the boundary layer growth and the crossflow in the boundary layer is influenced by W_1/W_2, $(W_1/W_2)/(lo/D_2)$ and $\Delta W_{\max}/W_m$.

The efficiency of each impeller is shown in Fig. 5. From these results, the maximum efficiency at the design flow rate is obtained when the inviscid relative velocity ratio W_1/W_2 is about 1.62–1.67 and the mean velocity gradient $(W_1/W_2)/(lo/D_2)$ is below 4.0.

According to the present analysis, the boundary layer migrates to the suction side of blade at the shroud. The radial velocity distribution at $r/r_2 = 1.05$ for impeller A is shown in Fig. 6. This was calculated from the total pressure distribution measured by a high frequency pressure transducer. In this calculation, the static pressure in the meridional plane is assumed to be uniform between the shroud and the hub. The circumferential unsteady static pressure was the value measured on the shroud wall. This indicates that the low momentum fluid accumulates on the shroud suction side. This was measured for impeller A. The blockage by the momentum thickness of the radial flow component was found to be 12 percent at the measured radius. From the present analysis, a blockage of 13 percent was obtained at the impeller exit. The variation due to mixing in the vaneless region to $r/r_2 = 1.05$ should be taken into consideration. The relation between the impeller efficiency and the loss $\Delta\eta$ is shown in Fig. 7 for the design flow rate. This means that the momentum thickness calculated by the present analysis represents the internal loss

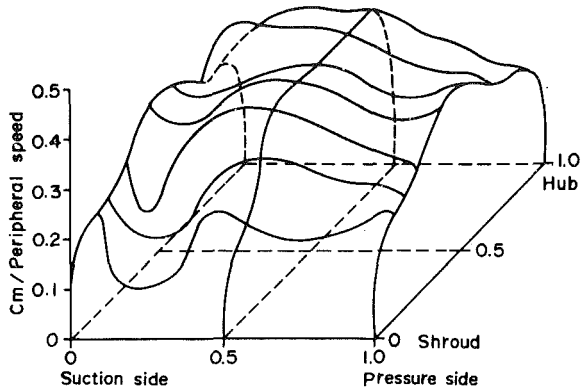

Fig. 6 Radial velocity distribution at $r/r_2 = 1.05$

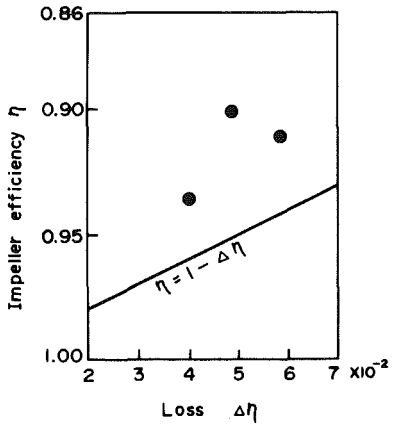

Fig. 7 Relation between impeller efficiency and loss $\Delta\eta$

and is related to the impeller efficiency. The loss $\Delta\eta$ is the calculation result.

Impellers A, B, and C have almost the same characteristics in the head coefficient. The velocity distribution at the impeller exit is nonuniform. Therefore, the peak of the time averaged meridional velocity is not located at the middle of diffuser width, but it is shifted toward the hub side. The meridional velocity is very low at the shroud side, though the tangential velocity is almost uniform. The time averaged velocity distribution at the impeller exit is shown in Fig. 8. The boundary layer blockage due to the displacement thickness at the exit of the impeller is 3.8 percent for impeller A, 6.6 percent for impeller B, and 4.3 percent for impeller C in the design condition. The absolute velocity was used to calculate the blockage.

Static Pressure Recovery in Semivaneless Region

In this paper, the semivaneless region means the space from the impeller exit to the diffuser throat. The static pressure recovery was calculated by the iteration between the inviscid core flow analysis and the boundary layer analysis, which is the same method used for the impeller. The core flow at the inlet condition of the diffuser was assumed to be uniform and axisymmetric flow. The boundary layer displacement thickness and momentum thickness at the inlet of the diffuser were determined from experimental data measured by a cobra probe. For these calculations, the inlet conditions of the diffuser were varied in accordance with the operating flow rates. The comparison between the calculated and measured static pressure recovery, C_{pi}, is shown in Fig. 9. The measured static pressure recovery was calculated as $C_{pi} = 2(P_{th} - P_2)/\rho\bar{C}_2^2$, where $\bar{C}_2$ is the area-averaged impeller exit velocity. P_2 is the static pressure which is determined by averaging measured values at three points on same radius of $r/r_2 =$ 1.05. P_{th} is the averaged static pressure at the throat. All measured and calculated values, in which off-design conditions are included, are shown in Fig. 9. The small discrepancies between the calculated and the measured values are believed to be due to inlet distortion and incidence.

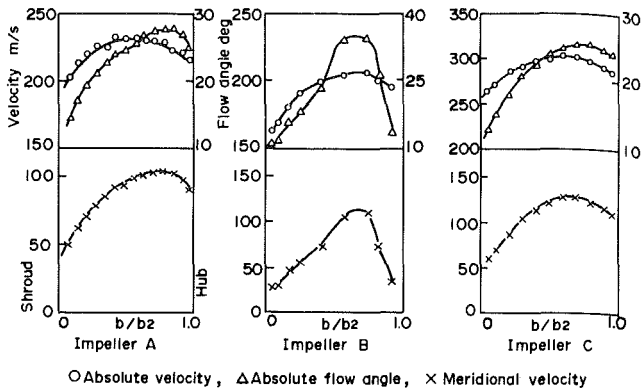

○ Absolute velocity, △ Absolute flow angle, × Meridional velocity

Fig. 8 Velocity distribution at impeller exit

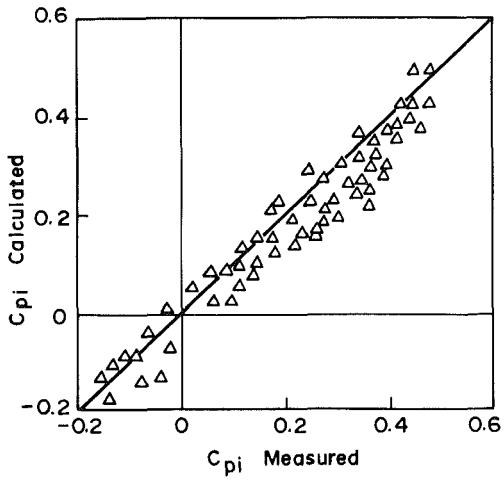

Fig. 9 Static pressure recovery in semivaneless region

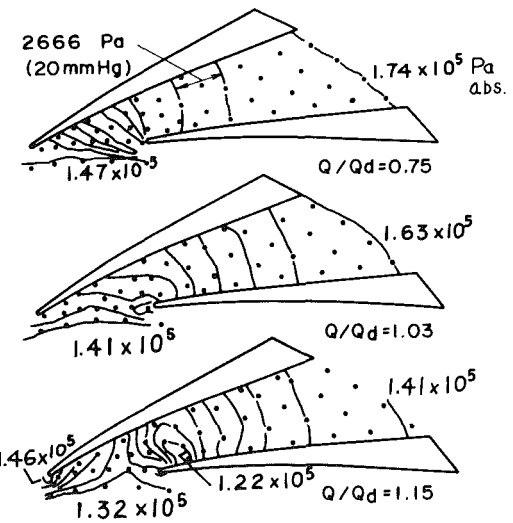

Fig. 10 Isobars of static pressure in the diffuser, diffuser b2

The isobars of static pressure in the diffuser, measured for diffuser b2, are shown in Fig. 10. The static pressure distribution in the semivaneless region varies in accordance with operating conditions. The incidence angle at the leading edge is minus 0.5 deg at design flow rate $Q/Q_d = 1.0$, and the wedge angle is about 12 deg, so the angle between velocity $\bar{C}_3$ and suction surface is minus 6.5 deg. The incidence angle to

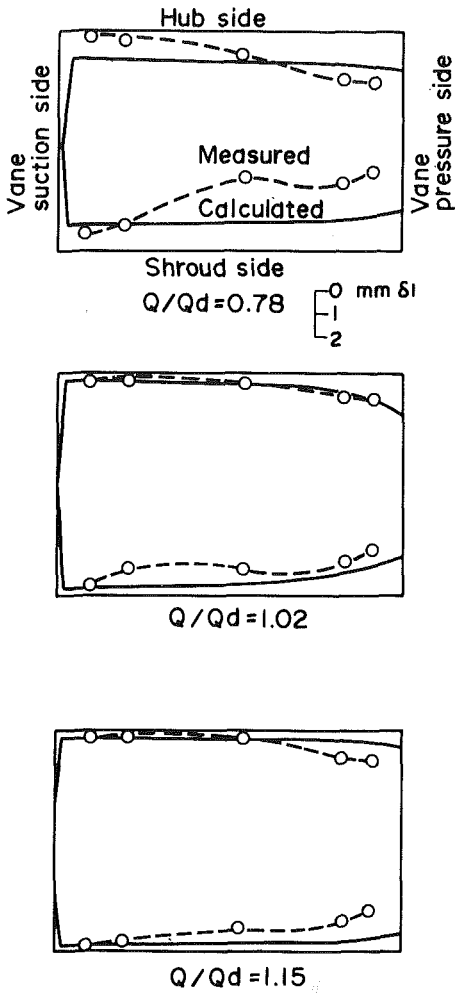

Fig. 11 Boundary layer distribution in throat, diffuser b2

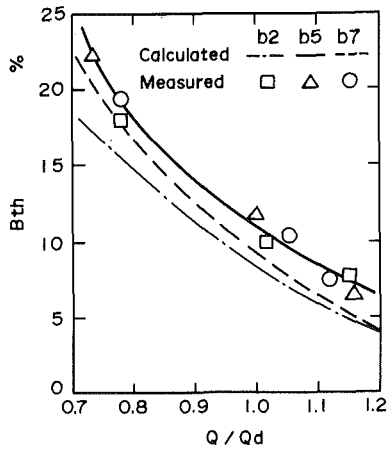

Fig. 12 Boundary layer blockage at throat

the camber line is +6.0 deg at $Q/Q_d = 0.75$, so the angle between velocity $\bar{C}_3$ and the suction surface is almost zero; the isobars are therefore nearly normal to the suction surface.

The boundary layer distributions in the throat section are shown in Fig. 11 for diffuser b2. In this figure, the calculated line was determined by the present analysis, and the measured value is displacement thickness determined from velocity distribution measured by a traversing yawmeter.

The scale of the boundary layer thickness, δ_1, in this figure is shown as twice as that of the throat area. The boundary layer blockage B_{th} at the throat is shown in Fig. 12. From these results, the boundary layer distribution is not uniform in

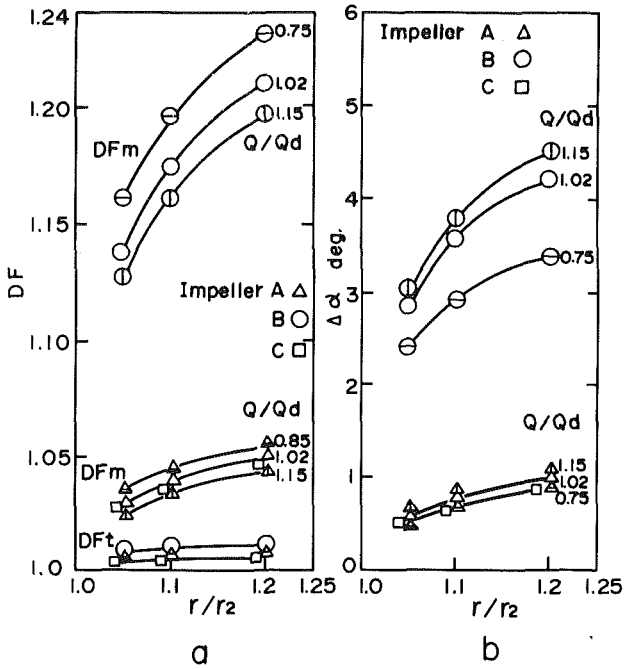

Fig. 13 Velocity distortion in vaneless diffuser

the semivaneless space and the throat section. There is a large growth of the boundary layer on the pressure side, though it is a very small amount on the suction side.

It seems that the three-dimensional boundary layer growth at the leading edge is included in this thick boundary layer on the pressure side. The smaller the flow rate is, the larger the throat blockage becomes. This is mainly due to the large velocity deceleration. In the case of diffusers b5 and b7, blockages are approximately 12 percent at $Q/Q_d = 1.0$ and 22 percent at $Q/Q_d = 0.73$.

Incidence Angle and Diffuser Performance

The velocity distribution in the semivaneless region is affected by the incidence angle, as shown previously. The flow distribution at the impeller exit, even after the jet and the wake are mixed, is three-dimensional and the flow angles of each point across the diffuser width are different.The flow angle between the absolute velocity and a tangential line is small at the shroud side. The velocity distortion factors for the meridional and the tangential components, DF_m and DF_t, were determined for each radius by measuring the velocity distribution in the vaneless diffuser. These results are shown in Fig. 13. For example, in the case of impeller B, DF_m in condition of $Q/Q_d = 0.75$ is 1.16 at a radius of $r/r_2 = 1.05$, and it increases to 1.23 at $r/r_2 = 1.20$.

The smaller the flow rate is, the more the flow is distorted. DF_t is nearly unity and almost constant. The incidence angle at the vane leading edge seemed to be evaluated more accurately by using flow angle $\bar{\alpha} = \tan^{-1} \bar{C}_m/\bar{C}_t$, determined from the mass averaged velocity, than by using flow angle $\bar{\alpha} = \tan^{-1} \bar{C}_m/\bar{C}_t$, determined from the area averaged velocity. The difference between $\bar{\alpha}$ and $\bar{\alpha}$, $\Delta\alpha = \bar{\alpha} - \bar{\alpha}$, is shown in Fig. 13(*b*) as a function of the radius. This value is fairly large. For example, in impeller B, $\Delta\alpha$ is about 3 deg at a radius of $r/r_2 = 1.10$. This is important in order to find the optimum incidence angle.

The channel, downstream of the throat, is two-dimensional. The flow distribution at the entrance of the channel, namely the throat, is nonuniform, so the performance of the channel is different from that which has a uniform inlet condition. The static pressure recovery of the

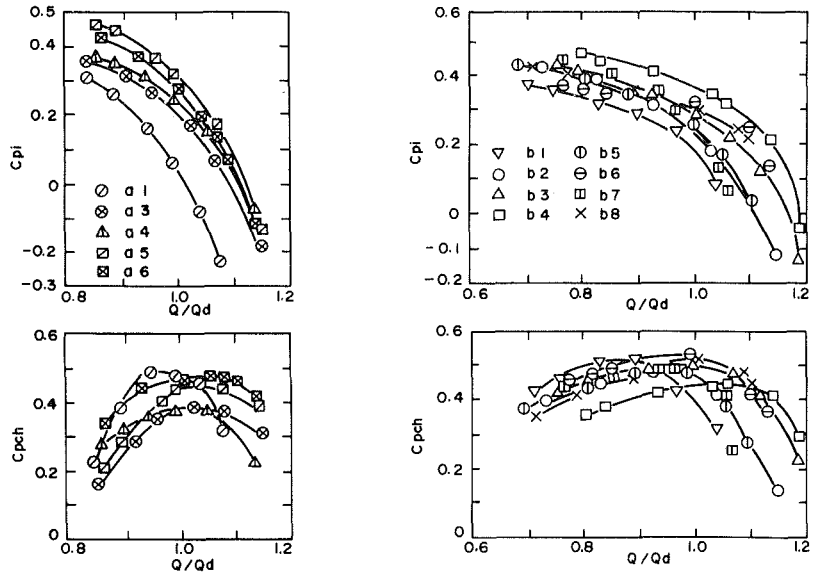

Fig. 14 Static pressure recovery coefficients of semivaneless region and channel

Table 3 Optimum incidence angle, at the vane leading edge

Vane	Q/Q_d at peak of C_{pch}	$\bar{i}$ deg	$\Delta\alpha$ deg	$\bar{\bar{i}}-\bar{i}-\Delta\alpha$ deg
a1	0.94	−1.5	0.9	−2.4
a2	0.98	−2.0	0.9	−2.9
a3	1.02	−2.5	0.9	−3.4
a4	1.00	−0.5	0.9	−1.4
a5	1.02	−0.5	0.9	−1.4
a6	1.05	+1.3	0.9	+0.4
b1	0.88	+1.0	3.3	−2.3
b2	0.92	+2.0	3.4	−1.4
b3	1.00	+2.0	3.6	−1.6
b4	1.06	+2.0	3.7	−1.7
b5	0.97	+0.5	3.5	−3.0
b6	0.99	+2.0	3.6	−1.6
b7	0.96	+0.5	3.5	−3.0
b8	1.02	+1.0	3.6	−2.6

channel was compared with straight two-dimensional diffuser data of Reneau [8] in order to evaluate the effects of the nonuniform inlet conditions on the diffuser performance. The tested diffuser channel is not straight but slightly curved. This effect of curvature was corrected by using the experimental data of Sagi [9].

The static pressure recovery coefficients of the semivaneless region and the channel are shown in Fig. 14. The relation between the static pressure recovery of the channel region in the vaned diffuser and that of the straight two-dimensional diffuser is defined as follows:

$C_{pch} = C_{ps} + \Delta C_{p1} + \Delta C_{p2}$

C_{pch} = static pressure recovery coefficient of tested diffuser channel

C_{ps} = static pressure recovery coefficient of straight two-dimensional diffuser

ΔC_{p1} = effect of nonuniformity on pressure recovery

ΔC_{p2} = difference of static pressure recovery between straight and curved diffuser, vane number

a1 - a5 $\Delta C_{p2} = 0.00$

a6 $= -0.02$

b1 - b8 $= -0.03$

The values of ΔC_{p1} are shown as a function of the incidence angle in Fig. 15. The incidence angle, $\bar{i}$, where ΔC_{p1} is maximum, was approximately −2 deg for diffuser a-series and +2 deg for diffuser b-series. This difference of 4 deg was caused by the inlet distortion at the throat. Namely, as shown in Table 3, when incidence angle, $\bar{i}$, determined by correcting

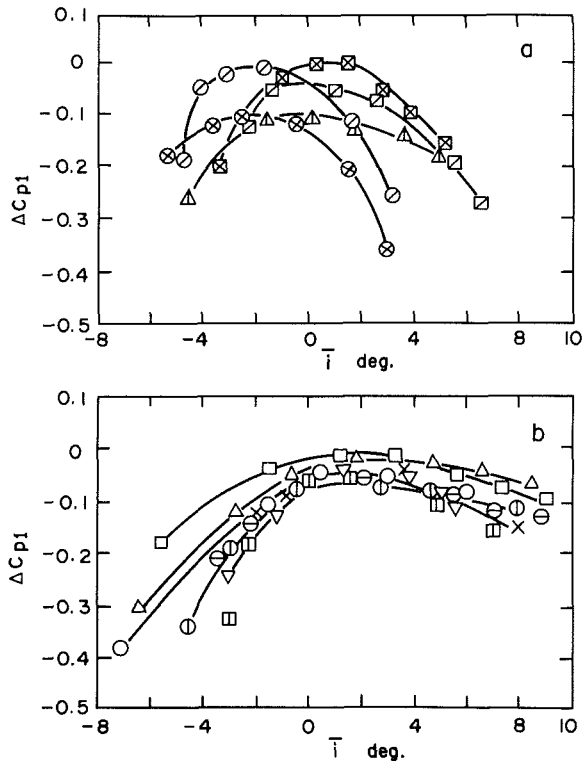

Fig. 15 Value of ΔC_{p1}

$\bar{i}$ with $\Delta\alpha$, shown in Fig. 13, is used for evaluation, approximately −2 deg is obtained as the optimum incidence angle for all diffusers. In the case of the uniform inlet condition, the maximum pressure recovery is obtained at zero incidence. However, when the inlet flow is nonuniform such as the centrifugal diffuser channel, the maximum pressure recovery is obtianed at about a −2 deg incidence angle of the mass-averaged flow.

These phenomena are due to the following reasons. The boundary layer in the semivaneless region migrates and affects the blockage and velocity distribution at the throat. The boundary layer growth on the suction surface of the semivaneless region is restrained by the dynamic pressure component normal to the surface. So the pressure recovery in the channel becomes maximum at about a −2 deg incidence

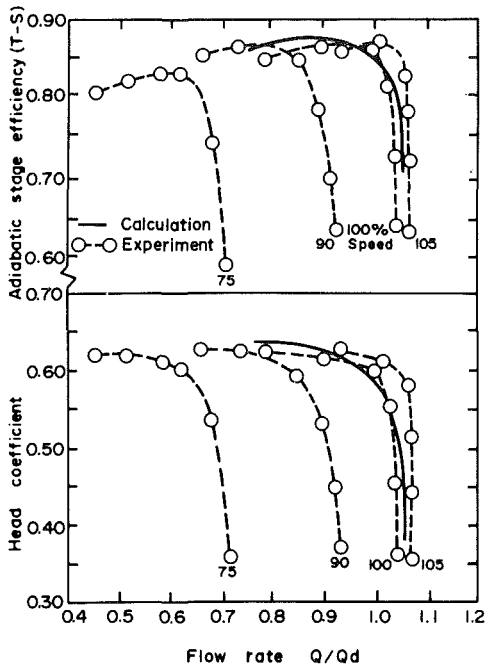

Fig. 16 Adiabatic stage efficiency and head coefficient, impeller C and diffuser b5

angle, due to the balance of deterioration by the incidence and effect of restraint of the boundary layer growth.

The surge of a centrifugal compressor is caused by the stall in the impeller or the diffuser in many cases. In this performance test, the flow rate Q/Q_d, when surge occurred, is clearly larger in the case of the vaned diffuser than in the case of the vaneless diffuser. The static pressure recovery coefficients of the channel, shown in Fig. 14, were determined as $C_{pch} = 2(P_4 - P_{th})/\rho \bar{C}_{th}^2$ based on dynamic pressure at the throat. P_4 is the static pressure at the diffuser exit. The value of C_{pch} in the off-design condition is smaller than in the design condition. The values of diffusion ratio $\bar{C}_2/\bar{C}_{th}$ are between 1.4 and 1.6 for all tested diffusers at the flow rate which is close to the surge initiation. The calculated maximum shape factor H_{12} of the boundary layer at the throat is between 1.5 and 1.6. However, the maximum measured shape factor is 1.9. This measured value is the maximum value in all diffusers and is obtained at the pressure side of the throat.

It does not seem that there is a thick boundary layer on the vane suction surface judging from the velocity distribution at the throat. The stream trace of coating film also indicates that there is no low momentum, namely a thick boundary layer, on the vane suction surface. These phenomena depend on the boundary layer migration from the suction side to the pressure side due to the static pressure unbalance as shown in Fig. 10. There is a possibility that the boundary layer at the throat pressure side begins to separate before the surge. This may be the three-dimensional separation at the leading edge. According to Fig. 14, the pressure recovery C_{pch} decreases at a small flow rate before surge. This decrease of the pressure recovery in the channel is caused by the throat blockage and the flow separation on the pressure surface in the channel. The small flow separation on the pressure surface of the channel was observed in the operating condition between the surge and the design flow rate. This small separation becomes larger, and the pressure recovery of the channel becomes low and the diffuser stall eventually occurs.

Stage Performance and Application to the Actual Machine

The adiabatic stage efficiency and head coefficient for impeller C and diffuser b5 are shown in Fig. 16. In this figure, the comparison between predicted values and measured values are shown. These show fairly good agreement, and high efficiency was obtained.

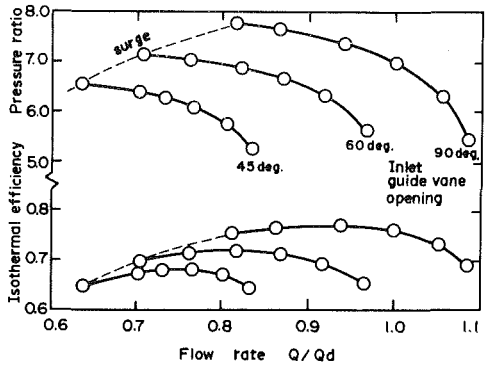

Fig. 17 Characteristic curve of isothermal centrifugal compressor

These results were applied to the one-shaft, four-stage isothermal centrifugal compressors in which the speed is about 90 percent of the stage experiment. The desired high efficiency was obtained. The characteristic curve, which was obtained from a field test, is shown in Fig. 17. This isothermal efficiency of 76 percent, which is the ratio of a theoretical isothermal compression work and a shaft power, is the highest level in the world. The three compressors have already been in operation. One of them handles the air of 70 m^3/s, which is the largest in the world for this application of a centrifugal compressor. It was demonstrated that because of its high efficiency and mechanical toughness the centrifugal compressor was suitable for a large isothermal compressor. According to our new design method, it is possible to design up to the capacity of 112 m^3/s and a pressure ratio of 8.

Conclusions

1 The boundary layer analysis, which considers the secondary flow and is combined with the core flow, predicts the condition of the internal flow. The results show fairly reasonable agreement with the experimental data.

2 The impeller efficiency is influenced by the boundary layer momentum thickness which is predicted roughly by the present analysis. The present prediction is useful for designing high-efficiency impellers. The maximum efficiency is obtained at $W_1/W_2 = 1.62 \sim 1.67$ as in the inviscid flow analysis.

3 The velocity distribution at throat is nonuniform. The boundary layer is thicker on the pressure surface than on the suction surface. The result of the calculation shows a similar distribution. The calculated blockage factor is almost same as the measured one.

4 The pressure recovery of the vaned diffuser channel, downstream of throat, is different from the two-dimensional straight diffuser. This difference is minimum when the incidence angle, which is determined from the mass averaged velocity, is about -2 deg. The minimum difference of pressure recovery is between -0.1 and 0.

5 It became possible to design the large isothermal centrifugal compressor which had a high efficiency.

Acknowledgments

The authors wish to express their appreciations to Mr. M. Ito, Mr. K. Kajiki, Mr. T. Sasaki, and Mr. N. Ishiguro for their performance test of the actual machines. The authors also acknowledge the Rotating Machinery Works for permission to publish the paper.

References

1 Dallenbach, F., "The Aerodynamic Design and Performance of Centrifugal and Mixed-Flow Compressors." SAE Technical Progress Series, Vol. 3, 1961, pp. 2–30.

2 Rodgers, C., "Impeller Stalling as Influenced by Diffusion Limitations," *Centrifugal Compressor and Pump Stability, Stall, and Surge*, ASME, New York, 1976, pp. 37–67.

3 Eckardt, D., "Flow Field Analysis of Radial and Backswept Centrifugal Compressor Impellers, Part 1: Flow Measurements Using a Laser Velocimeter," *Performance Prediction of Centrifugal Pumps and Compressors*, ASME, New York, 1980, pp. 77–86.

4 Fowler, H. S., "Some Measurements of the Flow Pattern in a Centrifugal Compressor Impeller," ASME Paper 65-WA/GTP-7, 1965.

5 Mager, A., "Generalization of Boundary Layer Momentum Integral Equations to Three-Dimensional Flow Including Those of Rotating Systems," NACA Report 1067, 1952.

6 Prahlad, T. S., "Mean Velocity Profiles in Three-Dimensional Incompressible Turbulent Boundary Layers," *AIAA Journal*, Vol. 11, No. 3, Mar. 1973, pp. 359–365.

7 Head, M. R., "Entrainment in the Turbulent Boundary Layer," A.R.C.R. & M. 3152, 1958.

8 Reneau, L. R., Johnston, J. P., and Kline, S. J., "Performance and Design of Straight, Two-Dimensional Diffusers," Trans. ASME, Series D, Vol. 89, No. 1, Mar. 1967, pp. 141–150.

9 Sagi, C. J., and Johnston, J. P., "The Design and Performance of Two-Dimensional, Curved Diffusers," Trans. ASME, Series D, Vol. 89, No. 4, Dec. 1967, pp. 715–731.

10 Runstadler, P. W., Jr., and Dean, R. C., Jr., "Straight Channel Diffuser Performance at High Inlet Mach Numbers," Trans. ASME, Series D. Vol. 91, No. 3, Sept. 1969, pp. 397–422.

11 Wolf, S., and Johnston, J. P., "Effects of Nonuniform Inlet Velocity Profiles on Flow Regimes and Performance in Two-Dimensional Diffusers," Trans. ASME, Series D, Vol. 91, No. 3, Sept. 1969, pp. 462–474.

12 Senoo, Y., and Nakase, Y., "An Analysis of Flow Through a Mixed Flow Impeller," Trans. ASME, Series A, Vol. 94, No. 1, 1972, pp. 43–50.

13 Katsanis, T., "Computer Program for Calculating Velocities and Streamlines on a Blade-to-Blade Stream Surface of a Turbomachine," NASA TN, D-4252, 1968.

Casing Wall Boundary-Layer Development Through an Isolated Compressor Rotor

I. H. Hunter
Ontario Hydro,
Toronto, Canada

N. A. Cumpsty
Whittle Laboratory,
University of Cambridge,
Madingley Road,
Cambridge, England

Detailed measurements were made of the casing wall boundary layer development across a large-scale, low-speed axial compressor rotor blade row. An important feature of the work was the use of blading which allowed the tip clearance to be varied. A conventional pressure probe was used to obtain time-averaged measurements of the outer-wall boundary layer downstream of the rotor whilst a hot-wire anenometry technique yielded the three-dimensional, blade to blade structure of the flow. The downstream boundary layer was found to thicken as the rotor loading and blade-end clearance were increased, with fluid tending to accumulate towards the pressure side of the passage. By its pronounced effects upon wall boundary layer development, tip clearance had a deleterious effect upon the performance of the compressor.

1 Introduction

It is well known that the pressure rise, stall point, and efficiency of axial compressors are limited by the boundary layers which develop on the hub and casing walls. It is therefore surprising how little is known about the behaviour of these boundary layers and how shaky are the foundations on which their prediction is based. The explanation is that the flow is both exceedingly complicated and difficult to examine experimentally.

Much research effort has been concerned with the development of various analytical techniques which attempt to provide the turbomachinery designer with means of accounting for the effects of wall boundary layers. Because the flow is invariably highly three-dimensional in nature, a considerable number of simplifying assumptions are required before workable solutions can be obtained. Over the past 25 years or so, the prediction methods have developed essentially along two lines.

In Classical Secondary Flow Theory (e.g., Hawthorne [1], Horlock [2], Horlock and Lakshminarayana [3]), the major part of the endwall flow is taken as inviscid, and solutions are obtained for the development of the streamwise component of vorticity as the boundary layer progresses through a blade row. This quantity can be used to evaluate the induced secondary velocity field. The obvious limitation of this approach is its inviscid basis, but equally serious is the restriction to small perturbations and the necessary simplifying of the geometry. Although useful predictions of blade outlet flow angle variations are obtainable, no information on losses is provided.

With boundary-layer theory the endwall flow is treated as a viscous flow problem. This approach developed primarily as a design tool for the prediction of annulus blockage effects in axial flow compressors. Most of the calculation methods are circumferentially or passage averaged, which makes them compatible with the commonly available axisymmetric models of the mainstream flow. As a further simplification, it is normal to integrate the equations of motion over the boundary-layer thickness. The development of the endwall flow is therefore described by the overall defect integral properties rather than in terms of the detailed boundary-layer profiles themselves (e.g., Horlock and Perkins [4], Mellor and Wood [5], Hirsch [6], Bario et al. [7]), and it is at this stage that considerable empirisism is required.

On the experimental side a large number of studies have been undertaken, some specifically to provide data for checking theoretical models, others to gain some insight into the physical nature of the flow processes. A significant proportion of these investigations have been concerned with stationary, linear cascades, in which, however, a number of important turbomachinery effects are missing. In fact, the flow along the endwalls of a stationary cascade is different in most important respects from that over a rotor tip or hub root, since the flow in these is characterised by quite high dynamic head right down to the wall, but with variation in direction (skewing). Even in the simpler cascade configurations the endwall flow has been found to be severely disturbed in its progress through the blades and many limitations in the various analytical models have been highlighted. While comparatively little data of a detailed nature currently exists for endwall flows in actual compressor stages, it is important to point out remarkable paper on multistage compressors by Smith [8], which we have cause to refer to later.

The present research, much of which is documented by Hunter [9], makes use of one of the large-scale, low-speed rotating cascade wind tunnels at the Whittle Laboratory, Cambridge. A comprehensive series of measurements were

Contributed by the Gas Turbine Division and presented at the International Gas Turbine Conference, London, England, April 18–22, 1982, of THE AMERICAN SOCIETY OF MECHANICAL ENGINEERS. Manuscript received at ASME Headquarters November 23, 1981. Paper No. 82-GT-18.

made of the development of the casing (outer) wall boundary layer across an isolated compressor rotor, with a view to revealing details of the flow phenomena. An investigation of the role of tip clearance, which is known to exert a significant influence upon the development of the endwall flow (e.g., Lakshminarayana and Horlock [10], Rains [11] and Dean [12]) formed an important aspect of the experimental work. The integral scales of the boundary layer entering the stage were found to be comparable to the minimum tip clearance in the first experiments and a subsequent series of tests were therefore carried out with an artificially thickened boundary layer.

2 Experimental Rig and Instrumentation

The experimental equipment is described fully in Hunter [9] and so only a brief account will be given here.

The research compressor is shown schematically in Fig. 1. A large inlet section with honeycombs and screens precedes the tunnel working section which has a 1.524-m (5-ft) outer dia and hub-to-tip ratio of 0.4. The rig contains two independent rotors, the research rotor and 1.829 m downstream of this, an auxiliary axial fan. Further downstream still is a throttle to atmosphere. Each rotor is driven by variable speed electric motor. There is great flexibility in the operation of the tunnel whereby the rotational speed of the research cascade and the air flow rate may be varied independently.

The work described in this paper was conducted with an isolated rotor, i.e., no inlet guide vanes or stator blades were installed. The compressor rotor comprises 22 blades of a 152-mm (6-in.) chord, and the aerodynamic design, described fully by Gregory-Smith [13], is such as to give a free vortex flow at a flow coefficient ϕ equal to 0.7.[1] There is a wide operating range and stall commences at about $\phi = 0.39$ for the minimum rotor tip clearance and inlet boundary layer thickness. With the thickened inlet boundary layer, stall occurs at $\phi = 0.41$. The blades were manufactured with epoxy resin reinforced with glass fibre. The important blading details are summarised in Table 1.

In an initial series of tests, a conventional rotor blade set was used for which the tip clearance, t, was about 0.7 percent of chord. In the remaining and major part of the work, the tip portion was made up of 4 individual sections (see inset to Fig. 1). The radial gap between the blade end and the tunnel casing could be varied by detaching appropriate sections of blade. The tip-clearance values investigated are summarised in Table 2. The precise value of the minimum tip clearance varied slightly due to tolerances in the assembly, notably a slight noncircularity of the casing. Some tests with the naturally developed inlet boundary layer were performed with a clearance of 1 mm ($t/c = 0.7$ percent), the majority with a clearance of 1.5 mm ($t/c = 1$ percent). These agreed closely with one another and remarkably well with measurements made earlier by Gregory-Smith [13] with a tip clearance of 2.4 mm ($t/c = 1.6$ percent). It was therefore felt that clearances in the range 1.0 to 2.0 mm could be regarded as comparable. All the tests with the thickened boundary layer were made with a tip clearance of 2 mm.

The research rotor was run at a constant speed of 525 rpm and the air flow rate adjusted by means of the throttle and auxiliary fan until the upstream axial velocity to produce the desired flow coefficient was obtained. The velocities encountered in the tunnel are such that the flow may be regarded as being incompressible. The resultant Reynolds numbers, based upon blade chord and relative inlet velocity at the casing wall boundary layer edge, range only between 5.0×10^5 at $\phi = 0.7$ and 4.4×10^5 at $\phi = 0.40$. These values are sufficiently large that the blade-endwall, boundary-layer

[1] The flow coefficient is defined by $\phi = V_x/U_m$, where V_x is the mean axial velocity and U_m is the blade speed at mean height.

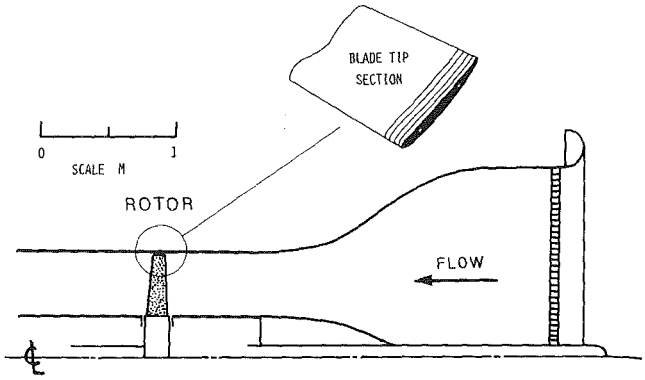

Fig. 1 Experimental compressor

Table 1 Important blading details at rotor tip section

Profile—C4 profile on circular arc camber line
Chord—152 mm (6 in.)
Overall span—457 mm (18 in.)
Blade inlet angle—64.9 deg
Blade outlet angle—56.7 deg
Design outlet flow angle—60.7 deg
Stagger angle—60.7 deg
Max. thickness/chord—8.0 percent
Pitch/chord—1.428

Table 2 Summary of tip clearance values investigated

Blade set	Mean radial tip clearance	
	t (mm)	t/c (%)
1	1.0	0.7
2	1.5	1.0
"	4.7	3.1
"	7.8	5.1
"	14.0	9.2

Nomenclature

t = tip clearance
c = blade chord
ϕ = flow coefficient
U = blade speed
v = flow velocity inside boundary layer
V = flow velocity at boundary layer edge
ρ = density
f_T = tangential blade force inside boundary layer
F_T = tangential blade force at boundary layer edge
F_x = axial blade force at boundary layer edge
ΔP = static pressure rise
ΔP_0 = total pressure rise
ψ = overall static pressure rise coefficient
β = relative flow angle referenced to axial direction
ξ = vorticity
δ = boundary layer thickness
δ^* = boundary layer displacement thickness
θ = boundary layer momentum thickness
ν_T = tangential force deficit thickness
ν_x = axial force deficit

Subscripts

x = axial direction
Z = radial direction
θ = tangential direction
1 = upstream (of blade row)
2 = downstream (of blade row)
tip = blade tip
m = mean height

interactions were representative of much current high speed practice.

The work carried out comprised measurements of the overall performance of the compressor and of the development of the casing wall boundary layer by conventional pressure probe and by hot-wire anemometry. Overall performance was evaluated in terms of the static pressure rise across the rotor measured with outer wall tappings located upstream and downstream of the blade row.

Measurements of the flow within the casing wall boundary layers were taken with a small three-hole "cobra" probe of head thickness 0.7 mm. The probe was calibrated so as to obtain dynamic and static pressures when nulled in yaw. A strain-gauge type differential pressure transducer was used to measure the probe pressures. The flow was traversed with the pressure probe at positions 210 mm and 33.5 upstream of the blade leading edge and 30.5 mm and 186.0 mm downstream of the trailing edge.

The full, three-dimensional, blade-to-blade structure of the rotor exit flow was determined by hot-wire anemometry. The technique used is an extended version of that developed originally by Whitfield et al. [14], employing a single hot-wire sensor inclined at 54.7 deg to the probe axis. The probe is rotated through successive 120 deg increments and data obtained for each of three mutually orthogonal orientations of the wire sensor. From these measurements the components of the flow velocity may be evaluated.

The inclined hot-wire technique was used in conjunction with the laboratory computer which provided on-line data acquisition and processing. The procedure mades use of phase-lock sampling and ensemble averaging. The recording of the linearized, hot-wire output voltage was initiated once every revolution of the rotor by a reference pulse. For each orientation of the hot-wire, a total of 80 ensembles each of 256 discrete measurements, covering the progress of three complete blade passages, were taken, and corresponding values were arithmetically averaged to produce the ensemble averaged distribution. This corresponded to the velocity signal linked solely to the passing of the rotor blades, unsteady random signals having been effectively removed. The ensemble average results at each orientation could then be used with the calibration data for the hot-wire to obtain the axial, tangential, and radial distributions of velocity.

The hot-wire probe assembly (consisting of a 1.0-mm length of 5-μm platinum-coated tungsten wire across two steel prongs set in a 2-mm dia stem) was introduced radially into the tunnel behind the rotor at a distance of 16.5-mm axially from the blade trailing edge.

3 Results and Discussion

The experimental results are described in the following manner. First of all, the overall performance characteristics of the rotor are considered. The details of the casing wall boundary layers are next described in terms of the averaged pressure probe data and then in terms of the high frequency hot-wire measurements. In both instances the minimum rotor tip clearance is examined first, and then attention directed towards increased gap sizes.

3.1 Overall Compressor Performance. The unstalled static pressure rise characteristics for each rotor tip-clearance configuration are given in Fig. 2. The compressor was known to be a tip-stalling machine, and hence blade end clearance was expected to have a profound effect upon this aspect of its performance. A significant (25 percent) increase in the stall onset flow coefficient was observed when the clearance was raised from t/c = 1.0 to 3.1 percent. With the two larger clearances, the limit of stable operation was reached at approximately the same flow coefficient as that for the t/c = 3.1 percent case. Tip clearance is seen to influence markedly the

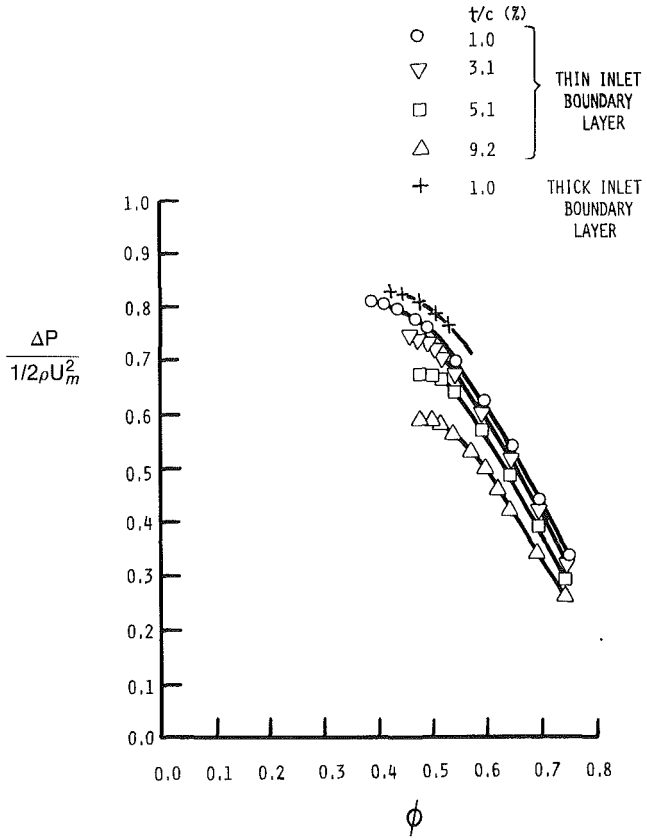

Fig. 2 Compressor overall performance characteristics

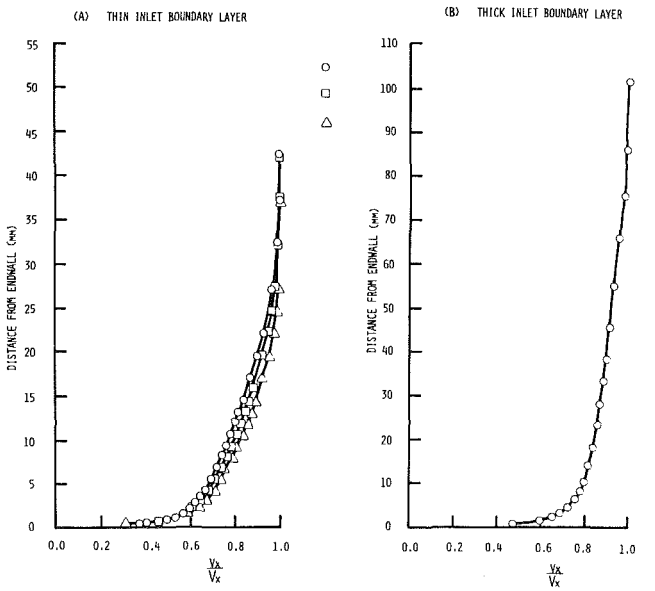

Fig. 3 Casing wall boundary layer velocity profiles upstream of rotor

aerodynamic behaviour of the machine away from stall, and pressure rise is lost continuously throughout the operating range as the gap size is increased.

The thickened inlet boundary layer (at minimum tip clearance) shows an increased static pressure rise but also an increased flow coefficient at stall. The increase in pressure rise is probably related to local streamline curvature effects near the wall produced by boundary layer thinning.

3.2 Pressure Probe Results. Before discussing the data itself, a statement is required on the identification of the wall boundary-layer edge. Downstream of the compressor rotor the total pressure and axial velocity outside the wall boundary

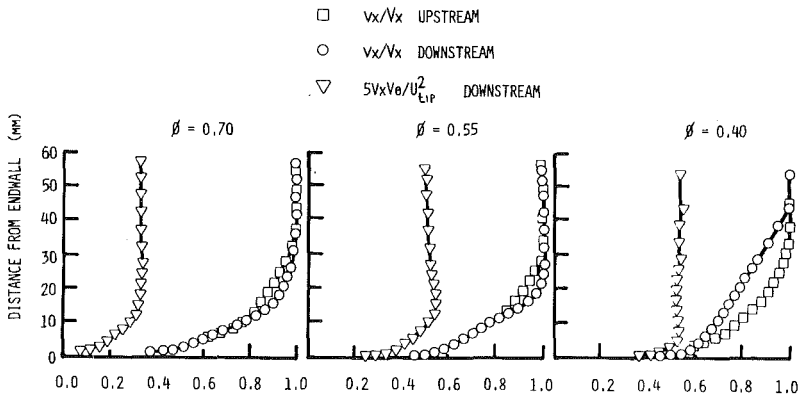

Fig. 4 Profiles upstream and downstream of rotor tip, natural (thin) inlet layer, t/c = 1.0 percent

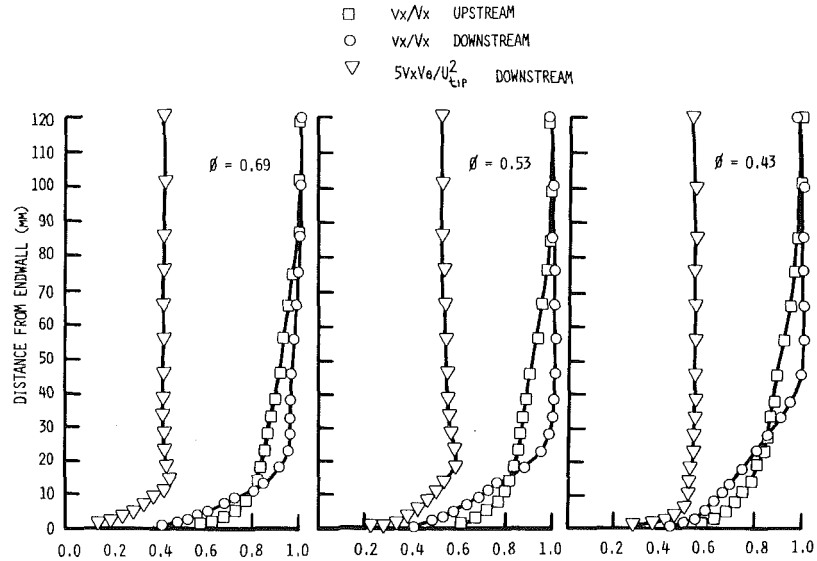

Fig. 5 Profiles upstream and downstream of rotor tip, thickened inlet layer, t/c = 1.0 percent

layer are strictly uniform only at design operating conditions when the flow is free-vortex. Nevertheless, the actual variations were sufficiently gradual off-design compared with those inside the boundary layer that a layer edge could be located with confidence in the majority of cases. Generally, the most convenient definition appears to be where the axial velocity either reaches a peak or reaches the uniform value of the free-stream.

3.2.1 Upsteam Flow. The velocity profiles of the axial casing wall boundary layer upstream of the rotor are shown in Fig. 3. All the layers are turbulent and well developed. The artifically thickened profiles were virtually independent of flow coefficient and so only a single distribution is shown in the figure. For the naturally developing layer there was a slight thinning with decreasing flow coefficient. This is attributed to the favourable pressure gradient on the wall immediately ahead of the rotor, the strength of the gradient increasing as the flow coefficent is reduced.

3.2.2 Minimum Tip Clearance (t/c = 1.0 percent). In this discussion of the wall boundary layer on the downstream side of the rotor, selection of the more important features of the flow associated with the minimum blade tip clearance are considered now whilst further details are revealed presently when the data associated with the other gap sizes is examined.

Figures 4 and 5 show the axial velocity profiles for the natural inlet boundary layer and the artificially thickened layer, respectively. Each is shown for three flow coefficients, but there are slight differences in the values of ϕ used for each set. The tip clearances are not quite the same, but this discrepancy is within the tolerance possible on the rig and is not thought to be significant. The profiles also show the tangential blade force (multiplied by 5 for convenience of plotting) derived from the downstream measurements as $v_x v_\theta$ and nondimensionalized by the square of the blade tip speed.

The axial profile in Fig. 4 is not greatly affected by the rotor at the two larger flows. At the flow coefficient close to stall, ϕ = 0.4, the profile is less full with a marked increase in displacement thickness.

In contrast with the thicker inlet boundary layer, there is a pronounced thinning of the layer across the rotor even for the flow coefficient close to stall (Fig. 5). The downstream boundary layers are actually quite similar for both inlet layer cases, suggesting that there is a "natural" outlet condition determined primarily by the blading. This becomes rather clearer when the integral parameters are considered.

The blade force shown in Figs. 4 and 5 remains fairly constant until very close to the endwall. The loss in blade force becomes smaller as the blade loading increases, i.e., the compressor moves toward stall. This may be explained by a rise in the swirl velocity close to the wall which more than compensates for the drop in axial velocity as the flow coefficient is lowered.

The integral parameters, which are convenient to compare, are the axial displacement thickness,

$$\delta_x^* = \int_0^\delta \left(1 - \frac{v_x}{V_x}\right) dZ,$$

Table 3 Summary of boundary layer integral parameters (minimum tip clearance condition)

	Flow coefficient	Upstream		Downstream				
	ϕ	$\delta_x{}^*$	θ_x	$\delta_x{}^*$	θ_x	ν_T	$\delta_x{}^*/t$	ν_T/t
Thin inlet	0.70	6.3	4.3	5.7	3.6	3.7	3.8	2.5
boundary layer	0.55	5.6	3.8	4.8	3.2	1.4	3.2	0.9
t = 1.5 mm	0.40	5.6	3.8	9.3	6.5	0.9	6.2	0.6
Thick inlet	0.69	10.5	8.4	7.1	5.0	3.2	3.6	1.6
boundary layer	0.53	10.4	8.2	6.2	3.6	1.1	3.1	0.55
t = 2 mm	0.43	11.7	9.2	9.6	6.4	7.9	4.8	0.95

All dimensions in mm

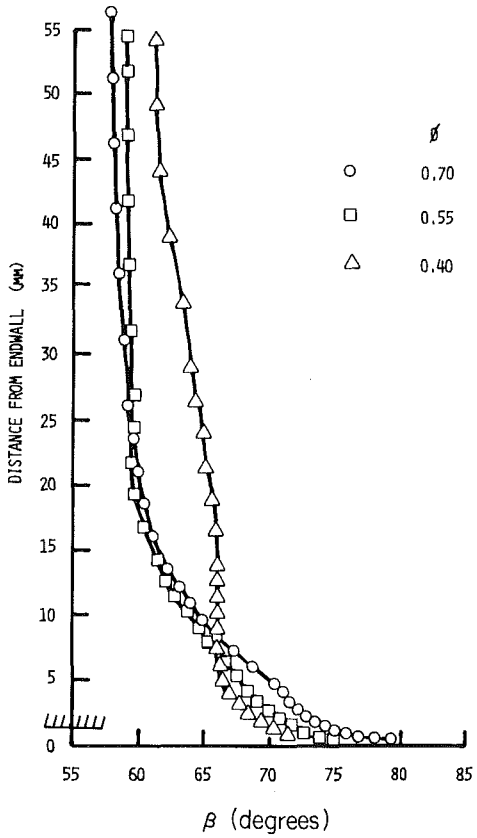

Fig. 6 Variation of rotor relative outlet flow angle with flow coefficient, t/c = 1.0 percent

the axial momentum thickness,

$$\theta_x = \int_0^{\delta} \left(1 - \frac{v_x}{V_x}\right) \frac{v_x}{V_x} dZ$$

and the tangential force deficit,

$$\nu_T = \int_0^{\delta} \left(1 - \frac{f_T}{F_T}\right) dZ$$

The boundary layer edge, δ, is somewhat arbitrarily taken where v_x reaches the maximum value V_x. The tangential force is given by $f_T = v_x v_\theta$ and at the boundary layer edge, $f_t = F_t$. All of these integral parameters are approximate since they neglect the variation in cross-sectional area with radius, but are adequate in view of the smallness of the thickness in comparison with outer wall radius.

The variations in integral parameters are summarised in Table 3. The table shows the outlet thickness $\delta_x{}^*$ and ν_T nondimensionalised with respect to tip clearance, according to ideas which are elaborated upon later.

The first thing to draw attention to is the similarity in the downstream $\delta_x{}^*$ and θ_x for the thin and thick boundary layers, suggesting strongly that there is a natural condition for the blading. For the thin boundary layer at the higher flow, the inlet and outlet layers are very similar in their axial thickness, and only close to stall is there a significant thicknening.

The tangential blade force deficit appears to be distinctly more erratic. The order of magnitude is that of the tip clearance, and the general trend is for the tangential force deficit to decrease as the blade loading is increased. No entirely satisfactory explanation for this phenomenon is yet available.

Plots of rotor relative outlet flow angle are shown in Fig. 6 and are derived from the measurements immediately downstream of the blade row with the thin inlet boundary layer. It is observed that for each flow coefficient the fluid in the boundary layer is turned in the opposite sense to that controlled by the camber of the blades, i.e., the flow is underturned. This underturning and its trend with flow coefficient, are predictable from secondary flow theory, of which a simplified analysis is given in the Appendix. The net deflection of the fluid is dependent upon the relative magnitudes of (*a*) the inlet streamwise vorticity arising from the skewing of the boundary layer flow at entry to the blade row, and (*b*) the passage vorticity produced by the turning effect of the blades. The former influence, directing the fluid towards the pressure side of the blade passage (that is underturning) is shown to dominate at all flow coefficients for this low-camber tip section.

The secondary flow analysis neglects the effect of tip clearance, though it is probable that this has a fairly major effect on the degree of underturning. In the stationary frame of reference, the downstream boundary layer flow has higher swirl than in the free-stream.

Figure 7 presents the radial distributions of two quantities of fundamental interest in compressor work, the rise in total pressure, and the work input. The former was derived from flow traverses made upstream and downstream of the blade row, allowance being made for the (small) radial shift of the streamlines, whilst the work input was calculated from Euler's equation, $\rho U \Delta v_\theta$. The results demonstrate that the rotor performs extra work within the wall bondary layer, yet the total pressure rise which is achieved is essentially that in the mainstream. The flow processes become increasingly less efficient as the wall is approached, the effect being enhanced and extended over a greater depth as the flow coefficient is reduced.

The radial distributions of static pressure downstream of the rotor are not plotted here but were found, for this minimum tip-clearance case and for each flow coefficient investigated, to be sensibly constant through the boundary layer and in close agreement with a measurement taken on the wall.

3.2.3 Increased Tip Clearance. All of the tests with increased blade clearance were carried out with the natural (thinner) inlet boundary layer.

The effects of increased tip clearance on the distribution of

Table 4 Summary of boundary layer integral parameters (4.7 mm tip clearance, thin inlet boundary layer)

Flow coefficient	Upstream		Downstream				
ϕ	$\delta_x{}^*$	θ_x	$\delta_x{}^*$	θ_x	ν_T	$\delta_x{}^*/t$	ν_T/t
0.70	5.1	3.7	8.0	4.2	2.3	1.9	0.5
0.55	5.6	4.1	11.9	5.7	5.1	2.8	1.2
0.47	7.4	5.1	16.7	9.9	10.4	3.9	2.4

All dimensions in mm

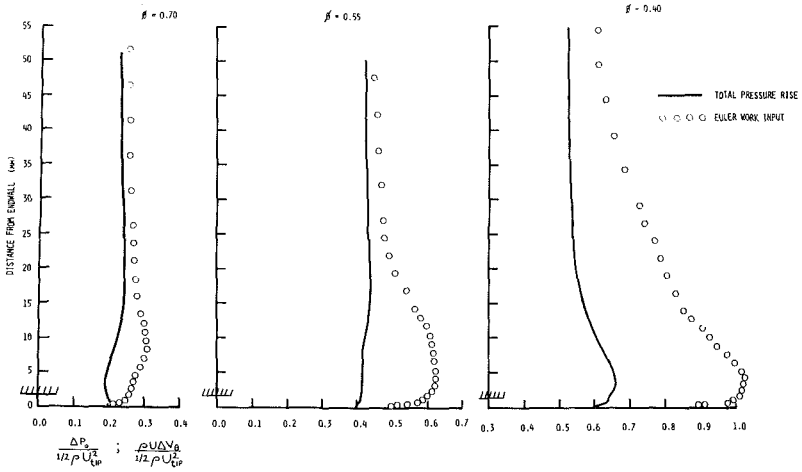

Fig. 7 Variation of total pressure rise and Euler work input with flow coefficient, t/c = 1.0 percent

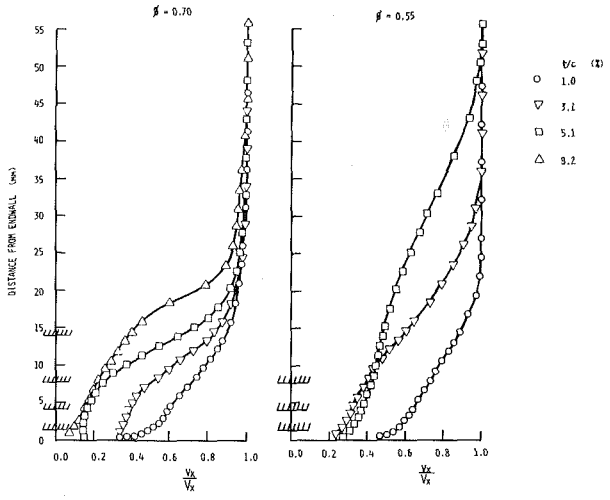

Fig. 8 Variation of axial velocity downstream of rotor with tip clearance

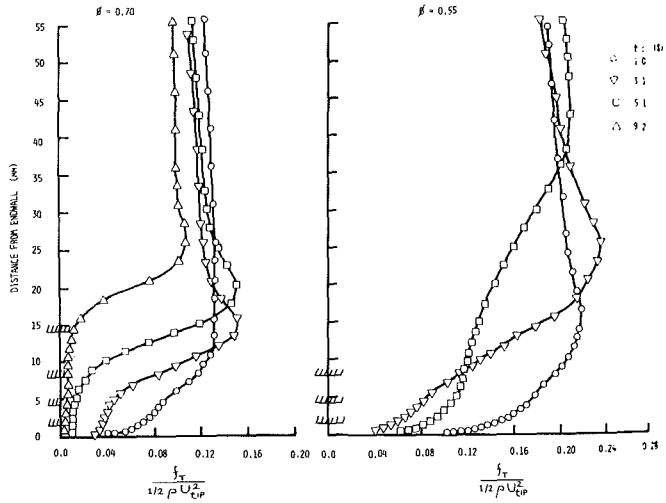

Fig. 9 Variation of rotor tangential force with tip clearance

the axial components of flow velocity just downstream of the rotor are shown in Fig. 8. For both flow coefficients the profile becomes less full as the gap size is enlarged. This depletion is far more pronounced at the larger flow coefficient and lower blade loading, indeed at the maximum clearance investigated the boundary layer *appears* to be close to separating. Although the profile distribution appears more severe at the lower loading, this is because the effect is more concentrated near the wall and the dispacement thicknesses are actually greater at the higher loading. The distributions through the endwall region of the tangential component of the blade force were deduced and are presented in Fig. 9.

The behaviour of the bounary layers is further demonstrated with reference to the integral properties of the layer shown in Table 4 and by Figs. 10–12, where the abscissa is the axial distance. At the smaller tip clearances, there is little change in the integral properties of the axial component of the boundary layer across the blade row. At flow coefficients of 0.7 and 0.55 there is a slight reduction in the momentum and displacement thickness.

For medium to high tip clearances the axial displacement thickness, and hence blockage effect, increases markedly with clearance and with blade loading. The displacement thickness remains of the same order, but usually greater than, the tip clearance.

The reductions in the displacement thickness on moving further downstream of the rotor illustrates the way in which the velocity profile tends to "fill-out" again as the flow irregularities mix out in what is nominally a zero-pressure gradient flow. The variations in momentum thickness are generally very small, as would be expected, and the increase for $t/c = 5$ percent at $\phi = 0.7$ may be erroneous. The force deficit thickness is less than the tip clearance in some cases and the explanation lies with the increase in the force on the

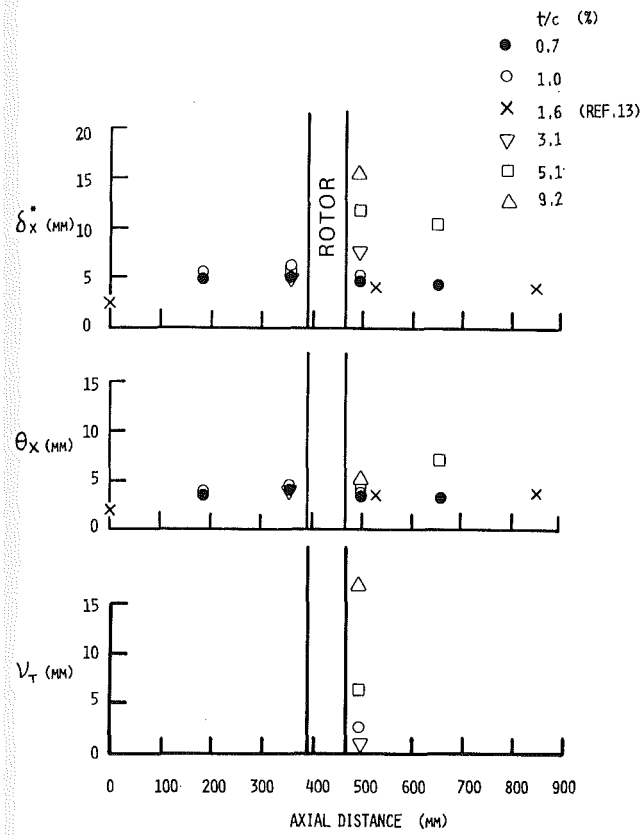

Fig. 10 Integral properties of casing boundary layer, $\phi = 0.70$

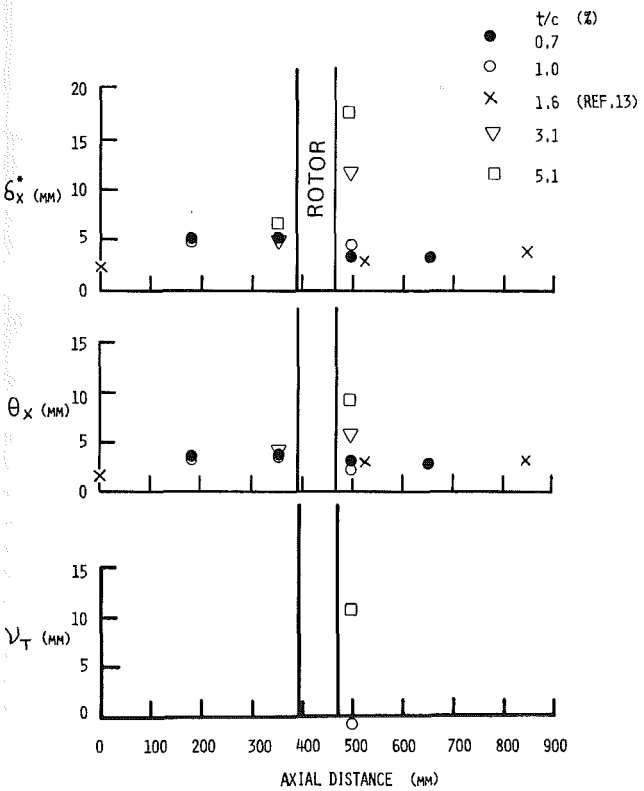

Fig. 11 Integral properties of casing boundary layer, $\phi = 0.55$

blades produced by the flow through the gap. The appearance of force "peaks" a little inward from the blade tip (see Fig. 9) is very similar to observations made in cascade experiments by Lakshminarayana and Horlock [10], who attributed the phenomena to effects of tip leakage vorticies on the blade

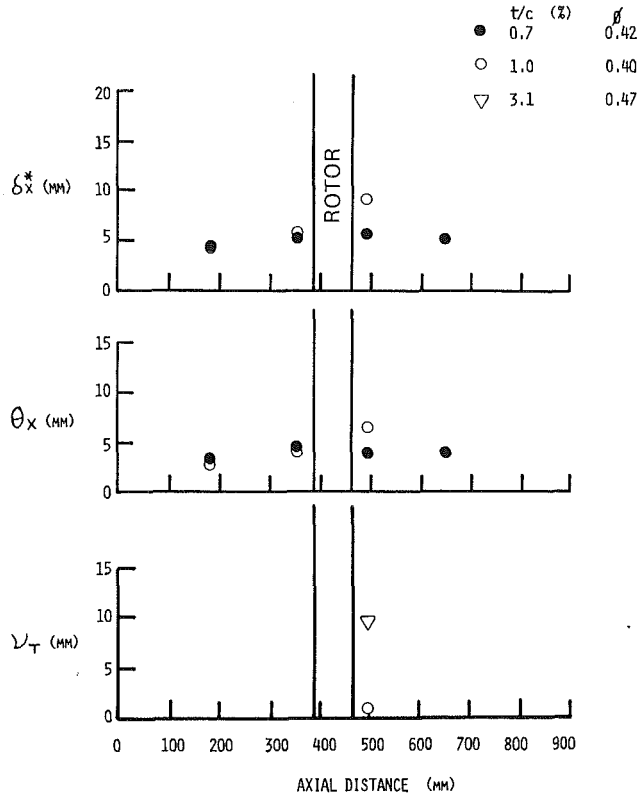

Fig. 12 Integral properties of casing boundary layer, $\phi = 0.4$

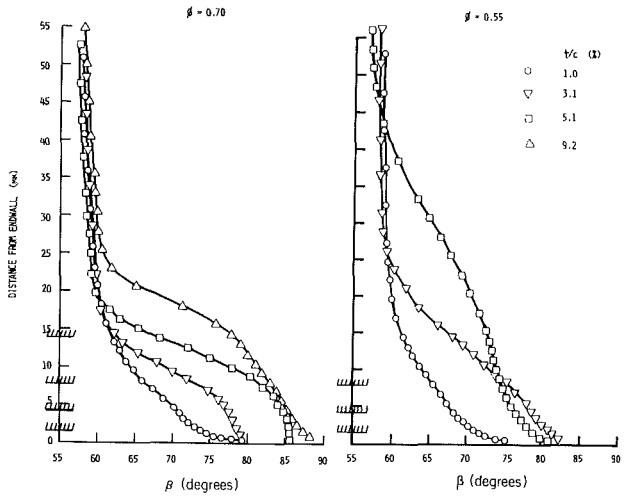

Fig. 13 Variation of rotor relative outlet flow angle with tip clearance

surface pressure distribution. For the more highly loaded case, $\phi = 0.55$, the loss in blade force seen in Fig. 9 with increasing clearance is neither as large nor as well defined as for the design flow coefficient. Generally the order of magnitude of the tangential blade force deficit is that of the tip clearance although it seems to be more often smaller than greater.

From the distributions of relative flow outlet angle, Fig. 13, it can be seen that the underturning of the flow is strongly reinforced as the tip clearance increases.

Whilst demonstrating the overall behaviour, the "self averaged" pressure probe data provides a somewhat limited appreciation of the flow in the region of the casing. The manner in which the instrument responded to the unsteady flow represents an additional uncertainty. For a number of the more important cases, the flow field was examined in greater detail by hot-wire anemometry. The results of these experiments are described in the following section.

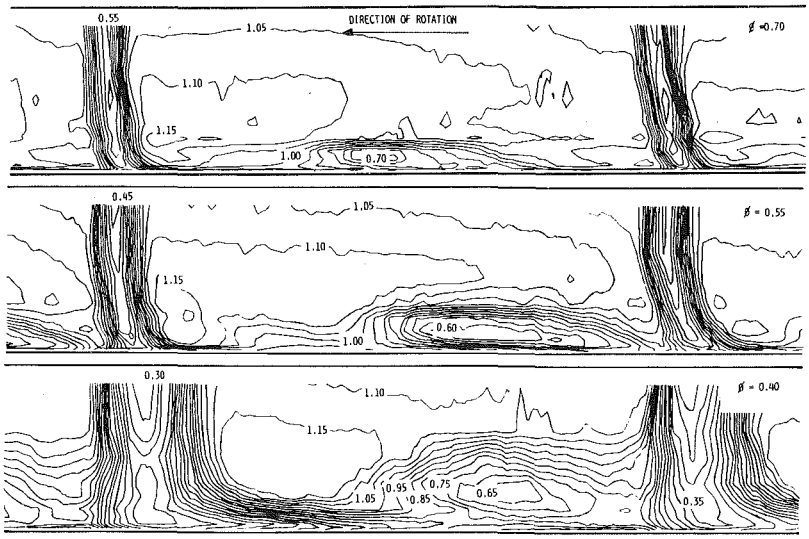

Fig 14 Contours of rotor exit relative dynamic head, t/c = 1.0 percent

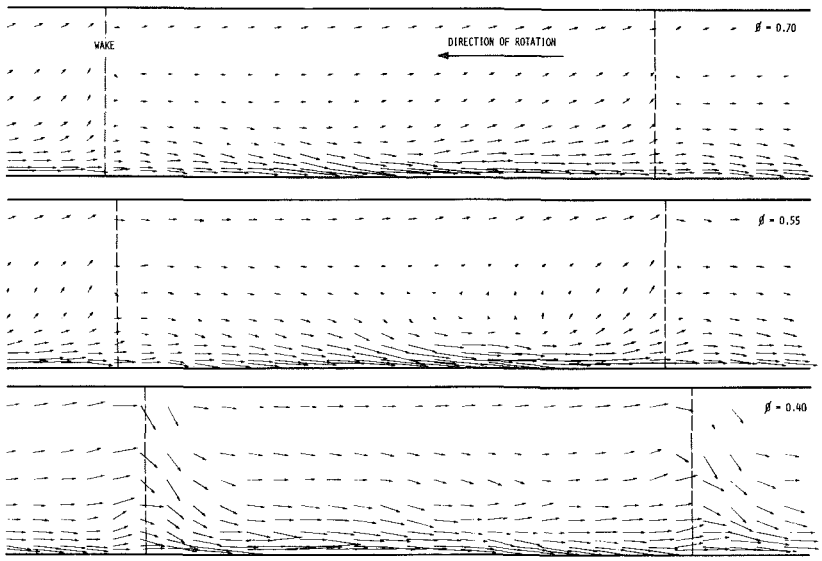

Fig. 15 Rotor exit relative secondary flow velocities, t/c = 1.0 percent

3.3 Hot-Wire Measurements. The velocity data obtained by hot-wire anemometry is presented in contour and vector form. It consists mainly of properties observed relative to the moving blades. The region of interest has been simplified to a rectangle representing the flow within a circumferential distance of just over one blade pitch and a radial height of 57 mm. The quantities shown by contours are non-dimensionalised where appropriate with respect to the corresponding circumferentially averaged value at the boundary layer edge. The secondary flows relative to the blades are illustrated by the distribution in vector form, of the velocity components which represent departures from the design potential flow field. The averaged relative velocity at the boundary layer edge was used to normalise the secondary flow components, which were computed, for all flow coefficients, relative to the design outlet flow angle distribution, Table 1.

3.3.1 Minimum Tip Clearance (t/c = 1.0 percent). In Fig. 14 contours of the rotor exit relative dynamic head (relative velocity squared) are given for three flow coefficients. The hot-wire anemometry technique provides a considerably enhanced appreciation of the overall flow structure. The data reveal an endwall flow which is highly nonuniform between the radial blade wakes. It is remarkable how the blade wakes extend right through the wall boundary layer region, and without any appreciable broadening. Close to stall at ϕ = 0.40, the wakes occupy a significant proportion of the passage area.

It is notable how the contours reveal the tendency for the fluid immmediately adjacent to the wall to be of high dynamic head, having attained the wall velocity in the relative frame of reference. It can be further seen that low energy fluid accumulates in a discrete heap or core, which thickens and moves from a midpassage position towards the pressure (leading) side of the blade passage as the flow rate is reduced from design to near stall conditions. This behaviour is in contradiction with the secondary flow calculations, which were apparently supported by the pressure probe results. These had suggested that the underturning of the flow within the wall boundary layer (and, one presumed, the convection of fluid towards the pressure side) decreased as the flow coefficient was reduced. The low dynamic head core is anyway too deep to be accounted for by flow swept up from the inlet boundary layer. The relative flow entering the blades for this design has a minimum dynamic head of $1/2\ U_{tip}{}^2$ (this corresponding to a particle on the wall with vanishing axial velocity). The relative dynamic head of the incoming flow will be higher than this by an amount depending on the flow

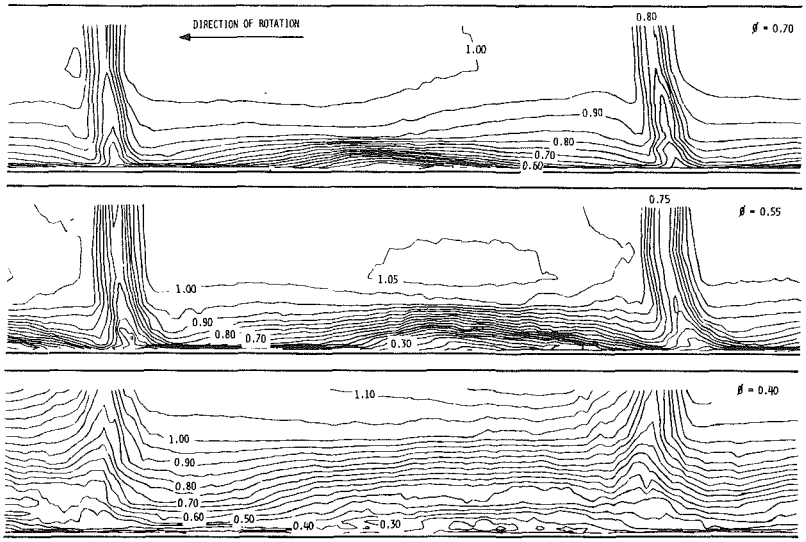

Fig. 16 Contours of rotor exit axial velocity, t/c = 1.0 percent

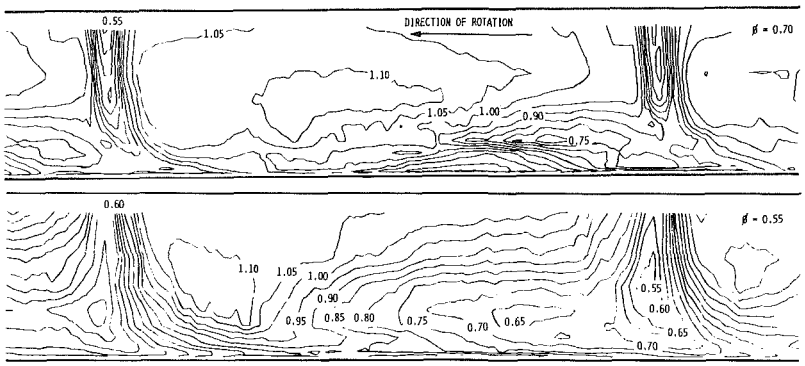

Fig. 17 Contours of rotor exit relative dynamic head, t/c = 5.1 percent

coefficient. On this basis[2] one would expect the core of the high-loss region to have dynamic heads of about 0.97 at ϕ = 0.40 and 0.80 at ϕ = 0.70. The values observed are much less than this and it seems probable that the core is the downstream evidence of the tip leakage.

The relative secondary velocities are shown vectorially in Fig. 15. The cross-passage flow directed towards the pressure side is clearly in evidence, particularly as the loading is increased, but much of this is deviation of the flow unconnected with the effects of the casing boundary layer. However, there is no evidence of large scale circulatory vortex motions which might be associated with the tendency for the endwall fluid to accumulate in cores. Here it is perhaps worth pointing out the contrast of these results with stationary cascade tests where clear evidence of vortex cores is normally found. The vorticies in stationary cascades usually originate in the stagnation point ahead of the leading edge when the lower velocity boundary layer flow is exposed to the pressure field about the blade. (This behaviour has been very clearly shown for stationary turbine cascades, for example Langston et al. [16], and was apparent in the flow visualisation tests of Hansen et al. [17]). With the moving blade the dynamic head of the flow very close to the wall is still quite high (certainly for highly staggered blades), and there is no reason to expect strong vorticies originating from a stagnation point. This is not to say that they will not exist in some weak form, but that they will not be important as they are for stationary cascades.

Large velocity components are apparent down the suction side of the blade wake for the ϕ = 0.40 condition (Fig. 15(*c*)). The thick blade boundary layers clearly provide increased opportunity for the radial transfer of fluid under the action of centrifugal force.

The axial velocity contours, seen in Fig. 16, are packed close to the wall except for the case near stall. The region of lower axial velocity, like the low dynamic head, moves from the centre of the passage to the pressure side as the flow coefficient is reduced. At the same time, the area of low velocity increases rapidly. For ϕ = 0.4, the growth is such that the blade wakes are barely distinguishable from the rest of the flow.

3.3.2 Increased Tip Clearance (t/c = *5.1 percent*). It could be reasonably inferred from the pressure probe data that the effects of rotor tip clearance on the endwall flow were more pronounced at the lower blade loading, i.e., ϕ = 0.7. However, the detailed hot-wire measurements for t/c = 5.1 percent presented in Fig. 17 firmly indicate the opposite trend.

At the design flow condition, as shown in Fig. 17(*a*), the blade wakes appear to be truncated just above the blade end, while the accumulation of low energy endwall fluid is more diffuse than before and has undergone some slight circumferential and radial displacement from its position at the smaller clearance. With ϕ = 0.55, the above trends are very much greater, indeed the flow pattern shown in Fig. 17(*b*) bears little resemblance to that for t/c = 1.0 percent (Fig. 14(*b*)). The accumulation of low dynamic head fluid on the endwall is seen to have grown in size considerably and has engulfed the blade boundary layer on the pressure side. Curiously though, no truncation of the wakes is noticeable here. It is worth noting that the value of the dynamic head is

[2] Assuming uniform flow upstream of rotor outside boundary layer

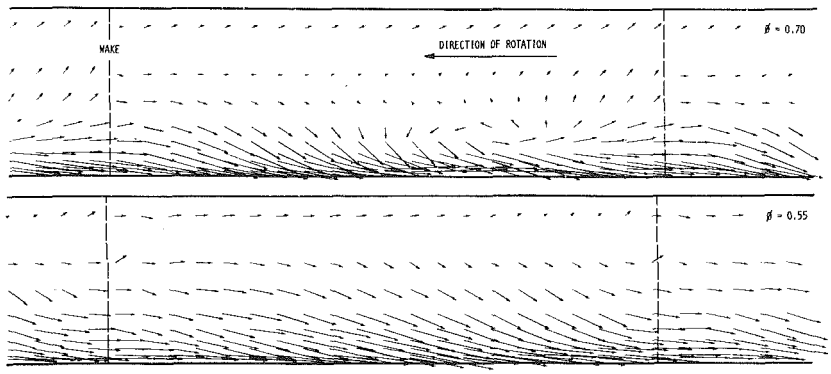

Fig. 18 Rotor exit relative secondary flow velocities, t/c = 5.1 percent

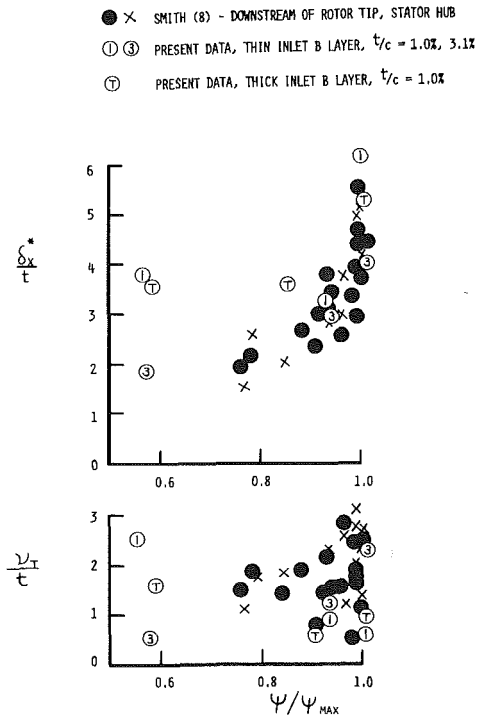

Fig. 19 Downstream displacement and tangential force deficit thickness versus pressure rise

the centre of the core is very similar to that for t/c = 1 percent even though the extent is much greater.

The secondary flow vector plots (see Fig. 18) show that the effects of increased gap size are largely confined to the clearance height for ϕ = 0.7, but at the more heavily loaded condition a much greater spanwise portion of the flow is involved. These observations are consistent with the pressure probe data. At the ϕ = 0.55 condition the vectors indicate a strong tendency for fluid to be drawn into the pressure surface/endwall corner.

The flow data obtained for the more heavily loaded conditions firmly suggests that a localised separation of boundary layer fluid, leading to the stall of the row, will be associated with blockage at the junction of the endwall and the pressure side of the passage. The suction side of the passage appearing to be washed by a relatively high energy stream. This process is evidently accentuated by increased cross-passage flow arising from larger tip-clearance gaps.

4 Discussion

Attention has been drawn repeatedly to the significance of tip clearance, both in determining the downstream deficit thicknesses and the shape of the profiles. The emphasis on tip clearance as a crucial parameter is far from new. It was given by Rains [11], who used water as his working fluid and recognized a cavitating vortex as originating with the tip clearance, and Hansen et al. [17], using smoke to show how clearance altered the endwall flow pattern. The evidence was there, and it is perhaps surprising that academic research has been so reticent to confront this. Once reason may be the great difficulty in carrying out any sort of calculation which realistically includes the fluid mechanics of a transverse jet close to the wall.

Without some analytic or numerical model there is a danger that experimental studies may fizzle out with a few statements of generalities. A paper which did not fall into this trap is that by Smith [8] who directed his attention to the repeating stage of a mutistage compressor. (A repeating stage is one in which the flow velocities entering and leaving are the same, the conditions having settled down to a type of equilibrium). The idea of the repeating stage is very important; as well as seeming to be a good physical description of the flow, it greatly simplifies our thinking. The ideas and correlations developed by Smith were shown by him to lead to predictions of pressure rise and efficiency agreeing well with measurements.

With such a body of data for multistage compressors available, it was natural to wonder whether the present data, obtained with an isolated rotor, could be compared usefully with it. Any comparison between different compressors must make assumptions about the salient geometric variables. We, for example, have used blade chord to nondimensionalise tip clearance, whereas Smith has used staggered spacing. For most designs, chord and staggered spacing vary in a way somewhere near to in-proportion. In a test on a multistage compressor[3], where the blade chord was held constant but the staggered spacing was doubled, we convinced ourselves that staggered spacing was not of particular significance. Smith has nondimensionalised displacement thickness with respect to staggered spacing and tangential force deficit thickness with respect to displacement thickness. These ratios have been plotted against the ratio pressure rise/maximum pressure rise (ψ/ψ_{max}) and lines of constant clearance nondimensionalised with staggered spacing superimposed. We have chosen to plot δ_x^*/t and ν_T/t against ψ/ψ_{max} directly. The results are shown in Fig. 19. Most of the points have been taken from Figs. 6 and 7 of reference [8]. It is very striking that the present results fit in with the multistage data very well, except perhaps for the very low values of ψ/ψ_{max}. It should be remarked that most of the tip clearances are much greater than the minimum of the present results and in the multistage the minimum seem to be in the range of about 4 percent of chord. This presentation does bring out rather clearly the overriding significance of tip clearance.

The plotting of annulus wall boundary layer thickness

[3] Unpublished Cambridge data

against ψ/ψ_{max} implicitly assumes that a correlation exists between the maximum pressure rise and the annulus boundary layer. In other words it postulates that the profile boundary layers have a secondary role in determining maximum pressure rise. But this begs the question of how the blade loading affects the boundary layer? The unravelling of this mystery is still conjectural and of a qualitative nature, but it seems that until these issues are clear, correlation procedures are castles built on sand.

One of the simplest yet most interesting considerations of annulus boundary layer development is due to Stratford [18]. Essentially, he took an axial section through the annulus so that he considered the axial projection of the blade row. He then enclosed a blade with a control volume and applied conservation of axial momentum. If F_x denotes the axial blade force per unit-cross-sectional-area at the edge of the boundary layer then, neglecting higher order terms,

$$F_x \nu_x = \rho(V_{x2}^2\,\theta_{x2} - V_{x1}^2\,\theta_{x1} + (V_{x2} - V_{x1})V_{x2}\,\delta_{x2}^*)$$

where V_{x1} and V_{x2} are the velocities at the boundary layer edge upstream and downstream of the blade row, θ_x and δ^*_x are axial momentum and displacement thicknesses and ν_x is the deficit thickness of the axial blade force.

What the application of momentum consideration has done is point out that the axial component of blade force balances the pressure difference and decelerates the flow. The part which balances the pressure difference can be substracted out and the growth in momentum thickness is proportional to the deficit in blade force. Physically this is what happens, for the axial boundary-layer flow could never surmount the pressure rise imposed if this were not almost entirely balanced by the blade force. To give an example, for $t/c = 1$ percent and $\phi = 0.55$, it can be seen from Fig. 2 that $\Delta P/1/2\rho\, U^2_m = 0.65$. This corresponds to $\Delta P = 2.3\,(1/2\rho V_x^2)$, whereas a turbulent boundary layer will separate normally (that is, without the aid of an equivalent blade force) when $\Delta P = 0.6\ 1/2\rho V_x^2$). It is a corollary of this reasoning that quite small proportional reductions in blade force close to the wall will have disproportionate effects on the boundary layer.

For many applications, including the rig on which the present measurements were made, the change in axial velocity at the boundary layer edge is very small across the blade row. In this case the equation can be simplified to

$$F_x \nu_x = \rho V_x^2(\theta_{x2} - \theta_{x1})$$

A look at the data tabulated for the naturally developing inlet bondary layer and the results shown in Figs. 10 and 11 will suggest that $\theta_{x2} \approx \theta_{x1}$, except close to stall and for large tip clearances. The axial force deficit away from stall is therefore very small, and sometimes even negative, if the clearance is not too large. This appears to be very similar to results for the tangential blade force deficit. The reason for this is not hard to find. If the shear stresses responsible for blade force are very small, which seems highly probable, the blade force is produced by the pressure distribution around the profile. When the boundary layer is thin compared with the chord it is clear that that pressure distribution will be almost unchanged until very close to the end of the blade. This was confirmed by measurements of rotor pressure distribution by Gregory-Smith [13], but not at conditions near to stall. Put another way, the length scale in the spanwise direction is so much less than the blade chord that it precludes a gradual reduction in lift. In this consideration it is inappropriate to think of overall boundary layer thickness, since most of the velocity deficit is much nearer to the wall, and displacement thickness may be a more appropriate scale. When the tip clearance is equal to or greater than the displacement thickness one may expect the force deficit to become appreciable and the momentum thickness to rise. This appears to be borne out by the results shown in Figs. 10 and 11, where for $t/c = 3$ percent (4.5 mm) the momentum thickness does rise substantially.

For the artificially thickened inlet boundary layer, the axial momentum thickness is decreased across the blade row, implying a negative force deficit or extra large axial force. It is also notable that the tangential blade force deficit was very small in this case. Very probably the blade is giving higher lift in the outer part of the boundary layer because of the increased incidence. The balance between this and the increase in thickness caused by the clearance is what establishes a "natural" thickness for the blade.

It is highly probable that the type of clearance flow vortex observed by Rains [11] and later by Lakshminarayana and Horlock [10] is producing an additional force reducing the force deficit below the value of the tip clearance. The vortex produces locally reduced pressures on the suction surface.

Although the momentum thickness on the downstream side is very similar to that at entry for the thin boundary layer at small clearance and low loading, there is a marked increase at loadings close to stall. The change in the axial velocity at the boundary layer edge across the blade row is still very small (no more than about 6 percent) and the implication is therefore that the axial blade force has diminished. The tangential blade force deficit does not, however, show a corresponding rise. The explanation appears to lie with the displacement thickness.

If the momentum thickness increase is determined by the deficit in axial blade force, no comparable relation appears to fix the displacement thickness. The hot-wire traces make it clear that the flow is distinctly nonuniform in the circumferential direction, with large blockage towards the pressure side of the passage and a comparatively thin boundary layer on the annulus wall towards the suction side. The circumferentially averaged displacement thickness greatly underestimates the amount of flow nonuniformity close to stall. The increase in the nonuniformity, reflected in the increase in displacement thickness as stall is approached, establishes the condition in which the blade force can be reduced with consequent rise in momentum thickness. Probably the most important cause of the displacement thickness increase for a rotor tip (or stator hub) is the tip-clearance flow. Not only will this increase as the blade loading rises but the direction in which it emerges, approximately normal to the blade chord, is predominantly in the upstream direction. Simple experiments with smoke emerging from a slot in the wall of a wind tunnel have confirmed Rains's [11] findings; a narrow slot is capable of producing an extensive region of affected flow similar to the regions evident in Fig. 14.

It would be misleading to give the impression that the rise in displacement thickness and momentum thickness, or force deficit thickness, are independent. All the processes are connected and the sequencing described above is heuristic in the extreme. The true process may emerge from detailed measurement between the rotor blades.

The same arguments about blade force and momentum thickness must be applicable to the endwalls of linear cascades. In this case, a stagnation point ahead of the leading edge is to be expected, since the fluid in the boundary layer has lower dynamic head, and two vorticies emerge from it. In the presence of adverse pressure gradients these vorticies provide an excellent means for blockage to increase bringing with it the reduction in blade force and establishing the well known phenomena of limited cascade pressure rise. The difference with rotor rows lies in the change of frame of reference so that flow on the endwall does not have vanishingly small dynamic head and no stagnation point and separation on the endwall ahead of the blades is required. It is probable that there is a three-dimensional region of separation in the tip region of rotors, and these have certainly

been noted in the endwall region of linear cascades. It seems that three-dimensional separations do not inevitably have the catastrophic nature normally found with two-dimensional separations. On the other hand, the conditions leading to a three-dimensional separation may be more varied and more difficult to classify or predict. A very elegant demonstration of this is given by Han and Patel [19].

While the blockage out of the rotor may be vital, the efficiency may be as important or more so. This has been referred to only obliquely because no measurement of torque was available for the rotor. Efficiency can be inferred from results such as those shown in Fig. 7, but this is not without pit-falls. The total pressure recorded by the probe right down to the wall may not be utilized by a following stator row. The flow entering the rotor had the lowest possible dynamic head (zero swirl) whilst the flow leaving has elevated swirl; the performance of a stator will determine whether this swirl is useful or is merely a step towards a rise in entropy.

Concluding Remarks

The flow around blade tips is very complicated and using measurements made upstream and downstream inevitably means that there is considerable uncertainty about the processes inside the blade passage. The experimental difficulties in making measurements inside rotor passages are very real, but the effort seems justified; some measurements made by Smith [20] show how different the flow may be to the simplified ideas emerging from tests on stationary cascades. Although skewed inlet flow is a very pronounced feature of the flow, the tip-clearance flow appears to be the most important. This is apparent from the in-passage measurements of Smith [20]. It is also evident from the effect of tip-clearance flow on overall performance (Fig. 2), and the extent to which the integral parameters (δ_x^*, and ν_T) can be correlated by it and the interpretation of the contour plots from hot-wire measurements downstream of the rotor.

It had been suspected that the results would form a different class from those measured in multistage compressors, and it was therefore rather a surprise when δ_x^* and ν_T fitted in the scattered band of results given by Smith [8]. It does seem, therefore, that ideas emerging from the detailed measurements described here should find application in multistage machines where the importance of casing boundary layers is usually much greater.

It would be satisfying if explanations could be found for the results obtained. Unfortunately, this is not so in most cases. The ideas originating with Stratford [17] are helpful, but do not explain the rise in blockage evident as the growth in displacement thickness. For blades of modest to high aspect ratio, and with boundary layers thin compared to the chord, the assumption of a small deficit in axial blade force seems appropriate without the agonizing that has sometimes incurred in the past. Close to stall, the situation is altered and this seems to be the most interesting area for further study. In principle these measurements should yield the deficits in tangential and axial blade force from which the variation in the direction of the force could be deduced. In practice, these measurements are too inaccurate to justify this.

Although there is a need for further experiments, particulary in between the blades, the great hope for clarification must lie with appropriate numerical treatment. At first sight, the rapidity with which the flow passes through the blades suggests that diffusive processes will not be very important and the model for turbulent shear stress not crucial. Nevertheless, the presence of the tip clearance flow entering the main flow at right angles probably means that turbulent mixing is crucial to determining blockage and, if the ideals described in this discussion are correct, to determining blade force and stall point as well.

Acknowledgment

The authors wish to express their indebtedness to Mr. C. Freeman of Rolls Royce Ltd. for his encouragement and his invaluable assistance in interpretting the results, and to Mr. E. Morishita of Mitsubishi Ltd. who made the measurements with the thickened inlet boundary layer.

References

1 Hawthorne, W. R., "The Applicability of Secondary Flow Analysis to the Solution of Internal Flow Problems," *Fluid Mechanics of Internal Flow*, edited by G. Sowan, Elsevier, Amsterdam, 1967.

2 Horlock, J. H., "Recent Developments in Secondary Flow," AGARD Conference Preprint No. 214, March 1977.

3 Horlock, J. H. and Lakshminarayana, B., "Secondary Flows; Theory Experiment and Application in Turbomachinery Aerodynamics," *Annual Review of Fluid Mech.*, Vol. 5, 1973, pp. 247-279.

4 Horlock, J. H. and Perkins, J. H., "Annulus Wall Boundary Layers in Turbomachines," AGARD Monograph No. 185, 1974.

5 Mellor, G. L. and Wood, G. M., "An Axial Compressor Endwall Boundary Layer Theory," *Journal of Basic Engineering*, June 1971.

6 Hirsch, C., "Endwall Boundary Layers in Axial Compressors," ASME Paper No., 76-GT-72, 1976.

7 Bario, F., Leboeuf, F., and Papaillou, K. D., "Study of Secondary Flows in Blade Cascades of Turbomachines," ASME Paper No. 81-GT/GR-4. Presented at Symposium, University of Patras, Greece, June 1981.

8 Smith, L. H., "Casing Boundary Layers in Multi-Stage Axial Flow Compressors," *Flow Research on Blading*, edited by L. S. Dzung, Elsevier, Amsterdam, 1970.

9 Hunter, I. H., "Endwall Boundary Layer Flows and Losses in Axial Turbomachines," PhD thesis, University of Cambridge, 1979.

10 Lakshminarayana, B. and Horlock, J. H., "Leakage and Secondary Flows in Compressor Cascades," ARC R & M 3483, 1965.

11 Rains, D. A., "Tip Clearance Flows in Axial Flow Compressors and Pumps," Report No. 5, Hydrodynamics and Mechanical Engineering Laboratories, California Institute of Technology, 1954.

12 Dean, R. C., "The Influence of Tip Clearance on Boundary Layer Flow in a Rectilinear Cascade," Gas Turbine Laboratory, Report 27-3, MIT, 1954.

13 Gregory-Smith, D. G., "Annulus Wall Boundary Layers in Turbomachines," PhD thesis, University of Cambridge, 1970.

14 Whitfield, C. E. Kelly, J. C., and Barry, B., "A Three-Dimensional Analysis of Rotor Wakes," *Aeronautical Quarterly*, 1972, pp. 285-300.

15 Squire, H. B. and Winter, K. G., "The Secondary Flow in a Cascade of Aerofoils in a Nonuniform Stream," *Journal of Aeronautical Sciences*, Vol. 18, April 1951.

16 Langston, L. S., Nice, M. L., and Hooper, R. M., "Three Dimensional Flow Within a Turbine Cascade Passage," ASME JOURNAL OF ENGINEERING FOR POWER, 1977, pp. 21-28.

17 Hansen, A. G., Herzig, H. Z., and Costello, G. R., "A Visualisation Study of Secondary Flows in Cascades," NACA TN 2947, 1953.

18 Stratford, B. S., "The Use of Boundary-Layer Techniques to Calculate the Blockage From the Annulus Boundary Layer in a Compressor," ASME Paper No. 67-WA/GT-7, presented at ASME Winter Annual Meeting, November 12-17, 1967.

19 Han, T. and Patel, V. C., "Flow Separation on a Spheriod at Incidence," *Journal of Fluid Mechanics*, Vol. 92, 1979, p. 643.

20 Smith, G. D. J., "Casing Treatment in Axial Compressors," Ph.D. thesis, University of Cambridge, 1980.

APPENDIX

A simple inviscid Secondary Flow Analysis is presented here in order to predict the nature of the induced secondary flow at the exit of the experimental rotor tip section and to establish its variation with flow coefficient.

From Squire and Winter [15], the streamwise vorticity produced by turning effect of blades is given by,

$$\xi_{sec} = -2\epsilon\xi_n \tag{A1}$$

where, ξ_{sec} = secondary streamwise vorticity

ϵ = deflection

ξ_n = normal vorticity = $\dfrac{dV_1}{dZ}$

More generally, $\xi_{S2} - \xi_{S1} = -2\epsilon\xi_n$ (A2)

where, ξ_{S1} = streamwise vorticity at entry

ξ_{S2} = streamwise vorticity at exit

Working in coordinates relative to the moving blades, ξ_{S1} and ξ_n are, respectively, the absolute vorticity resolved parallel to and perpendicular to the relative flow direction at the rotor inlet. Hence,

$$\xi_{S1} = \frac{dV_1}{dZ} \sin \beta_1 \tag{A3}$$

$$\xi_n = \frac{dV_1}{dZ} \cos \beta_1 \tag{A4}$$

Noting that,

$$\tan \beta_1 = \frac{U_{TIP}}{V_1} = \frac{U_m}{0.7\, V_1} = \frac{1}{0.7\, \phi} \tag{A5}$$

and

$$\epsilon = \beta_2 - \beta_1 \tag{A6}$$

Assuming the inlet normal vorticity is of the form (for a power law boundary layer),

$$\frac{dV_1}{dZ} = \frac{V_1}{m\delta} \left(\frac{\delta}{Z}\right)^{\frac{m-1}{m}} \tag{A7}$$

substitution into (2) gives,

$$\xi_{S2} = -2(\beta_2 - \beta_1) \frac{dV_1}{dZ} \cos \beta_1 + \frac{dV_1}{dZ} \sin \beta_1 \tag{A8}$$

Normalizing with respect to dV_1/dZ, which is taken as unity at the design flow coefficient of 0.7, the following results are obtained using measured angles β_1 and β_2

ϕ	β_1	β_2	$\beta_2 - \beta_1$	$\frac{\xi_{S1}}{dV_1/dZ}$	$\frac{\xi_{sec}}{dV_1/dZ}$	$\frac{\xi_{S2}}{dV_1/dZ}$
0.70	63.9°	57°	6.9°	0.898	−0.106	0.792
0.55	68.9°	60°	8.9°	0.733	−0.088	0.645
0.40	74.4°	62°	12.4°	0.550	−0.067	0.483

The streamwise vorticity at the blade exit is therefore in the same sense as that produced at the inlet, leading to flow underturning, and the magnitude of this diminishes with reducing flow coefficient.

Working in coordinates relative to the moving blades, ξ_{S1} and ξ_n are, respectively, the absolute vorticity resolved parallel to and perpendicular to the relative flow direction at the rotor inlet. Hence,

$$\xi_{S1} = \frac{dV_1}{dZ} \sin \beta_1 \tag{A3}$$

$$\xi_n = \frac{dV_1}{dZ} \cos \beta_1 \tag{A4}$$

Noting that,

$$\tan \beta_1 = \frac{U_{TIP}}{V_1} = \frac{U_m}{0.7\, V_1} = \frac{1}{0.7\, \phi} \tag{A5}$$

and

$$\epsilon = \beta_2 - \beta_1 \tag{A6}$$

Assuming the inlet normal vorticity is of the form (for a power law boundary layer),

$$\frac{dV_1}{dZ} = \frac{V_1}{m\delta} \left(\frac{\delta}{Z}\right)^{\frac{m-1}{m}} \tag{A7}$$

substitution into (2) gives,

$$\xi_{S2} = -2(\beta_2 - \beta_1) \frac{dV_1}{dZ} \cos \beta_1 + \frac{dV_1}{dZ} \sin \beta_1 \tag{A8}$$

Normalizing with respect to dV_1/dZ, which is taken as unity at the design flow coefficient of 0.7, the following results are obtained using measured angles β_1 and β_2

ϕ	β_1	β_2	$\beta_2 - \beta_1$	$\frac{\xi_{S1}}{dV_1/dZ}$	$\frac{\xi_{sec}}{dV_1/dZ}$	$\frac{\xi_{S2}}{dV_1/dZ}$
0.70	63.9°	57°	6.9°	0.898	−0.106	0.792
0.55	68.9°	60°	8.9°	0.733	−0.088	0.645
0.40	74.4°	62°	12.4°	0.550	−0.067	0.483

The streamwise vorticity at the blade exit is therefore in the same sense as that produced at the inlet, leading to flow underturning, and the magnitude of this diminishes with reducing flow coefficient.

DISCUSSION

L. H. Smith, Jr.[4]

The authors are to be congratulated for obtaining measurements in such detail and then examining them so critically to deduce their physical significance. It is expected that this set of data will be of much use in the future by those endeavoring to create analytic models of the rotor tip flow process.

The question has again been raised concerning the most appropriate linear dimension with which to normalize boundary layer thicknesses. As the authors point out, this discusser, in reference [8], chose to use staggered spacing, and that choice may certainly be challenged. Obviously it is the wrong choice when the solidity is extremely high or low or if the stagger is extremely high. It was chosen because endwall boundary layer secondary flow analyses done in a Trefftz plane, whose width is more or less like the staggered spacing, indicate that the penetration away from the endwall of

[4] General Electric Company, Aircraft Engine Group, Cincinnati, Ohio 45215

Casing Boundary Layers

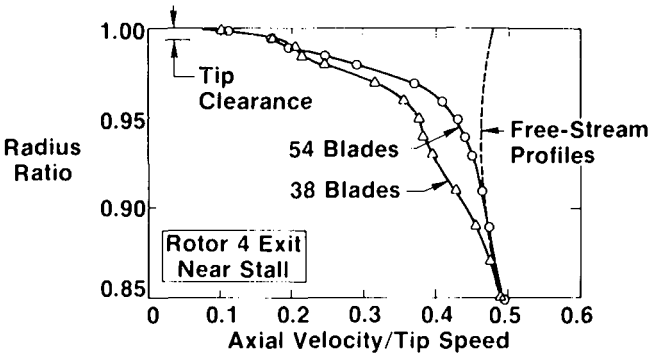

Fig. 20

significant secondary velocities depends more on that width than on the size or shape of the inlet boundary layer. Betz (reference [21]) makes a similar choice for his analysis of tip clearance flows.

Another reason that this discusser has preferred to normalize with staggered spacing is that it seems to be justified by most of the data of which he is aware. An example is offered here. Configuration 5 of [8] contained 54 rotor blades and 53 stator vanes in each of its four stages. This same blading was also tested as configuration 7 with reduced solidity (38 rotor blades and 37 stator vanes). Figure 20 shows axial velocity distributions in the outer half of the annulus at rotor 4 exit with the compressor operating near stall in each case. It can be seen that the larger blade spacing (38 blades) has yielded a thicker boundary layer; in both of these cases the displacement thickness is 22 percent of the rotor tip staggered spacing. Similar results were obtained at rotor 3 exit. At stator 3 exit this pattern was not followed at near-stall throttle settings; the calculated displacement thickness was larger with the smaller spacing. It was observed, however, that the flow in the stator was badly separated near the casing in both cases, with local regions of back flow noted, so that the flow angles and the circumferential averaging method used are suspect. For throttle settings further from stall, the normalization with staggered spacing again appeared to be good (see Fig. 6(*a*) of [8]).

The authors mention some unpublished Cambridge data that do not support the use of staggered spacing as a normalizing length. Perhaps they could elaborate on the particulars of that configuration.

Additional References

21 Betz, A., "Introduction to the Theory of Flow Machines," translated by D. G. Randall, Pergamon Press, 1966, Sections 40 and 41, pp. 138—141.

Author's Closure

The authors would like to thank Dr. Smith for his kind remarks. They would like to emphasize that nothing in their work suggests that staggered spacing is an incorrect or

inappropriate dimension with which to nondimensionalize the boundary layer thicknesses. The decision to use tip-clearance to nondimensionalize data was taken to emphasize the authors' point of view that this is probably the most important variable in compressor geometry. This is not really at odds with the correlation proposed by Dr. Smith, in which a strong effect of tip-clearance is also included. To some extent the decision to emphasize tip-clearance does also reflect the feeling that the classical approach to secondary flow analysis, which does naturally lead to stagged spacing, is not very helpful in considering the annulus boundary layer flow around rotor tips.

Dr. Smith asks for information about the four-stage compressor referred to in the paper. This was the Intermediate ϕ^* build machine tested by Day and described by Day and Cumpsty [22]. The configuration tested by Day had 72 blades in rotor and stator rows; in the present tests the same build was used (solidity 1.14), as was a build with 36 blades in each row (solidity 0.57). The boundary layer thicknesses were greater for the lower solidity build, but the differences were significantly smaller than those implied by the correlation of reference [8] based on staggered spacing.

Reference

22 Day, I. J., and Cumpsty, N. A., "The Measurement and Interpretation of Flow Within Rotating Stall Cells in an Axial Compressor," *Journal of Mechanical Engineering Sciences*, Vol. 20, No. 2, 1978.

Secondary Flows and Losses in Axial Flow Turbines

D. G. Gregory-Smith
Lecturer, Department of Mechanical Engineering,
University of Durham,
Durham, England

A simple approach to the estimation of angle variation and losses produced by the secondary flows near the hub and casing of a turbine is presented. The angle variation is predicted by 'classical' secondary flow theory, and the loss by estimating three components of the loss and adding them together. The method is in an early stage of development, but initial results obtained by comparing with data from turbine blade rows are encouraging.

1 Introduction

The presence of secondary flows in turbines due to the hub and casing wall boundary layers has two main effects. The first is to produce a variation of angle with radius at exit from a blade row. The second is to produce an increase in loss, termed secondary loss. Recently some attention has been given to estimating these effects by the use of three-dimensional viscous flow calculation methods applied to the blade channel. Such methods require considerable computer time and a lot of data preparation. In the early stages of designing turbines, such data may not be available, and so the aim of this work was to produce a simple method for estimating secondary flow angles and losses with reasonable accuracy. The method should be suitable to form a sub-routine of the larger design method.

The secondary flow angles are calculated using 'classical' secondary flow theory. The losses are estimated by identifying three sources of loss which are calculated independently and added together. Results from this simple approach are encouraging, and some are presented here. There is scope for development and improvement of the method so that it should be applicable to a wide range of turbine blade row designs.

2 Secondary Flow Angles

A computer program has been written using 'classical' secondary flow theory originally produced by Hawthorne [1] and developed by many other workers. The streamwise component of vorticity at exit from the blade row is calculated from the inlet streamwise and normal components of vorticity, using the formula of Came and Marsh [2]. The secondary velocities in the blade exit plane are calculated by the numerical solutions of the equation for the secondary flow stream function, Ψ, produced by Glynn and Marsh [3]. In polar coordinates the equation is:

$$\frac{1}{\cos \alpha_2}\frac{1}{r^2}\frac{\partial^2 \Psi}{\partial \Theta} + \frac{\mathrm{Cos}\,\alpha_2}{r}\frac{\partial \Psi}{\partial r} + \mathrm{Cos}\,\alpha_2 \frac{\partial^2 \Psi}{\partial r^2} = \zeta + u\frac{\mathrm{Cos}\,\alpha_2}{r}\frac{d}{dr}(r \tan \alpha_2)$$

where α_2 is the exit flow angle (measured from the axial direction), ζ the streamwise vorticity component, u is the local axial velocity, and ψ is defined by

$$v - u \tan \alpha_2 = \frac{\partial \Psi}{\partial z}, \quad w = \frac{\partial \Psi}{\partial y}$$

where v and w are the velocities in the Θ and r directions.

It should be noted that this equation differs from that produced by Hawthorne and Novak [4] and used by various other workers. In the continuity equation, Hawthorne and Novak assume that at blade exit the velocity derivative with respect to the axial direction is zero, whereas Glynn and Marsh make the better assumption that the derivative with respect to the downstream direction (which is included at an angle α_2 to the axial) is zero. It can also be seen that secondary velocities will arise even when there is no streamwise vorticity if the design is not free-vortex (i.e. $d/dr\,(r \tan \alpha_2) \neq 0$).

The application of the program is to the flow relative to the blade row, so that if the row is rotating, transformations between the stationary and rotating frames of reference has to be made. The program produces the variation of exit angle from the secondary velocities, taking about three seconds for a typical blade row on an IBM 360.

3 Secondary Losses

3.1 Physical Nature of Secondary Flows. The flow pattern near the end of a blade row is very complex, and a number of flow visualisation studies have helped to give an understanding of the physics of the flow, see for example Marchal and Sieverding [5], and Langston, Nice, and Hooper [6]. The approaching boundary layer on the end wall rolls up into a horse-shoe vortex around the leading edge of a blade, with one leg curling around onto the suction surface of the blade and the other leg crossing the passage to meet the suction surface of the adjacent blade (see Fig. 1). The position of this pressure side leg of the vortex and where it meets the adjacent blade depends on the blade geometry, but it usually moves a little away from the end wall up the suction surface of the adjacent blade as the trailing edge is approached. Because it crosses the passage, the leg rolls up most of the inlet boundary layer which is thus discharged from the blade row in the form of a loss core on the suction surface a small distance from the end wall. The passage vortex, which is predicted by the secondary flow theory of section 2, rotates in the same direction as this leg of the horse-shoe vortex, and the two

Contributed by the Gas Turbine Division and presented at the International Gas Turbine Conference, London, England, April 18–22, 1982, of The American Society of Mechanical Engineers. Manuscript received at ASME Headquarters November 23, 1981. Paper No. 82-GT-19.

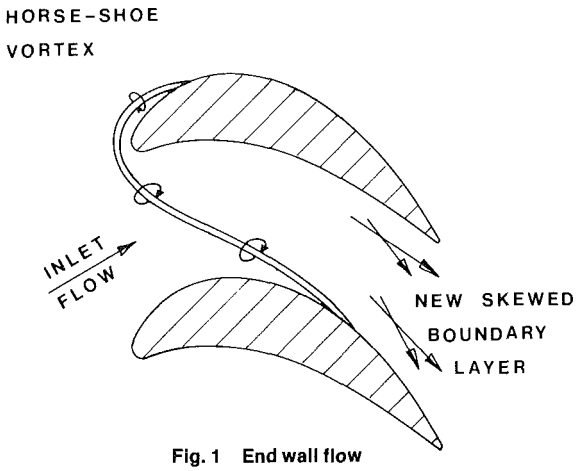

Fig. 1 End wall flow

merge together. A new highly skewed boundary layer forms on the end wall downstream of the pressure side leg of the horse-shoe vortex.

The above simplified picture refers essentially to cascade flows. In real turbines there are a number of additional effects. The radial pressure gradients will cause migration of low energy fluid along the suction surface of the blade. In a nozzle or stationary row this migration will be inwards, tending to spread out the loss core on the outer wall. Conversely in a rotating row the migration will be outwards. There will also be effects due to blade tip clearance, discontinuous end walls, curved end walls, and the interference of one blade row on a following row.

3.2 Prediction of Losses. Present prediction methods of secondary losses are largely empirical, such as that of Dunham [7]. It is not very reliable nor does it give the spanwise distribution of loss. A three-dimensional viscous flow calculation in the blade channel might be the ultimate prediction method, but even if possible, would require a lot of data preparation and computer resources. So, as a first stage, a method was sought which would be based on the features of cascade secondary flows, making use of classical secondary flow angle prediction. Some of the additional effects in real turbines may be added as a later development.

The secondary losses were divided into three components:

(a) the upstream boundary layer which is shed downstream as a loss core;

(b) the new skewed boundary layer on the end wall; and

(c) an extra secondary loss due to the vortex and its interaction with the blade and end wall boundary layers. The total or gross secondary loss is the summation of (a), (b), and (c).

3.3 The Loss Core. The loss core was assumed to be formed from the upstream boundary layer and to have the same mass flow and kinetic energy deficit as the upstream boundary layer. The shape of the loss core was assumed to be triangular, this shape being chosen for ease of analysis (see Fig. 2). The minimum stagnation pressure was made equal to the upstream static pressure, and its position specified arbitrarily; a distance from the end wall of the order of the upstream boundary layer thickness seemed reasonable.

A power law velocity variation was assumed from the point of minimum pressure to the outer velocity contour. Thus the position of the outer contour and the power law exponent could be determined from the upstream boundary layer thickness and its power law exponent. The resulting loss distribution could then be mass averaged across the pitch to get a spanwise loss variation

The resulting loss variation is a reasonable representation of a loss core, although there is a sharp peak due to the assumed triangular shape. Figure 3 shows the calculated loss core compared with the cascade results of Marchal and

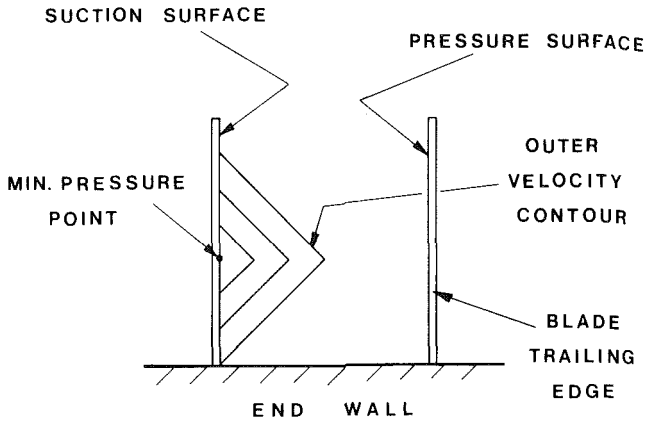

Fig. 2 Triangular loss core

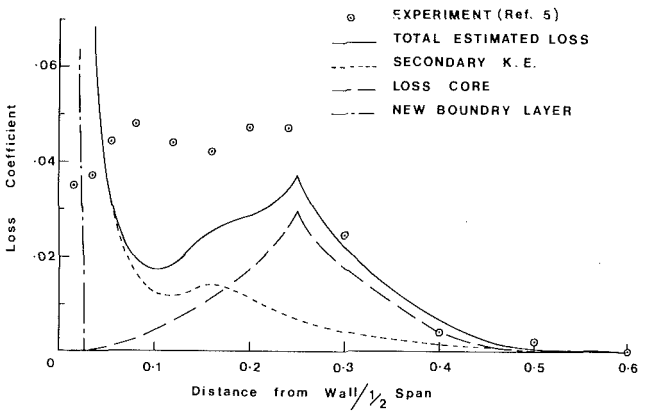

Fig. 3 Cascade secondary loss, reference [5]

Sieverding [5]. The loss coefficient is defined as the loss in stagnation pressure divided by the upstream dynamic pressure.

3.4 The New Boundary Layer. The new boundary layer was calculated along the mid-passage line using a two-dimensional boundary layer calculation method [8] (neglecting, at this stage, the effect of the skew). The starting conditions for the calculation are theoretically uncertain. However, because of the rapid acceleration up to the throat, the starting conditions have very little effect and the boundary layer may be assumed to be turbulent and to start at the throat. In comparison with experimental results, the position of the traverse plane has to be known, since the boundary layer continues to grow downstream of the blade row. Figure 3 shows the loss distribution due to the new boundary layer, which is concentrated near the end wall.

3.5 The Extra Secondary Loss. The Dunham [7] loss correlation stems from the original Ainley and Mathieson [9] correlation of secondary drag coefficient being proportional to the square of the lift coefficient. It is possible to show that the secondary kinetic energy is proportional to the square of the lift coefficient, and so it seemed reasonable to seek a relationship between the extra secondary loss and the secondary kinetic energy as predicted by classical secondary flow theory. As a first attempt, the relationship was assumed to be one of equality. The kinetic energy of the secondary flow was obtained from the computer program mentioned in section 2. Figure 3 shows the secondary kinetic energy distribution, which has a hump some distance from the end wall and then rises rapidly towards the wall.

3.6 The Summation of the Components. Figure 3 also shows the summation of the three components, and this may be compared with the experimental results, which were at the trailing edge plane. Reasonable agreement is obtained, except that the loss is predicted too high close to the wall and too low

Tabel 1 Total secondary loss coefficient for cascade, reference [5]

Observed value	0.011
Estimated values	
Loss core	0.0050
New boundary layer	0.0046
Secondary kinetic energy	0.0035
Total	0.0131
Observed loss / Estimated loss	0.84

Table 2 Total secondary loss coefficient for N.G.V. – thin inlet boundary layer

	Hub	Casing	Combined
Observed value	0.157	0.089	0.120
Estimated values			
Loss core	0.029	0.036	0.033
New boundary layer	0.057	0.031	0.043
Secondary kinetic energy	0.031	0.034	0.033
Total	0.117	0.101	0.108
Observed loss / Estimated loss	1.34	0.88	1.11

Table 3 Total secondary loss coefficient for N.G.V. – thick inlet boundary layer

	Hub	Casing	Combined
Observed value	0.163	0.149	0.155
Estimated values			
Loss core	0.058	0.070	0.065
New boundary layer	0.063	0.039	0.049
Secondary kinetic energy	0.027	0.034	0.031
Total	0.148	0.143	0.145
Observed loss / Estimated loss	1.10	1.04	1.07

further away. The total mass averaged loss coefficient may be obtained from the spanwise distribution, and these are presented in Table 1. The total observed loss is 16 percent less than the predicted loss, probably an acceptable error for design purposes.

4 Results for Nozzle Guide Vanes

The flows in the nozzle guide vanes of a single stage research turbine have been investigated by Hunter [10]. The method has been applied to this row and the results are presented here.

4.1 Losses. Table 2 shows the estimation of the mass averaged total pressure loss coefficient based on the upstream velocity. Some uncertainty exists about the observed value of secondary loss, since this is obtained from the total loss less an estimated profile loss. The profile loss was taken as the loss at some distance from the end wall where the loss became nearly constant with radius. The higher value on the hub may be due partly to the higher turning and also to migration radially inwards of the blade boundary layers. The hub region extends from the hub to the mean radius, and the casing region from the mean radius to the casing.

Three components of the estimated loss are shown, together with the total estimated and the ratio of the observed to estimated value. Table 3 shows the same quantities but for a thicker inlet boundary layer than that for Table 2. The distribution of loss with radius is shown in Figs. 4 and 5 for the two inlet boundary layers.

It can be seen from the tables and figures that the hub has a larger secondary loss than the casing. The loss core due to the upstream boundary layer is well defined there, where as it is much more diffuse on the casing. This may well be due to the radial inflow of low energy fluid in the blade boundary layers, and this effect is not included in the calculation method.

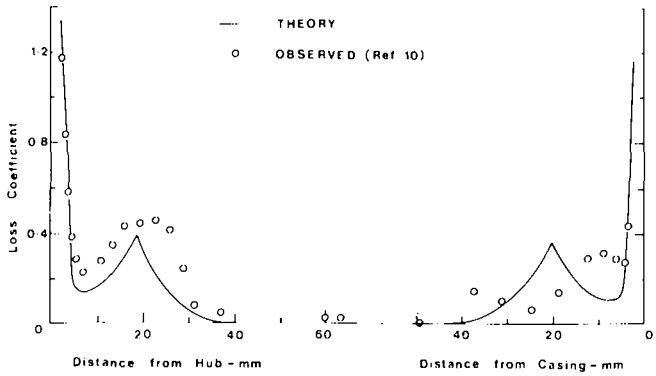

Fig. 4 N.G.V. loss—thin boundary layer

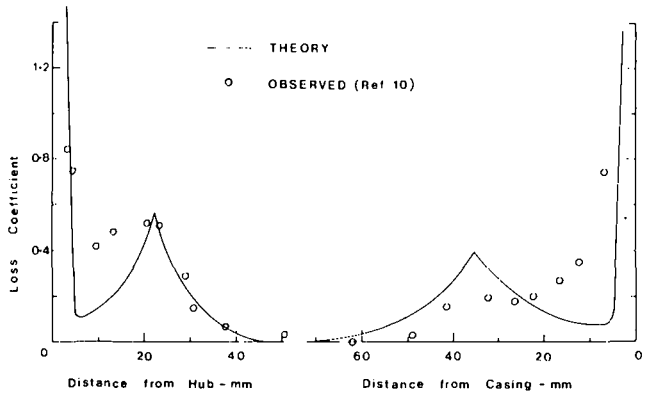

Fig. 5 N.G.V. loss—thick boundary layer

The estimated mass averaged loss coefficients are in reasonable agreement with the observed values, but the distribution of loss is less satisfactorily estimated. Apart from the loss core from the upstream boundary layers, the estimated loss is concentrated too close to the wall, due mainly to the new boundary layer being very thin. In reality some of this new boundary layer will be swept up on to the suction surface, and, thus, distribute the loss further away from the end wall.

Comparing the thinner and thicker inlet boundary layer results in Tables 2 and 3, it can be seen that most of the increased loss in the latter arises from the upstream boundary layer. The kinetic energy loss is slightly less, since the thicker boundary layer induces less intense secondary flows, and the new boundary layer loss shows a slight increase due to a slightly higher primary flow angle (see later) and the reduction in mass flow due to the thicker boundary layer at inlet.

4.2 Exit Angle. Figures 6 and 7 show the variation in exit flow angle. The assumed primary flow angle is shown, and, of course, this should be the same for both boundary layers. For the thin boundary layer case, the assumed primary angle was made 0.9 degree less than the blade exit angle to get the agreement with the measured flow angle at midspan. Hunter [10] has suggested the difference between the measured midspan values may be due to instrumentation zero error.

The thin boundary layer case shows quite good agreement between predicted and observed flow angles, the main difference being that the underturning is predicted a little too close to the wall. This may be due to the lack in the theory of any radial movement of the Bernoulli surfaces (surfaces of constant total pressure). In fact, the rolling up of the upstream boundary layer into a loss core indicates considerable distortion of the Bernoulli surfaces, and it may be considered surprising the agreement is as good as it is shown here.

For the thick boundary layer two calculated curves are shown. One is for the power law profile fitted to the inlet boundary layer profile, the other is for the actual profile input

numerically into the program. The power law profile shows poor agreement because it gives too much vorticity in the outer part of the boundary layer. The actual profile gives a result in quite good agreement at the hub. It underestimates the maximum underturning at the casing by 1.5 deg, but predicts its position accurately.

5 Future Development

The method of prediction of secondary flow angles and losses has been applied to other cascade data and results were obtained similar to those shown here. The variation of secondary flow angle is predicted quite well, which may be surprising in view of the complex nature of the flow. The total loss coefficient is estimated quite well, although the distribution usually shows too much loss predicted near the wall.

A useful development would be to trace the distortion of the Bernoulli surfaces through the blade row, which task has been attempted by Glynn [11]. This would modify the angle prediction results slightly, and would allow a less arbitrary positioning of the centre of the loss core. It would also help to distribute some of the new boundary layer loss further away from the end wall. There is also scope for developments of the three components of loss. For instance, the shape of the loss core could be varied, the effect of skew on the new boundary layer could be included and some other relationship between the extra secondary loss and the secondary velocities could be tried.

The real turbine effects such as those mentioned earlier, would probably be best included by empirical modification to the results. However, the difficulty in obtaining the accurate experimental data and the wide variety of conditions encountered might cast doubt on any such modifications at the present time.

6 Conclusions

The prediction of secondary flow angles by classical secondary flow theory has been shown to give reasonable results over a range of blade rows. Classical secondary flow theory assumes no spanwise flow and, thus, no Bernoulli surface distortion, but this limitation seems to cause little error for the nozzle guide vanes presented here. With the inclusion of Bernoulli surface distortion in the future, the predictions of angle variation should be improved, especially for high turning rotor blades.

The three loss component model has been derived from a physical description of the flow, and the estimation of total loss by summation of the three components if fairly satisfactory. However, the distribution of the loss is less satisfactory and needs improvement. It is hoped that development of the method will yield reliable estimates of the effects of secondary losses in turbines, while being much quicker and easier to apply than viscous three-dimensional flow calculation methods.

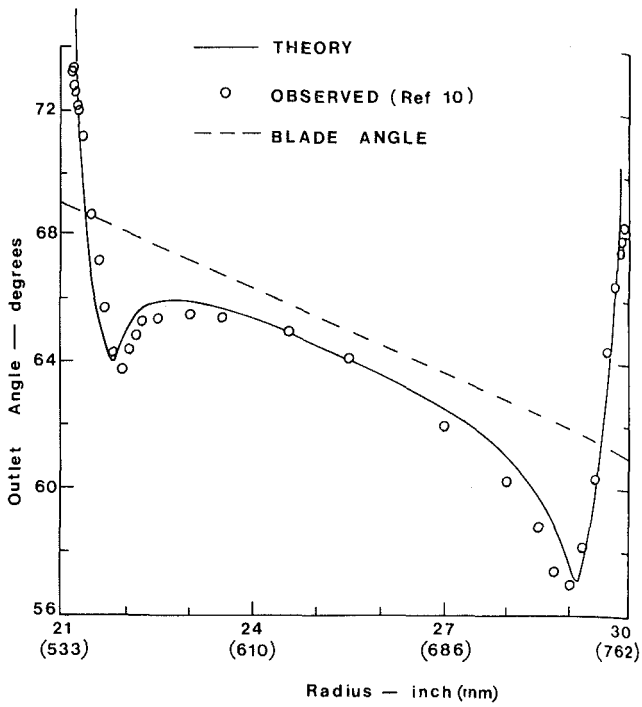

Fig. 6 N.G.V. angles—thin boundary layer

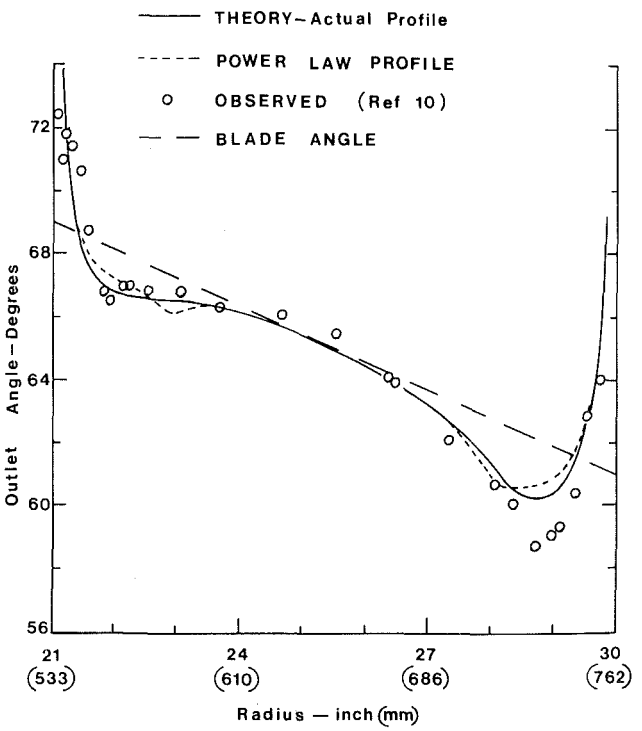

Fig. 7 N.G.V. angles—thick boundary layer

References

1 Hawthorne, W. R., "Some Formulae for the Calculation of Secondary Flows in Cascades," Aero. Research Council Report, 17.519, 1955.

2 Came, P. M., and Marsh, H., "Secondary Flow in Cascades: Two Simple Derivations for the Components of Vorticity," *J. Mech. Eng. Sci.*, Vol. 16, 1974, pp. 391-401.

3 Glynn, D., and Marsh, H., "Secondary Flows in Annular Cascades," *International Journal of Heat and Fluid Flow*, Vol. 2, No. 1, Mar. 1980, pp. 29-33.

4 Hawthorne, W. R., and Novak, R. A., "The Aerodynamics of Turbomachinery," *Annual Review of Fluid Mechanics*, Vol. 1, 1969, pp. 341-366.

5 Marchal, P., and Sieverding, C. H., "Secondary Flows Within Turbomachinery Bladings, *Secondary Flows in Turbomachines*, AGARD-CP-214, Paper 11, 1977.

6 Langston, L. S., Nice, M. L., and Hooper, R. M., "Three-Dimensional Flow Within a Turbine Cascade Passage," ASME JOURNAL OF ENGINEERING FOR POWER, Vol. 99, No. 1, Jan. 1977, pp. 21-28.

7 Dunham, J., "A Review of Cascade Data on Secondary Losses in Turbines," *J. Mech. Eng. Sc.*, Vol. 12, No. 1, 1970, pp. 48-59.

8 Duncan, W. J., Thom, A. S., and Young, A. D., *Mechanics of Fluids*, Arnold, London, 1960, pp. 335-338.

9 Ainley, D. G., and Mathieson, G. C. R., "A Method of Performance Estimation of Axial Flow Turbines," Aero. Research Council, R & M 2416, 1946.

10 Hunter, I. H., "Endwall Boundary Layer Flows and Losses in Axial Turbomachines," Ph.D. thesis, University of Cambridge, 1979.

11 Glynn, D., "Secondary Flow Calculation Including the Effects of Vorticity Convection and Bernoulli Surface Rotation," unpublished work at *University of Durham*.

Design and Development of a 12:1 Pressure Ratio Compressor for the Ruston 6-MW Gas Turbine

F. Carchedi
Principal Design Engineer.

G. R. Wood
Chief Design Engineer.

Ruston Gas Turbines, Ltd,
Lincoln, England

The paper describes the design and development of a 15 stage axial flow compressor for a 6-MW industrial gas turbine. Detailed aspects of the aerodynamic design are presented together with rig test data for the complete characteristic including stage data. Predictions of spanwise flow distributions are compared with measured values for the front stages of the compressor. Variable stagger stator blading is used to control the position of the low-speed surge line and the effects of the stagger changes are discussed.

Introduction

Over the last two decades considerations of fuel consumption and material costs have produced a trend of steadily increasing cycle pressure ratios and turbine inlet temperatures, in both the aero and industrial sector of the gas turbine industry. Calculations for a simple, open-cycle, 6-MW gas turbine, [1] showed that if an overall turbine thermal efficiency of 30 percent is to be achieved, a cycle pressure ratio of 12:1 at 1000°C maximum firing temperature would be required. Having selected the power at 6 MW the mass flow required is 27.3 kg/s, and in order to achieve the target thermal efficiency, the individual component efficiencies must be maintaned as high as possible; in this case a compressor polytropic efficiency of .89 must be achieved.

Feasibility studies for a suitable compressor covered a range of concepts including multistage axial, both transonic and subsonic, all-centrifugal and combined axial-centrifugal designs. At this size of engine an all-centrifugal compressor designed to the state-of-the-art could not achieve the required efficiency, while a combined axial-centrifugal in a single spool would need a considerable amount of development to achieve good matching and adequate surge margin. For all the configurations considered, twin spool designs were ruled out because of the increased mechanical complexity of this arrangement. The investigation was therefore reduced to the transonic and subsonic-all axial compressor.

It would be expected that a slightly higher efficiency would be achieved by the subsonic compressor over the transonic design, but when the complete gas generator is considered, calculations shows the performance of the two designs to be comparable. The higher rotational speed of the transonic compressor allows the use of a more efficient low hub/tip ratio turbine thus compensating for the lower compressor efficiency. The overriding factors affecting the choice are then narrowed down to development costs and time-scale.

Contributed by the Gas Turbine Division of THE AMERICAN SOCIETY OF MECHANICAL ENGINEERS and presented at the 27th International Gas Turbine Conference and Exhibit, London, England, April 18–22, 1982. Manuscript received at ASME Headquarters November 20, 1981. Paper No. 82-GT-20.

The requirement for a pressure ratio of 12:1 indicated that the compressor would require some form of variable geometry to ensure an acceptable sure margin for start and load acceptance conditions. For this design variable, stagger stator blading was judged to offer the most control.

In the assessment of the subsonic compressor it was shown that a design could be based on the existing 12 stage TB compressor described in [2]. The hub/tip ratio of the front stage on the TB compressor being relatively high at 0.642 would allow for the addition of two zero stages at the front. Also the required mass flow of 27.3 kg/s could be achieved without scaling of the compressor at a combined pressure ratio of 10.2:1. The required pressure ratio of 12:1 may then be achieved by the addition of a rear stage making 15 in all. Overall this reduces the hub/tip ratio of the front stage to 0.52 and increases it at the rear to 0.9; both these being acceptable.

The study on a transonic compressor indicated that the 12:1 pressure ratio could be achieved in nine stages by a highly loaded design. This compressor, although having a number of advantages, would require extensive development to ensure its performance and integrity and in view of the time-scale for the new engine the subsonic route was chosen.

Design of the Compressor

Existing TB Design. The compressor is a twelve stage axial machine with inlet and outlet guide vanes. The blading is a 50 percent reaction design using C4 aerofoils on a circular arc camber and giving equal temperature rise per stage. Moderate stage loadings are adopted and as a result a high blading efficiency is achieved. The annulus is of a constant outside diameter for the first five stages and constant inner diameter for the remainder. This effectively gives good control of the major aerodynamic parameters such as hub/tip ratios, loading, and Mach numbers and at the same time providing for economical manufacturing. The vortex distribution of the compressor is based on the "constant α_2" concept (i.e. constant stator inlet angle) and the first rotor tip Mach number is 0.75.

To reduce manufacturing costs there are four sets of rotor blades and four sets of stator blades with stages 1, 4, 7, and 10 being the masters for each set. The correct blade height for each stage is obtained by cropping the blade tips. The method of grouping and number of blades in a group have been carefully selected to minimise aerodynamic mismatch and manufacturing costs.

The rotor blades employ dovetail roots which are located between adjacent disks, with the whole disk pack held together by a central through-bolt. Stator blades are also retained by dovetail roots in grooves machined in the stator casing which is split on the horizontal centre line.

Matching of the New Front Stages. With knowledge of the TB compressor design and performance a matching point was selected. The basis for choosing the match point was to allow for sufficient stall margin on the early stages and for the match point to be at maximum efficiency.

By iteration, with an assumed polytropic efficiency of 0.89 for the two new stages, the required mass flow is achieved at a combined temperature rise of 42.2°C. This then provides a pressure ratio of 1.504 for the new stages and the new compressor speed becomes 11085 rpm. The temperature rise of 42.2°C is to be equally split between the two stages.

The next important parameter to be determined is the annulus shape to accommodate the new stages. Here a compromise has to be reached between mechanical and aerodynamic requirements. With the use of journal anti-whirlbearing, the space available at the rotor hub is limited while at the outside casing the relative Mach number onto the first rotor is the controlling parameter, due to the decision to extend the C4 blading to the new stages. The result of the above is a slightly increased outside diameter at the inlet to the compressor with hub/tip ratio of 0.52. Detailed design of the hub line will be covered in the following section.

Use of Throughflow Analysis. In previous work carried out by the authors' company extensive use has been made of the Turbomachinery Throughflow Analysis Program [5]. "Throughflow" is the result of a continuing development program into turbomachinery analysis techniques.

The program uses a finite difference technique to compute the flow conditions (i.e., velocity components, density, pressure, enthalpy, and entropy) throughout the axisymmetric part of the machine. As the calculation proceeds, the development of the annulus wall boundary layers are computed and allowance for their effects on blockage, blade force, and secondary flow losses are introduced. Each cascade is described by blade sections at eight radii; the pressure loss and flow deflection for each section are computed with due allowances for the effects of incidence, inlet Mach number, and Reynolds number.

Comparison between the measured and predicted characteristics for the TB compressor, Fig. 1, confirms the validity of the throughflow program. The program has also been tested on the TA 1750 and TA 2500 compressors [3] and has given excellent correlation. On this strength the design of the fifteen stage compressor could be tackled with great confidence using this analysis method.

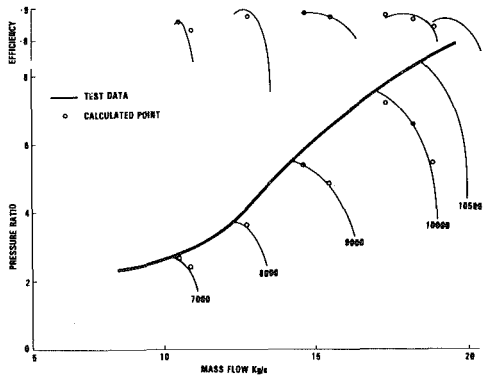

Fig. 1 TB compressor characteristic

Choice of Vortex Distribution. There are various vortex distributions, such as constant reaction, exponential, constant α_2, free vortex, etc., which have been adopted and proved to be equally successful in compressor design. The final choice is influenced by a number of factors such as ease of manufacture, calculation complexity, and, not least, by the individual designer's preference. In choosing the vortex for the new stages, the existing design philosophy of the TB compressor must be considered; it would be undesirable to have an abrupt change at the interface which may lead to velocity and temperature profiles being distorted at speeds other than design. As stated previously the TB adopts the "constant α_2" vortex with the subsequent assumption of a constant axial velocity along the span. This dictates that the flow onto the first TB rotor (from now on termed rotor 3) must be as uniform as possible and, therefore, the second new stage must be close to a "constant α_2" design. The first stage may in principle be a stage of this type, but because of the low hub/tip ratio and the need to limit the rotor tip Mach number, a design controlling the flow parameters in the radial direction is required.

In the representative meridional plane the flow equation, which results from averaging local conditions across the blade pitch, may be written in the form.

$$\frac{1}{2}\frac{\partial Vm}{\partial m} = \frac{\partial H}{\partial r} - T\frac{\partial s}{\partial r} - F\theta\tan\beta$$

$$-\frac{1}{2}\frac{1}{r^2}\frac{\partial (rV\theta)^2}{\partial r} - \frac{Vm^2}{rm}\cos\lambda + Vm\sin\lambda\frac{\partial Vm}{\partial m} \qquad (1)$$

By considering some of the terms individually, their influence on the flow may be assessed:

(*i*) $\partial H/\partial r$—Many designs of compressors, including the TB, have fixed $\partial H/\partial r$ at zero, but it is reasonable to assume that a compressor will accept an enthalpy gradient rather than a severe velocity gradient. For the type of design under consideration $\partial Vm^2/\partial r$ is always negative at the rotor outlet; therefore, $\partial H/\partial r$ must be positive to compensate for this (i.e., increasing work along the span).

(*ii*) $T\,\partial s/\partial r$—In a good design this is usually small and has to be minimized whichever philosophy is employed.

(*iii*) $F\theta\tan\beta$—This term is the magnitude of the blade force component acting along the span when dihedral angle β

Nomenclature

F = blade force
H = enthalpy
M = distance in meridional plane
r = radius
s = entropy
V = velocity
U = blade speed
α_2 = stator inlet angle
β = angle of inclination of stream surface to the radial line
η_p = polytropic efficiency
λ = angle of streamline relative to centreline
ϕ = flow coefficient, Va/U
ψ = pressure coefficient $2\Delta H\eta_p/U^2$

Subscripts

a = axial direction
θ = tangential direction
m = meridional plane

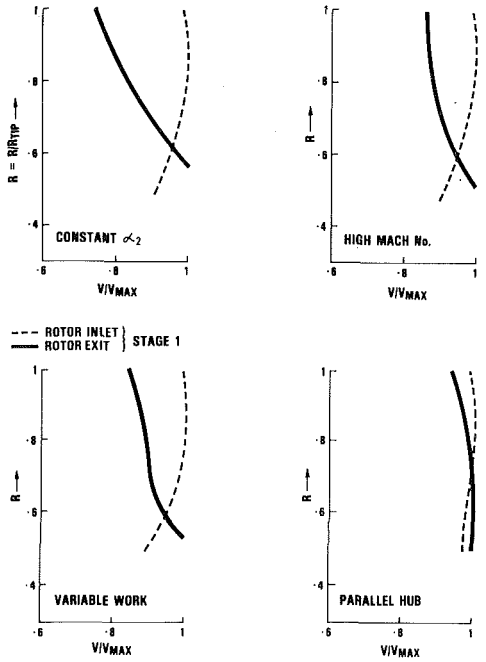

Fig. 2 Axial velocity gradients

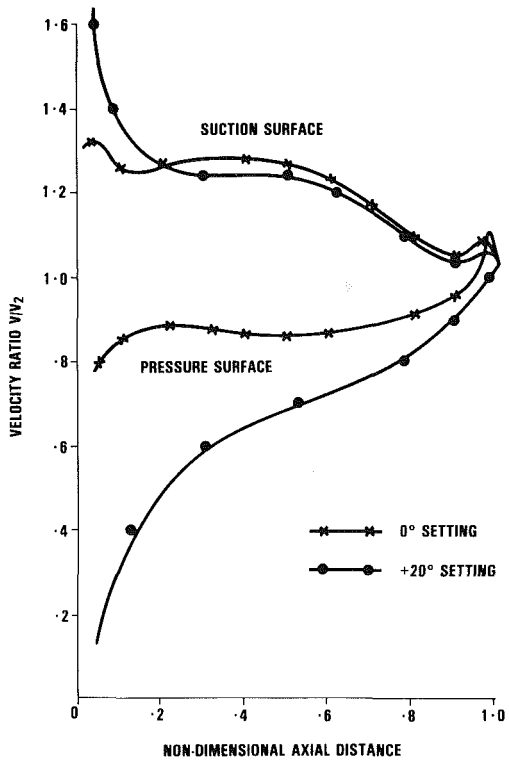

Fig. 3 Inlet guide vane velocity distributions mid-section

exists. If the blade force, $F\theta$, is large giving the blade some dihedral can have a pronounced effect on the flow distribution in the blade row.

(*iv*) $\partial(rV\theta)^2/\partial r$—This represents the contribution of the tangential velocity distribution to the flow variation and can be described arbitrarily.

(*v*) Terms containing λ—These which represent the effect of the curvature of the streamlines on the flow distribution are not always within the designers control but can influence the flow significantly.

By considering the preceding parameters several design options were tested using "throughflow.":

1 "Constant α_2" design as the TB compressor
2 High Mach number design
3 "Constant α_2" including dihedral
4 Varying radial work distribution
5 Forced vortex based on the "constant α_2" with parallel first rotor hub

In designs using the above vortex distributions all the normal constraints such as diffusion factors, Mach numbers, stress and vibrations have to be considered as an integral part of the design.

Constant α_2 Design. Examination of the flow using this design showed a large variation in axial velocity leaving the first stage and the migration of flow towards the root has lead to a high Mach number at the stator hub. The distortion is carried through to the existing twelve stages and their performance reduced. Figure 2 shows the axial velocity distribution across the first stage rotor.

High Mach Number Design. In an attempt to control the flow, a design between "constant α_2" stator outlet angle and free vortex was tested on the first stage, with a transitional second stage. This design as shown on Fig. 2 improved the flow out of the first stage rotor but the high Mach numbers were not acceptable for the C4 profiles.

Constant α_2, Including Dihedral. To assess the influence of dihedral a modified "constant α_2" design was selected and dihedral angles of up to −30 deg on the IGV, +20 deg on the first stator and +10 deg on the second stator were examined. Dihedral did show to have considerable effect but as the front stators and IGV's are to be of variable stagger the amount of dihedral which could be tolerated is small and therefore rendered this design unacceptable.

Varying the Work Distribution. If equation 1 is written in a finite difference form and applied between root and tip sections of the blade the following expression can be obtained.

$$\frac{1}{2}(Vm_1^2 - Vm_2^2) = (H_1 - H_2) - \frac{V\theta^2}{r}(r_1 - r_2)$$

$$-\frac{1}{2}(V\theta_1^2 - V\theta_2^2) + R(r_1 - r_2)$$

where R represents the residuals in the equation and are the curvature terms; $\partial s/\partial r$ and $F\theta\tan\beta$ have been assumed to be zero. The value of R may be determined from previous results.

This analysis, in the attempt to maintain $\partial Vm/\partial r = 0$, results in a temperature rise of 18.72°C at the root increasing to 23.29°C at the tip of the first rotor. Figure 2 shows the improvement in the axial velocity profiles as a result of the variable work distribution.

Forced Vortex. The aim of the design employing a parallel first stage rotor hub was to use the curvature effects and controlled diffusion to manipulate the flow. The effect of the parallel hub was to reduce the curvature effects at rotor outlet to 1/5 of the magnitude of those in designs employing a flared inner wall. The basis of the design is still "constant α_2," but with modifications to the hub and tip sections to account for radial equilibrium and the parallel rotor; the vortex may now be termed "forced." Figure 2 shows the velocity profiles achieved which can be seen to be superior to all previous designs.

The annulus shape for the following blade rows is then dictated by the requirement to match the first stage rotor to the existing third stage.

The second stage design is then based on the "constant α_2"

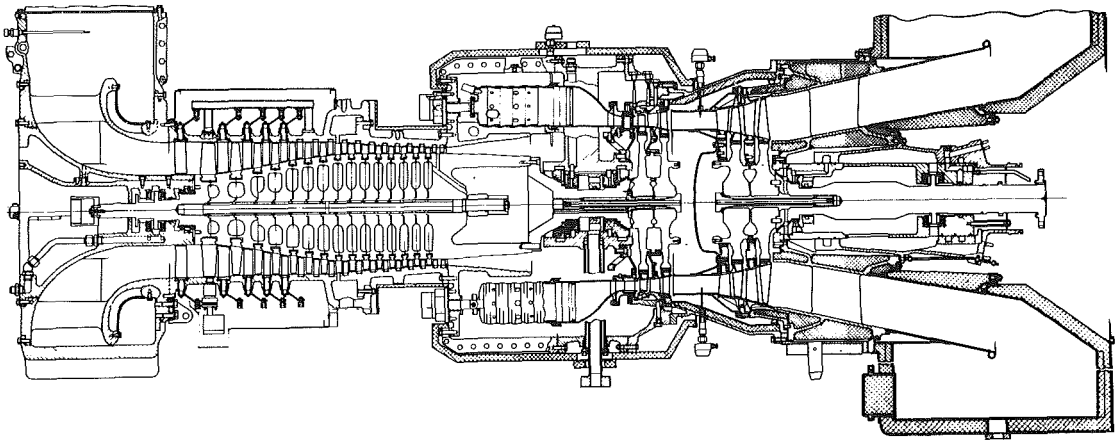

Fig. 4 Tornado cross section showing compressor gas path

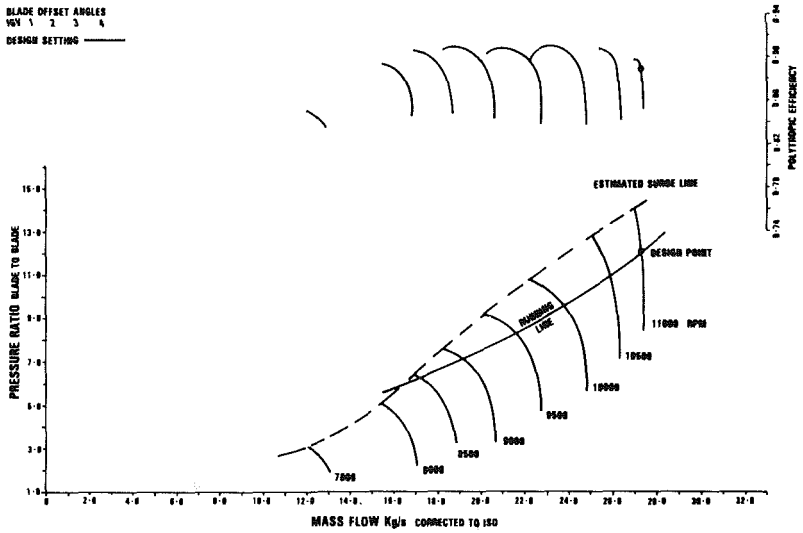

Fig. 5 Throughflow predicted characteristic

concept but with modifications to allow for radial equilibrium.

After due consideration the parallel rotor design was chosen for the new stages. The reasons are as follows:

(*i*) The flow conditions onto the existing compressor were more uniform than those achieved in any other design, thus maintaining the spanwise incidence onto the third rotor under full control.

(*ii*) The design philosophy of the new stage matched that of the existing compressor and therefore off-design and at variable stagger the blading would behave similarly.

(*iii*) All the aero-thermodynamic and mechanical constraints on the new stages were achieved.

Inlet Guide Vane Design. In parallel with the new stages the Inlet Guide Vane (IGV) to provide the required whirl was designed. Previous designs within the authors' company have adopted compressor profiles on circular arc cambers. On this compressor the opportunity was taken to design a "turbine" type of cascade. This would ensure convergence along all radial sections and give improved control over deviation. Also the vanes would be required to operate over a large range of stagger and hence the incidence acceptance must be high. The vanes were designed and tested using blade to blade methods, the results of one section are shown in Fig. 3.

Last Stage Design. The design of the additional rear stage was carried out for the same match point as the front stages. With the high hub/tip ratio to be found at the rear of the compressor, the changes in blade angles radially and from one stage to the next are small so that the new stage could be manufactured from the existing TB twelfth stage, the annulus height being adjusted to compensate for the change in density across the stage. Use of the existing stage allows the TB exit guide vane to be used in the new design.

The gas path of the fifteenth stage compressor is shown in Fig. 4, and the blading parameters are shown in the following table

First stage leading parameters:		
Inlet hub/tip ratio	=	.52
Inlet axial Mach number	=	.65
Design rotor tip speed	=	289 m/s
Rotor hub solidity	=	1.29
Rotor tip solidity	=	0.69
Rotor aspect ratio	=	2.156
Fifteenth stage leading parameters:		
Inlet hub/tip ratio	=	.90
Stage exit axial Mach number	=	.36
Rotor hub solidity	=	1.125
Rotor tip solidity	=	.98
Rotor aspect ratio	=	2.156

Performance Calculations of the Fifteenth Stage Compressor. The results of the "throughflow" analysis of the

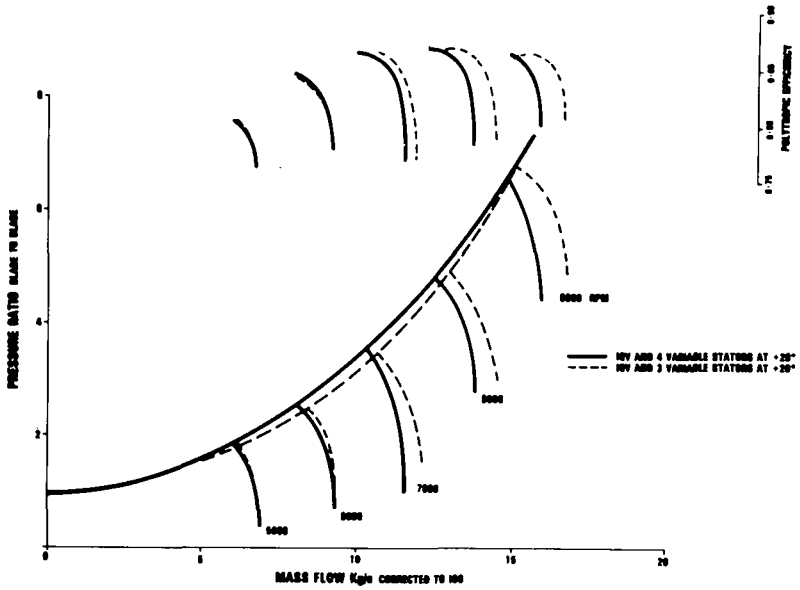

Fig. 6 Effect of number of variables

design are presented in Fig. 5 in the form of a compressor characteristic. Examination of the results shows that the mass flow of 27.3 kg/s and pressure ratio of 12:1 are achieved with the required efficiency.

In order to assess the amount of variability which will be required to effectively control the low speed surge line some estimate must be made of the stable operating range of the compressor.

The surge line of the compressor was estimated by inspection of the individual computed state characteristics. As expected, the choice of a pressure ratio of 12:1 on a single spool gives rise to low speed surge problems as indicated by the proximity of the running line to the surge line at low speed with blades at the design point setting.

Effect of Variable Stagger Blading and Bleed. For sensitivity of the compressor to the number of variable stages, it was tested by comparing the results of the IGV and three or four stages at various stagger settings. Figure 6 shows the computed effect of the stators and IGV's all at +20 deg (i.e., in a closed position). To ensure that adequate surge margin is achieved, four stators and IGV's are made variable on the compressor.

Along with variable stagger blading, interstage bleed has a significant effect on the surge line and when considering the matching of the compressor to the compressor turbine, also on the position of the running line. As a test compressor was to be built to check the design point performance and to optimise the variable stagger blading positions, a facility for interstage bleed was designed enabling between 15 and 20 percent of the mass flow to be bled off over the eighth stage.

Mechanical Design of Compressor. The mechanical design of the compressor is as described in [1] and therefore will not be covered here in great detail. Figure 7 shows the two additional rotor blades.

A feature of the first rotor is its large chord which is primarily dictated by the need to avoid flutter. The low aspect ratio is also beneficial to flow stability and in addition makes the blading less susceptible to damage and fouling.

With the addition of the front stages and existing blading now operate in a higher density field and at 10 percent higher speed. Stress and vibration calculations showed that all the blading and disks still meet the requirement of infinite life. A typical stress plot for the eighth stage disk is shown in Fig. 8.

The variable stators and inlet guide vanes are located in the

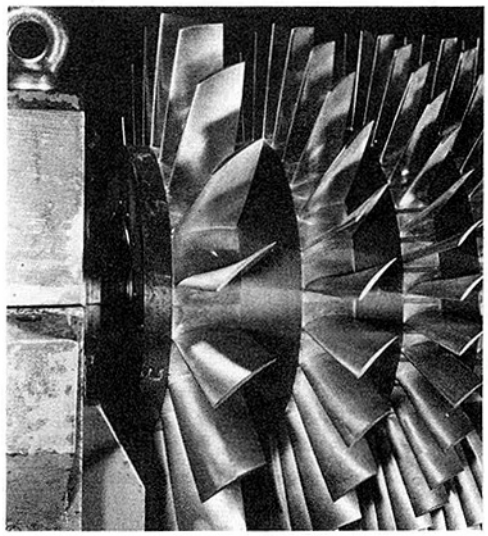

Fig. 7 Rotor front stages

low pressure casing and each blade is "ganged" together by levers attached to unison rings, which in turn are operated simultaneously via push rods connected to a torque shaft.

A feature worthy of note is that to minimise endwall losses the variable blading platforms are contoured to match the gas path while at the inner diameter the tips, which are unshrouded, are double ground; once at the design setting and once at the low speed setting. This ensures minimum tip clearance over a wide operating range.

Compressor Test and Performance

Test Program. As outlined in [1], the compressor was investigated in two phases. The first phase was accomplished by testing of the two zero stages on the front of a TB compressor in a modified TB 5000 gas turbine. The second phase was the testing of the complete compressor on a test rig over the full characteristic. As most of the results to be presented are from the full compressor rig, it will suffice to state that phase 1 tests confirmed the matching and design performance of the zero stages to the existing compressor, and thus gave confidence to the 6-MW engine design program at an early stage.

The compressor rig is illustrated in Fig. 9 and full details regarding the rig construction, instrumentation, and datalogging are presented in [4]. Two Ruston TB 5000's driving through a common gearbox and torquemeter power the compressor rig over the full speed range. Above 90 percent speed it becomes necessary to operate at reduced pressure levels in the intake. The pressure ratio of the compressor is controlled by two throttle valves downstream of the compressor.

Wall static tappings provide the stage characteristics, while total head rakes in the inlet and exit plane are used in the overall compressor assessment; temperature measurements, by the use of resistance thermometers, are carried out at the inlet and outlet planes of the compressor. Overall compressor performance measured with the above instrumentation is continually monitored and compared with the torquemeter result. Mass flow measurement is achieved by the use of an orifice plate.

In addition to the above instrumentation, total head probes and thermocouples are fitted spanwise along the first five stators, referred to as leading edge instrumentation (for further details see [4]).

Associated with the rig is a sophisticated computer-based data acquisition and processing system. This allows for immediate access to the results in engineering units. On the spot assessment of individual stage and full compressor performance may be made, which is critical when dealing with variable stagger blading.

From the outset of the compressor design it was envisaged that the variable stagger blading position would be modulated with compressor speed. The aim was to allow the engine to start and idle with the blading in the closed position while at the high speed it would be in the open position. In the intermediate range a modulation of angle versus speed was to be used. This therefore allowed the main testing to be split into three main parts:

(*i*) High-speed investigation to ensure design point performance and surge margin

(*ii*) Low-speed investigation to determine optimum

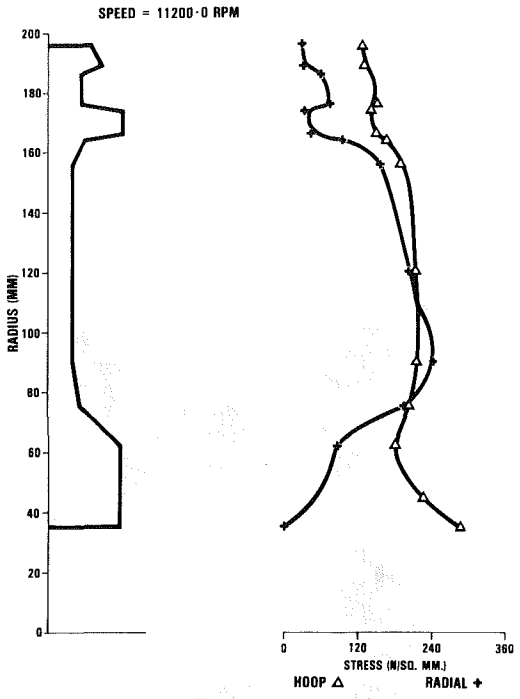

Fig. 8 Compressor disk 8 stress distribution

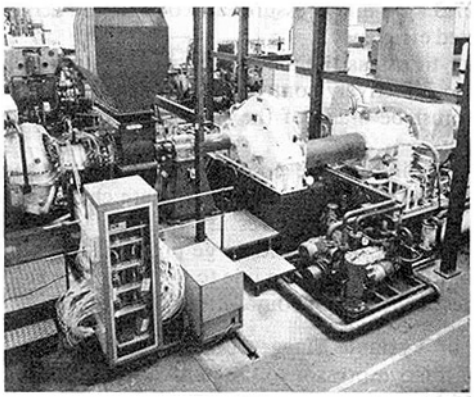

Fig. 9 Compressor test rig

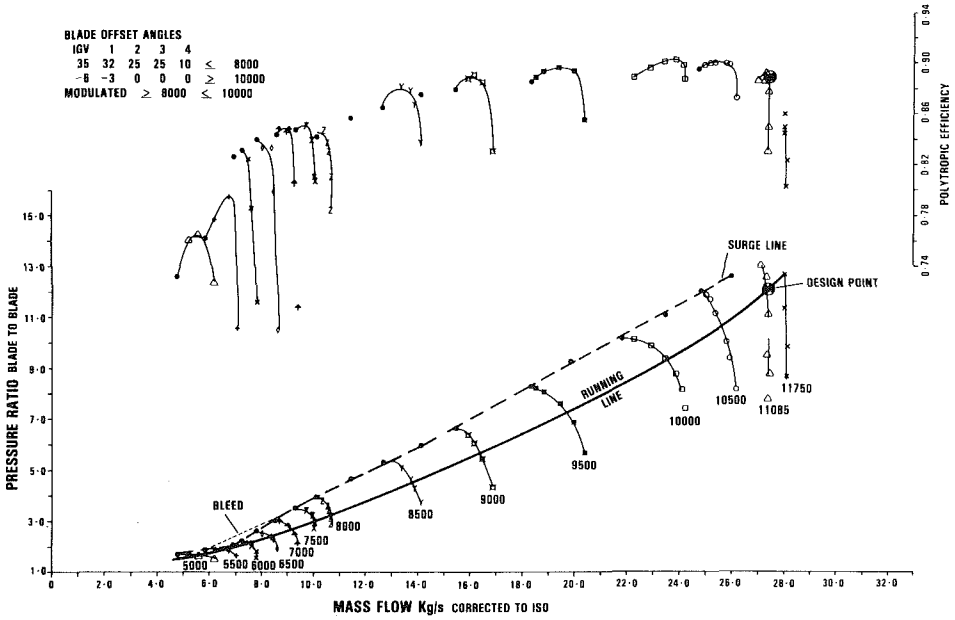

Fig. 10 Overall measured compressor characteristic

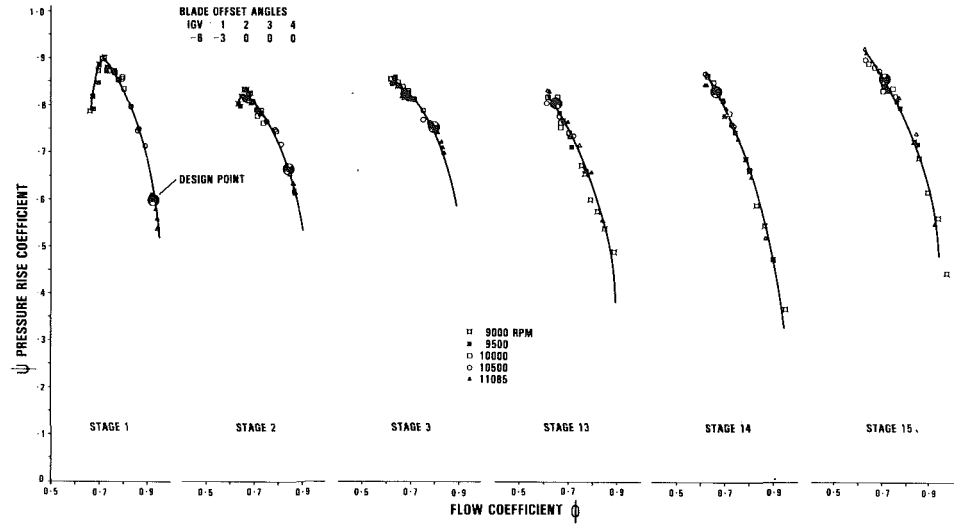

Fig. 11 High-speed setting stage characteristics

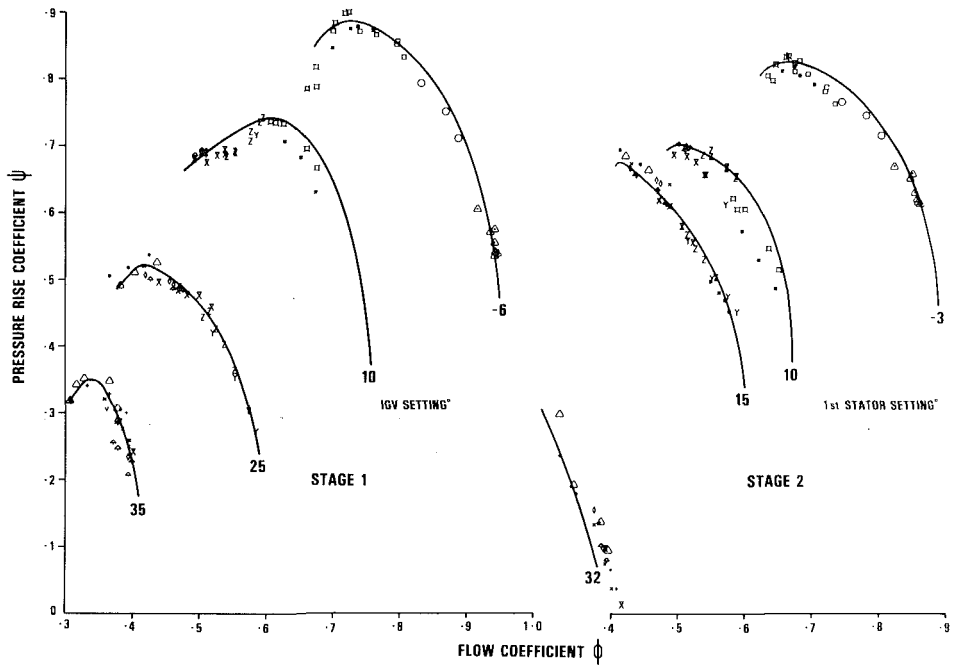

Fig. 12 Modification to stage characteristics by variable stagger blading

variable geometry setting to give maximum surge margin and efficiency

(*iii*) Intermediate range between high and low speed using the specified modulation

A fourth test on selected points would then be carried out using the leading edge instrumentation.

Overall Compressor Performance and Stage Matching. The overall performance produced by the fifteenth stage compressor is given on Fig. 10, and it shows the compressor meets its target performance. There is ample surge margin over the whole range, and when the free power turbine running line is superimposed it may be observed that it runs along the peak efficiency contours at all running speeds, hence ensuring excellent part speed engine performance.

The first tests on the high-speed performance indicated that the IGV and the first stator row needed a marginal change in design stagger to achieve the design mass flow of 27.3 kg/s.

As shown, the use of the variable geometry has removed the "knee" from the intermediate speed range to a speed well below the estimated engine idle point.

Also shown on the figure is the "softening"effect of bleed on the surge line around the "knee."

Stage characteristics for the front and rear stages with the variable geometry set at the design stagger position are shown on Fig. 11. Matching of the new zero stages to the existing stage is confirmed by the operating point on stage 3, which is at the optimum point on the characteristics, while clearly stage 1, because of the high operating Mach number, is controlling the high-speed flow. The last stage, as designed, is matched relatively high on its characteristics, thus allowing for the maximum range before choking at low speeds.

The characteristics also show the narrow working range in terms of speed if the variable geometry were not available. Primarily this is a result of the overall pressure ratio and number of stages.

At low-speed, Fig. 12 shows the effect of variable stagger

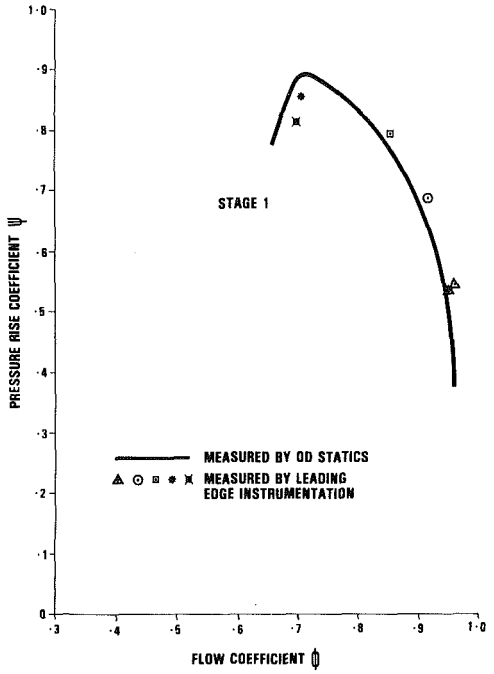

Fig. 13 Comparison of o.d. statics and blading edge measured stage characteristic

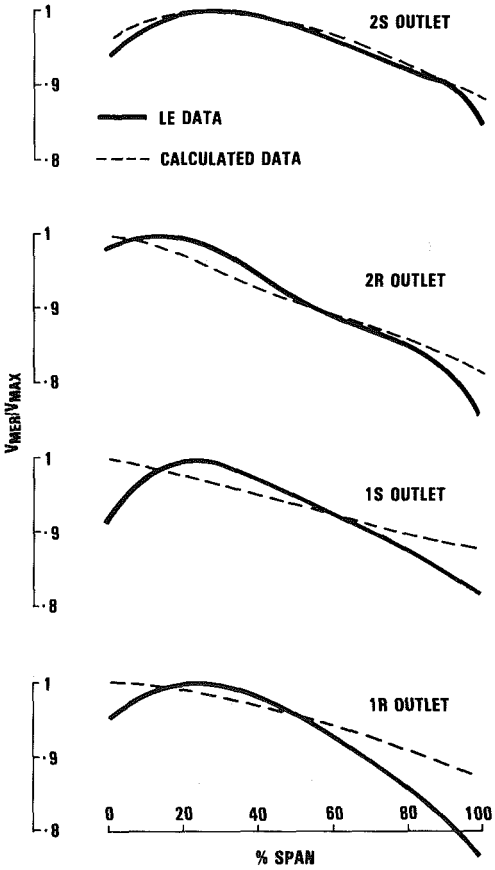

Fig. 14 Spanwise meridional velocity distribution

blading on the first and second stages. The characteristic is moved bodily to lower flow coefficients as the stagger is increased. This is mainly a result of the change in whirl imparted on the flow from the previous stator or IGV and the new axial-velocity profile at the inlet to the rotor leading edge.

The efficiency correction required for changes in Reynolds number caused by running at depressed inlet pressures have

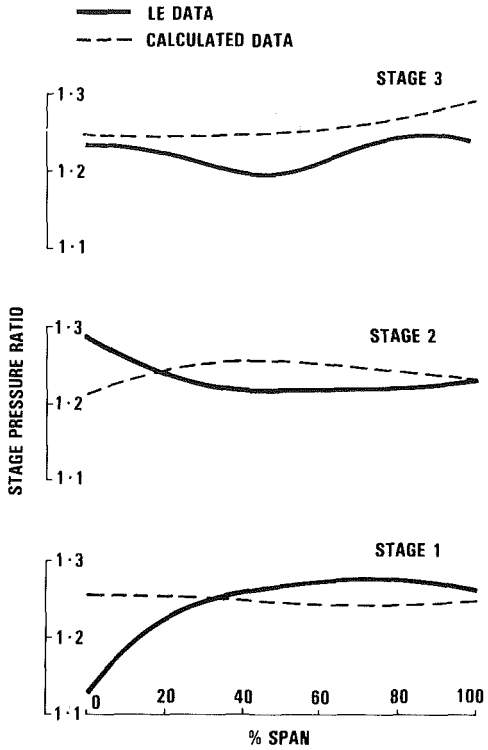

Fig. 15 Spanwise pressure ratio distribution

been shown to be small (see [4]). Various empirical methods indicate that at the design point mass flow of 27.3 kg/s with depression of .67 kpa and a mean diameter first stage rotor Reynolds number of 5.1×10^5 a correction of 0.5 percent is to be made.

Leading Edge Instrumentation and Results. To analyse the results from the leading edge instrumentation a modified streamline curvature analysis program is utilised. Within the analysis program three main assumptions are made

(*i*) Blockage factor along the compressor is estimated by the annulus wall boundary layer calculations within "throughflow." As the analysis deals with the early stages where total blockage is low no serious errors are imposed on the calculations.

(*ii*) Deviation and pressure loss at stator exit are computed from correlations within the program. Again well established routines are utilised.

(*iii*) The flow between the inlet and exit plane is assumed to be axisymmetric. This is necessary in order to minimise flow interference by excessive intrusive instrumentation. Results from the measured total pressures at the IGV inlet plane show this assumption to be fully justified.

Figure 13 shows a comparison of the first stage characteristic as indicated by the outer wall statics and the leading edge instrumentation. The similarity of these characteristics give confidence in both sets of instrumentation, particularly in the use of outer wall statics for low hub/tip ratio stages.

Figure 14 shows the development of the meridional velocity through the new stages, and it is seen that the uniform flow required and predicted for the existing compressor has been achieved. Out of the first rotor there is some error in the prediction with a measured lower velocity at the tip and higher at the root. Primarily this discrepancy may be attributed to the underestimation of the rotor hub deviation. The result of this discrepancy is indicated on Fig. 15, which shows the variation of radial stage pressure rise. It may be seen that a lower pressure ratio than required is achieved at the hub of the first stage.

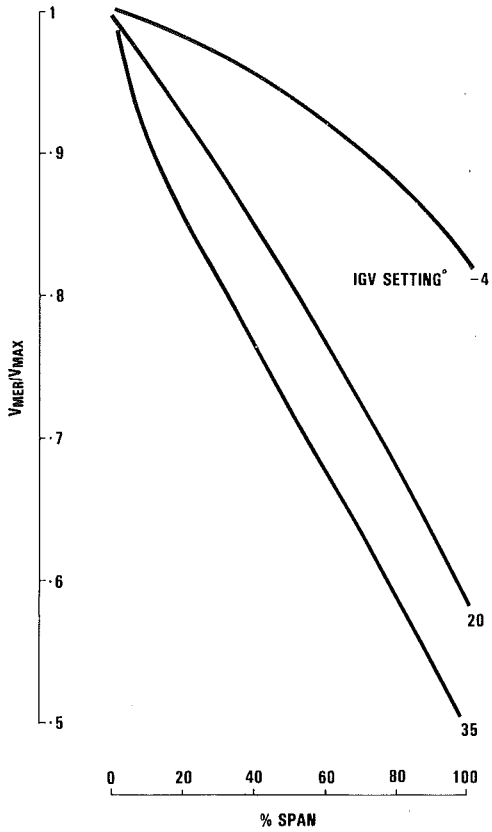

Fig. 16 Meridional velocity at IGV outlet

The stage efficiency measurements from the leading edge instrumentation were not totally satisfactory, due to the relatively small temperature rise across the stage and to phenomena associated with the averaging of the flow behind the rotor which must be strongly time-dependent. This is a topic for future investigations, but, nevertheless, useful quantitative results have been obtained.

As mentioned previously, the change in stagger of the blading has significant effect on the radial flow distribution. Figure 16 shows the meridional flow distribution out of the IGV at various settings. The consequences of the large change in stagger is that, although the average whirl is maintained under control, the radial variation will cause the rotor tip section to stall at low speed.

Some Mechanical Aspects of Testing. During the intensive test program the compressor rig has been run over 300 hrs and, in determining the stable operating boundaries, surged over two hundred times, including pressure ratios beyond design, without damage.

The rotor proved to be vibration free and no rubs were experienced on either the variable or fixed blading.

Conclusions

The results of the development program first and foremost proved that the performance of the compressor met design targets: a mass flow of 27.3 kg/s at a pressure ratio of 12:1 at design speed and at the design efficiency. This confirmed its suitability for the 6-MW gas turbine.

Modifications to the surge line achieved with variable stagger blading and bleed will ensure a rapid start up and surge free operation during load transients.

The mechanical integrity of the compressor has been proven over its entire working range.

Results from the compressor proved the validity of the throughflow analysis in all respects and confirm it to be a valuable tool for design and analysis of high-subsonic, high-pressure ratio compressors.

The leading edge results also confirmed the validity of the internal flow model in calculating the meridional flow in the early stages and identified small discrepancies in the deviation rule currently used.

References

1 Wood, G. R., "The Ruston Tornado: A 6-MW Gas Turbine for Industrial Application," ASME Paper No. 81-GT-171.

2 Tyler, J. R., "A 3-MW, Two-Shaft Industrial Gas Turbine, Ruston TB 4000," GEC *Journal of Science and Technology*, No. 1, 1975, pp. 9–15.

3 Andronowski, P. M., "A 2500-hp Addition to the Ruston Range," ASME Paper No. 79-GT-205.

4 Reusch, A. C., and Timperley, S., "Test Facility and Data Handling System for the Development of Axial Compressors," ASME Paper No. 82-GT-73.

5 Perkins, H. J., "The Turbomachinery Throughflow Analysis Program," GEC Internal Report M.E.L.W./M (3B), Nov. 1973, p. 1833.

CFD Technology for Propulsion Installation Design—Forecast for the 80s

G. C. Paynter
Principal Engineer,
Boeing Military Airplane Company,
Seattle, Wash. 98124

Competition for the world aerospace market will continue to be intense through this decade. The aircraft industry will use CFD in this period to gain an advantageous market position by reducing the cost and risk of achieving viable configurations and removing the test-derived data base as a design constraint. Use of CFD for design implies that parametric analysis will reduce reliance on parametric testing as the basis for configuration selection. Industry will increasingly emphasize development of the technology necessary to support this. Most of the industry will follow a zonal modeling strategy and take advantage of the large vector processing computers now commercially available. Areas which will pace the development of the necessary flow analysis technology include turbulence modeling, numerical error assessment and mesh generation, and experiments for code validation.

Introduction

One objective of this paper is to outline the primary role of CFD[1] in the aerospace industry and to clarify why CFD will be of increasing interest to industry in the 1980s. A second objective is to present current trends in CFD along with an explanation of these trends. Finally, key problem areas are defined which will pace the application of CFD technology by industry.

The goals of a typical corporation are to maximize profit and ensure survival of the corporation. One strategy for accomplishing this is to market a technically superior product at a competitive price. A technical advantage has tremendous leverage in the marketplace. The aerospace market is very competitive, both nationally and internationally. Because of the large size of aerospace corporations and the merging of corporate and government interests, the security and economic welfare of countries or coalitions of countries may be at stake. The high stakes and intense competition in the aerospace marketplace require a constant high sustained effort to develop improved products and to satisfy rapidly changing market requirements. The industry attempts to complete in this marketplace through application of the Research and Development process.

The Research and Development process was defined by the Wright Brothers.[(1)] It is ubiquitous through the industry and has remained essentially unchanged since the period of the Wright Brothers. In a typical Research and Development cycle to develop a new aircraft, reasonable overall performance objectives, based on past experience as embodied by preliminary design tools, are defined and translated into specific performance objectives for the components. For example, for a given vehicle the wing, control system, propulsion system, inlet, nozzle, installation, etc., each would have specific performance objectives defined from the preliminary design process. A detailed plan is prepared which will lead to achievement of the desired component and overall objectives. Work on the various components of the aircraft is closely coordinated to ensure component compatibility and to avoid duplication of effort in the integration process. Potential problem areas are defined as early as possible and research to resolve these problems is coordinated within the constraints of the overall program.

Aircraft design is by component build-up as shown in Fig. 1. In a typical design process, once a design concept has been defined for a given component or assembly, parametric model scale tests are run to define performance for a range of

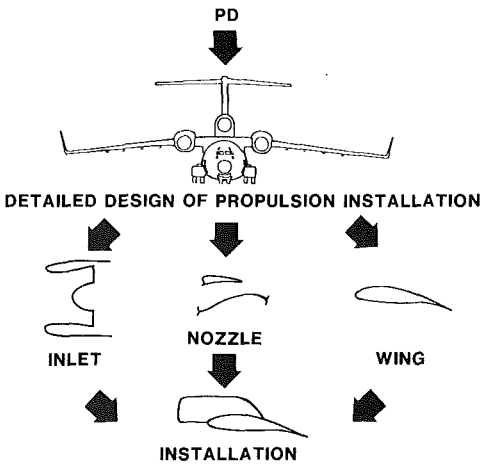

Fig. 1 Design by component buildup

[1] Computational Fluid Dynamics, CFD

Contributed by the Gas Turbine Division of THE AMERICAN SOCIETY OF MECHANICAL ENGINEERS and presented at the 27th International Gas Turbine Conference and Exhibit, London, England, April 18–22, 1982, Manuscript received at ASME Headquarters November 25, 1981. Paper No. 82-GT-21.

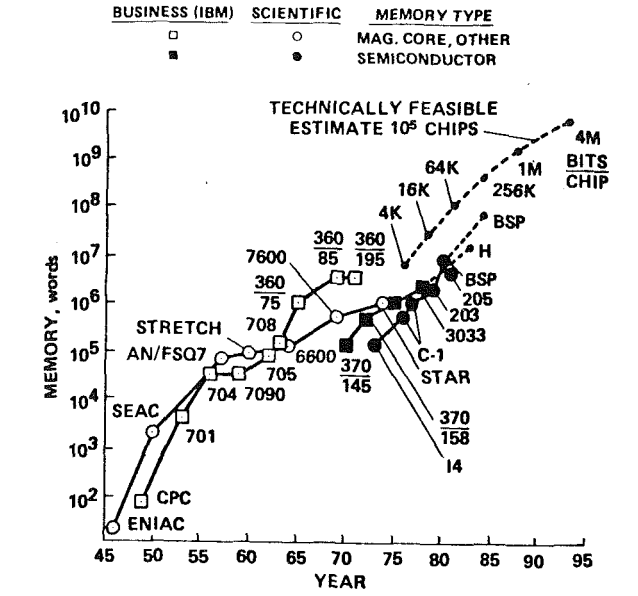

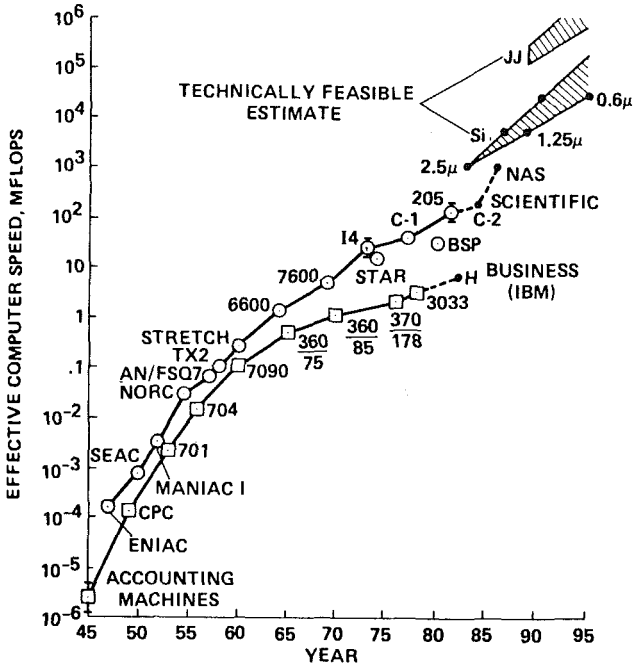

Fig. 2 Growth in computer memory and speed

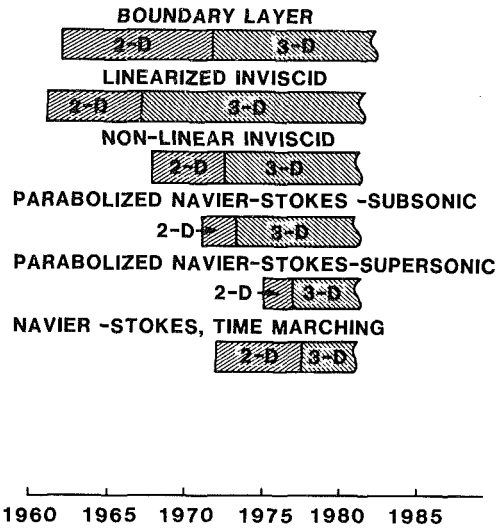

Fig. 3 Chronological development of computational methods

configurations. On the basis of this performance information, configurations are selected for full scale validation and optimization. Full-scale tests are run to confirm that the results of the model scale parametric tests can be scaled to predict full scale performance. On the basis of the full scale test results, a final design is chosen for flight test or for production. The potential role of CFD in this is to minimize parametric model scale testing and use parametric analysis as the basis for configuration selection. The rising cost of wind tunnel testing means fewer configurations can be evaluated in a given design exercise using a test based approach. This implies that the risk of not achieving a successful design is increased. The increasing availability of powerful computers and rapid progress in algorithms for solution of the partial differential equations of fluid mechanics make CFD an increasingly attractive alternative to parametric model scale testing in the design process. Use of parametric analysis rather than parametric testing for design offers the advantages of reduced development cost, time, and risk. It also removes as a design constraint the existing test data base. At present, the design process is a mix of test and analysis based approaches. The available analyses are used to reduce the size of the configuration test matrix. The analysis is also used to scale and interpret the test results. As prediction methods improve in accuracy, availability, cost, usability, etc., and as the aerospace community becomes more comfortable with CFD, the design process will use more analysis and less testing.

Because of the potential market advantages, the aerospace industry is hard at work developing a CFD analysis technology which will predict the flow through or about aircraft. Current trends in CFD are described in the Flow Analysis Development section below. Goals, approaches, problems, pacing items and technology trends expected in the next decade are discussed in the final section titled "Key Elements in CFD for the 80s."

Flow Analysis Technology Development

The overall goal with our CFD technology is an improved ability to predict in a design environment the flow characteristic of modern aircraft. These flows are complex, three-dimensional, and viscous. The design environment implies hundreds of configurations may have to be considered. It also implies the use of commercially available computers. The time and effort required to set up, run, and understand a flow with a given analysis procedure or procedures is a significant part of the cost of a design process. Experience indicates that the use of CFD for design must cost an order-of-magnitude less than an equivalent test based approach if it is to be accepted by industry as an alternative to parametric testing. This is primarily because the limitations and uses of a model test simulation are well understood while an analytical simulation is generally considered less reliable. The accuracy of the analytical result may be lower than desired because of numerical errors, modeling errors or inexperience on the part of the user. As these problems are corrected, users should be willing to accept more costly analysis studies.

The storage capacity and speed or commercially available computers and the cost per calculation are important constraints on the use of CFD for design. Chapman [2] has recently reported that growth in available speed and storage since 1945 and has projected the growth of these quantities through 1995 as shown in Fig. 2. In many possible applications of CFD for design, cost per calculation rather than the speed and storage of the available computer determines whether or not CFD is used. In many instances, only a fraction of the available storage capacity is actually utilized

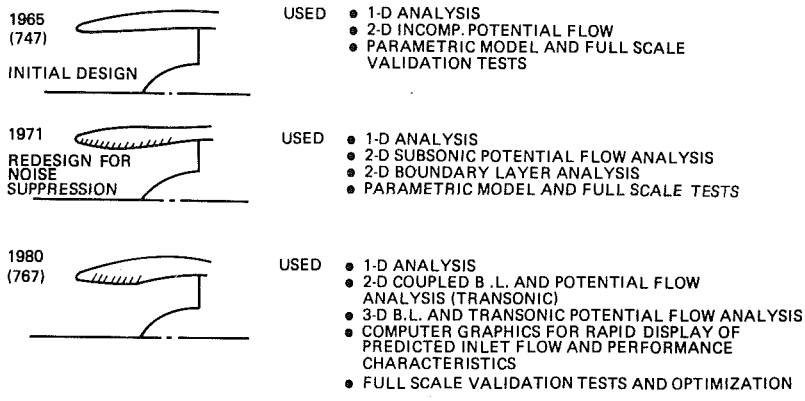

Fig. 4 Evolution of the inlet design procedure

because cost rather than machine capacity is the limiting factor. Increases in available speed and storage are important, however, because they imply that the cost to compute a given flow is reduced.

The growth in the availability of computational methods is illustrated in Fig. 3. The development time for an analysis procedure suitable for design is extraordinarily long. For example, three-dimensional linearized inviscid methods have been available for at least 15 years and these are constantly being upgraded while being utilized. A common misconception is that the development of a powerful new analysis technique will make obsolete much of the existing technology. In fact, there exists a hierarchy of methods ranging from very simple to very complex which can be applied to a typical problem. The availability of a powerful new analysis usually reduces the amount of testing rather than the amount of analysis with less sophisticated methods. This concept is illustrated in Fig. 4 showing the evolution of the design procedure at Boeing for subsonic inlets.

Because of limitations in the available computer storage capacity and speed and in the cost considered acceptable to compute a given flow for design, a zonal flow analysis strategy is gaining increasing acceptance. Zonal analysis is the use of multiple analyses in several flow regions to take advantage of simplifications that are available through the local nature of the flow. The analyses are coupled or interacted in a way appropriate for the flow to be predicted. For example, a three-dimensional potential flow analysis coupled to a three-dimensional parabolized Navier-Stokes procedure might be used for a nozzle installation with a close coupling between the aerodynamic flow over the wing and the flow from the turbo fan engine as illustrated in Fig. 5. In this case, the viscous and inviscid solution regions overlap and the solutions in the two regions are iterated until convergence is obtained for flow properties in the overlap region. A zonal modeling strategy is used because the use of a single analysis for the complex flows of a real aircraft would imply solution of the three-dimensional Navier-Stokes equations for large flow regions. This is impractical on current and projected commercially available computers because of the large storage required, high cost, and difficulty in setting up the solution. As the cost of flow analysis is reduced, the number of zones used to compute a given flow should decrease. Solution of the full Navier-Stokes equations is generally unnecessary because the flow in most regions of interest in adequately described with simpler inviscid and boundary layer or thin shear layer methods. Zonal modeling is also very compatible with aircraft design by component buildup. It is very desirable to be able to use analyses of varying levels of cost and accuracy depending on the stage of the design process as shown in Fig. 6.

Zonal modeling implies the existence of a system of flow codes which can be coupled or combined in a way appropriate

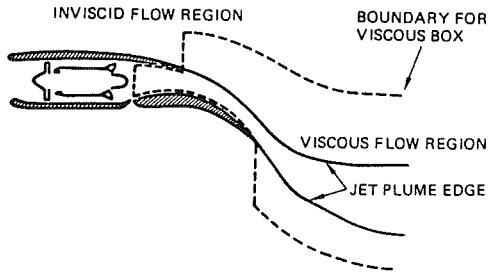

Fig. 5 Zonal flow analysis of a powered lift installation

for a given flow. Desirable features of this system include use of body fitted meshes, common input and output formats, common turbulence modeling, common code architecture and compatible numerics. These features minimize the difficulty in coupling and interfacing the several codes which might be utilized in a given analysis. These features also minimize the training and skill required on the part of the user to achieve a successful result. The available flow codes and other technologies may eventually be accessed through "User Friendly" work stations as shown in Fig. 7.

In a typical application, a zonal analysis strategy is developed, a geometry description is prepared, and computational meshes are developed for the various flow regions. Initial condition information is prepared for input, code boundary condition modifications are made if required, and the flow is computed on a trial mesh. If possible, a mesh refinement and convergence study is done to assure the user that residual and truncation errors are controlled to meet the goals of the analysis. Finally, computed results are manipulated and plotted in formats which highlight performance differences between configurations or which allow easy comprehension of the important flow phenomena.

A typical application of a zonal analysis strategy was reported recently by Kulfan [3]. Kulfan analyzed the flow of a supersonic transport model operating at mach 1.4 as shown in Fig. 8. The model had flow-through sharp lip nacelles through which the capture flow could be controlled by means of a variable position plug. Kulfan simulated the overall model flow field with the PANAIR panel method and the flow in the region of the inlet with Navier-Stokes procedure [4]. For inlet capture mass flows less than one, the inlet spills and a normal shock stands in front of the inlet. The Navier-Stokes analysis was used to compute the shock stand-off distance and a stream tube about the nacelle on which the flow is everywhere supersonic. The paneling was modified to treat this stream tube as an inlet of larger diameter positioned further forward to position the inlet shocks correctly and the flow was recomputed with the panel method for the wing pressure distribution. Computed results are presented in Fig. 9 for a

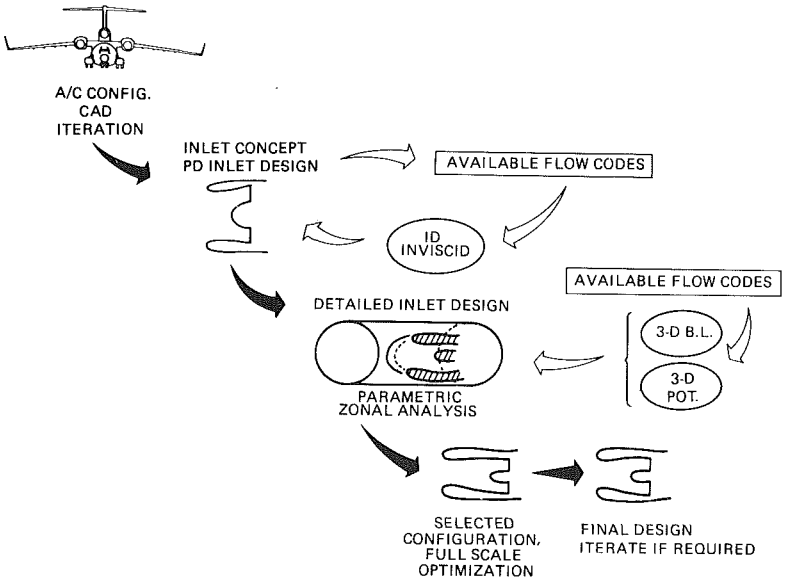

Fig. 6 Analysis based design – inlets

case with a capture mass flow ratio of 0.8. In this case, an iterative coupling was unnecessary since the flow was supersonic except in a local region upstream of the inlet.

A "broad front" strategy [5] is advantageous for the development of the necessary flow analysis technology. This strategy is characterized by an early identification of key problem areas and a coordinated effort on the individual analysis components to achieve specific goals. This strategy minimizes the time and resources required to develop a strong flow analysis capability since many component analyses of the overall analysis system have common problem elements. Typical problem elements are (*i*) numerics and mesh generation, (*ii*) turbulence modeling, (*iii*) modeling and validation experiments and (*iv*) data handling and display. The current status and recent trends in the first three of these areas are as follows.

Numerics and Mesh Generation. Putting aside for a moment questions pertaining to the adequacy of our modeling, we can in a practical sense solve the PDE's associated with many two-dimensional and some three-dimensional flows. Our latest codes are designed to be vectorizable on the new commercially available class-6 computers. Many problems which can be solved with conventional algorithms on these machines are still impractical for design, because the cost of the solution is too high. New implicit solution algorithms and multigrid methods seem to offer order-of-magnitude reductions in cost; substantial development of these methods is necessary however, to make them, practical for design.

Numerical error assessment is at present a tedious and difficult task. Data on the residual error as a function of iteration cycle and truncation error as a function of mesh density, distortion, and location are gathered by repetitive solutions for various meshes. Computer codes are commonly "validated" for a given flow by comparing computed results with experimental data. Examples of flow calculations with an inadequate mesh in which poor agreement between computed and measured flow properties is attributed to inadequate turbulence modeling are all too familiar. As noted by Forester [6], automatic error monitors and mesh adjustment procedures must be developed so that we can sort modeling errors from grid related errors. Multigrid methods appear to be particularly well suited to resolving these problems [6]. Since multigrid methods use a range of mesh densities, truncation error information is readily available as the solution develops. Error information should be useful for solution acceleration and provide guidance for mesh adjustment.

In the area of mesh generation, the progression has been

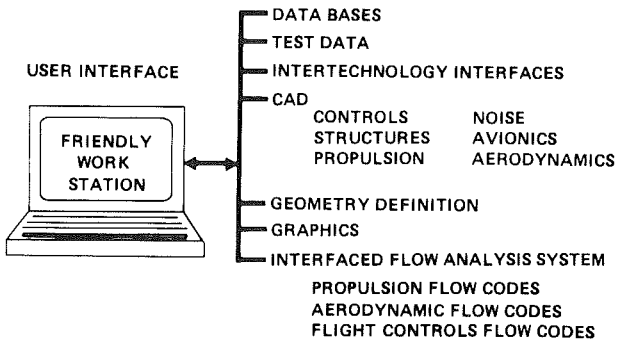

Fig. 7 Computer aided flow analysis design (CAFAD)

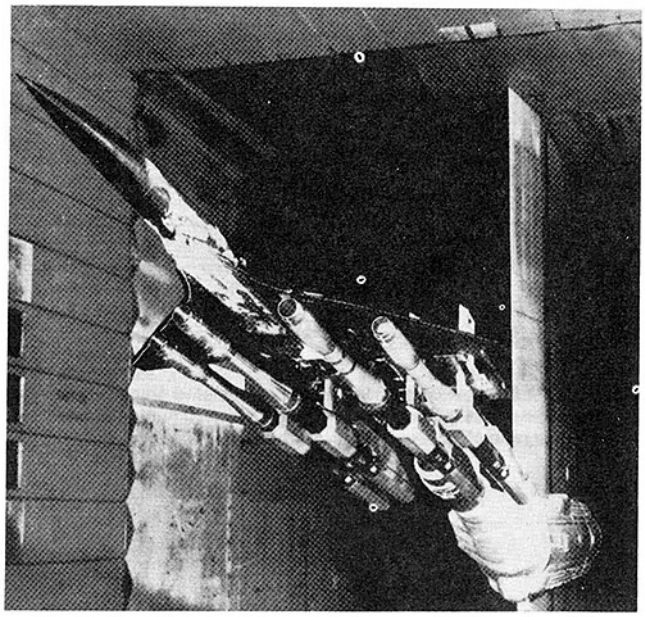

Fig. 8 Nasa Nacelle airframe interference wind tunnel model

from Cartesian meshes to Poisson-equation generated body-fitted meshes [7], to algebraic body-fitted meshes [8] and finally to subregion mesh strategies [9]. Cartesian meshes are simple but were found to lead to irregular surface cells, complex differencing logic, and inefficient use of the mesh. Body-fitted mesh generators based on the solution of a Poisson equation allowed the analysis of more complex geometries but were found to be, however, difficult to control and the mesh equations were difficult to solve. Algebraic mesh generators offer better control of the mesh and are easier to solve. The subregion strategy allows body-fitted meshes to be used for very complex geometries. The progression of development in the area of mesh generation is shown in Fig. 10.

Turbulence Modeling. With available turbulence modeling, many two-dimensional flows and a few three-dimensional flows of interest can be predicted. Available models are based primarily on two-dimensional data; the argument for their use for three-dimensional flows is that turbulence phenomena are essentially three-dimensional even when the mean flow is two-dimensional. Therefore, models developed for two-dimensional flows should work for at least some three-dimensional flows of interest. As noted recently by Hall [10], the available turbulence models seem to work reasonably well for most flows where the turbulence structure changes slowly. Examples of these flows are boundary layers, mixing layers, and wakes or jets in mild adverse or favorable pressure gradients. The available models don't seem to work where rapid changes in turbulence structure occur. Examples of these flows are regions of separation, reattachment, and shock boundary layer or shear layer interaction.[2]

[2] Mean flow properties through such interactions are predicted reasonably well with current methods. The relaxation of the turbulent layer downstream of the interaction is not well understood.

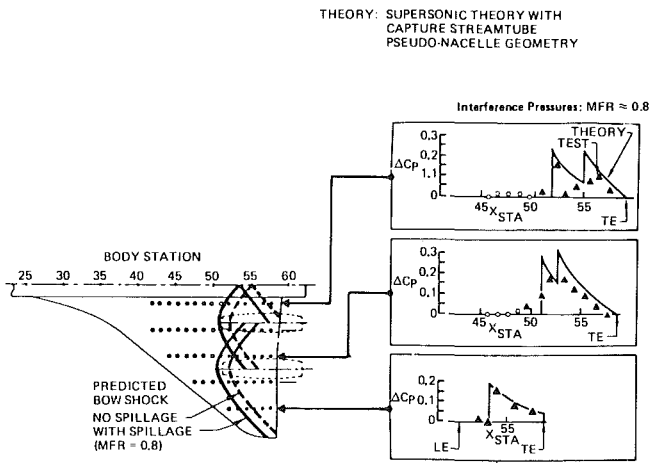

Fig. 9 Effect of normal-shock spillage on isolated Nacelle pressures and wing lower surface pressures at Mach 1.4, zero angle of attack, and a mass flow ratio of 0.8

The overall objective in the turbulence modeling area is an improved ability to predict the two-dimensional and three-dimensional complex turbulent flows of real aircraft. Flows of interest range from low subsonic to high supersonic Mach numbers and Reynolds number ranging from transition to flight values. Desirable turbulence modeling features are compatibility with the available numerical procedures, simplicity to minimize the computing cost, and a wide range of application.

The 1980-81 Stanford meetings[3] resulted in a selection of trustworthy data sets for a wide range of complex flows, the creation of a data library with those flows available on magnetic tape, an an evaluation of the available turbulence models and computational methods through comparisons between computed results and the experimental data for these flows. There still does not exist, however, an overall approach to the modeling of the complex three-dimensional turbulent flow phenomena of real aircraft. The problem is that an infinite number of flows must be considered if the flows are classified on the basis of geometry. Because of this, we must expect that most flows encountered in practical applications will differ in some important way from any previously studied flow. Bradshaw [11] has proposed classifying flows on the basis of flow phenomena rather than geometry because the former are much fewer than the latter. Progress has been encouraging but a tremendous amount of work must yet be done before we can claim to have any general ability to compute turbulent flows.

Modeling and Validation Experiments. The present predictive capability is built on the existing experimental data base. The expansion of our current predictive capability [12], [13] requires (*i*) experiments to support model development, and (*ii*) detailed flow data for complex flows of practical interest. The first experiments are detailed studies of separate flow phenomena or combinations thereof designed to check a modeling hypothesis. The second experiments are designed to validate the analysis for selected flows. As the complexity of the flows we wish to predict increases, the difficulty and expense of experimental studies which support the development of this predictive capability also increases. In practical terms, the number of flows which can be studied with a more or less fixed budget decreases. The development of an approach to turbulence research that coordinates the model development, and the experimental design is needed if significant progress is to be made.

Most of the flows encountered in industrial applications are complex and three dimensional, and the available modeling is being used to compute these complex flows. Almost no detailed data exist. Documentation of at least a few flows of current interest as "benchmarks" against which current models can be evaluated is badly needed. Flows which might be considered are those associated with (*i*) multielement

[3] 1980-81, AFOSR-HTTM – Stanford Conference on Complex Turbulent Flows.

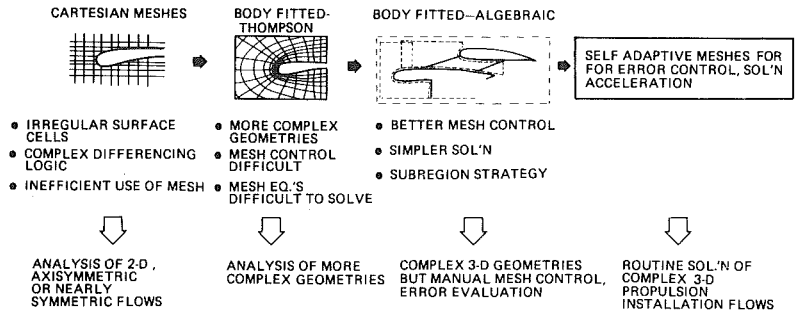

Fig. 10 Mesh generation

airfoils, (*ii*) multielement airfoils with control surfaces, (*iii*) multistream engine exhaust/nacelle flow interactions, (*iv*) the near wake of single and multielement airfoils, and (*v*) vortex generators under shear flows.

Key Elements in CFD for the 80s

Aircraft designed in the next decade will face new constraints such as stealth or improved fuel economy and will take advantage of technological advances in a number of areas. These advances should result in a fairly radical departure from aircraft being designed today. Significant improvement in aerodynamic performance is still possible through improved integration of the propulsion and control systems and through an improved understanding of local flow phenomena. The industry will continue to design aircraft by component buildup although integration will be increasingly emphasized. A substantial amount of model scale testing will continue to be used through this decade. As our CFD capability increases, however, the purpose of these tests will shift from providing overall performance information to demonstrating that the analysis procedure used for the parametric analysis studies is valid.

CFD for aircraft design is new and has developed only over the last fifteen years. While substantial advances have been made, we are now just on the threshold of predicting the three-dimensional complex flows of real aircraft. An intense challenge of U.S. dominance of the world aerospace market through the use of CFD for aircraft design is becoming apparent. For example, over 70 percent of the flows computed at the recent 1981 Stanford meeting on complex turbulent flows were computed by European participants.

Most of the industry will use a zonal modeling strategy to bring the cost of an analysis based design process down to an acceptable level. Key areas which will pace the development of the CFD capability are the development of solution acceleration and numerical error assessment methods, the development of a successful strategy for modeling complex three-dimensional turbulent flows, and the completion of modeling and validation experiments which support this.

What are the implications of the developing CFD technology? In the aerospace market, CFD is becoming increasingly important to the success of corporations competing for this market. CFD technology may in itself become a marketable commodity and an important arena in the competition for the aerospace market. Wind tunnel testing will be gradually de-emphasized. In the U.S. the current administration's emphasis on cost cutting may result in the closure of redundant facilities. In the universities, steps are already being taken[4] to close the gap between the training and research provided by the universities and industrial needs. Industry may be forced to train both new graduates and experienced engineers with obsolete skills in the use of CFD if the demand for this skill exceeds the supply. For the traveler, the lower aircraft development cost and improved performance implied by CFD should at least partially offset the higher fuel costs. In the area of defense, CFD will be used to design high-performance strategic and tactical aircraft and missiles with low observables. This, coupled with the apparent inability of the eastern bloc countries to keep pace in the development of scientific computers, should result in an improved defense posture for the U.S.

[4]NASA Centers of Excellence in CFD have been established at seven universities in the United States.

Acknowledgment

The role of CFD and the objectives and approach to the development of a competitive flow analysis capability are continuously reviewed and debated within the Boeing Company. The views stated in the present article reflect a consensus of the managers and engineers of the Propulsion System Fluid Mechanics Group. Key contributors of this are S. F. Birch, C. K. Forester, and E. Tjonneland.

References

1 Ritchie, M L., "The Research and Development Methods of Wilbur and Orville Wright," *Astronautics and Aeronautics*, July/Aug. 1978, pp. 56-57.

2 Chapman, D. R., "Trends and Pacing Items in Computational Aerodynamics," *Proceeding of the Seventh International Conference on Numerical Methods in Fluid Dynamics*, Stanford University, June 28-29, 1980.

3 Kulfan, R. M., and Sigalla, A., "Airframe Propulsion System Aerodynamic Interference Predictions at High Transonic Mach Numbers Including Off-Design Engine Airflow Effects," AGARD Symposium on Aerodynamics of Power Plant Installations, Toulouse, France, May 1981.

4 Peery, R. M., and Forester, C. K., "Numerical Simulation of Multistream Nozzle Flows," *AIAA Journal*, Vol. 18, N. 9, Sept. 1980, pp. 1088-1093.

5 Welliver, A. D., "Propulsion Research Requirements for Powered Lift Aircraft," *Proceedings of the Workshop on Engine-Airframe Integration*, PROJECT SQUID, 1977, pp. 199-242.

6 Forester, C. K., "Advantages of Multigrid Methods for Certifying the Accuracy of PDE Modeling," Symposium on Numerical Boundary Condition Procedures and Multigrid Methods, NASA Ames Research Center, Oct. 21-22, 1981.

7 Thompson, J. F., Thames, F. C., and Mastin, C. W., "Automatic Numerical Generation of Body Fitted Curvilinear Coordinate System for Field Containing Any Number of Two-Dimensional Bodies," *Journal of Computational Physics*, V. 15, 1974, pp. 299-319.

8 Kowalski, E. J., "Boundary Fitted Coordinate Systems for Arbitrary Computational Regions," Workshop on Grid Generation, NASA Langley Research Center, Oct. 6-7, 1980.

9 Forester, C. K., "Body Fitted Three-dimensional Full Potential Flow Analysis of Complex Ducts and Inlets," presented to the 19th Aerospace Sciences Meeting, Jan. 12-15, 1981, AIAA Paper No. 81-0002.

10 Hall, M. G., "Computational Fluid Dynamics—A Revolutionary Force in Aerodynamics," AIAA Paper No. 81-1014.

11 Bradshaw, P., "Review-Complex Turbulent Flows," ASME *Journal of Fluids Engineering*, June 1975, pp. 146-154.

12 Tjonneland. E., "Prediction of Turbulent Flows—A Boeing View," Presented to the 1980-81 AFOSR - HTTM - Stanford Conference on Complex Turbulent Flows, Sept. 1981.

13 Tjonneland, E., and Birch, S. F., "Application of Viscous Analyses to the Design of Jet Exhaust Powered Lift Installations," ASME JOURNAL OF ENGINEERING FOR POWER, Vol. 102, July 1980, pp. 626-631.

Investigation of Blade Vibration of Radial Impellers by Means of Telemetry and Holographic Interferometry

U. Haupt
Research Assistant.

M. Rautenberg
Professor.

Institute for Turbomachinery,
University of Hannover, West Germany

On a high-pressure, high-mass flow, centrifugal compressor blade vibration measurements are carried out to determine the excitation mechanism in various operating ranges. For these experiments semiconductor strain gages were used. For the transmission of the signals, an 8 channel telemetry system has been installed. A research program was started with blade vibration measurements in different operating ranges of the compressor such as rotating stall, surge and flutter ranges and for the case of nonuniform flow conditions. The results of vibration tests with the impeller at rest showed the stress distribution and the strain directions during blade vibration. This information was used for the choice of the strain gage position on the blade. The experimental results were confirmed by a finite-element calculation considering a segment of the impeller with one blade, which determined the different vibration modes. Further, the steady strain distribution of the impeller due to centrifugal force and temperature was calculated. The investigations were completed by optical measurements to find out the vibration modes of the different blades in rotating operation. These tests were carried out by means of a holographic interferometric system with an optical derotator. The results show the various vibration modes of the blade up to a rotational speed of the compressor of 13,000 rpm.

Introduction

Radial compressor development tends to higher power concentration of the machine, which means higher pressure ratios and massflows. This can be obtained by increasing the circumferential velocity of the impeller, requiring the use of better material and the reduction of the blade thickness. This has brought as a consequence the problem of blade vibrations, which is today an essential factor in the stress calculation of modern radial impellers. The importance of research activities in this field, to get information on the vibration behavior of radial blades is generally accepted.

Some years ago a wide research program in this subject was established in the Institute for Turbomachinery of Hannover. An experimental investigation was necessary to get information about the intensity of vibration in different operating ranges of the compressor and about the excitation mechanism.

Vibration modes and frequencies of even complicated blade-geometries meanwhile can be calculated by modern finite element methods.

Methods of Investigation

First activities dealt with the question of which measurement techniques and what type of signal transmission would be suitable for these investigations. Semiconductor strain gages were chosen because of their great sensitivity factor. As a result of this preparatory work we needed to compare them with foil strain gages on the blade. This was carried out in a calibration test before the investigation, to insure sufficient acccuracy in the measurements.

Slip rings for the transmission of the blade vibration signals from the rotating machine could not be used because of the high rotational speed of the compressor in conjunction with the relatively great shaft diameter of our machine. Consequently a telemetry system was selected and first tests with a battery-supplied 1 channel system proved very successful. The necessity to get information from more than one blade led to the decision to use a multichannel transmission.

For these investigations, special emphasis was laid on the following four important excitation phenomena documented in [1]:

- Blade vibration excitation by aerodynamic nonuniformity of the flow in the inlet or exit range of the compressor. Resonance occurs between the blade frequencies and the engine orders.
- Self-excited blade vibrations by operating the machine in the flutter regions of the compressor map
- Blade excitation by the cells of rotating stall
- Blade excitation by surge of the compressor

The test facilities for the experimental investigation are

Contributed by the Gas Turbine Division of THE AMERICAN SOCIETY OF MECHANICAL ENGINEERS and presented at the 27th International Gas Turbine Conference and Exhibit, London, England, April 18–22, 1982. Manuscript received at ASME Headquarters November 30, 1981. Paper No. 82-GT-34.

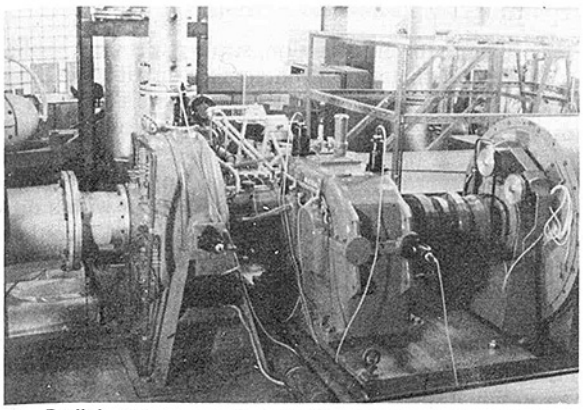

Fig. 1 Radial compressor test facility for the blade vibration investigation

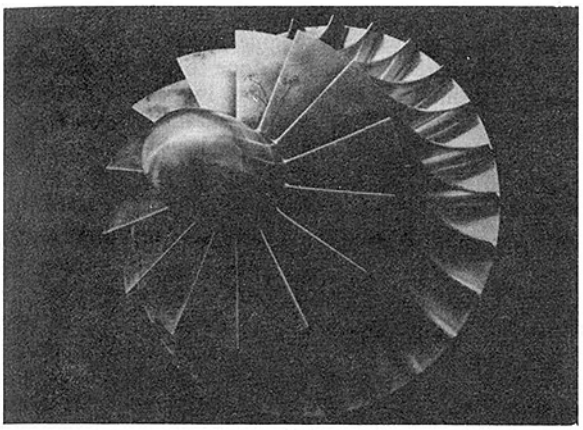

Fig. 2 View of the impeller

shown in Fig. 1. The 1350-kW d-c motor in connection with a gearbox drives the centrifugal compressor. A photograph of the test impeller is shown in Fig. 2. There are 28 blades at the outlet with every second blade cut back at the impeller inlet. The view of the very thin blades show the good suitability of the impeller for the vibration investigations. The large spherical cap was mounted to cover the telemetry transmitter.

Computation of Blade Stress and Strain Directions

The material stress of the impeller blade is the sum of the static stress due to the centrifugal force and the dynamic stress by the blade vibration. A measurement of both components was estimated to be very difficult, because this would not give the desired information about the dynamic component of the whole signal with sufficient accuracy. So we decided to measure only the vibrational part of the stress, while the strain due to the centrifugal forces was calculated by means of the finite element method. Figure 3 shows the part of the impeller used for this calculation and the element distribution. According to the illustration shell elements were used for the blades and cube elements for the impeller hub. The result of this computation for a rotational speed of n = 20,000 rpm, for which a measured temperature distribution was taken into account, is illustrated in the right graph of this figure. Maximum stresses of the blade occur in different hub sections while the stresses in the impeller reaches a maximum near the shaft, where additional vibration stresses can be neglected.

Much work had to be carried out to choose the best measuring points on the blade where the strain gages had to be applied. For this purpose, a detailed knowledge, not only of the strain distribution during the vibrational motion, but also of the principal stress directions was essential. By means of a

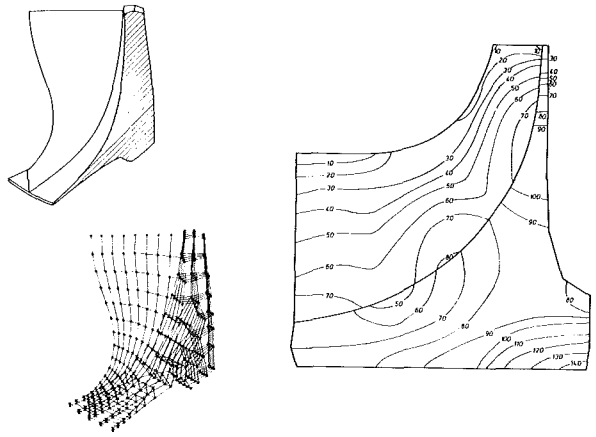

Fig. 3 Computed equivalent stress of the test impeller due to centrifugal force and temperature with cutout sector of the impeller for the computation and element distribution: n = 20,000 rpm and σ_v = equivalent stress in N/mm^2

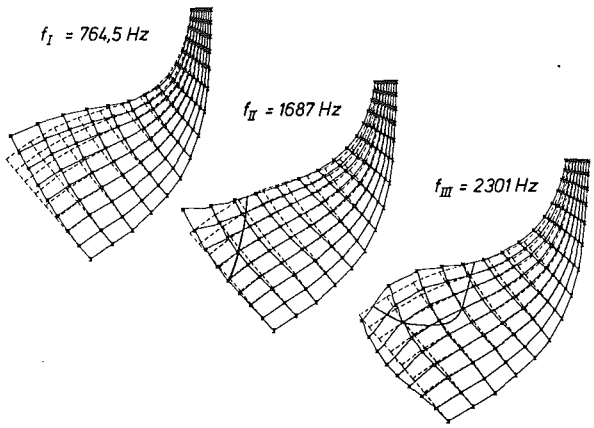

Fig. 4 Computed first three mode shapes of the radial blade of the test compressor: f = natural frequency

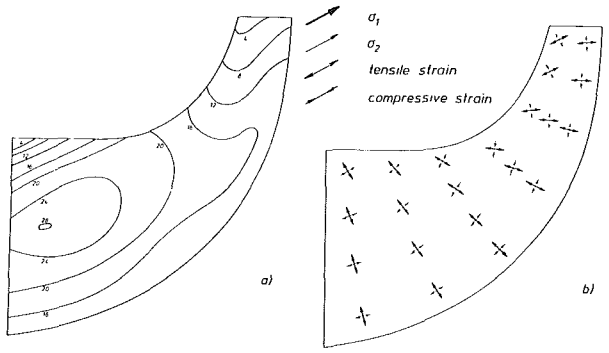

Fig. 5 Computed strain distribution at the impeller blade for the vibration in the first mode: (*a*) curves of constant equivalent stress in N/mm^2, (*b*) directions of the principal strains

FE-program at first the natural frequencies and the mode-shapes for the radial blade were computed. Figure 4 shows the results of this calculation for the important first three modes with nodal lines for the second and third mode. A computation of the strain and the principal strain directions of the vibrating blade gave the distributions as they are illustrated in Fig. 5 for the example of the first vibrational mode. For a displacement of the inlet tip of 1 mm a maximum strain of σ_v = 28 N/mm^2 was obtained at half of the inlet blade-height, where we got tensile strains for σ_1 and σ_2.

This work was completed with an experimental investigation, where one blade of the impeller at rest with 37

applied strain gage rosettes was excited to vibration and where the stress amplitudes were measured. One of the results of these experiments is illustrated in Fig. 6, again for the example of the first mode. While the arrows signify the amount of principal strain at that point of the blade, the small triangles indicate the direction of these strains. With the maximum strain at the blade inlet at half of the blade height, these results confirm those obtained by the FE-computation.

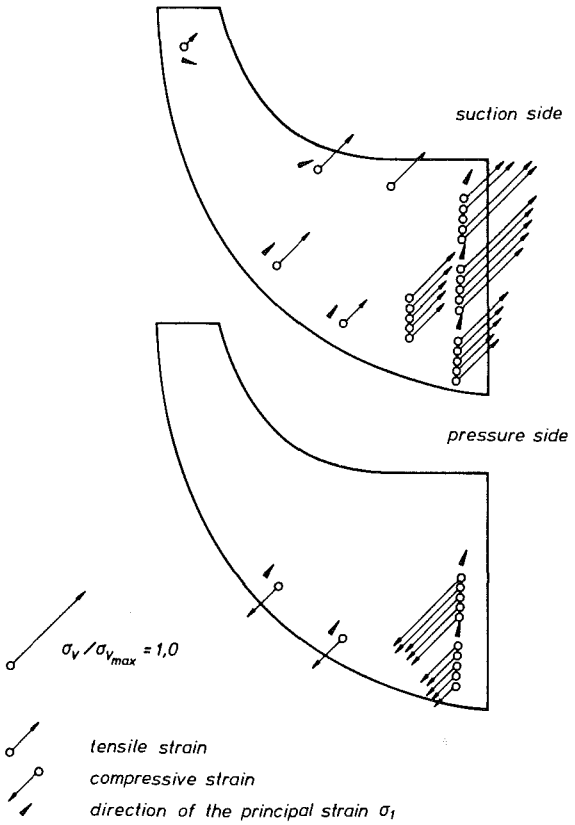

Fig. 6 Results of blade vibration tests with strain gages for the first mode: σ_v = equivalent stress, f_I = 794 Hz

Preparatory Experimental Activities

According to this information, strain gages were applied on all the blades with a wiring contact to a distribution pin plate in the spherical cap of the impeller, where the strain gages chosen for every measurement could be connected to the transmitter. For the first investigations a 1-channel telemetry system was used to get some experience in these measurement methods. The vibration tests were carried out with a diffuser with 19 aerodynamic blades and at constant throttle-valve position. The results shown in Fig. 7(*a*) are illustrated in a Campbell-diagram, where only maximum blade stress amplitudes are considered. Resonances with the first vibration mode and different engine orders are obtained, but also great vibration excitation by the 19 diffuser blades occurs especially at a rotational speed of approximately n = 18,000 rpm.

A similar measurement was carried out with a vaneless diffuser. The test results in the diagram of Fig. 7(*b*) show a very different blade vibration behavior with considerable amplitudes only at the resonance position between the second vibrational mode with the engine orders above n = 13,000 rpm. Much work is still to be done to repeat measurements like these at multiple blades and to investigate the excitation reasons by analyzing the vibration and the flow data.

Installation of a Multichannel Telemetry System

It was mentioned above that information from one blade only would not be sufficient for this investigation. This was realized by some preparatory tests with the impeller at rest, where different vibration behavior of the blades with respect to the eigenfrequencies and the vibration amplitudes was observed. This is due to manufacturing tolerances and the coupling effects between adjacent blades, which influence the natural frequencies. For this reason we tried to install a multichannel telemetry system in the compressor. After a long period of research and tests we found that the development of such multichannel transmission systems under ambient conditions, like high temperature, acceleration, oil, and the presence of rotating metallic components, was not sufficiently advanced. Only recent publications, such as [2], report the use of multichannel telemetry installations of very small sizes in

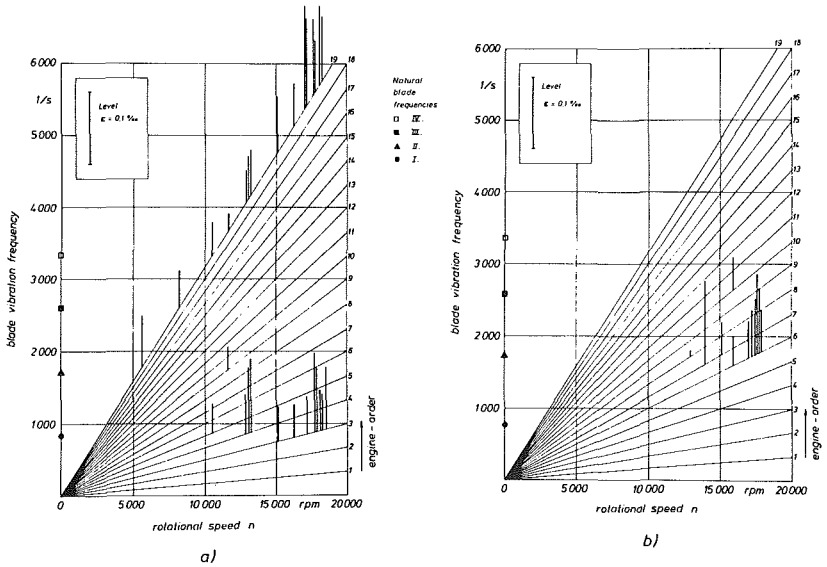

Fig. 7 Blade vibration measurements by means of a 1-channel telemetry system: (*a*) aerodynamic diffuser with 19 blades, (*b*) vaneless diffuser

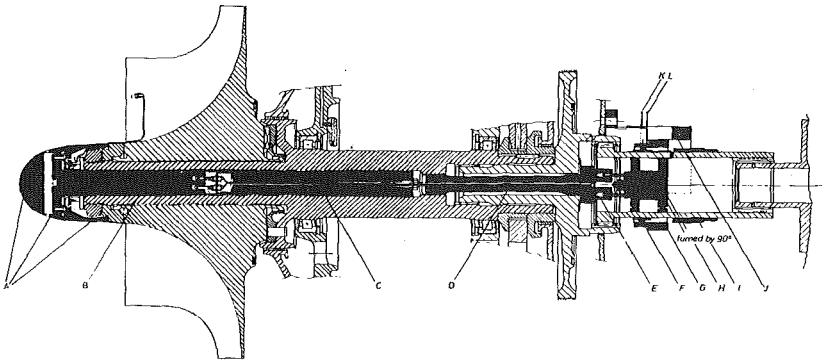

Fig. 8 Centrifugal compressor with installations for the telemetry transmission

A modified hub section
B 8-channel telemetry transmitter
C wiring-tube
D tension bolt with central bore
E adapter with pin-connector
F secondary coil with rotating antenna
G primary coil with coil carrier
H voltage converter for the inductive power supply
I slotted tube for shaft speed measurement
J adjustable coil mounting
K stationary antenna
L inductive power supply

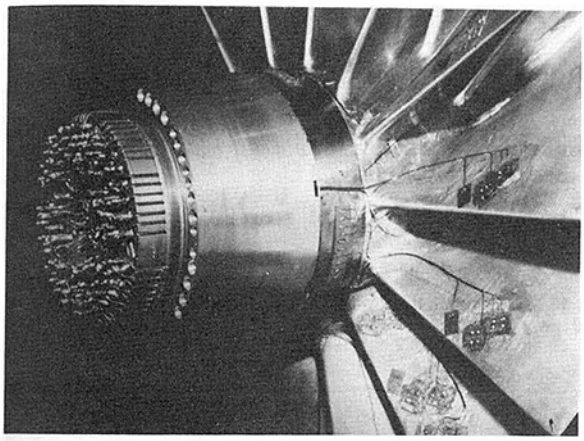

Fig. 9 Radial impeller with strain gages and mounted 8-channel telemetry transmitter

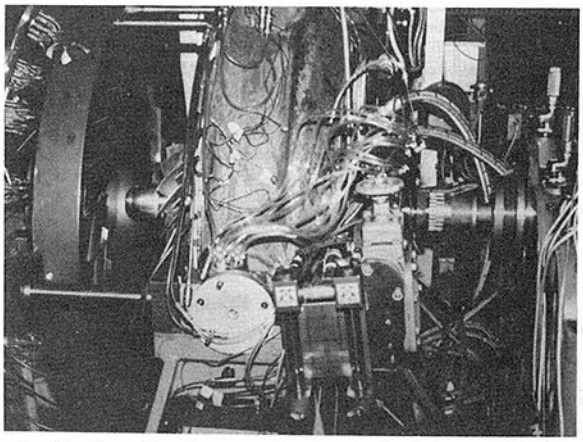

Fig. 10 Centrifugal compressor test facility before assembly

turbomachines. A power supply of the system—by battery for example—was not suitable because of the high ambient temperatures in the axis due to the heat generated by the bearings. Attempts in this respect lasted for a year with many disappointments and finally led to the present situation, in which we succeeded in installing an 8-channel telemetry system with an inductive power supply that has just proved operational up to highest rotational speeds of more than n = 18,000 rpm. Figure 8 shows the sectional view of the compressor with the new components of the telemetry system identified by the dark colour. The transmitter with its plate with the contacts to the strain gages is situated in the bore of the impeller shaft as shown in Fig. 9. It is connected with the components of the inductive power supply mounted in the socket-tube coupling of the compressor and the gear-box. To facilitate frequent assembly and disassembly, all parts had to be constructed with pins and sockets. The vibration signals leave the transmitter by the wiring for the power supply and they are transmitted at the coil system of the inductive supply. An additional receiver antenna finally could improve the transmission conditions. Figure 10 gives an impression of the test facilities at the moment just before the compressor was reassembled.

Blade Vibration Measurements at a Rotating Radial Compressor by Means of Holographic Interferometry

One fundamental disadvantage of strain gage measurements is the fact that information is obtained from

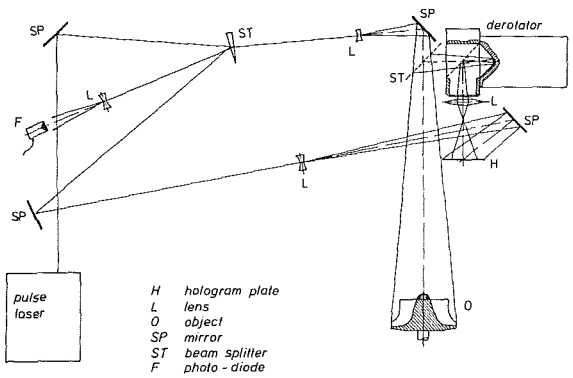

Fig. 11 Holographic setup for the blade vibration measurements

one point only. So different stress signals from two adjacent blades at the same measuring point do not necessarily mean that these stresses are characteristic for these two blades. It already has been mentioned above that coupling effects between all the blades of an impeller influence the mode shapes and so the stress maxima probably will be found at different points on the blade. The investigation with respect to this phenomenon at an impeller at rest would not be satisfactory because essential ambient conditions like the centrifugal force and the flow would not be taken into account.

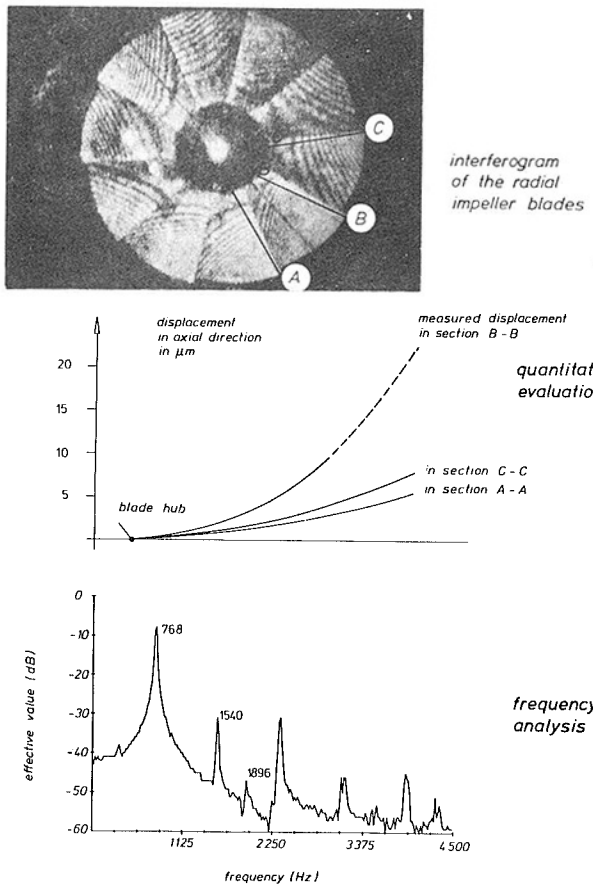

Fig. 12 Results of the optical blade vibration measurements, n = 3000 rpm

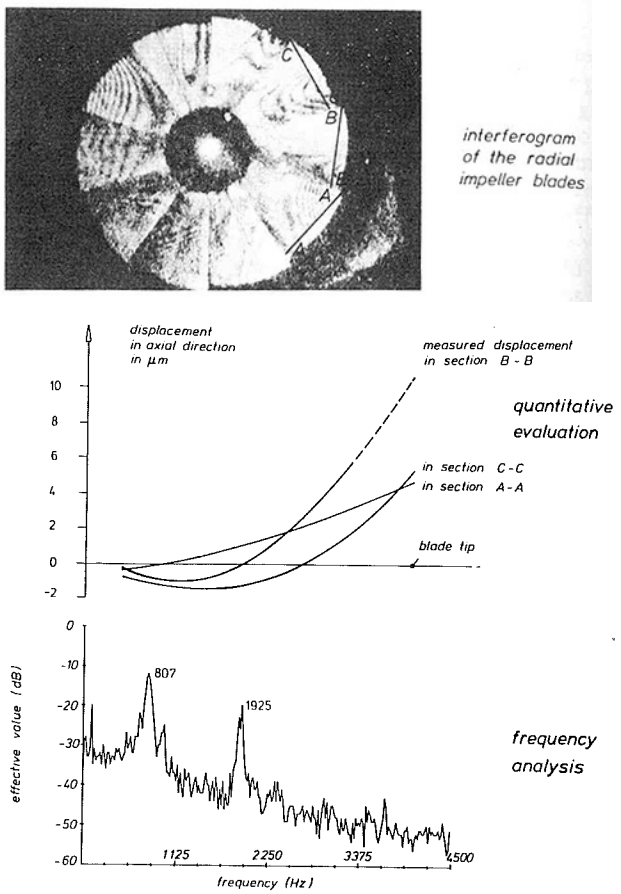

Fig. 13 Results of the optical blade vibration measurements, n = 6500 rpm

The cooperation with the "Bremer Institute für angewandte Strahltechnik (BIAS)" recently gave us the possibility to go one step forward in this problem. An optical method of investigation to measure vibrations in rotating systems had been developed, and its reliability could be proved in laboratory tests. This method, the holographic interferometry by use of a rotating prism, is described in detail in [3]. If it would be possible to apply it under the rough conditions of a highly loaded compressor, information about the mode shapes in the rotating state of every blade of the impeller would be attainable.

The principle system of the holographic setup as it was used at one of our radial compressors is illustrated in Fig. 11. The holographic interferometry is coupled with a rotating prism, a derotator, eliminating the rotating motion of the impeller. The main problem in applying this method to our machine was to mount all the optical components in a vibration isolated manner in spite of considerable motion of the operating compressor. Further, a great difficulty was to ensure that the prism rotated exactly at the rotational speed of the impeller. This was achieved by scanning 200 markers from the reverse of the impeller disk by a photo cell using a glass fiber.

For the first fundamental investigations of the compressor, the inlet tube was removed, because this method employed some optical components in the rotating axis. The whole compressor with the measurement setup was covered by a black plastic foil to keep it light-proof during the double pulse exposure. A vibration signal telemetered from one blade ensured driving the compressor in an operating range, where blade excitation occurs. First results are shown in Fig. 12, with the interferogram, the analysis of the blade displacement, and the frequency analysis. At n = 3000 rpm,

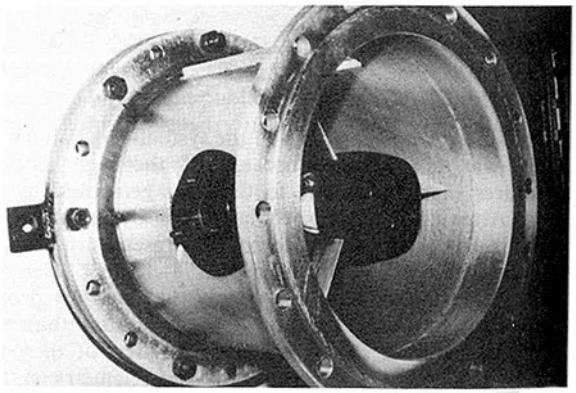

Fig. 14 View of the new compressor inlet tube with the installations for the laser beam displacement

all blades vibrate in, the first mode excited by the teeth of the gear wheel. The interferogram shows the same mode shape for all blades with different displacements due to coupling effects between the blades and manufacturing tolerances. These results are typical for resonance operation, while Fig. 13 illustrates an operating state of the compressor without excitation near the blade frequencies. At n = 6500 rpm, different mode shapes were observed. The interferogram shows variations of the first two modes with different displacements as indicated in the analysis of the telemetered blade signal. The vibrational modes on the left side of the impeller are similar to the first mode. We find nodal lines typical for the second mode on the right side. Other interferograms for the same rotational speed show different

displacement distributions of the impeller inlet section with always similar vibrational modes of the blades as in Fig. 13.

These investigations with the duration between pulses of 50 μs were carried out up to a rotational speed of $n = 8000$ rpm, where the measurements were limited by a considerable suction force of the inlet flow. Thus an application of the method with a closed inlet was desired, and, in fact, only this would mean realistic flow and excitation conditions. A new inlet tube as shown in Fig. 14 was manufactured with a glass window with parallel faces for the entry of the laser beam. To turn it into the rotating axis a surface mirror was mounted on a holder fixed in the inlet tube by three aerodynamic carrier blades. Another window was provided on the top of the tube for the purpose of adjustment of the mirror.

With this new setup measurements were carried out up to a rotational speed of $n = 13{,}000$ rpm. Further tests are underway to get information about the mode shapes at still higher speed.

This optical investigation extends considerably the possibilities of research on the nature of blade vibrations at the operating compressor and will complete the measurements by telemetered strain gage signals.

Summary

The stress distribution due to centrifugal force of a radial impeller with extremely thin blades has been calculated. The strain due to the vibrational motion of the blades was investigated experimentally and theoretically. With this information, strain gages could be applied to an impeller of a test compressor to carry out blade vibration measurements. For the signal transmission from the rotating shaft an 8-channel telemetry system with inductive power supply was installed and tested.

Further an optical method of measuring the mode shapes of the vibrating blades of an operating compressor was presented. Results were obtained up to a rotational speed of $n = 13{,}000$ rpm by mounting a special compressor inlet tube carrying the installation of an adjustable mirror system.

Acknowledgment

Funds of the work dealt within this paper were provided by the German Research Association (DFG) and the FVV (Forschungsvereinigung Verbrennungskraftmaschinen). The authors thank them for their support.

The advice of Dr. Jäger (MTU) in the preparation of the vibration measurements and the good cooperation with Dr. Kreitlow in the optical investigations are gratefully acknowledged.

References

1 Haupt, U. and Rautenberg, M., "Zur Untersuchung von Schaufelschwingungen an Laufradern hochbelasteter Radialverdichter mittels Datentelemetrie," MTZ 39, Vol. 4, 1978, pp. 177–183.

2 DeRose, R. D., "Low Profile Strain Gage Applications Telemetered from Rotating Machinery," Joint Fluids Engineering/Gas Turbine Conference and Products Show, New Orleans, Mar. 10–13, 1980.

3 Beeck, M. A. and Kreitlow, H., "Conditions and Examinations of Vibration Analysis of Rotating Blades with the Help of the Holographic Interferometry," *Proceedings of the Laser 77-Opto-Electronics Conference.*

P. J. Vermeulen
Associate Professor,
Department of Mechanical Engineering, University of Calgary, Calgary, Alberta, Canada
Assoc. Mem. ASME

J. Odgers
Professor Titulaire,
Universite Laval,
Quebec, Quebec, Canada

V. Ramesh
Research Associate.
Department of Mechanical Engineering,
University of Calgary,
Calgary, Alberta, Canada

Acoustic Control of Dilution-Air Mixing in a Gas Turbine Combustor

A small combustor of normal design employing acoustic control of the dilution-air flows has been successfully tested up to "half-load" conditions. It has been shown that this technique can be used to control the exit plane temperature distribution; also the ability to trim the temperature profile has been convincingly demonstrated. The acoustic driver power requirements were minimal, indicating that driver power at "full-load" will not be excessive. The nature of the acoustically modulated dilution-air flows has been clearly established as that of a pulsating jet flow with superimposed toroidal vortices. The pressure loss of the unit and its combustion efficiency were insignificantly affected by the acoustic drive. The work contributes to the design of combustors such that a desired exit plane temperature distribution may be achieved.

Introduction

A previous investigation [1] of a model combustor of gas turbine type showed that acoustic control of the dilution-air jet flows was possible. Temperature measurements demonstrated that acoustic modulation of the dilution-air flows can be used to selectively and progressively control the exit plane temperature distribution. These results were restricted by the model combustor being one of too poor a traverse quality, low dilution-air jet velocity, no film cooling air, essentially a dump casing (annulus being very large), and stabilization by means of an unswirled "pepper pot" instead of the more usual swirl stabilized primary zone. The geometry was therefore not fully representative of typical gas turbine combustors.

The work to be described uses a small typical tubo-combustor which removes many of the restrictions just mentioned. In order to be able to exercise acoustic control over the dilution-air flows, modifications to the combustor casing were necessary. These changes evolved on a trial and error basis to produce a final geometry which was effective in controlling the dilution-air mixing processes and hence also the temperature traverse quality.

The previous work [1] was unable to investigate the nature of the dilution-air flows when under acoustic control, and it was assumed, from experiments on a single orifice, that the modulated dilution flows in the combustor consisted of a modulated jet flow with superimposed toroidal vortices. An objective of this work was, therefore, to attempt to clarify the nature of the modulated dilution-air flows.

Besides the development of a suitable acoustic control system an important objective was to test the combustor at more representative conditions using natural gas (methane) and kerosene-type fuels. The work to be presented describes the tests using natural gas.

Experimental

The Combustor. A diagram of the combustor, unmodified for acoustic control, is shown in Fig. 1, which also indicates the major air distribution. The usual atomizer has been replaced by a conical gas distributor for the burning of natural gas. Combustion air was supplied by a centrifugal blower delivering air to a venturimeter prior to entering the combustion chamber. The fuel, from high-pressure bottles, was metered by a choked orifice before passing to the gas injector in the swirl stabilized primary zone. Ignition was by means of a high-energy spark. Inlet air static and stagnation pressures and temperature were measured, also the side-hole pitot tube could be traversed in order to obtain inlet velocity profiles. The velocity profiles, measured for "low" and "high" air mass flow rates, were typical turbulent profiles of good symmetry about the flow centre-line. The exit plane temperature distribution was measured by six, shielded, radially traversed thermocouples circumferentially spaced at 30 deg. Downstream static and stagnation pressures were also measured, and to check that reverse flow did not take place in the tail pipe, seven additional cylindrical pitot tubes (making eight equally spaced) were mounted to monitor stagnation pressures near the wall. No reverse flows were observed. Can wall temperatures were also measured by thermocouples attached to the outside diameter in the planes of the primary and dilution zones. Figure 2 shows a schema of the test rig assembly and instrumentation unmodified by acoustic control devices.

The crucial problem was how to control acoustically the dilution-air flows. For the convenience of easy variation of power and frequency, conventional loudspeakers of 150-W

Contributed by the Gas Turbine Division of THE AMERICAN SOCIETY OF MECHANICAL ENGINEERS and presented at the 27th International Gas Turbine Conference and Exhibit, London, England, April 18-22, 1982, Manuscript received at ASME Headqurters November 30, 1981. Paper No. 82-GT-35.

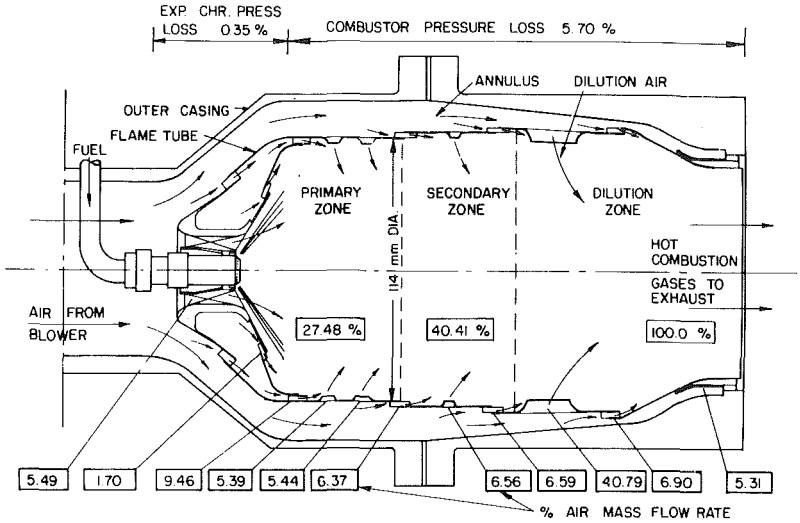

Fig. 1 Cross section through the combustor showing the air distribution

capacity were used as modulators, one speaker driving two dilution holes, for a total of three speakers. Fluid mechanical methods of driving are possible but are not yet developed. The main difficulty was to accomplish driving across the annulus between the outer casing and flame tube in the plane of the dilution holes. Success was finally achieved by rerouting the dilution-air such that it was tapped-off upstream of the combustor entrance, run through six tubes parallel to the combustor axis outside of the casing; then each tube was turned inwards at right angles to pass through the casing and join up with a dilution hole in the flame tube. Thus, air from the annulus no longer entered the dilution holes. Pairs of the air by-pass tubes were connected by "T" junctions to a driver tube and loudspeaker. To prevent acoustic energy passing upstream via the bypass tubes a Helmholtz resonator was teed to each bypass tube between its air intake and the point where it was teed to the driver tube. Figure 3 shows details of the arrangement. The Helmholtz resonator acts as a fairly broad-band rejection reactive filter centered around the natural frequency [2]. Bench testing of a driver tube bypass tubes system indicated that the Helmholtz resonator designed was effective over the acoustic frequencies likely to be used for

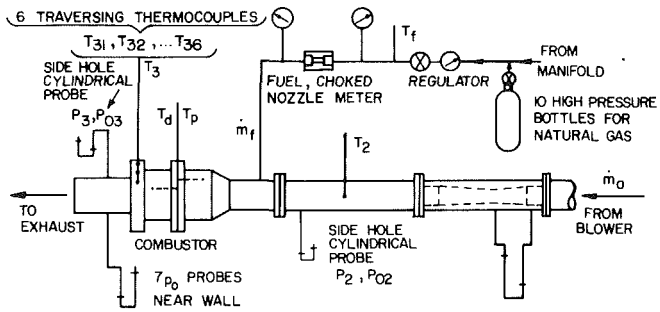

Fig. 2 Schema of test rig assembly and instrumentation (no acoustic devices)

dilution-air modulation, and that the drive at the dilution hole end was strengthened.

Such a system is acoustically complex, and despite bench testing to find the strongest resonance mode, it was still necessary to determine the frequency of the strongest resonance mode of the full assembly by progressively changing the drive frequency (keeping power constant) and

Nomenclature

A/F = air/fuel ratio (by mass flow rate)
f = frequency
$\dot{m}_a$ = air mass flow rate
$\dot{m}_f$ = fuel mass flow rate
M_{ref} = reference Mach number based on maximum i.d. of casing
p_2 = inlet static pressure
p_{02} = inlet stagnation pressure
p_3 = exit static pressure
p_{03} = exit stagnation pressure
Q = temperature traverse quality
Q_{radial} = radial temperature traverse quality
r = radial position
S_T = standard deviation
$\bar{S}_T$ = standard error of the mean
$\frac{S_T}{T_{3m}}$ = dimensionless standard deviation
T = temperature[1]
T_d = dilution zone wall temperature
T_f = fuel temperature
T_p = primary zone wall temperature
T_2 = inlet temperature
T_3 = exit plane temperature
T_{3m} = exit plane mean temperature
$T_{3\max}$ = exit plane maximum temperature
T_{3r} = exit plane mean "radial" temperature
$T_{3r\max}$ = exit plane maximum "radial" temperature
$\bar{T}$ = dimensionless temperature
$\bar{T}_r$ = dimensionless "radial" temperature
ΔT_{meas} = measured mean temperature rise
ΔT_{th} = theoretical mean temperature rise
η_{meas} = measured combustion efficiency
η_{th} = theoretical combustion efficiency
ϕ = equivalence ratio $\left(\frac{\text{stoic } A/F}{\text{actual } A/F}\right)$

[1] This is strictly stagnation temperature, but because of low flow velocity stagnation temperature closely equals static temperature and the distinction can be ignored.

Table 1 Relevant test conditions

Test	$\dot{m}_a$ kg/s	A/F^a	ϕ overall	T_2K	p_2kP$_a$	M_{ref}	$\frac{p_{02}-p_{03}}{p_{02}}$% calculated at inlet conditions	Driver No. and "max" power W @ 220 Hz		
								1	2	3
9	0.0984	62.9	0.272	308	90.28	0.0172	0.55	57.4	54.2	57.4
10	0.1344	67.3	0.255	307	90.15	0.0239	1.05	59.0	59.1	59.0
11	0.0981	62.5	0.275	309	89.76	0.0174	0.56	18.1	19.3	18.1
13	0.0978	62.7	0.274	309	89.57	0.0174	0.56	–	–	71.7
14	0.0974	63.7	0.269	310	89.09	0.0174	0.56	–	–	12.4
15	0.1693	90.5	0.190	307	90.42	0.0302	1.68	–	–	73.5
22	0.0983	55.7	0.308	307	90.30	0.0170	0.53	–	–	12.6
23	0.0984	90.3	0.190	306	90.25	0.0170	0.53	–	–	12.5
Theoretical full-load nominal	1.1657	60.4	0.286	476	395.4	0.057	5.97	standard combustor		

[a]Stoichiometric $A/F = 17.16$

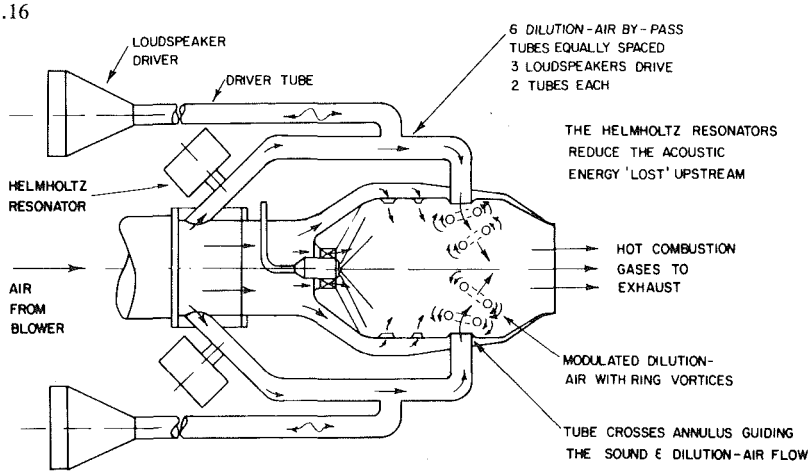

Fig. 3 Scheme of current apparatus for acoustic control of dilution mixing processes

observing the effect on the exit plane temperature distribution. A frequency of 220 Hz was judged to be the most effective for the geometry adopted, but it is possible that a different geometry would be more effective at a different frequency.

The combustor pressure loss, $p_{02} - p_{03}$, was measured over the full air mass flow rate range under cold conditions, and

$$\left[\frac{p_{02}-p_{03}}{p_{02}}\right]^{1/2}$$

was plotted against Mach number M_{ref} and compared with theoretically calculated values from the combustor aerodynamic analysis. As is usual for this type of combustor, M_{ref} was calculated at the maximum inside diameter of the casing (142.9 mm i.d.). The agreement is excellent, giving confidence in the test rig measurements and in extrapolating the results for aerodynamic scaling purposes.

Table 1 lists the range of test conditions used and indicates quite clearly that the experimental test conditions never exceeded the "half-load" value based upon the Mach number aerodynamic scaling factor M_{ref}. This was due to limitations of the test rig air supply. Because of this limitation, it has been necessary to justify the results by extrapolation to the "full-load" condition.

It is important to recognize, however, that acoustic driving of the dilution-air was being attempted at flow conditions of relevance to "full-load" operation. Furthermore, it should be noticed that the combustor was operated over approximately its full range of air/fuel ratio.

This particular combustor, without acoustic control, is one of three designed for a series of scaling experiments. The combustor is designed to operate on kerosene fuel and to give combustion efficiencies of 99 percent or better at an inlet temperature of 450 K, and above, at pressures exceeding 400 kPa. At these conditions, the design traverse qualities are Q $\simeq$ 15 percent and $Q_{radial} \simeq 6$ percent, with peak temperatures towards the turbine blade tips.

Combustor Measurements and Accuracy. The traversing thermocouples measuring the exit plane temperature distribution could be radially prositioned to ± 0.05 mm with circumferential deviation from the radial track of about ± 0.25 mm. The temperature was measured at eleven points across each of six diameters, nine situated at centers of equal annular area, with an additional two midway between the center-line (center of the fifth annulus) and center of the fourth annulus for graph plotting purposes, thereby dividing the exit plane into 66 measurement positions. The chromel-alumel thermocouples were accurate to ± 1 1/2 percent over the experimental range, which also encompassed errors due to fluctuations in a particular measurement. The flame tube wall thermocouples were similar.

The air and fuel mass flow rates were accurate to ± 1 1/2 percent, and ± 3 percent, respectively.

The stagnation pressures p_{02} and p_{03} were usually measured on the flow center-line except when p_{02} was being traversed to measure the inlet velocity profiles. Typical accuracy of the associated manometers was ± 1/4 percent, based on a manometer deflection of 200 mm.

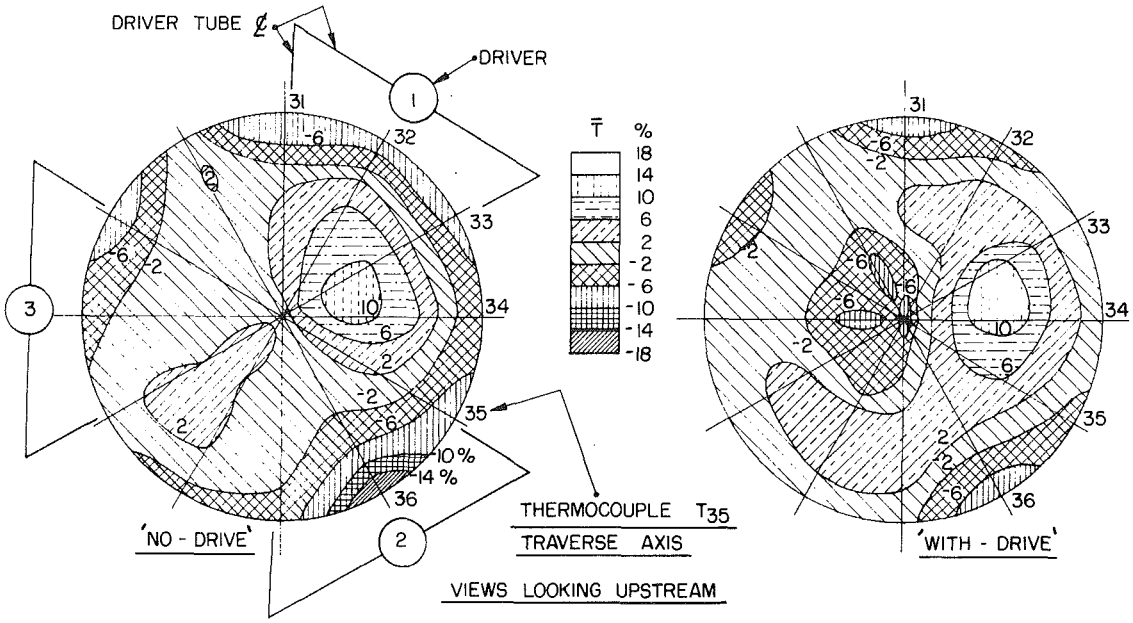

Fig. 4 Exit plane dimensionless temperature maps, test number 11 (see Table 1 for test conditions)

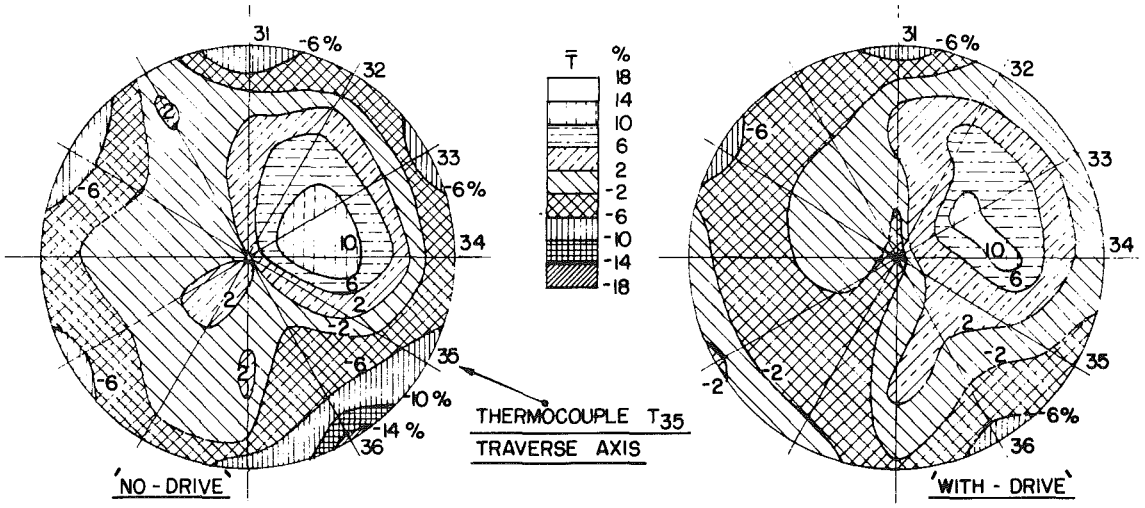

Fig. 5 Exit plane dimensionless temperature maps, test number 10

During the acoustic driving tests two amplifiers were used, one driving two loudspeakers in parallel, the other amplifier driving the remaining speaker. This was necessary in order to get the best impedance match and, hence, greatest power to the speakers. The same signal generator supplied a sinusoidal voltage to both amplifiers at the chosen frequency. Input power to a loudspeaker was measured by an a-c voltmeter and ammeter; the "maximum" power was then computed from the product of current and voltage.

Traverse Quality Results. The objectives of these measurements were to establish:

(*a*) that the temperature traverse was satisfactory, and typical, without acoustic drive;

(*b*) that the temperature pattern did not vary greatly with reasonable changes of running condition; and

(*c*) to determine the magnitude of changes in the temperature distribution brought about the introduction of acoustic drive.

In order to facilitate comparisons, the data are presented in terms of the local temperature defined in the nondimensional form

$$\bar{T}\% = \frac{T_3 - T_{3m}}{T_{3m} - T_2} \times 100$$

These dimensionless temperatures were plotted in contour form, for the various tests, for easy visual comparison. In addition, mean values were obtained for each depth of immersion, i.e., the six readings at one radial position were averaged, nondimensionalized in terms of

$$\bar{T}_r = \frac{T_{3r} - T_{3m}}{T_{3m} - T_2}$$

and plotted against radial position to give dimensionless "radial" temperature profiles. These correspond (approximately) to the radial temperature profiles in the annular section upstream of the turbine nozzle guide vanes, and indicate the sort of temperature distribution which would be "seen" by the turbine blades.

Both sets of data can be summarized in terms of the traverse qualities Q and Q_{radial}, where

$$Q = \frac{T_{3\max} - T_{3m}}{T_{3m} - T_2} \text{ and } Q_{\text{radial}} = \frac{T_{3r\max} - T_{3m}}{T_{3m} - T_2}$$

The temperature, T_{3m}, was obtained by averaging all the 66 measured individual values, and since equal annular area zones had been defined this was an energy averaged T_3. These values were then used in a statistical analysis of the tem-

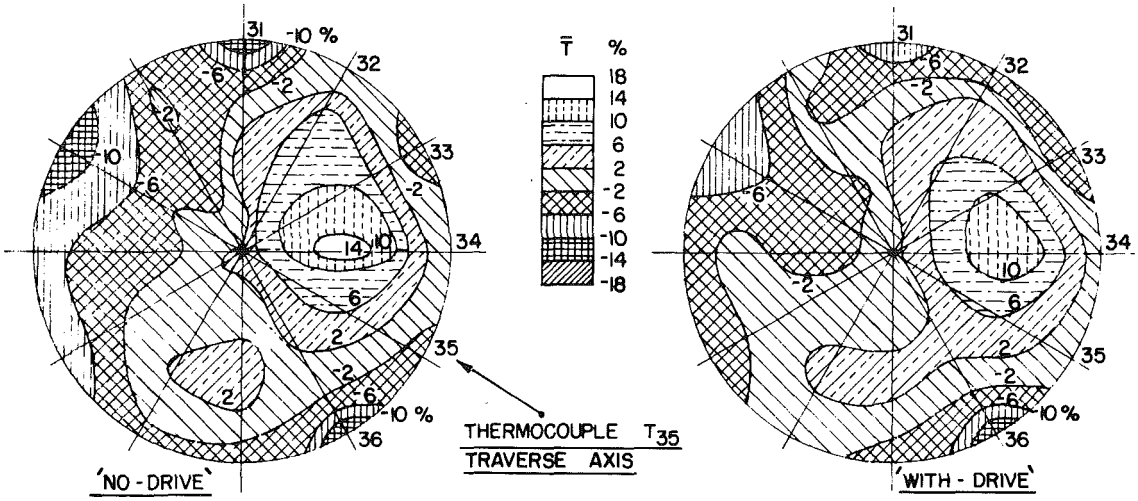

Fig. 6 Exit plane dimensionless temperature maps, test number 23

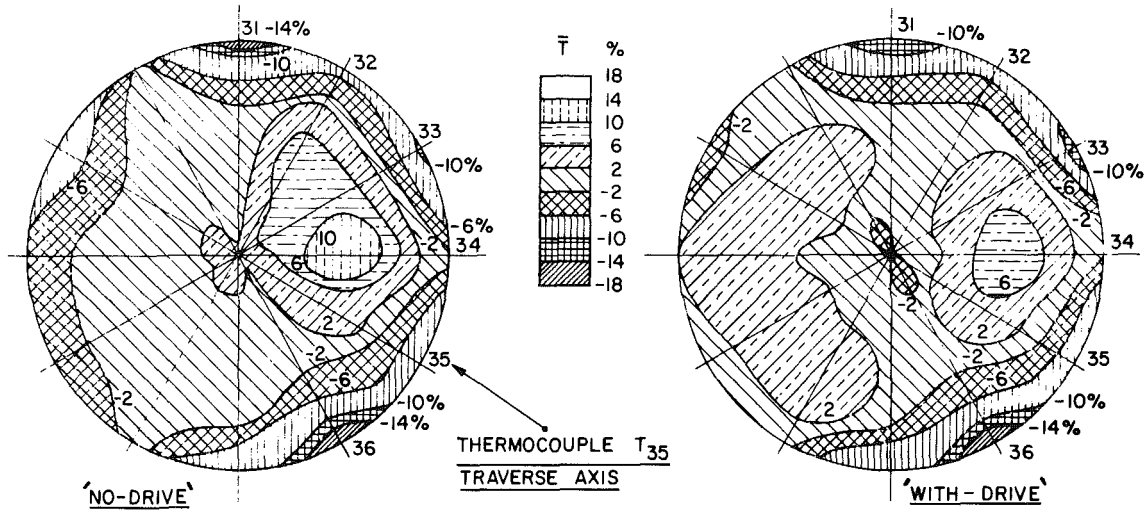

Fig. 7 Exit plane dimensionless temperature maps, (Test number 15)

perature distribution data. The results are summarized in Table 2.

Test Results "Without Acoustic Drive." Figures 4 to 8 show sample "no-drive" dimensionless temperature results. The similarity of the temperature distributions is immediately apparent as were the results for the three other tests. The "no-drive, radial" temperature profiles are typified by Fig. 8, good similarity between tests having been obtained. Both sets of data show an acceptable repeatability based upon comparisons between tests of similar $\dot{m}_a$ and A/F. The results show a temperature traverse that is satisfactory and typical for this kind of combustor without acoustic drive. The consistent behaviour of these results, over the full range of test conditions, adds to the excellent pressure loss performance reinforcing confidence in the extrapolation of data to other conditions. The traverse qualities Q and Q_{radial} are given in Table 2 and upon examination show a tendency to increase with increase of operating Mach number, which is normal. Thus the data suggests a traverse quality, Q, of about 18 percent at the nominal "full-load" condition. This is about 3 percent above design point, but considering that an undeveloped gas injector was used for these tests, it is considered to be satisfactory. The trend in Q_{radial} suggests a full-load value of some 9 percent, which is somewhat high but still acceptable. The standard deviation data for "no-drive",

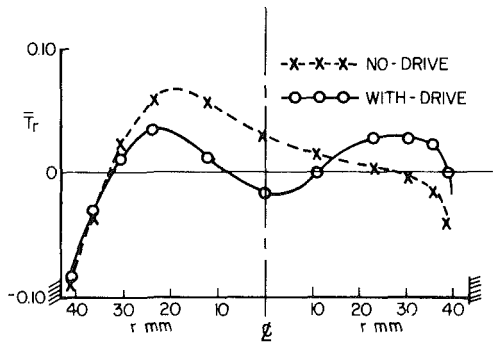

Fig. 8 Exit plane dimensionless "radial" temperature profiles, test number 23

Table 2, shows no discernable trends, the values of S_T/T_{3m} generally falling within normal test repeatability.

Test Results "With Acoustic Drive." Figures 4 to 8 also present typical dimensionless temperature distribution data for the "with-drive" condition for a drive frequency of 220 Hz. Two driver patterns have been explored as well as several driver powers, Table 1. It will be recalled that a major objective of the present tests was to examine whether or not acoustic modulation (at a low power level) could be successful in changing the temperature pattern of a combuster already

Table 2 Statistical analysis of the data and values of the temperature traverse qualities

Test number		T_{3m}K	S_TK	$\bar{S}_T$K	$\frac{S_T}{T_{3m}}$	Q	Q_{radial}
9	ND	925.1	30.30	3.73	0.0328	0.125	0.0583
	WD	927.2	34.11	4.20	0.0368	0.123	0.0696
10	ND	887.9	30.97	3.81	0.0349	0.121	0.0723
	WD	897.1	24.38	3.00	0.0272	0.112	0.0628
11	ND	926.8	30.61	3.77	0.0330	0.115	0.0610
	WD	928.2	27.36	3.37	0.0295	0.120	0.0720
13	ND	924.5	31.05	3.82	0.0336	0.111	0.0580
	WD	919.8	35.85	4.41	0.0390	0.139	0.0669
14	ND	916.3	30.00	3.69	0.0327	0.117	0.0598
	WD	913.2	27.38	3.37	0.0300	0.096	0.0415
15	ND	690.8	22.56	2.78	0.0327	0.154	0.0792
	WD	691.6	17.99	2.21	0.0260	0.135	0.0694
22	ND	989.3	33.33	4.10	0.0337	0.117	0.0537
	WD	986.4	29.69	3.65	0.0301	0.098	0.0388
23	ND	723.7	22.03	2.71	0.0304	0.100	0.0588
	WD	720.3	17.21	2.12	0.0239	0.080	0.0349

Where: ND = "no-drive" The mean $T_{3m} = \frac{1}{n}\sum_{i=1}^{n}(T_3)_i$ Standard deviation $S_T = \left[\frac{\Sigma(T_3)_i^2 - nT_{3m}^2}{n-1}\right]^{1/2}$

WD = "with-drive" Standard error of the mean $\bar{S}_T = \frac{S_T}{\sqrt{n}}$

possessing an acceptable outlet temperature distribution. It takes little more than a cursory glance at Figs. 4–8 to realize that this can be accomplished. Seven of the eight tests showed significant differences between "drive" and "no-drive" whilst the eighth showed dectectable differences. Table 2 summarizes the changes from the viewpoint of the combustion engineer. The observed changes are generally small (but definite), but this is not too surprising considering the good initial temperature distribution. The statistical results, Table 2, show no significant difference in T_{3m} for "drive" and "no-drive", as would be expected for mixing process effects only. The standard deviation S_T/T_{3m}, however, does show a significant difference between "drive" and "no-drive" conditions.

Wall Temperature, Hot Pressure Loss, and Weak Extinction Limit Measurements. For the "no-drive" condition the flame tube wall temperatures and hot pressure loss data were normal for this type of combustor and did not change significantly for the "with-drive" condition. The weak extinction measurements showed a normal richening of the A/F ratio as the air mass flow rate was increased, and no significant changes due to "drive" were observed. Under "with-drive" conditions the fuel mass flow rate remained constant and changes in the air mass flow rate were negligibly small.

Effectiveness of the Helmholtz Resonators. Two kinds of tests were run in an attempt to determine the effectiveness of the Helmholtz resonators. Both tests were run at conditions where the acoustic drive was most effective, namely at a low air mass flow rate, and a comparison made between performance with and without the resonators present (they could easily be disconnnected and the union blanked off). The first kind of test was made for the most successful arrangement, that of completely guiding the sound and dilution-air flows across the combustor annulus. The second kind of test was made with no guiding tubes across the annulus, and thus in this case the dilution-air was being supplied both from the dilution-air bypass tubes and the combustor annulus.

Maximum power at the loudspeakers was used for the same two driver patterns adopted in the temperature traverse quality measurements. Because of the time consuming nature of a full temperature distribution measurement, performance was assessed by exit plane temperature measurements with the six thermocouples (T_{31}, T_{32}, . . . T_{36}) set in a fixed pattern, at positions sensitive to changes caused by the acoustic drive, based on previous measurements. The possibility exists that for no guiding across the annulus the thermocouple positions chosen may not be sensitively located; however, they will give a relative measure but not necessarily an estimate of maximum changes. The data obtained are presented in Table 3 where it is readily seen that the Helmholtz resonators do not produce significant temperature changes. On the other hand, the increased acoustic effect, with full guidance across the annulus, is most marked.

Nature of the Modulated Dilution-Air Flows. A Thermal Systems, Inc. hot film anemometer was used to monitor the flow through one of the dilution ports. The hot film sensor was inserted radialiy through the elbow of the appropriate bypass tube and positioned inside the flametube some 16–20 mm downstream from the exit plane of the dilution-air hole. Because the sensor available was unsuitable for measurements in gas flows above 150°C, only cold air flows could be investigated. It was possible, however, to make measurements at air mass flow rates spanning the experimental range of the main tests. The turbulent nature of the flow made measurements difficult but as Fig. 9 shows, for low air mass flow rate, a pulsating flow with superimposed toroidal vortex has been detected. These data were obtained with the sensor at the edge of the air jet flow. Moving the sensor into the jet core showed pulsations only, confirming that the velocity structure

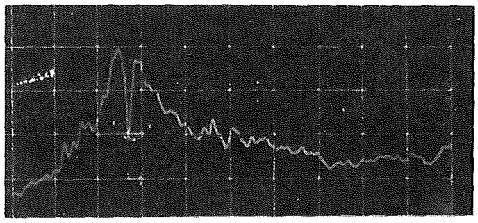

Oscilloscope trace showing vortex core

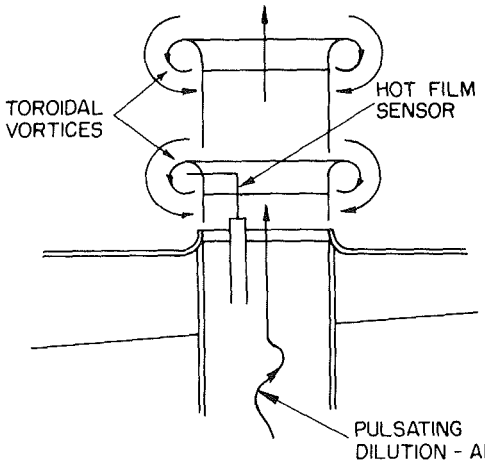

Fig. 9 Nature of the modulated dilution-air flows with interpretive sketch

at the edge was that of a toroidal vortex. Increasing the driver power increased the pulsation amplitude as well as the angular velocity of the vortex core. Increasing the air mass flow rate to maximum increased the turbulence level such that the vortex core was barely recognizable, although the pulsating nature was plainly evident. For the same driver power increasing the air mass flow rate was observed to decrease the vortex effects as well as the pulsation amplitude. Positioning the sensor inside the bypass tube, 20 mm from the dilution hole exit plane, showed good sinewave-like velocity pulsations at the driver frequency.

Whilst interpreting these results it must be remembered that the stationary sensor measures velocity magnitude only, and because of high flow turbulence, shaking of the dilution-air jet flow is equivalent to axial (combustor axis) shaking motion of the sensor. Thus it was very difficult to obtain measurement of a complete cycle of events at the same position relative to the flow.

By traversing the hot film sensor it was possible to measure approximately the inclination of the dilution-air jet flow boundary to the combustor axis. At the low mass flow rate of 0.099 kg/s the angle was 62 deg, whilst at the high mass flow rate of 0.171 kg/s the angle was 65 deg, both for no acoustic drive.

Derived Results – Combustion Efficiency. In order to obtain a measure of the combustion efficiency at the exit plane, the values of final temperature, T_3, with dissociation were calculated for methane/air mixtures having an air inlet temperature of 300 K. Then, knowing the operating air/fuel ratio (or equivalence ratio ϕ) for any condition, it was possible to compute the theoretical mean temperature rise through the combustor. From this and the actual mean temperature rise the combustion efficiency, η_{meas} was calculated. Then following the methods of reference [3], for the various tests, a theoretical efficiency, η_{th}, was calculated.

A comparison of the predicted results for combustion efficiency with those measured was made and is shown below for the best and worst cases:

Test	State	ΔT_{th}°C	ΔT_{meas}°C	η_{meas}	η_{th}
9	"no-drive"	688	618	0.898	0.897
	"with-drive"		617	0.897	
10	"no-drive"	657	581	0.884	0.852
	"with-drive"		589	0.897	

The agreement is considered to be satisfactory, and is all that can be expected bearing in mind the rather poor accuracy of combustion efficiency determinations made by thermocouples. On the basis of this agreement, two conclusions may be drawn:

(*a*) There is no evidence to suggest that the acoustic drive has any significant effect upon the overall combustion efficiency, nor is any expected since the combustion processes should be virtually completed before the flow enters the dilution zone.

(*b*) The reasonable agreement between the experimental values of combustion efficiency and the predicted ones suggests that predicitons could be made to other conditions with fair accuracy.

Discussion

The Temperature Measurements. Figures 4 and 5 show typical dimensionless temperature traverse data for all six dilution-air ports active for the "with-drive" condition. For these tests and test 9, the air/fuel ratio was maintained approximately constant and the power to all three drivers was balanced when in operation. Figure 4 shows the effects of simply increasing the driver power; a cool central core has been created whilst the hot peak remains. At the larger power of test 9, overpenetration occurred. These trends are indicated in Table 2, where test 9 shows a worsening of S_T/T_{3m} "with-drive," but test 11 (Fig. 4) shows a slight improvement indicating a flattening of the temperature distribution. However, the qualities Q and Q_{radial}, show a slight worsening because they are defined in terms of peak values. Increasing $\dot{m}_a$ for the higher drive condition removes the cold core but the hot spot remains, although reduced in size, Fig. 5 (test 10). Table 2 shows an improvement in S_1/T_{3m}, together with the qualities demonstrating generally a more even temperature distribution with acoustic drive.

Because of the persistent hot spot (at the 3 o'clock position looking upstream) experimentation with unbalanced driver powers was carried out, and it was found that the two dilution ports driven by No. 3 loudspeaker at 9 o'clock were effective in trimming this temperature peak. This effect is clearly shown in Fig. 6 (test 23) and by tests 14 and 22, where $\dot{m}_a$ and the drive power has been kept constant but the air/fuel ratio has been varied over the full range. The traverse qualities, Table 2, show improvement with acoustic drive substantiated by improvement in S_T/T_{3m}. There is still a tendency for a cooler central core under acoustic drive, also the region closest to the driven ports increases with temperature, together suggesting that the driven dilution-air jets have greater penetration properties. Test 13 demonstrated this quite dramatically, here the driver power was increased six times keeping $\dot{m}_a$ constant. A new hot spot ($\bar{T}$ = 14 percent) appeared at the wall in the 9 o'clock position, with a strong reduction in the hot spot at 3 o'clock ($\bar{T}$, 10 percent to 2 percent) and a marked change in the temperature contours, clearly a case of overdrive. The deterioration in the traverse qualities and in S_T/T_{3m} reflects this situation. Increasing the air flow rate to rig capacity and increasing the modulation power to half speaker capacity (considered to be a safe limit to avoid voice coil burn-out under sinusoidal current conditions), with A/F the same as in test 23 (Fig. 6), test 15 (Fig. 7), showed an improved temperature profile. The traverse qualities were improved as was S_T/T_{3m}, confirming this change.

Table 3 Effectiveness of the Helmholtz resonators

Thermo-couple	ΔT, Six driven ports, full guide tubes °C		ΔT, Six driven ports, no guide tubes °C	
	Helmholtz resonator	No resonator	Helmholtz resonator	No resonator
T_{31}	−12	−22	18	14
T_{32}	15	22	6	8
T_{33}	47	41	3	4
T_{34}	6	1	−1	−1
T_{35}	−29	−34	2	2
T_{36}	−76	−70	−23	−20
$\dot{m}_a$ kg/s	0.0974		0.0982	
A/F	63.6		64.8	

Where: ΔT = T 'No-Drive' − T 'With-Drive'

Driver	f, Hz	Power, W
1	220	57.2
2	220	69.5
3	220	57.2

Thermo-couple	ΔT, Two driven ports, full guide tubes °C		ΔT, Two driven ports, no guide tubes °C	
	Helmholtz resonator	No resonator	Helmholtz resonator	No resonator
T_{31}	53	54	14	12
T_{32}	51	50	21	11
T_{33}	70	66	23	17
T_{34}	47	44	5	2
T_{35}	15	7	−2	−2
T_{36}	−1	−2	−3	−4
$\dot{m}_a$ kg/s	0.0972		0.0982	
A/F	63.8		64.8	

Driver	f, Hz	Power, W
1	–	–
2	–	–
3	220	75.0

Comparing the "no-drive" and "with-drive" results of Figs. 6 and 7, and tests 14 and 22 for the L.H. half sector, shows an evening out of the temperature distribution suggesting better mixing effectiveness, probably due to the toroidal vortices. There has been a general temperature increase consistent with increased dilution-air jet penetration carrying the coolant to the R.H. half sector to reduce the temperature peak there.

The "radial" profiles, typified by Fig. 8, present generally the same picture as just discussed, though by definition the information is spatially less specific.

It is clear from the evidence presented, that significant changes in the temperature distribution of a "good" combustor are possible by acoustic control of the dilution mixing processes. Furthermore, even at the maximum air mass flow rate used, the driver power required to produce a significant effect was very small. The facts that the mean temperature (T_{3m}) was not significantly affected and the temperature changes were self compensating are what would be expected of processes with a predominantly mixing nature. It should be noticed that the radial flow and driving direction of the dilution-air flows is a constraint leading naturally to a cool central core. Other directions might be contemplated, but for this study were avoided in order to ensure minimum changes in combustor geometry. The ability to separately, acoustically control each dilution-air flow is obviously desirable but could not be carried out at this time because of the extra costs of additional amplifiers and loudspeakers. Compared with the previous work [1] the changes in traverse quality are not large but this cannot be expected when the traverse quality is already good at the outset. However, the ability to trim the temperature profile has been convincingly demonstrated and overall the results are sufficiently encouraging to further develop the technique.

Performance of the Acoustic Control System. Despite the care which had been taken to ensure a tuned driving system the discrepancy betwen the Helmholtz resonator frequency of 145 Hz and the test rig best driver frequency of 220 Hz indicates mismatched conditions. This was confirmed by the experiments which showed that the Helmholtz resonators when installed had little effect on the temperature profiles. Furthermore, the number of variables affecting the tuning mitigated against "hitting" the optimum conditions by purely experimental methods in the time available.

The loudspeakers were all operated in phase, and no significant change in the temperature pattern was observed when one speaker was operated 180 deg out of phase with the other two. It would appear that the driving phase of the dilution-air flows is not critical, however, a thorough investigation of this possibility will be attempted when the driving system has been fully tuned.

The fact that full guidance of the dilution-air flow across the combustion chamber air annulus enhanced the acoustic effects suggests that a completely contained flow up to the exit port is essential. Apparently acoustically driving the annulus is too "open" a situation to produce a modulated dilution-air jet.

Because the driver system appears to be mismatched, there is little point in trying to extrapolate the results to "full-load" engine conditions in order to estimate the acoustic power requirements. Compared with the previous tests in reference [1] however, the combustor operation has been increased from "one-tenth-load" to the "half-load" value. The total power at the drivers for significant effects has increased from 76 to 177 W, and at the maximum $\dot{m}_a$ currently used a single driver at 74 W driving two dilution-air ports was effective. In comparison to the energy conversion rate of the combustor, under the current test conditions of 100 kW, this driver power requirement is negligible.

Overall, the acoustic control system is not yet fully developed but has been adequate for the purposes so far.

The Dilution-Air Flows. The evidence presented clearly shows that the acoustically driven dilution-air flows consist of pulsating jet flows with superimposed toroidal vortices, confirming the assumption of the previous work [1]. This investigation was rather rudimentary but the flow nature was positively identified. Because of the turbulent nature of the flow it was not possible to make measurements to decide the relative importance of the flow modulation versus the toroidal vortices. General trends were established showing that increasing the driver power increased the pulsation amplitude and vortex strength, whilst increasing $\dot{m}_a$ (driver power constant) decreased the pulsation amplitude and vortex strength.

As was pointed out in the section on "The Temperature Measurements," the results obtained by driving only two dilution ports indicated a better mixing effectiveness than without drive. Reference [1] presents data showing that the field of influence of a jet one jet diameter downstream of its nozzle exit is about quadrupled by the superposition of a vortex. Thus the effective mixing diameter of the dilution-air

jet issuing from its 19.6 mm dia. port is doubled to about 40 mm, thereby affecting a sector from about the 7 o'clock to 11 o'clock positions (for two ports). This coincides with the observed zone of improved mixing effectiveness shown by Figs. 6 and 7, and, hence, it is probable that the improved mixing is due to vortex action. It is clear that a future experimental program is required to completely study the detailed behaviour of the modulated dilution zone flows; however, the nature of the modulated dilution-air jets has now finally been established.

The measured inclination to the combustor axis of the dilution-air jet flow of 62 deg to 65 deg compares favourably with the 60 deg of the standard combustor. Hence this factor has not had an active influence on the exit plane temperature profiles.

Conclusions

A small combustor of normal design employing acoustic control of the dilution-air flows has been successfully tested. The combustor, although still tested at "off-load" conditions, is much more representative of an engine combustor than the early one [1]. Overall it has been shown that acoustic modulation of the dilution-air flows can be used to control the exit plane temperature distribution. In particular, for an already good traverse quality, it is possible to trim the temperature profiles, and the results are sufficiently encouraging to further develop the technique. The study contributes to the design of combustors such that a desired exit plane temperature distribution may be achieved.

The nature of the acoustically modulated dilution-air flows has been clearly established as that of a pulsating jet flow with superimposed toroidal vortices. Because of the turbulent nature of the flow it was not possible to make measurements to decide the relative importance of the flow modulation versus the toroidal vortices. The temperature profile behaviour, however, indicates that improved mixing may be due to vortex action. Successful flow modulation was achieved up to "half load" conditions, indicating that driver power requirements at "full-load" will not dramatically increase.

There appears to be no effect due to the acoustic drive upon combustion efficiency. The latter, as predicted by the Odgers-Carrier equation shows reasonable agreement with the measured values.

The pressure loss of the unit, as measured, is in agreement with the theoretical value based upon the aerodynamic survey. It is typical of an aircraft combustor. Furthermore, the increase in pressure loss with acoustic drive was found to be insignificant.

Acknowledgments

The authors are indebted to Mr. J. Holdsworth, Chief Technical Supervisor, and to Mr. J. B. Wilkinson, Workshop supervisor, and their staffs for careful work in the building of the combustor test rig. Particular thanks are due to Mr. R. W. Gustafson, Technician, for expert help with measurement problems and to Miss Diane Bilozir, undergraduate, for competent and dedicated assistance in carrying out the experimental work and the analysis of data.

The work could not have taken place without the financial support of the National Science and Engineering Research Council of Canada, under Grant No. A7801, nor could it have been brought to timely completion without the award of a Killam Resident Fellowship to the first author.

References

1 Vermeulen, P. J., and Odgers, J., "Acoustic Control of the Exit Plane Thermodynamic State of a Combustor," ASME 24th Gas Turbine Conference, San Diego, Calif., Mar. 12–15, 1979, Paper No. 79-GT-180, pp. 1–12.

2 Kinsler, L. E., and Frey, A. R., "Resonators and Filters," ch. 8, *Fundamentals of Acoustics*, 2nd Ed., Wiley, New York, 1962, pp. 205–207.

3 Odgers, J., and Carrier, C., "Modeling of Gas Turbine Combustors: Considerations of Combustion Efficiency and Stability," ASME JOURNAL OF ENGINEERING FOR POWER, Vol. 95, No. 4, Apr. 1973. pp. 105–113.

K. V. L. Rao
Scientist,
Propulsion Division,
National Aeronautical Laboratory,
Bangalore, India

A. H. Lefebvre
Reilly Professor of Combustion Engineering
Purdue University,
West Lafayette, Ind.

Flame Blowoff Studies Using Large-Scale Flameholders

Experimental and theoretical studies are made of the factors governing the blowoff velocities of stabilized flames supplied with flowing gaseous combustible mixtures. The test program includes wide variations in effective pressure, obtained using the water injection technique, and also covers wide ranges of velocity, flameholder size, and flameholder blockage. An equation is derived for predicting blowoff velocities which shows good agreement with the experimental data.

Introduction

A widely used method for stabilizing a flame in a flowing stream of combustible mixture is by the insertion of a bluff object such as a disk, cone, or "Vee"-gutter, which produces in its wake a low-velocity recirculatory flow region in which combustion can be initiated and sustained. The mechanism of flame spread to other regions of the flow is by the transport of heat and active species from the shear layer which surrounds the recirculation zone to the adjacent fresh mixture.

The stabilizing performance of a bluff-body flameholder is usually described either in terms of the range of equivalence ratios over which stable combustion can be achieved, or by the maximum flow velocity that the system can tolerate before flame extinction occurs. Both aspects are important in practical combustion systems. Ballal and Lefebvre [1, 2] have investigated in detail the factors that govern the lean blowoff limits of bluff-body stabilized flames supplied either with homogeneous combustible mixtures or with heterogeneous mixtures of fuel drops of air. Their model for the mechanism of lean blowoff provides very satisfactory correlation of their experimental data as well as the results obtained by other workers [3]. Unfortunately, the model is valid only for equivalence ratios below around 0.7. This limitation provides the main motivation for the present work, which is to develop a model for predicting peak blowoff velocities which usually occur at or near the stoichiometric fuel/air ratio. Another objective is to determine experimentally the peak blowoff velocities of large-scale flameholders, of comparable size to those employed in practical combustion systems.

Due to apparatus limitations, in particular the difficulty and high cost of providing high air flow rates at low (subatmospheric) pressures, most of the previous work on bluff-body flame stabilization has utilized fan air. This is essentially at atmospheric pressure, so that where the flameholders tested have been of a practical size, the results have usually been confined to very weak or very rich mixtures. Where tests have been carried out in the most interesting fuel/air ratio range, i.e., near stoichiometric, either velocities have been very high or dimensions very small. In either event extrapolation to practical velocities or practical dimensions has been a somewhat dubious process. It is difficult to extrapolate dimensions because any such extrapolation must also take into account effects arising from a change in "blockage". It is equally difficult to extrapolate velocities because at high velocites compressibility effects can change the flow pattern in and around the combustion zone.

In the present study this problem is surmounted using the well-established "water injection technique" in which low pressures are simulated by injecting water or steam into the fuel-air mixture flowing into the combustion zone. This approach allows complete stability loops to be drawn for large flameholders, up to 8cm in effective width, at simulated pressures down to one-twentieth of an atmosphere.

Water Injection Technique

The main advantage of the water injection technique is that it allows the combustion performance of large-scale combustion systems to be fully evaluated while operating within their normal range of velocities and fuel/air ratios. Air is supplied at normal atmospheric pressure, usually from a fan, and lower pressures are simulated by introducing water into the combustion zone. The success of the method relies on the inability of the reaction zone to detect the difference between a reduction in gas pressure and a reduction in reaction temperature which, in this instance, is accomplished by the addition of water.

The apparatus employed is shown schematically in Fig. 1. Essentially, it comprises a supply of air at atmospheric pressure, a preheat combustion chamber, a working section containing the flameholder under test, and provision for injecting kerosine and water in well-atomized form into the flowing gas upstream of the flameholder. Sufficient time and temperature is provided between the planes of injection of water and kerosine and the flameholder to ensure that both liquids are fully prevaporized and premixed upstream of the reaction zone.

The test procedure is quite simple. The velocity and temperature of the gas flowing over the stabilizer are adjusted to the desired values; the fuel is turned on and a flame established in the recirculation zone downstream of the stabilizer. Water is then gradually admixed with the kerosine in increasing amounts until extinction occurs. This process is repeated at a sufficient number of fuel flow rates for a complete stability loop to be drawn.

Contributed by the Gas Turbine Division of THE AMERICAN SOCIETY OF MECHANICAL ENGINEERS and presented at the 27th International Gas Turbine Conference and Exhibit, London, England, April 18-22, 1982. Manuscript received at ASME Headquarters November 30, 1981. Paper No. 82-GT-36.

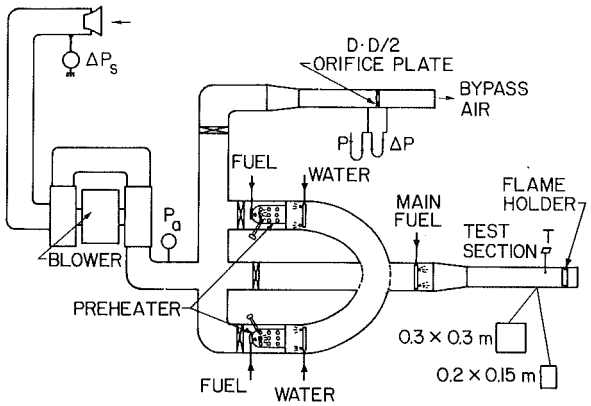

Fig. 1 Schematic diagram of test rig

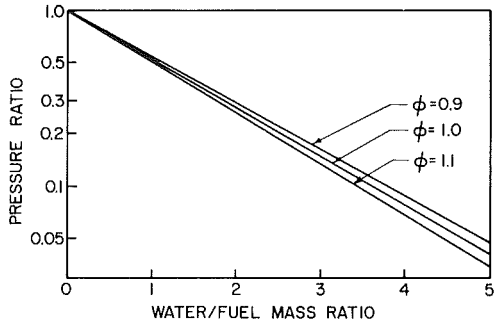

Fig. 2 Relationship between water/fuel mass ratio and effective pressure ratio

Curves of this type provide a useful means for comparing the basic stability of various designs of flameholder. The only assumption involved is a reasonable one, namely that the flameholder requiring the largest amount of water to cause flame extinction has the best stability. The value of the technique is greatly enhanced by the relationship which has been derived from global reaction rate considerations between the amount of water added and the equivalent reduction in gas pressure [4, 5]. This relationship is illustrated in Fig. 2. In general, it is found that injecting into the combustion zone a quantity of water equal to the kerosine flow rate is equivalent to halving the gas pressure.

Experimental

Two rectangular test sections, size 0.15 × 0.2m and 0.3 × 0.3m, were employed in order to separate the effects of flameholder size from those of flameholder blockage. Several Vee-gutter flameholders were constructed with included angles of 30, 45, 60, 90, and 180 deg. Normally the flameholder was mounted vertically at the center of the test section with its apex pointing upstream. However, one series of tests was conducted with a 180 deg gutter (i.e., a flat plate) fitted to the top of the test section. The purpose of this

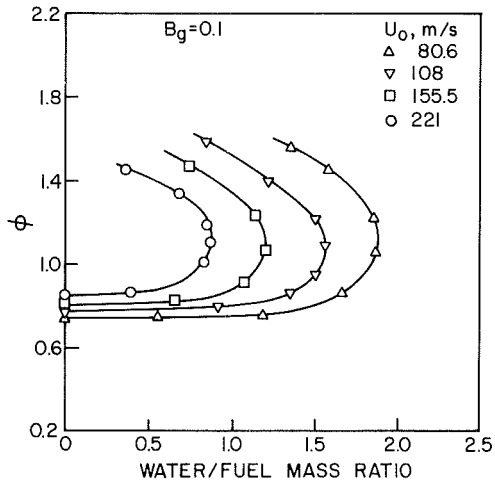

Fig. 3 Stability loops for a 30 deg Vee-gutter: D_c = 0.02m, test section 0.15 × 0.2m

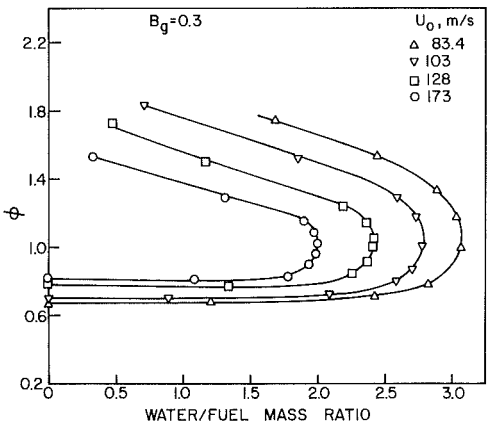

Fig. 4 Stability loops for a 30 deg Vee-gutter: D_c = 0.061m, test section 0.15 × 0.2m

arrangement was to produce a single-vortex flow pattern in the flameholder wake instead of the usual double-vortex formation.

The experimental program covered the following ranges of velocity, temperature, and effective pressure as measured in the gases just upstream of the flameholder.

Velocity	30–220 m/s
Temperature	373–565 K
Effective pressure	4.2–35.2 kPa

The effect of flameholder size on stability is illustrated in Figs. 3 and 4 for the 0.15 × 0.2m test section, and in Figs. 5 and 6 for the 0.3m square test section. Increase in flameholder size improves stability by extending the residence time of the reactants in the wake region. This is indicated in the figures by

Nomenclature

B_a = aerodynamic blockage of flameholder
B_g = geometric blockage of flameholder, flameholder csa/duct csa
C_s = flameholder shape factor, B_a/B_g
c_p = specific heat at constant pressure
D_c = characteristic dimension (geometric) of flameholder
k = thermal conductivity
$\dot{m}_m$ = mass rate of mixture consumed per unit volume
n = reaction order
P = pressure
Pr = Prandtl number, $c_p\mu/k$
R = gas constant
Re = Reynolds number based on flame speed ($S_L D_c \rho_0/\mu_0$)
S_L = laminar flame speed
T = temperature
t_c = time required for combustion
t_r = residence time in wake region
U = velocity
U_{BO} = blowoff velocity
α = thermal diffusivity, $k/c_p\rho$
μ = dynamic viscosity
ρ = density P_{eff}/RT_0

Subscript

0 = value just upstream of flameholder

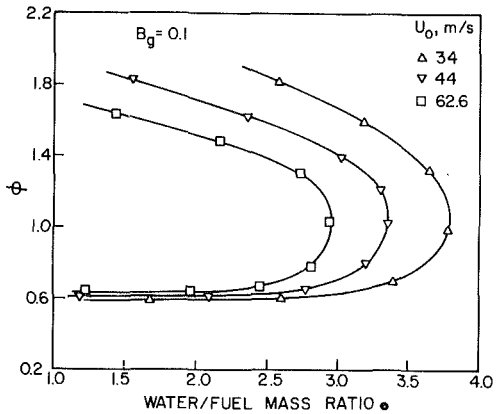

Fig. 5 Stability loops for a 30 deg Vee-gutter: D_c = 0.0305m, test section 0.3 × 0.3m

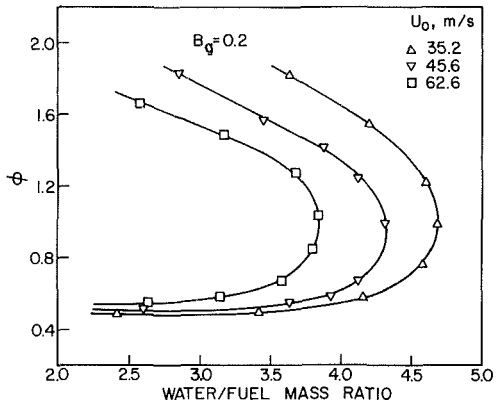

Fig. 6 Stability loops for a 30 deg Vee-gutter: D_c = 0.061m, test section 0.3 × 0.3m

the additional quantity of water needed to effect flame extinction with the larger flameholders.

The influence of flameholder shape on flame blowoff is illustrated in Fig. 7. The five stability loops drawn in this figure represent five Vee-gutters, all havig the same geometric blockage (B_g = 0.2) but different included angles (30, 45, 60, 90, and 180 deg). The work of Barrere and Mestre [6] showed that the shape of a bluff-body flameholder affects its stability characteristics through its influence on the size and shape of the wake region. For Vee-gutters an increase in included angle increases the size of the recirculation zone and thereby extends the residence time of the reactants in the combustion zone. The beneficial effect on stability due to increase in included angle is very apparent in Fig. 7. These results support Barrere and Mestre's suggestion that the flame-stabilizing properties of a bluff-body flameholder should be based not on its geometric width, but on the maximum width of the wake created behind it. It follows, of course, that the fresh mixture velocity of most relevance to stability is the velocity calculated downstream of the flameholder in the plane of maximum aerodynamic blockage. A method for calculating the aerodynamic blockage, B_a, of any given size and shape of flameholder has been described by Lefebvre [7], and is discussed later.

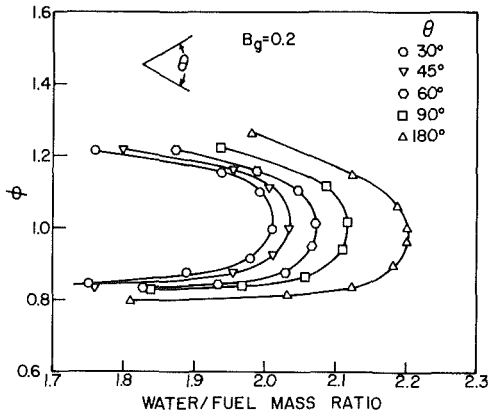

Fig. 7 Graphs illustrating the effects of flameholder forebody shape on stability

Increase in stream velocity affects stability adversely by reducing the time available for combustion. This is illustrated in Fig. 8 which shows four stability loops obtained with a rectangular flatplate flameholder, size 0.0406 × 0.15m, mounted vertically at the center of the 0.15 × 0.20 test section. Similar results were obtained when the flat plate flameholder was mounted at the top of the test section to create a large single flow recirculation in its downstream wake, as illustrated in Fig. 9. Comparison of Figs. 8 and 9 shows the superior stabilizing characteristics of the single vortex flow pattern for the same geometric size of flameholder. This point is further illustrated in Fig. 11. In general it was found that blowoff velocities for flameholders featuring single-vortex flow were around 25 percent higher than for flameholders of the same geometric blockage employing conventional double-vortex wake regions.

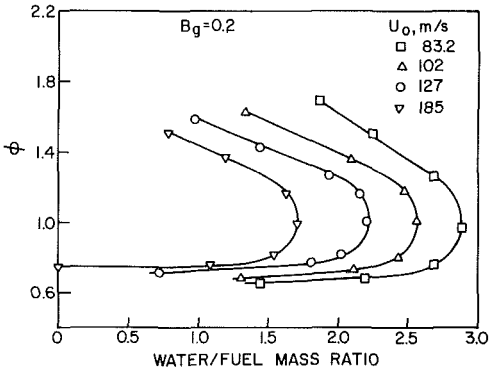

Fig. 8 Graphs illustrating the effect of approach stream velocity on the stability performance of a flat plate flameholder, D_c = 0.041m

Theoretical Aspects

Many theoretical studies have been carried out on bluff-body flame stabilization and several models have been proposed to account for the experimental observations on flame blowoff. Most of these models tend to fall into two main categories. One of these, following Longwell et al. [8], views the wake region of a bluff-body essentially as homogeneous chemical reactor. Flame extinction occurs when the time available for chemical reaction becomes less than the time required to generate sufficient heat to raise the fresh mixture up to its ignition temperature. The other category

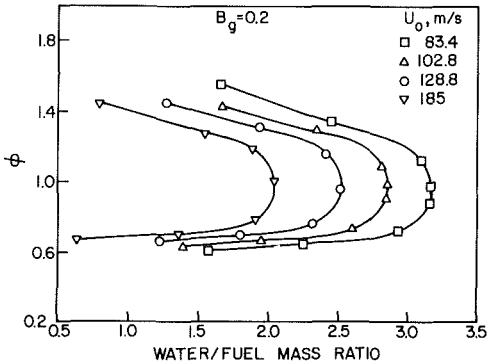

Fig. 9 Stability loops for a flat plate flameholder, D_c = 0.041. Plate is mounted across top of test section to produce a single-vortex flow pattern.

includes models in which attention is focused mainly on the shear layer surrounding the wake region [9, 10, 11]. According to Zukowski and Marble [9], ignition of the fresh mixture occurs in the shear layer when it is turbulently mixed with combustion products from the recirculation zone. The burning mixture then flows downstream through the shear layer and, in turn, ignites neighboring mixture kernels. When it reaches the end of the wake region some of the burning mixture continues to flow downstream, and the remainder is entrained into the recirculatory flow, which conveys it upstream to mix with and ignite the shear layer. Through continuation of this process a flame is anchored on the baffle. Blowoff occurs when the fresh mixture does not spend enough time in the shear layer to be ignited by the hot recirculation zone. Thus the criterion for blowoff is that the ignition delay time be equal to the residence time in the shear layer adjacent to the recirculation zone.

Which of these two basic approaches has the most fundamental significance and relevance to flame stabilization is uncertain but, fortunately, is of academic interest only as far as the development of a suitable correlation for blowoff velocity is concerned. This is because the time spent by the fresh mixture in the shear layer, and the residence time of the combustion products in the recirculation zone, are both proportional to the characteristic dimension, D_c, of the flameholder. Since the material entering the recirculation zone at its downstream edge has already passed through the shear layer it would seem more logical to define the residence time as the sum of the times spent in the shear layer and the recirculation zone. However, since this total time is also proportional to D_c, this assumption does not change the resulting correlation. This, of course, is why many workers who appear to base their analyses on a seemingly different set of assumptions, all arrive eventually at the same general conclusion, namely, that the equivalence ratio at blowoff is a function of $U P^x D_c^y T_0^z$, where U is the velocity past the baffle, P is pressure, and T_0 is the inlet gas temperature. Although the experimental data show some variation in the values of x and y, apart from tests carried out at low Reynolds number, both x and y are usually fairly close to unity. For information on the values x, y, and z obtained experimentally prior to 1960, reference should be made to the survey papers of Longwell [12], Penner and Williams [13], and Herbert [14]. The purpose of this brief discussion is to point out that, from a practical viewpoint, the best correlating parameter is the one which has the greatest ease and breadth of application, regardless of how simple or sophisticated are the assumptions employed in its derivation.

In recent years, Ballal and Lefebvre [1, 2] have investigated the blowoff characteristics of bluff-body flameholders in some detail. However, their analysis, which includes both gaseous and heterogeneous fuel-air mixtures, is valid only for equivalence ratios of less than 0.7. For near-stoichiometric mixtures, corresponding to peak blowoff velocities, these workers [3] adopted a different approach, along the following lines.

The residence time in the wake region, t_r, is given by

$$t_r \propto D_c/U \tag{1}$$

The time required for combustion, t_c, is obtained as

$$t_c \propto \rho_0/\dot{m}_m \tag{2}$$

where $\dot{m}_m$ is the mass rate of fresh mixture consumed per unit volume. At blowout, i.e., when $U = U_{BO}$, then $t_r = t_c$ and

$$\frac{D_c}{U_{BO}} \propto \frac{\rho_0}{\dot{m}_m}$$

or

$$U_{BO} \propto D_c \dot{m}_m/\rho_0 \tag{3}$$

Now volumetric heat release rates can be related to laminar flame speeds by an expression of the form

$$S_L \propto \left[\frac{\dot{m}_m \alpha_0}{\rho_0}\right]^{0.5} \tag{4}$$

Substituting for $\dot{m}_m$ from equation (4) into equation (3) gives

$$U_{BO} \propto C_s (D_c S_L^2/\alpha_0)$$

where C_s is a shape factor whose value depends on the various parameters that influence the shape of the wake region, such as flameholder geometry and base drag coefficient. The analysis of published data on U_{BO} conducted by Ballal and Lefebvre [3] showed that the constant of proportionality in this equation is unity, so that

$$U_{BO} = C_s (D_c S_L^2/\alpha_0) \tag{5}$$

Equation (5) was used to correlate blowout data obtained by Haddock [15], De Zubay [16], Zukowski and Marble [9], and Longwell [12]. The very satisfactory agreement obtained between the theoretical predictions on the effects of variations in pressure, temperature, and baffle size, and the actual experimental data lend support to the validity of the simple model for blowout velocity described above.

Equation (5) can be derived more directly by defining the combustion time as the ratio of the flame thickness to the flame speed, δ/S_L. Since $\delta \propto \alpha_0/S_L$, the combustion time is obtained as

$$t_c \propto \frac{\alpha_0}{S_L^2} \tag{6}$$

Equating (1) and (6) and introducing the shape factor, C_s, leads once more to

$$U_{BO} = C_s (D_c S_L^2/\alpha_0) \tag{5}$$

Similar relationships indicating the same dependence of blowout velocity on laminar flame speed and flameholder dimensions have been proposed by Putnam and Jensen [17], Spalding [18], Loblich [19], and Radhakrishnan et al. [11].

For a flameholder in a duct, equation (5) becomes

$$U_{BO} = C_s (1 - B_a) (D_c S_L^2/\alpha_0) \tag{7}$$

where B_a is the aerodynamic blockage, which is related to B_g, the geometric blockage, by the expression (7),

$$[1/(1 - B_a)^2 - 1] = \Omega[B_g/(1 - B_g)^2] \tag{8}$$

For the Vee-gutters employed in the present experiments

$$\Omega = 3.7\left(\sin\frac{\theta}{2}\right)^{0.25} \tag{9}$$

Equations (8) and (9) also define the shape factor, C_s, since for a ducted system $C_s = B_a/B_g$. Appropriate values of C_s for flameholders located in a free stream have been reported by Ballal and Lefebvre [3].

Substituting for $\alpha = k/c_p\rho$, and $k = c_p\mu/\mathrm{Pr}$, allows equation (7) to be written in dimensionless form as

$$U_{BO}/S_L = C_s (1 - B_a)\,\mathrm{Re}\,\mathrm{Pr} \tag{10}$$

where Pr is the Prandtl number of the fresh mixture, and Re is a "Reynolds number" ($D_c\ S_L\ \rho_0/\mu_0$) based on laminar flame speed.

Figure 10 shows the measured peak values of U_{BO}, as obtained by the water injection technique, plotted against the right hand side of equation (10). The level of agreement between the predicted values of U_{BO} and the actual experimental data is clearly very satisfactory.

Equations (7) and (10) show that U_{BO} is directly proportional to the wake width, $C_s D_c$. Pressure affects U_{BO} via S_L and ρ_0. Since $S_L \propto P^{(n-1)/2}$, we have

$$U_{BO} \propto P^{(n-1)} \tag{11}$$

where n is the reaction order. The experimental data show that $U_{BO} \propto P$, thus indicating a value of $n = 2$ for kerosine. The influence of inlet temperature on U_{BO} is also manifested through S_L and ρ. In the present analysis the temperature dependence of S_L was assumed to be the same as that observed by Dugger et al. [20] for propane. For stoichiometric kerosine/air mixtures this gives

$$S_L = 0.129 + 3.42 \times 10^{-6} T_0^2 \text{ m/s} \quad (12)$$

Figure 11 shows the peak blowoff velocities obtained with the flat-plate flameholder fitted across the top of the test section. Also shown in this figure are the corresponding data for the same plate when located centrally in the same test section. The superior stability of the single-vortex system is very evident in this figure; in fact its blowoff velocty is on average 25 percent higher than for the double-vortex system. Presumably this is due to the longer residence time provided by the single-vortex flow pattern. Further tests are planned to investigate this aspect in more detail.

Conclusions

From simple considerations of residence time and chemical reaction time in the wake region of bluff-body stabilized flames, it is concluded that the influence of operating conditions and flameholder size, geometry, and blockage is adequately described by the relationships

$$U_{BO} = C_s(1 - B_a)\,(D_c\, S_L^2/\alpha_0)$$

or

$$U_{BO}/S_L = C_s\,(1 - B_a)\ \text{Re Pr}$$

Thus for premixed combustible gases blowoff velocity is governed mainly by inlet air temperature and pressure, and the flow velocity downstream of the flameholder in the plane of maximum aerodynamic blockage. Blowoff velocities are also extended by an increase in flameholder size and reduction in flameholder blockage.

Predictions of blowoff velocity based on the above equations show good agreement with the corresponding experimental values obtained for kerosine-air mixtures over wide ranges of effective pressure, temperature, velocity, flameholder size and flameholder blockage.

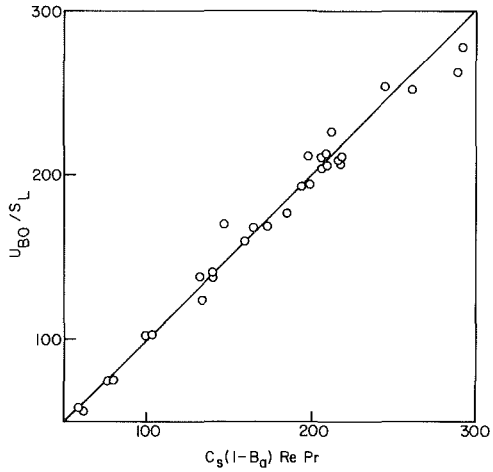

Fig. 10 Comparison of measured values of peak blowoff velocity with predicted values from equation (10)

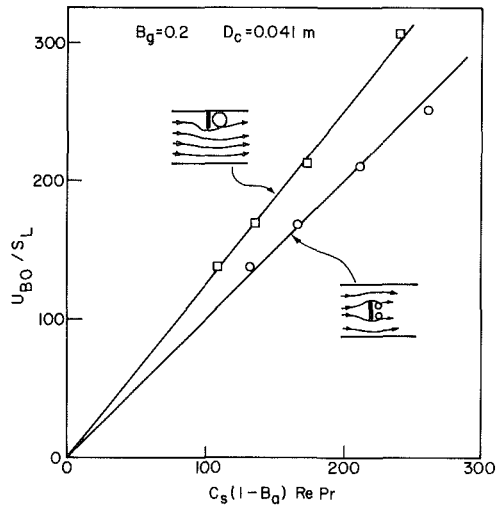

Fig. 11 Graphs illustrating higher peak blowoff velocities obtained with single-vortex wake region

Acknowledgment

Support of the work reported here by the U.S. Air Force Office of Scientific Research, with Dr. B. T. Wolfson serving as technical monitor for the project, is gratefully acknowledged.

References

1 Ballal, D. R., and Lefebvre, A. H., "Weak Extinction Limits of Turbulent Flowing Mixtures," ASME JOURNAL OF ENGINEERING POWER, Vol. 101, No. 3, 1979, pp. 343-348.

2 Ballal, D. R., and Lefebvre, A. H., "Weak Extinction Limits of Turbulent Heterogeneous Fuel/Air Mixtures," ASME JOURNAL OF ENGINEERING POWER, Vol. 102, No. 2, 1980, pp. 416-421.

3 Ballal, D. R., and Lefebvre, A. H., "Some Fundamental Aspects of Flame Stabilization," *Fifth International Symposium on Air-breathing Engines*, Bangalore, India, Feb. 1981.

4 Greenhough, V. W., and Lefebvre, A. H., "Some Applications of Combustion Theory to Gas Turbine Development," *Sixth Symposium (International) on Combustion*, The Combustion Institute, Pittsburgh, 1956, pp. 858-869.

5 Lefebvre, A. H., and Halls, G. A., "Simulation of Low Combustion Pressures by Water Injection," *Seventh Symposium (International) on Combustion*, The Combustion Institute, Pittsburgh, 1958, pp. 654-658.

6 Barrère, M., and Mestre, A., "Stabilisation des Flammes par des Obstacles," *Selected Combustion Problems: Fundamentals and Aeronautical Applications*, in French; English summary, Butterworth Scientific Publications, 1954, pp. 426-446.

7 Lefebvre, A. H., "A Method of Predicting the Aerodynamic Blockage of Bluff Bodies in a Ducted Airstream," *CoA Report Aero. No. 188*, College of Aeronautics, Cranfield, Bedford, England, Nov. 1965.

8 Longwell, J. P., Frost, E. E., and Weiss, M. A., "Flame Stability in Bluff Body Recirculation Zones," *Industrial and Engineering Chemistry*, Vol. 45, No. 8, 1953, pp. 1629-1633.

9 Zukowski, E. E., and Marble, F. E., "The Role of Wake Transition in the Process of Flame Stabilization on Bluff Bodies," *AGARD Combustion Researches and Reviews, London*: Butterworths Scientific Publishers, 1955, pp. 167-180.

10 Plee, S. L., and Mellor, A. M., "Characteristic Time Correlation for Lean Blowoff of Bluff-Body-Stabilized Flames," *Combustion and Flame*, Vol. 35, 1979, pp. 61-80.

11 Radhakrishnan, K., Heywood, J. B., and Tabaczynski, R. J., "Premixed Turbulent Flame Blowoff Correlation Based on Coherent Structures in Turbulent Flows," *Combustion and Flame*, Vol. 42, 1981, pp. 19-33.

12 Longwell, J. P., "Flame Stabilization by Bluff Bodies and Turbulent Flames in Ducts," *Fourth Symposium (International) on Combustion*, The Williams and Wilkins Company, Baltimore, Md, 1953, pp. 90-97.

13 Penner, S. S. and Williams, F., "Recent Studies on Flame Stabilization of Premixed Turbulent Gases," *Applied Mechanics Reviews* 10, June 1957, pp. 229-237.

14 Herbert, M. V., "Aerodynamic Influences on Flame Stability," *Progress in Combustion Science and Technology*, Vol. 1, edited by J. Ducarme, Melvin Gerstein, and A. H. Lefebvre, New York, Pergamon Press, 1960, pp. 61-109.

15 Haddock, G. W., "Flame-Blowoff Studies of Cylindrical Flame Holders in Channeled Flow," Progress Report 3-24, May 1951, Jet Propulsion Laboratory, California Institute of Technology, Pasadena, Calif.

16 De Zubay, E. A., "Characteristics of Disk-Controlled Flame," *Aero Digest*, Vol. 61, No. 1, 1950, pp. 54-56 and 102-104.

17 Putnam, A. A., and Jensen, R. A., "Application of Dimensionless Numbers to Flashback and Other Combustion Phenomena," *Third Symposium (International) on Combustion*, The Williams and Wilkins Company, Baltimore, Md., 1949, pp. 89-98.

18 Spalding, D. B., "Theoretical Aspects of Flame Stabilization," *Aircraft Engineering*, Vol. 25, Nov. 1953, pp. 264-276.

19 Loblich, K. R., "Semitheoretical Consideration on Scaling Laws in Flame Stabilization," *Ninth Symposium (International) on Combustion*, Academic Press, New York, 1963, pp. 949-957.

20 Dugger, G. L., and Heimel, S., "Flame Speeds of Methane-Air, Propane-Air, and Ethylene-Air at Low Initial Temperatures," NACA TN 2624, 1952.

Flame Imprinted Characteristics of Ash Relevant to Boiler Slagging, Corrosion, and Erosion

E. Raask

Central Electricity Research Laboratories,
Kelvin Avenue,
Leatherhead, Surrey, United Kingdom

Pulverized fuel flames imprint marked characteristics on different particulate species which influence their subsequent behavior in boiler plant. The paper discusses some of the high temperature changes, namely, the transformation of irregularly shaped mineral granulates to spherical shapes found in ash, coal/ash interface behavior and the surface properties of semi-molten ash particles, combustion of the ash-rich coal particles, and the release of potassium from alumino-silicates. This is followed by a brief assessment of relevance of the findings to boiler slagging, corrosion and erosion.

1 Introduction

Pulverized coal firing is likely to remain the principal mode of converting the fuel energy to electricity for several decades to come. The chief advantage of the system is its versatility, and large boiler units can be designed to utilize different types of solid fuel mined at present, i.e., peat, lignite, sub-bituminous and bituminous coals, and anthracite. The mineral matter in solid fuels can cause many boiler operation difficulties resulting in reduction of power generating efficiency or in a shutdown of boiler plant.

This paper sets out to examine the physical changes and chemical reactions of the silicate minerals in pulverized coal during their passage through boiler flame. This is followed by a discussion on relevance of the findings to some of the major boiler operation problems, namely slagging, high temperature corrosion, and the erosion wear of economizer water preheater and low temperature steam tubes caused by impaction of the gas borne ash particles.

2 Shape Transformation of Flame Borne Silicate Particles

Silicate minerals, together with silica (quartz) constitute the major impurity fraction in most coals and it is therefore essential to consider the physical changes and chemical reactions which take place when the particulate coal minerals are subjected to rapid heating in a boiler flame. Figure 1 shows the temperature/time plot for the particulates carried through the flame and subsequently through the heat exchange sections of a 500 MW pulverized coal fired boiler [1].

During the short heating period, hydrated silicate minerals undergo endothermic dehydration reactions which commence at about 300 K with a loss of surface-adsorbed and inter-lattice water. Dehydroxylation of "chemically" bounded water in the clay minerals, chiefly kaolinite, montmorillomite and illite commences at 650 K. Above 1100 K the endothermic lattice destruction and the exothermic phase transformation of the clay minerals will take place. The dehydration, dehydroxylation, lattice degradation and phase transformation reactions have been usually studied by the differential thermal analysis (DTA) techniques where the heating rates are low, i.e., between 1 and 20 K per min. By contrast, the heating rate of particulate silicates in a coal flame is higher by several orders of magnitude as shown in Fig. 1 which gives calculated temperatures of the ash. It is therefore probable that the pre-fusion changes are not fully completed before vitrification of crystalline mineral species and transformation of shape of the flame-borne particles commences.

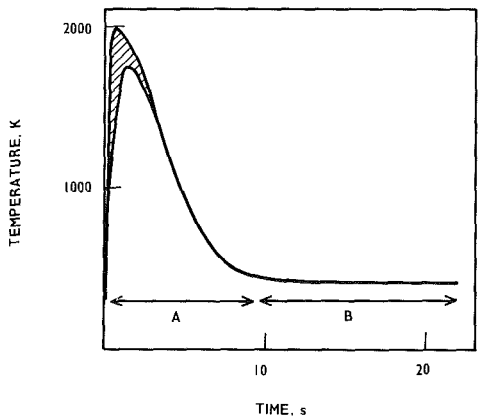

Fig. 1 Temperature/time plot for ash particles in a 500-MW pulverized coal fired boiler—0.1 μm (top curve) to 100 μm (lower curve) sizes. Section A: combustion and heat exchange chambers. Section B: electrical precipitators and chimney.

The change in shape of silicate particles on heating is a result of the action of surface tension on the shape edges of small irregular shapes which force the particles to assume a spherical form. The rate of transformation is dependent on viscous relaxation, and thus the surface tension and viscosity

Contributed by the Fuels Division and presented at the Joint Power Generation Conference, St. Louis, MO, October 4–8, 1981 of THE AMERICAN SOCIETY OF MECHANICAL ENGINEERS. Manuscript received at ASME Headquarters June 2, 1981. Paper No. 81-JPGC-Fu-1.

Table 1 Viscosity of mineral matter for deformation of particles of different sizes

Particle Radius, μm	10^{-2}	10^{-1}	10^{0}	10^{1}	10^{2}
Viscosity, N s m^{-2}	2.5×10^{7}	2.5×10^{6}	2.5×10^{5}	2.5×10^{4}	2.5×10^{3}

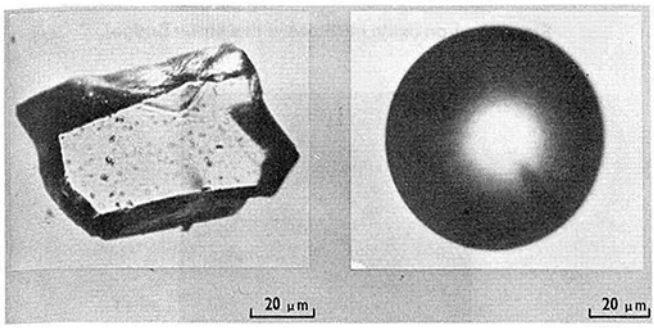

Fig. 2(*a*) Surface fused particle Fig. 2(*b*) Spheroidized particle

Fig. 2 Gas borne particles heated in laboratory furnace

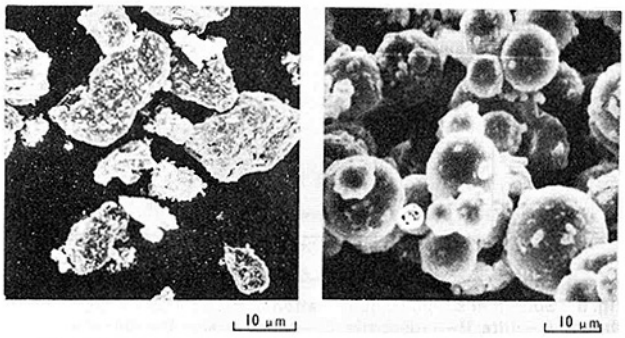

Fig. 3(*a*) Coal minerals Fig. 3(*b*) Spherical ash particles

Fig. 3 Nonspherical coal minerals and boiler flame spheroidized ash

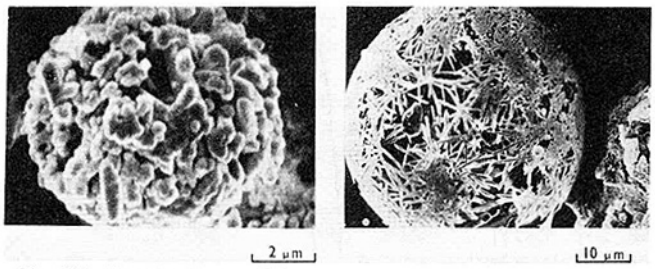

Fig. 4(*a*) Quartz microcrystals Fig. 4(*b*) Mullite needles

Fig. 4 Crystalline skeletons of ash particles after removal of glass matrix

of the particulate matter govern the change at a given temperature. The magnitude of the acting stress depends on the surface tension (γ) and on the radius of curvature (ρ) of the surface,

$$f = 2\gamma/\rho \tag{1}$$

Frenkel [2] has shown that the time of transformation (t), of an irregularly shaped particle to sphere is given to a first approximation by:

$$r = r_0 e^{-t/z} \tag{2}$$

where

$$z = 4\pi\eta r_0/\gamma \tag{3}$$

and r is the distance of a point on the original surface from the center of a sphere of equivalent volume having radius r_0, η is the viscosity and γ is the surface tension.

Equation (2) permits us to calculate the approximate time required for a particle to assume a spherical shape when the surface tension, viscosity, size and initial shape of particle are known. Alternatively, an estimate of the viscosity for the change to take place, can be made when the residence time of particles at a given temperature is known. Table 1 gives the calculated values of viscosity when the time for the change is 1 s. It was assumed that the thickness of moving surface layer was about ten percent of the radius, and the surface tension of fused ash was taken to be 0.32 N m^{-1} (Section 3).

It is clear from Table 1 that the small irregularly shaped particles should transform to spheres in a coal flame when the viscosity of the material is several orders higher than that required for bulk flow under gravity, which is about 25 N s m^{-2}. Raask [3] has used a laboratory furnace to determine the minimum temperature at which coal mineral species are transformed to spherical shapes. Particles of 10 to 200 μm dia range were introduced into a gas stream and then passed through a vertical furnace. The temperature of the furnace was varied from 1175 to 2025 K and was measured by a radiation pyrometer and by thermocouples attached to the furnace tube. The residence time of particles in the furnace after they had reached a steady temperature was calculated from Stoke's law, taking account of the velocity, viscosity and density of the gas stream. It was 0.5 s for small particles, whereas for large particles it was only 0.2 s. Air, and mixtures of nitrogen and oxygen (95 N_2 + 5 O_2 and, 99 N_2 + 1 O_2 by volume were used as the carrier gas. The particles were collected at the bottom of the tube and were later examined for their shape by the optical and stereo-electron microscopes.

Figure 2(*a*) shows a surface-fused silicate particle and Fig. 2(*b*) shows a similar particle after it was passed through the laboratory furnace. Figure 3(*a*) shows a typical sample of mineral particles in pulverized coal and Fig. 3(*b*) shows a sample of boiler ash taken from the electrical precipitator. On cooling, the vitrified silicate ash particles are recrystallized and they consist usually of microcrystals (Fig. 4(*a*)) and needles (Fig. 4(*b*)) dispersed in a glassy matrix. The glassy material in silicate ash can be removed by dissolution in a 0.1 HF (hydrofluoric acid) solution in which the crystalline silica (quartz) or silicates (mulliate) are insoluble [4].

Figure 5 shows the temperature range at which change of shape occurs for different minerals. The behavior of chlorite mineral illustrates the case where two components separate on heating and fuse at different temperatures (curves D_1 and D_2). The high temperature phase (D_2) had the same fusion characteristics as native quartz. Curve C shows that particles of native quartz changed their shape in the temperature range of 1775 to 2025 K. For this to occur, the viscosity of silica must have been in the range of 10^2 to 10^4 N s m^{-2}, whereas the viscosity of pure silica is between 10^5 and 10^7 N s m^{-2} in this temperature range. The probable explanation here is that the sample of native quartz contained impurities which sharply reduced its viscosity.

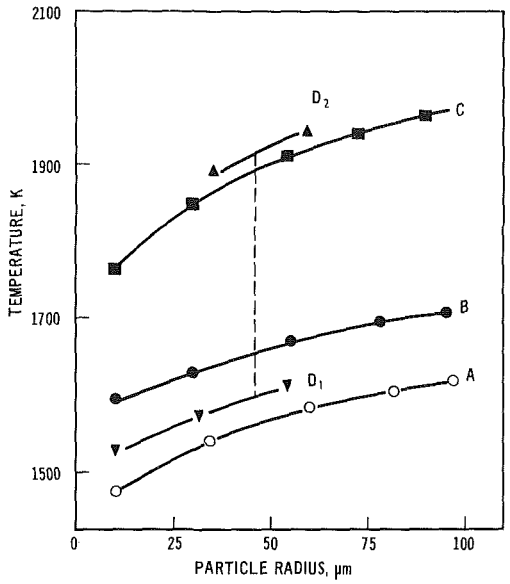

Fig. 5 Spherical shape transformation of granular minerals in hot gas stream: A—illite; B—muscovite; C—native quartz; D—chlorite

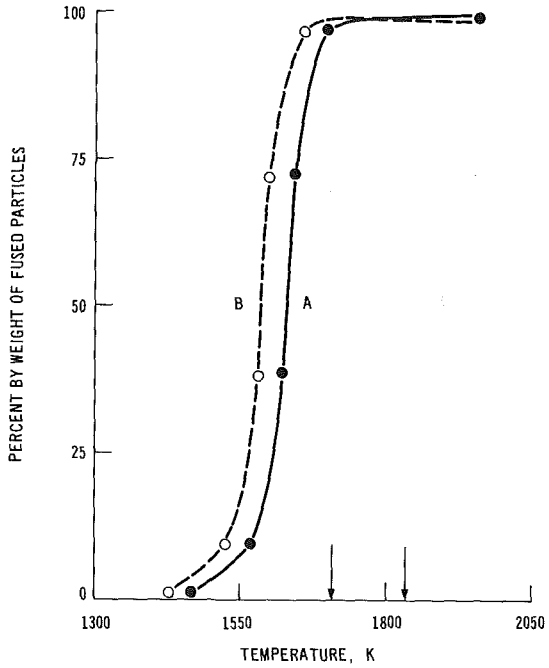

Fig. 6 Fusion of particulate minerals in coal: A—in tube furnace, residence time 0.2 to 0.5 s; B—in boiler furnace, residence time 2 to 5 s

Particle fusion characteristics of the mineral matter in pulverized coal when passed through the laboratory furnace is shown in Fig. 6 where curve *A* shows the percentage of rounded particles in the total at different temperatures. About ten percent of particles, chiefly pyrites, fused below 1575 K, the bulk of the irregular particles changed to spheres between 1575 and 1725 K and about five percent of the particles chiefly quartz changed their shape between 1725 and 1975 K. The fusion behavior of the particulate mineral matter in a large boiler is expected to be similar to that in the laboratory furnace. The only essential difference is that the residence time of particle in the boiler is up to ten times longer, thus the curve *A* in Fig. 6 would be displaced to curve *B*. This means that the majority of silicate and iron oxide particles (Fig. 3(*b*) and Fig. 7(*a*)) emerging from the flame would be spherical,

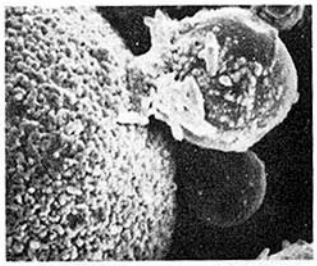

Fig. 7(*a*) Iron oxide particles with a sinter bridge

Fig. 7(*b*) Unfused quartz particle

Fig. 7 Spherical iron oxide and unfused quartz particles in ash

with the exception of large quartz particles (Fig. 7(*b*)) which would retain their original shape.

3 Slag/Coal Interface Characteristics and Surface Tension Measurements

A Leitz heating microscope has been used to observe the wetting characteristics of coal ash slag and synthetic silicate melts on different surface [5]. Figure 8(*b*) shows spreading of a droplet of coal ash slag on a wetting surface and it was found that the slags wetted all refractory oxide materials which were tested, i.e., alumina, zirconia and magnesium oxide, and also silicon carbide and platinum metal. Wetting of a refractory oxide surface by slag can be explained by assuming that there is an interaction between liquid and solid resulting in a lowering of the interfacial tension. Wetting of platinum took place probably because a film of platinum oxide formed on the metal surface. On silicon carbide there was a layer of silica which constituted on compatible surface for slag to spread.

In the absence of a solid oxide layer or absorbed film on carbon or graphite at high temperatures the nonoxide surface is incompatible with that of silicate melts and coal ash slags. As a result there is large contact angle between the surface of graphite, coke or coal residue and molten slag globule as shown in Fig. 8(*c*). The nonwetting property of coal ash slag on the surface of graphite permits measurements of the surface tension of molten slags by the sessile drop method [5]. The technique involves photographing a molten slag globule on graphite plate which can be conveniently carried out in a Leitz heating microscope. From the enlarged photograph the equatorial (horizontal) diameter and the height of the apex above the plane are measured. The density of slag may be determined from the volume of the drop as measured on the photograph. The shape of the drop depends upon parameter (β), i.e.,

$$\beta = \frac{gDR^2}{\gamma} \tag{4}$$

where g is the force of gravity, D is the density of slag, R is the

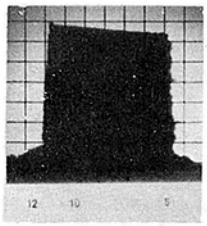

Fig. 8(a) Ash pellet

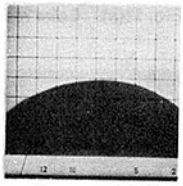

Fig. 8(b) Slag on alumina

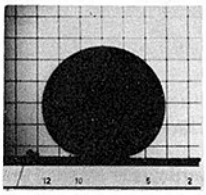

Fig. 8(c) Slag on carbon

Fig. 8 Ash fusion on wetting and nonwetting surface 0.5 mm gird

radius of curvature of the drop and γ is the surface tension. The geometric deviation parameter (β) and the necessary ratio tables to calculate the surface tension values from the measurements have been published by Brockris, White and Mackenzie [6].

The surface tension measurements were carried out with a number of slags in the temperature range of 1600 and 1750 K. The results thus measured were in the range of 0.25 to 40 N m^{-1} with an average value of the surface tension of 0.32 N m^{-1} at 1675 K. Evolution of gas bubbles inside the molten droplets of slag when resting on a graphite plate limits the accuracy of the sessible drop method of measuring the surface tension of coal ash slags. The bubbles distort the shape of the droplet and give erroneous results as to the density of the slag. It is therefore necessary to photograph the globule immediately after escape of the gas bubble and before a new one can develop.

4 Combustion of Mineral Rich Coal Particles and Coalsecence of the Inherent Ash

The fact that coal ash slag does not wet or spread on the coke residue particles, is of fundamental importance in high temperature combustion. In particular, the nonwetting behavior is a significant factor in the process of combustion of the middlings, i.e. the ash rich particles of pulverized coal. A technique of liquid density separation can be used to grade pulverized fuel into three fractions,

- low ash coal particles of ash content below 5 percent, with the particle density below 1300 kg m^{-3},
- high ash coal particles of ash content between 5 and 50 percent, with the density between 1300 and 2000 kg m^{-3}, and
- mineral particles of low, below 40 percent, coal content, with the density above 2000 kg m^{-3}.

Table 2 shows the relative amounts of "pure" coal, middlings and pure mineral fractions in a selection of British

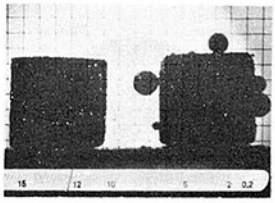

Fig. 9(a) Slag globules on coal particle (RHS)

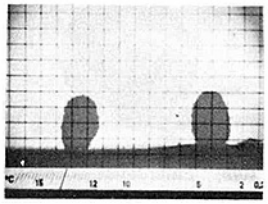

Fig. 9(b) Progress of combustion

Fig. 9 Combustion of carbon particle with slagged ash (RHS) 0.5 mm grid

(bituminous) coals. It is to be expected that the middlings content of U.S. bituminous coals when pulverized would show a similar distribution range, but the density distribution of mineral matter in nonbituminous coals and lignites can be markedly different when the coal impurity elements are present chiefly in the form of organo-metal complexes.

Noninterference of slag on combustion of ash rich coal particles has been demonstrated by heating two small pieces of carbon, one of which was coated with coal ash, in a heating microscope [5]. Figure 9(*a*) shows that the ash coating on coal particle had broken to small globules of slag when heated above the ash fusion temperature in nitrogen. At this point air was turned on, and Fig. 9(*b*) shows that the presence of the slag globules on the surface of burning carbon particles had no appreciable effect on the rate of combustion. Partially burnt particles of coal residues may be buried inside slag globules or in the surface layer of molten slag on furnace walls, in particular in cyclone and slag-tap boiler. Coal particles buried in the slag emerge at the surface as a result of gas evolution as demonstrated in Fig. 10. The slag globule (*a*) has a carbon particle buried in it, in stage (*b*) the particle is emerging and it is later ejected (*c*) as a result of formation of gas bubbles at the coal/slag interface [5].

Table 2 Relative amounts of clean coal, middlings and ash-rich fractions in pulverized fuel [7] (weight percent of coal)

Coal	Clean Coal	Middlings	Ash Rich Fraction	Ash in Ungraded Coal
1	65.8	30.7	3.5	5.4
2	67.9	25.6	6.5	7.0
3	50.3	33.2	16.5	16.2
4	56.4	27.5	16.1	16.4
5	55.8	27.9	16.3	17.2
6	14.1	69.9	16.0	17.3
7	49.3	33.5	17.2	18.3
8	54.0	27.1	18.9	18.6
9	38.2	42.0	19.8	18.7
10	48.1	34.1	17.8	19.1
11	64.0	16.4	19.6	22.9
12	48.0	31.9	20.1	23.5
13	47.9	29.7	22.4	23.7
14	3.9	66.6	29.5	32.6

When the temperature of burning particle is not sufficiently high to form slag beads but it is high enough to form a layer of sintered ash, the rate of combustion can be significantly reduced. This was demonstrated by experiments in the heating microscope with ash-coated carbon particles, where 0.1 mm

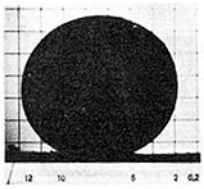

Fig. 10(*a*) Ash globule with embedded coal particle

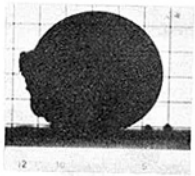

Fig. 10(*b*) Emergence of coal particle

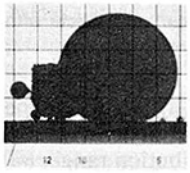

Fig. 10(*c*) Ejection of coal particle

Fig. 10 Ejection of coal particle from slag—0.5 mm gird

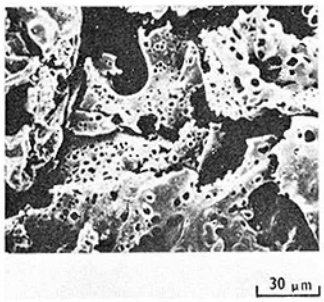

Fig. 11(*a*) Coke residue

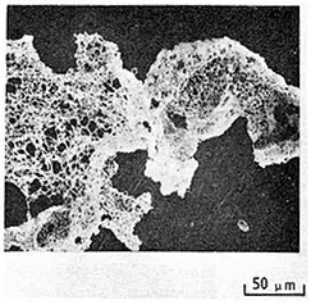

Fig. 11(*b*) Ash skeleton in coke

Fig. 11 Coke particles in ash and the inherent ash in coke

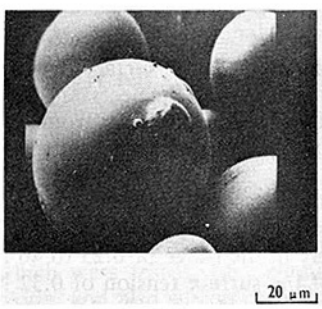

Fig. 12(*a*) Cenospheres

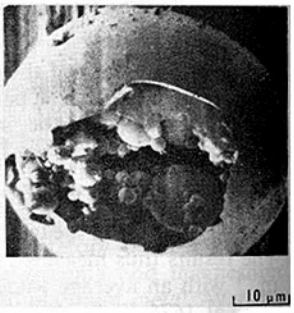

Fig. 12(*b*) Plerosphere

Fig. 12 Low density particles in pulverized coal ash

thick layer of sintered ash effectively prevented combustion taking place. Unburnt carbon residue present in pulverized coal (Fig. 11(*a*)) usually contains a skeleton of sintered ash (Fig. 11(*b*)) which is revealed when the carbonaceous matter is removed by burning the particles in air at 900 K. It has not been established whether or not the internal lacework of sintered ash has the effect of reducing combustion of coke particles in boiler flue gas.

Mineral matter in the ash rich coal particles (middlings) is usually present in the form of clay dispersion of the particle size of 0.1 to 10 μm. Thus, a 50 μm sized coal particle may contain several thousands of mineral particles which coalesce on combustion to form only one or a few ash particles [8]. During combustion of the ash rich particles, ash envelopes may be created which can take the form of a cenosphere [9] or a spheres-inside-a sphere formation (plerosphere) as shown in Figs. 12(*a*) and (*b*).

Coalescence of the inherent ash in pulverized coal particles is likely to be extensive, since the boiler fly ash contains a significantly smaller amount of the particles in the size range of 0.5 to 5.0 μm when compared with that of a laboratory ash prepared from the same coal (Fig. 13). The laboratory ash was obtained by burning coal at 900 K and at that low temperature the small silicate particles of the coal inherent ash do not coalesce.

5 Release of Potassium From Aluminosilicates in Boiler Flame

Potassium aluminosilicates, muscovite and illite species, usually constitute between 30 and 50 percent of the total mineral matter in coal. Muscovites contain around 11 percent by weight potassium, expressed as K_2O, and have an approximate chemical formula of $K_2O.2Al_2O_3.6SiO_2.H_2O$. Illite minerals contain between 5 and 6 percent K_2O and their chemical composition can be expressed approximately as $2K_2O.3(Ca, Mg, Fe)O.8Al_2O.24SiO_2.12H_2O$[10, 11, 12].

The potassium mineral particles vitrify in pulverized coal flame and change their shape to spherical forms as described in Section 2. The bulk of potassium remains dissolved in the glassy material of the aluminosilicate particles, but a fraction escapes into the vapor phase and the volatilized alkali metal is subsequently converted to sulphate in the presence of sulphur gases in the flue gas. The results of analysis of corrosive boiler deposits of alkali metal sulphates [13] gave rise to a suggestion that the process of potassium volatilization was enhanced in the presence of sodium chloride vapor in the flame, and an exhange reaction of sodium for potassium in aluminosilicate ceramic material has been demonstrated by Jackson and Duffin [14]. Sodium chloride was injected into propane flame which was constrained in a ceramic tube. The exchange of potassium for sodium took place in the glazed surface layer of the ceramic material at about 1675 K, and the chloride deposit on a cooled target contained up to 0.22 mole fraction of KCl.

Release of potassium from aluminosilicates has been investigated by the use of a bomb calorimeter where a gram quantity coal was burnt in an oxygen atmosphere [15]. Samples of coal were ground to the same fineness as that of the fuel burnt in pulverized coal fired boilers, that is, 75 percent of weight fraction passing through a 76 μm sized sieve. The combustion temperature as measured by a thermocouple embedded in the fuel bed was 1700 K, and it per-

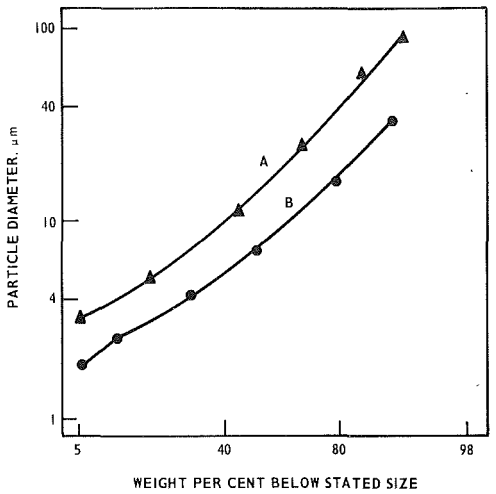

Fig. 13 Log probability partizle size distribution of pulverized fuel ash: A—boiler ash, flame temperature 1750 K; B—laboratory ash, combustion temperature 950 K

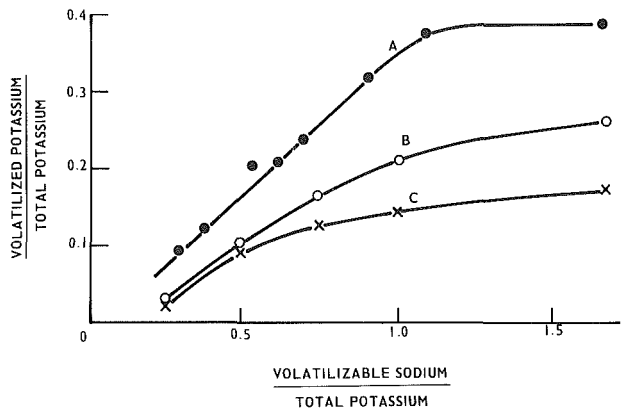

Fig. 14 The effect of sodium chloride on release potassium from silicates: A—coal silicates; B—muscovite; C—orthoclase

sisted at this value for 7 s. Experiments were made also with synthetic mixtures of potassium aluminosilicates, sodium chloride and benzoic acid as a fuel, to study the release of potassium from different silicate minerals.

The amount of potassium volatilized from silicate minerals during combustion can be readily determined by chemical analysis. Volatilized potassium is present after combustion in the form of chloride or sulphate, and these compounds are readily soluble in water. By comparison, the rate of leaching of potassium from silicates is low. Thus, the difference between the total potassium content and that of water soluble potassium represents the amount of metal combined in silicates. The same applies for the distribution of sodium in the soluble nonsilicate compounds and nonsoluble silicates. Table 3 gives the soluble and nonsoluble fractions of the two alkali-metals in coals before combustion and in the residue washings after combustion.

The data in Table 3 show that with the exception of one coal (sample 4) there was a net transfer of alkalis to silicate residue on combustion when expressed in terms of equivalent weight of sodium (last column). On the average, 50 percent of potentially volatile sodium was captured by the silicate residue. The release of potassium present in the potassium aluminosilicates in coal and in synthetic mixtures was dependent on the amount of the nonsilicate sodium originally present in the samples. On the average, 0.3 mole equivalent of potassium to one mole of sodium was released from the coal silicates and lesser amounts from the synthetic mixes.

Figure 14 shows the effect of sodium chloride on the release of potassium from the synthetic mix silicates and from coal silicates in bomb combustion. It is evident that with each type of mineral, a limiting release value was reached after which further addition of sodium chloride did not have any effect. Further, it was noticeable that relatively higher amounts of potassium were released from the coal silicates than those released from the synthetic mixture silicates. This was probably because coal ash residues had a lower viscosity than that of the synthetic mix residues, and consequently diffusion potassium from the silicate particles and sodium into the ash residue was enhanced.

According to the thermodynamic data on silicates published by Kelly [16] and those on chlorides published by Villa [17] the alkali-metal exchange reactions have a net (positive) free energy (ΔG) value between 12 and 25 kJ mole^{-1} at 1675 K:

$$mK_2O.xSiO.yAl_2O_{3\,(fused)} + 2NaCl_{(gas)} =$$

$$(m-1)K_2O.Na_2O.xSiO_2.yAl_2O_{3\,(fused)} + 2KCl_{(gas)} \quad (5)$$

$$\Delta G = -RT1g\frac{P_{(KCl)}^{\ 2}}{P_{(NaCl)}^{\ 2}} \quad (6)$$

A positive ΔG value means that after the high temperature exchange reactions the molar concentration of unreacted NaCl-vapor should be higher than that of KCl. This is in accordance with data given in Fig. 14, which shows that for one mole of MaCl 0.15 to 0.35 mole equivalent of potassium was released from the silicates.

6 Relevance of Flame Imprinted Properties of Ash to Boiler Deposits and Ash Impaction Erosion

6.1 Boiler Fouling and Slagging. Coalescence of the deposited particles by viscous flow is the principal mode of formation of sintered and slag deposit on boiler tubes [18], and the basic equation of the phenomenon was derived by Frenkel [2]:

$$\frac{x^2}{r^2} = \frac{3\gamma t}{2\eta r} \quad (7)$$

where x is the radius of neck growth between the spherical particles of radius r, γ is the surface tension, η is the viscosity of fused ash, and t is the time. The $(x/r)^2$ ratio can be taken as a criterion of the degree of sintering, i.e., the strength of boiler deposit (s) developed in time t, that is:

$$s = k\left(\frac{x}{r}\right)^2 \quad (8)$$

and the rate of deposit strength development is:

$$\frac{ds}{dt} = \frac{3k\gamma}{2\eta r} \quad (9)$$

where k is a constant.

Equation (9) shows that the rate of buildup boiler deposit and its strength development is proportional to the surface tension (Section 3) and inversely proportional to the viscosity and particle size of deposited ash. Earlier (Section 4) it was shown that a significant degree of coalescence of the small particles of clay minerals dispersed in coal takes place in the flame before deposition on boiler tubes. As a result the rate of their subsequent sintering by viscous flow is correspondingly reduced. For example, the rate of sintering of 25 μm in diameter particles is 50 times less than that of 0.5 μm particles. However, there remains a significant number of submicron sized particles in pulverized coal flame, and a large number of small particles are created from volatilized species [19]. It is, therefore, unlikely that coalesence of small particles of coal inherent ash in the flame will markedly influence the rate of buildup of deposits on boiler tubes.

Table 3 Silicate and nonsilicate alkalis in coals and in combustion residues (weight percent of coal)

Coal Sample	Before Combustion				
	Silicate		Nonsilicate		
	Na	K	Na	K	
1	0.105	0.480	0.119	0.004	
2	0.106	0.395	0.192	0.003	
3	0.123	0.197	0.197	0.003	
4	0.010	0.426	0.207	0.002	
5	0.453	0.646	0.139	0.06	
6	0.744	0.619	0.244	0.008	
7	0.125	0.438	0.340	0.006	
8	0.192	0.478	0.294	0.008	
Coal Sample	After Combustion				Net Capture of Alkalis, Na Equivalent
	Silicate		Nonsilicate		
	Na	K	Na	K	
1	0.155	0.412	0.069	0.072	0.010
2	0.125	0.306	0.083	0.092	0.058
3	0.227	0.120	0.093	0.080	0.059
4	0.032	0.314	0.185	0.114	−0.044*
5	0.555	0.600	0.037	0.052	0.076
6	0.730	0.512	0.058	0.115	0.124
7	0.284	0.272	0.181	0.172	0.062
8	0.317	0.309	0.169	0.177	0.026

*net release

The principal ash property which controls the rate of deposit formation is the viscosity/temperature characteristics of the silicate ash material landing on boiler tubes. The findings in Section 2 show that the silicate ash particles deposited on cooled boiler tubes are likely to consist of a mixture of crystalline material (Fig. 4) dispersed in a glassy matrix. It is the glassy surface layer which forms sinter bridges between the deposited ash particles [20] although its viscosity may be as high as 10^{10} N s m^{-2}. By contrast, a crystalline material has an infinitely high viscosity, i.e., above 10^{14} N s m^{-2}, and the rate of sintering of the particles by a lattice diffusion mechanism is much lower than that of viscous flow. It is therefore evident that the rate of sinter coalescence of deposited ash depends markedly on the ratio of crystalline to glassy material of the captured particles on boiler tubes. One possible method of enhancing the degree of crystallization of the surface layer of vitrified silicate ash particles, and hence reducing boiler slagging, is to use appropriate additives, and some success in this field has been reported by Kiss, et al. [21].

6.2 Fireside Corrosion Enhanced by Potassium Release in Coal Flame. Silicate ash deposit in the form of crystalline materials in a glassy matrix on boiler tubes does not constitute a corrosive medium for rapid attack on tube metals. The protective oxide layer on steels will dissolve in molten silicates at high temperatures, but coal ash slag and sintered deposits have a high viscosity, above 10^{10} N s m^{-2}, at temperatures below 1000 K and the rate of oxide dissolution is insignificant. However, silcate coal minerals containing potassium, chiefly illites and muscovites, constitute a source for volatilized potassium in the boiler flame as discussed in Section 4. Volatilized alkali-metals, chiefly sodium and potassium, are converted to sulphates [22] in the boiler flue gas and are preferentially deposited on cooled furnace wall and superheater tubes. Potassium rich sulphates in particular can form a low temperature melting and corrosive phase in boiler deposits [13]. K^+-ions have a low charge to ionic size ratio and thus they are capable of exerting a marked polarizing and stabilizing effect on aluminum, iron, and chromium sulphates which are otherwise unstable in boiler deposit in the temperature range of 800 and 950 K. As a result, the protective oxide on boiler tube metals may dissolve rapidly causing severe fireside corrosion.

The above findings are consistent with the observations made by Reese, et al., [23] that potassium rich sulphates are much more corrosive than that caused by sodium sulphate. According to their findings the total sodium content of coals is less important than the ratio of potentially volatilizable potassium to sodium in the boiler flame.

Deposition of sulphate (Na_2SO_4 and K_2SO_4) has been measured by inserting a cooled probe [24] in the superheaters of pulverized coal fired and cyclone fired boilers [25,26,27]. The results shows that the rate of sulphate deposition in a cyclone fired boiler was significantly higher than that measured in a pulverized coal fired boiler burning coals of the same quality. A probable reason for the high rate of sulphate deposition in the cyclone boiler was that at the high temperatures coal ash slag did not absorb much of volatilized alkali-metal. As a result there was significant quantity of volatilized sodium and potassium available for the formation of sulphates. It is therefore probable that some coals of moderate chloride (alkali) content when burnt in a cyclone boiler produce more corrosive deposits in comparison to those occurring in pulverized coal fired boilers burning coals of the same chloride content.

The risk of fireside corrosion by low temperature melting sulphates in pulverized fuel fired boilers burning high chlorine coal can be reduced by coal washing designed to remove the water-soluble chlorides, chiefly NaCl. Removal of sodium chloride would result in a lesser amount of sodium being available for the formation of Na_2SO_4 and for the release of potassium from aluminosilicates in boiler flame as discussed in Section 5. Consequently, a smaller amount of K_2SO_4 would be present in boiler deposits. Reduction of NaCl-content of coal would decrease also the risk of severe boiler fouling by sintered deposit [28].

6.3 Boiler Tube Erosion of Ash Impaction. The abrasive property of pulverized coal depends mainly on the amount of hard, sharp-edged quartz and pyrites present in the fuel. The pyrite particles undergo a complete physical and chemical change in coal flame resulting in the formation of spherical, less abrasive particles of iron oxide. The transformation of pyrites (FeS_2) proceeds via an intermediate product [22] which melts at about 1400 K and the particles take a spherical shape which is retained on further oxidation to FeO and Fe_3O_4 (Fig. 7(*a*)).

Abrasive characteristics of the heat-treated quartz particles (Fig. 7(*b*)) found in pulverized coal ash depends largely on the flame temperature. At exceptionally high temperatures the hard, sharp-edged particles vitrify and are transformed to less abrasive, spherical shapes as discussed in Section 2. It is therefore to be expected that the high temperature in a cyclone fired boiler results in a complete vitrification of quartz and the ash does not contain significant quantity of abrasive quartz particles. The peak flame temperature of a pulverized coal fired ("dry ash") boiler is usually 150 to 200 K less than that of a cyclone fired boiler. As a result between 25 and 50 percent of quartz originally in coal survive the flame treatment [29] and the particles in ash can retain their abrasive property [30]. In particular this may be the case with ashes from nonbituminous coal fired boilers where the flame temperature may be lower than that of bituminous coal flame. As a result the abrasive quartz particles preserve their original erosion wear-causing characteristics of the hardness and sharp-edged shapes.

The rate of erosion wear of boiler tubes caused by ash impaction depends also on the size of impacting particles. Particles of diameter <5 μm produce no significant damage, irrespective of their abrasive characteristics [31]. When the particle diameter is in the range of 56 to 50 μm the rate of erosion wear is proportional to the size, and above 50 μm the wear rate is independent of particle size.

7 Conclusions

7.1 The change of irregularly shaped mineral particles in pulverized coal to spherical ash particles in boiler flame is the result of the action of surface tension force. The rate of transformation depends on the viscosity of silicious ash and on the size of particles. A flow on the glassy surface layer takes place when the viscosity is in the range of 10^3 to 10^5 N s m^{-2} which is greater by several orders of magnitude than that required for viscous flow in bulk slag due to the gravitational force.

7.2 The inherent mineral matter in ash rich coal particles of pulverized fuel do not markedly reduce the rate of combustion at high temperatures where the incombustible residue fuses to small globules which do not wet or spread on the surface of burning particles. At lower temperatures a network of sintered ash may constitute a barrier to gas diffusion and thus reduce the rate of combustion of coke residue particles.

7.3 The inherent mineral matter in pulverized coal consists usually of a dispersion of clay particles of 0.1 to 5 μm in diameter, and a coal particle may carry several thousands of ash particles into the boiler flame. From those one or two dense ash globules, cenospheres or plerospheres are formed and thus there is an extensive coalescence of the inherent ash in a pulverized coal flame.

7.4 Volatilization of potassium originally combined in aluminosilicates is enhanced by the presence of sodium chloride vapor in pulverized coal flame. The release of potassium results from an exchange reaction whereby potassium in the silicates is partly replaced by sodium, and up to 40 percent of potassium can be transferred into the vapor phase.

7.5 Silicate ash particles deposited on the boiler tubes consist of a crystalline material in the form of microcrystals and needles, and of a glassy material which provides the matrix. The rate of coalescence of the ash particles by viscous flow sintering depends largely on the viscosity of the glassy phase at deposit-forming temperatures.

7.6 Potassium volatilized from aluminosilicates is converted to sulphate, and together with sodium sulphate it can form a corrosive medium of low melting sulphates for dissolution of protective oxide layer on boiler tube steels.

7.7 Abrasive characteristics of pulverized coal ash depends markedly on the amount of unfused particles of quartz in ash. The ash from some of the nonbituminous coals can be highly abrasive: The large quartz particles are not changed to spherical, less abrasive shapes. Particles size also influences the rate of erosion wear on ash impaction. Particles below about 5 μm in diameter do not cause any significant erosion wear, irrespective of their abrasive characteristics.

Acknowledgment

This work was carried out at the Central Electricity Research Laboratories. The paper is published by permission of the Central Electricity Generating Board.

References

1 Losel, G., and Schmucker, H., "Temperature Behaviour of Ash Particles at Combustion Chamber Exit," *VGB Kraftwerkstechnik,* Vol. 57, 1977, p. 839.

2 Frenkel, J. S., "Viscous Flow at Crystalline Bodies under the Action of Surface Tension," *Journal of Physics* (Moscow), Vol. 9, 1945, p. 385.

3 Raask, E., 1969, "Fusion of Silicate Particles in Coal Flames," *Fuel,* Vol. 48, 1969, p. 366.

4 Raask, E., and Bhaskar, M. C., *Pozzolamic Activity of Pulverized Fuel Ash, Cement and Concrete Research,* Vol. 5, 1975, p. 363.

5 Raask, E., "Slag-Coal Interface Phenomena," ASME JOURNAL OF ENGINEERING FOR POWER, 1966, p. 40.

6 Bockris, J. O. M., White, J. L., and Mackenzie, J. D., *Physio-Chemical Measurements at High Temperatures,* 1959, Butterworths, London.

7 Littlejohn, R. F., "Mineral Matter and Ash Distribution in As-Fired Samples of Pulverized Fuels," *Journal of Institute of Fuel,* Vol, 39, 1966, p. 59.

8 Sarofim, A. F., Howard, J. B., and Padia, A. S., "The Physical Transformation of the Mineral Matter in Pulverized Coal under Simulated Combustion Conditions," *Combustion Science Technology,* Vol. 16, 1977, p. 187.

9 Raask, E., "Cenospheres in Pulverized Fuel Ash," *Journal of Institute of Fuel,* Vol. 43, 1968, p. 339.

10 Dixon, K., Skipsey, E., and Watt, J. T., "The Distribution and Composition of Inorganic Matter in British Coals," *Journal of Institute of Fuel,* Part 1, Vol. 37, 1964, p. 485, Part 2, Vol. 43, 1970, p. 124, Part 3, Vol. 43, 1970, p. 229.

11 Kirsch, H., "The Behaviour of Coal Ash at High Temperatures," *Technische Überwachung,* Vol. 6, 1965, p. 203.

12 Rao, C. P., and Gluskoter, H. S., "Occurrence and Distribution of Minerals in Illinois Coals," Illinois State Geological Survey, Circular No. 476, 1973, Urbana, Il.

13 Adams, A. M., and Raask, E., "Complex Sulphates in Coal-Fired Boiler Plant," *Proceedings of International Conference on Mechanism of Corrosion by Fuel Impurities,* Marchwook U.K., 1963, Butterworths Publication, p. 496.

14 Jackson, P. J., and Duffin, H. C., "Laboratory Studies of the Deposition of Alkali-Metal Salts from Flue Gas," *Proceedings of International Conference on Mechanism of Corrosion by Fuel Impurities,* Marchwood, U.K., 1963, Butterworths Publication.

15 Raask, E., "The Behaviour of Potassium Silicates in Pulverized Coal Firing," *Mitteilungen VGB,* Essen, Germany, Vol. 48, 1968, p. 348.

16 Kelly, K. K., "Heats and Free Energy of Formation of Anhydrous Silicates," U.S. Bureau of Mines, Report No. 5901, 1962, Washington, D.C.

17 Villa, H., "Thermodynamic Data of the Metallic Chlorides," *Journal of the Society of Chemical Industry,* No. 1, 1950, p. 9.

18 Raask, E., "Boiler Fouling—The Mechanism of Slagging and Preventive Measures," *VGB Kraftwerkstechnic,* Vol. 53, 1973, p. 248.

19 Raask, E., "Characterization of Captured Ash, Chimney Stack Solids and Trace Elements," *Journal of Institute of Energy,* Vol. 54, 1981, to be published.

20 Raask, E., "Sintering Characteristics of Coal Ash by Simultaneous Dilatometry-Electrical Conductance Measurements," *Journal of Thermal Analysis,* Vol. 16, 1979, p. 91.

21 Kiss, L. T., Lloyd, B., and Raask, E., "The Use of Copper Oxychloride to Alleviate Boiler Slagging," *Journal of Institute of Fuel,* Vol. 45, 1972, p. 213.

22 Halstead, W. D., and Raask, E., "The Behaviour of Sulphur and Chlorine Compounds in Pulverized Coal Fired Boilers," *Journal of Institute of Fuel,* Vol. 42, 1969, p. 344.

23 Reese, J. T., Jonakin, J., and Koopman, J. G., "How Coal Properties Relate to Corrosion of High Temperature Boiler Surfaces," *Proceedings of American Power Conference,* Vol. 24, 1961, p. 391.

24 Jackson, P. J., and Raask, E., "A Probe for Studying the Deposition of Solid Material from Fluegas at High Temperatures," *Journal of Institute of Fuel,* Vol. 34, 1961, p. 275.

25 Raask, E., "Formation of Superheater Deposits in Coal Fired Boilers Burning East Midlands Coals," 1962, Unpublished work.

26 Raask, E., "Formation of Superheater and Air Heater Deposits in a Cyclone Boiler Fired with East Midlands Coals," 1961, Unpublished Work.

27 Raask, E., "Reactions of Coal Impurities during Combustion and Deposition of Ash Constituents on Cooled Surfaces," *Proceedings of International Conference on Corrosion by Fuel Impurities,* Marchwood, UK, 1961, Butterworth Publication, p. 145.

28 Jackson, P. J., and Ward, J. M., "Operational Studies of the Relationship between Coal Constituents and Boiler Fouling," *Journal of Institute of Fuel,* Vol. 29, 1956, p. 154.

29 Raask, E. "Quartz, Sulphates and Trace Elements in PF Ash," *Journal of Institute of Energy,* Vol. 53, 1980, p. 70.

30 Raask, E., "Impact Erosion Wear Caused by Pulverized Coal and Ash," International Conference on Erosion by Liquid and Solid Impact, 1979, Cambridge, UK.

31 Goodwin, J. E., Sage W., and Tilley, G. P., "Study of Erosion by Solid Particles," Institute of Mechanical Engineers Publication, UK Vol. 184, 1969, Part 1.

Combustion Roar as Observed in Industrial Furnaces

A. A. Putnam
Battelle, Columbus Laboratories,
Columbus, Ohio 43201
Fellow, ASME

Factory noise in recent years has become a source of increasing attention, both because of the action of regulatory bodies and because of increased industrial awareness of possible detrimental effects to workers. This paper concerns one significant source of factory noise, namely, combustion roar. Combustion roar accompanies any turbulent flame, premixed or diffusion. Generally, it increases with the rate and intensity of combustion. The effects of several variables, such as firing rate, turbulence intensity, and burner type, on the noise output of flames in an acoustically-infinite situation are first considered. Then, the available information on the changes in the acoustic performance of burners when they are placed in furnaces is discussed. Finally, some remarks are made concerning the suppression of combustion roar.

Introduction

Combustion-produced noise can be classified as one of two types—either combustion roar or combustion-driven oscillations. Combustion roar accompanies any turbulent combustion process. For a simple flame, in the absence of reflecting surfaces, it has a smooth noise spectrum (Fig. 1(*b*)) and a relatively low efficiency of conversion of chemical energy to noise [1] in the range of 10^{-8} to 10^{-5}. The various aspects of combustion roar, as based on observations of industrial burners, are the subject of this discussion.

In contrast, combustion-driven oscillations are characterized by a discrete frequency (Fig. 1(*a*)), the presence of a feedback cycle, and a relatively high efficiency of conversion of chemical energy to noise (about 10^{-4}) [1]. In residential, commercial, or industrial combustion systems, the noise amplitude from combustion-driven oscillations is often sufficiently high to cause severe noise and/or fatigue problems requiring immediate action. This phenomenon has been widely discussed in the literature [2] and will not be considered further herein.

A simple theory of production of combustion roar, based on Bragg's basic treatment [3], is first presented. Results on several industrial burners in an acoustically-infinite system are next presented. Then, experimental studies of the effect of the furnace enclosures are outlined. Pertinent concluding remarks complete the discussion.

Combustion Roar Theory

Figure 1(*b*) shows a typical combustion roar noise spectrum for a natural-gas diffusion flame, as might be obtained from a burner in a anechoic chamber or an acoustically-open furnace. The spectrum has no specific high energy frequencies. Rather, it has a broad band of noise that has a basic form similar to a jet noise spectrum. The peak frequency varies with fuel and is strongly related to the chemically controlled reaction rate per unit volume for the fuel [4]. In the presence of strong vortex-shedding action of some burner components, or of some flow noise, some flame amplification of these noise sources can also be produced. Often, this noise is in the same frequency range as the chemically controlled frequency spectrum. This distorts the shape of the overall or observed spectrum, with a mild effect of the flow rate imparted to the peak frequency. On the other hand, cases have been observed where the spectra are definitely separated.

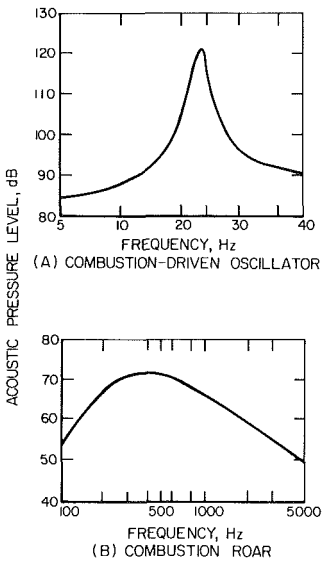

Fig. 1 Typical noise spectra for combustion-driven oscillations and combustion roar

Returning to the suggestion that the peak frequency is related to the chemically controlled reaction rate per unit volume, we note that for many types of burners, there is a

Contributed by the Fuels Division and presented at the Winter Annual Meeting, November 15-20, 1981, Washington, D. C., of THE AMERICAN SOCIETY OF MECHANICAL ENGINEERS. Manuscript received at ASME Headquarters July 14, 1981. Paper No. 81-WA/Fu-8.

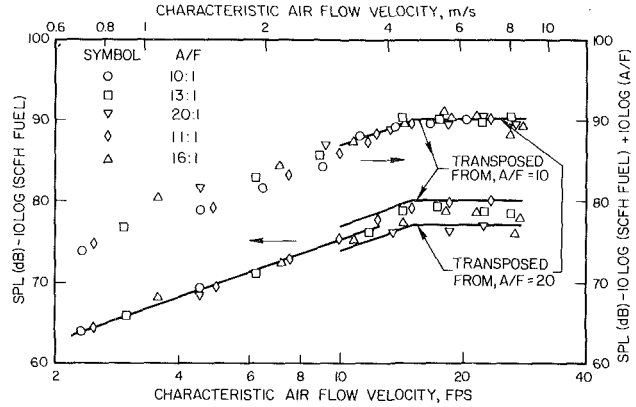

Fig. 2 Burner ARP: nozzle-mix nonswirl gas burner: 5-1/8 in. (130mm) exit dia, 580 SCFH (4.56×10^{-3} m^3/s) natural gas at rated firing rate. Air inlet velocity is 27.8 times characteristic velocity based on cold air flow and exit area

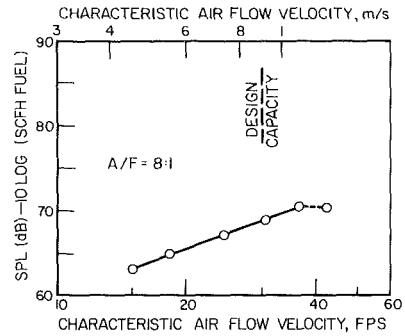

Fig. 3 Burner FRP, premix with annular flame retention: characteristic velocity based on 3-in. (75mm) dia exit rather than 1-1/2 in. (38 mm) dia accelerating nozzle

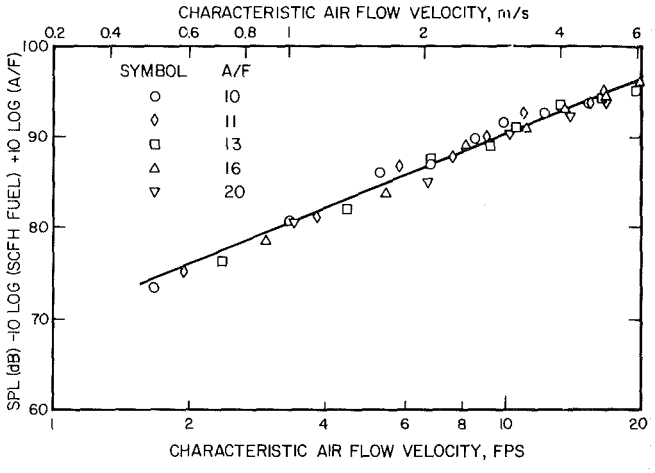

Fig. 4 Burner BBD: partly premix, nozzle mix, swirl rocket shaped burner: 5-1/2 in. (140 mm) dia combustion section, 700 SCFH (5.51×10^{-3} m^3/s) natural gas at rated capacity. Exit diameter is 1-11/16 in. (43 mm). Air inlet velocity is 16 times characteristic velocity

primary fuel rich premixed flame followed by a secondary diffusion flame. Consideration of the relative reaction rates indicates a possibility of two separate spectra occurring. Data that can be interpreted in this manner have been observed.

Concerning the overall noise level, Bragg [3] suggested in 1963 that a turbulent flame could be considered as an array of monopole noise sources; that is, the turbulent flame can be considered from the noise standpoint as an array of balloons expanding and contracting at various rates and frequencies. From a variation of Bragg's derivation [5], the ratio of the acoustic power output to chemical energy input, η, is given by

$$\eta = [(\gamma - 1)(E - 1)(S/c)/4\pi](u'/c)^2 \quad (1)$$

where γ is the ratio of specific heats; E is the volume expansion ratio of the burned to the unburned gas; S is the laminar burning velocity; c is the velocity of sound; and u' is the turbulence component of the velocity. Note that the efficiency of conversion, η, is a function of the product of a term depending on the fuel and the mixture ratio, and a term depending on the turbulence level of the combustion region.

For smaller turbulent flames of the simple Bunsen type (say, under about 100,000 Btu/hr or 30 kW [6,7]), buoyancy and vortex shedding effects lead to complications of this simple formula that result generally in stronger effects of burning velocity, flow rate, and burner size. Strahle [8] empirically fit to data from a large series of tests on this specific type of hydrocarbon flame (falling on both sides of the approximate breakover ratio) a somewhat more complex relation than given earlier, including a Reynolds number, Prandtl number, and fuel mass fraction term.

Acoustically Open Flames

Burners are seldom used in acoustically open situations, that is, in situations in which there is no noise reflection from walls or other obstacles. Even the noise spectrum of an open flame in a large room shows the effects of the normal room frequencies [6]. Furthermore, burners, because of the lack of recirculating hot gases, may not perform the same in the open as in a furnace situation. Nevertheless, studies of flames in an acoustically-open or infinite situation reveal the basic acoustic features of the flame and form a common basis of comparison of various burners. In this discussion, the effects of a number of variables on the basis acoustic amplitude and spectra of burners in an acoustically-open situation are considered. These are useful in considering methods of reducing combustion noise in practical situations.

Firing Rate. Figure 2 presents a typical curve of a noise level as a function of firing rate for a nozzle mix burner of 580,000 Btu/hr (170 kW) design capacity [1,9]. This burner has eight nonswirl air jets surrounding the single axial fuel jet. The reference velocity is the flow velocity through the burner tile referred to standard conditions. The overall noise level measurements were made 37 in. (0.94 m) from the burner axis and in the plane of the burner face. The subtraction of the log of the fuel flow rate (left-hand coordinate) puts the data on a noise production efficiency basis.

Figure 3 presents similar data for a premix burner of 670,000 Btu/hr (200 kW) design capacity [9]. Three other nozzle mix burners and two other premix burners were studied in the same programs [10]. All gave noise levels varying with the cube (or slightly less, probably from Reynolds number effect) of the flow rate; efficiencies of conversion of chemical energy to noise (Figs. 2 and 3) varied as the square (or slightly less) of the flow rate. This is in agreement with the Bragg theory as previously outlined. Custard ran tests on similar burners of similar capacity with similar results [11]. Further, Bertrand and Michelfelder [12] reported a value of the exponent of 2.80, as compared to the theoretical value of 3, for a natural gas fired swirl burner operating up to about 7,000,000 Btu/hr (2 MW).

Fuel/Air Ratio. The noise data for turbulent diffusion flames are simpler to interpret than those for premixed flames. Figure 2 (left hand coordinate) shows diffusion flame data for a range of natural gas/air mixture ratios from 1:10 to 1:20; on the noise efficiency basis, there is no effect of mixture ratio [10].

Premixed flames seem to occur more frequently than one

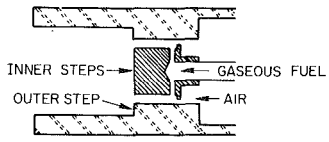

Fig. 5(a) Original

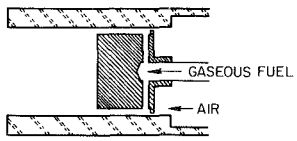

Fig. 5(b) Modified

Fig. 5 British gas design of modular burner

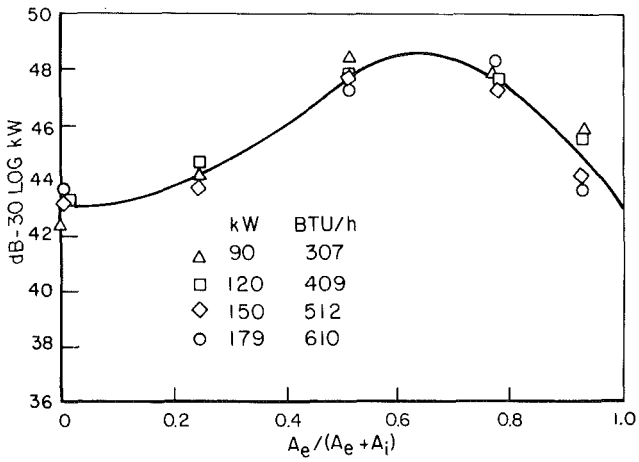

Fig. 6 Normalized sound power as a function of external to total step area ratio

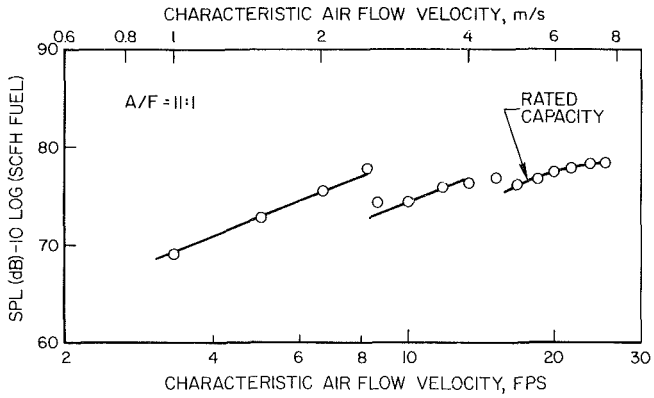

Fig. 7 Burner DMA, nozzle-mix multiple step gas burner: 4-3/4 in. (120 mm) exit dia, 3-5/8 in. (92 mm) dia and 2-1/4 in. (57 mm) dia steps, 675,000 Btu/hr (198 kW) rated capacity

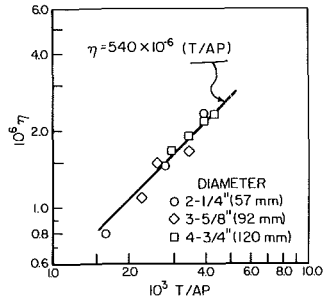

Fig. 8 Efficiency of noise production as a function of normalized thrust for burner DMA

might expect. When burner ARP was overfired, the flame moved from its normal holding position and stabilized in a region where premixing occurred prior to combustion. Further overfiring resulted in the flame largely moving out of the burner, and the slope changed from the theoretical. Finally, noise output is affected by mixture ratio. However, a correlation still can be obtained as shown by the right-hand side coordinate system of Fig. 2.

Burner BBD (Fig. 4), while based on a nozzle mix burner design, actually had a small amount of premixing. Furthermore, it was actually a rocket-shaped burner with internal combustion. This resulted in a premix burner performance, as shown in Fig. 4. Again, a further arbitrary correction for the A/F ratio works.

A similar result was obtained with burner EEE wherein the mixture entered the combustion chamber through a porous cylinder.

The effect of air/fuel ratio on noise production from the premixed flames can be explained on the basis of equation (1). As the mixture ratio moves farther from stoichiometric, the mixture dependent portion of the equation takes on a smaller value, and the predicted efficiency of noise production becomes less. However, with a diffusion flame, the burning occurs at a variety of mixture ratios distributed narrowly about the maximum buring velocity composition. Thus, for diffusion flames, there is no effect on air/fuel ratio.

Turbulent Intensity. With an increase in turbulence level, there is a general increase in the noise output; the noise spectrum increases nearly uniformly in amplitude while maintaining its shape [6,13]. Equation (1) indicates that the noise power output at constant firing rate will vary with the second power of the turbulence intensity. There are few data, however, where a direct measurement of turbulence intensity has been made to check this result. In a study of burner FRP, a perforated plate was installed alternatively at upstream distances of 12 in. (0.30 m) and 40-1/2 in. (1.03 m) from the end of the potential core of the flame (region of maximum noise production in the flame). Using the classical 5/7 power of turbulence decay for the turbulence generated by a grid, a 7.5 dB difference is indicated. This corresponds exactly with the measured difference in dB level.

Custard [11] outlines the development of a quiet industrial burner through a systematic change in size of the inner and outer recirculation zones behind corresponding steps in the burner tile to minimize the turbulence intensity in the combustion zone. Figure 5 shows the original version of the burner and the final version of the burner. In the experiments, the areas of the inner and outer steps were varied. Figure 6 shows the sound data normalized to eliminate the effect of firing rate; the noise level is seen to minimize when either the inner or external step was absent and maximize when about two-thirds the area was in the external or outer step.

Noise Jump Phenomena. When the position at which a flame is seated shifts suddenly as the firing rate increases, a sudden change in the noise level also may occur. The jump can be either up or down in amplitude. Putnam [1,9,10] termed this "superturbulent combustion noise" in reviewing several instances reported in the literature. As an example, Fig. 7 for a nozzle-mix burner (DMA) with multiple steps on the tile shows corresponding steps in the noise level. These relate to changing positions of flame stabilization. It was also found that the efficiency of conversion of chemical energy to noise was directly proportional to the burner thrust divided by the pertinent holding area. This result is shown in Fig. 8. A check on the proportionality constant between the noise parameter and thrust parameter showed that it varied from a low value for premix burners to high values for nozzle-mix burners [10].

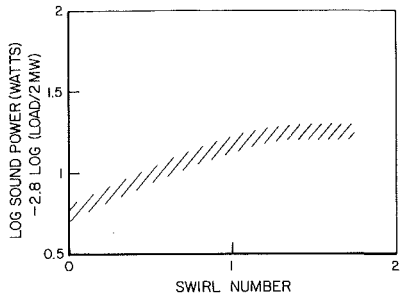

Fig. 9 Efficiency of noise production as a function of swirl

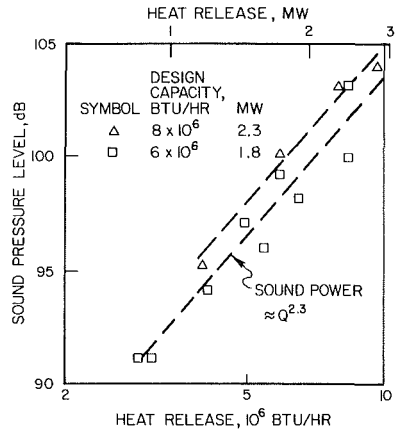

Fig. 10 Comparison of noise output of two propane fired refinery burners

The general effect of swirl in burners is to increase the intensity of combustion and also the noise level. Figure 9, based on studies of a gas-fired swirl burner in an acoustically-open situation [14], shows that the noise level first increases with swirl and then levels off. In some instances, a phenomenon like that of the jump phenomenon previously discussed may occur [15].

Burner Size. If a homologous series of burners is considered, each firing at its rated capacity and pressure drop, then (neglecting Reynolds number effects) u'/c which is proportional to $\sqrt{\Delta p}$ is a constant. From equation (1), the efficiency of conversion is also a constant. Thus, the noise power at design capacity is proportional to the firing rate. It follows that a change in the number of burners for a given application, if from the same series and all fired at the rated capacity, will not change the combustion roar output.

Some experimental data appear to conflict with this conclusion, but the observed results can be explained. Seebold [16] discussed results obtained by Bitterlich [17] on two propane-fired refinery burners of different design size. As shown in Fig. 10, the data, though scattered, show a change of noise power output with the 2.3 power of the firing rate, as compared to the theoretical value of 3. The data scatter is similar to that found in our studies with industrial burners lacking symmetry due to side ports for ignitors, sensors, and constructional defects. On this basis, the presence of a jump phenomenon in the smaller burner could explain a deviation of all the data from a straight line with a slope of about 3. However, the burner could have been designed on the basis of a constant intensity of combustion at design rate; this could also explain the difference of the two design capacities.

Payne [19], in a study of three burners in a triangular array in a furnace as contrasted to one burner of equal capacity, found that there was a general tendency for the noise to decrease with increased spacing when the one burner was

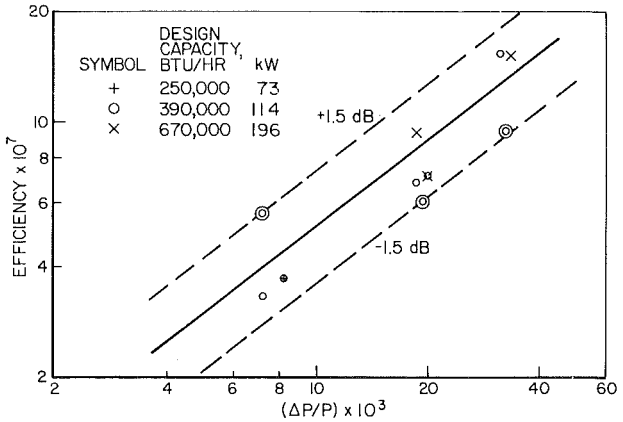

Fig. 11 Efficiency of conversion of chemical to acoustic energy as a function of dimensionless pressure drop

twice the other two in capacity, but no consistent effect when all three were the same capacity. Beer [20] suggested that these results are related to an observation in another flame study that noise was attenuated as it passed through multiple flame surfaces [21].

Giammar and Putnam [6] showed that, for a constant firing rate natural gas diffusion flame, the noise level increased as the intensity of combustion increased and flame size decreased; this was as expected. But they also showed a cutoff of higher frequencies which extended to lower frequencies as the flame size increases. Thus, one might also expect some decrease in noise level in a homologous series of burners as the firing rate increased. This size effect is very important in analyzing data for flames with high reaction rates per unit volume, such as ethylene and hydrogen. Cutoffs lower than the predicted peak frequencies can result, thus reducing the apparent peak frequency.

However, the explanation may simply lie in the observed noise suppression effect of a lower velocity and temperature jet on a higher velocity and temperature jet [22].

Giammar and Putnam [5] used a series of three sizes of flame retention premix burners, singly and in pairs with 20 in. (0.5m) separation, to examine the effect of number of burners and burner size. Figure 11 shows the results in terms of noise efficiency as a function of dimensionless pressure drop. The data show no consistent effect of using one or two burners at a given firing rate.

Summarizing, there is no clear-cut evidence for preferring multiple small burners to one large one on a noise basis, if they are designed in a homologous series.

Preheat. Few data are available on the effect of preheat temperature on burner noise production. From equation (1), one would expect the noise level to increase with preheat, both because of the effect on flow velocity and the effect on burning velocity. Smith and Lowes [15] report data on three gas-fired swirl burners in a furnace. Preheats were varied to give from 25 to 480°C air temperature. Up to about 200° C, the noise level increased somewhat faster than expected from theory; above 200°C, the increase was about as expected. However, consideration of the data recording method indicates that the deviation from the theory could be a result of the specific recording procedure.

Flames in Enclosures

While the basic nosie spectrum of a turbulent flame is shaped much like the spectrum from jet noise, components of the spectrum are amplified at the natural frequencies of the surrounding enclosure. As an example, a burner tile around a flame can amplify the combustion roar at the natural axial

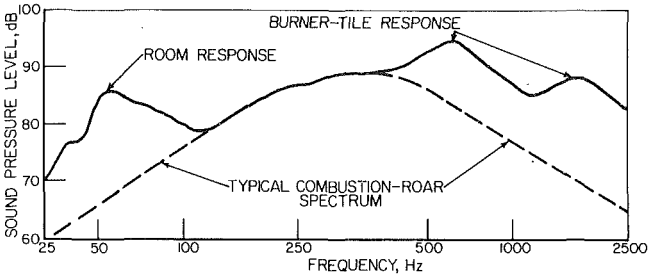

Fig. 12 Effect of environmental amplification of typical combustion-roar spectrum for a nozzle-mix burner

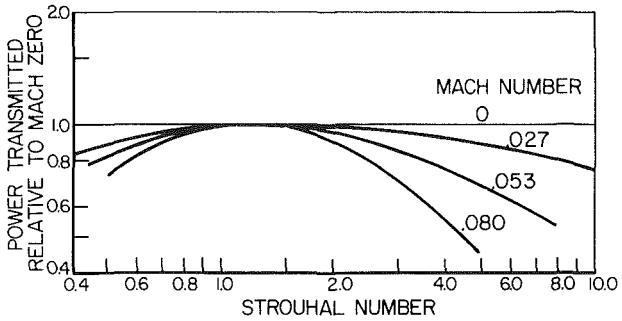

Fig. 13 Effect of Strouhal number and Mach number on noise power transmitted from duct

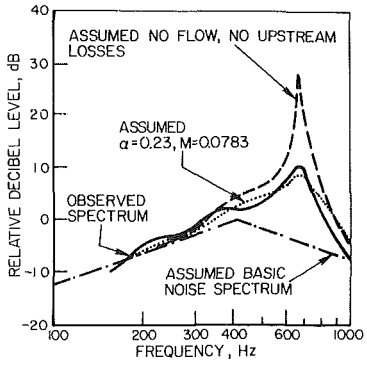

Fig. 14 Comparison of theoretical spectrum with experimental spectrum for burner tile: 9 in. (229 mm) x 4 in. (102 mm) dia tile, 440 SCFH (12.5 m^3/h) of natural gas, 10.2 air/fuel ratio, assumed average combustion duct temperature of 1800°F (986°C)

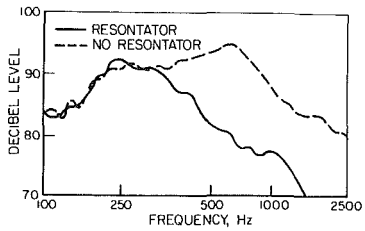

Fig. 15 Effect of Helmoltz resonator in burner tile on combustion-roar spectrum of an industrial nozzle-mix burner

modes of the tile. Figure 12 shows such an example of first mode amplification at about 600 Hz for a burner similar to burner ARP discussed earlier [1,6]. In Fig. 12, amplification at 50 Hz results from the lowest natural frequency of the room in which the burner was fired. The same phenomenon occurs from a burner in a furnace. Several factors enter into altering the spectrum shape and amplitude of the combustion roar of a burner when it is inserted into a furnace, beyond the obvious external factors of distances and orientation of the observation point in the region surrounding the furnace or stack. These include the internal shape of the furnace or burner duct, the acoustic properties of the furnace lining, the transmission of noise upstream into the fuel and air supply systems, and the transmission and reflection characteristics of the walls. In this discussion, the assumption is made that the walls are rigid; for a residential heating unit, this assumption is not justified. Furthermore, the effect of fan or blower noise is not discussed herein; yet in many instances, the blower noise from a furnace air supply can be of the same magnitude or higher than the combustion roar [23].

In the following section, the amplification of burner noise by tiles, ducts, and radiant tubes is first covered, and then the amplification by furnaces.

Duct Amplification. When a burner is inserted into a duct of infinite length in both directions, theory shows the noise from the array of monopole sources is amplified significantly. Strahle [24] confirmed this theoretical prediction experimentally. Further, simple theory indicates that a long unflanged tube with a burner deep within it, and with no acoustic reflection from upstream, will emit the same noise from the end as would the burner in the open at the position of the tube opening. That is, the amplification of the burner noise in one direction by the presence of the duct is canceled out exactly by the reflection from the open end. In practical burners, more complications arise.

Putnam [25] discussed the results of measurements of sound reflection back into the duct and transmission out through the end of a duct from noise generated in the duct, at several flow velocities, on the net sound power transmitted to the surroundings from the sound source. At a critical Strouhal number, that is, the product of frequency and duct diameter divided by the flow velocity, there was no effect of flow. Either side of this Strouhal value, there was a decrease in the transmitted power, the amount of decrease increasing with increasing Mach number. Figure 13 shows the effect.

The results were used to predict the noise spectrum external to a radiant tube burner about 10 ft (3.05 m) long, and a short tile about 9 in. (0.23 m) long. In both instances, it was found that the effect of upstream losses (i.e., transmission of signal upstream into fuel and air supply ducts) was far more important than the effect of flow [25]. In both cases, the temperature interface between the flame and the surroundings was neglected on the basis that such an interface would be present both for flame in a duct and a flame in an acoustically-open situation, and would have the same effect. In the case of the tile, some data were available on the noise spectrum of a burner. Unfortunately, experimental absolute values were not available, but matching the noise spectrum at the low frequency end showed an excellent agreement between theory and experiment over the rest of the spectrum [25]. Figure 14 shows the result. It may be concluded that the essential features of the noise produced by a burner in the tight enclosure of a duct are adequately understood.

The duct amplification of combustion roar, such as in Figs. 12 and 14, may be reduced by use of sound absorption material, especially at higher frequencies. However, such materials have practical limitations in this type of industrial use. The results of an alternative approach are shown in Fig. 15, for a nozzle-mix burner with a 5 in. (127 mm) dia by 6-1/2 in. (165 mm) long tile [6].It is noted that the noise level has been lowered 15 dB above 600 Hz. In this alternative approach, the tile is replaced by a set of reactive mufflers designed in a conventional manner. For the specific case shown, all orifices were distributed on the inner surface, but the enclosed volume was so divided as to produce six Helmholtz-type mufflers of three different design frequencies covering the range of desired frequency suppression. The similarity of this approach to one that can be used for various thrust producing devices is obvious.

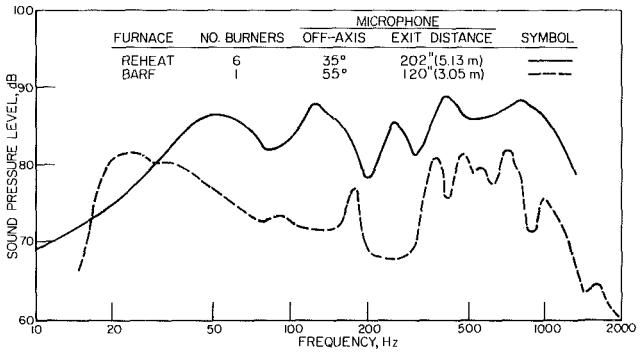

Fig. 16 Comparison of 10^6 Btu/hr (293 kW) burner in reheat furnace and BARF furnace. BARF data corrected for number of burners, 1/10 octave band width to 1/3 octave width, and distance to furnace exit

Furnace Amplification The situation of a burner in a furnace is different than that in a duct. First, from several cold flow studies, it appears that there is no net position or negative amplification because of flow through the exit openings for flows of interest in this study (in contrast to result of Fig. 13). Second, there can be significant damping effects as the results of the furnace lining. Third, far more acoustic modes are available in a furnace; these include not only transverse and combined modes of reasonably low frequency, but also a very low Helmholtz frequency. For simple furnace shapes, assuming a simple temperature profile, an exact solution can be obtained for the noise power propagated to the exterior of the furnace. The author was successful in calculating the noise power propagated to the exterior of a furnace for a cylindrical hard-walled furnace with a centrally-located flame at one end and a centrally-located short exhaust at the other end. However, furnaces are usually more complex in shape and more difficult to handle analytically.

Abrishaman [26] suggests dividing the problem into three frequency ranges, typically classified as lumped element acoustics for low frequencies, wave theory acoustics for medium frequencies, and geometric acoustics or statistical energy method for high frequencies. Considering that the peak frequency of combustion roar is usually in the 100-500 Hz range, the corresponding half wavelength in a hot furnace is the order of 2–10 ft (0.6–3 m). Much smaller furnaces could probably be treated adequately by the lumped-element approach. Much larger furnaces could be treated by the statistical energy method. Some success has also been reported using this later approach well into the region where wave theory should be used [26]. This simplification in approach is more acceptable for cases where only the coarse octave band analysis is required, and there is appreciable damping.

Putnam [1] compared the noise outside the exit of a 6 ft (1.83 m) dia by 6 ft (1.83 m) long furnace with a flat-flame burner within (dashed line of Fig. 16) to the noise spectrum for a similar design of flat-flame burner in the open (curve not shown). No exact comparison was possible, but a similar spectrum shape was noted. The small ripples above about 400 Hz, not present in the open burner data, are related to the exit duct modes. The 180 Hz frequency is an amplification at the first axial mode of the furnace interior, and the Helmholtz frequency is about 25 Hz. Both these modes also distorted the open burner spectrum.

Using reasonable assumptions for damping of the furnace liner material, a noise spectrum was developed for the burner in an acoustically-open situation. This, of course, would be the aim of a full calibration of a Burner Acoustic Rating Furnace (BARF), namely, to develop a rating correction factor from the measurement to the correct burner spectrum in an acoustically-open but flow and thermally-closed furnace situation. The developed spectrum was reasonably close to that observed for the similar burner.

In another comparison, the noise level of the above furnace was checked against a 6,000,000 Btu/hr (20 MW) reheat furnace. The burners were identical with the one used to obtain the dashed curve in Fig. 16. Interestingly, the furnace volume per burner and per design firing rate, and the exit area per burner, were nearly identical in the two furnaces, though the Helmholtz frequencies were different. The data from the burner in the rating furnace (BARF) were corrected to the conditions of the measurements of the reheat furnace. Figure 16 shows the comparison. The general shape is not too different; the lowest mode in the reheat furnace is the Helmholtz frequency at about 50 Hz (as contrasted to above 25 Hz for BARF), and the other modes are axial furnace modes. The greatest difference is an average of about 6 dB of the reheat furnace above the rating furnace.This brings out another important point. External noise measurements for the rating furnace were made in an acoustically open situation. The noise level measurements for the reheat furnace were made in a factory situation. The 6 dB agreed with the expected difference because of this room enclosure [27].

Other effects of furnace enclosures have been noted. For instance, Bertrand and Michelfelder [12] reported that the noise power in the maximum energy octave band, a, of a swirl burner in a furnace increased with the 3.6 power of the firing rate while the overall noise power, b, increased as the expected third power like the noise power on both bases, a and b, in an acoustically open situation. The furnace enclosure in this instance appears to have caused an increase in the peakedness of the spectrum as the firing rate increased. This may be related to the observation by Putnam [24] on tube burners relative in the effect of flow velocity.

Abrishaman [26] reported a series of both cold flow and fired results on a furnace with inside dimensions of $4 \times 4 \times 6$ ft long ($1.2 \times 1.2 \times 1.8$ m long). The furnace, for most tests, was lined with 4-1/2 in. (114 mm) of 2300°F (1260°C) insulating firebrick. The burner (under cold conditions a loudspeaker or air jet) was in the center of one end, and the flow exit was in the center of the other end. Burner ARP was used at design capacity.

In a series of cold flow tests, constant area exits from round to 2.5:1 slots showed no significant difference in transmission of noise. With exit areas over a 4:1 ratio, the external noise level increased linearly with area. In a series of tests on 3 in. (76 mm) dia exits of about 7 to 24 in. (178 to 610 mm) long, amplification at the natural frequencies of the ducts was found, but overall there was no effect of length on the noise level. Comparative tests at no flow and 0.13 Mach number exit velocity showed no significant differences. In one test, the furnace had an additional 3 in. (76 mm) of glass fiber lining added. This did not greatly reduce the overall noise level as compared to the rather porous firebrick, but it did eliminate the resonant frequency peaks.

Following these tests, Abrishaman used a jet to produce a noise spectrum inside a furnace after calibrating it in an acoustically infinite environment. For this small furnace, observation and prediction of interior noise level using the geometric acoustic method agreed within 3 dB for octave bands from 125 to 8000 Hz, with the overall predicted valued about 1 dB high. For the exterior, the agreement was again within 3 dB, for 63 to 8000 Hz octave bands, with the overall prediction about 1 dB low.

In the hot flow tests, using Burner ARP, the lack of effects of exit shape was confirmed, as was the linear effect of exit area on outside sound level. The hot and cold differences in internal and external sound pressure levels were compared. For the hot furnace, the drop in level for the interior to ex-

terior was 3.5 dB less at 500 Hz band; the difference fell off to zero in the 4000 Hz band, and between the 63 and 32.5 Hz bands. Comparing the measured external noise level with that calculated from the data on the burner in an acoustically open situation, using the geometric acoustic method [22,25], showed an agreement of overall noise level within 1 dB. However, this was felt to be an anomalous result, since octave band variation ranged up to 11 dB for the 31.5 Hz octave band, with three deviations of about 5 dB. In the case of 11 dB, the observed noise level with burner inside the furnace was high. The Helmholtz frequency is within this ocatve band, and it is not surprising that the geometric method failed. However, Giammar and Putnam [6] earlier noted a similar occurrence.

Concluding Remarks

The data discussed hereinbefore concerning the combustion roar of industrial burners make it clear that the turbulence level in the combustion zone of a flame has a significant effect on the noise level. This is in essential agreement with simple theory. The flow velocity, flow rate, and excess air should be as low as possible, and there should be no turbulent generators in the burner beyond those needed for the proper performance and shape of flame.

Muffling the furnace of burner is quite effective. For instance, Seebold [16] has shown that dissipative mufflers on the inlet of inspirating burners can reduce the noise level by the order of 20 dB. Reactive mufflers have also been used as part of a burner wall to reduce combustion roar by a significant amount [6].

If a furnace is hard-walled, a significant reduction in combustion roar can be achieved by using a more sound absorbent lining. In a similar manner, the noise from the furnace discharging into hard-wall enclosures may be suppressed by improved wall treatment.

There is no clear evidence that using an increased number of smaller burners will either increase or decrease the noise level. The basic design philosphy used for a series of burners has a significant control on the result, but the way burners are distributed and the relative sizes of the flames also influence the result.

As a final comment, it is expected that in the not-too-distant future burner manufacture will be able to supply basic combustion roar output for a burner, plus guidance in predicting from this information the external noise of any particular furnace design.

References

1 Putnam, A. A., "Combustion Noise in Industrial Burners," *Noise Control Engineering*, Vol. 7, July/Aug. 1976, pp. 24-34.

2 Putnam, A. A., *Combustion-Driven Oscillations in Industry*, American Elseveier, 1971.

3 Bragg, S. L., "Combustion Noise," *Journal Institute Fuel*, Vol. 36, 1963, pp. 12-16.

4 Giammar, R. D., and Putnam, A. A., "Combustion Roar of Turbulent Diffusion Flames," ASME JOURNAL OF ENGINEERING FOR POWER, Vol. 92, 1970, pp. 159-165.

5 Giammar, R. D., and Putnam, A. A., "Combustion Roar of Premix Burners, Singly and in Paris," *Combustion and Flame*, Vol. 18, 1972, pp. 435-438.

6 Giammar, R. D., and Putnam, A. A., "Noise Generation by Turbulent Flames," *American Gas Association*, Cat. No. M00080, 1971.

7 Shivashankara, B. N., Strahle, W. C., and Handley, J. C., "Combustion Noise Radiation by Open Turbulent Flames," *Progress in Aeronautics and Astronautics*, Vol. 37, MIT Press, 1975.

8 Strahle, W. C., and Shivashankara, B. N., "A Rational Correlation of Combustion Noise Results from Open Turbulent Premixed Flames," 15th Symposium on Combustion, The Combustion Institute, 1975, pp. 1379-1385.

9 Putnam, A. A., Fischer, R. D., Rodman, C. W., and Freeze, T. W., "Superturbulent Combustion Noise," Battelle Report to A.G.A., Feb. 18, 1976.

10 Putnam, A. A., "Combustion Roar of Seven Industrial Gas Burners," *Journal Institute Fuel*, 1976, pp. 135-138

11 Custard, G., "The Suppression of Noise in Heating Plants," *Gas Engineering and Management*, Vol . 17, 1977, pp. 422-428.

12 Bertrand, C., and Michelfelder, S., Report on the AP-5 Trials, International Flame Research Foundation, Doc Nr F 37/a/3, 1978 (Fig. 4.6.2).

13 Putnam, A. A., "Combustion Noise in Industrial Furnaces," Seminar on New Developments in Combustion Engineering, Penn State Univ., 1971.

14 Bertrand, C., and Michelfelder, S., "Experimental Investigation on Noise Generated by Large Turbulent Diffusion Flames," 16th International Symposium on Combustion, The Combustion Institute, 1977, pp. 1757-1769.

15 Smith, R. B., and Lowes, T. M., "Report on AP-4 Trials," *International Flame Research Foundation*, Doc Nr F 37/a/1, 1974.

16 Seebold, J. G., "How to Control Combustion Noise in Process Plant Furnaces," *Oil and Gas Journal*, Jan. 3, 1972, pp. 48-51.

17 Bitterlich, G. M., "Some Findings on Burner Noise and Its Suppression," Symposium on Burner Noise, 35th Mid-Year Meeting on API Division of Refining, May 1970.

18 Putnam, A. A., "Your Combustion Noise—What Type It Is ? Session III, Paper 2, *Proceedings of 3rd Conference on Natural Gas Research and Technology*, American Gas Association, Mar. 1974.

19 Payne, R., "Report on the Multiple Burner Trials—MJ3, "International Flame Research Foundation," Doc Nr F 35/a/11, 1977.

20 Beer, J. M., Private Communication.

21 Gupta, A. K., Syred, N., and Beer, J. M., "Fluctuating Temperature and Pressure Effects on the Noise Output of Swirl Burners," 15th International Symposium on Combustion, The Combustion Institute, 1975, pp. 1367-1377.

22 Shivashankara, B. N., and Bhat, W. V., "Noise Characteristics of Two Parallel Jets with Unequal Flow," *AIAA Journal*, Vol. 19, 1981, pp. 442-448.

23 Faulkner, L. L. (editor), Handboook of Industrial Noise Control, Industrial Press, Chapter 12, Case Study 4, 1976.

24 Strahle, W. C., "Combustion Noise," *Progress Energy and Combustion Science*, Vol. 4, 1978, pp. 157-176.

25 Putnam, A. A., "Transmission of Combustion Roar from Burners and Furnaces," *ASHRAE Transactions*, Vol. 84, Part 1, 1978, pp. 477-487.

26 Abrishaman, M., "Summary Report on Effect of Furnace Design on Combustion Noise," Battelle Report to American Gas Association, July 19, 1977.

27 Peterson, A. P. G., and Gross, E. E., Jr., *Handbook of Noise Measurements*, 7th ed., Fig. 8.8 General Radio, 1972.

Naturally Occurring High-Chloride Coal and Superheater Corrosion—A Laboratory Study[1]

A. L. Plumley

W. R. Roczniak

Combustion Engineering, Inc.,
Windsor, Conn. 06095

DOE Provided funds for C-E to investigate the fireside corrosion potential of commercial boiler tube alloys at elevated temperatures when exposed to the combustion products from a series of coals. The results of the laboratory and field tests were previously reported. In a supplementary phase of the program, C-E tested for the effect of chloride on similar alloys while firing a naturally occurring high chloride Midwestern bituminous coal in the same laboratory furnace. On the basis of exposure in the convection pass at temperatures from 1100–1700°F, Inconel Alloy 690 was found to have very good resistance to corrosion while Incoloy 800H and Tp-310 s. s. were good transitional materials. Poor materials were T-22, 316 s. s., Inconel 617, and Inconel 671.

Introduction

An earlier publication [1] described a Department of Energy (DOE) funded investigation to determine the fireside corrosion potential of a series of commercial boiler tube alloys and coatings for advanced power cycles. These cycles may operate at higher temperatures, but with lower pressure and possibly with circulating fluids other than steam. The alloys and coatings were tested at elevated temperatures when exposed to the combustion products from a series of coals. The results of this investigation, a series of four laboratory tests and four field tests, were reported earlier by the Kreisinger Development Laboratory (KDL) of Combustion Engineering [2].

This investigation did not concentrate on coal with particular chemical cnstituents, but used four coals of geographic and economic significance (Eastern bituminous, Midwestern bituminous, Western subbituminous and Texas lignite). Chloride, however, is one chemical constituent of fuel that has made itself conspicuous. Large amounts of chloride in fuel have been shown to lead to increased fireside wastage in coal-fired boilers in England, and in incinerators and chemical recovery boilers. Consequently, in a supplementary phase of the program, the effect of naturally occurring high-chloride (>0.3 percent) coal[2] on the previously evaluated corrosion resistant alloys was tested. The alloys were exposed for 300 hrs in the same laboratory facility that was used in the previous investigation [1, 2].

Experimental

Materials. In the earlier investigation the available alloys had been surveyed and the field narrowed to twenty-two commercial alloys, based on mechanical properties (creep strength data) and resistance to fireside corrosion at elevated temperatures (1600–1800°F, 870–980°C). From the twenty-two, seven had been selected for testing based on the additional factors of ease of manufacture, availability, economics, and previous performance in the boiler and power turbine industry.

Of the original seven metals and coatings tested in the initial program, two metals and all the coatings were dropped. Haynes 188 was not included because of its limited availability and prohibitive cost. Sandvik 12R72 and the previously evaluated coatings were omitted due to their relatively poor performance in previous testing. For the two metals dropped, two were added: Inconel 690 and T-22. Inconel 690 was a newly available alloy recommended by the vendor for application in high chloride environments. T-22 (2¼ Cr, 1 Mo) was added for testing at the lower temperatures to allow comparison of the resistance of a lower alloy ferritic steel, a conventional superheater material, to the high chloride coal combustion products.

The exposed alloys were classified into four categories. The first category consisted of the austenitic steels TP-310H and TP-316H, the second category consisted of the nickel-chromium-cobalt alloys Inconel 617 and 671, the third category was the nickel-chromium-iron alloy Incoloy 800H, and the fourth category consisted of T-22 (Table 1).

In these tests, ring specimens were fabricated from the alloys, mounted on temperature controlled probes, and exposed to the products of combustion resulting from burning a raw 0.45 percent chloride Illinois interior coal, which could be classified as bituminous high volatile C. The source of this high chloride coal was Illinois No. 6 Seam—Old Ben Mine No. 21. The probes were located in a convection pass of the laboratory test facility whose nominal gas temperatures range between 1700–2200°F (925–1205°C). Metal temperatures

[1] Work included in this paper was partly funded under DOE Contract ACO1-76 ET 1050 (Formerly (#49-18)-2045).

[2] No coal with these levels of chloride is currently burned in U.S. boilers without blending.

Contributed by the Fuels Division of THE AMERICAN SOCIETY OF MECHANICAL ENGINEERS and presented at the Winter Annual Meeting, November 15-20, 1981, Washington, D.C. Manuscript received at ASME Headquarters July 15, 1981. Paper No. 81-WA/Fu-10

Table 1 Alloys being exposed for 300 hrs on KDL-FTPF in high-chloride Illinois coal

Type	Group	[a]Creep rupture values, KSI (MPa) 1200°F	(650°C)	1450°F	(785°C)	Major constituents	Relative[b] price index
T310H	Std. austenitic S.S.	6.0	(41)	2.0	(14)	25Cr-20.5Ni-25C	1.7 X
T-316H	Std. austenitic S.S.	11.4	(78.6)	2.6	(18)	16Cr-13Ni-2Mo	1.6 X
Inconel 617	Alloys strengthened by solution hardening and carbide dispersion	21.5	(148)	9.0	(62)	22Cr-54Ni-9Mo-12.5Co	11.5 X
Inconel 671	Alloys strengthened by solution hardening and carbide dispersion					Clad (50/50 Cr-Ni on 800H)	6.1 X
Incoloy 800H	Alloys strengthened by solution hardening and carbide dispersion	9.8	(68)	4.5	(31)	21Cr-32Ni-46Fe-.1C	2.7 X
Incoloy 690		4.8	(33)	<1.0	(<6.9)	29Cr-60Ni-8Fe	3.5 X
T-22		2.4	(17)			2¼ Cr-1Mo-Bal Fe	0.4 X

[a]Ave. 100,000 hrs values
[b]X for 304 s.s. – 1.0

Table 2 FPTF typical operating data

Combustion data	Conventional units	S.I. units
Total heat input (X 10^6)	3.54 Btu/hr	3.74 kJ/h
Coal feed rate	273 lb/hr	124 kg/h
Primary air flow	395 lb/hr	179 kg/h
Primary air temp.	71°F	22°C
Secondary air flow	2618 lb/hr	1188 kg/h
Secondary air temp.	697°F	370°C
0_2 (% in flue gas)	4.1	4.1
Combustibles (% in flue gas)	0.0	0.0
Furnace pressure (H_2O)	−0.35 in.	0.89cm
Lower furnace temperature	2690°F	1476°C
Lower furnace residence time (s)	0.97	0.97
NHI/PA (X 10^6)	0.637 Btu/hr-ft^2	7.23 kJ/hr-m^2
Vol. heat release rate	46680 (Btu/hr-ft^3)	1.739×10^6 kJ/h-m^3
Waterwall test panel		
Metal surface temp.	700°F	371°C
Therminol inlet temp.	503°F	262°C
Therminol outlet temp.	521°F	272°C
Therminol flow rate	8.0 g/min	30 l/min
Superheater probes		
Gas temperature		
Duct I	2260°F	1238°C
Duct II	2080°F	1138°C
Duct III	1960°F	1071°C
Gas velocities		
Duct I	63.8 fps	19.5 m/s
Duct II	59.6 fps	18.2 m/s
Duct III	56.8 fps	17.3 m/s

ranged from 1200–1800°F (650–980°C) corresponding to anticipated temperatures in advanced thermal power cycles.

Test Equipment. The six probes used in this supplementary study contained five test sections per probe. Each controlled temperature corrosion probe system was comprised of a number of subsystems. Included were the probe assembly, an electronic temperature controller (to fix the assigned temperature), an air distribution system (pneumatic controller), a multipoint temperature recorder, thermocouples, lead wire, and required air and electrical sources. Details of the fireside performance test facility (FPTF) and the test probe system have been reported elsewhere [1].

Furnace Operation. Typical operating data for the FPTF in this test are shown in Table 2. The average coal feed rate was 273 lb/hr (124 kg/h). The firing at this feed rate in combination with preheated secondary air at a temperature of 697°F (370°C) resulted in a total heat input of 3.54 × 10^6 Btu/hr (3.74 × 10^6 kJ/h). The lower furnace gas temperatures were relatively stable at 2690°F (1476°C) throughout the test. Figure 1 presents a schematic of the FPTF. Typical gas temperatures were 2260°F (1238°C), 18 in. (45 cm) downstream from the furnace outlet; 2080°F (1138°C), 48 in. (122 cm) downstream; 1960°F (1071°C), 85 in. (216 cm) downstream; and 1780°F (971°C) at the end of the superheater test section.

Refractory wall surface temperatures were as high as 2000°F(1094°C). There was substantial ash deposition on the refractory walls with deposits reaching a maximum thickness of approximately 1½ in. (3.8 cm). In the combustion zone, refractory wall deposit outer surfaces were molten and fluid during operation.

Furnace operation was relatively stable throughout most of the test. There were a few instances where clinkers dislodged from the refractory roof and fell on top of the burner. In most of these cases, furnace stability was only slightly disrupted in that the furnace pressure fluctuated very little. Occasionally similar clinkers were sucked into the superheater duct, resulting in high draft losses (partial pluggage). However, in all cases, the clinkers were removed within one hour to minimize furnace fluctuations.

The laboratory analysis of the as-fired pulverized high-

chloride Illinois coal is shown in Table 3. Analyses of both the Illinois interior and Pennsylvania Appalachian coals used in the earlier tests are included for reference. The heating value of this fuel was 11,480 Btu/lb (26,703 kJ/kg), and the ash content was 17.1 percent. In the previously completed laboratory tests using Illinois coal, the fuel analysis indicated 12,170 and 13,270 Btu/lb (28,307 and 30,866 kJ/kg, respectively) with ash contents of 12.6 percent. The ash fusibility temperatures were relatively low with a softening temperature of 2120°F (1160°C) and a fluid temperature of 2670°F (1466°C). The fluid temperature of the high chloride coal was about 400°F (200°C) higher than that of the originally tested Illinois coal—2280°F (1249°C)—but was comparable to that of the Pennsylvania coal—2260°F (1460°C). The screen analyses showed that 81.1 percent of the pulverized fuel passed through a 200 mesh sieve. By pulverizing with a mill outlet temperature between 140°F and 150°F (60° and 66°C), the moisture content of the coal was reduced to 2.6 percent. These procedures are typical of all test runs on this facility.

Superheater Probes. Surface metal temperature of superheater probes were controlled at 1100, 1200, 1300, 1425, 1575, and 1700°F (593, 649, 704, 773, 857, and 927°C). There were three thermocouples located along the length of each probe, approximately 2½ in. (6.35 cm) apart. The controlling thermocouple was located in the center.

Superheater probe deposits formed during this 300-hr test were very similar to those formed during the firing of previously tested Illinois coal. Superheater probe deposits usually consist of three layers, specifically referred to as the initial layer, inner layer, and outer layer. The initial deposit consisted of a thin coating of dry, gray-white powder which covered the face of the probe. This deposit was generally less than 1/32-in. (0.07-cm) thick. The inner deposit was a very dense, reddish brown material. The deposit had a coarse, compact structure and covered the initial deposit completely. The particles forming this deposit thickness varied along the length of the probe, being thickest in the center and tapering to each end. At the end of the test and deposit thickness in the center of the probes was approximately ½ in. (1.27 cm) in

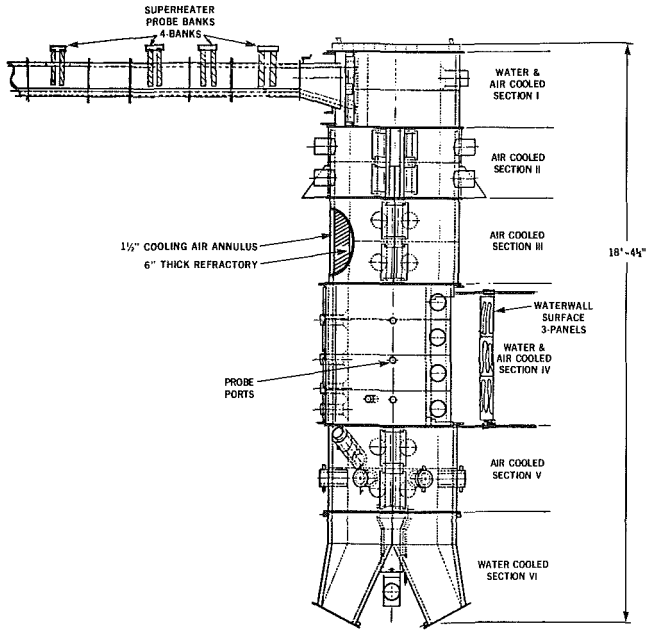

Fig. 1 Schematic of fireside performance test facility

Table 3 Analysis of as-fired coals 300-hr test FPTF

	Pennsylvania Appalachian pulverized coal	Illinois interior pulverized coal, low-chloride	Illinois interior pulverized coal, high-chloride
Proximate, Wt. %			
Moisture	0.7	2.1	2.6
Volatile matter	32.3	31.5	32.2
Fixed carbon	54.4	53.8	48.1
Ash	12.6	12.6	17.1
Total	100.0%	100.0%	100.0%
HHV,	13,270 Btu/hr 30,866 kJ/kg	12,170 Btu/hr 28,307 kJ/kg	11,480 Btu/hr 26,703 kJ/kg
Ultimate, Wt. %			
Sulfur	1.4	3.6	1.8
Chloride	0.16	0.06	0.45
Ash fusibility, °F			
I.T.	2370 (1299°C)	1960 (1071°C)	2030 (1110°C)
S.T.	2510 (1377°C)	2020 (1105°C)	2120 (1159°C)
H.T.	2560 (1405°C)	2170 (1188°C)	2380 (1304°C)
F.T.	2660 (1460°C)	2280 (1249°C)	2670 (1465°C)
Ash composition, Wt. %			
SiO_2	51.1	42.0	54.6
Al_2O_3	30.7	15.2	21.4
Fe_2O_3	10.0	18.4	9.0
CaO	1.6	7.1	4.8
MgO	0.9	1.0	1.0
Na_2O	0.4	0.9	1.1
K_2O	1.7	1.3	2.3
TiO_2	2.0	1.0	0.9
SO_3	1.4	8.9	4.5
P_2O_5	0.1	0.2	---
Total	99.8	96.0	99.6
Base/acid ratio	0.174	0.49	0.295
Fe_2O_3/CaO ratio	6.25	2.59	1.88
Water soluble Na	0.01	0.075%	not determined
Water soluble K	0.01	0.008%	not determined
Acid soluble Na	0.02	0.06%	0.07%
Acid soluble K	0.05	0.139%	0.10%

probe bank I (the duct area adjacent to the furnace) to less than ⅛ in. (0.32 cm) in bank III (Fig. 2). In bank I, all the probes had massive outer deposits, while the probes in banks II and III had much less outer deposit. The outer deposits were generally crystalline and porous and adhered relatively weakly to the inner layer of deposit. At the high gas temperatures in bank I (2260°F, 1238°C), the outer deposits became somewhat tacky (plastic) and less friable. At no time was the overall appearance of the deposit molten. Outer deposits formed at lower gas temperatures, banks II and III, were friable and tended to slough off the probes at thickness of 3 in. (7.6 cm) and 1½ in. (3.8 cm), respectively, for bank II and bank III. Overall, the physical nature and growth rate of deposits were affected by both flue gas and surface metal temperatures. (Deposition rate on downstream probes, banks II and III was influenced by the scrubbing or collecting action of the probes in bank I, which effectively reduced particle loading of downstream probes.)

Laboratory analyses and fusibility temperatures of the deposits are listed in Table 4. Initial deposits were not available for analyses from the test probes since the primary objective of the test was determination of gross weight loss and penetration. Representative inner deposits from banks I and II show significant increases in iron (as Fe_2O_3) when compared to the as-fired coal ash.

The bonding strength of the inner deposit to the superheater probe was comparable to that previously experienced when burning Pennsylvania and greater than that found when burning Illinois coal. It was bonded tenaciously and resisted removal by soot-blowing.

Physical Measurements. The physical data on the coupons before and after exposure are presented in this section of the report. A total of thirty separate coupons were exposed for 300 hrs to the products of combustion resulting from burning this bituminous high volatile C coal containing 0.45 percent chloride.

The physical measurements discussed inthis report include:

(*i*) Weight loss data expressed in grams and also calculated as milligrams weight loss per unit area of exposed surface (mg/cm2)

(*ii*) Metal thickness on each coupon expressed in mills

The metal thickness readings were taken on each coupon at various locations. These readings were taken at eight points about the circumference of each coupon. The first point is directly in line with the gas flow and the successive readings were taken clockwise about each coupon.

Referring to Fig. 2, it can be seen that two probes, A and B, were located in the first superheater duct where gas temperature averaged 2260°F (1238°C). Following that, probes C and D located in the second duct experienced gas temperatures of 2080°F (1138°C). The third duct contained probes E and F. Temperatures at that point were at approximately 1950°C (1066°C).

Proceeding in Table 5, the probes are identified alphabetically and with decreasing average probe control temperature. Following are two columns which outline the temperature ranges each probe experienced during the 300 hr run, including the averaged deviation from the desired control point. Note that at the high gas temperatures, the range was largest and it decreased as the gases cooled along the succeeding ducts. The reason for better temperature control at the lower control point is the decrease in deposition of slag on the back end probes which allows for more uniform heat transfer to the metals. Slagging and subsequent surface cleaning accomplished by soot blowing in the first duct creates erratic and wide ranging temperature profiles on those probes (similar metal temperature variations may also be expected on actual tube surfaces during slag build-up and fall-off).

Figures 3 and 4 graphically represent the wastage rates of each alloy exposed to the flue gas from high chloride Illinois coal in terms of skin metal temperature. It can be seen that some coupons experienced only slight wastage.

These curves are similar to the ones developed while firing bituminous high volatile C coal in the laboratory test facility for this 300 hrs of exposure.

Chemical and Metallurgical. This discussion is directed to

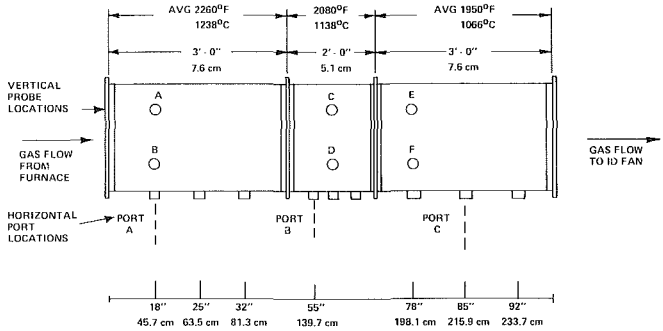

Fig. 2 Probe orientation in superheater duct section of the FPTF

Table 4 Superheater probe deposit analysis high-chloride Illinois coal

	Bank I		Bank II		Bank III	
Fusion temperatures	Probe A outer	Probe A initial	Probe C outer	Probe C initial	Probe E outer	Probe E initial
I.T., F (C)	2100 (1149)	1910 (1043)	2110 (1154)	1920 (1049	2120 (1160)	I.S.
S.T.	2190 (1199)	1950 (1066)	2170 (1188)	1960 (1071	2280 (1249)	--
H.T.	2400 (1316)	2020 (1104)	2420 (1327)	2090 (1143	2510 (1377)	--
F.T.	2660 (1460)	2140 (1170)	2650 (1454)	2180 (1193	2700 (1482+)	--
Ash Composition, Wt. %						
SiO_2	59.7	21.6	57.0	20.6	59.7	22.2
Al_2O_3	20.4	8.4	19.4	8.9	21.6	9.2
Fe_2O_3	8.4	57.5	8.8	58.5	7.1	40.5
CaO	4.0	4.5	5.2	5.3	3.0	6.7
MgO	1.1	0.7	1.1	0.6	1.1	0.5
Na_2O	1.2	0.6	1.1	0.8	1.3	2.6
K_2O	2.5	0.9	2.5	1.3	2.7	2.0
TiO_2	0.5	0.6	1.0	0.7	1.2	0.7
SO_3	0.5	3.5	2.0	2.6	2.7	13.1
Total	98.3	98.3	98.1	99.3	100.0	97.5
Base/acid ratio	0.22	2.10	0.24	2.20	0.18	1.63
Fe_2O_3/CaO	2.10	12.8	1.69	11.0	2.37	6.04
Chloride, Wt. %	2.9	1.4	--	--	--	--

I.S. = insufficient sample

Table 5 Summary of operating data

Probe	Probe control point, °F (°C)		Probe actual temp. range, °F (°C)		Average temp. deviation from C.P., °F (°C)	
A	1700	(927)	1400–1900	(760–1038)	−45	(−25)
B	1575	(856)	1380–1780	(749–971)	−10	(−5.5)
C	1425	(773)	1300–1600	(704–871)	+35	(19.4)
D	1300	(704)	1250–1430	(677–777)	+25	(13.9)
E	1200	(649)	1160–1280	(627–693)	+25	(13.9)
F	1100	(593)	1080–1280	(582–693)	+80	(44.4)

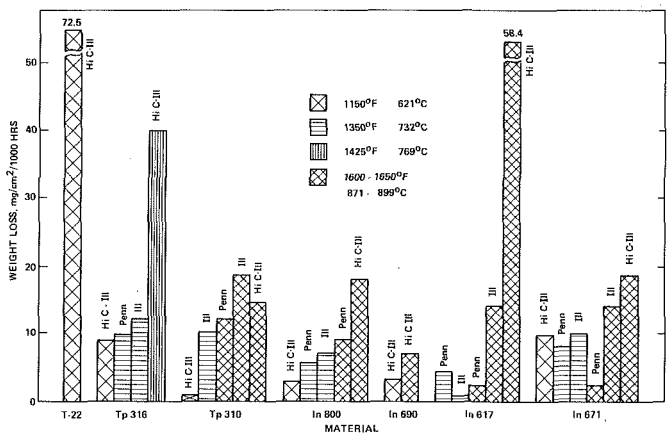

Fig. 3 Average weight loss 300 hr laboratory test mg/cm²/1000 hrs

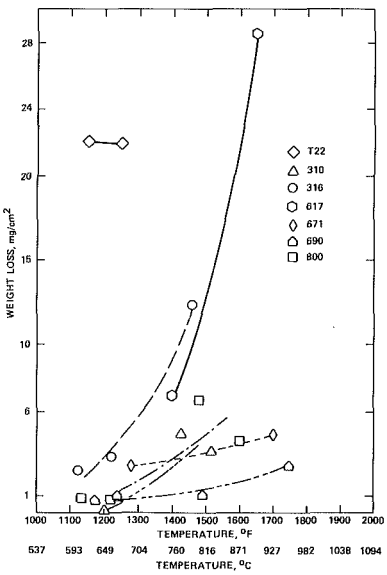

Fig. 4 Weight loss as a function of temperature for each material (after 300 hrs)

the analysis of deposits removed from the exposed coupons. Significant differences in results from this test run are compared to the previously tested Illinois coal.

Coal burned during this test was analyzed and is presented in Table 3. High-chloride Illinois coal analysis indicates an "increased" potential for corrosion, based on the potassium-to-sodium ratio. However, the coal analysis reveals that the amount of alkaline earth materials—calcium and magnesium—available will only reduce corrosion approximately 50 percent in the low temperature range between 1100 and 1300°F.

This is based on a nomograph developed by C-E in a previous OCR test relating bituminous coal constituents to high-temperature corrosion [3].

Identical procedures for sample selection, preservation, and removal with those of the previous laboratory tests were employed. Deposit analyses were by x-ray fluorescence and diffraction.

Logical material family groupings are employed in discussing the results from tested alloys. Comparison of results obtained from this test are made to those results obtained from the original laboratory test of Illinois coal and Pennsylvania coal.

In the absence of an aqueous phase, test conditions were not conducive to stress corrosion cracking and no evidence of attack of this type was observed.

To provide a basis for comparison with deposits obtained from the corrosion probes during this run, fly ash was collected and subjected to chemical analysis as in the previous tests [2].

Ferritic Steel.

Type T-22 (2-¼ percent Chromium, 1 percent Molybdenum). Specimens of T-22 material were exposed at the lower temperatures to evaluate presently utilized steels of construction in this high-chloride coal. This material was not evaluated in the previous laboratory or field tests since its application is limited to low temperatures, i.e., below 1150°F(621°C).

Chromium concentration in the deposits exposed at 1150°F and 1240°F (621 and 671°C) shows a relatively slight increase over that found in flyash from this coal. Increased sulfur concentration was also observed. Microscopic examinations revealed almost no detectable difference in the as-received sample and the exposed sample. Incipient oxide penetration of about 0.5 mils and a layer of surface scale was observed on the exposed specimen (Fig. 5).

Austenitic Steels.

Type 316H Stainless Steel. Specimens of TP-316H were exposed over essentially the same temperatures while burning this high-chloride Illinois coal as with the original Illinois coal tested. The deposits obtained from the specimen exposed at 1460°F (793°C) revealed a significant increase in chromium, nickel, and molybdenum concentrations over levels found in the flyash. Sulfur concentration also increased. This effect of surface temperature on wastage was observed in the previously conducted tests [2].

Metallurgical evaluation of the samples revealed essentially no differences due to exposure to high chloride coal. Sensitized grain boundaries and o.d. surface due to the machining operation were observed but no indications of corrosive attack or surface deterioration were noted.

Type 310H Stainless Steel. Deposits from exposure at similar temperatures to those from the original Illinois coal firing, showed an increase in chromium and nickel concentrations with temperature. In the sample exposed at 1460°F (793°C), there was a significant increase, indicating corrosive attack. Concurrent with this increase, a significant increase in the sulfur concentration was observed in all the deposits, suggesting a role for this species in the attack.

Metallurgical examination indicated surface penetration from almost nil at the lower temperatures to 2.5 mils at the highest temperature. Very little attack to this material was noted during the previous laboratory test.

The microstructure of these exposed samples showed a relatively uniform, large grain size when compared to the nonuniform duplex grain size of the earlier tested samples.

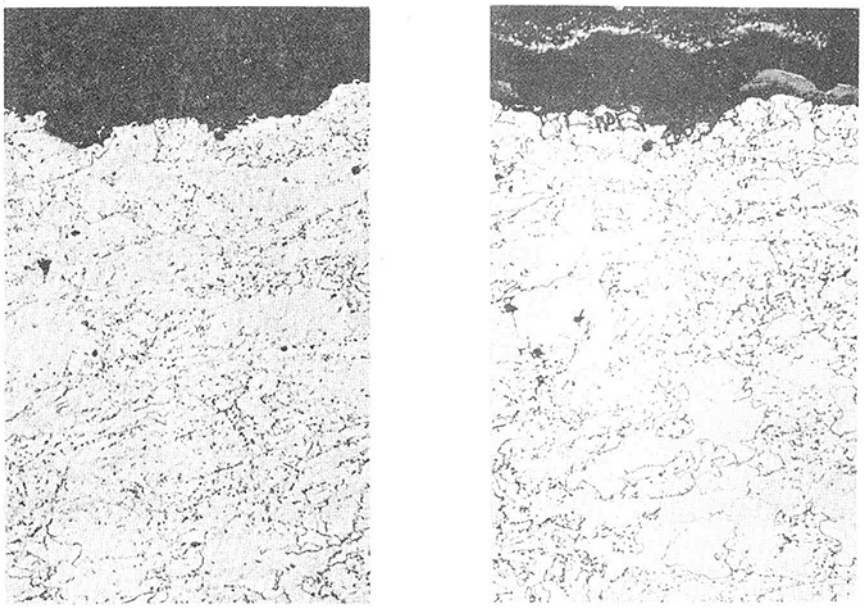

Fig. 5 SA-213, T-22, Nital etch, 200X mag.

Grain boundary carbide coarsening and the apparent chromium depleted layer at the surface were more apparent in these samples exposed to high-chloride Illinois coal as compared to the previously tested Illinois coal. Figure 6 shows minimal surface depletion of chromium concentration at the metal interface.

Nickel-Chromium-Iron Alloy.

Incoloy 800H. Baseline comparison was made to the sample prepared from Incoloy 802 material since In800H was not used in the earlier studies. Very slight composition differences are found between Incoloy 802 and 800H. These differences primarily affect strength characteristics.

Deposit analyses, indicate an increase in sulfur concentration in all the deposits when compared to the previous laboratory test. The sample exposed at 1450°F (788°C) indicates corrosive attack to this material. The nickel and chromium concentrations have increased significantly in this sample.

Metallurgical examination showed grain boundary coarsening (Fig. 7) as a function of temperature. Also, a depleted surface layer was noted in all samples congruous to increased temperatures. Similar conditions were observed with the Incoloy 802 material exposed in the previous laboratory test [1, 2].

Inconel 690. This alloy (60 percent nickel and 29 percent chromium) was not evaluated in the previous tests in the laboratory or the field. This relatively newer material was recommended by the manufacturer for application in high-chloride environments.

Deposits analyses of samples exposed during this laboratory test show increases in the sulfur concentration over ash composition. The sample exposed at 1490°F (810°C) shows slight increases in nickel and chromium concentration, usually resulting as corrosion byproducts. These increases do not indicate any corrosive attack from this exposure of 300 hrs.

Microscopic examination (Fig. 8) of the sample exposed at the highest temperature revealed a thin, depleted layer on the surface. No other significant features were observed.

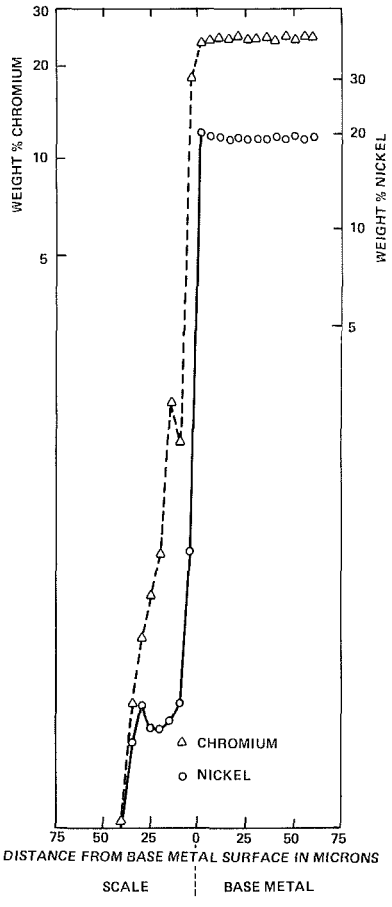

Fig. 6 Test probe B-1, type 310 SS, chromium and nickel concentration profiles at o.d.

Inconel 671 (50/50 Chromium/Nickel Clad on Incoloy 800H). Deposit analyses indicate only an increase over ash

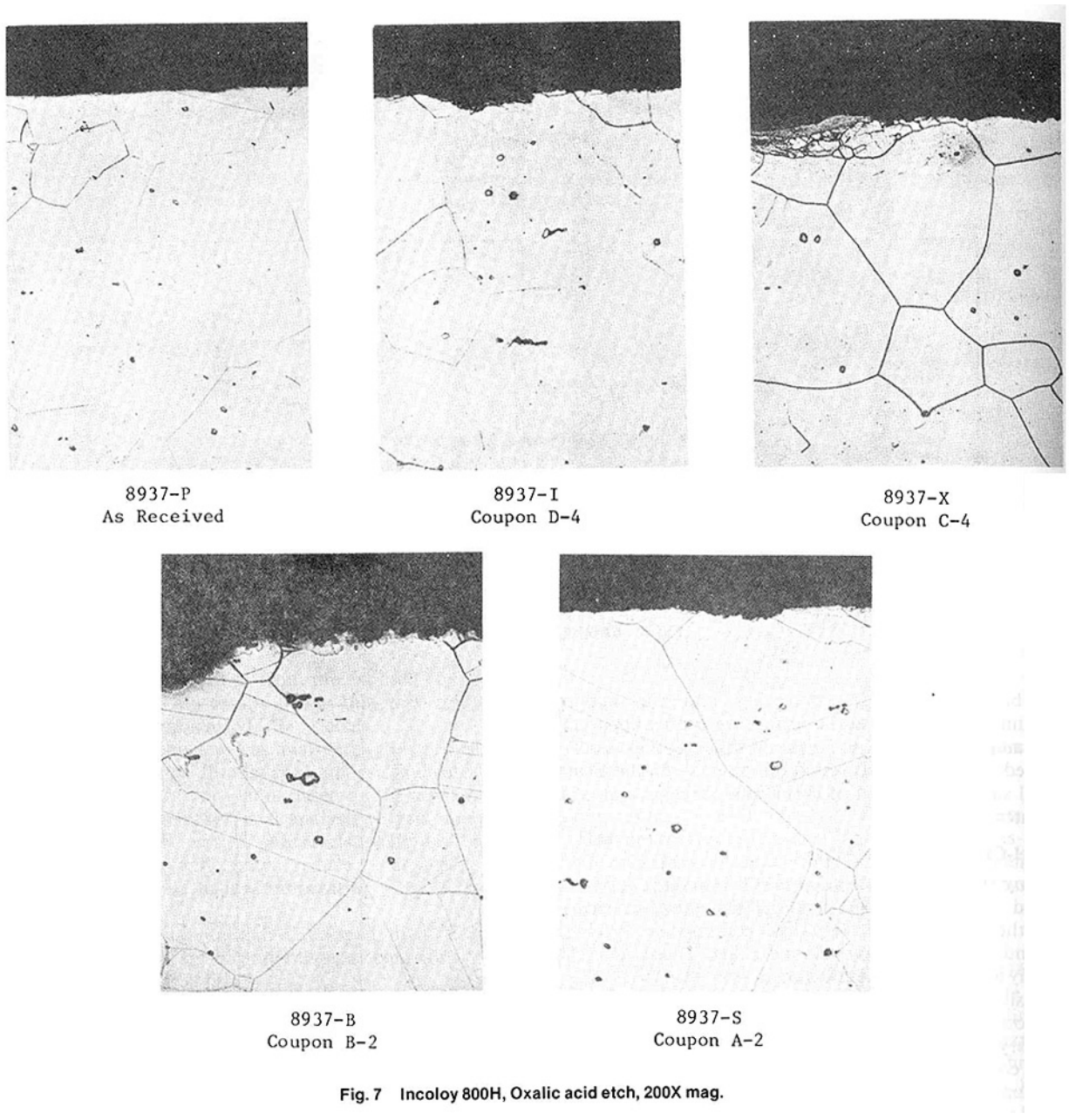

Fig. 7 Incoloy 800H, Oxalic acid etch, 200X mag.

composition in sulfur concentration in all the samples examined. No other increases indicating corrosive attack were determined (Table 4).

Metallurgical examination revealed only slight surface deterioration, even at the highest test temperature of 1700°F (927°C). The maximum depth of surface penetrations was about 1.5 mils (.038 mm), as shown in Fig. 9. The previously exposed samples showed the same evidence of preliminary surface attack.

Nickel-Chromium-Cobalt Alloy.

Inconel 617. Deposit analyses obtained from this alloy revealed a significant increase in sulfur concentration over that formed in the flyash as well as in flyash from previously evaluated Illinois coal. Also increasing significantly were chromium, nickel, cobalt, and molybdenum. The increases indicate corrosive attack to this alloy which was not observed when this alloy was exposed in the previous laboratory test using Illinois coal.

Metallurgical examination of this alloy revealed an obvious difference from those exposed to low chloride testing. These samples exhibited a more uniformly refined grain size (Fig. 10).

Results

The wastage rates per 1000 hrs and the chemical and metallurgical data are presented in Tables 6 and 7 for this 300 hr laboratory test burning high chloride (0.4 to 0.5 percent) Illinois Coal. Similar laboratory results obtained while burning low chloride Midwestern bituminous and Eastern bituminous coals are included to facilitate comparison with currently used coals of economic significance. Detailed results are contained in the final report [4].

Summary

1 The exposed alloys did not reveal any accelerated wastage of the type observed on conventional superheater operating in a metal temperature range of 1000–1300°F (538–704°C). Skin metal temperature range was 1100–1700°F (593–927°C).

2 Wall thickness loss of alloys after 300 hr exposure was

8937-Q
As Received

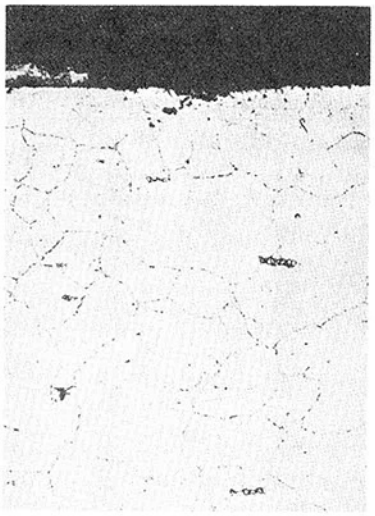

8937-E
Coupon B-5

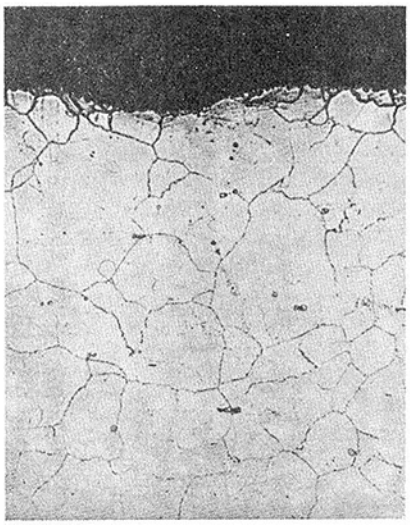

8937-V
Coupon A-5

Fig. 8 Inconel 690, Oxalic acid etch, 200X mag.

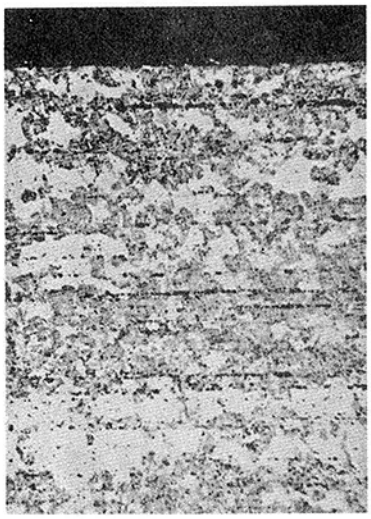

8937-O
As Received

8937-G
Coupon D-2

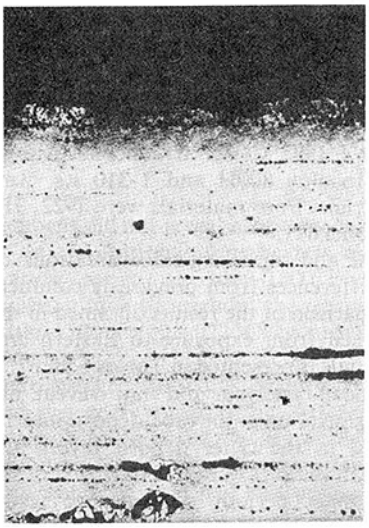

8937-U
Coupon A-4

8937-D
Coupon B-4

Fig. 9 Inconel 671 clad, Oxalic acid etch, 200X mag.

8937-M
As Received

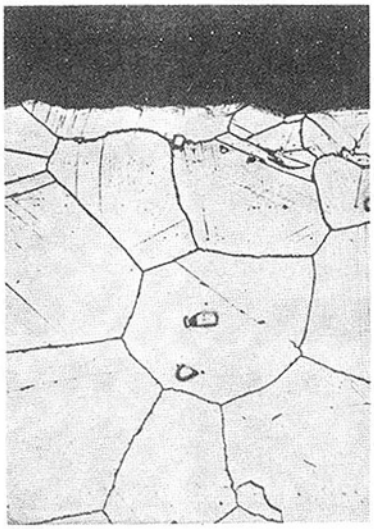

8937-W
Coupon C-3

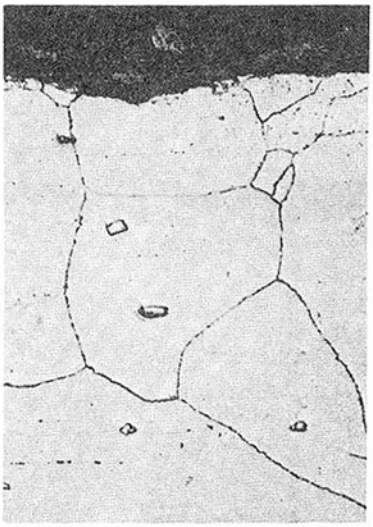

8937-C
Coupon B-3

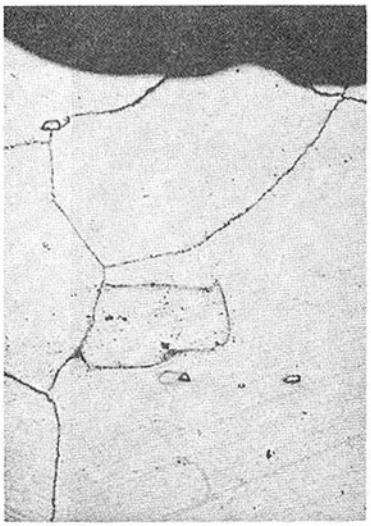

8937-T
Coupon A-3

Fig. 10 Inconel 617, 60% HNO_3 etch, 200X mag.

generally so slight as to be within accuracy of the measurement instrument (micrometer). Wall thickness losses ranged between 0.001 and 0.002 in. (0.025 and 0.05/mm).

3 Although there was generally only slight wastage noted during the firing of this coal, the significant difference was observed in the performance of the cobalt based alloy, Inconel 617. Pitting attack to this material was visually observed on the pieces exposed at 1500°F and above. Such pitting was not seen in the previous tests.

4 The samples of ferritic steel, T-22 (2¼ percent Chromium, 1 percent Molybdenum), experienced quite high wastage values in this test. Exposure of this material was included to demonstrate the validity of the test by confirming significant wastage in a material known to be unsuitable for superheater service in a coal-fired boiler at 1100–1700°F (593–927°C).

5 All other previously tested materials evaluated in this laboratory test performed in approximately the same manner as they had during similar exposure while burning Midwestern bituminous coal with a nominal chloride level.

6 With respect to ranking the test alloys for wastage potential on the basis of exposure at temperatures from 1100°F–1700°F (593°C–927°C), Inconel Alloy 690 was very good while Incoloy 800H and T-310 s.s. were good transitional materials. Poor materials were T-22, 316 s.s., Inconel 617, and Inconel 671.

7 Chemical and metallurgical evaluations did not reveal significant differences from previously conducted laboratory tests. A comparison of the results obtained in this exposure to results obtained from exposure to Eastern and Midwestern bituminous coals is presented in Tables 6 and 7.

8 The deposit analyses did not reveal any significant chloride concentration at the tube-deposit interface. Chlorides were detected in the outer deposit layers and were more concentrated in samples obtained during very short periods of exposure. Longer periods of exposure resulted in lesser concentrations of chloride in the deposits examined.

Conclusion

Physical, chemical, and metallurgical evaluation of

Table 6 300-hr laboratory studies average weight loss data (mg/cm²/1000 hrs)

Alloy	Low-chloride Temp. °F (°C)		Eastern bituminous	Midwestern bituminous	High-chloride Temp. °F (°C)	Midwestern bituminous
316	Avg. low	1350 (732)	9.80	12.1	1150 (621)	8.9
	Avg. high	1650 (899)	-	-	1425 (769)	40.5
310	Avg. low	1350 (732)	43.9[a]	9.7	1150 (621)	0.2
	Avg. high	1650 (899)	12.0	18.2	1600 (871)	14.2
12R72	Avg. low	1350 (732)	20.0	26.4	-	-
	Avg. high	1650 (899)	-	-	-	-
800H	Avg. low	1350 (732)	5.5	6.8	1150 (621)	2.7
	Avg. high	1650 (899)	8.9	51.8[a]	1600 (871)	17.8
617	Avg. low	1350 (732)	4.3	0.7	-	-
	Avg. high	1650 (899)	2.2	13.9	1600 (871)	58.4
671	Avg. low	1350 (732)	7.8	9.9	1150 (621)	9.6
	Avg. high	1650 (899)	2.2	13.9	1600 (871)	18.4
188	Avg. low	1350 (732)	-	-	-	-
	Avg. high	1650 (899)	6.3	34.7[a]	-	-
690	Avg. low	1150 (621)	-	-	1150 (621)	2.7
	Avg. high	1600 (871)	-	-	1600 (871)	6.7
T-22	Avg. low	1150 (621)	-	-	1150 (621)	72.5

[a]Mechanical damage
denotes not tested

Very good – <5 mg/cm² loss /1000 hrs
Good—transitional – 7-10 mg/cm² loss/1000 hrs
Marginal—bad – >20 mg/cm² loss/1000 hrs

Table 7 300-hr laboratory studies summary chemical and metallurgical data

	Eastern bituminous		Midwestern bituminous		High-chloride coal	
	Chem.	Met.	MO	S	Chem.	Met.
316 s.s. Low temp.	MO	S	MO	S	L	MI
High temp.	H	S	MO	S	L	VS
310 S.S. Low temp.	L	VS	L	VS	L	MI
High temp.	L	VS	L	VS	L	MI
12R72 Low temp.	MO	S	L	S	-	VS
High temp.	MO	S	L	S	-	-
802 Low temp.	L	VS	L	S (800H)	L	MI
High temp.	L	VS	L	VS	MO	MI
617 Low temp.	L	S[a]	L	S	L	S
High temp.	MO	S[a]	L	S	MO	S
671 Low temp.	L	S	L	S	L	MI
High temp.	L	S	L	S	L	VS
188 Low temp.	L	MI	L	MI	-	-
High temp.	L	MI	L	MI	-	-
690 Low temp.	-	-	-	-	L	MI
High temp.	-	-	-	-	L	MI
T-22 Low temp.	-	-	-	-	L	S

[a]surface cracks in material "as received"
-denotes not tested

Key: Chemical (deposit concentration of Cr, Ni, Mo, Co, etc.)
Low (L) 0.25%
Moderate (MO) 1.5%
High (H) 1.5%

Metallurgical (magnification for visible defects)
Minimal (MI) = high magnification required 200X
Very slight (VS) = medium magnification required 50X
Slight (S) = low magnification (10X) or visible to eye

laboratory specimens did not reveal accelerated wastage of the type observed on conventional superheaters operating in a metal temperature range of 1000–1300°F. There was, however, sufficient attack throughout the temperature range under study 1100–1700°F (593–927°C) to provide a ranking of the alloys tested.

Although there was generally only slight wastage observed during firing of this coal, a significant difference from the previous tests was observed in the performance of the cobalt-based alloy, Inconel 617. All other previous tested materials evaluated in this laboratory test had approximately the same results while the low-alloy ferritic steel, T-22, experienced quite high wastage values in this test.

With respect to ranking the tested alloys for wastage potential on the basis of exposure at temperatures from 1100–1700°F (593–927°C), the following can be concluded:

(*a*) Very good—690 <5 mg/cm² loss/1000 hrs
(*b*) Good—transitional —800, 310 7–10 mg/cm² loss/1000 hrs
(*c*) Marginal—bad—316, 617, 671, T-22 >20 mg/cm² loss/1000 hrs

Without consideration of the economics of substitution of the various materials, this test program has established that operation of coal-fired boilers as part of advanced power cycles at elevated 1300–1600°F (704–871°C) metal temperatures is technically feasible, although the high-chloride coal appears to decrease corrosion resistance of the higher alloys previously found effective for high-temperature advanced power cycles [2]. A slight increase in the corrosion resistance of 316, 310, and 800 (Table 7) at 1350°F and below

may be attributable to lower sulfur content in the high-chloride coal.

Recommendations

Further evaluation of the materials that were very good and good-to-transitional, i.e., Inconel Alloy 690, Incoloy 800H and Tp-310 s.s., should be considered. These materials could be evaluated for six months to one year on probes exposed at controlled temperatures 1200–1700°F (649–927°C) in units that presently burn high chloride coals, i.e., U.S. industrial units or utility units in England and Australia.

References

1 Plumley, A. L., Accortt, J. I., and Roczniak, W. R., "Evaluation of Boiler Tube Materials for Advanced Power Cycles," presented at the NACE-DOE Corrosion-Erosion Conference, Berkeley, Calif., Jan. 1979, Combustion Engineering Publication TIS-6105.

2 Plumley, A.L., Accortt, J. I., and Roczniak, W. R., "Evaluation of Boiler Tube Materials for Advanced Power Cycles," Final Report Vols. I, II, III. DOE Contract (49–18)–2045, July 1979.

3 Borio, R. W., Hensel, R. P., Ulmer, R. C., Grabowski, H. A., Wilson, E. B., and Leonard, J. W., "The Control; of High-Temperature Fireside Corrosion in Utility Coal-Fired Boilers," OCR R&D Report No. 41, 1969.

4 Plumley, A. L., and Roczniak, W. R., Supplement I to "Evaluation of Boiler Tube Materials for Advanced Power Cycles—A Laboratory Study to Evaluate the Effects of Firing a Naturally Occurring High Chloride Coal," Final Report DOE Contract AC01-76 ET 1050 (formerly (49-18)-2045) Dec. 1980.

Small Particle Transport Across Turbulent Nonisothermal Boundary Layers[1]

D. E. Rosner
Professor,
Department of Chemical Engineering.

J. Fernandez de la Mora
Assistant Professor of
Theoretical Fluid Mechanics,
Applied Mechanics Section.

High Temperature Chemical Reaction
Engineering Laboratory,
Yale University, New Haven, Conn. 06520

Based on the importance of thermophoretic drift in transporting small particles across a turbulent thermal boundary layer, and the relatively small Brownian diffusivity of such particles, we present a simple asymptotic theory of particulate transport to aerodynamically smooth, solid surfaces cooled below, T_e, the mainstream gas temperature. Numerical calculations based on a law-of-the-wall equilibrium velocity profile, and the assumption that the effective eddy diffusivities for mass, energy, and momentum diffusion are equal, are well-represented by

$$-\dot{m}_p'' \approx \rho_e u_e \omega_{p,e} \cdot \mathrm{St}_h \cdot (\alpha_T \mathrm{Le})_w \frac{[(T_e - T_w)/T_w]}{\{1 + [(T_e - T_w)/T_w] \cdot [0.07 + 0.93(\alpha_T \mathrm{Le})_w]\}}$$

where St_h is the local heat-transfer coefficient (Stanton number) and $(\alpha_T Le)_w$ is the ratio of the particle thermophoretic diffusivity to the gas mixture heat diffusivity. While currently being extended to cover particle size ranges for which (i) the Brownian diffusion sublayer is not negligible in thickness compared to the viscous sublayer, or (ii) eddy impaction sets in, the present theory provides a rational improvement over previous estimates, and explains several important features of the recent data of Nomura et al [1] on the fouling rate of internally air-cooled, gas turbine blades exposed to the products of combustion of Vanadium-containing residual fuel oil.

1 Introduction

Two recent trends in the gas turbine (GT) industry have been to (*a*) increase turbine inlet temperatures (to raise thermodynamic efficiency), and (*b*) use lower grade, cheaper fuels. The first of these factors requires higher GT blade cooling rates because the metal temperature is limited by structural considerations, while the larger concentration of contaminants (ash, salts) present in the combustion products of lower grade fuels leads to the formation and possible deposition of particles. Under these combined circumstances *thermophoresis* leads to highly accelerated blade fouling rates, as demonstrated by the recent GT cascade experiments of Nomura et al. [1]. These authors measured rates of particle deposition to an air cooled GT blade cascade immersed in the gaseous stream resulting from the combustion of low-grade fuel (Mideast residual oil, 70–80 ppm (by wt) Va). Vermes [2] analyzed these and other (field) data and showed that the deposition rate increases systematically with the difference between mainstream and blade temperature, concluding that thermophoresis (particle drift in a temperature gradient) provided the main driving force. Indeed, the fouling rates observed by Nomura et al. [1] were larger than those measured on similar uncooled solid blades by more than one order of magnitude. In view of the foregoing experimental evidence and the additional data assembled in [3] it appears that for particle sizes just below the onset of inertial effects, thermophoresis is the leading mechanism for deposition on actively cooled turbine blades. Moreover, even "uncooled" (e.g., utility) GT turbine blades run cooler than the gas dynamic adiabatic wall (aw) temperature, and thermophoresis can more than double the rate of sub-0.1 μm particle capture by them [4]. Even when most of the mass in the prevailing particle size distribution (PSD) is in the size range in which inertial effects (e.g., eddy impaction)[2] dominate thermophoresis, the latter may still be important in determining system performance since the smaller particles may be more corrosive and may provide the "glue" for larger particle deposit adherence [4].

In the present paper, we quantitatively treat the interaction between turbulent diffusion, Brownian diffusion, and particle thermophoresis in the attainable limit of vanishing particle inertial effects.[3]

[1] Supported in part by AFOSR (Contract F49620-76C-0020) and NASA-Lewis Research Center (Grant No. NAG-3-201).

Contributed by the Gas Turbine Division for publication in the JOURNAL OF ENGINEERING FOR POWER. Manuscript received by the Gas Turbine Division February 26, 1981.

[2] The onset of appreciably eddy impaction augmentations in particle transport across a turbulent boundary layer (TBL) may also be "delayed" (shifted to larger size particles) on a suction surface owing to the presence of streamwise curvature-produced centrifugal particle drift [5].

[3] We show in Appendix 1 that, in the absence of effects due to streamwise curvature and thermophoresis, this limit implies that the dimensionless particle stopping time t_p^+ must be smaller than about 12 $(\mathrm{Sc})^{-1/3}$. This provides a conservative limit for the validity of the present results as well, except on concave (pressure) surfaces [5]. The coupling between eddy impaction and thermophoresis will be treated elsewhere. For a treatment of the coupling between thermophoresis and inertial effects in laminar flows see reference [7].

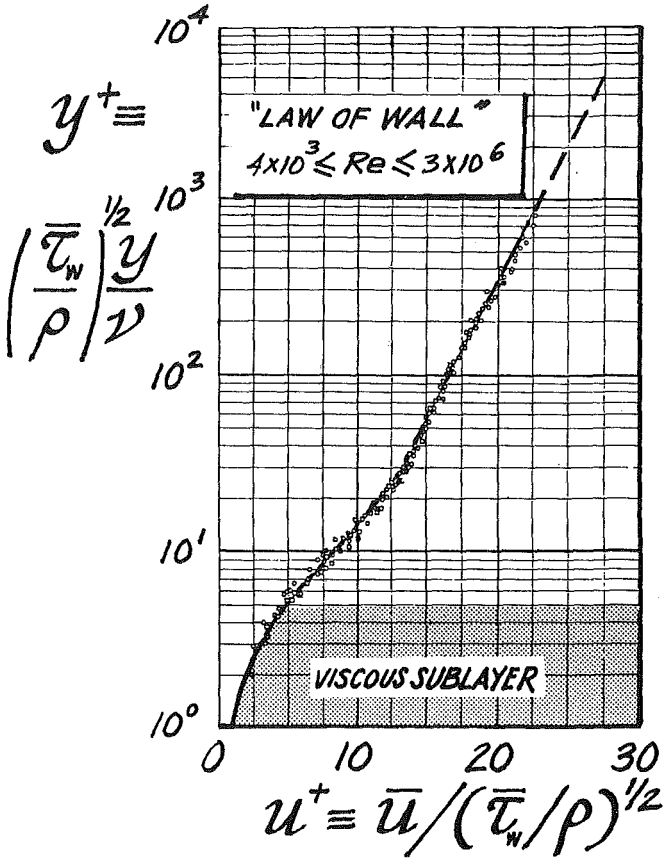

Fig. 1 Universal time-averaged streamwise velocity profile in the vicinity of a smooth solid wall (replotted from data in reference [26])

2 Previous Theoretical Studies

To the authors' knowledge, at least three papers have dealt with thermophoretic transport of particles in turbulent flow [2, 7–12][4] (for the laminar case, including vapor transport, see the works of Goren [15], Walker et al. [16], Talbot et al. [17] and Rosner et al. [7, 8, 18–22]). Most contain the inaccurate assumption that the ratio between the particle concentration near the wall and its mainstream value is unity (see section 4.2). As shown below (and in analogy to the laminar case), this ratio is generally considerably *less* than unity for strongly cooled walls, being of the order of the ratio of the wall and free-stream temperatures.

In addition to calling attention to the importance of thermophoresis in gas turbine blade fouling, Vermes [2] proposed a theoretical particle capture model. However, as outlined in references [4, 8, 20], his approach is oversimplified and must be improved in several ways. First, he used a particle trajectory analysis, not only neglecting (as in [15] and [16]) Brownian diffusion, but also neglecting eddy transport. In support of this latter point, Vermes notes that observed deposition rates are more than one order of magnitude larger with thermophoresis than without. However, this argument is misleading for the following reasons.

Vermes's analysis [2] is based on the "limiting trajectory" described by a particle that hits the trailing edge of the blade and starts its trip at some critical distance from the turbine at its leading edge station. His approach would be essentially correct if this limiting trajectory was completely embedded inside the viscous sublayer, but this is rarely the case.[5] A deterministic "trajectory analysis" loses its meaning in turbulent flow, where two particles initially arbitrarily close to each other may ultimately find themselves far apart. The fact that pure eddy mixing leads to very small deposition rates does not imply that eddy transport is unimportant *everywhere*, only that it is negligible *somewhere* in the boundary layer—this being the well-known viscous sublayer adjacent to the wall. While turbulence is very efficient in transporting mass from the mainstream to the outer edge of the viscous sublayer, this mechanism is strongly damped as one approaches the wall. Then, Brownian diffusion is *normally* the only available transport mechanism sufficiently close to the wall, and because particle diffusivities are very small, transfer rates will be negligible unless some other driving force, like thermophoresis, alters the picture by assisting mass transfer across this otherwise "insulating" zone. Thus, *both* processes—thermophoresis and eddy diffusivity—will be important in their respective zones of influence. Turbulence will increase the mass flux, not only by increasing the temperature gradient across the viscous sublayer, but also by efficiently transporting mainstream particles up to the partially laminar ("buffer") layer where thermophoresis can begin to "take over." Accordingly, here we present the details of an Eulerian, turbulent boundary layer model, briefly outlined in references [8, 20].

[4] Owen's estimate [12] also contains a numerical error in his use of Epstein's formula [13] for the thermophoretic force on a single particle. For particles comparable to or smaller than the prevailing gas mean-free-path, this formula must be generalized to include rarefaction effects [14].

[5] Even so, [2] has neglected the important effect of the simultaneous transverse ("displacement") velocity present within developing boundary layers.

Nomenclature

a = dimensionless numerical constant in equation (17)
B_T = "blowing" (suction) parameter associated with particle thermophoresis, equation (18)
c_f = local skin friction coefficient, $\tau_w/(\frac{1}{2}\rho_e u_e^2) = 2(u_*/u_e)^2$
d_p = particle diameter (aerosol)
D_p = Brownian diffusivity for particle transport in host gas
Kn_p = particle Knudsen number (ratio of mean-free-path to diameter)
k = Boltzmann constant
Le = Lewis number (ratio of D_p to gas heat diffusivity)
$\dot{m}_p''$ = particle mass deposition flux at surface ($y = 0$)
m = individual particle mass
Pr = Prandtl number (of host combustion products)
Re = Reynolds number
Sc = Schmidt number (ratio of gas kinematic diffusivity to D_p)
St_h = local Stanton number for heat transfer
St_m = local Stanton number for mass transfer, equation (7)
t_p = particle stopping time (see, e.g., reference [33] and footnote 12)
t_p^+ = dimensionless particle stopping time, $u_*^2 t_p/\nu$
T = absolute temperature
u = gas velocity parallel to (local) blade surface
u_* = friction velocity $(\tau_w/\rho)^{1/2}$
v = gas velocity perpendicular to (local) blade surface
v_T = thermophoretic drift velocity; $-\alpha_T D_p\, \partial \ln T/\partial y$
$\overline{u'v'}$ = velocity correlation in yx component of the Reynolds stress
$\overline{\rho\omega'v'}$ = eddy diffusion flux of particles

3 Theoretical Approach

Our starting point is the particle phase mass conservation equation for a two-dimensional BL, including the thermophoretic flux term $-\rho\omega D\alpha_T(\partial lnT/\partial y)$ [18] directed toward the cold wall:

$$\rho\frac{\partial\omega}{\partial t}+\rho u\frac{\partial\omega}{\partial x}+\rho v\frac{\partial\omega}{\partial y}=\frac{\partial}{\partial y}\left[\rho D\frac{\partial\omega}{\partial y}+\omega\rho D\alpha_T\frac{\partial lnT}{\partial y}\right] \quad (1)$$

Here, ω is the mass fraction of the suspended particles (or any species transported since, in the absence of inertia, particles and vapors obey identical transport laws), ρ, u and v are the carrier gas density and velocity components, D is the diffusion coefficient of the particles (or transported species) in the mixture and α_T is the dimensionless thermophoretic (or thermal diffusion) coefficient, values for which are discussed in detail by Talbot, et al. [17], Talbot [14], and Rosner [18] (for the case of vapors). Upon time averaging (equation (1)), in addition to the traditional eddy diffusion term $\overline{\omega' v'}$ (arising from the nonlinear convective term), a new "correlation" term appears which we have called "eddy thermophoresis." It arises from the simultaneous fluctuation of the thermophoretic speed and particle concentration fields. The latter term may be expected to be small in the viscous sublayer (where turbulent diffusion is strongly damped) and also in the outer turbulent region where the mean temperature gradient (thus, the thermal drift) is small. Furthermore, all correlation terms are generally small compared with those originating from the nonlinearity in the advective term (the eddy diffusivity here, or the Reynolds' stresses, in the momentum conservation equation). Accordingly, we neglect eddy thermophoresis everywhere. There is no rigorous way of defending or relaxing this assumption short of recourse to direct measurement; however, an indication of its validity may be obtained by using a mixing-length hypothesis. This exercise (not included here) shows that for a nondeveloping boundary layer, eddy thermophoresis is indeed negligible. Moreover, there is little point in attempting a very careful modeling of all terms appearing in this problem since the temperature variation across the boundary layer probably introduces comparable effects (e.g., additional correlation terms associated with the temperature dependence of the host gas density or the transport coefficients). For the present preliminary approach it thus seems more than sufficient to ignore variable property effects, simply adding the mean thermophoretic term to the standard time-averaged linear transport equations. For simplicity, we adopt the formalism used by Spalding [23] for the turbulent flow near a flat plate in the analogous heat-transfer problem. It is assumed that sufficiently far downstream from the location of transition an equilibrium time-averaged velocity profile (law-of-the-wall) is attained. Particle turbulent diffusivities are based on this "law of the wall," with turbulent Prandtl and Schmidt numbers set equal to unity, and a constant value of the shear stress across the boundary layer (see also [24]).

The final time-averaged mass conservation equation in nondimensional (x^+, u^+) coordinates is,

$$u^+\frac{\partial\omega}{\partial x^+}=\frac{du^+}{dy^+}\frac{\partial}{\partial u^+}\left[\left(\frac{1}{\mathrm{Sc}_{\mathrm{eff}}}\cdot\frac{\partial\omega}{\partial u^+}+\omega\cdot\frac{\alpha_T}{\mathrm{Sc}}\frac{\partial lnT}{\partial u^+}\right)\frac{du^+}{dy^+}\right] \quad (2)$$

with $\mathrm{Sc}_{\mathrm{eff}}$ being an effective (overall) Schmidt number, accounting for both Brownian and eddy diffusivity:

$$\frac{1}{\mathrm{Sc}_{\mathrm{eff}}}=\frac{1}{\mathrm{Sc}}+\left(\frac{dy^+}{du^+}-1\right) \quad (3)$$

Except for our dropping the overbar for time-averaged quantities, the notation is standard (see Nomenclature).

Equation (2) has to be solved along with the following equation giving the time-averaged temperature T [23]:

$$u^+\frac{\partial T}{\partial x^+}=\frac{du^+}{dy^+}\frac{\partial}{\partial u^+}\left[\left(\frac{1}{\mathrm{Pr}_{\mathrm{eff}}}\frac{\partial T}{\partial u^+}\right)\frac{du^+}{dy^+}\right] \quad (4)$$

with

$$\frac{1}{\mathrm{Pr}_{\mathrm{eff}}}=\frac{1}{\mathrm{Pr}}+\frac{dy^+}{du^+}-1 \quad (5)$$

In total analogy with equation (3), $\mathrm{Pr}_{\mathrm{eff}}$ is an effective Prandtl number, and Pr is the usual Prandtl number, or the ratio between the gas kinematic viscosity and its thermal (heat) diffusivity. Pr is the usual Prandtl number, or the ratio between the bath kinematic viscosity and its thermal diffusivity.

Note that the field equations for ω and T use u^+ rather than y^+ as the independent variable, both of them being related via the law-of-the-wall; viz: $u^+ = u^+(y^+)$ [see, e.g., Fig. 1]. This expression is also necessary to evaluate the term dy^+/du^+ appearing in equations (2–5). Thus, once the law of the wall is specified, closure is achieved in the present approximation, and we may proceed to the solution as soon as the boundary conditions are specified.

4 Solutions for Instructive Limiting Cases

As a first step we follow the early examples of Prandtl [25] and Deissler [26], who neglected the streamwise variation term $u^+\,\partial/\partial x^+$. This assumption is certainly valid for slowly

Nomenclature (cont.)

x = distance measured along blade (or vane) surface
x^+ = running integral of $(u_*/\nu)dx$
y = distance measured normal to local blade (vane) surface
y^+ = $u_* y/\nu$
α = thermal diffusivity of carrier gas $(\lambda/(\rho c_p))$
α_T = dimensionless thermophoretic diffusion factor [8, 13, 14, 17]
$\alpha_T\mathrm{Le}$ = thermophoretic diffusivity/gas thermal diffusivity ratio
δ_m = mass-transfer boundary layer thickness (Brownian diffusion sublayer)
τ_w = shear stress at wall
ρ = local density of the dusty gas mixture
ω = local mass fraction of particle phase (for a specified size class)
ν = local kinematic viscosity of the host gas mixture
λ = thermal conductivity of the carrier gas

Subscripts

aw = adiabatic wall (at the local "recovery" temperature)
eff = effective (based on turbulence-augmented diffusivities)
e = outer edge of the gas thermal boundary layer at station x
m = at the outer edge of the Brownian diffusion sublayer, or pertaining to mass transfer (e.g., St_m)
p = particle
w = at the surface
t = turbulent contribution (e.g., $\nu_{\mathrm{eff}} = \nu + \nu_t$, etc.)

Superscripts

$+$ = made dimensionless with the friction velocity u_* and the kinematic viscosity ν of the fluid.

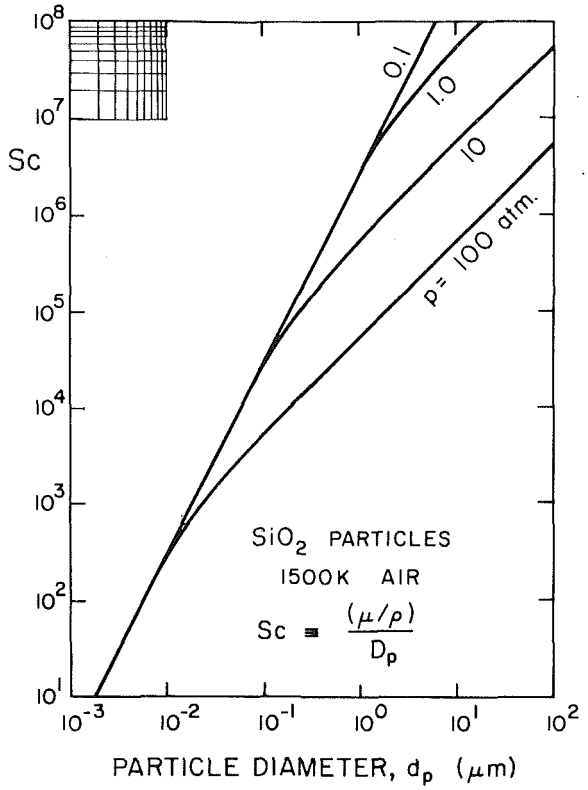

Fig. 2 Schmidt number for SiO_2 particle diffusion in 1500K air [19]

developing flows when the flux of matter to the walls is sufficiently small as to negligibly perturb the concentration profiles from station to station. Then the governing equations (2) and (4) become ODEs, easily solved[6] using the same techniques employed by Deissler [26]. For the results reported below, the expression used for the law-of-the-wall was a generalization of Spalding's simple inverted formula [23], with an improved near-wall behavior to allow accurate calculations of heat or mass transfer rates at large Prandtl or Schmidt numbers.[7]

4.1 Limit of Very Large Schmidt Numbers. The large Schmidt number limit is of greatest interest to particle deposition;[8] however, considerable care is needed in the use of numerical methods owing to the singular behavior of the mass-transfer problem near the wall, i.e., large variations of particle concentration occur within an extremely thin Brownian diffusion sublayer at the "base" of the viscous layer, necessitating much higher spatial resolution than normally provided by numerical methods. Fortunately, this fact simplifies rather than complicates the picture, allowing an asymptotic treatment in negative powers of the Schmidt number, very much like Goren [15], and Walker et al. [16] have outlined for the laminar case. The translation of Goren's conclusions to the present situation is straightforward for, at sufficiently large Schmidt numbers (i.e., $> 10^2$), the Brownian sublayer is so thin that it does not modify the mass flux carried to the Brownian sublayer edge by thermophoresis:

$$j''_w \cong -\left[\omega D\rho\alpha_T \frac{\partial\, lnT}{\partial y}\right]_m \tag{6}$$

Here the symbol m stands for the conditions near the wall, but still outside the Brownian diffusion sublayer. The group $D\alpha_T \partial\, lnT/\partial y$ does not vary appreciably across this sublayer, but ω does change quite abruptly to satisfy the wall boundary condition (usually $\omega(0) = 0$); thus, for what follows, it is important to keep in mind that ω_m is not the true wall boundary value, but rather the exterior solution equation (2), which assumes $Sc^{-1} = 0$. It is equally important to realize that ω_m *in general differs appreciably from the mainstream* value ω_e and this ratio, ω_m/ω_e, is calculated below. Ironically, at the wall itself, thermophoretic transport vanishes (when $\omega(0) = 0$) and Brownian diffusion "takes over."

4.2 Particle Concentration Depletion Outside of the Brownian Sublayer. Equation (6) can be used to obtain an expression for the dimensionless mass-transfer coefficient (Stanton number):

$$St_m \equiv -j''_w/(\rho_e u_e \omega_e) \tag{7}$$

in terms of the particle concentration ratio ω_m/ω_e established across the BL outside of the Brownian sublayer. We assume that the Schmidt number is large enough so that $T_m \approx T_w$, $(\partial T/\partial y)_m \approx (\partial T/\partial y)_w$, and we neglect the difference between $c_p(T_m)$ and the mean c_p between T_e and T_w. Then, since St_h is defined such that:

$$[\lambda(\partial T/\partial y)]_w = \rho_e u_e\, St_h \cdot c_p(T_e - T_w) \tag{8}$$

Equation (6) may be rewritten in the nondimensional form,

$$\frac{St_m}{(St_m)_0} = \frac{\omega_m}{\omega_e} \cdot (-B_T) \tag{9}$$

where we have introduced the thermophoretic ("suction") parameter [18]:

$$-B_T \equiv (\alpha_T \mathrm{Le})_w \cdot \frac{St_h}{(St_m)_0} \cdot \frac{T_e - T_w}{T_w} \tag{10}$$

Here α_TLe is the ratio of the thermophoretic particle diffusivity $\alpha_T D$ to the carrier gas heat diffusivity (see Fig. 3), and the subscript 0 on the mass-transfer coefficient St_m refers to the condition of no thermophoresis. The important term ω_m/ω_e, which remains to be determined, is what we have previously called [8, 18, 19] the "outer sink" factor. It is near unity in problems where the heat- and mass-transfer boundary layers are equally thick [Sc/Pr = 0(1)] but becomes significantly different from unity in the present limit ($Sc >> 1$) both for laminar and turbulent flows.

4.2.1 A Singular Case When α_TLe = 1. The special case when α_TLe = 1 is particularly instructive because (if consistent with the upstream boundary condition[9]), the outer solution has the form

$$\omega/\omega_e = T/T_e \tag{11}$$

which holds in the laminar situation, and may be generalized also to turbulent flows if the eddy diffusivities for mass and heat are equal. The proof may be given by taking the difference between equations (2) and (4) after dividing each by ω_e and T_e, respectively. This yields

$$u^+ \frac{\partial}{\partial x^+}\left[\frac{\omega}{\omega_e} - \frac{T}{T_e}\right] = \frac{\partial}{\partial y^+}\left[\frac{1}{(Sc)_t}\frac{\partial}{\partial y^+}\left(\frac{\omega}{\omega_e} - \frac{T}{T_e}\right) + \frac{1}{Pr}\frac{\partial\, lnT}{\partial y^+}\cdot\left(\frac{\omega}{\omega_e}\alpha_T \mathrm{Le} - \frac{T}{T_e}\right) + \frac{1}{Sc}\frac{\partial}{\partial y}\left(\frac{\omega}{\omega_e}\right)\right] \tag{12}$$

Away from the Brownian sublayer, the term proportional to

[6] The numerical integrations for intermediate Schmidt numbers were carried out at Yale University during the summer of 1980 by Sonia Vaziri under the direction of one of us (DER). Some TBL problems at high Pr or Sc also lead to ODEs even in the presence of streamwise convection (see footnote 11).

[7] There is still some uncertainty as to the proper near-wall behavior of ν_t/ν (proportional to $(u^+)^4$ or $(u^+)^5$? [27-29]). The present calculations used as inverted law-of-the-wall, $y^+(u^+)$, consistent with the former [26].

[8] This is clear from Fig. 2, which shows estimates [19] of the Schmidt number for SiO_2 particles in 1500K air at several pressure levels. For micron-sized particles near 20 atm, Sc is seen to be of the order of 10^5.

[9] The more general and commonly occurring case when a clean, dust-free cold jet is introduced through the wall (e.g., film cooling) is a clearcut example showing the interference of upstream boundary conditions [30].

Sc^{-1} is negligible (outer solution) and, in the special case $\alpha_T Le = 1$, the above expression becomes a homogeneous linear partial differential equation for $[(\omega/\omega_e) - (T/T_e)]$, which is zero at all the relevant boundaries (note that the wall does not fall into this category). The outer solution is first order for ω and only the boundary condition at infinity is relevant. The solution is therefore the trivial one: $[(\omega/\omega_e) - (T/T_e)] = 0$, which we set out to prove. The method is the same as that for the laminar problem, where the validity of equation (11) is confirmed by the numerical integrations of Goren [15] and Walker et al. [16]. Although actual values of the group $\alpha_T Le$ are always smaller than unity (see Fig. 3), they may reach values near 1/2, thus the outer sink effect may be expected to be of the order of the temperature ratio T_w/T_e, which can differ appreciably from unity.

4.2.2 "Outer Sink Strength" for $\alpha_T Le < 1$. It is clear from our experience with thermophoresis in high Sc laminar flows that equation (11), based on $\alpha_T Le = 1$, will overestimate the strength of the outer sink (hence, underestimate ω_m/ω_e) for values of $\alpha_T Le < 1$. For example, under subsonic laminar conditions, the data of Goren [15] and Walker et al. [16] (for flat plate and tube flows) fit well the expression [8],

$$\frac{\omega_m}{\omega_e} = \left(\frac{T_w}{T_e}\right)^{(\alpha_T Le)^{0.46}} \qquad \begin{pmatrix} Sc >> 1 \\ T_w/T_e > 0.5 \end{pmatrix} \tag{13}$$

while our own calculations at the stagnation point show the similar behavior [7]

$$\frac{\omega_m}{\omega_e} = \text{funct}\left[\left(\frac{T_w}{T_e}\right)^{(\alpha_T Le)^{1/2}}\right] \quad (Sc >> 1) \tag{14}$$

In what follows, we provide rational quantitative estimates of ω_m/ω_e for turbulent BL flow on a smooth solid surface, from which high Sc deposition rates can be calculated for realistic values of $\alpha_T Le$ (see Fig. 3). For this purpose we first adopt a simple two-layer model of the turbulent boundary layer and extract the functional form of the ω_m/ω_e relation. We then use this result to suggest a useful correlation of numerical calculations of ω_m/ω_e based on a more realistic law-of-the-wall model of turbulence within the thermal boundary layer.

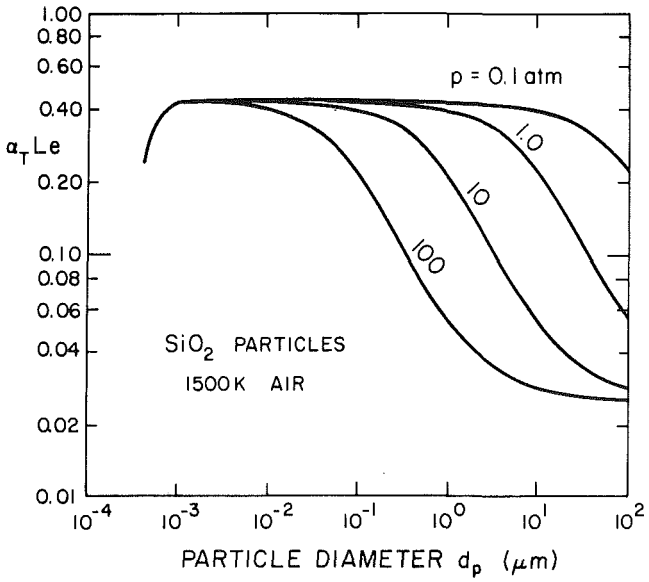

Fig. 3 Predicted ratio of particle thermophoretic diffusivity to host gas thermal diffusivity; SiO_2(c) in 1500K air [19]

4.2.3 Two-Layer Model. A very simple but successful method to estimate heat-transfer rates across turbulent boundary layers was derived independently by Prandtl and Taylor (see Schlichting [31], equation (23.18)) by assuming a two-layer flow field with an inner "laminar" region (with $u^+ \simeq y^+$) up to $u^+ = u_0^+$, followed by an outer "fully turbulent" region with unity turbulent Prandtl number. Prandtl and Taylor implicitly assumed negligible streamwise variations, $u^+ \partial/\partial x^+ = 0$. A three-layer model including a transition, or "buffer," region was subsequently introduced by von Karman [32], but the differences with the two-layer case are slight for Prandtl numbers of order unity (see Fig. 23.3 in Schlichting's book [31]). Since we are mainly concerned with aerosol deposition (with $Pr \simeq 0.7$), a two-layer model including thermophoresis is sufficient, as shown below.

Subject to the abovementioned assumptions, first integrals of equations (4) and (2) reveal that both $T(u^+)$ and $\omega(u^+)$ are piecewise linear functions, continuous at u_0^+. Imposing the known conditions at the outer edge of the Brownian sublayer when $Sc >> 1$ and in the mainstream (where $u_e^+ = (c_f/2)^{-1/2}$ we recover the well-known Prandtl-Taylor results for $T(u^+, Pr)$ and $St_h(c_f/2, Pr)$ [31]. However, for the mass-transfer problem in the limit $Sc >> 1$ we obtain [20]:

$$\frac{\omega_m}{\omega_e} = \left[1 + \alpha_T Le \cdot \frac{(T_e - T_w)}{T_w} \cdot \left(1 + \frac{u_0^+ Pr(1-\alpha_T Le)}{\alpha_T Le} \cdot \frac{St_h}{(c_f/2)^{1/2}}\right)\right]^{-1} \tag{15}$$

where $u_0^+ \approx 5$ in the simplest form of the Prandtl-Taylor two-layer model. The corresponding mass-transfer coefficient St_m follows immediately from equation (9).

4.2.4 Numerical Calculations With $\partial/\partial x^+ = 0$. Numerical calculations with the abovementioned continuous form of the law-of-the-wall confirm the predictions of the two-layer TBL model in the sense that the group $[\omega_e/\omega_m) - 1]$ depends linearly on $[(T_e/T_w) - 1]$, and their ratio is itself linear with the property group (diffusivity ratio) $\alpha_T Le$. Nonetheless, the Reynolds number dependence of the numerical results is slightly different than given by the two-layer model. Over the Reynolds number range of roughly 10^4 to 10^7 a good fit is obtained with the simple Re-independent expression:

$$\frac{\omega_e}{\omega_m} - 1 = \left(\frac{T_e}{T_w} - 1\right) \cdot [0.93\,(\alpha_T Le) + 0.07] \tag{16}$$

as shown in Fig. 4, which displays ω_m/ω_e as given by equation (16) versus its value obtained numerically for a number of values of the diffusivity ratio $\alpha_T Le$, Re and T_e/T_w. The agreement is better than acceptable.

5 Conclusions and Preliminary Comparison with Experiments

We conclude that in the parameter range of interest, thermophoresis augments the ordinary high Schmidt number mass-transfer coefficient St_m (eddy + Fick diffusion) by the factor F(outer sink) • F(thermophoretic suction), where:

$$F(\text{outer sink}) \approx \left\{1 + \frac{T_e - T_w}{T_w}[a + (1-a)\,(\alpha_T Le)]\right\}^{-1} \tag{17}$$

$$F(\text{thermophoretic suction}) \approx (\alpha_T Le) \cdot \frac{St_h}{St_{m,0}} \cdot \frac{T_e - T_w}{T_w} \equiv -B_T \tag{18}$$

with $a \approx 0.07$. Thus, if the conditions below are satisfied,

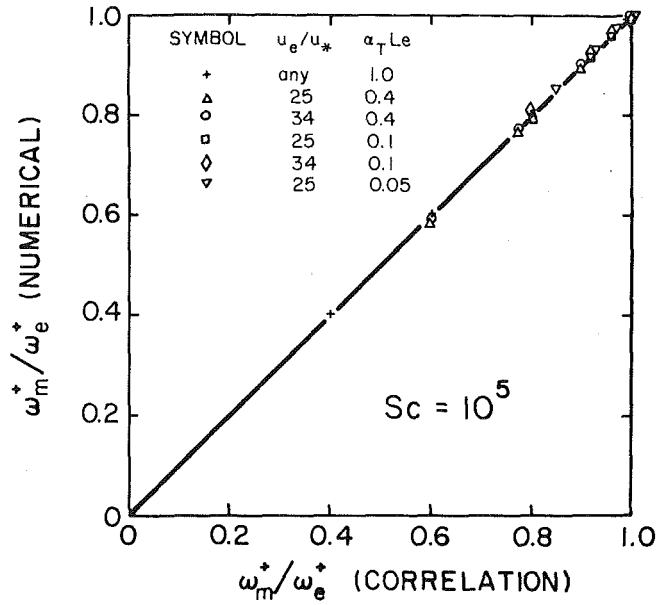

Fig. 4 Test of Sc >> 1 correlation (equation (17)) for ω_m/ω_e via numerical solution of fully developed form of equations (2) and (4) outside of the Brownian sublayer

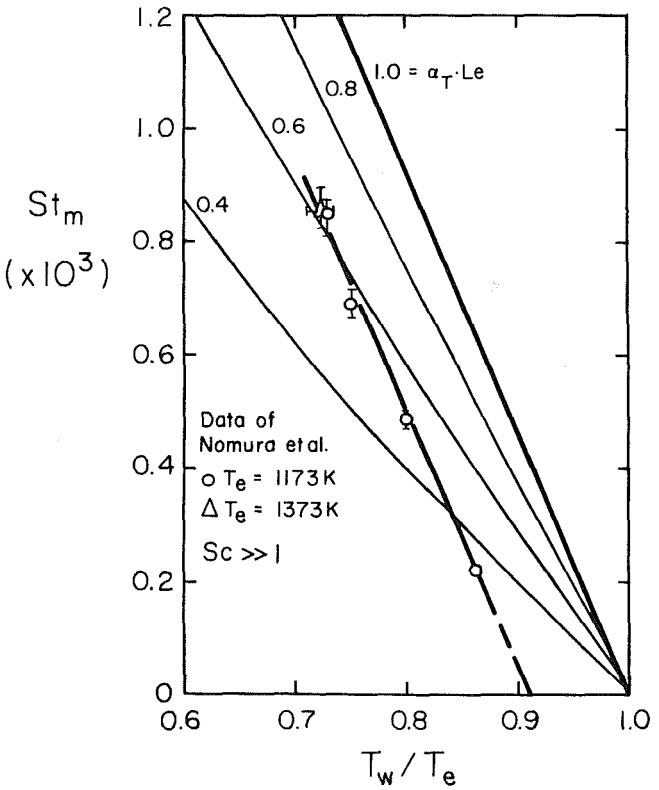

Fig. 5 Comparison between the simple two-layer Sc >> 1 thermophoretic theory and the experimental data of Nomura et. [1]

local particle mass deposition fluxes to a smooth solid surface can be estimated from:

$$-\dot{m}_p'' \approx \rho_e u_e \omega_{p,e} \cdot \mathrm{St}_h \cdot (\alpha_T \mathrm{Le})_w \cdot \frac{[(T_e - T_w)/T_w]}{\{1 + [(T_e - T_w)/T_w] \cdot [0.07 + 0.93(\alpha_T \mathrm{Le})_w\}} \quad (19)$$

where St_h is the local heat-transfer coefficient (Stanton number). Since α_TLe < 1 (Fig. 3), a convenient local upper bound to the thermophoretically augmented deposition flux is provided by the α_TLe = 1 singular case of equation (19), viz:

$$-\dot{m}_p'' < \rho_e u_e \omega_{p,e} \mathrm{St}_h \cdot \frac{T_e - T_w}{T_e} \quad (20)$$

However, especially if the particles or pressure levels are large enough to enter the continuum regime[10] (Kn_p < 1) and the particles are themselves poor thermal conductors, actual deposition rates (equation (19)) will be considerably lower than this simple upper bound (equation (20)).

For the asymptotic formula (19) to apply, we must have $(T_m - T_w)/T_w << 1$. Thus (Appendix 2), we require that the particles be large enough so that $\alpha_T [(T_e - T_w)/T_w] >> 1$. Yet the particles must be small enough so that eddy impaction does not set in [33], i.e., the dimensionless particle stopping time must satisfy (see Appendix 1) $t_p^+ < \delta_{m,0}^+$ (or, approximately $t_p^+ < 12(\mathrm{Sc})^{-1/3}$). Fortunately, these conditions are not uncommon. Moreover, even when the mainstream particle size distribution includes particle size classes for which one of these conditions breaks down, there will usually be important intermediate size particles present governed by the above mentioned deposition rate laws. Generalizations to embrace smaller (Sc = 0(1)) and larger particles (inertial effects) will be the subject of subsequent communications [34, 35].

Any comparison between these predictions and GT blade or cascade particle deposition experiments should be regarded only as indicative of general trends, since real blades have a laminar and transition region which may occupy a considerable portion of their total chord. In addition, large streamwise pressure gradients may be present locally, influencing the law-of-the-wall (implicit in equations (15) and (19)).[11] For these reasons alone one would be inclined to ultimately use more realistic computational models for the velocity, temperature and turbulent diffusivity fields (see e.g., Cebeci and Smith [37]), including also the effects of film cooling. However, such generalizations inevitably have to cope with the numerical problems discussed in section 4 and circumvented in section 5. Thus, dropping the wall boundary condition for ω and using equation (6) instead, as done here, would provide a reasonable approach to the calculation of F(thermophoretic suction) and F(outer sink) under these more general conditions too. Pending further studies, however, we recommend that equation (19) be used for local particle deposition rate estimates, where St_h is interpreted to be the prevailing local heat-transfer coefficient, provided all other basic assumptions discussed above are satisfied.

As a preliminary indication of the success of the present formulation we examined the 3 atm data of reference [1][12], and compared the experimental dependence of mass-transfer coefficient on wall temperature (see points, Fig. 5) with that

[10] An interesting consequence of equation (19) and Fig. 3 is that in the particle size range for which α_TLe ≈ const (and yet conditions 5-5 and 5-6 are satisfied) the mass deposition rate coefficient becomes independent of particle size. In general, however, the proportionality factor relating mass deposition flux to local mainstream particle mass fraction is particle size (class) dependent, in view of the particle size dependence of the parameters α_TLe and Sc.

[11] Provided the law-of-the-wall is locally valid, it is possible to rigorously include the streamwise convective derivative effects, as demonstrated in the interesting paper of Donovan, Hanna and Yerazunis [36] dealing with high Pr or Sc transport across developing, but "self-similar," TBLs. In such cases τ/τ_w is indeed approximately constant within the heat or mass diffusion sublayer and certain important transfer coefficient correction factors (e.g., effect of true blowing or suction) are, remarkably, the same as for the corresponding Couette-flow ($\partial/\partial x^+ = 0$) case.

[12] These data [1] exhibit a dramatic dependence of deposition rate on pressure level [5]. For low pressures (1.6 atm) the concave surface exhibits no deposit, while the convex part is covered with dust only downstream from an apparent dew point around the 30 percent of the blade chord. At higher pressures (3 atm), both convex and concave surfaces exhibit similar amounts of deposit, which increase linearly with the difference in temperature between mainstream and blade (see Fig. 5).

predicted from the present approach using the two-layer TBL model (which gives results very close to the present numerical calculations). It is noteworthy that both the data and the simple two-layer thermophoretic theory (Sc >> 1) plot nearly as straight lines (cf. the above mentioned particle trajectory model of Vermes [2] which predicts $\overline{St}_m \sim (T_e - T_w)^{1/2}$), and the slopes are in reasonable agreement for values of α_TLe of order unity. Such α_TLe-values are somewhat larger than expected from present thermophoretic theories [$(\alpha_T/Sc)_{max} \simeq 0.6$ [17]] or recent experiments [$(\alpha_T/Sc)_{max} \simeq 0.8$ [17]], but the general agreement is encouraging given the many indeterminacies and simplifications involved both in the GT cascade experiments and the calculations. Indeed, more refined computational models can hardly be justified given the present experimental situation. Among other things, the above mentioned data of Nomura et al. [1] were obtained with in situ formed particles of undetermined size distribution on an air-cooled GT blade with a portion of the coolant released near the leading edge. Thus, in bringing to bear the present solid-wall TBL results we are assuming that (*a*) the effective thermophoretic diffusivity ratio parameter α_TLe can be estimated (see Fig. 4), and (*b*) since this portion of the coolant was ejected in the laminar region, its effects on the rates of deposition in the turbulent zone, where most fouling occurred, should be small. These complicating effects on deposition rate, as well as those associated with aerodynamic roughness and mainstream turbulence, will have to be clarified in follow-on research [5].

In closing, it is interesting to note that this simple thermophoretic deposition theory predicts that the mainstream (recovery) temperature will play the role of an "apparent dew point for particles"—i.e., predicted deposition rates in a highly subsonic flow should extrapolate to zero at $T_w = T_e$. This is evidently not the case in the data of Nomura et al. [1]; however, it is not clear whether the ca. 100K "offset" is due to: (*i*) the existence of a competing particle removal process, (*ii*) errors in high temperature measurement, or (*iii*) artifacts of perimeter-averaging on a blade with highly nonuniform surface temperature. At this point it appears that simpler and more fully characterized experiments (especially with regard to mainstream particle loading and particle size distribution will be required to reliably guide theoretical model development [38-40].

Acknowledgments

We gratefully acknowledge the research support of AFOSR (Contract F49620-76C-0020) and NASA (Grant NAG-3-201), the computer programming assistance of S. Vaziri, and helpful discussions with R. Israel, S. Gokoglu, and A. Zydney.

References

1 Nomura, M., Morishita, T., and Kan, S., "An Experiment of Deposit Formation on the Surface of an Air-cooled Gas Turbine Blade," *Proceedings of the 1977 Tokyo Joint Gas Turbine Congress*, JSME/ASME, pp. 566-573.

2 Vermes, G., "Thermophoresis-enhanced Deposition Rates in Combustion Turbine Blade Passages," ASME JOURNAL OF ENGINEERING FOR POWER, Vol. 101, 1979, pp. 542-548.

3 DeCorso, S. M., and Vermes, G., "Description of Program to Develop Combustion Turbine Design Guidelines Based on Deposition/Corrosion Considerations," *Proceedings of the 1st Conference on Advanced Materials for Alternative Fuel Capable Directly Fired Heat Engines*, edited by J. W. Fairbanks and J. Stringer, Report #CONF-790749, 1979, pp. 287-300.

4 Rosner, D. E., and Fernandez de la Mora, J., "Inertial and Thermophoretic Effects on the Capture of Fuel Ash Particles by Gas Turbine Blades," (discussion of ASME Paper No. 81-WA/CD-1), ASME JOURNAL OF ENGINEERING FOR POWER, Vol. 103, 1981, pp. 558-560.

5 Rosner, D. E., and Fernandez de la Mora, J., "Correlation and Prediction of Thermophoretic and Inertial Effects on Particle Deposition from Nonisothermal Turbulent Boundary Layers," ASME *Symposium on Particle-Laden Flows in Turbomachinery*, St. Louis, Mo., June 7-15, 1982.

6 Rosner, D. E., Israel, R., and Zydney, A., "Effect of Thermophoresis on the Minimum Attainable Aerosol Diffusional Deposition Rate Before the Onset of Inertial Impaction," *ACS/IEC-81 Winter Symposium on Aerosol Systems*, Jan. 26-28, 1981.

7 Fernandez de la Mora, J., and Rosner, D. E., "Inertial Deposition of Particles Revisited and Extended; Eulerian Approach to a Traditionally Langrangian Problem," *Journal of Physicochemical Hydrodynamics*, Pergamon, Vol. 2, 1981, pp. 1-21.

8 Rosner, D. E., and Fernandez de la Mora, J., "Recent Advances in the Theory of Salt/Ash Deposition in Combustion Systems," *Proceedings of the DOE/EPRI 1st Conference on Advanced Materials/Alternate Fuel Capable Directly Fired Engines*, edited by J. W. Fairbanks and J. Stringer, Report #CONF-790749, 1979, pp. 301-330.

9 Byers, R. L., and Calvert, S., "Particle Deposition from Turbulent Streams by Means of Thermal Force," *Ind. Engrg. Chem. Fundam.* Vol. 8, 1969, pp. 646-655.

10 Sing, B., and Byers, R. L., "Particle Deposition due to Thermal Force in the Transition and Near Continuum Regimes," *Ind. Engrg. Chem. Fundam.*, Vol. 11, 1972, pp. 127-133.

11 Nishio, G., Kitani, S., and Takahashi, K., "Thermophoretic Deposition of Aerosol Particles in a Heat Exchanger Pipe," *Ind. Engrg. Chem.*, Process Des. Dev., Vol. 13, 1974, pp. 408-415.

12 Owen, P. R., "Dust Deposition from a Turbulent Airstream," in *Aerodynamic Capture of Particles*, edited by E. G. Richardson, Pergamon Press, New York, 1960.

13 Epstein, P. S., *Z. Physik*, Vol. 54, 1929, p. 537.

14 Talbot, L., "Thermophoresis, A Review," *12th Symposium on Rarefied Gas Dynamics*, Charlottesville, Va., 1980, *Progress in Astronautics and Aeronautics*, Vol. 74, edited by S. S. Fisher, AIAA, New York, 1981, pp. 467-488.

15 Goren, S. L., "Thermophoresis of Aerosol Particles in the Laminar Boundary Layer on a Flat Plate," *J. Colloid Interface Sci.*, Vol. 61, 1977, pp. 77-85.

16 Walker, K. L., Homsy, G. M., and Geyling, F. T., "Thermophoretic Deposition of Small Particles in Laminar Tube Flow," *J. Coll. Int. Sci.*, Vol. 69, No. 1, 1979, pp. 138-147.

17 Talbot, L., Cheng, R. K., Schefer, R. W., and Willis, D. R., "Thermophoresis of Particles in a Heated Boundary Layer," *Journal of Fluid Mechanics*, Vol. 101, 1980, pp. 737-758.

18 Rosner, D. E., "Thermal (Soret) Diffusion Effects on Interfacial Mass Transport Rates," *Physicochemical Hydrodynamics*, Vol. 1, 1980, pp. 159-185.

19 Rosner, D. E., "Mass Transfer from Combustion Gases," Paper No. 59a, Presented at the AIChE 73rd National Meeting, Chicago, Ill., Nov. 1980, pp. 16-20.

20 Fernandez de la Mora, J., *Deterministic and Diffusive Mass Transfer Mechanisms in the Capture of Vapor and Particles*, Ph.D. dissertation, Yale University Graduate School, Department of Engineering and Applied Science, Dec. 1980.

21 Srivastava, R., and Rosner, D. E., "A New Approach to the Correlation of Boundary Layer Transfer Rates with Thermal Diffusion and/or Variable Properties," *International Journal of Heat and Mass Transfer*, Vol. 22, 1979, pp. 1281-1294; see also Gokoglu, S., and Rosner, D., ibid. (1983)

22 Rosner, D. E., Chen, B. K., Fryburg, G., and Kohl, F., "Chemically Frozen Multicomponent Boundary Layer Theory of Salt and/or Ash Deposition Rates from Combustion Gases," *Comb. Sci. and Tech.*, Vol. 20, 1979, pp. 87-106.

23 Spalding, D. B., "A Single Formula for the 'Law of the Wall'," ASME *Journal of Applied Mechanics*, 1961, pp. 455-458.

24 Kestin, J., and Richardson, P. D., "Heat Transfer Across Turbulent Incompressible Boundary Layers," *International Journal of Heat and Mass Transfer*, Vol. 6, No. 2, 1963, pp. 147-190.

25 Prandtl, L., "Bemierkung über den Wärmeübergang im Rohr," *Zeit. Physik*, Vol. 29, 1928, p. 487; see also *Zeit. Physik II*, 1910, p. 1072.

26 Deissler, R. G., "Analysis of Turbulent Heat Transfer, Mass Transfer and Friction in Smooth Tubes at High Prandtl and Schmidt Numbers," NACA Rep. 1210, 1955.

27 Hanna, O. T., and Sandall, O. C., "Developed Turbulent Transport in Ducts for Large Prandtl or Schmidt Numbers," *AIChE Journal*, Vol. 18, N9. 3, 1972, pp. 527-533.

28 Sandall, O. C., and Hanna, O. T., "Large Schmidt Number Mass Transfer in Turbulent Pipe Flow," *AIChE Journal*, Vol. 25, No. 1, 1979, pp. 190-192.

29 Shaw, D. A., and Hanratty, T. J., "Turbulent Mass Transfer to a Wall for Large Schmidt Numbers," *AIChE Journal*, Vol. 23, 1977, p. 78.

30 Rosner, D. E., and Fernandez de la Mora, J., "Aerosol Deposition Behavior on Gas-Film Cooled Solid Surfaces," in preparation, 1982.

31 Schlichting, H., *Boundary Layer Theory*, 6th ed., McGraw-Hill, New York, 1968.

32 VonKarman, T., "Analogy Between Fluid Friction and Heat Transfer," Trans. ASME, Vol. 61, 1939, p. 705; see also *Engineering*, Vol. 148, 1939, p. 210.

33 Friedlander, S. K., *Smoke, Dust and Haze—Fundamentals of Aerosol Behavior*, J. Wiley & Sons, New York, 1977.

34 Rosner, D. E., Fernandez de la Mora, J., and Gökoglu, S., "Vapor and Small Particle Transport Across Turbulent Nonisothermal Boundary Layers," ASME Transactions, to be submitted, 1982.

35 Yaglom, A. M., "Similarity Laws for Constant-Pressure and Pressure-

Gradient Turbulent Wall Flows," *Ann. Rev. of Fluid Mech.*, Vol. 11, 1979, pp. 505-540.

36 Donovan, L. F., Hanna, O. T., and Yerazunis, S., "Similar Solutions of Turbulent Boundary Layer Heat and Mass Transfer Problems," *Chemical Engineering Science*, Vol. 22, 1967, pp. 595-610.

37 Cebeci, T., and Smith, A. M. O., "A Finite Difference Method for Calculating Compressible Laminar and Turbulent Boundary Layers," ASME *Journal of Basic Engineering*, Vol. 3, 1970, pp. 523-535.

38 Rosner, D. E., Seshadri, K., Fernandez de la Mora, J., Fryburg, G. C., Kohl, F. J., Stearns, C. A., and Santoro, G. J., "Transport, Thermodynamic and Kinetic Aspects of Salt/Ash Deposition Rates from Combustion Gases," *Proceedings of the 10th Materials Research Symposium: Characterization of High Temperature Vapors and Gases*, edited by J. W. Hastie, NBS Spec. Public. 561, & S. Govt. Printing Office, Oct. 1979, pp. 1451-1474.

39 Rosner, D. E., and Seshadri, K., "Experimental and Theoretical Studies of the Laws Governing Condensate Deposition from Combustion Gases," *Proceedings of the Eighteenth International Symposium on Combustion*, Combustion Institute, 1981, pp. 1385-1394.

40 Rosner, D. E., and Atkins, R. M., "Experimental Studies of Salt/Ash Deposition Rates from Combustion Products Using Optical Techniques," *Proceedings of the Engineering Foundation Int. Conference on Experimental Research into Fouling and Slagging Due to Impurities in Combustion Gases* (in press), edited by R. Byen, 1981.

APPENDIX 1

Simple Criterion for Neglect of Eddy Impaction [6]

To obtain a useful criterion for the onset of eddy impaction we find the particle size at which:

$$\mathrm{St}_{m,0}\{\text{eddy + Brownian diffusion}\} = \mathrm{St}_m\{\text{eddy impaction}\} \tag{A1-1}$$

However, at large Schmidt numbers [4, 29]:

$$\mathrm{St}_{m,0}(\text{eddy + Brownian diffusion}) \simeq 0.085(c_f/2)^{1/2}\,\mathrm{Sc}^{-2/3} \tag{A1-2}$$

and for $t_p^+ < 20$, experimentally [4, 5, 33]:

$$\mathrm{St}_m(\text{eddy impaction}) \simeq 6\times 10^{-4}(c_f/2)^{1/2}(t_p{}^+)^2 \tag{A1-3}$$

Equating these two expressions for St_m, and solving for t_p^+, we obtain:

$$t_p{}^+ \simeq 12(\mathrm{Sc})^{-1/3} \tag{A1-4}$$

It is interesting to note that equation (A1-2) also implies:

$$\delta_{m,0}^+ \simeq 12(\mathrm{Sc})^{-1/3} \tag{A1-5}$$

Comparing A1-4 and A1-5 we observe that eddy impaction sets in when $t_p^+ \simeq \delta_{m,0}^+$ or, when:

$$t_p \simeq \delta_{m,0}/u_* \tag{A1-6}$$

i.e., when t_p *is numerically equal to the time required to traverse the Brownian sublayer if traveling at the friction velocity,* u_*. Accordingly, the analysis of section 3 holds for particle diameters such that the stopping time t_p is much smaller than $\delta_{m,0}/u_*$. Equation (A1-1) or (A1-4) may be regarded as an equation for a particular particle size [6] *above* which inertial effects should be included[13], especially when the thermophoretic enhancements are modest.

APPENDIX 2

Criteria for the Validity of Asymptotic Treatment of Thermophoresis

Consider the conditions under which the thickness, δ_m, of the Brownian diffusion sublayer will indeed be small compared to characteristic thermal boundary layer thickness, δ_h. If the Schmidt number is large enough for the validity of equation (6), then δ_m can be estimated from:

$$-j_w{}''(\text{equation (6)}) \simeq D\rho\omega_m/\delta_m \tag{A2-1}$$

Thus, the condition $\delta_m/\delta_h \ll 1$ is equivalent to the condition:

$$\alpha_T(T_e - T_w)/T_w \gg 1 \tag{A2-2}$$

In view of Figs. 2, 3, this can be written:

$$\mathrm{Sc} > > \frac{\mathrm{Pr}}{(\alpha_T \mathrm{Le})[(T_e - T_w)/T_w]} \tag{A2-3}$$

For example, if $(\alpha_T \mathrm{Le}) \simeq 0.4$ (Fig. 3) and $\mathrm{Pr} = 0.7$ then inequality A2-3 gives $\mathrm{Sc} \gg 1.75[(T_e - T_w)/T_w]^{-1}$. Therefore, if $(T_e - T_w)/T_w \simeq (1400\text{-}1000)/(1000) = 0.4$, then Sc must be much greater than $(1.75)\,(0.4)^{-1} = 4.4$, which is certainly satisfied (Fig. 2) for particle diameters above 10^{-2} μm. The laws governing the thermophoretically enhanced deposition of still smaller particles will be taken up in reference [34].

It appears that, in view of equation (A2-1), the validity of equation (19) would require that the surface be smooth on the scale of δ_m, not merely δ_h and $5\nu/u_*$ (the maximum roughness height for aerodynamically smooth behavior). Fortunately such an ultrastringent condition is evidently *not* required for the case of cooled surfaces considered here. Rather, smoothness on the scale of δ_h and $5\nu/u_*$ should be sufficient, since for large Schmidt number particles (Fig. 2) there is a wide portion of the viscous sublayer where both Brownian and turbulent diffusion are negligible. There the particle mass conservation equation becomes effectively first order, exhibiting concentration versus distance behavior independent of the precise wall boundary conditions (section 4.1). Returning to the experiments of Nomura et al. [2], we note that their blades were smooth on the scale of δ_h and $5\nu/u_*$, but certainly very rough on the scale of δ_m (equation (A2-1) above). Yet, the observed deposition rate (Fig. 5) increased linearly with the temperature gradient, confirming our contention.

[13] The particle stopping time, t_p appearing here is closely related to the Brownian diffusivity D_p (implicit in Fig. 2) and the individual particle mass m_p. According to the Einstein relation: $t_p = (kT/m_p)^{-1} D_p$.

Gradient Turbulent Wall Flows," *Ann. Rev. of Fluid Mech.*, Vol. 11, 1979, pp. 505-540.

36 Donovan, L. F., Hanna, O. T., and Yerazunis, S., "Similar Solutions of Turbulent Boundary Layer Heat and Mass Transfer Problems," *Chemical Engineering Science*, Vol. 22, 1967, pp. 595-610.

37 Cebeci, T., and Smith, A. M. O., "A Finite Difference Method for Calculating Compressible Laminar and Turbulent Boundary Layers," ASME *Journal of Basic Engineering*, Vol. 3, 1970, pp. 523-535.

38 Rosner, D. E., Seshadri, K., Fernandez de la Mora, J., Fryburg, G. C., Kohl, F. J., Stearns, C. A., and Santoro, G. J., "Transport, Thermodynamic and Kinetic Aspects of Salt/Ash Deposition Rates from Combustion Gases," *Proceedings of the 10th Materials Research Symposium: Characterization of High Temperature Vapors and Gases*, edited by J. W. Hastie, NBS Spec. Public. 561, & S. Govt. Printing Office, Oct. 1979, pp. 1451-1474.

39 Rosner, D. E., and Seshadri, K., "Experimental and Theoretical Studies of the Laws Governing Condensate Deposition from Combustion Gases," *Proceedings of the Eighteenth International Symposium on Combustion*, Combustion Institute, 1981, pp. 1385-1394.

40 Rosner, D. E., and Atkins, R. M., "Experimental Studies of Salt/Ash Deposition Rates from Combustion Products Using Optical Techniques," *Proceedings of the Engineering Foundation Int. Conference on Experimental Research into Fouling and Slagging Due to Impurities in Combustion Gases* (in press), edited by R. Byen, 1981.

APPENDIX 1

Simple Criterion for Neglect of Eddy Impaction [6]

To obtain a useful criterion for the onset of eddy impaction we find the particle size at which:

$$\mathrm{St}_{m,0}\{\text{eddy + Brownian diffusion}\} = \mathrm{St}_m\{\text{eddy impaction}\} \tag{A1-1}$$

However, at large Schmidt numbers [4, 29]:

$$\mathrm{St}_{m,0}(\text{eddy + Brownian diffusion}) \simeq 0.085(c_f/2)^{1/2}\,\mathrm{Sc}^{-2/3} \tag{A1-2}$$

and for $t_p^+ < 20$, experimentally [4, 5, 33]:

$$\mathrm{St}_m(\text{eddy impaction}) \simeq 6\times 10^{-4}(c_f/2)^{1/2}(t_p{}^+)^2 \tag{A1-3}$$

Equating these two expressions for St_m, and solving for t_p^+, we obtain:

$$t_p{}^+ \simeq 12(\mathrm{Sc})^{-1/3} \tag{A1-4}$$

It is interesting to note that equation (A1-2) also implies:

$$\delta_{m,0}^+ \simeq 12(\mathrm{Sc})^{-1/3} \tag{A1-5}$$

Comparing A1-4 and A1-5 we observe that eddy impaction sets in when $t_p^+ \simeq \delta_{m,0}^+$ or, when:

$$t_p \simeq \delta_{m,0}/u_* \tag{A1-6}$$

i.e., when t_p *is numerically equal to the time required to traverse the Brownian sublayer if traveling at the friction velocity,* u_*. Accordingly, the analysis of section 3 holds for particle diameters such that the stopping time t_p is much smaller than $\delta_{m,0}/u_*$. Equation (A1-1) or (A1-4) may be regarded as an equation for a particular particle size [6] *above* which inertial effects should be included[13], especially when the thermophoretic enhancements are modest.

APPENDIX 2

Criteria for the Validity of Asymptotic Treatment of Thermophoresis

Consider the conditions under which the thickness, δ_m, of the Brownian diffusion sublayer will indeed be small compared to characteristic thermal boundary layer thickness, δ_h. If the Schmidt number is large enough for the validity of equation (6), then δ_m can be estimated from:

$$-j_w{}''(\text{equation (6)}) \simeq D\rho\omega_m/\delta_m \tag{A2-1}$$

Thus, the condition $\delta_m/\delta_h \ll 1$ is equivalent to the condition:

$$\alpha_T(T_e - T_w)/T_w \gg 1 \tag{A2-2}$$

In view of Figs. 2, 3, this can be written:

$$\mathrm{Sc} \gg \frac{\mathrm{Pr}}{(\alpha_T \mathrm{Le})[(T_e - T_w)/T_w]} \tag{A2-3}$$

For example, if $(\alpha_T \mathrm{Le}) \simeq 0.4$ (Fig. 3) and Pr = 0.7 then inequality A2-3 gives Sc >> $1.75[(T_e - T_w)/T_w]^{-1}$. Therefore, if $(T_e - T_w)/T_w \simeq$ (1400-1000)/(1000) = 0.4, then Sc must be much greater than $(1.75)(0.4)^{-1} = 4.4$, which is certainly satisfied (Fig. 2) for particle diameters above 10^{-2} μm. The laws governing the thermophoretically enhanced deposition of still smaller particles will be taken up in reference [34].

It appears that, in view of equation (A2-1), the validity of equation (19) would require that the surface be smooth on the scale of δ_m, not merely δ_h and $5\nu/u_*$ (the maximum roughness height for aerodynamically smooth behavior). Fortunately such an ultrastringent condition is evidently *not* required for the case of cooled surfaces considered here. Rather, smoothness on the scale of δ_h and $5\nu/u_*$ should be sufficient, since for large Schmidt number particles (Fig. 2) there is a wide portion of the viscous sublayer where both Brownian and turbulent diffusion are negligible. There the particle mass conservation equation becomes effectively first order, exhibiting concentration versus distance behavior independent of the precise wall boundary conditions (section 4.1). Returning to the experiments of Nomura et al. [2], we note that their blades were smooth on the scale of δ_h and $5\nu/u_*$, but certainly very rough on the scale of δ_m (equation (A2-1) above). Yet, the observed deposition rate (Fig. 5) increased linearly with the temperature gradient, confirming our contention.

DISCUSSION

G. Vermes[14]

The authors present an impressive application of fundamental heat and mass transfer methods to the problem of deposition of small particles from hot gases to cooled surfaces. The applicability of this approach is contingent on the successful assessment of the pertinent transfer coefficients for the problem at hand: once the various coefficients are known, the only variables to consider are temperatures (equation (6)). Figure 5 is an indication of how the method correlates with one set of test data, obtained from gas turbine type cascade tests.

Another type of approach to the assessment of particle transport due to gas/wall temperature differences is the "Lagrangian" method which tries to follow the fate of the individual particles in the gas path. This was the approach chosen by this discusser [2]. The key quantity to be assessed in this second approach is the distance of a limiting streamline from the vane surface (t_0^* in [2]) at the beginning of the problem (e.g., at the entrance to the blade path): all particles initially at this critical streamline (or at streamlines closer to the surface) will reach the wall; all particles originally at streamlines at a greater than t_0^* distance will not reach the surface while traversing the blade path.

[13] The particle stopping time, t_p appearing here is closely related to the Brownian diffusivity D_p (implicit in Fig. 2) and the individual particle mass m_p. According to the Einstein relation: $t_p = (kT/m_p)^{-1} D_p$.

[14] Fellow Engineer, Combustion Turbine Systems Division, Westinghouse Electric Corporation, Concordville, Pa 19331. Mem. ASME

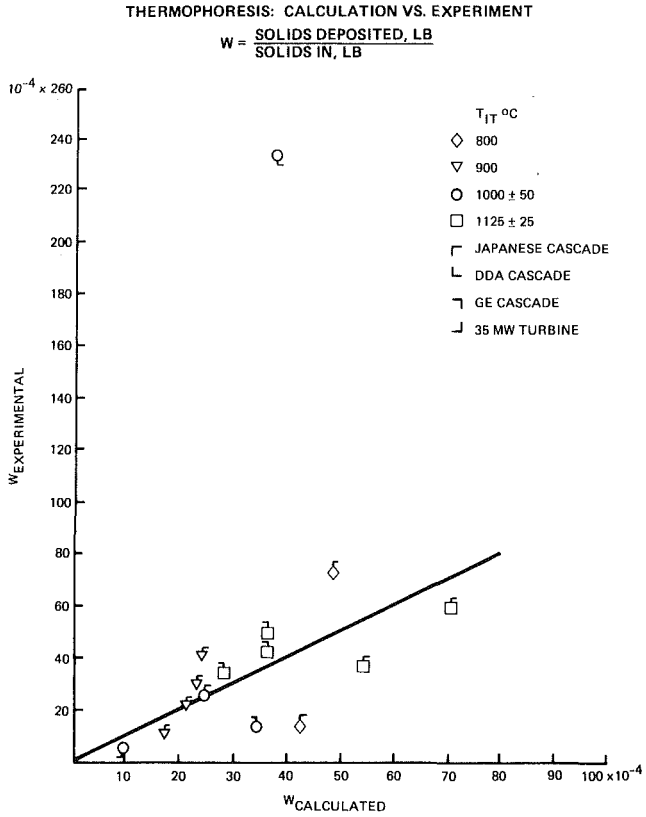

Fig. 6

In principle, the authors' "Eulerian" treatment and the "Lagrangian" approach of [2] are both legitimate avenues of problem solving in the fields of fluid mechanics and heat/mass transfer. In practice, however, numerous simplifications have to be accepted to make the task tractable for both approaches. Unless the simplifications inherent in one approach are such that gross departure from reality can be proven *a priori*, only a substantial amount of experimental evidence can decide which method should be pursued.

In comparing the two methods, the authors state that the "Lagrangian" approach of the "limiting trajectory" as proposed in [2], would be "essentially correct if this limiting trajectory was completely embedded inside the viscous sublayer, but this is rarely the case. Even so [this writer in [2]] neglected the important effect of the simultaneous transverse velocity present . . . ." The authors' comments indicate that they feel: the "Lagrangian" approach can be dismissed out of hand on the strength of the above arguments.

Both comments of the authors amount to, essentially, the same question: how does the distance of the "limiting streamline" from the surface (denoted t_0^* in [2]) compare with the thickness of the laminar sublayer δ_{VSL}? The significance of this question was recognized by Dr. G. P. Wachtell of the Franklin Research Center in his incisive discussion of [2]. He presented in his discussion a modification of the calculation procedure of this discusser's approach to obtain t_0^*. Dr. Wachtell's procedure incorporates the assumption into the "Lagrangian" calculation of [2] that the "limiting trajectory" is indeed inside the laminar sublayer. (His modification has other advantages as well.) Dr. Wachtell's derivation is fully explained in his published discussion to [2]. In the Author's Closure to [2], this writer suggested that – though the numerical results of his original calculations in [2] and Dr. Wachtell's improved method are not too different – the latter is clearly the more correct (and also more convenient way) to calculate t_0^*.

All this eventually, boils down to a numerical check, whether δ_{VSL} is smaller than t_0^* calculated with Dr. Wachtell's equation (34) (in [2]):

$$t_0^{*2} = mKST_s^{1/2}\left(\frac{T_{0G}-T_{0S}}{P_0 V_{0G}} + \frac{T_{1G}-T_{1S}}{P_1 V_{1G}}\right)$$

In the formula, T, V, and P are temperature, velocity, and pressure in the blade path entrance and exit (subscripts 0 and 1), measured in the free gas stream and the surface (subscripts G and S, respectively), and S is the chord length of the vane. Because of the assumption of the laminar sublayer, $m=1$. When using the CGS system (cm, dyn, °K, cm/s) the constant K was originally thought to be 34.7. In the Author's Closure to [2] it was explained that a 30–56 percent smaller value is more correct and 15 will be used. For the conditions of [1], t_0^* calculates on the order of 5×10^{-3} cm. For full sized turbines, the order of t_0^* is the same. The thickness of the viscous (laminar) sublayer can be obtained from the criterion

$$5 > \frac{u_* \delta_{VSL}}{\mu}$$

where

$$u* = 0.15 u_1^{1/8}\left(\frac{\mu}{\delta}\right)_{VSL}^{1/8}$$

and u_1 is the gas velocity parallel to the surface at the edge of the laminar (viscous) sublayer [31]. At turbine passage conditions (12 atm, 2060°R wall temperature, $500 < u_1 < 1000$ fps) the thickness of the viscous sublayer $(\delta)_{VSL}$ will be on the order of 10×10^{-3} cm. Note that the system pressure (P) is only inplicitly involved in the calculation ($V^{1/8} \sim P^{-1/8}$); because of the 1/8 exponent, the thickness of the sublayer will be about the same in a low pressure cascade [1] and in a field turbine – provided velocities and temperatures are similar. Properly designed cascade tests observe this latter criterion.

It appears that – comparing $\delta_{VSL} \sim 10 \times 10^{-3}$ cm and $t_0^* \sim 5 \times 10^{-3}$ – the thickness of the laminar sublayer and the position of the "critical distance" are compatible with the original assumption. It should be noted that outside of the laminar sublayer, there is a transition layer which is about fourteen times the width of the sublayer ([31]). This means that δ_{VSL}/t_0^* is actually $>>1$.

It is true that in the entrance to the blade path, the thickness of *any* boundary layer is – by definition – zero, therefore t_0^* is indeed $>\delta_{VSL}$ in the cascade entrance. It was pointed out in [2], however, that the interest of the turbine designer/operator is focussed on the downstream end of the passage, the "throat" of the cascade: turbine efficiency is most sensitive to restriction in this area of the blade path. It may be concluded, that the first criterion of validity of the "Lagrangian" approach noted by the authors' (i.e., $t_0^* < \delta_{VSL}$) is not an unreasonable assumption in a combustion turbine.

Considering the second comment of the authors' (that displacement velocities in the boundary layer interfere with the thermophoretic movement of the particles), it should be noted that transverse gas velocity in a laminar sublayer is practically nonexistent: if it is accepted that $t_0^* < \delta_{VSL}$ the author's second comment is also answered.

This writer would conclude that the paucity of experimental data at the present time does not yet allow us to make a reliable choice whether deposition rates in cooled turbine passages should be calculated using the method suggested by the authors or using [2]: as more material becomes available, this decision will be possible. It appears, however, that the "Lagrangian" approach of [2] can not be dismissed out of hand.

This writer very much agrees with the authors' comment that "more refined computational models can hardly be justified given the present experimental situation." This remark is especially welcome in view of the assumption used

by the authors as well as this writer in [2], that capture efficiency is 100 percent: "What arrives, sticks." Considering the fact that laboratory experiments are seldom run uninterrupted for several days whereas turbines in the field do, the accuracy of deposition tests in the laboratory is often influenced by the thermal shock of the shutdown, when deposits may peel off. This may not happen in a base loaded turbine for weeks.

It is felt that the next task at hand is a realistic assessment of the capture efficiency rather than computational refinement. Figure 6 is intended as an illustration of the problem. The experimental material on the figure includes the test data from [2] ("Japanese Cascade," "35-MW turbine") but also data from two additional cascade tests ("DDA Cascade," "GE Cascade"). Both investigations were sponsored by the Electric Power Research Institute (see, e.g., "Workshop Proceedings: Deposition in Utility Gas Turbines," Arthur Cohn and John Stringer, EPRI WS-80-121, May 1981). This figure shows the calculated deposition rate, using equation (34) of [2] versus the deposition rates deduced from the experiments. It is not impossible that the data scatter originated from two sources: the uncertainty of the 100 percent capture efficiency assumption and the assumption involved in the numerical value of the heat conductivity of the deposited material (the latter assumption caused the problem with K mentioned before). Heat conductivity influences the constant K in all W_{Calc} values: a K value different from what was used would make the slope of the line of equality different.

There is one test point which is quite different: the DDA cascade (refer to "Investigation of the Influence of Contaiminated Fuel on Turbine Vane Deposition, D. A. Nealy, W. H. Timmerman, and A. Cohn, Paper AIAA-80-1113, 1980). This cascade had a permeable skin: a special form of transpiration cooling ["Lamilloy"(R)]. The dramatic effect of the changed boundary layer structure is quite clear.

In summary, this discusser feels that the "Eulerian" and the "Lagrangian" assessment of thermophoretic deposition rates in turbines should coexist for a while, at least until more reliable test data become available.

Author's Closure

Our reasons for recommending the Eulerian boundary layer (BL) approach for predicting thermophoretically augmented small particle deposition rates in turbomachinery are briefly restated and amplified below.

If the limiting particle trajectory is close enough to the blade surface to never experience appreciable turbulence, yet each particle is not so small as to have an appreciable Brownian diffusivity, then the two approaches are fully equivalent, since, as demonstrated and discussed in [7], individual particle trajectories are, in fact, *characteristics* of the resulting first order *Eulerian* PDE governing the particle "phase" velocity field.

However, *the Eulerian formulation has the decisive advantage that it retains its conceptual and computational validity in the more general cases in which turbulence and/or particle Brownian diffusivity are not negligible.* Indeed, since small particle mass transfer distribution calculations are already made in the gas turbine industry using highly developed Eulerian boundary layer codes (see references [37, 41–44]), there is evidently nothing to be gained (and a penalty to be paid in lost generality!) by abandoning this approach in the presence of appreciable thermophoretic particle drift.

Inspection of the Eulerian PDE governing the local particle mass fraction reveals [18] that thermophoresis introduces two distinct effects, viz., (*i*) a thermophoretic convection ("suction") of particles toward the cold blade, which "competes" with the BL "displacement" velocity and any real (wall transpiration) blowing [45]; and (*ii*) a "pseudo-homogeneous sink" term governed by an effective rate constant proportional to the spatial gradient of the thermophoretic velocity. Indeed, these effects are readily included in the discretized Eulerian BL equations [43, 44]. On this basis we have recently developd and tested easy-to-use engineering correlations of thermophoretically augmented mass-transfer coefficients, $\text{St}_m/\text{St}_{m,0}$ [45, 46]. Moreover, in the large Schmidt number limit, (see Fig. 2) it is possible to develop an asymptotically exact method for incorporating the simultaneous effects of non-negligible *particle inertia* on the spatial distribution of thermophoretically augmented small particle deposition rate [5, 7, 47] at non-zero, but subcritical particle Stokes numbers. As briefly discussed in reference [7], the principal inertial effect is to alter (enrich or deplete) the *local* BL-edge particle mass fraction from its upstream reservoir value. Further illustrations of these previously unconsidered effects under combustion turbine and combustion gas heat-exchanger conditions will be the subject of follow-on publications from this laboratory.

Vermes's concluding comments pertain to the possible role of variations in particle capture coefficient and thermophoretic coefficient on preliminary comparisons of his deposition rate predictions with selected test data (Fig. 6). While further discussion of these points would require considerable additional detail best left for another occasion, we do wish to remark that: (*a*) the problem of making a realistic assessment of the intrinsic capture (sticking) coefficient, s, cannot really be divorced from the problem of making self-consistent deposition rate predictions; (*b*) because of the opportunities for multiple encounters, locally, diffusional and/or thermophoretically dominated deposition rate predictions will never be as sensitive to s as would inertially dominated deposition [40]; and, finally, (*c*) even at combustion turbine pressures the thermophoretic properties of submicron and/or micron-sized particles cannot be predicted on the basis of quasi-continuum (Stokes drag, etc.) behavior alone. At high temperatures the prevailing combustion gas mean-free-path is not really negligible on the scale of the particle radii; therefore, $\alpha_T\text{Le}$ (and, hence, Vermes's K, seen to be $(\nu p/T^{3/2})\cdot(\alpha_T\text{Le}/\text{Pr})$) will be larger than their corresponding "continuum" asymptotes (see, e.g., Fig. 3 and reference [14]).

Additional References

41 Menguturk, M., and Sverdrup, E. F., "A Theory for Fine Particle Deposition in Two-Dimensional Boundary Layer Flows and Application to Gas Turbines," ASME JOURNAL OF ENGINEERING FOR POWER, Vol. 104, No. 1, Jan. 1982, pp. 69–76.

42 Wenglarz, R. A., "An Assessment of Deposition in PFBC Power Plant Turbines," ASME JOURNAL OF ENGINEERING FOR POWER, Vol. 103, 1981, pp. 552–557.

43 Crawford, M. E., and Kays, W. M., "A Program for Numerical Computation of Two-Dimensional Internal and External Boundary Layer Flows," STAN5, NASA CR 2742, 1976.

44 Patankar, S. V., *Numerical Heat Transfer and Fluid Flow*, McGraw Hill, New York, 1980.

45 Gökoglu, S., and Rosner, D. E., "Correlation of Thermophoretically Modified Small Particle Deposition Rates in Forced Convection Systems with Variable Properties, Transpiration Cooling and/or Viscous Dissipation," *International Journal of Heat and Mass Transfer*, (submitted 1982).

46 Gökoglu, S., and Rosner, D. E., "Viscous Dissipation Effects on Thermophoretically Augmented Particle Transport Across Laminar Boundary Layers," *International Journal of Heat and Mass Transfer*, (submitted 1982).

47 Fernandez de la Mora, J. and Rosner, D. E., "Effects of Inertia on the Diffusional Deposition of Small Particles to Spheres and Cylinders at Low Reynolds Numbers," *Journal of Fluid Mechanics*, in press (1982).

An Approximate Method for Evaluating the Temperature Field in Tubesheet Ligaments of Tubular Heat Exchangers Under Steady-State Conditions

K. P. Singh
M. Holtz
Joseph Oat Corporation,
Camden, N.J. 08104

A method to determine the temperature field in a typical tubesheet ligament is developed. Using a numerical example, it is shown that, contrary to the common belief, a temperature gradient may exist throughout the thickness of the tubesheet in heat exchangers operating under "typical" conditions. Such thermal gradients can have significant influence on the exchanger's thermal and mechanical performance. The solution is developed with an eye to its suitability as a design tool.

Introduction

Tubesheets in shell-and-tube heat exchangers form a principal barrier between two pressure chambers, commonly referred to as "shell-side" and "tubeside" in the literature. The two chambers usually operate at different temperatures resulting in a thermal gradient in the body of the tubesheet. Gardner [1] showed that the ligament material of the tubesheet is mainly at the tubeside fluid temperature except for a thin skin facing the shellside fluid where a steep temperature gradient exists. Therefore, the so-called "thermal skin effect" produces only localized stresses (known as "peak stresses" in the lexicon of the ASME Codes). The body of the tubesheet does not experience a "global" thermal stress.

The intent of this paper is to show that under certain circumstances the thermal gradient may not be limited to the shellside skin. In fact, the thermal gradient may introduce significant rotation at the tubesheet rim resulting in leakage where the tubesheet is also used as a flange. Such a situation occurs whenever the shellside fluid heat-transfer coefficient is high, and the tube material possesses low thermal conductivity.

The knowledge of tubesheet/tubewall temperature field is especially important in the case of "rolled only" joints. The interfacial pressure between the tubewall and tubesheet provides the protection against leakage between the two pressurized chambers. Under the operating condition, the development of a differential temperature in conjunction with different coefficient of the wall expansion between the tubesheet ligament and tubewall may reduce the interface pressure below the threshold necessary to maintain a leak proof joint. Industrial design standards [2] provide empirical guidelines on the maximum allowable "joint temperature." A detailed knowledge of the temperature distribution in the tubewall and tubesheet ligament region is the first logical step towards the formulation of a mathematical criterion for determining the sealworthiness of "rolled only" joints.

A similar situation arises in the case of double tubesheet designs. The tubesheet in contact with the shellside fluid may be at a substantially different temperature than the tubeside tubesheet if the shellside heat transfer is much higher than the tubeside coefficient. In such an event, the tube segments spanning the two tubesheets may experience severe bending and shear stresses [3].

Gardner's Equation for tubesheet ligament temperature, despite its simplicity, is fairly accurate for commercial heat exchangers. However, as heat exchangers are deployed in ever more exacting situations, the need to formulate a solution capable of predicting the temperature field with accuracy becomes imperative. This paper is an attempt to fulfill this need.

While we seek to devise a solution of maximum generality, the need to keep the associated computation effort reasonably small is equally important. It is important that the method should lead to a solution procedure which can be utilized in a programmable calculator or a small computer. Availability of such a solution will most definitely encourage a check of tubesheet ligament temperatures during routine design work.

The solution described in this paper meets the foregoing criteria of simplicity and generality. Since the solution implies many approximations of heat-transfer equations, a thorough comparison with "Finite Element" solutions was performed to establish its accuracy and reliability. A typical comparison is described in this paper.

Due to the rather obscure source of Gardner's paper, an abstract of his solution is given in Appendix A for reference purposes. A numerical example illustrates a comparison between Gardner's formula and the solution constructed in this paper.

Contributed by the Nuclear Engineering Division and presented at the ASME Winter Annual Meeting, Washington, D.C., November 15-20, 1981. Manuscript received by the Nuclear Engineering Division November 19, 1981. Paper No. 81-WA/NE-12.

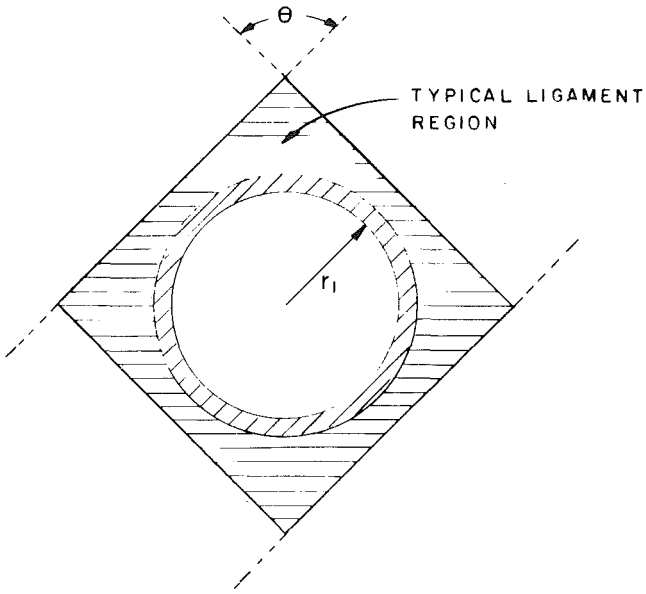

Fig. 1 Typical tube and its associated ligament cross section

In the following section a brief description of the mathematical model and its analysis is provided. Design engineers interested in using the final equations without the burdensome details of derivation may proceed directly to section 3 wherein a step-by-step description of the calculation procedure is given. Numerical illustration of the method and its comparison with a Finite Element Code solution is provided in section 4. Concluding remarks are contained in section 5.

Analysis

The cross section of a typical ligament surrounding a tube is shown in Fig. 1. During steady-state conditions, the temperature field in all ligaments will be identical, hence we will focus our attention on a composite region consisting of one tube, and its associated tubesheet ligament. It is also known that the variation of temperature is mainly in the direction of the tube axis.

In other words, the temperature changes in the lateral (in-plane) direction are, relatively speaking, quite small. These considerations lead us to model the tube-ligament assemblage as two interfacing coaxial cylinders. The inner cylinder is the tube which contains a fluid at temperature T_t. The outer cylinder is the tubesheet ligament. The noncircular cross section of the ligament is replaced by an equivalent circular section of equal cross-sectional area. This approximation is tenable so long as the temperature gradient in the lateral direction is small. It can be shown that the outer radius of the equivalent cylinder is given by

$$r_3 = p\left(\frac{\sin\theta}{\pi}\right)^{1/2} \tag{1}$$

where θ is the layout angle (Fig. 1), and p is the layout pitch. Thus, the idealized problem under consideration is that of two coaxial cylinders subject to a heat source at tempertures T_t on the inside cylindrical surface, T_s on the outside exposed surface of the inner cylinder and right lateral surface of outer cylinder, and T_t on the left lateral surface of both cylinders (Fig. 2). The inner cylinder is assumed to be infinitely long. For the purpose of analysis, the inner cylinder is subdivided into two regions, indicated by 1 and 1′ in Fig. 2. Assuming regions 1 and 2 to be at temperature T_1 and T_2 (functions of x) respectively, the governing heat-conduction equations are:

$$k_1 \frac{d^2T_1}{dx^2} + \frac{[h_t S_1 (T_t - T_1) - q_{12} S_2]}{a_1} = 0 \tag{2}$$

where

S_1 = circumference of inner tube surface
S_2 = circumference of tube outer surface
q_{12} = heat flux from region 1 to region 2
k_1 = conductivity of region 1 (tube) material
a_1 = cross-sectional area of region 1

Note: $S_1 = 2\pi r_1; S_2 = 2\pi r_2$ (3a)

$$a_1 = \pi(r_2^2 - r_1^2) \tag{3b}$$

Similarly, the governing equation for region 2 is

$$k_2 \frac{d^2T_2}{dx^2} + \frac{q_{12} S_2}{a_2} = 0 \tag{4a}$$

where $a_2 = \pi(r_3^2 - r_2^2)$ (4b)

Let $q_{12} = h_{12}(T_1 - T_2)$ (5)

where h_{12} is the equivalent inter-region heat-transfer coefficient. An approximate expression for h_{12} is derived later

Nomenclature

$[A]$ = coefficient matrix (4 × 4)
a_1 = lateral cross-sectional area of region 1 (Fig. 2)
a_2 = lateral cross-sectional area of region 2 (Fig. 2)
b_i = constants of integration, $i = 1,2,3,4$ (equation 11)
c_i = derived coefficients, $i = 1,2,3,4$ (equation 10)
d_i = constants of integration, $i = 1,2,3,4$ (equation 13)
$\{f\}$ = right hand side vector (4 elements)
h_{12} = heat-transfer coefficient corresponding to q_{12} (equation 5)
h_c = heat-transfer coefficient on the tubesheet surface in the tubeside chamber
h_t = in-tube heat-transfer coefficient
h_s = shell-side heat-transfer coefficient on the tube-sheet surface
h_s' = shellside heat-transfer coefficient on tube outer surface
k_1 = thermal conductivity of tube material
k_2 = thermal conductivity of tubesheet material
m_1, m_2 = quantities defined in terms of c_i ($i = 1,2$) (equation 12)
l = tubesheet thickness
p = layout pitch (equation 1)
q_{12} = heat flux from region 1 to region 2
r_1 = tube hole radius
r_2 = tube outer radius
r_3 = equivalent ligament radius (Fig. 3)
r', r'' = functions of r_1, r_2, and r_3 (equation 22)
S_i = circumference corresponding to radius r_i ($i = 1, 2, 3$)
T_1 = average cross-sectional temperature of tube wall (function of x)
T_2 = average cross-sectional temperature of tube-sheet ligament (function of x)
T_1' = average tube wall cross-sectional temperature in region 1′
T_t = tubeside fluid temperature
T_s = shellside fluid temperature
α, β = parameters which define tube metal temperature in region 1′
θ = layout angle (Fig. 1)
ω_1, ω_2 = coefficients which relate d_i to b_i (equation 15)

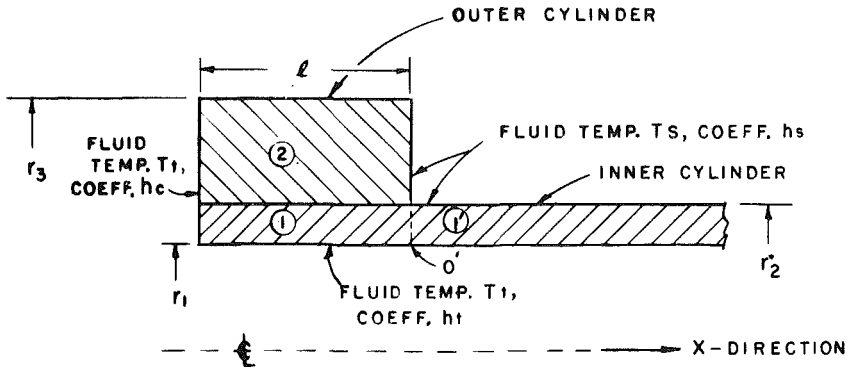

Fig. 2 Cross section of the idealized problem

Table 1 Comparison of analytical solution with finite element method (F.E.M.) results

Location x_1 (inch)	Mean tubewall temp., °F			Mean ligament temp. °F		
	Analytical solution	F.E.M. solution	Fractional difference $\times 100^a$	Analytical solution	F.E.M. solution	Fractional difference $\times 100^a$
0.0	211.4	210.4	0.50	215.4	213.8	0.80
0.12	215.6	214.4	0.60	218.2	216.8	0.70
0.24	219.7	218.7	0.50	222.1	221.2	0.45
0.37	224.6	224.2	0.20	227.0	226.7	0.15
0.49	230.6	230.9	−.15	233.1	233.6	−.25
0.61	237.7	239.1	−.70	240.4	241.9	−.75
0.73	246.1	248.6	−1.25	249.0	251.6	−1.3
0.85	256.4	260.4	−2.0	258.7	262.8	−2.05
0.98	273.6	268.3	2.65	269.3	268.5	0.40

[a]Fractional difference is defined as (analytical solution - F.E.M. solution) $(T_s - T_f)$

in this paper. Substituting for q_{12} in equations (2) and (4), and rearranging terms, yields

$$\left[k_1 \frac{d^2}{dx^2} - \frac{h_f S_1}{a_1} - \frac{h_{12} S_2}{a_1}\right] T_1 + \frac{h_{12} S_2}{a_1} T_2 + \frac{h_f S_1 T_f}{a_1} = 0 \tag{6}$$

$$\left[k_2 \frac{d^2}{dx^2} - \frac{h_{12} S_2}{a_2}\right] T_2 + \frac{h_{12} S_2}{a_2} T_1 = 0 \tag{7}$$

Hence

$$T_1 = \frac{a_2}{h_{12} S_2}\left(\frac{h_{12} S_2}{a_2} - k_2 \frac{d^2}{dx^2}\right) T_2 \tag{8}$$

Substituting for T_1 in equation (6) yields a fourth order ordinary differential equation in T_2

$$c_1 \frac{d^4 T_2}{dx^4} + c_2 \frac{d^2 T_2}{dx^2} + c_3 T_2 + c_4 = 0 \tag{9}$$

where

$$c_1 = \frac{-k_1 k_2 a_2}{h_{12} S_2} \tag{a}$$

$$c_2 = = k_1 + \frac{k_2 a_2}{h_{12} S_2}\left(\frac{h_f S_1}{a_1} + \frac{h_{12} S_2}{a_1}\right) \tag{b}$$

$$c_3 = \frac{-h_f S_1}{a_1} \tag{c}$$

$$c_4 = \frac{h_f S_1 T_t}{a_1} \tag{d}$$

(10)

The complete solution of equation (9) is given in terms of four undetermined constants of integration, b_i $(i = 1, 2, 3, 4)$,

$$T_2 = b_1 e^{m1x} + b_2 \bar{e}^{m1x} + b_3 e^{m2x} + b_4 \bar{e}^{m2x} - \frac{c_4}{c_3} \tag{11}$$

where

$$m_i = \left\{\frac{-c_2 + (-1)^{i+1}(c_2^2 - 4c_1 c_3)^{1/2}}{2c_1}\right\}^{1/2}; \quad i = 1,2 \tag{12}$$

By virtue of equation (8), we have:

$$T_1 = d_1 e^{m1x} + d_2 \bar{e}^{m1x} + d_3 e^{m2x} + \bar{d}_4^{m2x} - \frac{c_4}{c_3} \tag{13}$$

where

$$d_1 = \omega_1 b_1, \; d_2 = \omega_1 b_2, \; d_3 = \omega_2 b_3, \; d_4 = \omega_2 b_4 \tag{14}$$

and

$$\omega_i = \left[\frac{-k_2 a_2}{h_{12} s_2} m_i^2 + 1\right]; \quad i = 1,2 \tag{15}$$

The four constants of integration, b_i, are evaluated by utilizing the boundary conditions at $x = 0, l$. These are

region 2

$$\text{At } x = 0, \; k_2 \frac{dT_2}{dx} = -h_c (T_f - T_2)|x=0 \tag{a}$$

$$\text{At } x = l, \; k_2 \frac{dT_2}{dx} = -h_s (T_2 - T_s)|x=l \tag{b}$$

region 1 (16)

$$\text{At } x = 0, \; k_1 \frac{dT_1}{dx} = -h_c (T_f - T_1) \tag{c}$$

$$\text{At } x = l; \; \frac{dT_1}{dx} = \frac{dT_1'}{dx}|x=0 \text{ in region } 1' \tag{d}$$

To determine the temperature gradient in region 1′, we model it as a very long tube attached to a source at temperature T^* (say) subject to a heat transfer from a fluid at temperature T_f on its inside surface (coefficient h_f) and from a fluid at temperature T_s on its outside surface (coefficient

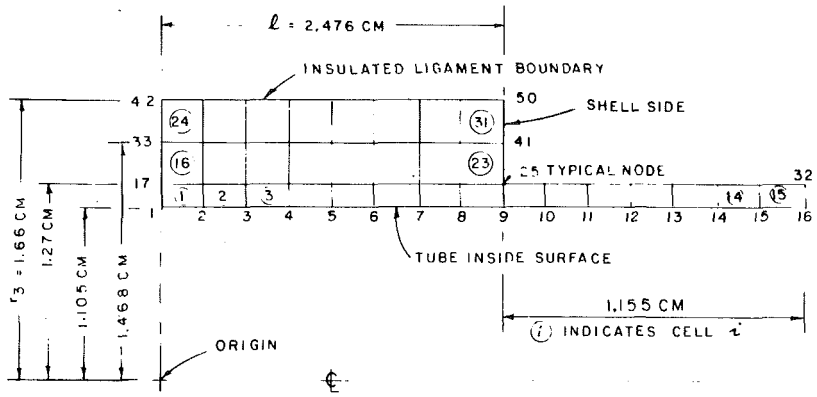

Fig. 3 Finite element grid for the sample problem

h_s'). The solution for the temperature field follows directly from the heat conduction equation

$$T_1' = c_1 e^{-\alpha x} + c_2 e^{\alpha x} + \frac{\beta^2}{\alpha^2} \tag{17}$$

where

$$\alpha^2 = \frac{h_s' S_2 + h_t S_1}{k_1 a_1} \quad \text{(a)} \tag{18}$$

$$\beta^2 = \frac{h_s' S_2 T_s + h_t S_1 T_t}{k_1 a_1} \quad \text{(b)}$$

region 1'

$x = 0$ occurs at point 0' in Fig. 2.

We require T_1' to be finite as x becomes large, which implies that $c_2 = 0$. Furthermore, at $x = 0$, $T_1' = T,^*$ which yields

$$c_1 = T^* - \frac{\beta^2}{\alpha^2}$$

Hence

$$T_1' = \left(T^* - \frac{\beta^2}{\alpha^2}\right) e^{-\alpha x} + \frac{\beta^2}{\alpha^2}$$

and

$$\frac{dT_1'}{dx} \Big| x=0 = -\alpha\left(T^* - \frac{\beta^2}{\alpha^2}\right) \tag{19}$$

equation (16*d*) can be combined with equation (19) to furnish an independent algebraic equation in the undertermined constants, b_i. Equations (16*a*)-(16*c*) provide the other three algebraic equations. The resulting system of four linear algebraic equations can be represented in subscript notation as

$$A_{ij}\, b_j = f_i;\ i = 1,4 \tag{20}$$

Summation on the repeated subscript ($j = 1, \ldots 4$) is implied in equation (20).

The coefficients of the [A] matrix and the $\{f\}$ vector are given in Appendix B.

Equation (20) is solved for the four b_i's using a standard Gaussian elimination subroutine. The expressions for T_1 and T_2 follow directly thereafter from equations (11) and (13), respectively. In this manner, the temperature field is completely described. At this point, the description for the entire solution scheme is complete, except for the intraregion coefficient h_{12}. We will now devise a simple expression for h_{12}, which is consistent with the level of accuracy of the total solution.

It is well known [4] that the general solution for temperature distribution in an axisymmetric long cylinder is a logarithmic function in the radius, r. Hence, it is reasonable to assume the temperature field to be logarithmic in radius r for the inner and outer cylinders. The unknown constants are evaluated using boundary and interface conditions; thus,

$$t_1(r) = m_1 \ln r + n_1;\ r_1 \le r \le r_2 \quad \text{(a)} \tag{21}$$

$$t_2(r) = m_2 \ln r + n_2;\ r_2 \le r \le r_3 \quad \text{(b)}$$

m_1, m_2, n_1, and n_2 are evaluated under the following conditions:

$$\text{At } r = r',\ t = T_1$$

$$r = r'';\ t = T_2$$

$$r = r_2,\ t \text{ is continuous}$$

$$r = r_2,\ k_1 \frac{dt}{dr} = k_2 \frac{dt}{dr}$$

Let r' and r'' be logarithmic mean radii in regions 1 and 2, respectively, i.e.,

$$r' = \frac{r_2 - r_1}{\ln \frac{r_2}{r_1}} \qquad r'' = \frac{r_3 - r_2}{\ln \frac{r_2}{r_1}} \tag{22}$$

The foregoing relationships determine the four undetermined coefficients in equation (21).

Recalling that the heat flux at $r = r_2 = h_{12}(T_1 - T_2)$, we obtain the final expression for h_{12}.

$$h_{12} = \frac{-k_1}{r_2 \ln\left[\left(\frac{r_2}{r''}\right)^{k_1/k_2} \left(\frac{r'}{r_2}\right)\right]} \tag{23}$$

Solution Procedure

A step-by-step description of the solution procedure is given in the following to facilitate direct use of the foregoing analysis without the encumbrance of assimilating the details.

(*a*) Input Data:

(*i*) Geometry Data—tubesheet thickness, l, tube inner and outer radii (r_1 and r_2).

Tube layout pitch, p, layout angle, θ. (Fig. 1)

(*ii*) Thermal property data[1]—tube material conductivity, k_1; tubesheet material conductivity k_2.

k_1; tubesheet material conductivity k_2.

(*iii*) Heat-transfer data—channel side heat-transfer coefficient, h_c; in-tube heat-transfer coefficient, h_t.

Shell side heat-transfer coefficients, h_s, on tubesheet surface; h_s' on tube surface.

[1] If a fouling factor on any of these surfaces is specified, then the corresponding coefficient should be accordingly adjusted to account for fouling.

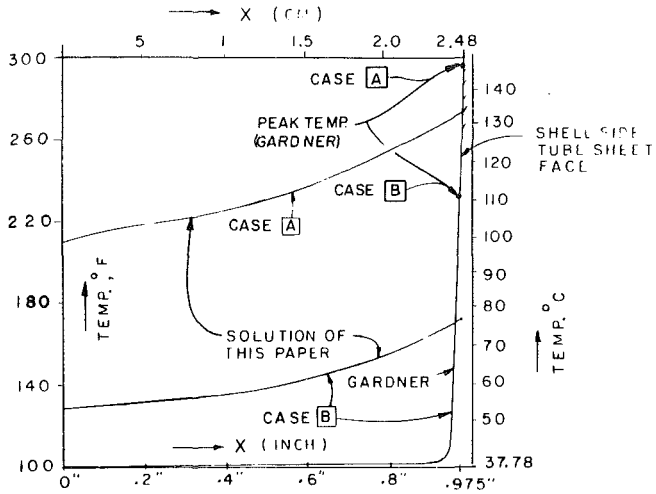

Fig. 4 Tubewall temperature distribution for the example problem

Tubeside fluid temperature, T_t; shell side fluid temperature, T_s.

(*b*) Compute r_3 from equation (1), and h_{12} from equation (22) and (23).

(*c*) Compute S_1, S_2 (equation (3), a_1 and a_2 (equation (3*b*) and (4*b*).

Compute c_1, c_2, c_3 and c_4 from equation (10); and m_i from equation (12); ω_i from equation (15), α and β from equation (18).

(*d*) Compute all 16 coefficients of A_{ij} and four terms of f_i (Appendix B).

(*e*) Solve 4 × 4 linear equation set (equation 20) to obtain values of b_1, b_2, b_3 and b_4.

(*f*) The temperature in the ligament is obtained as a function of x from equation (11). Determine d_i ($i=1, \ldots 4$) from equation (14)–(15). The tubewall temperature as a function of x is obtained from equation (13).

Numerical Example

A tubesheet in contact with tubeside fluid at 100°F (37.77°C), and shellside fluid at 300°F (148.89°C) is analyzed.

The basic data is given below:

(*a*) Geometry data—l = 0.975″ (2.48cm); r_1 = 0.435″ (1.105 cm) r_2 = 0.5″ (1.27cm) θ = 60 deg

(*b*) Thermal property data—Tube material conductivity k_1 = 9.3 Btu/Hr.-ft.-°F (16.1 J/msk) Tubesheet material conductivity, k_2 = 30 Btu/hr-ft-°F (51.92 J/msk)

(*c*) Heat-transfer data—channel side coefficient, h_c = 50 Btu/Sq. ft.-°F-Hr. (283.91 J/m^{2}sk) In-tube coefficient, h_t = 50 Btu/Hr.Sq.ft.-°F (283.91 J/m^{2}sk). Shell side coefficients, $h_s = h_s'$ = 1000 Btu/Hr.-Sq ft-°F (5678.3 J/m^{2}sk)

All surface fouling factors are assumed to be zero.

Table 1 shows the average tubewall temperature and average ligament temperature as a function of x. The same problem is solved using a finite element heat conduction-convection computer program. The finite element grid utilized is shown in Fig. 3. The computer program "FWILHEAT" is a general purpose heat-transfer computer program. The temperatures are computed at the node points. From the nodal temperatures, average cross-sectional temperature is computed for a series of values of x. Table 1 summarizes the F.E.M. results alongside the results obtained by the method proposed in this paper. The fractional difference is seen to be less than 3 percent at all locations.

The tubewall temperatures is plotted in Fig. 4 as a function of x_1. Figure 4 also shows the tubewall temperature variation when all coefficients are set equal ($h_t = h_s = h_c$ = 50 Btu/Hr.-Sq.ft.-°F) and the conductivities k_1 and k_2 are also set equal ($k_1 = k_2$ = 9.3 Btu/Hr.-ft.°F). This latter case is labelled as case B. For purposes of comparison, the solution produced by Gardner's formula is also plotted. The discrepancy between the two solutions is obvious. Whereas, Gardner's solutions shows a purely skin effect, the solution given herein indicates a nonlinear thermal gradient through the tubesheet. Therefore, a global thermal stress in the tubesheet will be developed, as opposed to only "peak stress" predicted by the Appendix A formula. Global thermal stresses produced are important in evaluating plastic breakdown of the structure under cyclic conditions. Peak stresses, on the other hand, are only significant in evaluating safety from multiple cycle fatigue. It is also to be noted from the foregoing examples that the skin effect predicted by the Appendix A formula grossly exaggerates the severity of the state of stress on the shellside face of the tubesheet.

Conclusion

A method to determine the temperature field in a typical ligament of a tubesheet has been developed. It is shown, via a numerical example, that significant thermal gradient throughout the body of the tubesheet may exist in ordinary heat exhangers. The thermal stresses so produced are "secondary stresses" rather than "peak stresses." Secondary stresses warrant closer attention in tubesheet design, especially in units subject to large operating cycles. Furthermore, an axial thermal gradient may produce "bowing" of the tubesheet. In designs where the tubesheet also serves as a flange, such a bowing may cause joint leakage. Less perceptibly, bowing of the tubesheet may cause the pass partition plates to lose contact on the tubesheet surface thereby inducing an interpass leakage. Equally important, tubesheet ligament temperature distribution under operating conditions has a great deal of impact on the sealworthiness of "rolled only" joint conditions.

The solution procedure given herein is intended to be used as a routine design tool. A programmable calculator should suffice to furnish a computing ability to handle the task.

Acknowledgment

We are thankful to Mr. Vytas Maciunas for his assistance in computer programing.

References

1 K. A. Gardener, Heat Exchanger Tubesheet Temperatures, The Refiner & Natural Gasoline Manufacturer, Mar. 1942.

2 Standard for Power Plant Heat Exchangers, 1st ed., Heat Exchange Institute, 1980, p. 10.

3 A. I. Soler, "Tube Stresses due to In-Plane Thermal Expansion of Tubesheets in Closely Spaced Double Tubesheets," *International Journal of Pressure Vessels and Piping*, Vol. 7, 1979, pp. 119–132.

4 M. Jakob, *Heat Transfer*, Vol. 1, Wiley & Sons, 1967, p. 133.

APPENDIX A

Gardner's Equations

Setting the origin of the axial coordinate, x, on the shellside face, the temperature of the tubesheet ligament, T, is given by equation (A1).

$$T = T_t + (T_s - T_t)\left[\frac{\text{Cosh}\,\frac{\Lambda x}{l} - \frac{\Lambda y_2}{y_1}\,\eta\,\text{Sinh}\,\frac{\Lambda x}{l}}{1 + \frac{\eta h_t}{h_s}}\right] \qquad \text{(A1)}$$

where x is directed towards the tubeside face, and

$$\Lambda = \left(\frac{y_1}{y_2}\frac{h_t l}{k}\right)^{1/2}$$

$$\eta = \frac{y_1}{y_2 \Lambda}\left[\frac{1 + \frac{y_1}{y_2 \Lambda}\tanh \Lambda}{\frac{y_1}{y_2 \Lambda} + \tanh \Lambda}\right] \tag{A2}$$

$$y_1 = 2\pi r_1 \tag{A3}$$

$$y_2 = (p^2 \operatorname{Sin} \theta - \pi r_1{}^2) \tag{A4}$$

In the foregoing, k is the thermal conductivity of tube and tubesheet material (assumed identical); h_t is tubeside heat-transfer coefficient; h_t and h_c are assumed to be equal; h_s and h_s (shellside coefficients) are also assumed to be equal.

APPENDIX B

Coefficients of [A] Matrix and $\{f\}$ Vector

$A_{11} = k_2 m_1 = h_c$; $A_{21} = (k_2 m_1 + h_s)\ e^{m_1 l}$

$A_{12} = k_2 m_1 - h_c$; $A_{22} = (-k_2 m_1 + h_s)\ e^{m_1 l}$

$A_{13} = k_2 m_2 - h_c$; $A_{23} = (k_2 m_2 + h_s)\ e^{m_2 l}$

$A_{14} = -k_2 m_2 - h_c$; $A_{24} = (-k_2 m_2 + h_s)\ e^{m_2 l}$

$f_1 = -h_c\left(T_t + \frac{c_4}{c_3}\right)$; $f_2 = h_s\left(\frac{c_4}{c_3} + T_s\right)$

$A_{31} = (k_1 m_1 - h_c)\ \omega_1$; $A_{41} = \omega_1 (m_1 + \alpha)\ e^{m_1 l}$

$A_{32} = -(k_1 m_1 + h_c)\ \omega_1$; $A_{42} = \omega_1 (-m_1 + \alpha)\ e^{m_1 l}$

$A_{33} = (k_1 m_2 - h_c)\ \omega_2$ $A_{43} = \omega_2 (m_2 + \alpha)\ e^{m_2 l}$

$A_{34} = -(k_1 m_2 + h_c)\omega_2$; $A_{44} = \omega_2 (-m_2 + \alpha)\ e^{m_2 l}$

$f_3 = -h_c\left(T_t + \frac{c_4}{c_3}\right)$; $f_4 = \frac{\beta^2}{\alpha} + \frac{\alpha c_4}{c_3}$

A Review of Fast Reactor Design Applications of Swelling and Irradiation Creep

J. P. Foster

A. Boltax

Westinghouse Electric Corporation,
Advanced Reactors Division,
Madison, Pa. 15663

The formulation of empirical swelling and irradiation creep equations from their respective independent data bases is reviewed. These equations are not inclusive of all reactor operating conditions, and the use and applicability of these equations is discussed. The application of swelling and irradiation creep equations in the design of core components is illustrated for both primary and secondary loading situations. The primary (external) loading illustrations include fuel pin performance and duct dilation. The agreement between measurements and predictions using swelling and irradiation creep equations indicates that these equations adequately describe available component performance data. Secondary (internal) loading is illustrated by duct bowing. The necessary component performance and model test data to determine the applicability of swelling and irradiation creep equations are currently in-progress in EBR-II or planned for early FFTF tests.

Introduction

A knowledge of inelastic deformation processes (swelling and irradiation creep) is necessary in order to understand and predict the behavior of fast reactor core components. High dose swelling [1] (1.4×10^{23} n/cm^2 [E>0.1 MeV]) and irradiation creep [2] (1.0×10^{23} n/cm^2 [E>0.1 MeV]) data have been reported for a variety of stainless steels. However, the data base is not sufficiently large for any one material to permit unambiguous determination of the functional dependencies of swelling and irradiation creep on dose, temperature, stress, and structure. The purpose of this paper is to present an assessment of swelling and irradiation creep relative to various design applications. First, the swelling and irradiation creep data base, the empirical design equations and their applicability will be reviewed, and then several design applications will be illustrated.

Swelling and Irradiation Creep

Swelling and irradiation creep, in the U.S. program, are measured independently using unpressurized and pressurized tubing samples, respectively. The equations derived from this data are assumed to apply to all cases of primary and secondary loading.

The stress-free swelling data consist of immersion density measurements. Figure 1 [1] shows that the data are nonlinearly dependent on fluence and temperature. The data can be described by an empirical equation of the form (see Fig. 2)

$$\frac{\Delta V}{V_0} = R\left[\phi t + \frac{1}{\alpha} ln\left(\frac{1+\exp(\alpha(\tau-\phi t))}{1+\exp(\alpha\tau)}\right)\right] \quad (1)$$

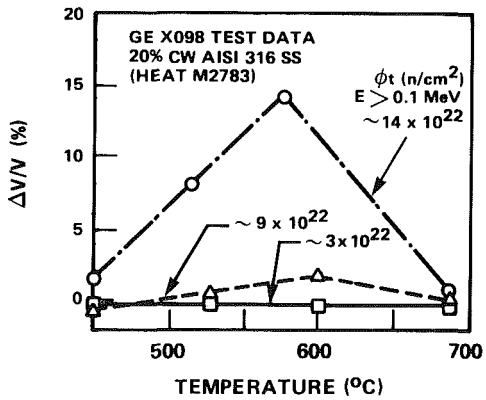

Fig. 1 Nonlinear temperature and fluence dependence of stress-free swelling

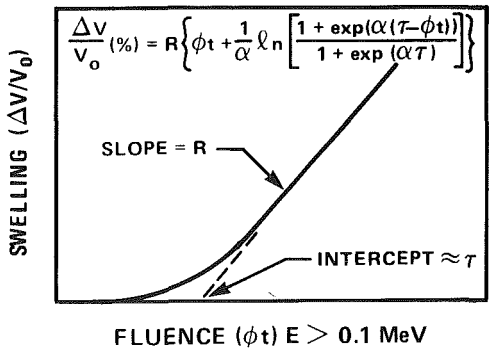

Fig. 2 Empirical swelling equation used for the design of 20 percent Cw AISI 316 SS core components

where $\Delta V/V_0$ is the volumetric swelling, R is the steady-state swelling rate, ϕt is the fast fluence, τ is the fluence intercept of

Contributed by the Nuclear Engineering Division and presented at the 1981 ASME Joint Conference of PVP Materials, Solar, and Nuclear Engineering Division, June 21-26, 1981 at Denver, Colorado. Manuscript received by the Nuclear Engineering Division March 22, 1982.

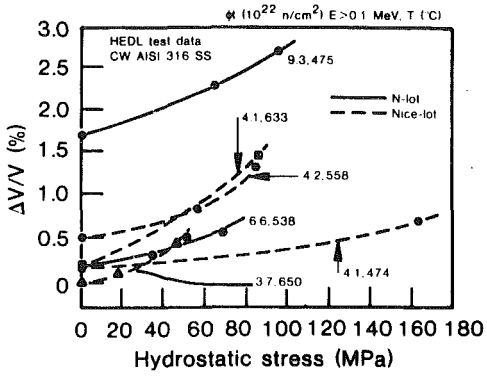

Fig. 3 Effect of hydrostatic stress on swelling

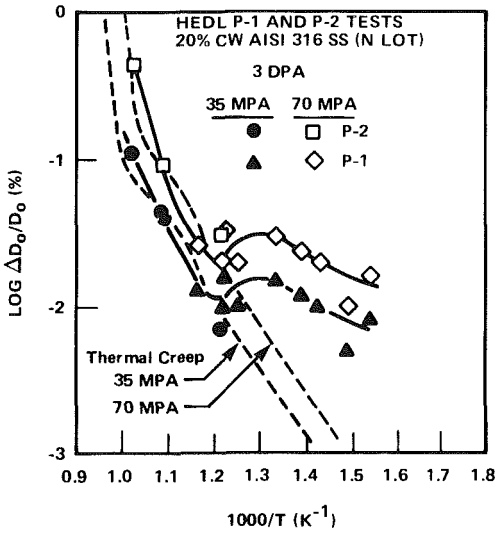

Fig. 4 Irradiation creep temperature dependence

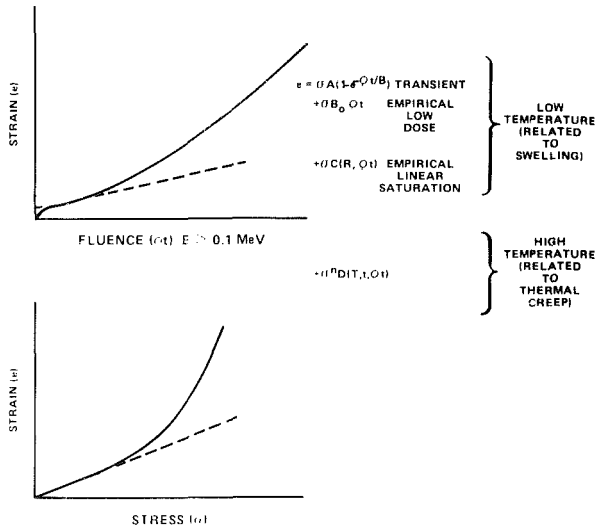

Fig. 5 Empirical irradiation creep equation used for the design of 20 percent CW AISI 316 SS core components

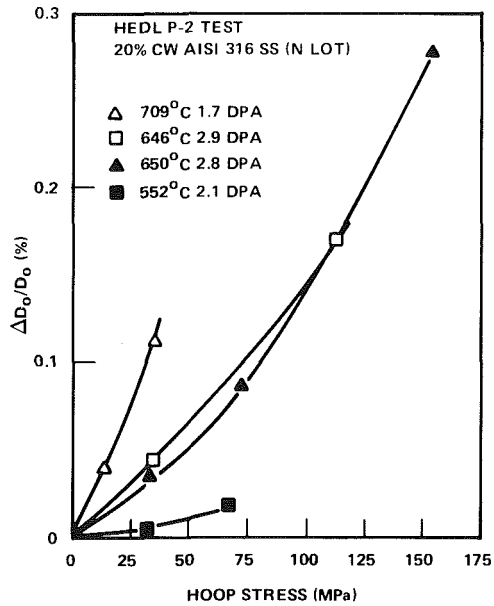

Fig. 6 Irradiation creep stress dependence

the steady-state swelling rate, and α is a curvature parameter which provides a smooth transition from zero to steady-state swelling. At low fluence levels, the initiation of swelling is masked by densification (due to the formation of higher density second phases), and this has led to different interpretations of the α and τ values [3]. At high fluence levels, the swelling rate appears to attain a constant value dependent on temperature. Confirmatory data are required to conclusively demonstrate this behavior.

Immersion density measurements on stressed (pressurized tube) samples show that stress enhances the stress-free swelling. Figure 3 [4] shows that this effect is small for temperatures below 600°C in comparison with stress-free swelling (and these conditions comprise most nominal reactor design and operating conditions). The primary effect of tensile stress appears to decrease the incubation fluence (τ) [4]. Compressive stress data are unavailable and are assumed to correspondingly increase the incubation fluence. Confirmatory data are necessary to verify the magnitude, the functional forms, and the behavior under compressive loading conditions.

Gas pressurized tubes (primary loading with a hoop-to-axial stress ratio of 2:1) provide the basic irradiation creep data source. The data include diameter and immersion density measurements which permit the separation of swelling and irradiation creep diametral strain contributions. Figure 4 [5] shows that irradiation creep exhibits a temperature peak at about 550°C which is similar to that exhibited by swelling (see Fig. 1). In fact, the CW AISI 316 SS temperature dependence of swelling and irradiation creep are similar until high temperatures ($T > 600$°C) when irradiation creep follows the temperature dependence of out-of-reactor thermal creep (see Fig. 4). The similarity of the swelling and irradiation creep temperature dependencies has been reported [2, 6] in other alloy systems, and appears to be a general result.

Irradiation creep, for empirical descriptive purposes, has been partitioned into low- and high-temperature components. The total irradiation creep strain is given by (see Fig. 5)

$$e = e_l + e_h \tag{2}$$

where the superscripts denote the low- and high-temperature components, respectively. The low temperature component is linear in stress [7] (see Fig. 6) and is given by

$$e_l = B(\phi t, T)\sigma\phi t$$

$$= \sigma[A(1 - \exp(-\phi t/B) + B_0\,\phi t + C(R, \phi t)] \tag{3}$$

where $B(\phi t, T)$ is a function of fluence and temperature and A, B, B_0, and C are material coefficients. The first term on the right-hand side of equation (3) is the initial transient strain component. The magnitude of A is relatively small for pressurized tube tests [2], but larger values have been reported for spring [8], bent beam [9] and uniaxial tension [10] tests.

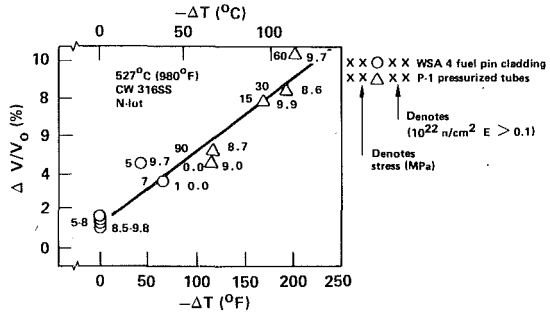

Fig. 7 Increase in swelling due to a temperature reduction during irradiation

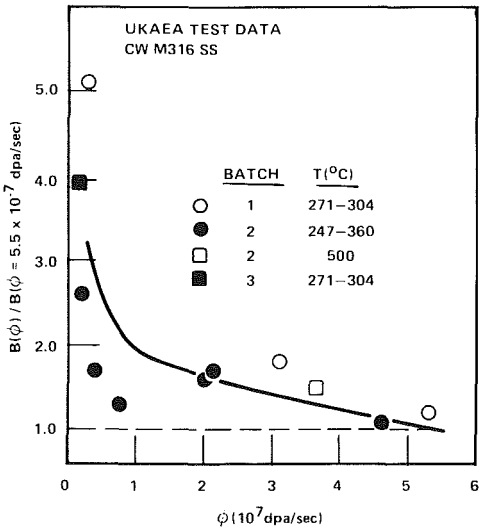

Fig. 8 Increase in the irradiation creep coefficient with decreasing neutron flux

The second term on the right-hand side of equation (3) represents steady-state creep and is empirically determined using low temperature data. The third term on the right-hand-side of equation (3) models the observed rapid acceleration of irradiation creep with fluence which occurs prior to swelling initiation [2]. This term exhibits the temperature dependence of the steady-state swwelling rate, R, and linear strain saturation is assumed at high fluences (this behavior is anticipated because of the apparent linear swelling saturation). High fluence data are necessary to confirm linear strain saturation. Figure 6 shows that for temperatures above 600°C that the irradiation creep strain exhibits an initial linear followed by a higher than linear stress dependence. This behavior is further evidence that high temperature in-reactor creep is related to out-of-reactor thermal creep. The high-temperature irradiation creep component is given by

$$e_h = D(T, t, \phi t)\,\sigma^n;\ n > 1$$

where $D(T, t, \phi t)$ is a function of temperature, time, and fluence.

The data base used to formulate the swelling and irradiation creep design equations presented above is not inclusive of all reactor design conditions. Many reactor design applications involve compressive stresses (e.g., beam bending), and in-reactor compression tests on CW AISI 316 SS have not been performed. Equation (2) is assumed to be applicable for compressive stresses, and this assumption is considered reasonable because of the good agreement between the steady-state irradiation creep components of primary loaded beams (in four-point bending) and pressurized tubes [2, 9].

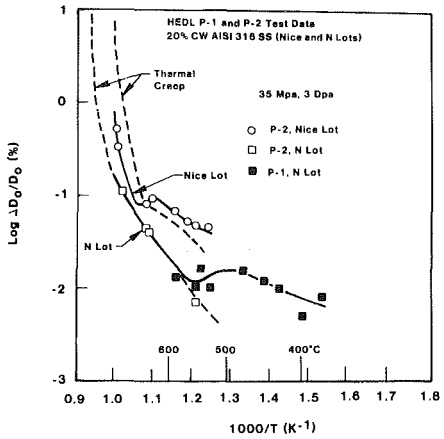

Fig. 9 Irradiation creep material dependence

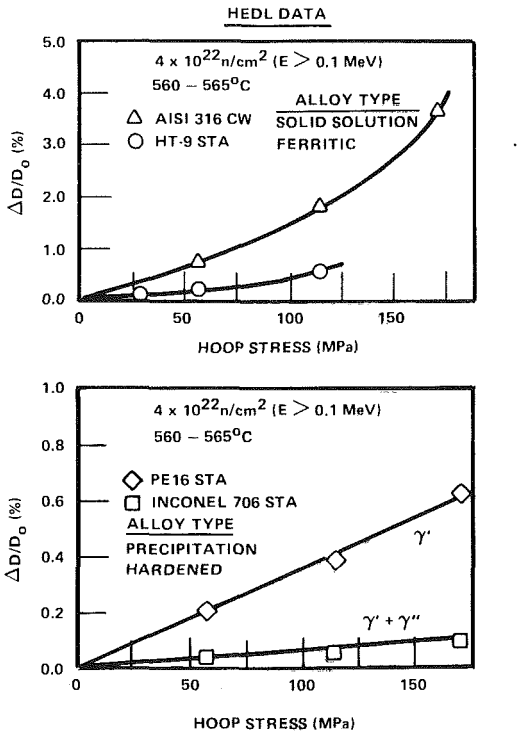

Fig. 10 Irradiation creep resistance of CW AISI 316 SS and advanced alloys

Swelling and irradiation creep have been reported to depend on the temperature history. Figure 7 shows that swelling increases are associated with temperature reductions during irradiation, [11, 12] whereas equation (1) would predict a decrease in swelling. Similar behavior has been reported for irradiation creep [12]. In the case of flux variations, Fig. 8 shows that the irradiation creep coefficient increases with decreasing neutron flux [13]. Similar results have been observed for swelling [14].

The coefficients of the empirical swelling and irradiation creep equations presented above are strongly dependent on alloy type. In fact, large variations in swelling [3] and irradiation creep [5] (see Fig. 9) have been reported for different heats of CW AISI 316 SS. Low fluence advanced alloy measurements show that large reductions in irradiation creep rates are possible [6, 7] (see Fig. 10).

Design Applications

Design applications of swelling and irradiation creep correlations include both primary and secondary type

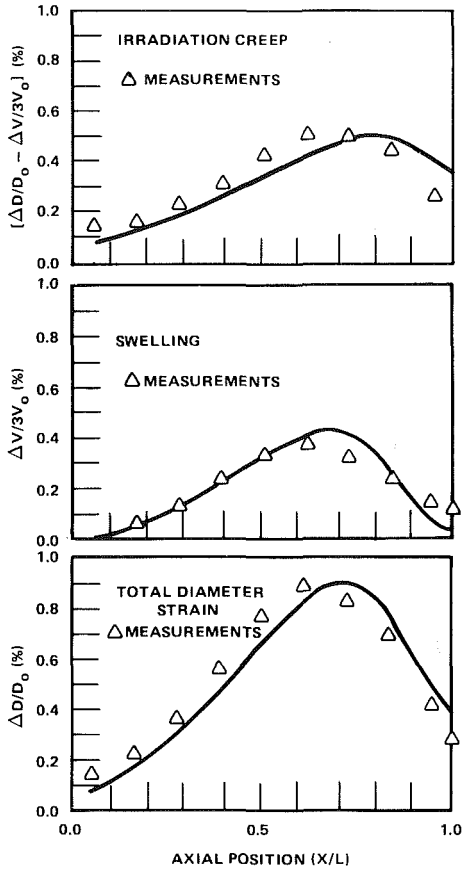

Fig. 11 Comparison of measured and calculated fuel pin strains

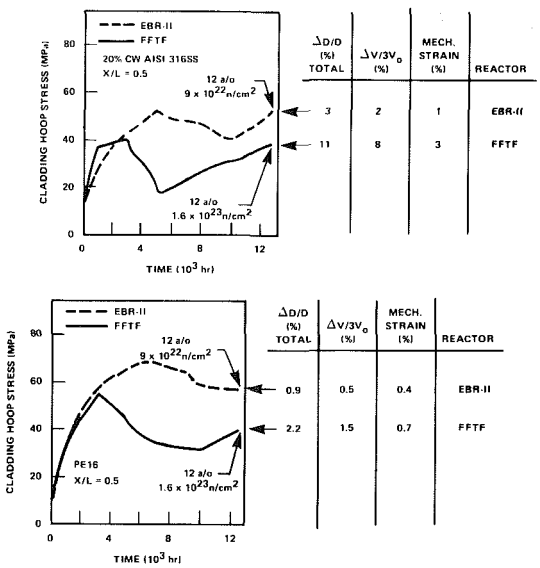

Fig. 12 Oxide fuel pin diameter growth

loading. In the case of primary loading (loading by an external stress) calculation of the deformation involves a simple superposition of swelling and irradiation creep. The plenum and fuel cladding regions of fuel pins represent typical examples of primary loading. In the plenum region the hoop-to-axial stress ratio is 2:1 because the external stress is primarily due to fission gas pressure. This method of loading is identical to the pressurized tube samples used to develop irradiation creep equations except that the stress increases with increasing burnup (or fluence) for fuel pins. Load history

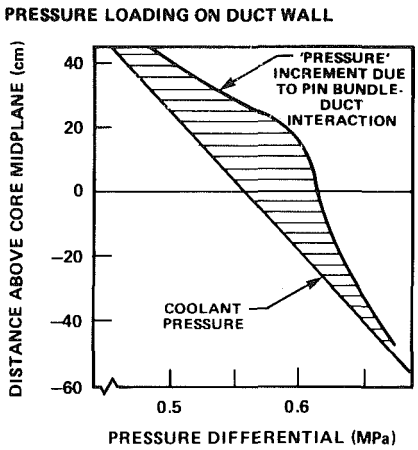

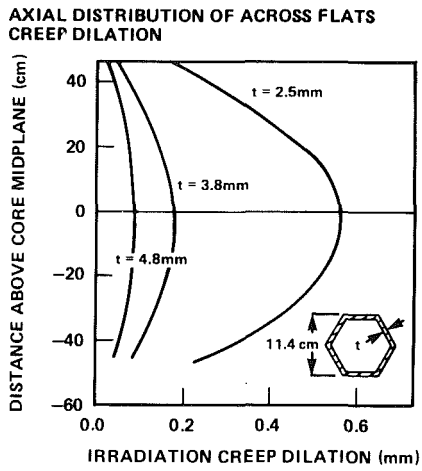

Fig. 13 Duct dilation

irradiation creep measurements show that the instantaneous in-reactor creep rate is not load history dependent [15]. In the fuel region, the stress ratio can vary from 2:1 to 1:1 depending on the extent of fuel-cladding mechanical interaction [16]. Further, the cladding stress history may be quite complex depending on fuel pin parameters and pin power history. Figure 11 illustrates that reasonable agreement is obtained using swelling and irradiation creep equation sets used to calculate the fuel pin diameter strain components [17].

The calculated impact of advanced alloys on fuel pin performance is illustrated in Fig. 12. The use of PE16 type cladding relative to CW AISI 316 SS increases the cladding stress level and decreases the diameter strain.

Duct dilation represents another application of primary loading. Figure 13 [18] shows that the load is due to the superposition of forced convection (coolant pressure) and fuel-pin, bundle-duct interaction. In this application, the total strain dilation is the superposition of swelling and irradiation creep strains, and the irradiation creep strain is primarily due to bending (note a small circumferencial stress is also developed). The dilation application is similar, but not identical to the four point bending tests discussed above. Figure 13 [18] also shows that the resulting dilation depends on the duct wall thickness.

Figure 14 shows a comparison of the measured mid-flat CW AISI 316 SS dilation with predictions for a EBR II duct with the flow orifice moved from the normal below-core position to the duct top [19]. The predicted dilation was calculated for both nominal and a ±10 percent environmental parameter uncertainty (temperature, pressure, and fluence). Figure 14 shows that the measurements are in reasonable agreement with the calculations. [19]

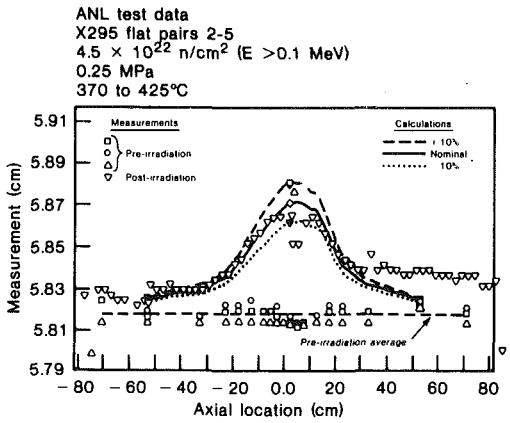

Fig. 14 Comparison of CW AISI 316 SS mid-flat dilation with predictions for nominal and ±10 percent uncertainty in temperature, pressure, and fluence

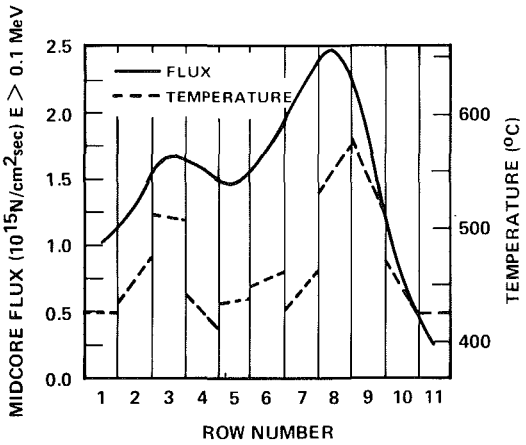

Fig. 15 Typical reactor core temperature and fluence gradients

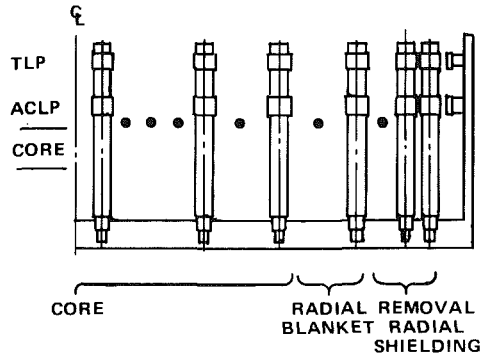

TLP DENOTES TOP LOAD PLANE
ACLP DENOTES ABOVE CORE LOAD PLANE

Fig. 16 Limited free bow core restraint concept

For the case of secondary loading, the stress is produced by differential swelling due to temperature and/or flux gradients. Two examples of secondary loading are the differential stress across the cladding wall thickness (radial variation of the hoop stress) and the bowing of ducts and fuel pins. The deformation due to secondary loading results from the opposition of swelling and irradiation creep, and will be illustrated for a typical FBR duct. Ducts bow initially on startup because of differential thermal expansion due to the reactor radial temperature gradient. After swelling is initiated the thermal bowing is enhanced by differential swelling. Differential swelling results because opposite duct flats with large temperature and/or gradients swell at significantly

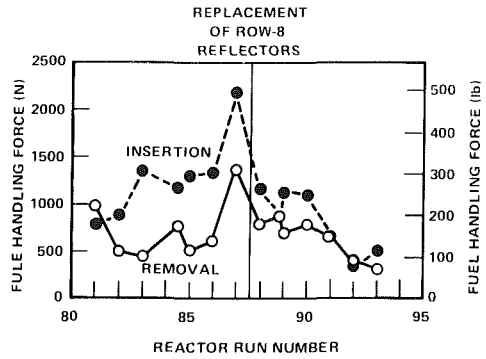

Fig. 17 Average fuel handling forces in row 8 of EBR-II as a function of run number

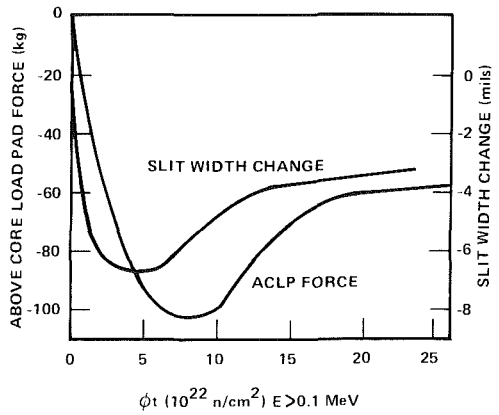

Fig. 18 Similarity between the ACLP force and the slit tube, slit width change as a function of fluence

different rates. The ducts freely bow until the load pad clearances are exceeded, and then contact at the load pads induces irradiation creep. Irradiation creep acts to limit the amount of bowing and thereby decreases the duct interaction loads whereas differential swelling acts to increase both the duct interaction loads and the bowing. The swelling and irradiation creep strain gradients occur in opposite directions, and, therefore swelling and irradiation creep are considered to act in opposition.

The largest bowing effects are exhibited in the reactor core region with the largest temperature and flux gradients. In Fig. 15, the largest gradients occur in rows 9 and 10 for the heterogeneous Clinch River Breeder Reactor core. This position is typically associated with outer core, radial blanket, and reflector positions (see Fig. 16).

The effects of differential swelling and irradiation creep on duct bowing have been observed in EBR-II. One measure of duct bowing (or interassembly contact forces) is the force required to either remove or insert a duct. Figure 17 [20] shows that the fuel handling forces in the EBR-II reflector region increased between runs 81 and 87, and these forces were decreased by inserting new (straight) replacements. The differential swelling induced bows of several assemblies were alleviated by continuing irradiation after a 180 deg rotation [20]. The rotation and continued irradiation allowed irradiation creep to "unbow" these ducts, as evidenced by a decrease in the fuel handling force [20]. Measurements are currently in progress to determine the bow magnitude as a function of fluence on selected ducts.

A slit-tube test has been fabricated and currently is under irradiation in EBR-II to provide swelling-irradiation creep opposition data for application to duct bowing. The predictions of duct bowing and interaction loads using swelling and irradiation creep equations developed from immersion density and pressurized tube data results in large

uncertainties in both duct position and the interassembly load magnitude [21]. The slit-tube test consists of small capsule tube samples with a radial temperature gradient due to an encapsulated fuel pin. The development of secondary stresses in this test occurs by the same mechanism as in duct bowing. Figure 18 shows the similarity in performance predictions between slit-tube test data and duct interassembly forces (above core load pad). The slit-tube test data are anticipated to qualify swelling and irradiation creep equations for secondary loading type applications.

Conclusions

Additional swelling and irradiation creep data are required for both primary and secondary loading applications in order to analyze and explain component performance and advance reactor design. In the case of primary loading, swelling and irradiation creep data are required at high fluence levels to confirm the anticipated rate saturation. Low swelling and irradiation creep advanced alloys appear attractive because large swelling and irradiation creep in stainless steels limit design. In the case of secondary loading, slit-tube data will be obtained to qualify swelling and irradiation creep design equations for secondary loading applications.

Acknowledgments

The authors wish to thank Mr. Thomas Moran at Argonne National Laboratory for permission to present Fig. 14. This work was performed under contract with the U.S. Department of Energy.

References

1 Kenfield, T. A., Appleby, W. K., Busboom, H. J., and Bell, W. L., "Swelling of Type-316 Stainless Steel at High Fluences in EBR-II," *Journal of Nuclear Materials*, Vol. 75, 1978, pp. 85–97.

2 Gilbert, E. R., and Chin, B. A., "In-Reactor Creep Measurements," *Nuclear Technology*, Vol. 52, 1981, pp. 273–283.

3 Bates, J. F., and Korenko, M. K., "Empirical Development of Irradiation-Induced Swelling Design Equations," *Nuclear Technology*, Vol. 48, 1980, pp. 303–314.

4 Garner, F. A., Gilbert, E. R., and Porter, D. L., "Stress-Enhanced Swelling of Metals During Irradiation," *ASTM 10th International Symposium on Effects of Radiation on Materials*, Paper No. HEDL-SA-2004, June 3–5, 1980, Savannah, Ga.

5 Gilbert, E. R., and Lovell, A. J., "Temperature Dependence of In-Reactor Creep of 20 percent Cold Worked Stainless Steel," in *Radiation Effects in Breeder Reactor Structural Materials*, edited by M. L. Bleiberg and J. W. Bennett, American Institute of Mining, Metallurgical and Petroleum Engineers, New York, 1977, pp. 269–276.

6 Paxton, M. M., Chin, B. A., and Gilbert, E. R., "The In-Reactor Creep of Selected Ferritic, Solid Solution Strengthened, and Precipitation Hardened Alloys," *Journal of Nuclear Materials*, Vol. 95, 1980, pp. 185–192.

7 Paxton, M. M., Chin, B. A., Gilbert, E. R., and Nygren, R. E., "Comparisons of the In-Reactor Creep of Selected Ferritic, Solid Solution Strengthened and Precipitation Hardened Alloys," *Journal of Nuclear Materials*, Vol. 80, 1980, pp. 144–151.

8 Mosedale, D., Lewthwaite, G. W., and Ramsey, I., "Further Creep Experiments in the Dounreay Fast Reactor," in *Irradiation Embittlement and Creep in Fuel Cladding and Core Components*, The British Nuclear Energy Society, London, 1972, pp. 233–238.

9 McSherry, A. J., Patel, M. R., Marshall, J., and Gilbert, E. R., "Irradiation Creep in Bending of CW AISI 316 at Low Fluence," *Transaction of the American Nuclear Society*, Vol. 28, 1978, p. 146.

10 Gilbert, E. R., Kaulitz, D. C., Holmes, J. J., and Claudson, T. T., "Fast Reactor Induced Creep in 20 Percent Cold Worked Type 316 Stainless Steel," in *Irradiation Embrittlement and Creep in Fuel Cladding and Core Components*, The British Nuclear Energy Society, London, 1972, pp. 239–252.

11 Foster, J. P., and Boltax, A., "Effects of Temperature Changes on the Swelling Behavior of 20 Percent Cold-Worked AISI Type 316 Stainless Steel," *Nuclear Technology*, Vol. 47, 1980, pp. 181–188.

12 Garner, F. A., Gilbert, E. R., Gelles, D. S., and Foster, J. P., "The Effect of Temperature Changes on Swelling and Creep of AISI 316," paper presented at the *ASTM 10th International Symposium on Effects of Radiation on Materials,* Savannah, Ga., June 3–5, 1980, Paper No. HEDL-SA-2003, Apr. 1980.

13 Lewthwaite, G. W., and Mosedale, D., "The Effects of Temperature and Dose-Rate Variations on the Creep of Austenitic Stainless Steels in the Dounreay Fast Reactor," *Journal of Nuclear Materials*, Vol. 90, 1980, pp. 205–215.

14 Porter, D. L., and Hudman, G. D., "The Apparent Dose Rate Dependence of Swelling in Austenitic Stainless Steels," *Transaction of the American Nuclear Society*, Vol. 34, 1980, pp. 230–231.

15 Wire, G. L., "Effects of Prior Stress History on Irradiation-Induced Creep," in *Irradiation Effects on the Microstructure and Properties of Metals*, American Society for Testing and Materials, Philadelphia, Pa., Paper No. ASTM STP-611, pp 1–31.

16 Foster, J. P., and Nayak, U. P., "Direct Observation of Fuel-Cladding Mechanical Interaction (FCMI) in Mixed-Oxide Fast Reactor Fuel Pins," Paper accepted for publication by *Journal of Nuclear Materials*, (Westinghouse Advanced Reactors Topical Report WARD-OX-94000-5, Sept. 1980).

17 Taylor, J. P., Gilbert, E. R., and Lovell, A. J., "A Comparison of Fuel Pin Deformations with Pressurized Tube Creep Tests," in *Effects of Radiation of Structural Materials*, American Society for Testing and Materials, Philadelphia, Pa., 1979, Paper No. ASTM STP-683, pp. 608–623.

18 Pennell, W. E., "Structural Materials Aspects of LMFBR Core Restraint System Design," *Nuclear Technology*, Vol. 16, 1972, p. 332.

19 Moran, T., Argonne National Laboratory, private communication, Feb. 1981.

20 Walters, L. C., and Walter, C. N., "Observations of Dilation and Bowing in Experimental Breeder Reactor II Ducts and Cladding," *Nuclear Technology*, Vol. 46, 1979, pp. 134–148.

21 Foster, J. P., Kalinowski, J. E., Swenson, D. V., and Boltax, A., "Technical Basis for Swelling-Irradiation Creep Opposition Testing," *Nuclear Engineering Design*, Vol. 61, 1980, pp. 399–413.

The Effect of Irradiation Induced Structural Material Deformations on Core Restraint Design

J. E. Kalinowski
Westinghouse Electric Corporation,
Advanced Reactors Division,
Madison, Pa. 15663

A summary of the major considerations in the design of LMFBR core restraint systems is presented. A discussion of these considerations is given using the design features and environment of the Clinch River Breeder Reactor Plant core restraint system design. A comparison of core restraint performance with an alternate concept is provided. Conclusions are drawn on the direction of current and future core restraint system designs.

Introduction

In the design of fast reactor cores, the positions of the core assemblies and their mechanical interactions with other core assemblies and the core supporting structures must be controlled in order to assure adequate core safety and performance. This gives rise to the definition and selection of mechanical features on the core assemblies and at core assembly – core support structure interfaces which permit core performance, safety, and interfacing component functions to be achieved. The composite of core assembly and core support structure mechanical features which affect core assembly positions and mechanical interactions defines the core restraint system. Core restraint system design is complicated by reactor core and external environmental considerations. These include: high temperatures and temperature gradients; high fast neutron flux and flux gradients; the potential for seismic events during the life of the plant. This presentation illustrates how these environmental considerations affect the design of the Clinch River Breeder Reactor Plant (CRBRP) core restraint system, with the focus of attention placed on the design problems introduced by the irradiation of core structural materials.

Reactor System Design Features

Figure 1 illustrates the relative location of the components which comprise the CRBRP reactor system. The reactor core assemblies are supported from below and laterally by the core support structure whose main structural components are the core support plate and the core barrel. Direct vertical support of the core assemblies is provided by the lower inlet modules and the bypass flow modules. The lower inlet modules are seated on inlet module liners which extend through penetrations in the core support plate. The bypass flow modules which support the low flow core assemblies are supported by the core support plate between the lower inlet modules and the core barrel. Peripheral support of the core assemblies is provided at two elevations: the above core load plane (ACLP) and the top load plane (TLP). At these elevations the core former structure, which limits the outward radial motion of the core assemblies, is supported by the core barrel.

The upper internals structure is located above the core assemblies and promotes mixing for the flows of differing temperatures which exit the core assemblies. Instrumentation posts which are located directly above the core assembly

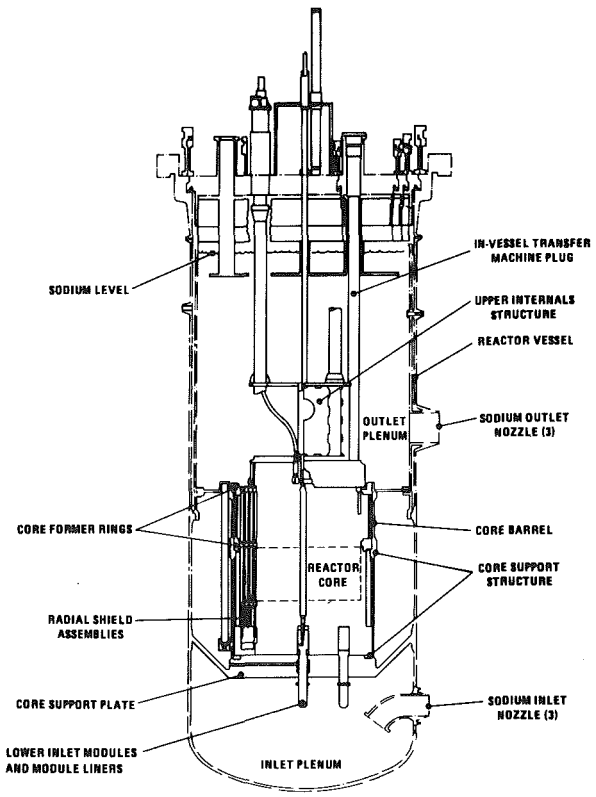

Fig. 1 Schematic of reactor

Contributed by the Nuclear Engineering Division for publication in the JOURNAL OF ENGINEERING FOR POWER. Manuscript received by the Nuclear Engineering Division March 22, 1982.

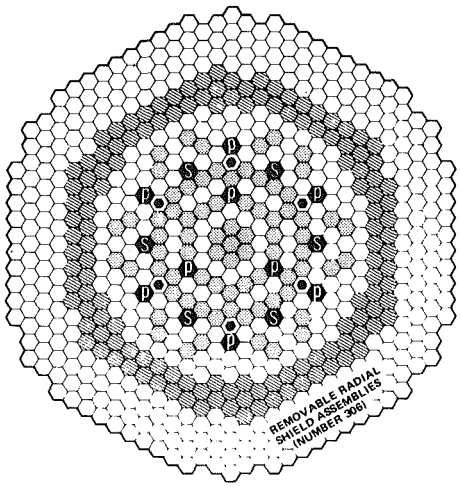

SYMBOL	COMPONENT NAME	NUMBER
	FUEL ASSEMBLY	156
	INNER BLANKET ASSEMBLY	76
	RADIAL BLANKET ASSEMBLY	132
	ALTERNATE FUEL/BLANKET ASSEMBLY	6
P	PRIMARY CONTROL ASSEMBLY	9
S	SECONDARY CONTROL ASSEMBLY	6

Fig. 2 Reactor core map

outlet nozzles provide support for core outlet thermocouples and provide backup holddown of the core assemblies.

During refueling, the upper internals are lifted 229 mm and rotated out of their operational position over the core. This allows the in-vessel transfer machine (IVTM) access to the core assemblies for replacement or relocation within the core. Assembly replacement is accomplished by the straight pull or push of assemblies out of or into their in-core positions.

The CRBRP core map is illustrated in Fig. 2. Fuel and inner blanket assemblies are interspersed in a hetrogeneous configuration which provides improved breeding ratio and a reduced sodium void effect. The fuel region is surrounded by the two rows of radial blanket assemblies and four rows of removable shielding assemblies. The main control and safety function is provided by nine primary control assemblies. The six secondary control assemblies provide alternate shutdown capability in the extremely unlikely event that the primary control system fails to shutdown the reactor.

The fuel assembly schematic is illustrated in Fig. 3(*a*). The fuel assembly provides support and a coolant flow path for the power generating fuel pins. The main fuel assembly structural members are the inlet nozzle, shield block, duct, and handling socket. Raised circumferential load pads are located at the above core and outlet nozzle elevations corresponding to the ACLP and TLP elevations of the core former structure. The external features of the blanket and control assemblies are similar to the fuel assemblies. The removable radial shielding assemblies differ in that the inlet nozzle extends to the base of the duct in the absence of a shield block region.

Core Environment

Liquid metal fast breeder reactor (LMFBR) core temperature environments are characterizezd by a large temperature rise from core inlet to core outlet. In CRBRP at full power conditions sodium enters the core at a temperature of 388°C and leaves the reactor vessel at 535°C. Typical core assembly duct axial and radial temperature profiles are shown in Fig. 3. The axial temperature change is shown in Fig. 3(*a*). The increase in temperature and temperature gradient occurs in the fuel region. Radially, the duct temperatures vary with assembly type. In a fresh core, the fuel assemblies run "hot" while the blanket assemblies run "cold." As fissionable plutonium builds up in the blanket assemblies, power generation and temperatures increase. At end-of-life conditions the blanket assemblies run as "hot" as the fuel assemblies. Assembly to assembly temperature gradients are due to interassembly heat transfer. At start-of-life, the steepest interassembly temperature gradients occur at the fuel-radial blanket interface. At end-of-life, the steepest temperature gradients occur in ducts adjacent to the control assemblies.

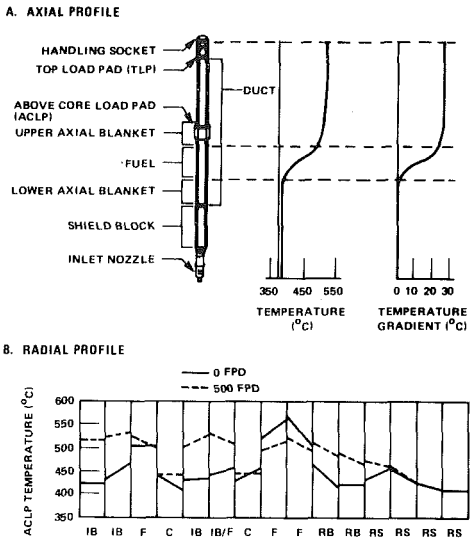

Fig. 3 Typical duct temperature profiles

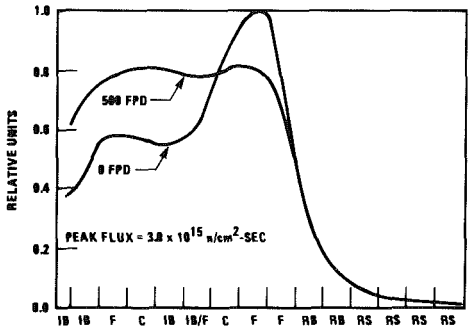

Fig. 4 Radial fast flux distributions at core midplane

The radial distribution of the fast flux is shown in Fig. 4 at the core mid-plane elevation. Because of the heterogenous configuration of the core, the neutron flux peaks in the outer fuel rows and is depressed in the center of the core. As plutonium builds up in the blanket regions, the flux shifts toward the core center and the peaking in the outer fuel region diminishes.

Nomenclature

B = blanket assembly
C = control assembly
F = fuel assembly
IB = inner blanket assembly
RB = radial blanket assembly
RRS = removable radial shield assembly

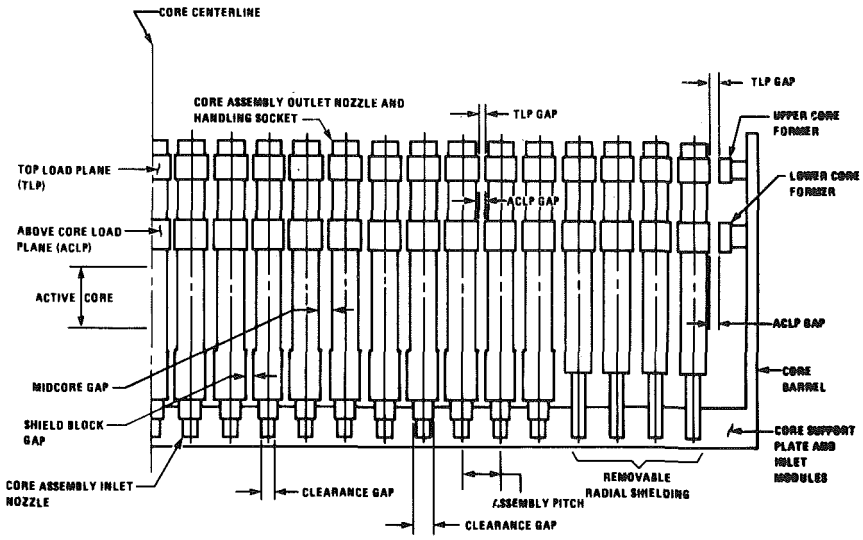

Fig. 5 CRBRP core restraint system mechanical interfaces

The reactor plant is designed to accommodate the effects of seismic events during the plant lifetime. Seismic motion is applied to the core at the inlet nozzle and load plane elevations by the core support structure. The magnitude of design seismic motions is sufficient to displace the entire core against the core support structure. The inertia loads generated within the core assemblies are reacted at the core formers and the inlet nozzle receptacles. At the ACLP and TLP, inertia loads are transmitted from assembly to assembly prior to being reacted aganist the core former rings. Consequently, duct seismic loads are maximum in those assemblies adjacent to the core formers.

Core Restraint Design Considerations

The mechanical features of the CRBRP core restraint system and significant interface parameters are shown in Fig. 5. The reactor assemblies are laterally supported at three elevations: inlet nozzle, ACLP and the TLP. The core assemblies are provided with circumferential load pads at the ACLP and TLP. Small interassembly gaps at the ACLP and TLP allow accommodation of limited assembly bowing motions and differential thermal expansion between the core and core support structures. Small clearance gaps at the inlet nozzle permit a limited degree of pivoting motion at the inlet nozzle. Gaps at the shield block level and between the ducts are sized to limit the degree of interassembly contact at non-load plane elevations. Peripheral restraint of the core array is provided by core formers at the ACLP and TLP. The location and sizing of the core restraint system mechanical features are determined by the following core restraint system requirements.

Reactivity. In a fast reactor core small motions of the fuel region give rise to changes in the core reactivity. Positive reactivity is added when the core assemblies displace radially inward. Core assembly motions are most likely during reactor startup when power is being increased at constant reactor flow. Core assembly temperatures and temperature gradients buildup from an isothermal state to the level shown in Fig. 3. Transverse duct temperature gradients cause the assemblies to bow and the resultant motion changes the core reactivity level.

The ACLP gaps (interassembly and peripheral) are chosen to limit assembly motions which would add positive reactivity. Likewise, locating the central of the three load planes above the core promotes negative assembly motion reactivity feedback when the reactor is at power. This occurs because at-

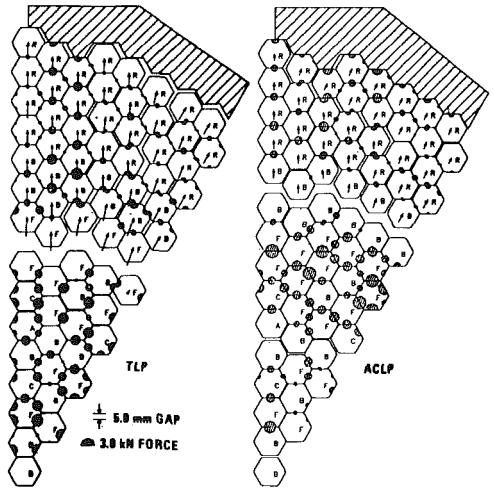

Fig. 6 Load pad gaps and forces at 0 FPD

power the ACLP gaps in the fuel region assemblies are closed and the active core zone of the high worth outer fuel region assemblies are forced to bow outward for an increase in power.

In addition to limiting assembly motions due to thermal bowing, the lower core former ring serves as a safeguard against any spurious reactivity insertions due to assembly sticking and slipping at the two load planes. Furthermore, the load pads are coated with a hard-surface, low-friction chromium-carbide coating to minimize the occurance of a stick-slip phenomenon.

Interassembly Loads. Contact loads between adjacent assemblies arise due to the three environmental sources discussed in the introduction: thermal, neutron flux and seismic. Figure 6 illustrates the interassembly contact and load pattern established at the ACLP and TLP due to the start-of-life duct temperatures of Fig. 3. Utilizing the symmetry in the core arrangement and environment, core restraint evaluations are performed for a 30° deg sector using the NUBOW-3D computer program [1] and employing the analysis techniques discussed in reference [2]. Figure 6 shows that the temperature gradients at the fuel radial blanket interface play a dominant role in establishing interassembly load and contact patterns. Assemblies inboard of the fuel-radial blanket interface are compacted inward toward the

reactor centerline. The radial blanket and radial shielding assemblies are displaced outward against the lower and upper core former rings. Interassembly contact loads tend to concentrate in a ring of assemblies extending from the sixth to the tenth radial rows at the ACLP. Outboard of row 10, the interassembly loads are generally radial in nature out to the core former rings. With irradiation (the action of neutron flux over time), the interassembly contact pattern remains generally the same, however, the level of the local pattern is predicted to decrease or increase depending on the dominant irradiation deformation mechanism (creep or swelling). This is discussed further below. The ACLP load pad is the critical elevation for design against core restraint loads. Circumferential load pads are sized to provide adequate structural margin against a combination of normal and design transient core restraint loads. secondary loading due to design transient temperatures, and seismic interassembly loads.

When the reactor is brought off-power for refueling, the core assemblies retain a residual bowing shape due to on-power irradiation structural effects. Restraint provided by the core former rings results in off-power interassembly load plane contact loads. The magnitude of the contact loads must be assessed in defining the push/pull capability of the core assembly refueling equipment. Likewise, interassembly loads must be limited to prevent galling at the load plane surfaces. Refueling loads are limited by making the interassembly load plane gaps sufficiently large to avoid exceeding conflicting requirements: reactivity at the ACLP and alignment at the TLP.

Alignment. Misalignment of the assembly top ends from their theoretical pitch positions is limited in order to permit the refueling equipment to locate the assemblies at refueling and to limit side loads on the control assembly driveline which could adversly affect reactor shutdown. The main parameters which determine that alignment considerations are satisfied are the interassembly and peripheral gaps at the TLP.

Irradiation Effects. Stainless steel is the typical structural material for fast reactor core assemblies. In CRBRP, the core assembly ducts will be fabricated from 20 percent cold worked AISI 316 stainless steel. Extensive small sample and full-size component tests have shown that this material exhibits swelling and creep during irradiation. Swelling of 20 percent CW 316 stainless steel initiates following an incubation period in the core flux environment. For duct temperatures in the range of Fig. 3, the swelling rate increases with temperature. The overall swelling at any location is nearly proportional to the product of the swelling rate and the difference between the actual fast fluence (flux X time) and the incubation fluence. The irradiation creep strain at a given location depends on the local temperature, neutron flux, and stress state. A more detailed discussion of irradiation creep and swelling on core assembly ducts is presented in reference [3]. THe overall effects of these phenomena on core restraint performance are examined below.

Figure 7 illustrates the primary deformation effects of swelling and creep on a core assembly. Duct dilation refers to the duct bulging at the active core elevation under the combined action of creep and swelling. Primary loading of the duct due to the coolant pressure as well as high temperature and flux are the active factors for this effect. Duct bowing occurs as a result of the differential swelling gradient across the duct. This gradient is especially pronounced in assemblies at the fuel-radial blanket interface where temperature and flux gradients are steepest. Axial growth of the duct is primarily due to the axial swelling strains. In the CRBRP core, limited amounts of each deformation type can be accommodated during core assembly lifetimes without impeding the functions of the core restraint and interfacing systems. This is accomplished by providing adequate gaps between

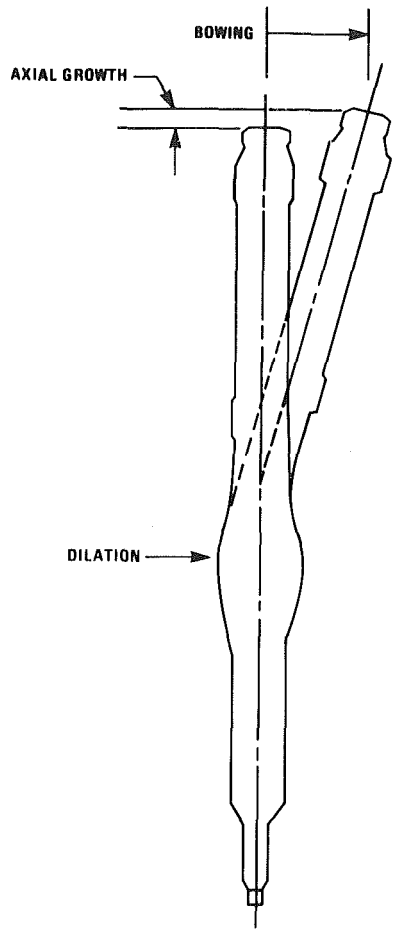

Fig. 7 Irradiation induced assembly deformations

ducts and above the assemblies to accommodate duct bowing dilation and axial growth. The provision of three load planes at the elevations selected (inlet nozzle, ACLP and TLP) permits irradiation creep to be utilized to offset the effects of swelling induced duct bowing. The ACLP is located at an elevation sufficiently above the active core where dilation effects are negligible.

Core Wide Irradiation Effects

Figure 8 illustrates the change in the on-power assembly bowing pattern during equilibrium fuel assembly life along a radial spoke extending from the core centerline to the core former structure. The dotted lines are shown for selected assemblies to illustrate the pattern of irradiation induced bowing deformation. Irradiation induced bowing is worst in the outer fuel region as a result of peak temperature and flux levels and gradients.

Off-power loading effects due to irradiation induced bowing at the core formers are illustrated in Fig. 9. The initial load buildup is due to the relaxation of thermal bowing stresses by irradiation creep which produces the initial bowing distortion in the core assemblies. Beyond 125 days, the ACLP core former loads diminish and the TLP core former loads increase slightly as swelling bows the assemblies in a direction opposite to that caused by irradiation creep. Another illustration of core wide effects is shown in Fig. 10, where the assembly motion reactivity at power changes with fuel assembly life. The pattern is primarily associated with the motion of the high worth outer fuel assemblies. The initial reactivity drop is due to irradiation creep relaxation of the themally induced bow. However, as the ducts begin to swell

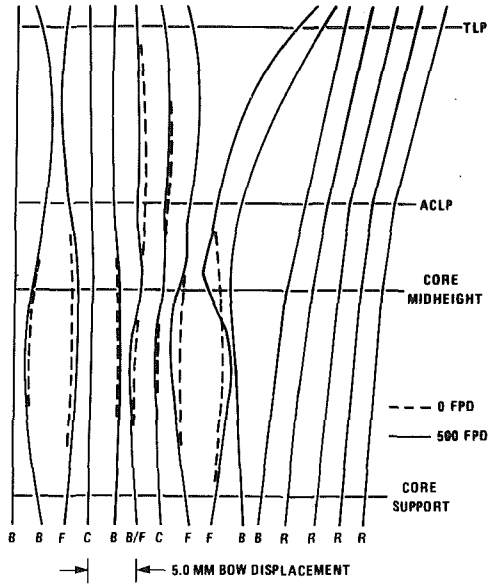

Fig.8 On-power restrained bow shape changes during fuel assembly life

and bow inward, reactivity is added to the core. At approximately 300 days, mid-core duct contact due to dilation initiates between the outer fuel assemblies impeding their further inward displacement and assembly motion reactivity change.

From the core wide standpoint, studies to date show that irradiation induced effects can be accommodated. Reactivity effects are minor. Loads are self limiting as creep and swelling act to offset each other. Duct dilation effects are limited as neighboring ducts come into contact cancelling the primary load driven creep bulge. Work is continuing on the refueling and seismic consequences of duct to duct contact patterns which may develop.

The CRBRP core restraint system is derived from the FFTF core restraint design. With operation of the FFTF reactor now in progress operational data in duct performance, core reactivity, and refueling loads will be used to confirm the conclusions drawn on the adequacy of the CRBRP core restraint system design.

Alternate Core Restraint Concepts

In smaller-sized fast reactor cores there is a greater sensitivity of core reactivity to assembly displacements. Consequently, earlier fast reactor designs emphasized control of assembly motion. In EBR-II and Phenix [4, 5] this was achieved by providing a greater degree of assembly restraint at the inlet nozzle but permitting more freedom to bow at the assembly top end. This concept is sometimes referred to as the "free standing" or "free bow" concept. In this concept the reactor assembly inlet nozzle consists of a lengthy stalk which is closely supported by a core support grid near the bottom and top of the stalk. Because of this, the lower end of the assembly is not free to pivot as in the limited free bow concept. In EBR-II, spacer buttons are located at the mid-core elevation, while in Phenix the buttons are located immediately above the core. During a rise to power, interassembly contact at the spacer button plane is established and the assemblies are displaced outward adding negative reactivity. Top loads pads are not provided in this concept and theoretically no contact at the top end occurs between assemblies due to thermal bowing. In practice, however, irradiation induced bowing will cause the top ends of the assemblies to contact at specific locations. Peripheral support of the core is provided by several rows of reflector or shielding assemblies whose inlet

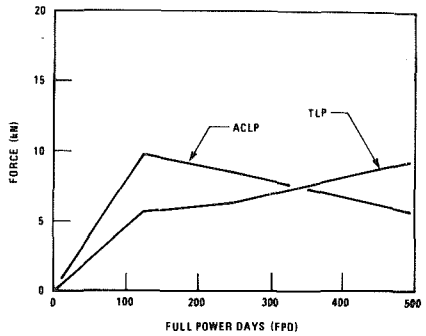

Fig. 9 Core former off-power loads

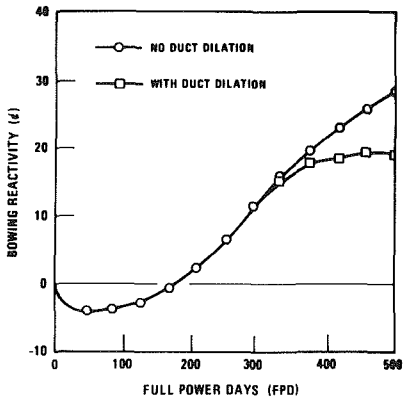

Fig. 10 On-power bowing reactivity

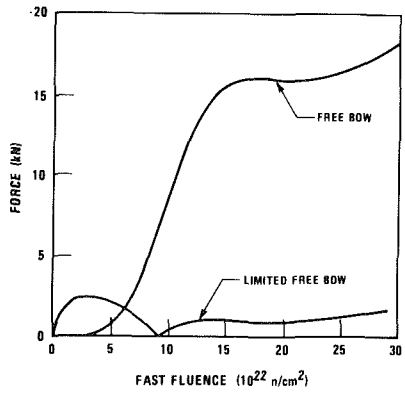

Fig. 11 Total lateral duct force at refueling on an outer fuel assembly

nozzles are restrained similar to the fuel assemblies. On the periphery at the elevation of the assembly top ends, a ring mounted to the core barrel acts as a stop for core seismic motions.

A disadvantage of the free standing concept is that the locations of the assembly support points do not permit irradiation creep to be utilized to offset selling induced bowing. Consequently, this concept is bowing limited especially at the outer fuel boundary where the the temperature and flux gradients are the steepest. This can be illustrated using the results of a single assembly analysis of the free bow and limited free bow concepts at a fuel radial blanket interface. Figure 11 [6] shows the sum of the lateral forces acting on the assemblies at refueling conditions as a function of time in life. Initially, loads build up due to irradiation creep in the limited free bow concept. However, when swelling initiates, the refueling load reduces as swelling causes the irradiation bow to reverse. The load increases again but stabilizes at a relatively low level when creep balance of swelling is achieved. At the end-of-life, the assembly would be

relatively straight with little bowing distortion. In the free bow concept the irradiation creep effect is small. Therefore, the refueling load induced by swelling builds up to a high level before sufficient creep occurs to offset swelling. Similarly, the high fluence bowing distortion of the free bow restraint assembly is excessive because of the small creep opposition of swelling. This analysis of the free bow concept has been verified by recent operations in EBR-II where assembly bowing distortion and refueling difficulties have been experienced in the reflector region [7]. Duct bowing will be less of a problem if duct alloys are developed in which swelling is negligible. However, for 20 percent CW 316 stainless steel duct bowing is a life limiting factor for the free bow concept.

The allowance of generous interassembly gaps at the top end also makes the assurance of control rod insertion for highly unlikely design transients more difficult. During a seismic event, misalignment of the core with the upper internals can give rise to high frictional forces on the control rod driveline retarding control rod insertion. Limitations of top end interassembly gaps reduces misalignment and assures that control rod performance will not be degraded for this event.

Conclusion

To achieve current goal core assembly lifetimes, the duct structural material must be irradiated to a level where irradiation induced distortion effects are significant. This is taken into account in the design of the core restraint system together with the need to meet system functional requirements. Given present day duct reference materials which exhibit both creep and swelling during irradiation, the limited free bow concept as utilized in CRBRP and FFTF permits both system and duct lifetime objectives to be met. As reactor core sizes are increased to commercial levels, the relative importance of the functional requirements will change but all will still need to be considered. Advanced materials with reduced creep and swelling will be used in future designs. However, operating the material to its limits will still require that irradiation induced effects be considered. Consequently, given that the safety and operational objectives of current reactor designs will be retained in future designs, it is expected that future core restraint designs will incorporate the major elements of the limited free bow design as employed in the CRBRP.

Acknowledgment

This work was performed under U.S. DOE Contract EYO76-C-15-2395.

References

1 McLennan, G. A., "NUBOW-3D (Inelastic): A FORTRAN Program for the Static Three-Dimensional Structural Analysis of Bowed Reactor Cores Including the Effects of Irradiation Creep and Swelling," ANL-CT-78-19, Mar. 1978.

2 Kalinowski, J. E., and Swenson, D. V., "Nonlinear Analysis of the Core Restraint System" in *Clinch River Breeder Reactor Plant Technical Review, Fall 1976*, CRBRP-PMC-76-06, pp. 7-30.

3 Foster, J. P., and Boltax, A., "A Review of Fast Reactor Design Applications of Swelling and Irradiation Creep." JOURNAL OF ENGINEERING FOR POWER, accepted for publication.

4 Bump, T. R., et al, "Analyses of EBR-II Core-Component Deformations," ANL-7986, Jan. 1973.

5 "Phenix, Prototype Fast-Neutron Nuclear Power Station," AEC-tr-7130, Feb. 1970.

6 Kalinowski, J. E., and Baumgartner, A. J., "Benchmark Problem Set Evaluation of the Revision 5 Creep and the Revision 8 Swelling Correlations for 20 percent CW 316SS" in *Core Restraint Development Quarterly Progress Report for the Period Ending May 31, 1979*," WARD-CR-94000-3, Oct. 1979, pp. 23-66.

7 Shields, J. A., "Bow in Experimental Breeder Reactor II Reflector Assemblies," *Nuclear Technology*, Vol. 52, Feb. 1981, pp. 214-227.

D. R. Goff
Project Engineer,
ITT, Electro-Optical Products Division,
Roanoke, Va.

J. F. Gardner[1]
Xomox Corporation,
Cincinnati, Ohio,
Assoc. Mem . ASME

D. A. Maxfield
Member Technical Staff,
TRW Energy Engineering Division,
Morgantown, W. V. 26505.
Assoc. Mem. ASME

Lockhopper Valve Testing and Development

As advanced processes are used commercially for converting coal to other forms of energy, reliable valves will be required for operating in lockhopper service at pressures to 1200 psig (8.3 MPa) and temperatures to 1600°F (870°C). The Department of Energy's Lockhopper Valve Testing and Development Project, being conducted at the Morgantown Energy Technology Center (METC), is cooperating with lockhopper valve manufacturers and users to improve the state-of-the-art capability of commercially available lockhopper valves. The test facilities and valve testing program currently being made available to valve manufacturers at METC are described. The performance of test valves currently in the program is summarized and design considerations for solids lockhopper service are discussed.

Introduction

Coal will play an important role in meeting the future energy needs of many nations as costs and availability make oil use less attractive. Processes, such as pressurized, fluidized-bed combustion and advanced coal gasification/liquefaction, will be increasingly important for converting the coal to more easily transported, more environmentally acceptable, and more economically viable forms of energy. Advanced gasification processes require handling solids at pressures as high as 1000 psig (6.9 MPa) at temperatures to 1200°F (650°C). Pressurized, fluidized-bed combustion processes operate at lower pressures (50–200 psig/0.3–1.4 MPa), but their temperature can be as high as 1750°F (950°C).

The system most commonly used in pilot plants (and the equipment specified in the preliminary designs for most early commercial projects) for feeding coal and other solids into pressurized reactor vessels, as well as removing char, ash, or slag, is a lockhopper. A typical lockhopper is shown in Fig. 1. It is a pressure vessel located between two process zones that are at different pressures. Lockhopper valves at either end of the pressure vessel can isolate it from either or both of the adjacent process zones. Initially, both valves are closed, and the lockhopper pressure vessel (hereafter referred to as the lockhopper) is empty. The pressure is equalized between the upper process zone and the lockhopper. Then the uppermost lockhopper valve is opened, and solids are fed into the lockhopper. Next, the solids flow is stopped, the upper lockhopper valve is closed, and the pressure is balanced between the lockhopper and the lower process zone. The lower lockhopper valve is opened, and the solids flow out of the lockhopper by the action of gravity. The lower lockhopper

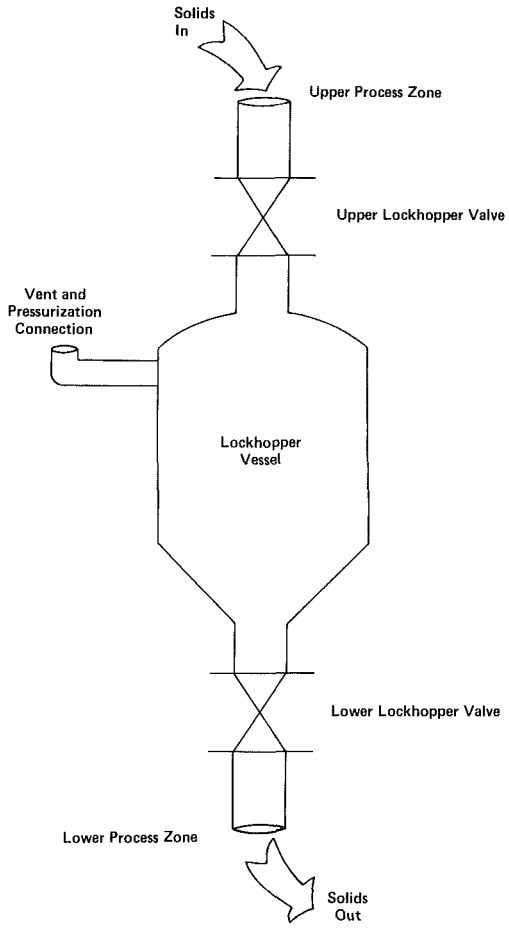

Fig. 1 Typical lockhopper system

[1] Formerly, Project Manager, Lockhopper Valve Testing and Development Project.

Contributed by the Advanced Energy System Division for publication in the JOURNAL OF ENGINEERING FOR POWER. Manuscript received by the Advanced Energy System Division July 25, 1981.

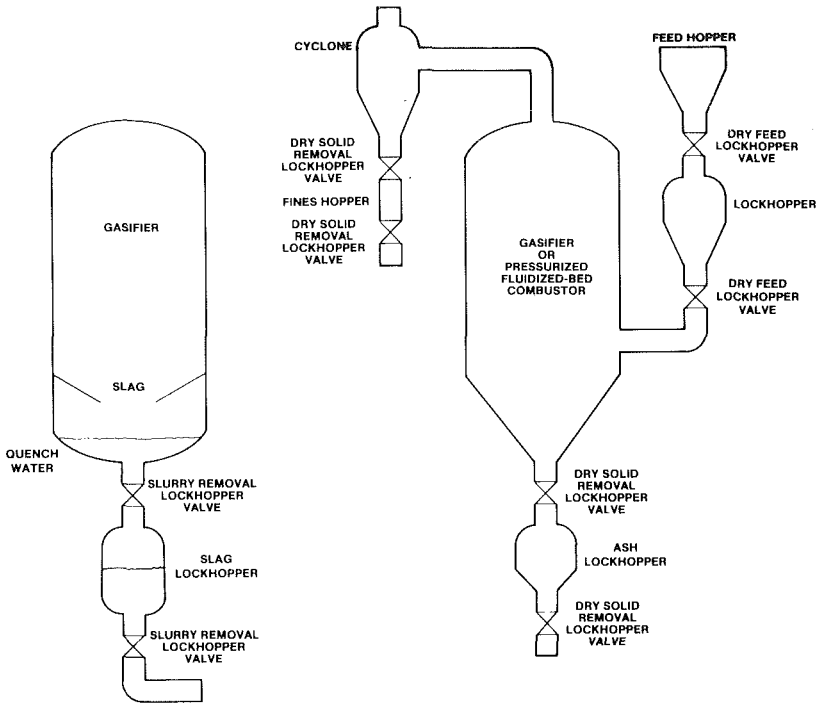

Fig. 2 Typical lockhopper valve applications for coal conversion and utilization processes

valve is then closed and the cycle repeated as often as necessary to provide the required feed rate.

Typical applications of lockhoppers in pressurized-fluidized bed combustors and advanced gasifiers are shown in Fig. 2. Coal and other dry solids, such as limestone for absorbing sulphur oxides, can be fed into the pressurized reactor vessels using lockhoppers. Lockhoppers can also be used to remove dry solid, such as char and ash, from the bottom of the reactor vessel and other process components, e.g., the cyclones that are used to remove solids from the product gas stream. Slagging processes will typically drop the molten slag into a water filled quench tank. The rapid cooling fractures the slag, resulting in a slurry which can be concentrated and them removed by a lockhopper system.

Experience in existing pilot plants has shown that it is difficult to obtain valves that will operate reliably in lockhopper service with coal solids at temperatures above 600°F (320°C) or pressure differentials above 600 psi (4.1 MPa). Circa 1976, the typical lockhopper valve life (i.e., time between major rebuilds) was 500 cycles. Today valve life is bring extended to as high as 15,000 cycles. Part of the improvement in valve life can be attributed to the work performed by the Department of Energy at the Morgantown Energy Technology Center (METC).

In 1976, METC was designated the U.S. Department of Energy's lead center for lockhopper valve testing. As part of this responsibility METC developed the State-of-the-Art Lockhopper Valve Testing and Development Project. The objectives of the project are described in Fig. 3. The goal of the project is to have commercially available lockhopper valves which will meet the specifications shown in Table 1. The approach being used in the project is shown in Fig. 4. Basically, this consists of providing the test facilities, feedback, and encouragement necessary for manufacturers of standard valves to upgrade their products to handle the demanding process conditions of coal conversion and utilization.

The test sequence shown in Fig. 5 has been developed for the evaluation of valves for lockhopper service. "Acceptance

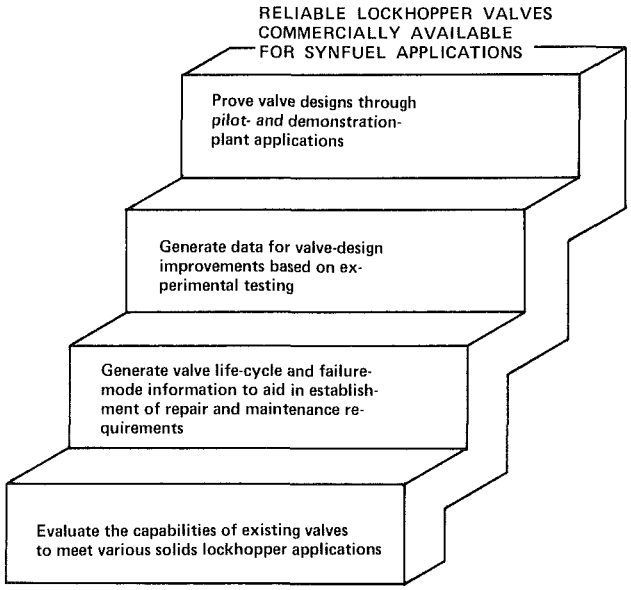

Fig. 3 Goal and objectives of the METC state-of-the-art Lockhopper Valve Testing and Development Project

testing" determines that the proper valve has been shipped, that it is operable, and that it meets the manufacturers' criteria for initial leakage. "Static testing" evaluates the effect of a range of differential pressures and valve body temperatures in the absence of solids. The test cycle performed takes the test valve through the sequence of actuations and differential pressures that a valve would be expected to experience in lockhopper service. The data obtained during this testing also provides a baseline for comparison of the test valve's performance in subsequent testing.

After static testing the test valve is disassembled. Detailed measurements and photographs are made of the internals to assist in projecting wear rates or analysis of failures. This procedure also provides an evaluation of the completeness of

Table 1 Lockhopper valve and requirements for advanced coal conversion and utilization processes

Characteristics	Dry solids feed service	Hot dry solids removal service	Slag/ash slurry removal service
Pressure range	10 to 1500 psig	10 to 1500 psig	
Typical	200-1000 psig gasification 200-300 psig PFBC	200-1000 psig gasification 200-300 psig PFBC	10 to 1500 psig
ΔP at operation	Less than 15 psig	Less than 15 psig	Less than 15 psig
Temperature range	Ambient to 850°F	600-1800°F	400-600°F
Typical	200-600°F	600-1400°F gasification 1000-1750°F PFBC	450-550°F
Medias handled	Coal and/or limestone	Char, ash	Water quenched or slurried char, ash, or slag
Media size range	2″ to -100 mesh	1 inch to -100 mesh	N/A
Typical	1″ to 50 mesh		
Valve size range	2 - 24 in. bore	2 - 24 in. bore	2 - 24 in. bore
Typical	4 - 12 in., pilot plant 8 - 16 in., demo plant	4 - 12 in., pilot plant 8 - 16 in., demo plant	4 - 12 in., pilot plant 8 - 16 in., demo plant
Seal requirements	1.0 scfm/in. NPS internal leakage, new 3.0 scfm/in. NPS max. in-service internal leakage 0.1 scfm external leakage	1.0 scfm/in. NPS internal leakage, new 3.0 scfm/in. NPS max. in-service internal leakage 0.1 scfm external leakage	1.0 scfm/in. NPS internal leakage, new 3.0 scfm/in. NPS max. in-service internal leakage 0.1 scfm external leakage
Desired life	25,000 cycles W/0 internal refurbishment	25,000 cycles W/0 internal refurbishment	25,000 cylces W/0 internal refurbishment
Applicable processes	Lurgi, Co-Gas, and many others	Lurgi, PFBC, Westinghouse	Texaco, Bi-Gas, Slagging Lurgi

NPS = Nominal Pipe Size

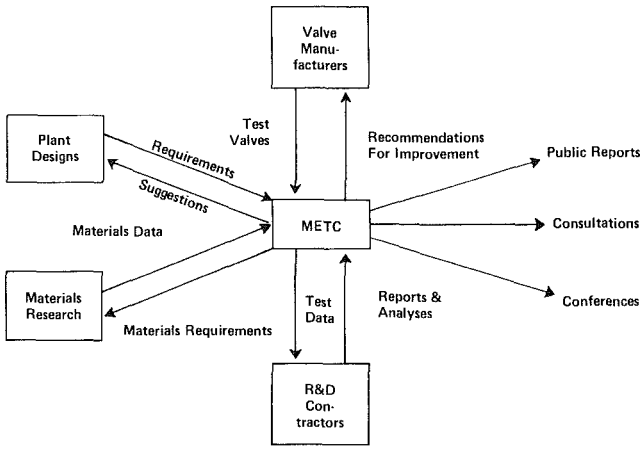

- Develop a strong, cooperative effort among industry manufacturers, the test/development project, and the coal-conversion pilot/pioneer commercial project teams
- *Provide adequate test facilities with realistic service conditions* to acquire meaningful test data to support manufacturers' improvements in design, new designs, and verification of all design concepts
- Feedback data from the test facilities, specifically acquired to fill the needs of the manufacturer, to implement design modifications or new valve designs
- Rapid transfer of experience and problems with operation of valves in pilot plants and pioneer commercial plants
- *Transfer materials development and testing technology to industry manufacturers, plant operators, and the private sector*
- Sponsor periodic conferences/workshops to bring together industry plant designers and operators and testing groups, e.g., Morgantown Valve Workshops (November 1977 and October 1980)

Fig. 4 State-of-the-art lockhopper valve testing and development project approach

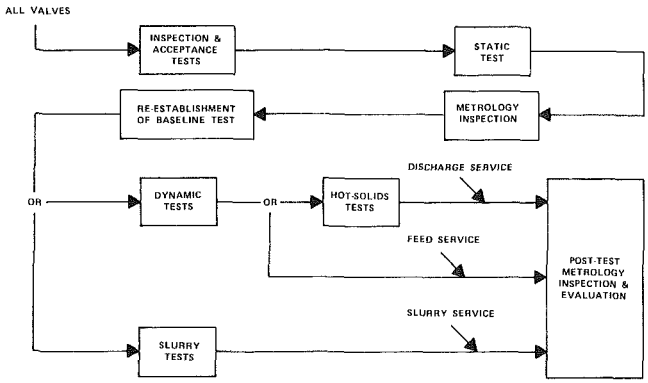

Fig. 5 Lockhopper valve testing sequence

the manufacturer's assembly instructions and the ease with which the test valve can be maintained in a plant maintenance shop (or even an in-line) environment. After reassembly, a "reestablishment of baseline test" is performed to verify that the test valve was indeed properly reassembled. At this point the path of the test sequence diverges. Test valves intended for slurry service proceed to "slurry testing," where the effects of moderate-temperature, high-pressure slurry are evaluated. Test valves intended for dry solids feed and removal service proceed to "dynamic testing." Here the effects of high-pressure and ambient-temperature solids on the test valve's performance are evaluated. Test valves intended for handling solids at higher temperatures proceed from dynamic testing to "hot solids testing." This testing evaluates the test valve performance under conditions simulating actual lockhopper service including pressures to 1600 psig (11.0 MPa) and solids temperatures up to 2000°F (1100°C).

At the end of their respective test sequences or in case of a failure, a "final inspection" is performed. This inspection documents the conditions of the valve at the end of testing and provides a data base for predicting valve life or analyzing a failure.

The capabilities of the test units are summarized on Table 2. Additional information on the test program and test units can be found in references [1-3].

Discussion of Test Results

As a result of a survey of valve manufacturers (reference [4]), fifteen valves were initially procured for testing. This selection considered not only valves with potential for

Table 2 Capabilities of METC lockhopper valve test units

Parameter	Valve static test unit (VSTU)	Valve dynamic test unit (VDTU)	Valve hot solids test unit (VHSTU)	Valve slurry test unit (VSLTU)
Pressure (psig):				
Nitrogen	1200	1200	1200	600
Air	2000	2000	2000	2000
Test media	Dry gas	Non-flammable solids up to 4 mesh	Non-flammable solids up to 4 mesh	Water slurry up to 50% solids
Media temperature	Ambient	Ambient	300-2000°F	Ambient-200°F
External heaters for valve body	100-850°F	100-850°F	None	None
Number of valves tested	One	Two or three	Up to five in two separate assemblies	One
Data recorded				
Gas	Pressure temperature	Pressure temperature	Pressure temperature	Pressure temperature
Valve leakage	Internal External	Combined	Combined	Internal External
Valve body	Temperature	Temperature	Temperature	Temperature
Valve actuator	Force/torque time	Force/torque time	Force/torque time	Force/torque time
Other			Solids Temperature	Slurry Temperature
			Strain gage or other measurements if transducers are installed on the test valve noise, vibration and various other technician observations	

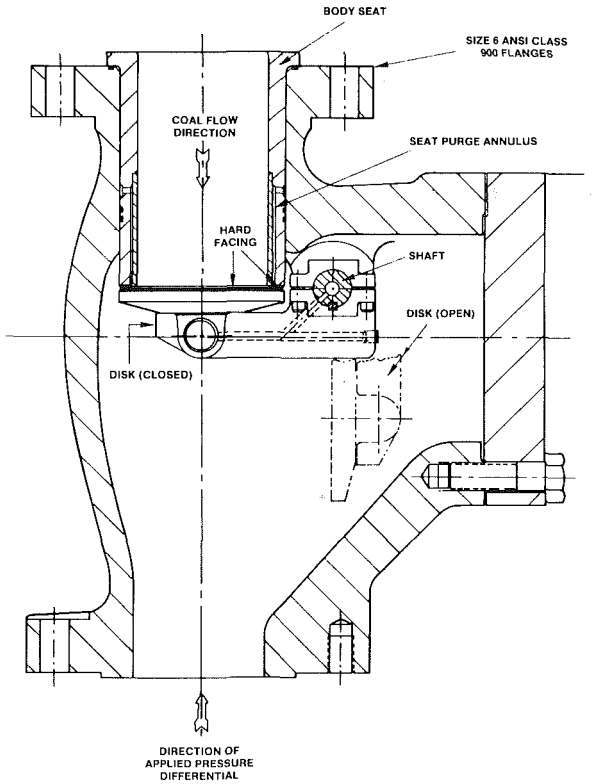

Fig. 6 Rockwell coal lockhopper valve

lockhopper service, but also included at least one valve from each major design type. An additional fourteen valves have been obtained through no-cost cooperative agreements with manufacturers or long-term loans.

To date forty-nine test runs have been performed. During these test runs, forty-three valve failures have been observed. Table 3 shows a breakdown by test unit and general cause of the failure. Essentially, most of the failures observed during

Table 3 Valve failures observed in testing

	Acpt.	Static	Rstb.	Dyn.	Slurry	Total
QC	2	12		2		16
Design		2	1	2		5
Solids				9	1	10
Test		2		2		4
Not Det.		7		1		8
Total	2	23	1	16	1	43

Examples:

Quality control -Wrong valve body, misassembly, failure to actuate, loose body bolts, wrong packing material, manufacturing defects
Design -Stripping of linkage, inappropriate materials
Solids -Internal cavities packing, mechanisms jamming
Test -Direction of applied pressure wrong, gasket failures in test unit, external heating effects

static testing can be attributed to quality control problems. For dynamic testing the majority of the problems are solids related.

Of the twenty-nine valves that have been tested, thirteen have had to be returned to the manufacturer or have had work performed on them at METC by the manufacturer before significant testing was performed. Significant testing means acceptance testing or the first few cycles of static testing. Problems encountered resulting from poor quality control or design defects have included shipment of the wrong ANSI class body, insufficient hardfacing thickness, loose bolts, actuator linkages breaking, assembly clearances that result in the valve galling, jamming or leaking excessively, sealants that are not adequate for the rated temperature of the valve, and gross machining defects of the body or internal components.

The next most significant problem observed has been the compaction of fines in critical areas. Deposits of fines have prevented valve actuation by blocking the movement of internal parts or creating sufficient drag that linkages have failed. Parts, such as springs, which require clearances to function properly have been plugged by deposits. Such deposits also produce nonsymmetrical loadings on the

operating mechanisms. It is suspected that these unusual loadings have contributed to the galling and abrasion observed, to some degree, on the stem of almost every valve tested.

A problem area which is expected to be more significant in future testing is thermal effects. To date, most of the testing has been performed at 300 and 600°F (150 and 320°C). Clearance type problems have become more frequent at the higher temperatures. Additional problems are expected with materials and clearances as test temperatures are increased over 600°F (320°C). Also at higher temperatures, the strength of metals is reduced significantly. This makes the design less tolerant of the dynamic loadings produced by the interaction of the valve intervals with the solids.

The number of valve figures observed to date has resulted in some generalizations concerning the requirements for lockhopper valves. Critical areas are:

- the flowpath through the valve,
- the seals between the set and body and between the seat and the closure member,
- the sizing of the actuator and the linkages that transmit the operating forces to the closure element,
- quality control in the design, fabrication, assembly, and documentation of the valves, and
- thermal design considerations.

Flowpath. The design of the valve body and the operating mechanism must result in a clear flow path through the valve body. The flow path should direct the solids away from seats, bearings and other critical areas. Any pockets or recesses should be minimized. If a valve design does have locations where solids accumulate, they must be designed so that a path is available for the solids to drain out of them.

A purge system can be used to clear out pockets, as well as clear particles off sealing surfaces. An effective purge system is absolutely necessary in some designs and advisable in almost all. To perform successfully, more than just a fitting in the side of the valve body is needed. The purge flow must be high velocity and large volume. It must be directed at the critical area so that particles are moved toward an outlet. The total purge volume can be minimized by using a short duration purge, suitably timed to the valve's actuation.

In addition to the flow path of the valve, the clearances between moving parts are also critical. They must be sized so that particles are either excluded or can move freely between the members; if not, excessive abrasion and jamming can occur. Abrasion and jamming can substantially increase the required operating forces. Most of the abrasion/erosion noted has occurred between moving parts rather than in the solids flow path. The low velocities and normal forces occurring in the free-flowing solids have not caused significant wear in any of the test valves to date.

Internal Leakage Considerations. Perhaps the most critical part of valve design for solids service is the seal between the seat and the closure member. The valves that have been successful in the test program to date have followed one of two philosophies. Either continuous contact is maintained between the sealing surfaces or else no rubbing contact is allowed whatsoever. If continuous contact is maintained between the sealing surfaces, care must be taken to prevent particles from becoming trapped between the two surfaces. Adequate forces must be applied to the surfaces to maintain their contact. If springs are used to generate these forces, they must be designed so that solids will not interfere with their operation. Also, the surfaces must be in complete contact. Any recesses or grooves will tend to entrap particles and scrape them across the opposite surface.

If no rubbing contact is allowed, the actuator must have sufficient force to effect a seal between the members. If the differential pressure is in the proper direction it can assist in holding the sealing members together. However, an adequate seal must be obtained to prevent excessive leakage at low pressure and initially to allow the pressure differential to be developed. If excessive leakage occurs even just at low pressure, erosion of the sealing surfaces can occur.

With a powerful actuator, care must be taken to control the actuation time of the valve. A rapid closing action will make purge timing more difficult and can produce impact damage to the sealing surfaces, especially if particles are trapped between them. In continuous contact designs, the wiping action of the closure member tends to clear particles from the sealing surfaces. In non-rubbing designs, some type of a wiping or purging action is necessary to prevent solids from being trapped between the seating surfaces.

Most of the sealing surfaces tested to date have been Stellite 6. These alloys have performed adequately with the limestone solids which have been used in most of the testing. Limestone is a reasonable material to use for simulating feed materials. However, slags and ashes can contain components much harder (and, therefore, more abrasive and erosive) than limestone. Simple comparison scratch tests, like those used for the Moh Hardness Scale, have shown some components of the bottom ash from the METC, 42-in. dia, stirred, fixed-bed gasifier to be harder than aluminum oxide. For comparison purposes, the relative hardness of aluminum oxide, limestone, stainless steel, and potential hardfacing materials are shown on Table 4. As can be seen, limestone is softer than most of the hardfacing alloys in current use, but aluminum oxide and fused ash are much harder than any of the hardfacing alloys. Only the cerments and ceramic materials have comparable hardnesses.

Hardness is only one variable that can affect a material's rate of wear and is not always the best indication of per-

Table 4 Relative hardness of solids media and hardfacing materials[a]

Material	Equivalent Vickers Hardness Number
Solid Media	
Coal[b]	<40
Limestone	110–130
Dolomite	130–150
Fushed Ash	800–2000
Aluminum Oxide	1800–2100
Hardfacing Alloys	
316 stainless steel	160–290
Stellite No. 6	400
Stellite No. 1	580
Haynes No. 40	630
Tribaloy T-800	650
METCO 19-E	600–700
Cermet and ceramic materials	
Silicon nitride	1400
Tungsten carbide	1600–1750
Silicon carbide	1900–3300
Boron carbide	3000
Tungsten titanium diborite over tungsten carbide (TMT-745)	~5000

[a]This data was compiled from vendor literature and standard reference sources. Where data was obtained by methods other than Vickers Hardness Number (VHN), approximations were used to convert the data to VHN.

[b]This is for carbonaceous material and is not representative of siliceous and other mineral inclusions which are common. The hardness on these range from 100 to over 1000.

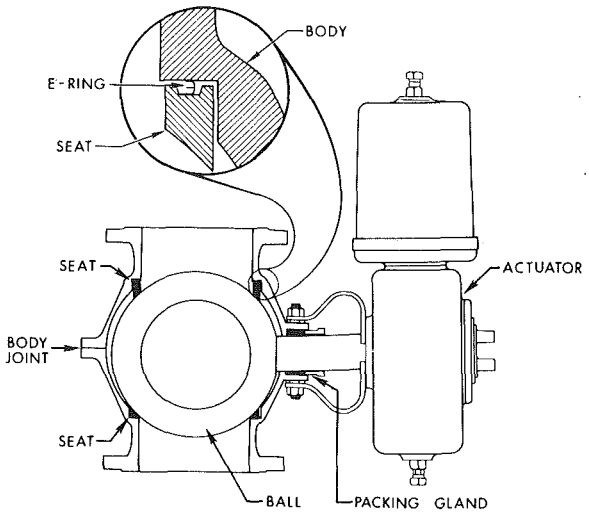

Fig. 7 Kamyr PD Series ball valve

Table 5 Recommendations made to valve manufacturers

Areas identified in which performance can be improved or allowable service condition expanded	-4
upgrade body/seat seal, higher seating faces, etc.	
Areas identified for review	- 4
duty cycle on actuator motor, slight abrasion or galling in packing box, etc.	
Specific problem areas identified	- 7
external seal leakage, low contact pressure between internal sealing surfaces, etc.	
Specific modifications	- 12
redesign of actuator linkage, modifications to set retainer, specific purge locations, etc.	
Improve purge system	- 5
Consider alternate materials	- 4

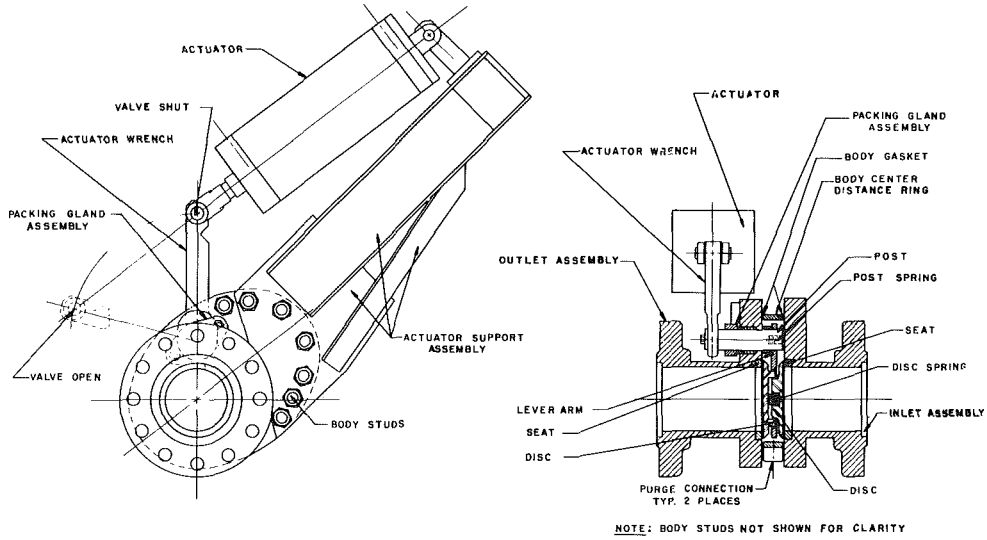

Fig. 8 Everlasting double-disk, coke-oven valve

formance. The particle size and shape can also affect the erosion or abrasion rate. However, the effects of the hardness difference between limestone and aluminum oxide have been observed in the testing that has been performed. More damage to the sealing surfaces has been observed, in test valves of both closure types, due to a few hundred cycles with aluminum oxide than from many thousand cycles with limestone.

The other seal that has occasionally been the source of excessive internal leakage is the seal between the body and the seat. It is a static seal, but allowances must be made for thermal expansion of the valve internals. In some designs it is the elasticity of this seal that provides the preload to maintain contact between the seat and the closure member. The elastomers and plastic type sealants used in many designs are limited in their temperature range. In fact, for most valves, it is the maximum allowable temperature of this seal that limits the service temperature of the valve. Many of the designs with higher operating temperature limits are using expanded graphite ribbon to good advantage to seal the seat to the valve body. The design of seals which can perform well at high temperatures, accept thermal transients, and will allow the seat to be replaced without removing the valve from the system, is an area where new ideas will be needed to produce valves that will perform well in the upper range of the process temperatures.

External Leakage Considerations. The two major sources of external leakage are the packing gland and the body joint. Most of the valves that have been tested with solids have experienced some degree of stem abrasion in the packing area, as well as galling between the stem and the packing follower. It is believed that transient bending moments in the stem due to the interactions between the internals and solid particles contribute to the galling problem. The abrasion under the packing is probably due to migration of the fines into the packing, but the bending moments in the stem could also contribute to it by slightly disturbing the packing and requiring that the packing gland be tightened more often.

Difficulties with sealing the body joints have resulted from inadequate gasket retention, distortion of parts during assembly, and thermal expansion of external body studs during elevated temperature testing. The expansion of the body studs can reduce the preload on the gasket and encourage leakage. This effect is aggravated by the use of induction heaters for high-temperature testing. The less massive studs tend to heat as fast, if not faster than, the heavier body members resulting in greater thermal expansion of the studs. In actual service the valve body and internals would normally

PARTS SPECIFICATION		
SL-1	INLET BONNET	CAST IRON, ASTM A 278 CL 30
SL-2	OUTLET BONNET	CAST IRON, ASTM A 278 CL 30
G-3	OUTLET SEAT	S.S. 440-C (59 Rc)
G-8	OUTLET DISC	S.S. 440-C (59 Rc)
G-4	LEVER ARM	STEEL
	POST	416 SS
G-5	POST GASKET	HARD ASBESTOS
G-5A	POST PACKING	ASBESTOS-TEFLON IMPREG.
G-9	DISC SPRING	S.S. 17-7PH
G-6	POST SPRING	S.S. 17-7PH
G-22	GLAND	CAST IRON
G-10	BODY GASKET	ASBESTOS
G-13	WRENCH(HANDLE)	STEEL
G-14	BEAM	STEEL

SIZE	B	E	H	L	P	Z	SIZE AIR CYL
1½	9½	5	6-3/4	19½	3-7/8	2	2½x4
2	10-1/8	6	7	19½	3-7/8	2	2½x4
3	13	7½	12½	24	6-1/8	2-1/4	4x8
4	15	9	17	32	7-3/8	2-5/8	4x12
6	17	11	21	42	8-5/8	3	5x18

Cylinder size based on 60 P.S.I. operating air for cylinder, 100 P.S.I. line pressure @ time of valve operation. For more accurate cylinder sizing advise specifics on line operating pressure and available air.

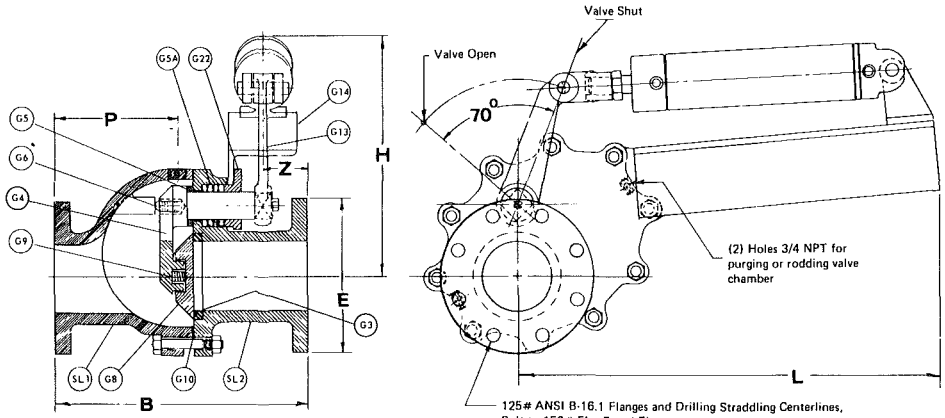

2 Way Slurry Valve Air Cylinder Operated

* Fig. 3075-A-30, Cl. 125, with iron seat and disc

* Fig. 3075-A-32, Cl. 125, with 440-C (59R_c) for abrasive service

** Fig. 3077-A-(30 or 32) Cl. 250, with 250# ANSI B-16.1 flanges

Fig. 9 Everlasting sliding-disk valve

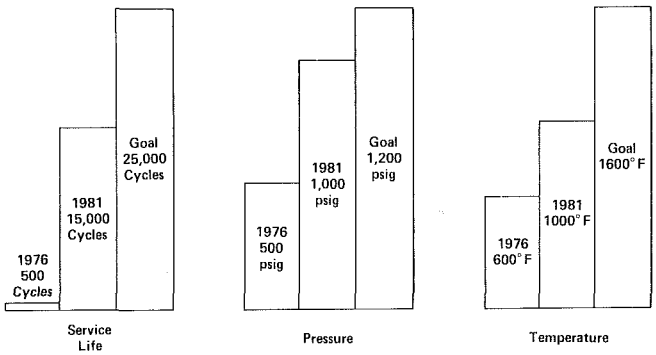

Fig. 10 Lockhopper valve state-of-the-art

be heated before the exterior studs, which would minimize any tendency for the body gasket to lose its preload due to thermal expansion of the body studs.

Actuators. The performance of the actuators, in most cases double-acting pneumatic cylinders, has been very reliable. The problems that have been observed are more the result of improper sizing of the actuator and the linkages needed to transfer the operating forces to the closure member. The actuator does not have to be sized to operate the valve with the full differential pressure across the closure member. Most process designs call for lockhopper valves to be actuated with a differential pressure of 20 psid (0.14 MPa) or less. However, an oversized actuator is required to overcome the drag and jamming tendency that can result from deposits of solids.

The linkages should be sized to transmit the full force developed by the actuator. If this is not possible, a force limiter or some type of shear pin should be used to limit the force that can be applied to a value that will not damage the valve internals. A feature that would be desirable for lockhopper service is a system that will sense an increase in the required operating force and reverse the actuator or possibly cycle and purge the valve repeatedly to clear any potential blockages or deposits.

Quality Control. As noted earlier, almost one-half of the test valves that have been tested have failed to meet their rated operating parameters due to manufacturing or assembly defects. While a raw material to finished product documentation and quality assurance program, such as used by the nuclear component industry, is neither necessary nor desirable, some quality control inspections and a set of standardized tests performed at the factory shortly before shipment should be encouraged. The extra cost of such a program is readily weighed against the cost of having to remove a valve from a system or potentially delay the start-up of a plant.

Additional quality control is also needed in the documentation that accompanies lockhopper valves, in particular the repair and maintenance procedures. Under severe service conditions the lockhopper valves will require regular maintenance. One reason for disassembling and reassembling the test valves as part of the test program is to evaluate the completeness and accuracy of the maintenance procedures and to identify any procedures that would be difficult to perform in a plant environment. The quality of the procedures supplied with the valves has been varied. Some have been complete and accurate; others have required repeated calls to the factory to fill in missing steps and even visits by factory personnel to demonstrate complicated alignments. Experience has shown that valves with critical assembly tolerances and complicated assembly procedures tend not to perform well in a solids handling service. The forces generated from the action of the solids in the valve can readily disrupt close tolerance alignments.

Thermal Design Considerations. As the operating temperature of the valves increases, the level of detail of the valve design process becomes more important. As the testing temperature was increased from 300 to 600°F (150 to 320°C), more problems became apparent. The effects of thermal expansion and degradation in the physical properties of many alloys and other materials of construction will become increasingly apparent as the operating temperature exceeds 1000°F (540°C). Careful design work will have to be done to evaluate these effects and compensate for them.

As temperatures increase, the thermal expansion of valve

internals and the relative thermal expansion between different materials or alloys become significant. For example, the expected change in length on a 12-in. (0.30-m) long austenetic stainless steel member when heated from 70 to 1000°F (21 to 540°C) is 0.18 in. (3.0 mm). This is 50 percent more than the 0.08 in. (2.0 mm) expected change in length for a 9 percent Cr-1 percent Mo alloy. If constrained, this expansion can overstress and even deform members. Such thermally induced changes in dimension can affect clearances and alignments critical to the operation and sealing of a valve.

An additional concern is that most of the thermal analysis currently being performed on valves assumes a constant body temperature. In lockhopper service it is more likely that a thermal differential will exist both axially and radially in the valve. The efects of this on the integrity and operability of the valve needs to be considered in order to achieve reliable operation at the higher media temperatures.

Best Designs. At the conclusion of the testing performed on a specific test valve a report is prepared summarizing the test result and analyzing the valve's performance. Where appropriate, recommendations are made suggesting improvements and pinpointing potential problems. The type of recommendations made are shown on Table 5.

As a result of the testing performed to date, eleven valves have been deleted from the project and four valves have been judged to show good potential for lockhopper service. Most of the valves that have been deleted from the project were valves that were included as representatives of different valve types and were not primarily intended for this type of service. After the test results were discussed with the manufacturer, it was decided that the particular valve was not suitable for the lockhopper applications. Some valves did show potential but require some degree of modification. In these cases, additional testing is performed if the manufacturer is willing to perform the indicated modifications.

The four test valves that have been the most successful to date are listed below. The order presented does not reflect the relative performance of the test valves.

- Rockwell-coal lockhopper valve, Fig. 6
- Kamyr-PD series, ball valve, Fig. 7
- Everlasting-double-disk, coke-oven valve, Fig. 8
- Everlasting-sliding-disk valve, Fig. 9

Each of these test valves has completed at least 8000 cycles of *Dynamic Testing* with only minor or readily correctable problems. The fact that out of four valves there are three different design types represented suggests that the valve type is not as important as is adapting the specific design to the service.

Summary

In 1976, when the state-of-the-art Lockhopper Valve Testing and Development Project was initiated, the maximum process condition for a lockhopper valve was a differential pressure of 500 psi (3.4 MPa) at an operating temperature of 600°F (320°C). In order to maintain acceptable performance at this condition the valve would have to be rebuilt approximately every 500 cycles. In the METC stirred, fixed-bed gasifier, feed lockhopper valves are now operating for 14,000 cycles at pressures of 165 psig (1.1 MPa) with temperatures of 450°F (230°C); cyclone dust removal lockhopper valves have been operated successfully for over 1500 cylces with 900 to 1200°F (480 to 650°C) gas and 550 to 700°F (290 to 370°C) solids. Test valves have performed well in simulated lockhopper conditions for 16,000 cycles at pressures to 1000 psig (6.9 MPa) and valve body temperatures to 600°F (320°C). This represents a significant improvement since the start of the project. It is believed that at this time valves can be purchased with a potential service life of 15,000 cycles at 1000 psig (6.9 MPa) and 1000°F (540°C).

As shown in Fig. 10, meeting the goal of 25,000 cycles at 1200 psig (8.4 MPa) and 1600°F (870°C) still requires almost doubling the service life, an increase of 200 psi (1.4 MPa) in pressure rating, and an increase of 600°F (320°C) in service temperature. In order to accomplish the testing necessary to develop valves for these services conditions, METC has constructed facilities that can simulate lockhopper service at pressures up to 2000 psig (13.7 MPa) with up to 600°F (320°C) simulated feed materials (limestone) or 2000°F (1100°C) simulated ash materials (aluminum oxide or silicon carbide). These facilities will be placed in operation later this year.

To date, METC facilities have been used to perform forty-nine test runs on twenty-nine test valves (fifteen purchased and fourteen obtained through cooperative agreements with valve manufacturers). Information on test results, new valve designs, materials testing, and pilot plant experience is being distributed through technical papers, project publications, presentations at Valve Manufacturers Association and other meetings, and through the sponsorship of conferences. The most recent conference, the 2nd Symposium on valves for Coal Conversion and Utilization (reference [5]), contributed significantly to informing valve manufacturers and plant designers of the valve needs of the emerging synthetic fuels industry.

The knowledge accumulated from this project is being assembled into a document, *Lockhopper Valve and System Design Criteria for Coal Conversion and Utilization Applications* (reference [6]). As further information is developed it will be included in this document. It is intended that this design criteria will eventually contain the sizing information, solids flow correlations, design trade-offs and sample specifications necessary for an engineer to size a lockhopper system and specify the required valves.

New candidate valves are still being evaluated for possible inclusion in the test program. Project plans call for the operation of the test facilities for evaluation of state-of-the-art lockhopper valves through 1983 and publication of the final results in 1984.

References

1 Gardner, J. F., and Maxfield, D. A., *Topical Report—Lockhopper Valve Testing and Development Projects*, United States Department of Energy (DOE/METC/SP-137), Mar. 1981.

2 Gardner, J. F., and Holtz, T. R., *State-of-the-Art Lockhopper Testing and Development Project Test Plan*, United States Department of Energy (DOE/METC/SP-139), Apr. 1981.

3 Gardner, J. F., and Holtz, T. R., *Prototype Lockhopper Valve Testing and Development Project Test Plan*, United States Department of Energy (DOE/METC/SP-143), Apr. 1981.

4 Gardner, J. F., Evaluation Report, *Survey of Valve Industry Capability to Furnish 6-Inch Valves for Coal Conversion*, United States Department of Energy, (DOE/METC 78/10), Feb. 8, 1977.

5 United States Department of Energy/Morgantown Energy Technology Center, and Valve Manufacturers' Association, *Proceedings of the 2nd Symposium on Valves for Coal Conversion and Utilization*, Oct. 15–17, 1980 (DOE/MC/14522-1), edited by TRW Energy Engineering Division, published Jan. 1981.

6 Gardner, J. F., and Holtz, T. R., and Maxfield, D. A., *Lockhopper Valve and System Design Criteria and Guidelines for Coal Conversion and Utilization Applications*, United States Department of Energy (DOE/METC/SP-138), Mar. 1981.

G. D. Dumbaugh
Kinergy Corporation,
Louisville, Ky. 40218

Coal or Lignite Handling Functions by Least Input Power

1 Introduction

All coal or lignite fired industrial power plants must unload, store and withdraw, feed, and sometimes screen or clean this needed fuel. This presentation discusses how to accomplish all of these functions by the least consumption of the plant's generated product; namely, electrical heat energy.

It will be shown how the unloading of bottom discharge rail cars, withdrawal of silos, bins, bunkers, and storage piles containing poor flow or non-self flowing characteristic fuel can be induced by least input power by taking advantage of gravity and the fuel's inherent natural, vertical flow pattern.

All non-gravity functions such as feeding, screening, or cleaning will be accomplished by the use of kinergy—which is non-heat, reactive, kinetic energy. This principle derives from the "drive-load" relationship of a vibratory mass inertia load being capable of being driven by nonheat energy.

In every application, the equipment's functional performance level will not be compromised. In some cases, performance may actually improved. Further, the initial cost of the equipment and its installation will at least be competitive with alternate methods. Operating costs will be markedly reduced. More significantly, precious heat energy is not unnecessarily wasted.

Finally, it is at least a step towards the manifest engineering law that lies in our professional future; namely, accomplishing the same functions as before—but with less input power requirements.

2 Gravity Flow Functions

Gravity flow functions include storage bins, bunkers, silos, storage piles, vertical or near vertical chutes, and bottom dump rail cars.

I Storage Bins or Bunkers. Storage bins (includes bins, bunkers, track hoppers, silos, and vertical chutes), and their proper withdrawal have long been an engineering headache for the coal, chemical, ore processing, wood processing, and cement industries. After World War II, these industries more quickly automated their process funcitons. The day of accurate instrumentation, telemetering, automatic controls,—capped by the introduction of computers—was here. Information could be automatically read, digested, decisions made, and executed without human assistance. However, they quickly learned that the know-how that existed with storage bins and their continual, reliable, and total withdrawal was sadly lacking. While the process downstream would function near perfectly, it was virtually useless unless the storage bin would give up the bulk solid raw material that was necessary to supply and sustain the process.

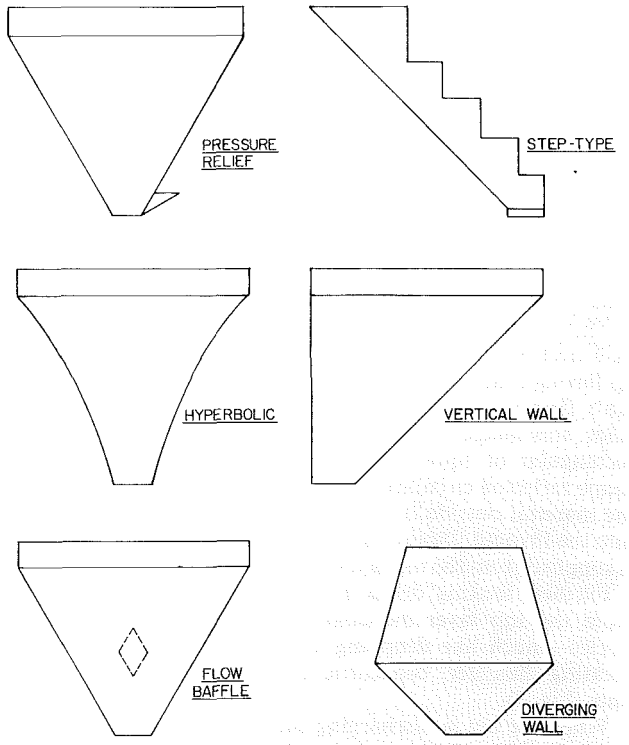

Fig. 1 Typical past bin designs to relieve pressure

In the late 50s and early 60s, storage bins began to receive much more dedicated, and definite engineering attention than ever before. Prior to this effort, all kinds of geometric shapes had been attempted with storage bins (Fig. 1). Some experienced limited success, and some no success at all. Also, high power consuming "forcing" devices were inserted within the storage bin itself or adjacent to its outlet in an attempt to accomplish this storage withdrawal. Before proceeding further, let's review known bin flow pattern basics.

1 Bin Flow Pattern Basics. When coal or lignite (or any other material) is placed in a storage bin for the first time, and filled to some level, a certain static pressure will exist against the side wall and on the bottom cone. However, when the outlet is opened, and assuming flow occurs, the pressure against the vertical side walls will increase (as much as three times for some materials), and the vertical headload on the conical bottom will actually decrease (Fig. 2). This is called

Contributed by The Fuels Division and presented at the Industrial Power Conference, October 21-24, 1979, Cincinnati, Ohio of The American Society of Mechanical Engineers. Manuscript received at ASME Headquarters July 9, 1979. Paper No. 79-IPC/Fu-2.

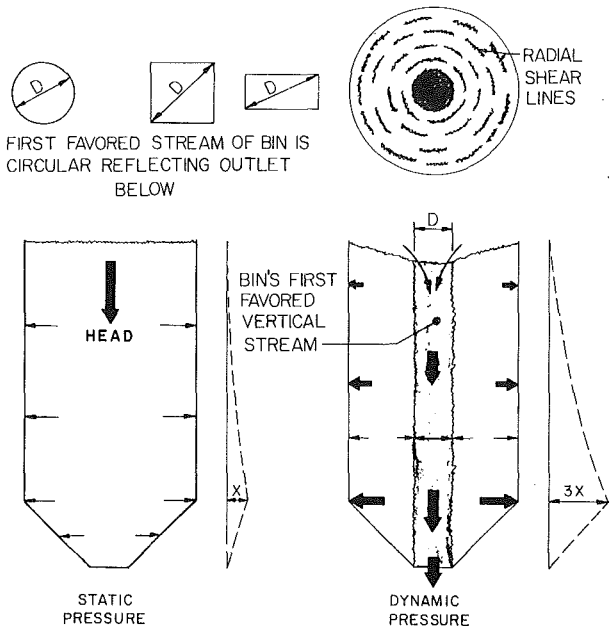

Fig. 2 Change in sidewall pressure from static loading to state of dynamic flow

the "dynamic" or flow pressure characteristic. And, this phenomena must be dealt with structurally.

The reason this change in pressure from static to dynamic flow occurs is that a circular reflection of the outlet, projected up through the height of the material in the bin, becomes the bin's first favored vertical flow stream. If the outlet is circular, this image is the diameter of the circle. If the outlet is rectangular or square, this image is the diagonal of either shape reflected circularly up through the material height. All the material outside this first favored stream attempts to get into the favored stream but is pushed back because this stream is supplied from the top layers of the bin (Fig. 2).

Further, looking down in plan view at the bin, the flow from the top layer increases in ever increasing concentric circles—much like dropping a rock into a pond. These increasing diameter, concentric circles are called radial shear lines (Fig. 2).

When the bin is discharging into "open" drop—such as a receiving railroad car or truck—the flow at the outlet will tend to be uniform across its full cross-sectional area. However, if a feeder of any type is introduced, the phenomena of introducing a localized feeder favored stream at the bin's outlet should be recognized.

If the contained coal or lignite is of relatively poor flow characteristics, it is definitely possible that the only withdrawal that will be accomplished is the initial first favored stream of the storage bin (that is, a reflection of the bin's outlet). The result is a "core" straight up through the height of contained material. This is called "plug" flow (or, funnel flow at rat-hole).

On the other hand, if the fuel is very free flowing, and near perfect bin design conditions exist, the top level will drop much like water, and all particles would flow downward with nearly uniform vertical velocities. This is called "mass flow."

Therefore, in basic bin design, the following four factors must be recognized and satisfied:

- The bin's first favored vertical flow stream must be known and identified. This will be a circular (plan view) reflection of the outlet.
- The bin design must maintain "command" of the sloughs. That is, product outside the initial favored vertical stream of the bin (reflection of outlet) must be commanded so that it will at least flow into the bin's first favored stream and be withdrawn.
- The bin should be withdrawn concentrically. That is, its full cross section should withdraw uniformly. Or, said another way, the top level drops uniformly (like water).
- It should be recognized that localized feeder favored streams exist at the outlet, and proper steps must be taken to minimize their effects. Otherwise, it could violate concentric withdrawal.

As we have said, many kinds of shapes and flow assist devices had been developed over the years. As a result of the engineering deliberation of the early 60s, we believe most solids fuel handling engineers will now agree that two acceptable basic approaches to storage bin response and withdrawal exist today. One is the "geometric static" bin design approach and the other is the "induced" vertical flow approach. They will not be discussed individually.

2 Static Geometric Bin Design Approach. One approach is defined as "static geometric." Here, the side walls of the storage bin are made relatively steep. These steep slopes would be related to the flow characteristics of the material contained. This relatively recent research effort was commenced in the U.S.A. by a grant given to the University of Utah, which assigned to it Dr. Andy Jenicke and Dr. Jerry Johanson. Later, Mr. Hank Colijn of Pittsburgh, Pa. added contributions.

In this approach, precise fuel flow characteristic tests are first conducted. The predicted and specific flow characteristics are taken into account to establish a bin design of specific side wall slopes. At times, special side wall construction is also specified, such as smooth stainless steel, or polyclutch epoxy liners. With proper design, the contained material or product will drop with a uniform velocity across its full cross section and mass flow will be obtained (Fig. 3).

This approach is by far the best from the standpoint of input power because the entire storage bin is static. No power is consumed. However, it does have potential engineering disadvantages that must be reckoned.

- First, it could require excessive head room (because of the steep conical side wall slopes). This means that possibly a coal or lignite fired power plant building may have to add one or two levels of height.
- The process engineer is still relying upon gravity as his motivating force to move the product from the storage bin. True, by conscientious design and accurate determination of flow characteristics, it is definitely possible to design a static bin with good flow properties. However, if those properties should be "abounds" because of changing fuel characteristics from a new supplier or weather conditions, the bin could go beyond its design limits and render poor flow.
- If the contained product takes on a "set" (that is, undergoes a fusion of particle to particle under pressure of its own weight with time in storage), there is no external force to unlock this so-called set. Gravity does not have the ability to overcome set.

Therefore, provided the fuel's flow characteristics are well defined and expected to be reasonably constant, and the head room required for steep wall slopes acceptable, the "static geometric" approach is recommended, obviously, because no power is consumed in withdrawal.

3 The Induced Vertical Flow Approach. An alternate to the static geometric approach is some form of external force withdrawal. Previously, this took the form of air pads, air jets, bin wall vibrators, rotary tables, etc. All of these devices have been set aside by the advent of the induced (not forced) vertical flow device identified as a bin discharger, bin activator, or vibrating hopper. The term "bin activator" has

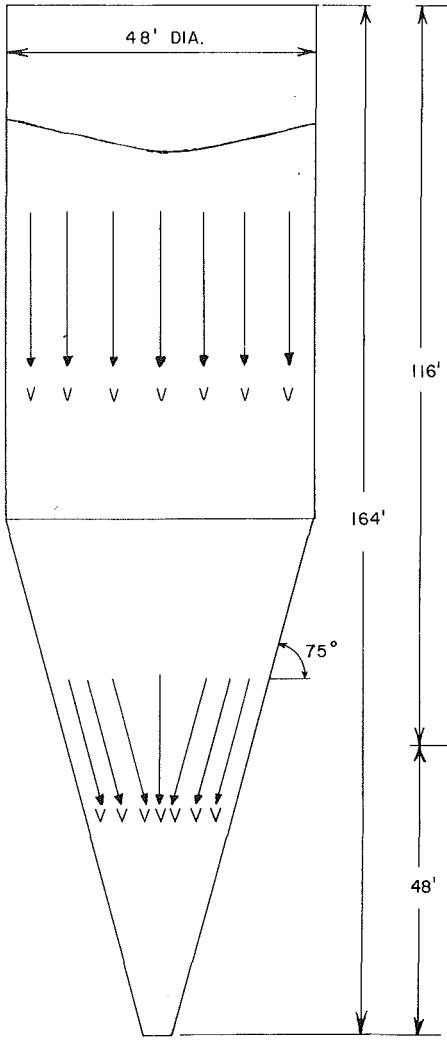

Fig. 3 *V* is vertical velocity of downward flowing coal or lignite

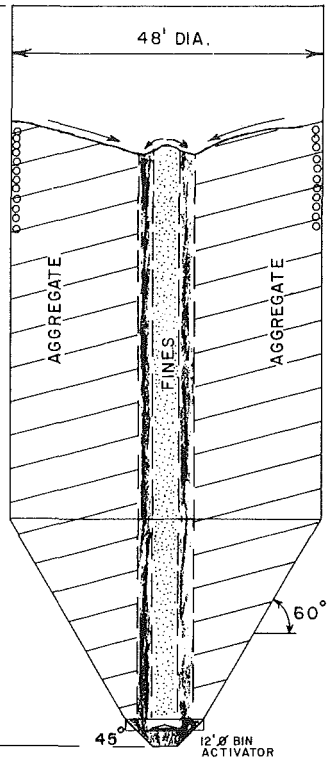

Fig. 4 A comparison of performance in withdrawal and height requirements of static geometric design (Fig. 3) versus induced vertical flow by means of bin activator (Fig. 4). Same volume of solids fuel in each bin.

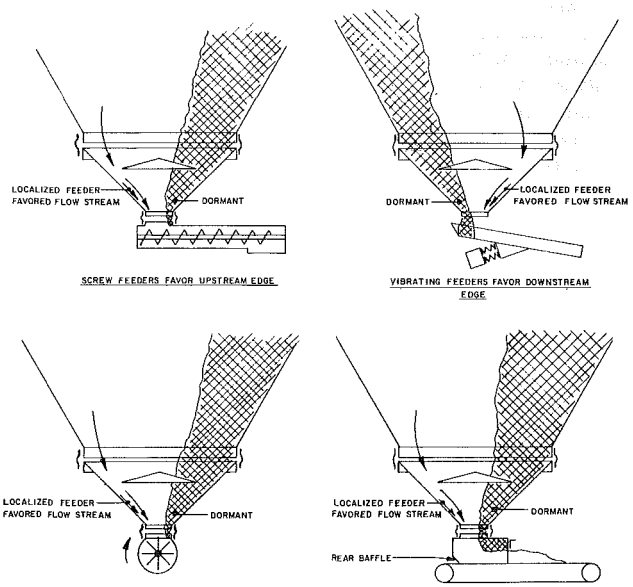

Fig. 5 *Influences of localized feeder flow streams adjacent to bin or bin activators outlet*

been more universally accepted, and will be used in this presentation.

The bin activator has the tremendous asset of withdrawing concentrically, and possessing a relatively high external force input capability to overcome particle fusion or set. Further, maintenance items do not exist inside the unit. These three reasons have caused it to conquer its conceptual competitors. And, by its method of operation, the added advantage of commanding sloughs and dealing with localized favored flow streams caused by feeders can be accomplished (Fig. 4).

If the bin activator discharges into an open railroad car, barge, or truck, its method of operation is far more arbitrary than if the bin activator discharges into some form of feeding device at its outlet. This is particularly true when its inlet diameter is less than the bin's diameter.

Steady, continuous operation of the bin activator is usually satisfactory for open drop discharging (because a feeder is omitted).

When a feeding device is introduced at a bin activator's outlet, the asset of concentric withdrawal (which the activator inherently possesses) can be robbed form the unit's performance. That's because all feeders set up a localized favored flow stream at the bin activator's outlet or at the inlet to the feeding device itself. Screw, vibrating, belt, apron, or other feeding devices all have their own individual feed favored stream characteristic.

If a bin activator in conjunction with a feeder is operated continuously, it will initially attempt to withdraw from the storage bin above concentrically. Further, it will try to pass the withdrawn product uniformly around its top bin stream deflector, baffle, or cone. However, because of the localized favored feeding stream adjacent to the activator's outlet, the premise of concentric withdrawal is discouraged. Eventually, because of this continuous running, dormant coal or lignite layers will actually "back up" from the outlet, around the bin stream deflector, to the full height of the material contained in the storage bin. The result in flow can actually show as a core straight up the bin equal to the inlet diameter of the activator. Or, a small funnel core could occur. In some instances, a bridge can actually occur above the bin activator in

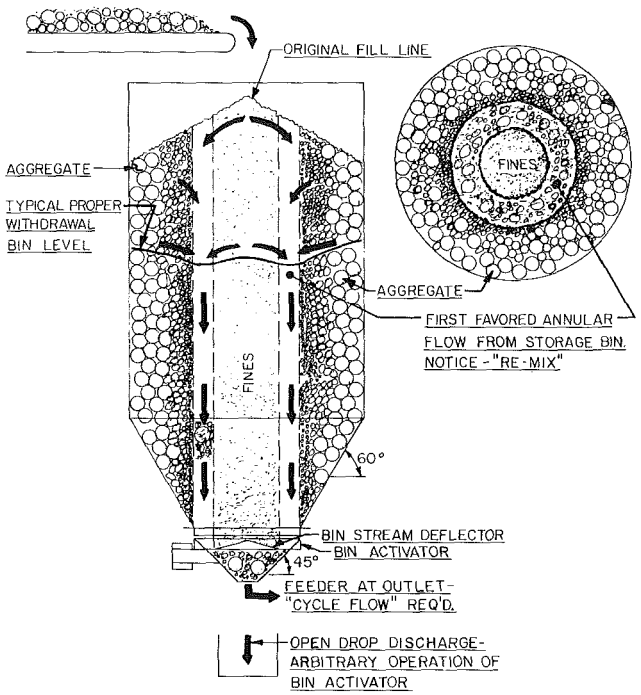

Fig. 6 Cross section of properly withdrawn storage bin with bin activator (Note: inherent classification or segregation upon filling, and remix that occurs by bin activator action)

the storage bin (Fig. 5). It also will cause continual, excessive maintenance to be required by the bin activator.

This violation of concentric withdrawal can be corrected by operating the bin activator on a proper on-off cycle. In this manner, the bin activator "nudges" the natural flow pattern within the storage bin itself; and maintains the desirable condition of concentric withdrawal. It does not change the localized favored feeding stream at the outlet. It simply makes it more tolerable. Cycling is accomplished by either a timer, starve switch, or a combination of both.

It is important to realize that even though a bin activator is cycled, it maintains a continuous steady flow of coal or lignite at its outlet. There is no interruption in flow to the feeder even though the bin activator is being turned on and off.

Each time the discharger comes on, it will induce a slough outside the bin's favored stream to fall in that stream. Because of this phenomena, coupled with the concentric withdrawal for its inlet diameter, essentially a "mass flow" characteristic is accomplished in the storage bin. That is, the top level drops with a uniform level (like water).

Another quality point of the bin activator is its ability to correct the classification or segregation that inherently occurs when the coal or lignite is placed in the storage bin. Whether the bin is fed in the center, or off center, it is virtually impossible for the loading design engineer to prevent classification of the coal or lignite particles upon loading. Larger particles will inherently go to the outboard side and the "fines" will tend to congregate in the center. Because the bin activator has a bin stream deflector (located near its inlet), it acts as a block for the fines located directly above its image. However, it does permit these fines to be supplied to the annular first favored stream of the storage bin above. Thus, this annular favored stream is withdrawing the aggregate from the side walls, and allowing fines from the center portion to re-mix. The result is the material coming from its outlet is essentially the same mesh distribution as it was before being placed in storage (Fig. 6).

Bin activators do not require any special flow inducing surfaces in the bin. However, if the sulphur content of the coal or lignite is excessive (4 percent or more), an 11 ga. SS-304 liner is recommended to thwart corrosion. Also, a 60 deg slope is adequate for the bin's conical section. Further, they increase the bin's first favored vertical stream to an annular flow equal to the activator's inlet diameter. But, they cannot always be arbitrarily operated. Particularly, with feeders at their outlets.

By vibratory excitor design efforts over the years, a high external force output capabilty has been accomplished by relatively low horsepower rating electric motors. And, when these excitors are operated on a "cycled" basis—which they are designed to do—the RMS (root-mean-square) power consumption for the function accomplished (namely, immediate response with full concentric withdrawal) is very low. For example, a 12 ft bin activator can withdraw a typical 50 ft dia silo at 1000 TPH of coal or lignite and have a RMS horsepower consumption as low as 2.0 hp (actual rating of excitor is 5.0 hp). Actually, this low power consumption is the reward for inducing the coal or lignite to flow in accordance with its own natural vertical flow pattern.

The bin activator is "sized" to the diameter or diagonal and vertical wall height of the bin or silo. The TPH discharge rate dictates the size of the outlet. For bins with vertical wall heights that do not exceed twice the bin's diameter, a bin activator whose inlet diameter is half the bin's diameter will totally withdraw the coal or lignite. Bin activators of 12 ft inlet dia are recommended and successfully applied to bins that exceed twice the activator's inlet.

Therefore, when coal or lignite flow characteristics are not clearly defined, or are expected to be subject to changing characteristics, or when fusion of the particles as a result of pressure of its own weight with time in storage is expected, the bin activator with its induced vertical flow characteristic is the recommended alternate choice. And, when it is operated on a cycle, you are not only catering to the natural gravity flow pattern of the bin itself, you are reducing the net overall power consumption to accomplish what heretofore has been called the toughest problem in industry: Namely, the fully reliable withdrawal of a coal or lignite storage bin or bunker on command, with quick response, and full concentric withdrawal. Further, no manual, physical effort or auxiliary flow inducing devices will be required.

II Storage Piles. Outside storage piles of coal or lignite can be reclaimed by various methods of surface reclaim. The alternative is to withdraw the pile through open ground level ports and utilize gravity in that withdrawal. In general, the decision of whether to use a surface reclaimer or a vertical flow withdrawal is simply a matter of economics and other related practical factors. One is the realization that induced vertical flow withdrawal can only approach the coal or lignite's natural angle of repose (assuming flat ground level storage).

Surface reclaimers will not be treated in this presentation.

If the induced vertical flow of the storage pile is the selected method, then the same problems of obtaining response, concentric withdrawal, or simply commanded vertical flow that existed with the storage bins will exist with the pile. Their vertical flow patterns are exactly the same (i.e., storage bins and storage piles, Fig. 7). A device has been developed to answer this need. It is called a storage pile discharger.

Physically, it has some similarity to the bin activator in that it is conical in shape, has an internal pile stream deflector; and a circular inlet reducing concentriaclly to a smaller outlet. However, it has the significant difference of possessing a "drawdown skirt" which projects above the ground. This drawdown skirt exists so that full contact with the storage pile throughout the withdrawal is fully assured. Also, it is generally excited by two electric motors instead of only one. By their mounting arrangement, these two vibratory excitors

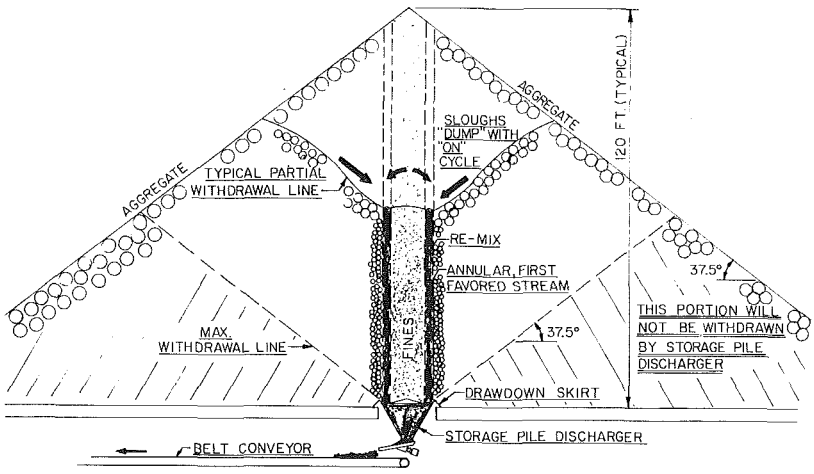

Fig. 7 A typical storage pile discharger, properly operated (cycled) during its withdrawal

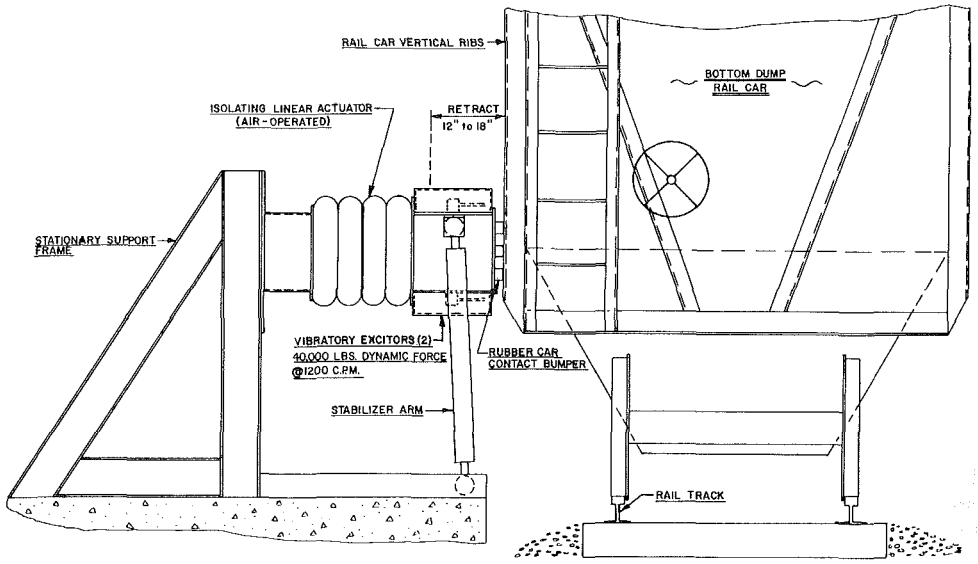

Fig. 8 Engaged trackside rail car discharger for bottom dump cars

provide a stroking action that is more favorable to pile penetration and ultimate drawdown capability.

Again, the same comments that apply to a bin activator in its concentric withdrawal from the storage bin above, when coupled with a feeding device which has a localized favored stream, must be considered. The corrective answer is the same and that is to cycle operate the storage pile discharger. (Storage pile dischargers and their application are fully discussed in ASME Paper 73-MH-11).

Each time the pile discharger is cycled on, a slough from the storage pile above will dump, even from rain soaked or frozen coal or lignite piles. The pile discharger will first draw an annular favored stream from the pile above equal to its inlet diameter. The re-mix of the inherent classification that occurs in pile loading reoccurs. The pile stream deflector located adjacent to the discharger's inlet causes this result. And, the pile discharger will continue to draw from its first favored vertical flow stream and move outboard in ever increasing concentric circles. Eventually, the storage pile discharger will withdraw the storage pile until it approaches the coal or lignite's natural angle of repose. It will not withdraw any further. Usually, this product is left for emergency reclaim by means of vehicular devices. And, the remaining coal or lignite has become more densified, thus retarding the spontaneous combustion characteristic found in non-induced fuel piles.

Flow inducing or wear protecting surfaces are not needed in pile dischargers. However, if excessive sulphur content coal or lignite (4 percent or more) is being withdrawn, an 11 ga. ss-304 liner is recommended to combat corrosion.

The input excitors of a storage pile discharger are of relatively low power consumption compared to their tremendous force output capabilty. And, when they are operated in accordance with the natural, vertical flow pattern of the storage pile above, they are cycled. As a result, the total RMS power consumed to obtain this withdrawal is of a very low value. For example, a 15 ft dia drawdown skirt with 12 ft inlet dia (the largest size standard storage pile discharger) discharging 2000 TPH has two 7.5 hp rated excitors and consumes a total RMS horsepower as low as 3.0 hp! And, the pile can be 150 ft high! Yet, it is fully withdrawn despite weather conditions to the point of approaching the fuel's natural angle of repose.

Here again, a vertical flow inducing device accomplishes what was heretofore a nasty task. The storage pile discharger with its low RMS power consumption by means of the cyclic operation accomplishes what was intended: namely, quick response, concentric withdrawal, and the overcoming of product "set" within the pile itself. And its performance is not markedly altered by changing coal or lignite flow characteristics.

III Rail Car Unloading. Bottom discharging rail cars can be difficult to unload. The inherent packing of the coal or

lignite, or the influence of weather conditions (particularly winter months) while in transit, can cause totally nonvertical flow conditions. When this occurs, some form of external force producing device is needed to induce the solid fuel to flow from the rail car.

In the past, the coal or lignite has been dug out of the car with bucket reclaimers. Or, high noise level, car damaging external vibrating, pounding devices have been utilized.

By advancing the concept of making the entire rail car act like a huge bin activator, a quiet, non-car-damaging, trackside rail car discharger has been developed. And, by its operation, the inherent natural vertical flow pattern of the fuel in the car can be catered. The result being a quickly unloaded, fully withdrawn rail car with an approximate RMS input power of 2.0 hp!

The trackside rail car discharger (Fig. 8) is permanently located alongside the rail track. And, the car to be unloaded is located with its approximate centerline adjacent to the discharger. By pneumatic operation, the discharger moves forward until its rubber lined "face" is pressed against the rail car's side. Then, high input force producing vibratory excitors are energized. Since minimal relative motion exists between the excitor's face and the rail car, it quitely causes the entire car to vibrate, as a complete entity, on its own supporting steel coil isolation springs. If the coal or lignite is removed as fast as it is discharged, a steady run is acceptable. But, if the material is discharged faster than the take away rate, the same "cycle" type operation for bin activators or pile dischargers is recommended. After the car is emptied, the discharger is de-energized and its contact face retracts. The emptied car is moved and replaced with a fully loaded coal car.

Assuming the coal or lignite can be taken away fast enough, 75 ton and 90 ton rail car emptying can be completed in a few minutes. And the quick establishment of vertical flow and complete car withdrawal can be accomplished despite the material being rain soaked or frozen at its top or side layers. Because the rail car is made to vibrate as a huge bin activator, the unloading system approaches acceptable sound levels and has long term, low maintenance characteristic.

3 Nongravity Flow Functions

For non-gravity coal or lignite movement functions, the implementation of kinetic energy is recommended to generate a significant portion of the total energy required to drive the machine performing that function.

To understand the employment of kinetic energy, a brief review of its concept will be made and then the practical expressions of that theory will be presented. Some future possibilities will also be explored.

I The Kinergy Concept. Two types of energy need to be reviewed. Namely, heat energy and kinetic energy. Heat energy can only be derived from the sun. The sun's heat has been stored for years in the form of coal, lignite, oil, wood, and natural gas or other substances known as fuels. And, these fuels must be burned to release their contained heat. Kinetic energy is the energy of motion. A moving boulder, or water flowing down a Penstock are examples. When a rolling boulder strikes another boulder, there is an exchange of energy. However, the exchange does not consume heat energy nor does it produce heat energy other than the frictional loss of rolling and striking. The point is that kinetic energy can take the form of non-heat energy.

There is a classic law of "conservation of energy" which cannot be ignored. This law states that energy cannot be created or destroyed. Further, energy is defined as the ability to do work. It is also defined dimensionally as force-distance (i.e., lbs.-in.). So is work. If work or energy is divided by time, it yields the unit of power.

Because heat energy is derived from the sun, its only source is defined. However, kinetic energy which can be a non-heat energy, can be generated, for instance, by means of resilient spring. Any spring when deflected has a contained inherent force. As this force is relieved, the spring will return to its original position. Therefore, a force is generated by deflecting the spring, and a distance quantity is introduced by relieving that deflection. Thus, a force-distance dimensional value can be accomplished or an energy output can be obtained. This energy output is work. But, it possesses no heat. To prevent confusing this specific kinetic energy generated by a spring

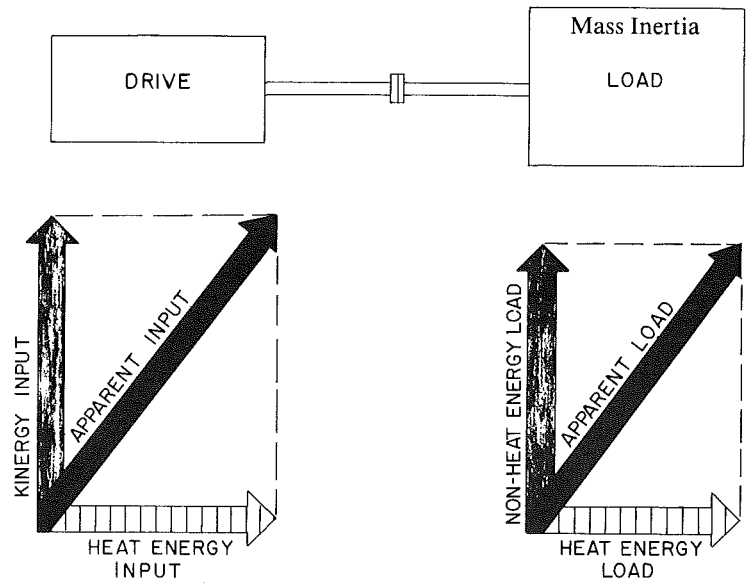

Fig. 9(*a*) Typical drive capabilty in vectoral form with kinergy employed. The total output of the drive (or what the load sees) is the apparent input vector. If kinergy were not employed, the drive would necessarily have to produce the apparent input vector itself.

Fig. 9(*b*) Typical mass movement load vectoral relationship. The total energy to drive this load is equal to the apparent load resulting vector.

Fig. 9 The vectoral relationship of the drive—load fundamentals for a mass inertial load machine

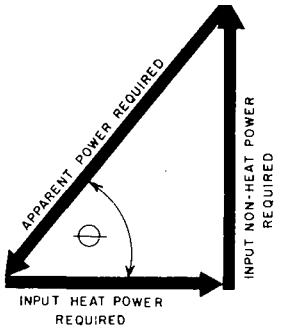

Fig. 10(*a*) Total power required to drive a load. This is a "power triangle." It exactly represents the power input required to drive a machine that *does not* have a kinergy drive component. If a kinergy drive component is provided, it effectively drives the non-heat required vector (Fig. 10(*b*)). Then, all that remains is the input vector shown in Fig. 10(*c*)

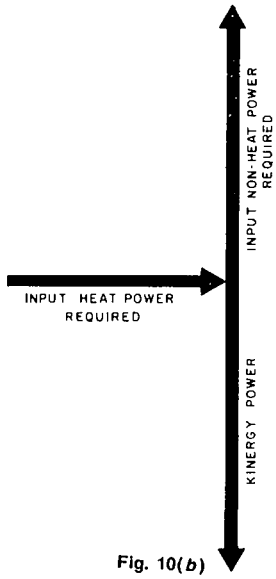

Fig. 10(*b*)

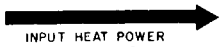

Fig. 10(*c*)

Fig. 10 Vectorally shows how kinergy driven units for mass inertial loads require only the heat input of the load as their external input. Or, heat in = heat out

with other forms of kinetic energy, or heat energy, it has been identified by the term kinergy or, the energy of a spring's motion.

A spring can be made to drive a mass or weight. This is called a mass inertia load. For two increments in the vibratory cycle which amount to one-half the cycle, the spring is driving the mass inertia load. For the remaining one-half cycle, the mass inertia is restoring the spring's spent energy. Therefore, in a kinergy drive system, the spring and the mass inertia load are simply exchanging their energy values. Thus, the law of conservation of energy is satisfied.

From thermodynamics, the most efficient engine or drive known is reported as the Carnot cycle. Simply stated, it means the heat output of a drive is approximately equal to the heat input to the load. And, this heat could be reversible from the load to the drive. This is the highest level of efficiency a drive-load combination could obtain. Obviously, any vibratory load driven by large quantities of heat energy, but having very little heat energy appear on the load side, is by this standard very inefficient. On the other hand, any vibratory load driven that has the necessary heat input of the drive system limited to the heat requirements of the load is very efficient. By utilizing kinergy, which is spring generated, reactive nonheat energy, the latter can occur. Namely, the drive system needs only to provide the heat losses of the load as its input power. Thus, a kinergy drive system is simply made more efficient from the standpoint of heat energy consumed as compared to other drive system arrangements.

Because heat energy is limited to the single source of the sun, it is very precious. The use of this heat energy to drive a non-heat energy requiring load is simply a waste of that heat energy. This waste is what kinergy corrects. Namely, kinergy drives the nonheat requirement of the load, and the heat loss of the load is all that is required from an external power source.

II Drive Versus Load Analysis for Vibratory Machines. A vibratory machine can have its vectoral force equation written as follows by taking advantage of the law of dynamic equilibrium:

$$F_{\text{spring effect}} + F_{\text{input force}} + F_{\text{mass inertia}} + F_{\text{friction}} = 0 \qquad (1)$$

Rearranging the terms, the following can be derived:

$$\text{DRIVE} = \text{LOAD}$$

$$F_{\text{spring effect}} + F_{\text{input force}} = F_{\text{mass inertia}} + F_{\text{friction}} \qquad (2)$$

$$\text{(non-heat energy)} + \text{(heat energy)} = \text{(non-heat energy)} + \text{(heat energy)} \qquad (3)$$

$$\text{Kinergy Generators} + \text{Input Motor} = \text{Total Inertial Load} + \text{Friction Loss} \qquad (4)$$

If $F_{\text{spring effect}}$ equals $F_{\text{mass inertia}}$, then they cancel, and equation (2) becomes:

$$F_{\text{input}} = F_{\text{friction or Heat in}} - \text{Heat out (ideal)}$$

The two terms on the right of equation (2) which are $F_{\text{mass inertia}}$ and F_{friction} represent the load requirements. The two terms on the left, $F_{\text{spring effect}}$ and F_{input} represent the drive. This gives a basis to analyze the vibratory machine as a drive versus load (see Fig. 9). Equation (3) shows the energy relationships. Equation (4) shows the realistic components. If these force terms were multiplied by velocity, it would represent the vectoral equation of power.

This analysis shows the need to drive any vibratory mass inertia load with *two separate* input drive components of work or power as opposed to a *single* input drive means. Or, *provide heat energy to that portion of the load that resists motion, but only supply non-heat energy to that portion of the load that opposes motion.*

III The Power Triangle. If the load is such that it requires a 100 percent continual supply of heat energy, there is nothing the engineer can do but provide it. Examples of this would be boilers, furnaces, and constant speed frictional loads. Kinergy cannot be of any assistance since it has no heat value. The load is a full heat energy quantity and therefore requires a full heat drive or input.

On the other hand, many loads are demands for changing accelerations or movements of a mass. This movement of mass could be accomplished by kinergy!

All mass inertial loads will require some heat input. This is required to overcome their frictional losses which of course take the form of heat. If this heat input load requirement is plotted horizontally, and is represented by a red vector because it is heat consuming; then, the non-heat requirement of the load (which is 90 deg out of phase) is plotted vertically upward. Since it possesses no heat demand, it is represented

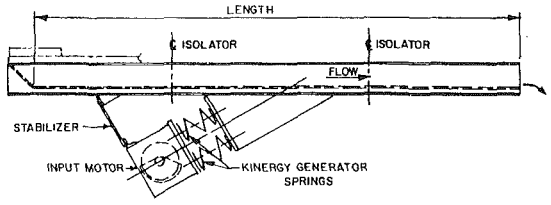

Fig. 11(*a*) Typical kinergy drive component feeder

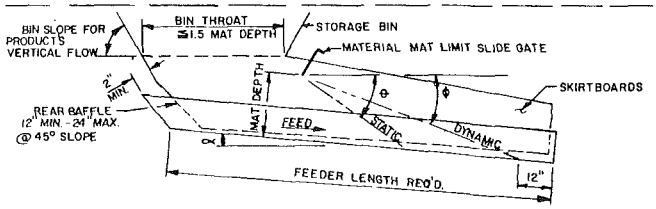

Fig. 11(*b*) Conveying rate—interface layout. Application: best interface arrangement for repeatability in feed rate for constantly changing coal or lignite flow characteristics. Also, recommended for feeders loacted under car dumps or often emptied and refilled bins.

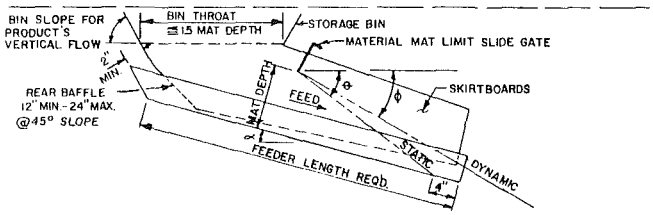

Fig. 11(c) Maximum capacity—interface layout. α = angle of declination—can be horizontal to 15 deg; θ = material static friction angle—this is the angle of repose; ϕ = material dynamic friction angle—this angle is 25 percent less than static friction angle. Application: best interface arrangement for economy as it provides the greatest capacity (TPH) per unit of width. Since this interface layout can be susceptible to capacity changes derived from marked change in material characteristics, it should be used when material characteristics are reasonably constant. For example, a material characteristic change could cause a reduction in capacity without a control.

Fig. 11 Two methods of interfacing a kinergy drive component feeder

by the "cold" color blue. The resultant load vector is called the "apparent power" vector. This is the total energy of power required to drive that load (Fig. 9(*b*)).

An electric motor (equipped with shaft mounted eccentric weights) can be sized to have a horsepower (or kilowatt) capability equal to the heat component required by the mass inertial load. However, the kinergy component of work or power can be provided by a group of springs called kinergy generators or drive springs which are sub-resonant tuned. The resultant vectoral resolution is the apparent energy or power output of the drive which is equal to or greater than the energy the load requires and thus the machine is driven (Fig. 9).

Because free wheeling, rotating eccentric weights are the heat energy input (as opposed to a crankshaft drive arm), the drive system has three significant advantages. One is the fact that it can be subresonant tuned. This gives it high load change capability (such as bin headloads). Secondly, it can be started and stopped frequently, under full load, without damage. That's because the input motor accelerates and de-accelerates independent of the non-heat energy generating springs. Finally, the entire drive system has a completely adjustable output from zero to maximum in infinite steps by simply varying the applied voltage to an a-c squirrel cage heat energy input motor. This important asset derives from the drive system's capability to continually separate and independently provide the heat energy and the non-heat energy requirements of the load at any driven speed (frequency) below its design or rated speed.

By the utilization of kinergy, a separate component of the required power to drive machines with mass inertial loads can be generated at the machine. All that remains is to provide the heat losses of the load and drive system from an external power source (Fig. 10). This mechanical drive system could well be the most efficient known. And, it has full inherent adjustable output from zero to maximum capacity in infinite steps.

IV Specific Kinergy Driven Applications. Today, feeders, sizing screens, dewater and desliming screens, conveyors, fluid bed dryers and coolers, and spiral elevators are all being

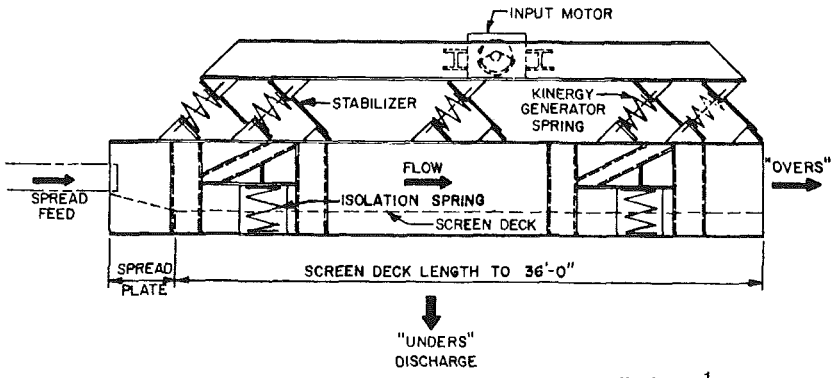

Fig. 12(*a*) Top drive system with full length unders discharge[1]

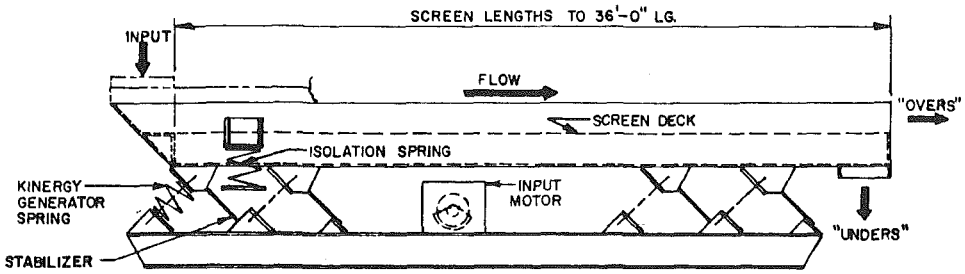

Fig. 12(*b*) Bottom drive system with full length "unders" conveying deck[1]

Fig. 12 Sizing screens driven by kinergy generating drive springs combined with a heat energy providing input motor* (all units inherently adjustable rate from zero to maximum)

[1] All units inherently adjustable rate from zero to maximum

driven with amazingly low input power! Specifically, feeders and sizing screens find application in coal or lignite fired power plants and will be specifically discussed.

1 Kinergy Driven Feeders are vibrating feeders designed to the drive versus load analysis. The drive or motivating power is *not* the input motor only but a *vectoral resolution* of both the input motor and the generating springs.

Vibrating feeders: offer low initial cost, full rate adjustment in infinite steps from zero to maximum output by simple electrical control means, nothing requiring routine maintenance in the fuel flow stream, can be equipped for operation in hazardous environments, quiet running, can withstand headloads, ease of installation, and are easy to adapt to simple or sophisticated control schemes. In short,

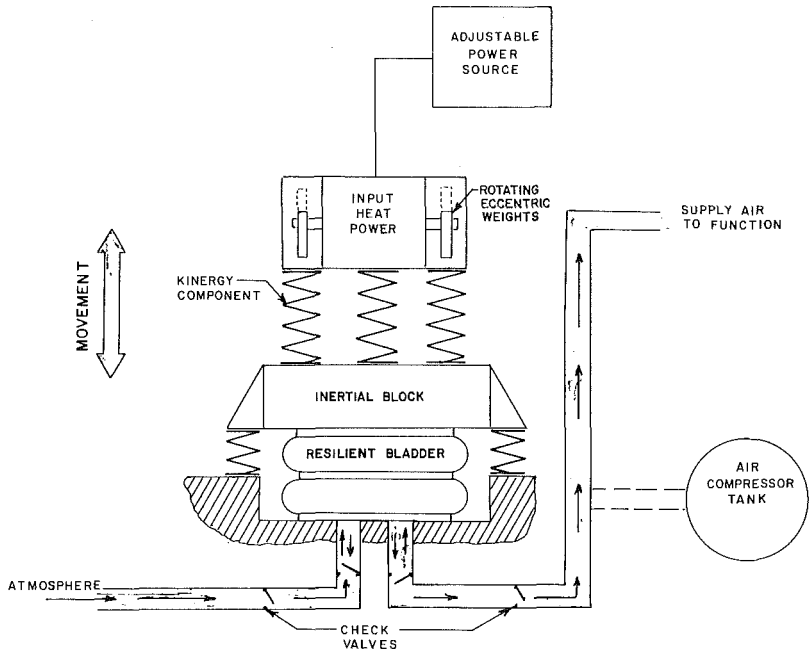

Fig. 13 Schematic of possible kinergy component drive system for the pumping of air

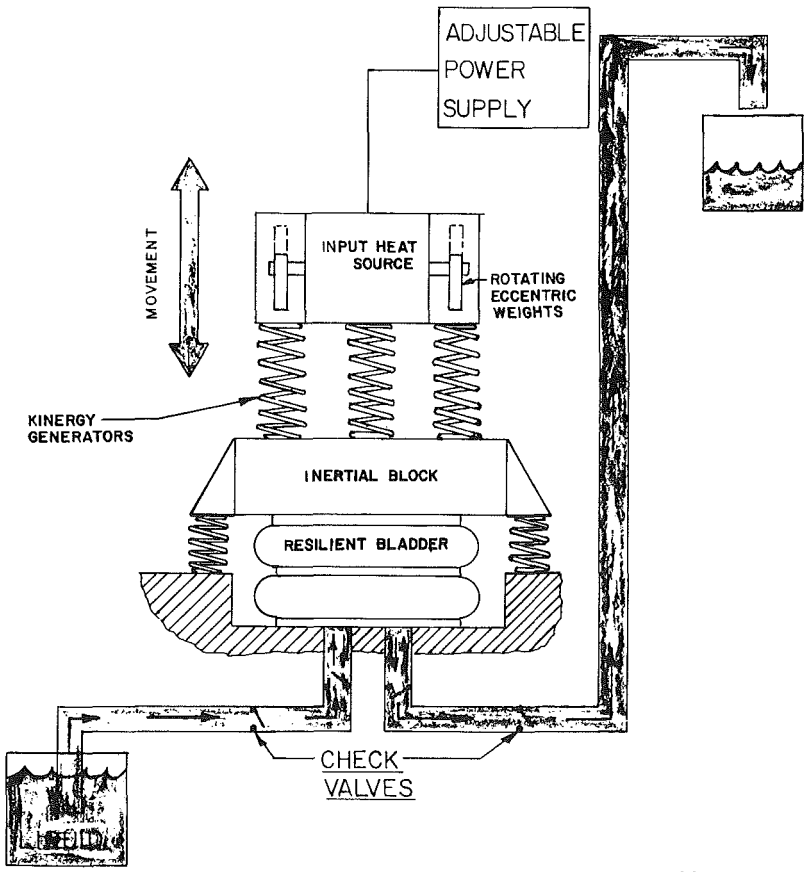

Fig. 14 Schematic diagram of possible kinergy component drive system for pumping liquid

they are probably one of the best bargins of all power plant equipment.

The key to a vibrating feeder's performance is its ability to possess stability in going from no load to full load, and its proper interface with the input coal or lignite source which is usually a bin, hopper, or silo.

(*a*) *Load Stability.* The effect of load being minimal is the responsibility of the feeder designer and manufacturer. The fuel carrying member must be of adequate mass or weight. Steel coil type drive springs are near perfect because they are virtually uneffected by changing ambient temperatures and require the least input power to sustain their non-heat energy generation (hysteresis loss). Thus, their producing constant spring rate contributes stable input power.

The input motor is an a-c squirrel cage type with specific starting, breakdown, and running torque versus speed characteristics. It also has adequate radial force capabilities in the form of spherical roller bearings. Finally, the complete drive system (springs and input motor) must be capable of sub-resonant tuning. The latter means the natural speed or frequency of the steel coil drive component springs is above the input motor's maximum running speed. As load is applied, this natural driving speed or frequency is reduced and approaches—but never equals—the input motor's speed. The result being the springs work more under load. Conversely, as load is removed, the springs work less. Because the input motor's eccentric weights are "free" (not directly connected) of the steel coil drive springs, the drive springs can move up and down independently in natural speed or frequency in answer to load demands.

Therefore, the combination of mass of the coal or lignite carrying member, type of generating spring and its producing spring rate, torque characteristics and mechanical strength of the input motor, and the independent changing of drive springs natural speed or frequency, all blend with sub-resonant tuning capability to give the drive system no load to full load stability with the least amount of input power required.

(*b*) *Interface.* The interface responsibility of the feeder is usually that of the solids fuel handling engineer or system design installation group. When specifically requested, and necessary information provided, the feeder manufacturer can perform this function. The lack of proper interfacing of vibrating feeders has long been a fuel handling system's major problem. A feeder's output (TPH) capacity is a function of its mat depth, mounting angle, width, coal, or lignite characteristics, stroke and frequency, bin throat length, and its respective interface trought length layout. The stroke and frequency, required mat depth, width, and mounting angle are specified by the feeder supplier.

(*i*) *Mat Depth*—The mat depth is the height of material (perpendicular to the feeder trough bottom) as it moves from under the downstream edge of the bin (usually a mat gate). Mat depths of at least 24 to 48 in. are common. 30 in. is a good design mat depth with manual adjustment to 36 or down to 24 in. (to agree with actual field conditions at start-up) for power plants.

(*ii*) *Stroke and Frequency*—The Stroke and frequency of the feeder's drive system is generally specified by the manufacturer. Typically, strokes of 1/4 in. nominal with capability of 3/8 in. by field adjustment at 855 cpm (900 rpm) is the usual design practice.

(*iii*) *Width*—In general, a feeder's capacity is directly proportional to its width.

(*iv*) *Mounting Angle*—The mounting angle can be horizontal to declined 15 deg. For continual bin emptying and refilling applications (such as track dump hoppers), the maximum recommended declination is 10 deg. For applications where the bin is continually with headload (such as crusher or reclaim feeders), the maximum declination recommended is 15 deg. The ability to obtain smooth zero to maximum output range control is independent of the angle of declination to 15 deg. However, more trough "over end" surge dumping could be experienced at more steep declines upon initial filling unless conveying rate layout with excess length is employed. Of course, the advantage of declining a feeder is more capacity per unit of width.

(*v*) *Coal or Lignite Characteristics*—Changes in flow property characteristics will effect a maximum rate interface layout much more then they will a conveying rate interface layout (Fig. 11). This is the primary reason conveying rate interface layouts are favored. If the static and dynamic friction angle of the material decrease because of size distribution or moisture content changes, the output of the feeder will remain essentially the same with conveying rate layout interfacing. However, it would effect a maximum rate layout interfaced feeder because the dynamic friction angle may no longer clear the trough end.

(*vi*) *Bin Throat*—The bin throat length is the responsibility of the interface designer. For mat depths of 24 in. or more, the bin throat should not exceed 1.5 the mat depth. Nor, should it be too short and require the vertical velocity of coal or lignite through the bin throat cross section area to exceed 125 fpm. Making the bin throat too long introduces vertical flow dormancy in the aft end of the feeder. (That's because the material is making a full turn – see Fig. 5). The latter robs a feeder of its stroke action capability (appears to excessively dampen under load).

(*vii*) *Interface Trough Length Layout*—The interface can be of the "maximum rate" or "conveying rate" type. Maximum rate provides the most output (TPH) per unit width and per degree decline. The feeder's trough length is dictated by the static friction angle (angle of repose) intersecting the trough bottom at a point no more than 4 in. from the discharge lip. But the TPH output can be effected by unanticipated but changing coal or lignite flow characteristics. This is a proper interface layout when constant flow characteristics are expected and economy is a strong dictating factor (See Fig. 11).

By using the conveying rate interface layout, the feeder's output will remain essentially consant even though the coal or lignite flow properties are changing. The feeder's trough length is long enough to have the dynamic friction angle (25 percent less than static friction angle) intersect the trough bottom with at least 12 in. of additional length remaining.

For either interface, it is imperative that the static friction angle intersect the trough. This is basic to stopping flow when the feeder is de-energized.

A mat depth gate that is manually adjustable is usually provided to allow start up adjustment to exact field conditions of static and dynamic friction angles.

In terms of capacity (TPH), a maximum rate interfaced feeder will feed 20 to 30 percent more solid fuel than will the same feeder with the conveying rate layout interface with all other application variables being the same.

Also, it should be understood that proper interfacing is applicable to any vibrating feeder. This specific interfacing is not only recommended for feeders that require low input power values but any vibrating feeder regardless of the inner power it consumes.

(*c*) *Input Power.* Observing the feeder design parameters of load stability, and having proper interface layout in installation, some noticeable reductions in input power requirements can be realized. For example, 400 TPH of fuel can be fed by consuming less than a kilowatt. 800 TPH of fuel can be fed with about 1 kW consumed. And, 2000 TPH of fuel is fed with a consumption of slightly more than 2 kW!

All of these applications have full zero to maximum controlled rate adjustment, declined 15 deg or less, reasonable

excess service factor (extra capacity), and low maintenance attention requirements.

2 *Kinergy Driven Screens* are vibrating screens designed to the drive versus load analysis. The input motor provides the heat energy losses and the kinergy generating drive springs provided the non-heat energy mass inertial load requirements.

The load stability of the screen is accomplished in exactly the same manner as described above for a vibrating feeder. The screen's input power requirement is very little. And, like the feeder, it is inherently adjustable rate (from zero to maximum) by electrical control means. (This allows pulsing.) These screens can be used for desliming and dewatering coal or lignite but power plant use is primarily "sizing" and this will be reviewed.

The drive system can be located above the screen deck for full length unders discharge or below the screen with full length unders conveying trough. Either unit can be built to 12 ft widths and 36 ft lengths as standard. They can be applied horizontal or declined (usually no more than 15 deg).

(*a*) *Crusher Screen Applications.* If 1200 TPH of coal or lignite is to be supplied to a crusher, for crushing to minus 1 in. and one-third of the supply (400 TPH) is less than 1 in., it is very practical to utilize a sizing screen to remove the minus 1 in. before the crushing operation. This means only 800 TPH requires crushing. Not only is the crusher sized smaller (800 TPH versus 1200 TPH), but the initial cost, operating cost (power consumed and wear of parts), and maintenance costs are lowered.

And, by taking advantage of the inherent zero to maximum rate control by electrical means, the screen could be made to automatically follow the crusher load. For example, if 1200 TPH of plus 1 in. coal or lignite was temporarily being screened in this example application, the crusher would have its drive motor become overloaded. This added burden to the crusher motor could be sensed and an electrical control signal sent back to the sizing screen to have it reduce its screening rate. When the burden was removed, the screen would speed up. In short, temporary crusher overloads could be automatically relieved.

(*b*) *Rotary Breaker Applications.* The same application as described for coal or lignite crushers is applicable to rotary breakers.

(*c*) *Scalping Screen Applications.* Kinergy driven screens can be applied to scalping functions to remove tramp material from the coal or lignite.

(*d*) *Input Power.* Maintaining the no load to full load stability as described above for feeders, coal, or lignite screening can be accomplished by minimal input power consumption. 4 ft wide by 12 ft long screens operated on the horizontal consume less than 1 kW. 8 ft by 16 ft screens, horizontally mounted, require about 2 kW! A 10 ft wide by 20 ft screen requires slightly more than 3.0 kW of input power!

All units have inherent zero to maximum controlled rate adjustment, electrical pulsing, horizontal to 15 deg declines in mounting, reasonable excess "service factor" (extra capacity), and low maintenance requirements.

V The Future of Kinergy. While it is recognized that the kinergy concept as derived from "drive versus load" analysis is taking a "new-in depth" look at existing natural frequency (resonant) principles, it does reveal more accurate design engineering approaches to currently applied vibrating equipment. And, this line of analytical logic (heat versus non-heat mechanical energy) does provide some added interesting and provocative progressive thinking to areas other than bulk solid movement functions. The realization of our wordly heat energy supply situation has caused it to be advanced with

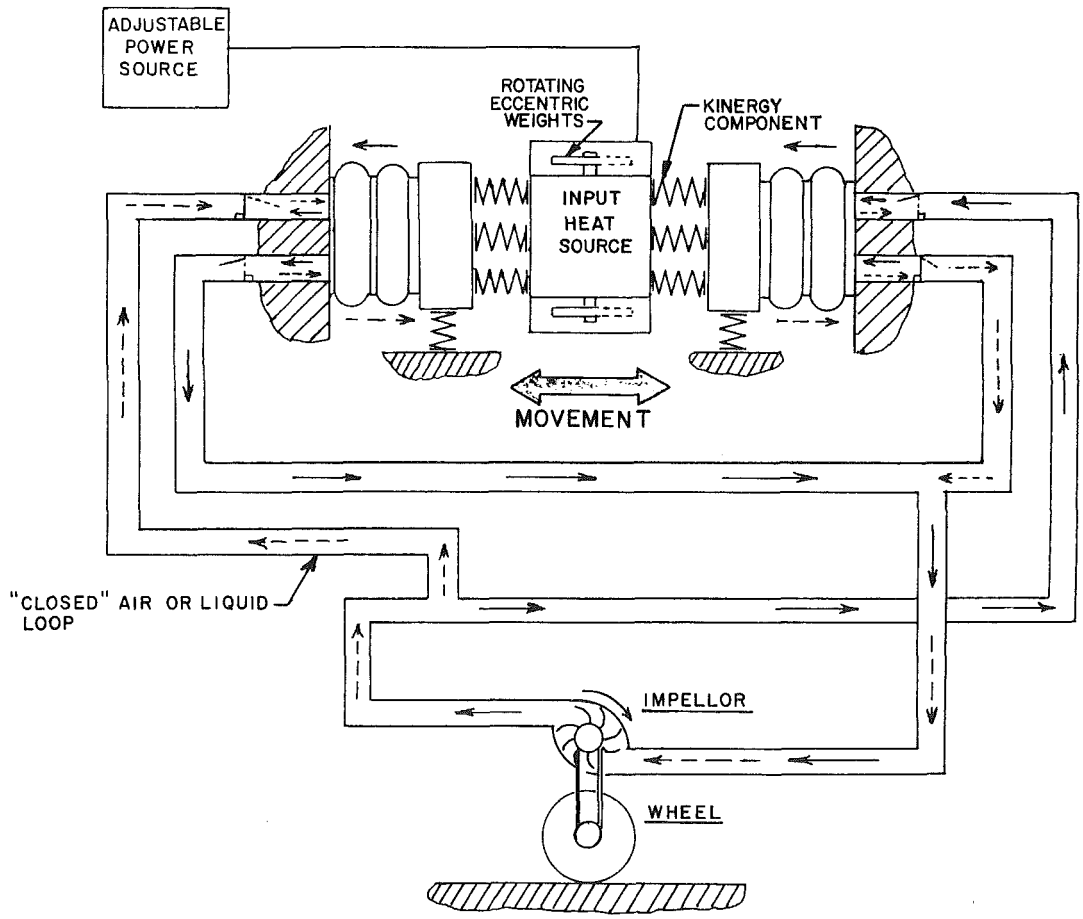

Fig. 15 Schematic of a possible kinergy component drive system for vehicles or other mass movement loads

more deliberation. Exploits are now being pursued outside the field of routine vibrating equipment.

For example, if a relatively low input horsepower electric motor is combined with kinergy generating steel coil drive springs (or any other spring system) and this in turn drove a resilient bladder or bag, through an inertia block; and if a piping system were so constructed to have inlet and outlet check valves (as is done with positive displacement piston pumps), it would be possible to pump air. In other words, it accomplishes the same function as a fan. Since the bulk of the power is utilized to move the air as a mass or weight, it could be provided by the kinergy component which is of course supplied by the spring system as a nonheat quantity. This means that fans that are moving a given amount of air against a given pressure through a given cross-sectional area duct and presently consuming, say, 100 hp input, could conceivable be moved by a kinergy drive component, combined vectorally with an input heat energy motor which only consumed, say, 25 hp from an external power source! (Fig. 13).

If, in Fig. 13, the output goes directly into a tank, the system could be operated as an air compressor, also with possible input power savings!

Further, if the above system were to have the air replaced by a liquid, then it becomes a liquid pump! Again, for the pumping of liquids which are now requiring 200 hp, it is possible that this mass movement (of the liquid) could be accomplished by an input power of say 40 hp with the help of kinergy! (Fig. 14).

Finally, if you will permit your mind to wander deep into the engineering dreamland of the future, it is believed possible to modify the same illustrations listed above to include an impellor in either a closed air or liquid circuit. This impellor would be driven by the movement of either the air or liquid. And, the impellor would be attached to a shaft which in turn drives a pair of wheels. With some definite, strong imagination, you could be looking at the drive system for vehicles of the future! (Fig. 15).

Therefore, the concept of applying the kinergy generating non-heat component along with the heat energy component to obtain a vectorally resolved apparent power output to drive "other" machines that have mass inertial loads could possibly be in our future. Significantly, these kinergy drives are all of the free mass type, which allows them to possess an inherent zero to maximum full range adjustable output. And, it can be accomplished by simple means.

Finally, the true kinergy drive concept is relatively little-known and newly practiced in the mechanical vibrations engineering field. However, its exact same principles have been utilized by electrical engineers for almost 100 years. It is identical to what has been done with electrical power distribution systems with so-called "true power," "reactive power," and "apparent power." Electrical engineers call it power factor correction.

4 Conclusion

For fuel bunkers, hoppers, silos, and storage bins, either the static geometric design or the induced vertical flow by means of bin activators designed and operated in accordance with the bin's natural flow principles should be employed.

For coal or lignite storage piles, the choice is surface reclaiming or induced vertical flow. Storage pile dischargers accomplish the latter.

For coal or lignite feeders, preparation screens, drain and rinse screens, or sizing screens, kinergy driven units should be utilized. Feeders should be properly interfaced and screens used to reduce crusher burden.

Following these recommendations, the total input power consumed by the coal or lignite handling portion of the power plant can be significantly reduced. Not only financial savings from power reduction is realized, but the cost of wiring and electrical controls is also reduced.

Further, as conscientious professional engineers, we are taking positive steps to deal with the inevitable. That is, the approaching, realistic energy crisis. And, we are commencing to adhere to the manifest engineering law of the near future: namely, accomplishing the same functions as we were before, but with less input power requirements.

References

1 Reynolds and Carter, "Design of Bunkers for Difficult Flowing Fuels," *Combustion*, 1962.

2 Brown and Hohmann, "BCR Easy Flow Hoppers," *Power Engineering*, 1962.

3 Ketchum, M. S., *Walls, Bins, and Grain Elevators*, McGraw-Hill, New York, 1919.

4 Jenicke, A. W., "Storage and Flow of Solids," Bulletin, University of Utah, 1964.

5 Johanson, J. R. and Colijn, H., "New Design Criteria for Hoppers and Bins," *Iron and Steel Engineering*, 1964.

6 Dumbaugh, G. D., "Concepts of Vibratory Hoppers," ASME Paper No. 65-MH-11, 1965.

7 Oszter, Z. F., "Comments on Specific Feeder Applications," *The Canadian Mining and Metallurgical Bulletin*, 1966.

8 Dumbaugh, G. D., "The Application of Storage Pile Dischargers," ASME Paper No. 73-MH-11, 1973.

9 Sadler, J. E., "More Research Needed in Coal Silo Technology," *Coal Mining and Processing*, May 1976.

10 Dumbaugh and Wilson, U.S. Patent Application 946,576, "Hopper Car Discharge Apparatus."

11 Halliday and Resnick, *Fundamentals of Physics*, John Wiley, 1974.

12 Dumbaugh, G. D., "Mechanical Work Generating Means," U.S. Patent No. 4,052,849, 1977.

ERRATA

Correction to the address and affiliation of "Application of Lifting Line Theory to Streamsurface Theory in Subsonic Flow," by P. T. Chang, published in the July 1982 issue of ASME JOURNAL OF ENGINEERING FOR POWER, pp. 642–649:

P. T. Chang
Research Associate,
Institute of Engineering Thermophysics,
Chinese Academy of Sciences,
Beijing 100080,
People's Republic of China